The University Of Sheffield.

Ultrasonic Measurements of the Strip Thickness, Lubricant Film Thickness, Roll Deflection and Roll Stress in the Roll Bite in the Cold Rolling of Steel

By:

Andrew Kevin Hunter

A thesis submitted in partial fulfilment of the requirements for the degree of Doctor of Philosophy

The University of Sheffield
Department of Mechanical Engineering

February 2018

Summary

In cold rolling the interface between the roll and strip, known as the roll bite, is key to the finish and geometry of rolled products. This interface is complex and operates in the mixed regime with part asperity contact and part fluid film. The factors which affect this are of interest to the cold rolling community. The inaccessibility of the interface has made direct measurement of its condition difficult. In this thesis ultrasonic approaches have been developed to measure the state of the roll bite, in-situ and in real time.

The thesis starts by introducing the background theory underpinning modern cold rolling. The theory behind the proposed ultrasonic measurements is developed. It is proposed that the proportion of longitudinal and shear waves reflected by the asperity and lubricant film components of the mixed mode interface are dependent on their respective stiffnesses. From these the lubricant layer thickness can be calculated. It is also shown how time-of-flight measurements can be used to measure strip thickness, roll stress, roll deflection and roll material properties.

Ultrasonic sensor systems were incorporated into pilot and semi-industrial cold-rolling mills. Measurements were taken as steel was rolled under a range of lubrication conditions, with rolling velocities from 25 m/min to 1200 m/min and elongations from 5% to 50%. Stiffness and lubricant film thickness measurements were demonstrated for films from 0.3 µm to ~6 µm. Roll bite contact lengths of 9.13mm to 15.34mm were recorded for elongations from 9.7% to 40%. For these same elongations average radial roll stresses of 180 MPa to 340 MPa and roll deflections of 30 µm to 55 µm at the roll bite centre were measured. Time-of-flight measurements yielded thickness profiles of strip reduced from 2.8mm to 2.154mm.

Validation was provided by multiple numerical models which showed good agreement with the ultrasonic results.

Acknowledgments

This thesis is just a small window into a process that has involved many late nights, early starts, successes, failures, moments of inspiration and months of head-scratching. Too many people to mention have helped me throughout this. In particular, it would be remiss of me to not give credit and my thanks to the following:

Firstly I'd like to thank my supervisor Rob Dwyer-Joyce for all his support and advice. It has been a genuine pleasure working under your guidance and I look forward to continuing working with you in the future. Thanks to everyone at the Leonardo Centre for Tribology who has assisted me directly and indirectly, especially Robin Mills and Dave Butcher for his technical wizardry.

I gratefully acknowledge the funding received from the European program RFCS (Research Fund for Coal and Steel) which enabled this research. Thanks to the whole Rollgap project team, it was a pleasure working with you. Specific thanks must go to Nicolas Legrand and Nathalie Labbe at Arcelor Mittal for all your support.

Thanks to Phil Harper. Phil I would not have had this opportunity were it not for you and I'm lucky to consider you both a mentor and a friend. Also thanks to the rest of the team at Tribosonics Ltd. and particularly Tapiwa Mutasa for his perspective on many problems.

Thanks to Yves Carretta at the University of Liège for his advice and computational modelling work.

Thanks to all my friends with a special mention to Henry Brunskill, I've never met anyone with such boundless infectious energy, and to Oscar for his endless humour.

My love and thanks to all my family for your support throughout the years, my Grandma, my brothers, James and Michael, and my Dad. I finally finished it!

And last, but not least, my wife Keeley. Thank you for the endless support, patience, love and care you have given me. I love you.

Table of Contents

Nomenclature

The following is a list of the characters and symbols used in this thesis. To maintain consistency with naming conventions in some cases the same character has been used to denote more than one parameter, although never within the same chapter. To avoid confusion, the chapter where each parameter has been used has been listed.

Parameter	***Units***	***Chapter***	***Description***
A	-	2	Proportion of asperity contact
A	-	3	Wave amplitude
A	-	3	Apparent area of contact
A_R	-	3	Real area of contact
A_{Ref}	-	7	Reference wave amplitude
A_0	-	3	Initial wave amplitude
a	m	2	Half contact width
a_1	m	2	Half contact width of the stick zone
α	Nepers/m	3, 8	Attenuation coefficient
α	-	4	Acoustoelastic constant
α	1/MPa	9	Pressure-viscosity coefficient
B	GPa	3	Bulk modulus
B_1, B_2, B_3	-	8	First, second and third reflection numbers
b	-	2	Simplifying factor defined in Equation 2.66
β	rad	2	Angular position of element
C	-	2	Constant of integration
C	pF/m	6	Cable capacitance
c	m	2	Half width of roll support bearing
c	m/s	3	Speed of sound
c_L, c_S, c_R	m/s	3	Longitudinal, shear and Rayleigh wave speed of sound
c_1, c_2	m/s	3	Speed of sound in the materials either side of an interface
c_{Light}	m/s	6	Speed of light in a vacuum (=2.9979x10^{8}m/s).
D	m	2	Roll diameter
D	m	5	Diameter of the piezoelectric element
d_0	m	4	Initial length
d	-	2	Draft or reduction
d	C/N	5	Piezoelectric charge constant
d_f	m	5	Diameter of the sensing spot
Δ	m	2	Roll deflection
Δf	Hz	8	Fast Fourier transform frequency step
$\Delta t_\rho, \Delta t_\delta, \Delta t_E$	s	4	Change in time of flight due to density, deflection and elasticity
δ	m	4	Deflection
E	Pa	2, 3	Young's modulus
E_R, E_S	Pa	2	Young's modulus of the roll and strip
$el\%$	%	2	Elongation percentage
ξ	-	2	Stick-slip ratio
ε_0	F/m	5	Permittivity of free space (= 8.85x10^{-12} F/m)
$\bar{\varepsilon}_{pl}$	-	11	Equivalent plastic strain
ε_r	-	5	Relative permittivity
ε_x, ε_y, ε_z	-	4	Strain in x, y, z directions
F	N	2	Roll Normal Force

F_q	N	2	Contribution to horizontal force made by the radial pressure
F_R	N	2	Radial force applied by the roll
F_τ	N	2	Contribution to horizontal force made by a shear stress
F_z	m	5	Transducer focal zone
f	N/m	2	Specific rolling force
f	Hz	3	Wave frequency
f_m	Hz	3	Resonant frequency of liquid layer
f_s	Hz	8	Sampling frequency
G	Pa	2, 3	Shear modulus
g	Vm/N	5	Piezoelectric voltage constant
g_x, g_z	m^2/s	4	Gradient of speed of sound array
H	-	2	Simplifying factor defined in Equation 2.76
h	m	2	Strip thickness
h	m	3	Fluid layer thickness
h_0, h_1	m	2	Entry and exit strip thickness
h_s	m	9	Inlet film thickness
K	N/m^2	3	Liquid layer stiffness per unit area
K_L, K_S	N/m^2	3	Longitudinal and shear stiffness of interface
K_σ, K_τ	N/m^2	3	Normal and shear stiffness of interface
k	N/m	3	Spring constant
k	Hz·s/m	3	Wave number
k	-	5	Electromechanical coupling factor
k	-	6	Dielectric constant of cable insulator
k	Pa	11	Yield shear stress
L	m	2	Roll bite contact length
L	µH/m	6	Cable inductance
L_0, L_1	m	2	Strip lengths before and after rolling
L_y	m	2	Centre to centre distance between the roll bearings
l	GPa	4	Third order elastic constant
l	m	6	Cable length
l	s	8	Pulse length
λ	m	3	Wavelength
λ	GPa	4	Second order elastic constant
m	kg	3	Mass
m	-	3	Mode of resonance
m	GPa	4	Third order elastic constant
μ	-	2	Friction coefficient
μ	-	4	Second order elastic constant
μ_0	H/m	6	Permeability of free space (=4πx10^{-7} H/m)
μ_C, μ_T	-	11	Coulomb and Tresca friction coefficients
μ_m	-	2	Minimum coefficient of friction
N	Hz·m	5	Frequency constant
N	m	5	Nearfield distance
N	-	8	Number of samples
N	-	12	Number of averages
n	-	3	Ratio of acoustic impedances as defined in Equation 3.79
n	GPa	4	Third order elastic constant
n	-	8	Number of pulse cycles
η	mPa·s	9	Viscosity

η_0	mPa·s	9	Viscosity at ambient pressure
η_g	mPa·s	11	Viscosity at the glass transition temperature
ω	Hz	3	Angular frequency
ω_0	-	3	Simplification as defined in Equation 3.14
P_I, P_R, P_T	Pa	3	Incident, reflected and transmitted wave pressures
P_m	Pa	3	Wave pressure
P_R	N	2	Radial roll force
p	Pa	2	Normal pressure
p_R	Pa	2	Radial pressure applied by the roll
p_{Max}	Pa	2	Maximum pressure
p_{Mean}	Pa	2	Mean interface normal pressure
φ_0	rad	3	Phase angle
Q	C	5	Piezoelectric charge
Q_m	-	5	Mechanical quality factor
q	Pa	2	Interface tangential stress
R	-	3	Reflection coefficient
R	m	2	Roll radius
R	m	5	Distance from the transducer
R'	m	2	Deformed roll radius
R_p	Hz	8	Pulse repetition rate
R_a, R_q,	µm	3	Roughness parameters
r_{RMS}	µm	3	Root mean square roughness
ρ	kg/m^3	3	Density
S_f	%	4	Forward slip
s	-	2	Symbolic variable giving the position from the centre of the contact
s	m^2/N	5	Elastic compliance
σ	Pa	2	Compressive stress
σ	-	12	Standard deviation
σ_1, σ_2	Pa	2	Tension at entry and exit to roll bite
σ_{SE}	-	12	Standard error
$\sigma_{1,xz}$	Pa	2	Principal stress 1
$\sigma_{2,xz}$	Pa	2	Principal stress 2
σ_{max}	Pa	2	Maximum stress
σ_{min}	Pa	2	Minimum roll pressure
σ_{yield}	Pa	2	Tensile yield stress
T	°C	6	Temperature
T	-	3	Transmission coefficient
T_0	s	3	Time period of wave
T_g	°C	11	Glass transition temperature
$tan(\delta)$	-	5	Dielectric loss factor
t_p	s	8	Excitation pulse width
τ_l	Pa	2	Interface shear stress
τ_a, τ_l	Pa	2	Shear stress, asperity and lubricant components
θ	rad	2	Angle dependant on position in roll bite
θ_1, θ_2	rad	3	Angle of incidence and refraction
θ_n	rad	2	Angular position of the neutral point
U	J	4	Strain energy
u	m	3	Spring extension
V	m^3	3	Lubricant volume
v_b, v_f	m/s	2	Roll bite backward and forward velocities

v_I, v_R, v_T	m/s	3	Incident, reflected and transmitted wave particles
v_{in}, v_{out}	m/s	2	Entry and exit strip velocities
v_r, v_s	m/s	2	Roll and strip velocities
v	-	2	Poisson's ratio
v_R, v_S	-	2	Poisson's ratio of the roll and strip
v_{Factor}	-	6	Velocity as a percentage of the speed of light in a vacuum
W	m	2	Strip width
w	-	2	Simplifying factor defined in Equation 2.67
x	m	2	Distance along roll bite
Z_{Cable}	Ω	6	Cable electrical impedance
z	m	2	Vertical distance from centre of strip
z, z_1, z_2	MNs/m^3	3	Acoustic impedances

Abbreviations

The following is a list of abbreviated terms used within this thesis:

ADC	Analogue to Digital Convertor
COTS	Commercial Off The Shelf
DA	Direct Application
DC	Direct Current
EHD/EHL	ElastoHydrodynamic Lubrication
EM	ElectroMagnetic
EMAT	ElectroMagnetic Acoustic Transducers
EMI	ElectroMagnetic Interference
FFT	Fast Fourier Transform
LSB	Least Significant Bit
MPH	Micro-Plasto-Hydrodynamic Lubrication
mpm	Metres Per Minute
Mtpa	Million Tons Per Annum
NDT	Non-Destructive Testing
PCI	Peripheral Component Interconnect
PHD	PlastoHydrodynamic Lubrication
Pk to Pk	Peak to Peak Amplitude
PRF/PRR	Pulse Repetition Rate/Pulse Repetition Frequency
PZT	Lead Zirconate Titanate
RE	Recirculated (lubricant)
RPM	Revolutions Per Minute
SNR	Signal to Noise Ratio
SoS	Speed Of Sound
TOEC	Third Order Elastic Constant
ToF	Time of Flight
UPR	Ultrasonic Pulser Reciever

1 Introduction

This thesis is concerned with ultrasonic measurements in cold metal rolling. The work presented builds on a range of previous research and aims to extend this in a number of areas. To give the work presented herein any meaning it is first important to understand the context in which the work is undertaken and foundations on which it builds. The following chapter aims to populate this back-story by giving an introduction to the topic of rolling, the historical context of the research put forward, the nature of the problem being researched and an overview of the aims, benefits and layout of the thesis.

1.1 The Development of Rolling

It is impossible to accurately identify a single inventor of the rolling mill. Like so many inventions the first rolling mill designs for which records exist were sketched by Leonardo da Vinci. These can be found in the *Codex Atlanticus* and *Paris Manuscript I*. The sketch in the Paris manuscript, as shown in Figure 1.1, is dated between 1497 and 1505. This shows sheet rolling with backup rolls. There is no evidence that these designs were ever built and it is believed that small hand driven rolls were used prior to this to flatten gold and silver for the manufacture of jewellery (Eppelsheimer, 1938).

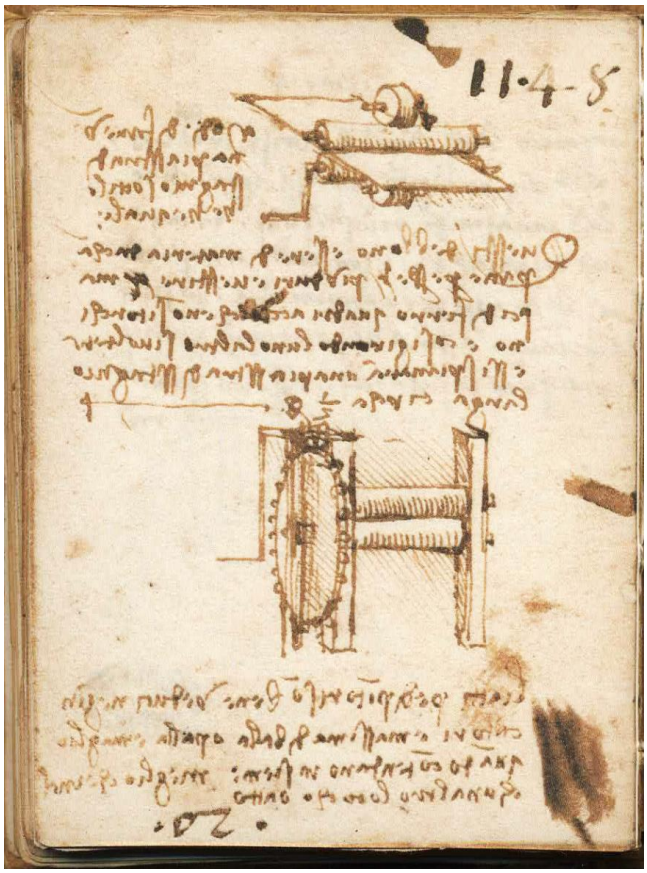

Figure 1.1: Rolling Mill designs sketch by Leonardo da Vinci, showing Sheet Rolling with Backup Rolls (Leonardo da Vinci, 1488–1505).

Metal rolling did not begin to gain particular significance until the end of the 16th century when a slitting mill was setup in Dartford, Kent by Godefroi de Bochs under a patent granted in 1588 to Bevis Bulmer (Tyson, 1996). The mill was powered by waterwheel and cut iron, which at the time was only available in plate form, for nail production (How, 2015). Similar mills in Germany

and Belgium were being developed around the same time. These were designed for use with softer metals, predominantly lead being produced for roofing, flashing and guttering (Roberts W. L., 1978).

The rolling of iron probably originated in Great Britain around the middle of the 17th century and it is known that in 1665 a rolling mill was in operation in the Parish of Bitton, near Bristol, that was used to roll iron into thin flats (Mackintosh-Hemphill, 1953). By 1682 water-driven rolling mills for ferrous metals were in operation at Swalwell and Winlaton, near Newcastle.

Over the next century rolling mill design gradually progressed with the introduction of various grooved rolls, rolling tables and reversing systems until in 1783 when William Playfield submitted a patent for a two-high single stand rolling mill that had a similar form to modern rolling mills, as shown in Figure 1.2 (Mackintosh-Hemphill, 1953).

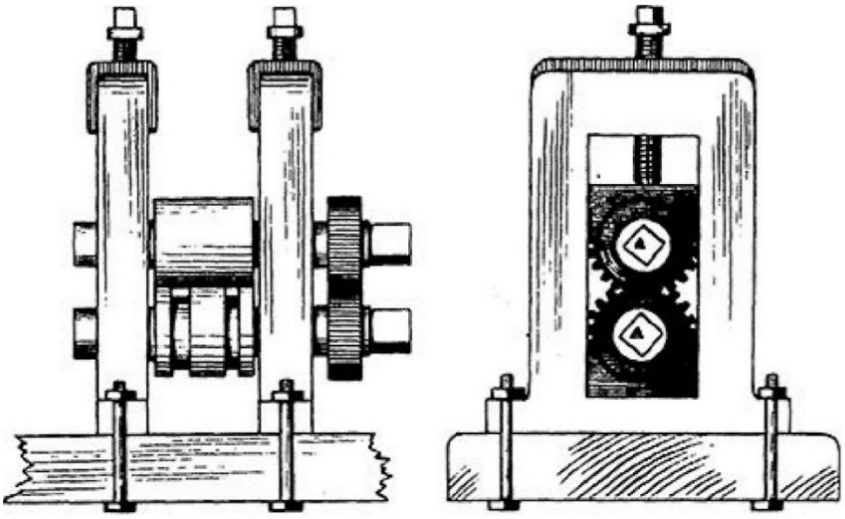

Figure 1.2: Two-high single stand mill design from William Playfield's 1783 patent (Roberts W. L., 1978).

In 1779, the Royal Navy's victualling commissioners approached noted ironmaster Henry Cort, offering him a contract to produce iron hoops for their barrels. Apart from supplying new hoops, the contract obliged Cort to convert old hoops into new at the rate of two tons old, to one ton new. Cort built a rolling mill at Fontley and began experimenting with grooved rollers instead of hammering to make the new hoops. In 1783 Cort patented this process which promised a possible eight-fold increase in the capacity of an average charcoal forge. Figure 1.3 shows a sketch of how such an ironworks would have looked, including a grooved rolling mill. The processes patented by Cort are credited with revolutionising iron production in Britain, paving the way for the cheap railway lines and the wire used in electric telegraphs which spurred on the industrial revolution (Eley, 2012).

In the 1780's the power source for industrial machinery began shifting from water power to steam engines. It is known that around this time John Wilkinson employed a Boulton and Watt steam engine to power, amongst other machinery, a rolling and slitting mill at his Bradley Works (Davis, 1987).

Successive stands (sets of rollers) were introduced by James Cockshutt and Richard Crawshay in a four-high tandem mill near Sheffield in around 1790, the top and bottom rolls of which were driven by separate weighted waterwheels that also acted as flywheels (Roberts W. L., 1978).

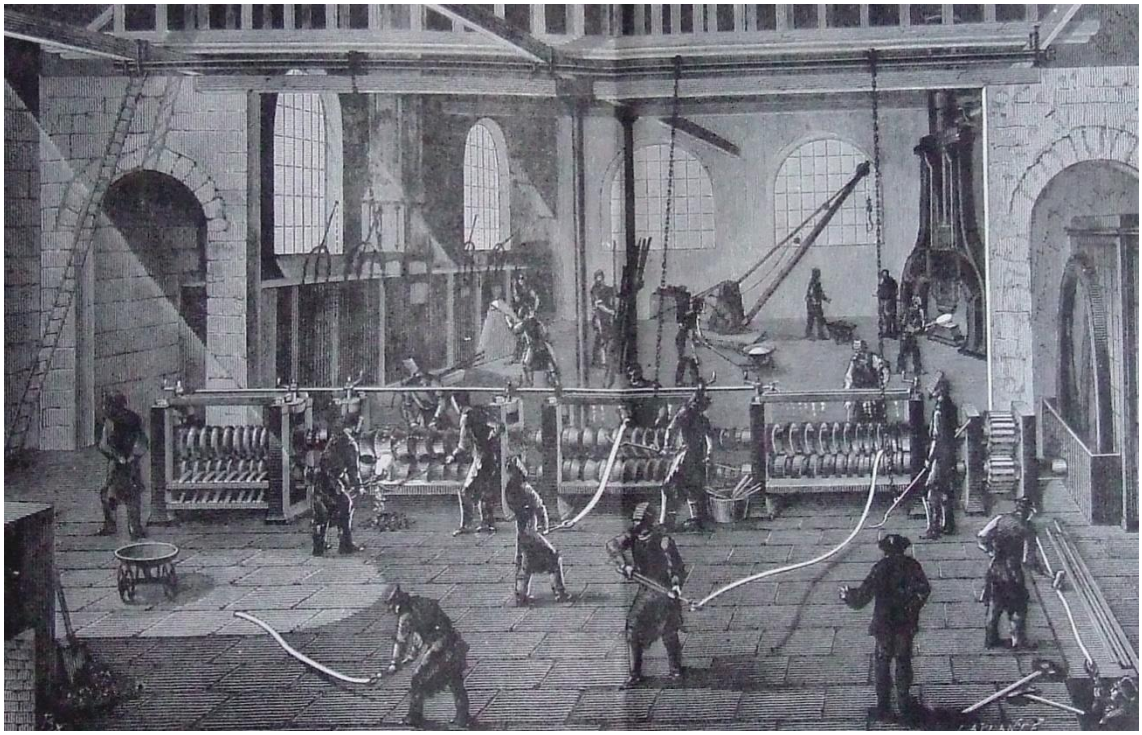

Figure 1.3: A sketch of an Ironworks typical of the early 19th century showing a water-wheel driven grooved rolling mill (Annandale, 1894).

A patent issued to Sir Henry Bessemer in 1857 which described the casting of metal between rollers, was the precursor to contemporary continuous hot mills. Bessemer's original sketch is shown in Figure 1.4. J.T. Newton of Ystalyfeva, Wales was issued a patent describing the predecessor to the modern cluster mill in 1862.

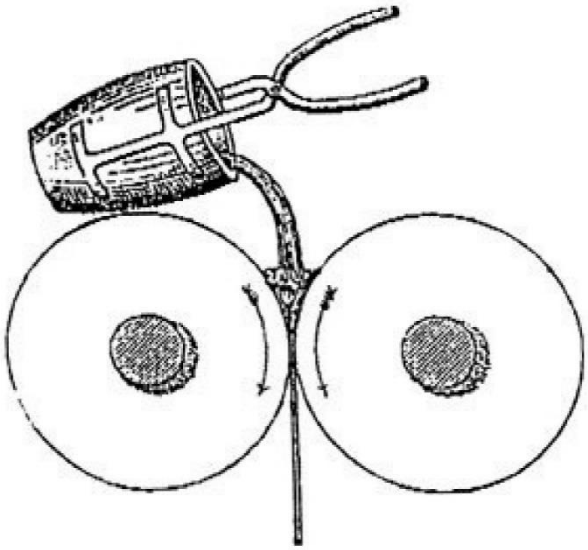

Figure 1.4: Sir Henry Bessemer's original sketch showing twin-roll casting of metals (KMM Metals, n.d.).

1.2 Rolling Today

Today greater tonnages of metals are processed by rolling than by any other technique (Roberts W. L., 1978). Approximately 40% of steel production goes to flat rolled products. As of 2007 this equated to approximately 480 Mtpa (million tons per annum) worldwide (Capital Market Days 2007, 2007). One estimate from 2012 put the revenue from flat rolled steel products as $7.3 billion in the US market alone (Steel Rolling & Drawing in the US: Market Research Report, 2012).

Rolling is just one in the long chain of processes that form the steel industry value chain. Industry terminology often categorises these processes as *Upstream* which includes the production of iron and steel, and *Downstream* processes which cover the production of semi-finished products like blooms, billets, slabs and ingots as well as finished plate and foil products. Figure 1.5 shows a typical chain of processes (SSAB Sheet Steel, n.d.), starting with the output from the steel manufacture. The actual set of methods used will depend on the requirements of the final product.

Within the industry a distinction is often made between *long* and *flat* products. Long products such as structural beams are rolled from rectangular section *blooms,* and smaller bars, rods and wires are rolled from square section *billets*. These products are most commonly used in civil and structural applications. Flat products such as plates and coiled sheets are rolled from flat cross-section *slabs*. Automotive and appliance manufacturers are the largest consumers of flat products (C. Egenhofer, 17 December 2013).

There are two key categories of rolling: *Hot Rolling* and *Cold Rolling*. Hot rolling is performed on a metal which has been heated to above its recrystallisation temperature, for steel this is around 920°C (Hot Rolled Vs. Cold Rolled Steel, n.d.). Hot rolling can be used to alter the as-cast structure of the material. During rolling the original grains change shape and careful control of the hot rolling variables can be used to control the resultant microstructure. Large deformations of the metal can be made when hot rolling. A primary drawback of rolling at these temperatures is the tendency for the strip to oxidise, causing the formation of surface iron oxide layers known as *mill scale* (United States Steel Corporation, Association of Iron and Steel Engineers, 1985). This is detrimental to the surface finish, coating ability and corrosion resistance of the rolled product. For these reasons hot rolling is predominantly used to manipulate material geometry rather than achieving precise surface finish and mechanical properties.

The alternative to hot-rolling is cold-rolling which is performed on metal that is below its recrystallisation temperature, typically at ambient. This generates dislocations in the metal's crystal structure. These dislocations resist further slip, resulting in work hardening of the metal. Cold rolling can therefore be used to alter the microstructure of the metal, adding strength. Also a more accurate thickness and smoother surface finish can be achieved in comparison to hot rolling. The hardening effects of Cold Rolling can cause the strip to become brittle and hard. Cold rolled strip is therefore often annealed to restore some formability to the strip (SSAB Sheet Steel, n.d.). Cold rolled sheet can be further processed by coating to provide protection against corrosion. For steel, hot-dip zinc galvanizing is one of the most common methods. Other widely used methods include, tin coating, chromium coating, aluminising and Terne coating (a mixture of 80% lead and 20% tin) (C. Egenhofer, 17 December 2013). Coated products may also be painted to further prevent corrosion. This is ineffective with hot rolled products due to scaling (EPA Office of Compliance, 1995).

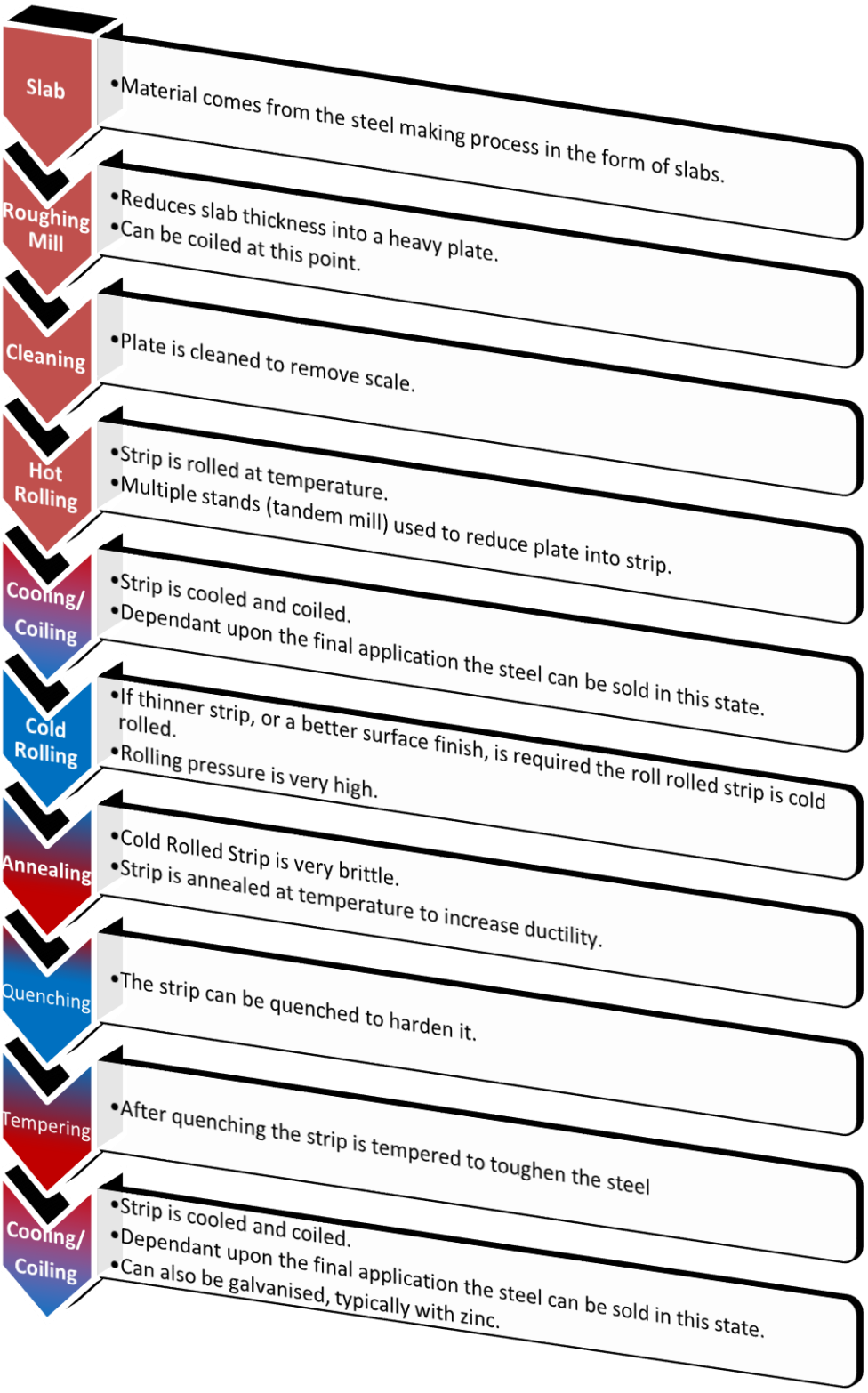

Figure 1.5: Typical Flat Steel Product Production Processes (SSAB Sheet Steel, n.d.).

A large part of the cost of producing flat steel product is its transportation. Another large contributor is the cost of energy (C. Egenhofer, 17 December 2013). Many of the processes in the chain are energy intensive, especially those that require elevated temperatures such as steel production, hot rolling and annealing. To reduce these costs and for practical reasons, such as the availability of power and transport links, the various processes are often integrated into one

plant. Plants are laid out based upon the material flow through the factory, and as such are often linear. For larger plants shipping is the only practical way to transport the quantity of steel produced and so these plants often incorporate, or are located near to, a port. It is normally only economical to build integrated plants which produce 2 Mtpa or more. Currently the largest integrated steel plant is located in Gwangyang, South Korea and is owned and operated by POSCO (formerly Pohang Iron and Steel Company). Gwangyang Steel works produced 19.5 million tons of crude steel in 2010 (POSCO, n.d.).

1.3 Modern Rolling Mills

Although the scale and complexity of rolling mills has evolved over time, their basic principles remain the same. The setup of a rolling mill will vary dependent upon the processing it is required to do. The yield, initial strip thickness, thickness reduction, rolling speed, surface finish, rolling force and required work hardening will all have an influence on the design used.

Despite this all modern rolling mills share a set of similar features and terminology. Figure 1.6 shows a schematic of the key components of a modern mill. It can be seen that the basic principle of the machine is fairly straightforward, however modern rolling mills are complex mechanisms which incorporate a plethora of measurement and control systems. As well as controlling the settings for the mill itself, it is also necessary to coordinate the lubricant delivery, strip tension and the uncoiler/coiler mechanisms.

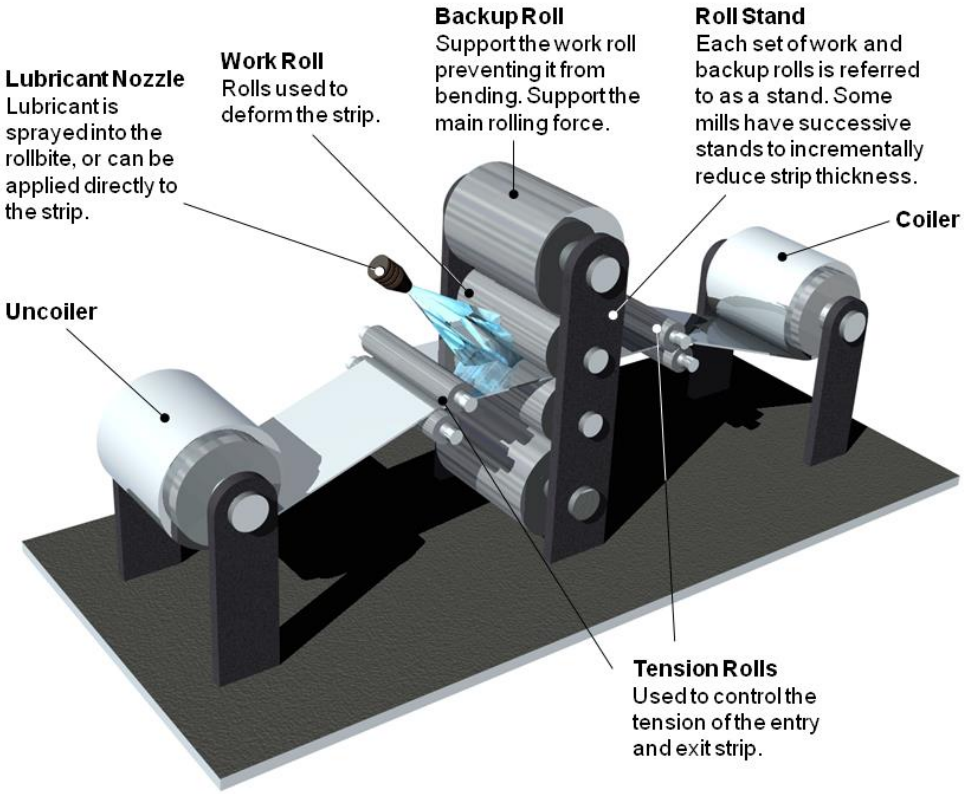

Figure 1.6: Schematic of a Modern Rolling Mill

Figure 1.7 shows a selection of some of the most common roll arrangements used in rolling mills. The most basic configuration are *2-High* mills, these are often small workshop mills. The rolling forces seen in larger mills tend to bend the work rolls resulting in inconsistent strip thickness. Therefore, backup rolls are used to support the main work roll and maintain its shape. The

purpose of the *4-High* and *Cluster* variants shown is to reduce the work roll deflection. *3-High* mills also achieve this by rolling two strips (or the same strip twice) at the same time. *Reversing Mills* are those which can operate in either direction, often passing the same piece of strip back and forth through the rolls, gradually reducing the strip thickness in several *Passes*. The advantage of this is that only one stand is required to produce a large elongation of the strip. However, both the length of strip and throughput are limited. For cases where long strip lengths, or large throughputs, are required, the strip reduction might be separated out into a number of successive roll stands, this is known as a *Tandem* mill.

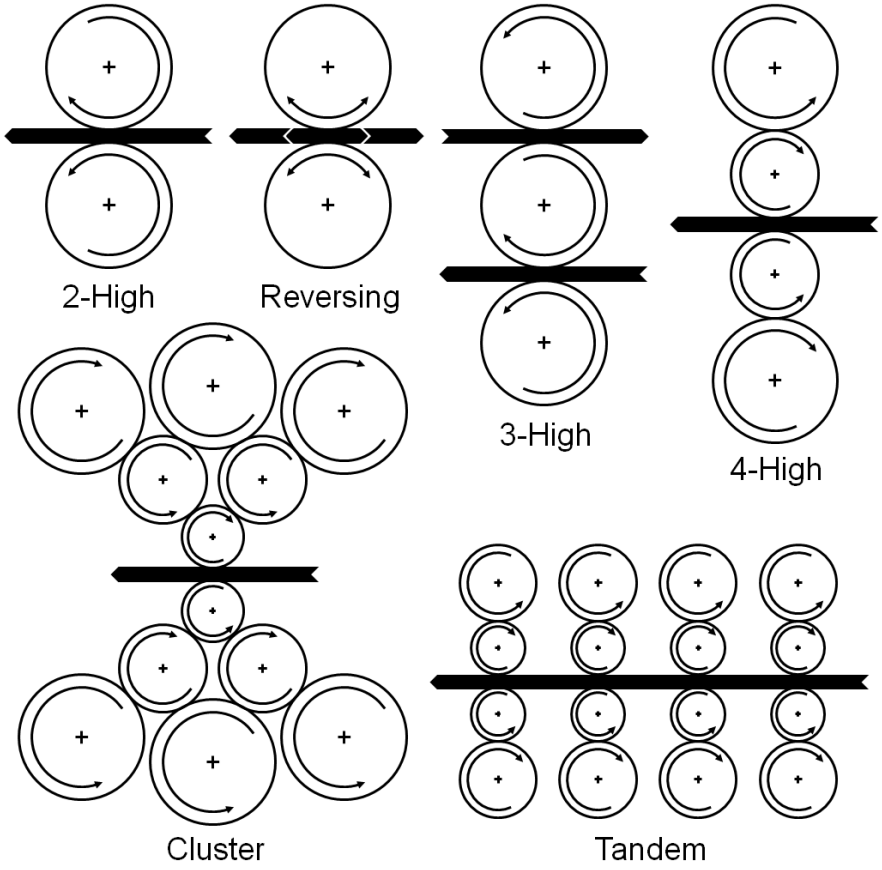

Figure 1.7: Rolling Mill Configurations

When multiple stands are used, these need to be synchronised. A change in reduction on one stand will alter the outgoing strip speed and therefore the incoming strip speed to the next stand. This adds yet another degree of complexity to the rolling mill control system. Greater detail on the specifics of the cold rolling mills used in this work are given in later chapters

1.4 Nature of the Problem

There is a constant drive for higher quality rolled strip. Aspects of specific interest are strip thickness, strip flatness and a strip surface free from defects. This drive is intensified due to the trend of modern rolling mills to combine higher rolling speeds, larger reductions, harder steel grades and thinner strip. In order to achieve higher product quality, and productivity, it is necessary to have a better understanding of the interaction between the strip and work roll surface in the roll bite, including an understanding of the friction, heat transfer and lubrication in the roll gap.

One area in which this greater understanding will help to contribute to improved product, are the preset and adaptation mathematical models used to setup rolling mills. Preset models are

used to determine the initial settings of a mill for a given rolling regime, including entry and exit strip thickness, rolling speed, entry, exit and intermediate tensions, rolling force, roll gap position, rolling torque, flatness actuators and cooling (F. Feldmann, 2009). Friction and heat transfers, both into and from the rolls, are two main input parameters for mill preset models. Current mill presets have poor performance due to the bad estimation of these two parameters. Poor estimation of these, and inability to measure them accurately in real-time has a knock-on effect on adaption models. These are the models used to adapt the initial mill settings during rolling for drift and inaccuracies, specifically in friction, heat transfer and rheology.

Mill preset models are actually made up of a number of sub-models covering tension, speed, roll gap, strip and roll temperature, roll thermal expansion, flatness, roll gap position and sensitivity of outputs to inputs (F. Feldmann, 2009). Most of these relationships are well understood and measured in modern mills, however while work has been completed to theoretically model the roll bite (Ford, Ellis, & Bland, 1951), the harsh conditions mean that little empirical evidence has been obtained.

Explaining rolling force and forward slip behaviours against rolling parameters (rolling speed, lubrication, roll roughness etc) has been a major question in modern rolling. Two main factors are considered as responsible for the observed behaviours, friction and strip rheology. Friction is typically considered using the friction coefficient of the Coulomb model. This describes a range of tribological phenomena related to lubrication, speed, temperature etc. However classic Coulomb or Tresca friction laws are over-simplified to describe the complex lubrication regimes present at the interface. Advanced mixed lubrication models have been developed recently to describe these lubrication regimes in cold rolling (Wilson & Sheu, Real Area of Contact and Boundary Friction in Metal Forming, 1988) (Wilson & Chang, Low Speed Mixed Lubrication of Bulk Metal Forming Processes, 1996) (Kosasih & Tieu, 2007). Again experimental data is missing to validate these models.

Inadequate friction conditions can lead to greater surface roughness, especially when lubrication reaches the hydrodynamic regime, and skidding where the work roll speed is higher than the strip speed. As well as degradation of surface finish, skidding can also result in uncontrolled vibrations in the mill stand leading to inconsistent strip thickness and strip breaks. Other surface defects, such as heat streaks resulting from thermal breakdown of lubricant film can also be an issue.

With friction of clear importance in the rolling process, metal rolling lubricants have a significant impact not just upon the product quality but also energy consumption and roll lifetime. The lubricant must therefore be matched to the rolling conditions. Without knowledge of how the lubrication conditions are affected by rolling force, speed, lubricant composition, reduction and strip tension the correct selection of lubricant and flow rate to match rolling conditions is difficult. Currently these variables are selected using a heuristic approach and adjusted by the mill operator, this leads to inefficiencies and inconsistencies on the process.

The issues mentioned so far relate equally well to both hot and cold rolling. Although this thesis is concerned primarily with the cold case, there is a large cross-over between the two processes and therefore some consideration should also be given to the issues seen in hot rolling.

In hot rolling the friction level in the roll bite and wear of the work rolls can lead to rolled-in-scale on the strip surface. There is currently no reliable online indicator or effective industrial

practice to prevent rolled-in-scale in hot rolling. Consequently, rolled-in-scale, not detected at the hot strip mill, is generally revealed on the subsequent pickling process where it is extremely difficult to remove. This gives rise to unacceptable surface defects and loss of product.

Modelling of hot rolling lubrication is much less advanced than in cold rolling. Therefore, prior to the development of a hot rolling lubrication model, a local friction and lubricant thickness measurement could be a useful to better understand lubrication regimes specific to hot rolling.

1.5 Proposed Solution

In cold rolling, the thin film of lubricant existing between roll and strip is clearly crucial to the quality of rolled product, as described above. The roll operates in boundary lubrication, and currently, the film thickness or the amount of asperity contact is experimentally unknown in rolling processes. Roll stress has been measured by means of strain gauges, however this often requires significant modification of the roll to ensure the measured part deforms in a specified manner. Similarly, a number of studies have measured rolling friction, however this often required modification of the rolling surface itself, deeming most such techniques unsuitable for industrial use.

A wealth of previous works have used ultrasonic techniques to measure the lubricant films (Dwyer-Joyce, Drinkwater, & Donohoe, The Measurement of Lubricant Film Thickness using Ultrasound, 2003) in a range of components, specifically piston rings (Harper, Dwyer-Joyce, Sjödin, & Olofsson, 2004), thrust pads (Dwyer-Joyce, Harper, Pritchard, & Drinkwater, 2006), hydrodynamic bearings (Dwyer-Joyce, Harper, & Drinkwater, A Method for the Measurement of Hydrodynamic Oil Films using Ultrasonic Reflection, 2004), EHL contacts (Dwyer-Joyce, Reddyhoff, & Zhu, Ultrasonic measurement for Film Thicknessand Solid Contact in Elastohydrodynamic Lubrication, 2011) and mechanical seals (Anderson, Salant, & Jarzynski, 1999) (Reddyhoff, Dwyer-Joyce, & Harper, A New Approach for the Measurement of Film Thickness in Liquid Face Seals, 2006). This thesis proposes the use of similar techniques to study the lubrication conditions in the roll-bite and stress conditions within the roll. If these techniques can successfully be applied it will allow measurements to be performed without the need to alter the rolling surface, ensuring the measurement process has minimal effect on the rolling process, and strip surface finish.

1.6 Aims

This thesis intends to develop an innovative approach, based upon ultrasonic reflection, to measure a number of roll gap parameters in situ. To achieve this the following aims have been set:

1. Develop the concept and underlying theory for a lubrication sensor based on reflected ultrasound. The proposed measurements will rely on the interaction of ultrasound with the system being studied. It is essential that a theoretical model for this interaction is developed so that the measured ultrasonic response can be linked to the associated lubrication condition.
2. Design and implementation of an in situ ultrasonic sensor to carry out measurements stated in the thesis aims. Different sensor designs are to be evaluated and compared in cold rolling conditions using laboratory, pilot and industrial mill tests. Various methods of sensor instrumentation are to be trialled. A successful design will be selected and tested

3. Design of data acquisition system to capture the required data in real-time. This must take into account the required acquisition rates and resolutions, as well as the implementation of real-time processing algorithms and data storage
4. Measurement of oil film thickness and asperity contact in situ. The oil film thickness for a range of cases will be recorded.
5. Measurement of roll stress in-situ. From this roll stress measurement rolling friction will also indirectly be obtained, based upon the relationship between roll stress and friction.
6. Measurement of strip thickness in-situ. Although other proven methods are available to measure strip thickness many of these happen externally to the roll bite. A by-product of the data captured for the other measurements taken is likely to be the ability to measure strip thickness in real-time in the roll bite.
7. The verification of the results obtained from testing by comparison with computer simulations

1.7 Benefits

The proposed work should contribute to the following direct industrial benefits, and wider benefits to society:

1. Improved strip thickness through better mill presets: Existing models for roll force calculation will be considerably improved through the data gained from the proposed sensor.
2. Decreasing strip surface defects: Currently, rolled-in-scale losses are estimated to £470k per year for one hot strip mill of 4 Mtpa. Assuming that 3% of rolled-in scale defects appearances could be avoided by the improved models obtained with these sensors, and given the annual EU hot coils production of about 80 Mtpa, means a potential saving in the order of £350k per year for the European steel industry alone. Similar benefits also exist in cold rolling.
3. Selecting roll steel grades: The criteria used by roll suppliers for roll steel grades selection and treatment are dependent on the temperature and stress in the contact and the relative motion between the strip and roll. The sensor should define these criteria more accurately.
4. Improve mill productivity by minimising roll degradation: A much better understanding of the interaction between the different roll damage mechanisms (fatigue, oxidation, abrasion) will generate more predictive fatigue and wear models that will decrease the problem. Currently, roll degradation generates losses estimated to £3.9M per year on a hot strip mill of 4 Mtpa. Extended across Europe this amounts to around £78M per year. If the sensor developed in this thesis contributes a decrease of 3% to these losses, benefits of about £2.3M per year can be expected in Europe alone.
5. Competitiveness: With the above industrial benefits, the competitiveness of the steel rolling sector should be increased as the productivity, quality of rolled products, and life of work rolls will be improved. Note that steel producers, roll suppliers and mill automation systems suppliers shall benefit from these advanced sensors by increasing their expertise.
6. Positive impact on occupational health, safety, and working conditions: The integrated sensors, through the better understanding of the roll bite phenomena, will minimise rolled strip quality defects and will avoid many critical situations such as strip breaks due

to bad friction conditions. A positive impact can therefore be expected on working conditions.

7. Preservation of natural resources, energy and environment: The sensor, by enabling a better understanding of roll bite phenomena and their use on industrial mills, will decrease roll and strip surface degradation as well as increase strip thickness accuracy. This should directly reduce material losses. Additionally, more effective and efficient use of rolling lubricant will hopefully result in a reduction of the amount required.

1.8 Layout of Thesis

This thesis is split into twelve chapters. Although successive chapters build on concepts in previous chapters, they are broadly self-contained. Each chapter aims to detail one aspect of the work completed.

This chapter offers an introduction to the thesis. Following on from this, chapters 2 to 4 cover various aspects of the underlying theory used throughout the thesis. The transducers, instrumentation, experimental design are covered in chapters 5 and 6. Results from preliminary testing performed to verify the proposed techniques and experimental setup are presented in chapter 7. The primary testing and results are shown in chapters 8 through 10, and the computer modelling validation work is detailed in chapter 11. The conclusions of this work and suggestions for future work are included in the final chapter. Referenced works are included at the end of the thesis.

2 Cold Rolling of Steel

This thesis sits at the intersection of three distinct areas of study, cold-rolling, ultrasonics and tribology. This chapter presents the fundamental theory behind the cold-rolling and related tribological aspects of the work. Equation proofs have been presented where they are of particular interest in this thesis, are used in later analysis or have been formulated by the author.

2.1 Mathematical Model Assumptions and Simplifications

The rolling process is a complex problem and even basic modelling requires an understanding of the interaction between interface tribology, roll mechanics and strip rheology. A number of assumptions have been made to simplify this analysis and these have been described below.

Unless it is stated otherwise the mediums under consideration are assumed to be perfectly homogeneous, isotropic, isothermal and elastic. For simplicity the theoretical work presented only considers a 2 dimensional cross section of the rolls and strip, on the plane perpendicular to the axis of the rolls, the X-Z plane as shown in Figure 2.1.

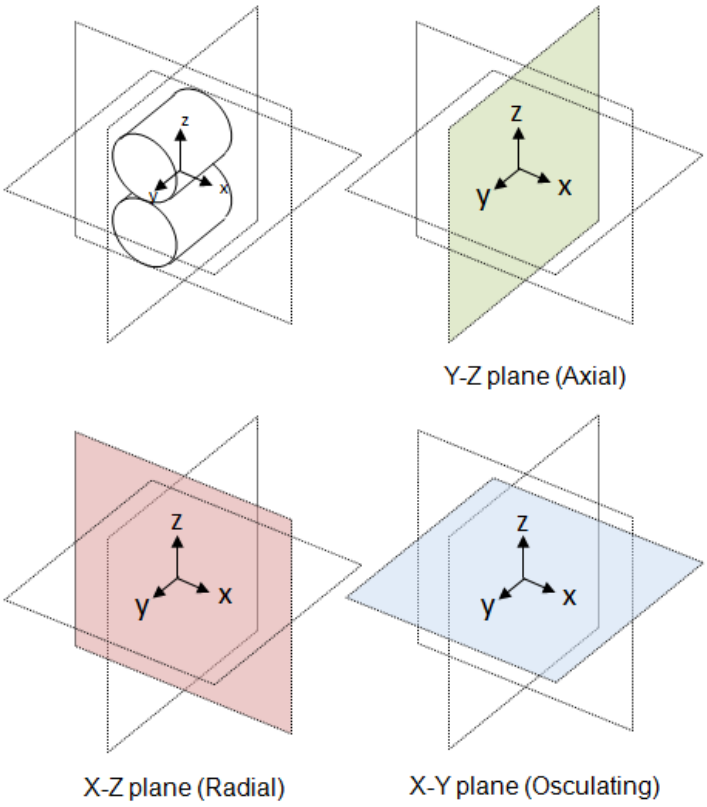

Figure 2.1: Axis and Plane Definitions

This plane is located across the midpoint of the roll, and it is assumed that there is reflective symmetry about this plane in the Y-direction. Spreading of the rolled strip in the Y direction is assumed to be negligible. Where forces are shown in diagrams the positive direction of the force corresponds to the direction of the arrow.

The dimensions of the rolls are large in comparison with the dimensions of the contact area. Therefore the stresses in the region of contact are not significantly dependent upon the shape and support of the rolls far from the contact. It is assumed that the stresses may be calculated

to good approximation by considering the rolls as semi-infinite bodies bounded by a plane surface. A mathematical model of this nature, in which only one boundary exists and all others are infinitely far away, is commonly known as a half-space.

2.2 Cold Rolling Model Overview

In its most basic form rolling is used to reduce an input strip to a predetermined thickness, by deformation between two cylindrical rollers. A range of more complex cases exist, such as the use of shaped rolls to create products with a non-uniform cross section, however only simple thickness reduction rolling is considered in this thesis. This reduction can be achieved either with a preheated strip (hot-rolling) or an unheated strip (cold-rolling), as described in the previous chapter. This thesis only considers the cold case, although much of the work is applicable to either.

The energy required to deform the strip can be thought of as coming from four sources, strip backward tension, strip forward tension, roll force and roll torque, as shown in Figure 2.2. Roll torque is transmitted to the strip via friction in the roll-strip interface. This interface is referred to as the *roll bite* and the characteristics of this interface strongly influence the effectiveness and efficiency of the rolling process. It is common for a lubricant, typically an oil-water emulsion, to be used in the roll bite for numerous reasons as described towards the end of this chapter.

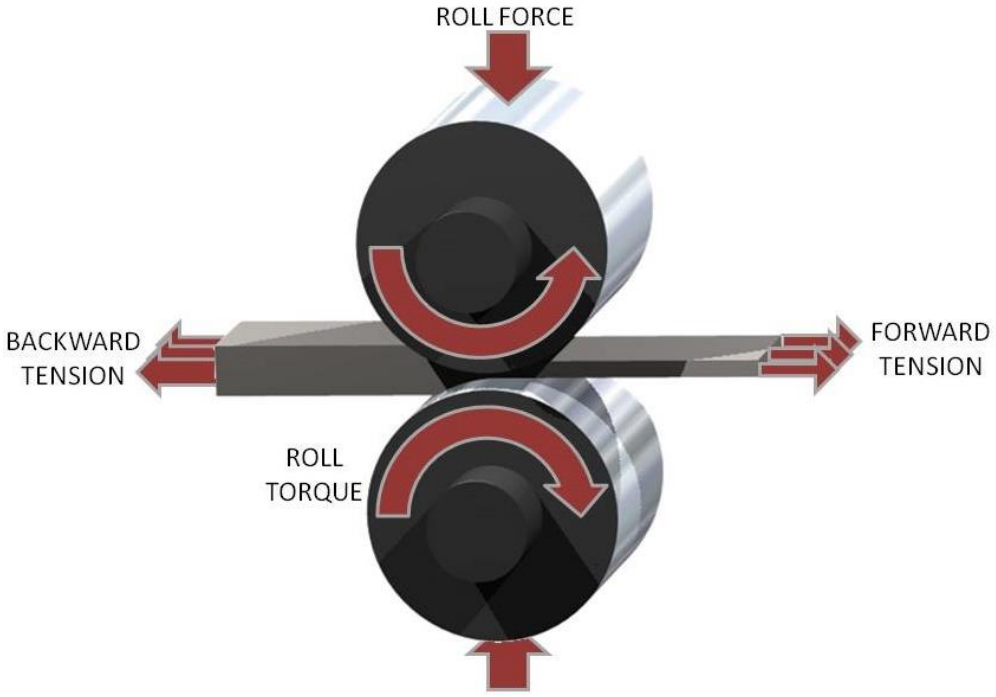

Figure 2.2: Primary Forces in Metal Rolling

As the deformation energy applied by the rolls is transmitted through the roll-strip interface the conditions and interactions here are the predominant interest in this work. To adequately understand this aspect of the system it is also necessary to look into the behaviour in the roll bulk and strip.

2.2.1 Draft and Elongation

Large loads are required during rolling to permanently deform the strip, and these can cause elastic deformation of the roll. The roll is flattened and the roll radius local to the contact area

increases from its nominal value *R* to its deformed radius *R'*. This slightly increases the roll bite contact length *L*, shown in Figure 2.3. It also results in stresses inside the roll. Understanding these stresses is important for both roll design and condition monitoring.

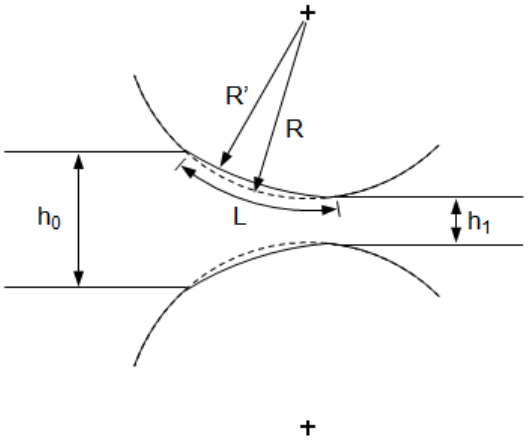

Figure 2.3: Roll Schematic

As shown in Figure 2.3 the strip thickness is reduced from h_0 to h_1 the difference between these being the draft, *d*, also referred to as the reduction.

$$d = h_0 - h_1 \tag{2.1}$$

If we assume conservation of mass and no density change, it must hold that there is no volumetric change. Combining this with the assumption that there is negligible flow of the strip across its width we can state:

$$h_0 L_0 = h_1 L_1 \tag{2.2}$$

Where L_0 and L_1 are the strip lengths before and after rolling. It is clear that a reduction in strip thickness results in an elongation of the strip length. It is useful to define this elongation in terms of percentage, *el%*, as given by:

$$el\% = 100\frac{L_0 - L_1}{L_0} \tag{2.3}$$

Rolling processes are normally defined by specifying elongation percentage rather than the draft.

2.2.2 Interface Profile

The roll bite length, as shown in Figure 2.3, is often of the order of millimetres. It is therefore useful to consider the profile of the roll bite on the microscopic scale. Figure 2.4 shows a schematic of the interfaces and lubricant in and around the roll bite. It can be seen that the contact between the roll and strip is a combination of direct asperity contact interspersed with lubricant filled pockets. This type of contact will be referred to as mixed mode.

Both the lubricant and solid asperity contact contribute to the interface normal pressure and shear stress, in the manner described in Equations 2.4 and 2.5:

$$p(x) = \big(1 - A(x)\big)p_l(x) + A(x)p_a(x) \tag{2.4}$$

$$\tau(x) = \big(1 - A(x)\big)\tau_l(x) + A(x)\tau_a(x) \qquad 2.5$$

Where *A* is the proportion of asperity contact, τ is the shear stress, *p* is the normal pressure and the subscripts *l* and *a* denote the lubricant and asperity components respectively. The proportion of asperity contact is therefore of great importance.

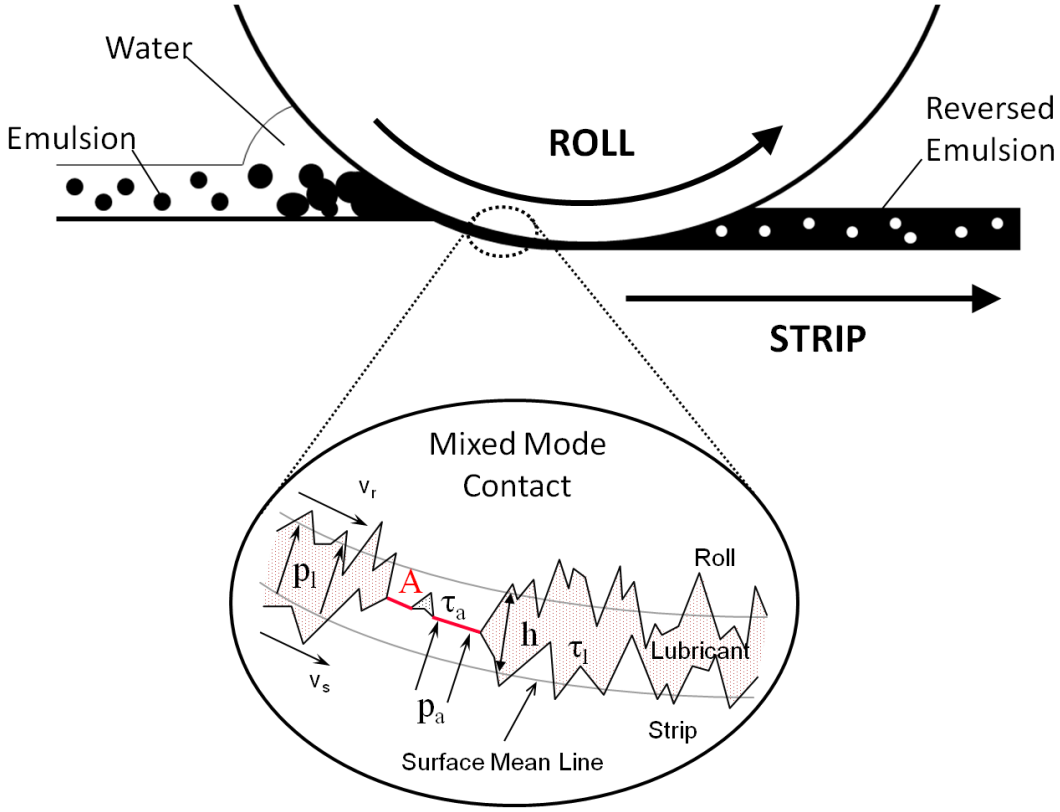

Figure 2.4: Roll Bite Interface Schematic

It is also worth noting that, as shown in Figure 2.4 the amplitude of the asperities can be of the same order as the film thickness. Defining a single value for film thickness is therefore non-trivial. In this thesis the surfaces are assumed to have an evenly distributed roughness and the film thickness is taken as the difference between the roughness mean-lines of the two surfaces. Most rolling occurs in the mixed lubrication regime, however at higher rolling speeds hydrodynamic lubrication with a continuous fluid film has been observed, although this rarely happens in practice (Atkins, 1974).

2.2.3 Roll and Strip Velocities

If a constant volume of metal is assumed, and no significant spread occurs across the width of the strip, the strip speed must increase relative to the roll surface speed through the roll bite. In normal rolling the incoming strip travels slower than the roll surface while the exiting strip travels at the same speed or marginally faster. This leads to a velocity difference, or slip, between the strip and roll. Part way through the roll bite there is transition point, known as the neutral point, where the slip changes direction. At this point the roll and strip are travelling at the same speed. These various velocities are shown in Figure 2.5.

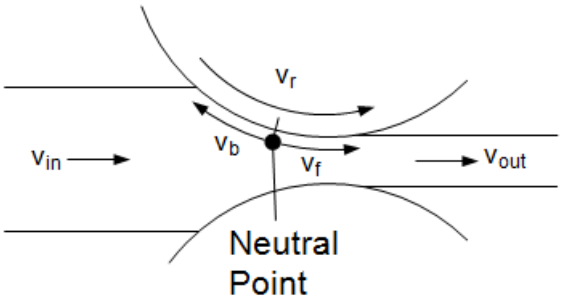

Figure 2.5: Roll Bite Velocities, v_b and v_f are the backward and forward velocities of the strip relative to the roll

Figure 2.6 shows the velocities of the roll and strip along with the aforementioned neutral point. The location of the neutral point is defined by the friction conditions in the roll bite. Many traditional models of rolling (Atkins, 1974) (Roberts W. L., 1978) put the neutral point near the centre of the roll bite, however in practice it is widely understood that the neutral point is actually nearer to the exit.

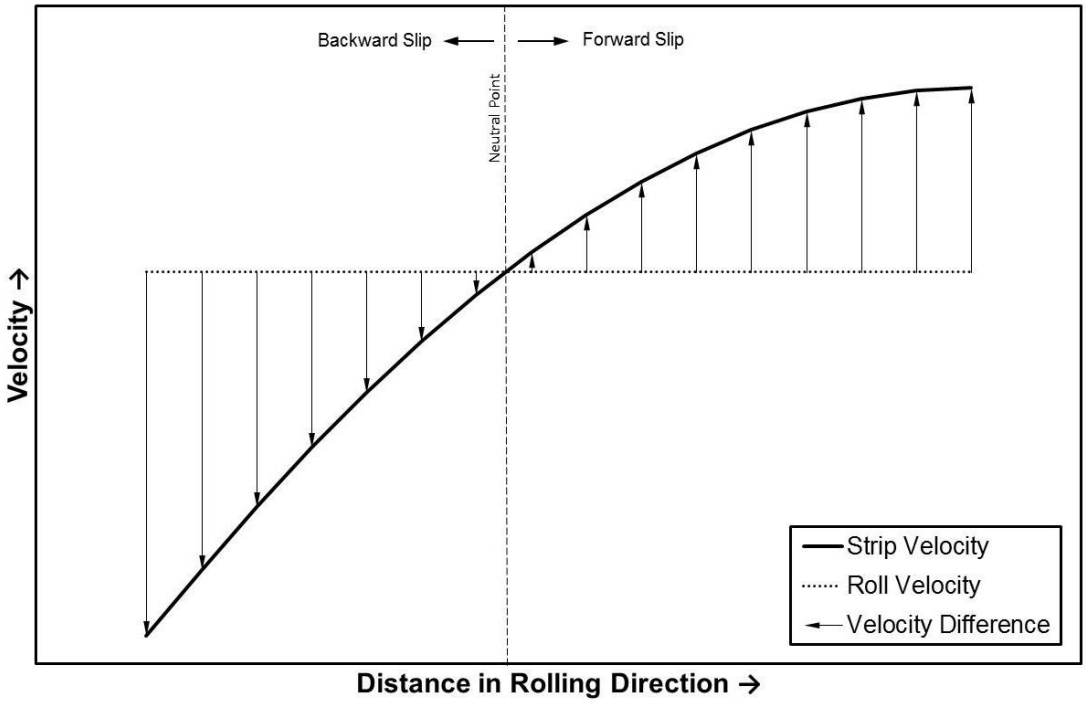

Figure 2.6: Roll and Strip velocity showing the neutral point

2.2.4 Interface Friction

Early models of cold rolling assumed Amontons' laws of friction to be applicable, that the ratio of shear to normal stress assumes a constant value along the entire arc of contact and that this ratio is equal to the coefficient of friction. Amontons' laws however only apply to dry interfaces and cannot be applied to the lubricated case.

Even later models which account for lubrication assume that this results in a uniform coefficient of friction across the roll bite. However this assumption does not hold true due to the partially hydrodynamic nature of the interface, and non-uniform pressure profile across the roll bite. In hydrodynamic lubrication the frictional effects should be higher at points of highest slip, for example the entry to the roll bite, and will be zero at the neutral point. On the other hand the thickness of the lubricant film is expected to decrease through the roll bite, and this will result in an increasing coefficient of friction due to boundary layer lubrication.

The magnitude of the friction coefficient between the strip and roll affects the relative slip. As the friction coefficient increases backward slip is reduced and the neutral point moves closer to the entry of the roll bite. Conversely as the frictional force is reduced the neutral point will move towards the back of the roll bite. Too little friction and the neutral point will move beyond the end of the roll bite, which results in the roll surface travelling faster than the strip at all points across the roll bite and the rolls skidding. If the frictional forces are too high then positive, or forward, slip occurs (where the strip exit speed is in excess of the roll surface speed) this can result in a poor surface finish and higher energy consumption.

It is therefore desirable to operate as close to the smallest value of friction coefficient before skidding occurs, this value is referred to as the minimum coefficient of friction, μ_m. For rolling of thin strip and foil products this can be as low as 0.01 (Roberts W. L., 1978). Friction is therefore of great importance to the rolling process. Many mathematical models characterise the roll bite with a constant coefficient of friction. While this is sufficient for simple analyses it is clear that this is not the whole story. Lubrication conditions will clearly have a large impact on this.

At the minimum friction level the pressure exerted by the rolls across the contact is essentially constant. When the coefficient is increased and the neutral point moves into the roll bite a *friction hill* is observed which results in a peak in the pressure exerted by the rolls at the neutral point (Seibel, Berichte des Walzwerksausschusses [Reports of the Rolling Mill Committee], 1924), as shown in Figure 2.7. It is worth noting that the rolling force per unit width can be calculated from the pressure curve by integrating the area underneath it. Various methods of modelling the pressure distribution are discussed later.

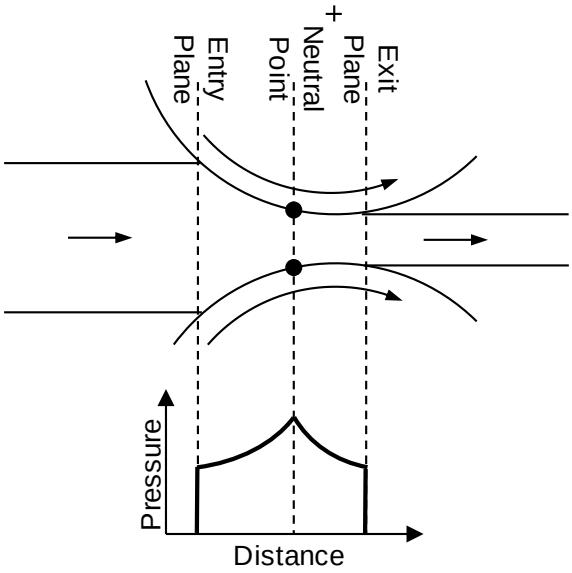

Figure 2.7: Schematic Illustrating the Hypothetical “Friction Hill" Pressure Distribution along the Arc of Contact

Figure 2.8 illustrates that for constant emulsion flow rate, but varying rolling speed, different lubrication regimes occur in the roll bite. For slow speeds the coefficient of friction decreases with speed. The emulsion is behaving like a pure oil and the lubricant is supporting more of the load. However at higher rolling speeds the friction level increases. This is due to the occurrence of starvation.

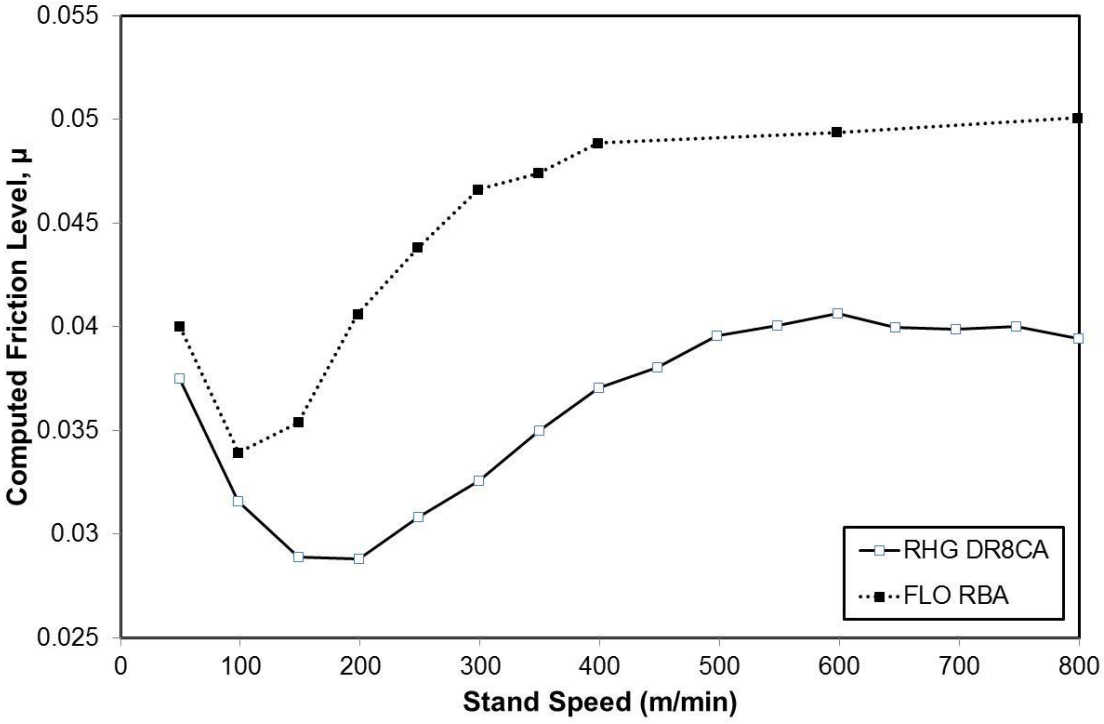

Figure 2.8: Stand Speed against Friction for two lubricants, reproduced from Fouratier et al. (A. Fouratier, F. Geißller, G. Endemann and B. Schmidt;, 2002).

It is clear that rolling is not a simple problem and that any attempt to model it must take into account numerous variables.

2.3 Roll Deformation

The deformation of the roll under normal operating conditions is elastic. The elastic deformation of contacting surfaces has been widely studied and much work has been put into mathematically modelling this. Two common approaches, Hitchcock and Hertzian, are presented here.

2.3.1 Hertzian Approach

Heinrich Hertz studied the elastic contact of spheres (Hertz, 1896), which was subsequently extended to a range of contacting bodies including a cylinder-on-plate. The cylinder-on-flat contact is treated as a special case of cylinder-on-cylinder contact where the cylinder used to represent the flat is assumed to have an infinite radius (R. G. Budynas, 2011). The cylinder axial lengths are equivalent to the strip width. This gives:

$$L = 2\sqrt{\frac{2F}{\pi W}\frac{(1-\nu_R^2)/E_R + (1-\nu_S^2)/E_S}{1/D}} \qquad 2.6$$

D is the diameter of roll, *E* and *v* are the Young's Modulus and Poisson's ratio of material, with the subscripts *R* and *S* representing the roll and strip respectively. The pressure distribution is elliptical. Rearranging and substituting for the specific force, *f*, we get:

$$L = 1.596\sqrt{fD\left(\frac{1-\upsilon_R^2}{E_R}+\frac{1-\upsilon_S^2}{E_S}\right)} \qquad 2.7$$

This Hertzian approach assumes elastic materials, this is a fair assumption for the roll, however as the strip plastically deforms its validity is questionable. This modelling approach would therefore be much better suited to modelling of the contact between the work roll and backup rolls. A more suitable approach for the roll-strip interface was formulated by Hitchcock (Hitchcock, 1935) who used the elliptical Hertzian pressure distribution to calculate deformed and undeformed roll radii.

2.3.2 Hitchcock's Approach

Hitchcock's equation for the roll bite length, accounting for a deformed roll is given here:

$$L = \frac{8R(1-\nu_R^2)\bar{p}}{\pi E_R}+\sqrt{\left[\frac{8R(1-\nu_R^2)\bar{p}}{\pi E_R}\right]^2+Rd} \qquad 2.8$$

Where *L* is the length of the arc of the deformed contact, *R* is the undeformed roll radius, ν_R is Poisson's ratio of the roll, E_R is Young's modulus of the roll, *d* is the reduction and $\bar{p}$ is the mean pressure. The mean pressure is the roll normal force *F* divided by the contact area, calculated from the roll bite length *L* and strip width *W*, as shown in Equation 2.9.

$$\bar{p} = \frac{F}{LW} \qquad 2.9$$

The deformed radius can be obtained from this by the following assumption:

$$L = \sqrt{R'd} \qquad 2.10$$

Where *R'* is the flattened roll radius. Combining with Equation 2.8 and simplifying to give the relationship in terms of the specific rolling force *f,* which is the force applied per unit width ($f = F/W$) gives:

$$R' = R\left[1+\frac{16(1-\nu_R^2)}{\pi E_R d}f\right] \qquad 2.11$$

As described at the beginning of this chapter a combination of strip tensions and roll torque, in addition to rolling force, contribute to the deformation of the strip. These are implicit in the reduction term used in Hitchcock's formula. Hitchcock's equations have since been shown to under predict the amount of roll deformation and a number of authors have suggested modifications to the equations (Roberts W. L., 1969) and the assumptions made in formulating the equation have been widely criticised (Lenard, 2013). It can be seen from the equation that Hitchcock's relationship defines the flattened roll shape by a simple radius value, the deformed shape is therefore assumed to be circular. Empirical evidence has shown that the work roll is in fact flattened. This is evident from a basic consideration of the profile as there must be a

transition between the unloaded and deformed profiles at the roll-bite exit and entry. However, Hitchcock's equation is still widely used as a simple and quick way to estimate both roll flattening and contact length

Figure 2.9 shows a comparison of the roll bite length predicted by the Hitchcock equations. Values representative of a real rolling case were used (E_R, E_S = 2.1x10^{11} Pa, ν_R, ν_S = 0.3, D = 0.4m)

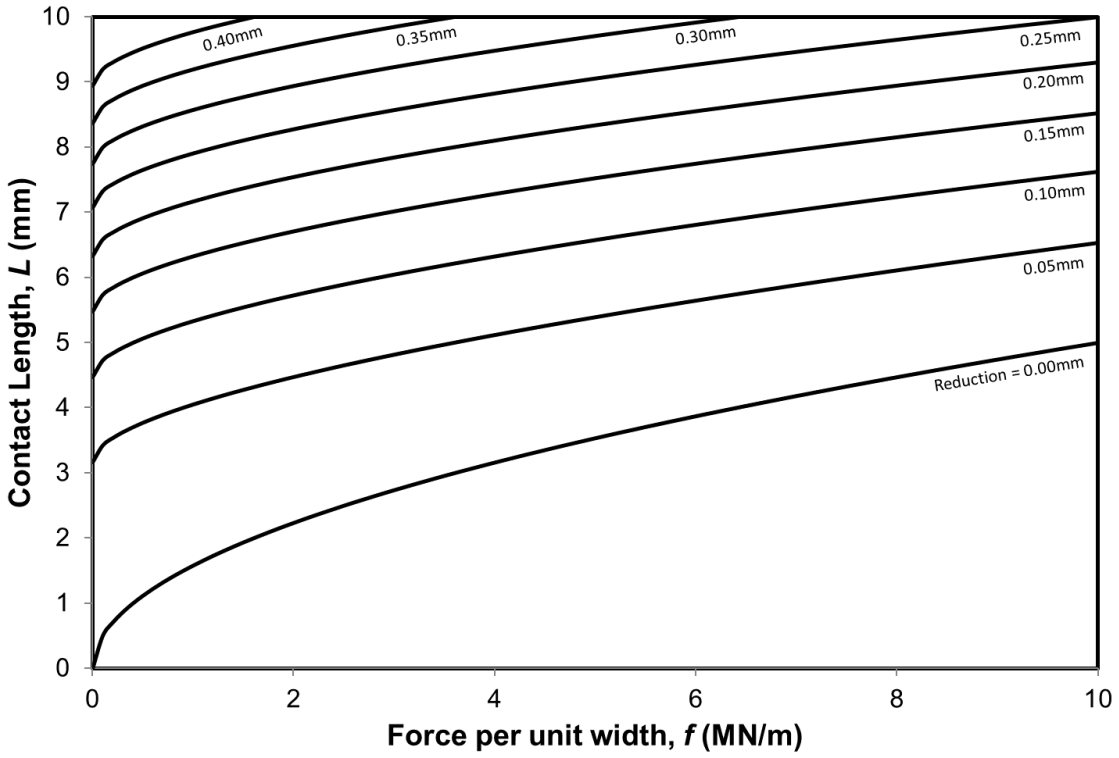

Figure 2.9: Contact Length predicted by Hitchcock (Equation 2.8) for a number of reductions

The mean pressure used in Hitchcock's equation was calculated from the force and contact length output from the Hertzian approach. For zero force, Hitchcock's equation can still be used to predict contact lengths for non-zero deformations, however clearly no reduction is possible without a deformation force. Conversely the zero reduction calculation will not hold for non-zero deformation forces, this has only been plotted in Figure 2.9 to represent the lower bound of contact lengths predicted by Hitchcock's formula.

2.4 Contact Pressure Distribution

The normal rolling force is the primary mechanism by which strip deformation is achieved. Only by matching the required rolling force to the strip deformation required can an accurate output strip thickness be attained. The preceding analysis allowed for an estimation of contact length, and using knowledge of the normal rolling force which is commonly measured on rolling mills, it is possible to get an estimation for the pressure distribution.

2.4.1 Stick-Slip Approach

Two cylindrical rollers of identical material in rolling contact with parallel axis (such that they make a rectangular contact) can be modelled as a plane strain problem with normal and tangential stress distributions at the contacting surfaces (Kalker, 1990).

As described earlier in this chapter there is slip between the surfaces of the roll and strip in cold rolling. This can be modelled by assuming a zone of sticking (zero relative velocity between roll and strip) and a zone of slip (Carter, 1926). This zone can be approximated to a strip shape, and is defined by a stick-slip ratio:

$$\xi = a_1/a \qquad 2.12$$

Where ξ is the stick slip ratio, *a* is half the contact length and a_1 is half the contact length of the stick zone.

2.4.1.1 Normal Pressure Distribution

According to classical contact mechanics the normal pressure distribution, *p(x)*, across the contact zone is elliptical (Johnson, 1987). If the maximum pressure is denoted as p_{Max} this leads to the following relationship for the normal pressure distribution, Equation 2.13.

$$p(x) = p_{Max}\sqrt{(1-(x/a)^2)} \qquad 2.13$$

Where *x* is the distance along the roll bite. The half contact width is half the roll bite contact length ($a = L/2$), although for simplicity in later calculations *a* is retained. Figure 2.10 shows the elliptical pressure distribution and equivalent average pressure.

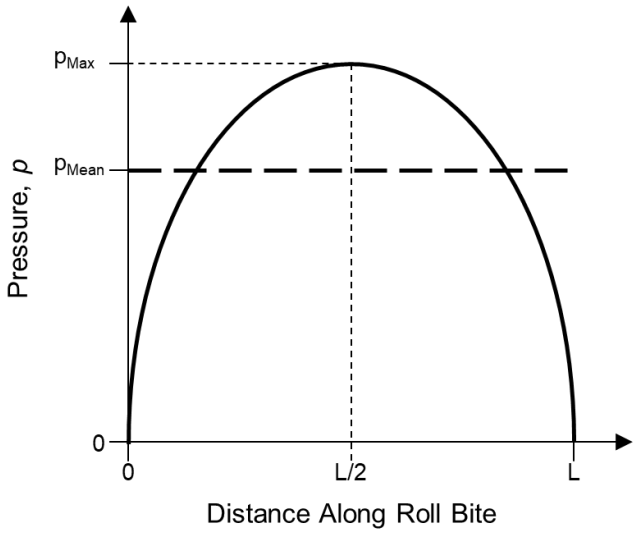

Figure 2.10: Elliptical Pressure Distribution.

The integral of these two functions must be equal across the width of the contact; it is therefore fairly straightforward to work out the p_{Max} from p_{Mean} using simple geometry to give Equation 2.14.

$$p_{Max} = \frac{p_{Mean}4}{\pi} \qquad 2.14$$

The average pressure is simply the ratio of normal force to contact area, Equation 2.15

$$p_{Mean} = \frac{F}{2aW} \qquad 2.15$$

Where *F* is the normal force applied to the rolls and *W* the width of the contact (strip width). Substituting Equation 2.15 into Equation 2.14 along with the force per unit length across the roll ($F = fW$) gives a value for the maximum pressure, Equation 2.16.

$$p_{Max} = \frac{2f}{a\pi} \tag{2.16}$$

This can be substituted into Equation 2.13 to give Equation 2.17, the normal pressure distribution across the contact:

$$p(x) = \frac{2f}{a\pi}\sqrt{1 - \left(\frac{x}{a}\right)^2} \tag{2.17}$$

This is only valid in the contact, where $|x| \leq a$, outside the contact the normal pressure is zero.

2.4.1.2 Tangential Stress Distribution

In the slip zone the tangential stress *q* is a function of the normal pressure *p* and friction coefficient μ, as shown in Equation 2.18.

$$q = \mu p \tag{2.18}$$

The tangential stress distribution *q(x)* over the contact zone is given by (Das Bakshi, Leiro, Prakash, & Bhadeshia, 2014):

$$q(x) = \begin{cases} 0, & |x| \geq a \\ -sgn(s)\frac{\mu 2f}{a\pi}\sqrt{1 - \left(\frac{x}{a}\right)^2}, & -a \leq x < a - 2a\xi \\ -sgn(s)\frac{\mu 2f}{a\pi}\left[\sqrt{1 - \left(\frac{x}{a}\right)^2} - \sqrt{\xi^2 - \left(\xi + \frac{x}{a} - 1\right)^2}\right], & a - 2a\xi \leq x \leq a \end{cases} \tag{2.19}$$

where

$$sgn(s) = \begin{cases} +1, & s > 0 \\ 0, & s = 0 \\ -1, & s < 0 \end{cases}$$

Here *s* is a symbolic variable giving the position from the centre of the contact, as shown later in Figure 2.18. The tangential and normal stress distributions where calculated using Equations 2.17 and 2.19. A friction coefficient of μ=0.3 was used, and the stress was normalised by dividing through by the ratio f/a. The results are plotted in Figure 2.11.

As described in its derivation the normal force distribution is elliptical, and is unaffected by the stick-slip ratio or friction coefficient. The tangential force distribution changes markedly with a change in the stick-slip ratio, as expected from the form of Equation 2.19. The figure also shows that in the slip zone the tangential force is of the same elliptical form as the normal force distribution, but scaled by the friction coefficient.

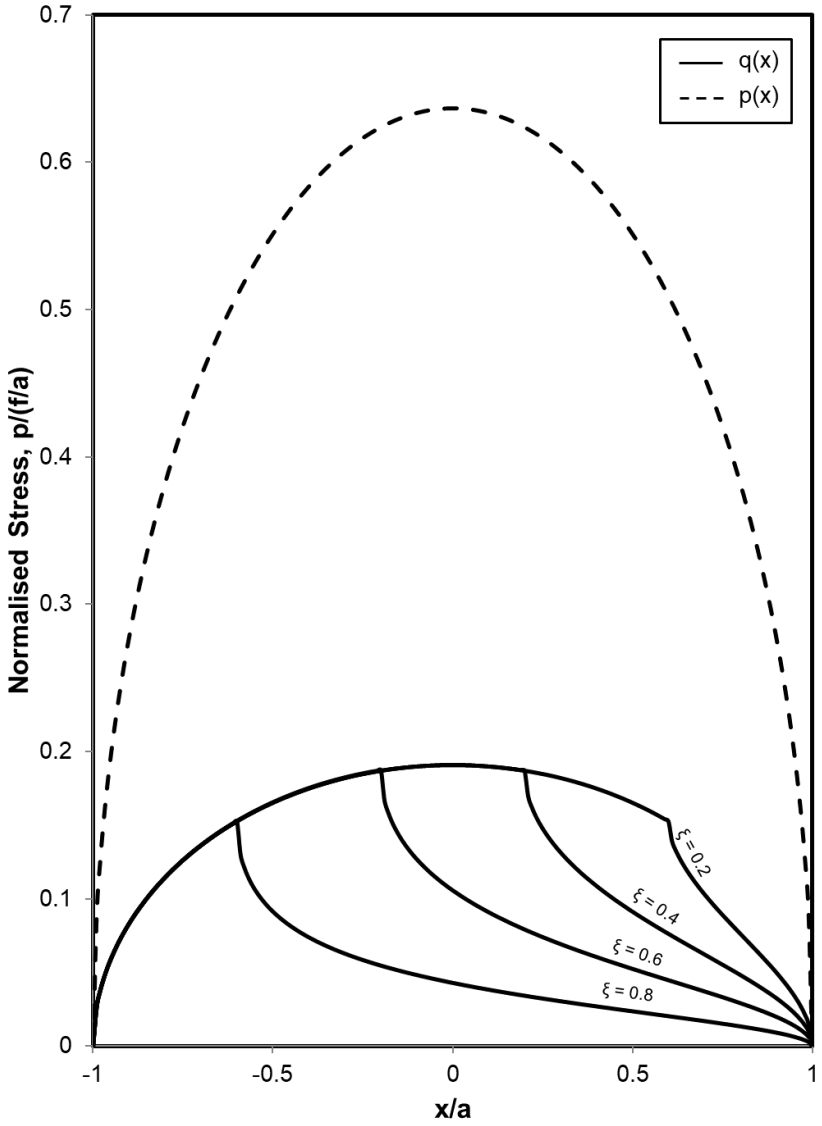

Figure 2.11: Normal and Tangential Stress Distribution for a range of ξ, with μ = 0.3.

2.5 Strip Deformation

The primary purpose of most rolling processes is to reduce the thickness, or alter the cross sectional geometry, of the input material. There are number of other advantages that can be gained by rolling.

Deforming the strip between smooth rollers imprints the surface roughness onto the strip improving the finish. Plastic deformation of the strip induces a residual stress, which is often undesirable. The effect of residual stresses can be decreased by annealing which is used when subsequent processes require the material to have good ductility.

Rolling can also be used to join dissimilar materials in laminates to give improved performance of the final product.

2.5.1 Strip Flow

During rolling the strip is deformed in all 3 dimensions. In cold rolling the strip is typically many times wider than it is thick. For this reason, we can assume that the problem is only 2 dimensional, with deformation occurring to the strip thickness and length. While some transverse effects do occur these are concentrated on the outer edges of the strip, so this assumption is appropriate.

In the preceding calculations isothermal conditions are assumed, this implies that all rolling energy is absorbed by the strip and goes into plastic deformation. However, in practice the plastic deformation actually causes some heating of the strip.

Rolling will alter the grain structure of a metal, making it anisotropic, with elongated grains in the direction of rolling. A sketch showing how the strip material flows through the roll bite can be seen in Figure 2.12.

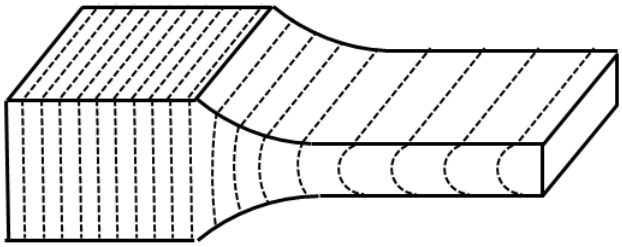

Figure 2.12: Strip Flow

Clearly a reduction in strip thickness requires material flow. It is convenient for our analysis to assume that this is entirely plastic, however in reality a certain amount of elastic recovery occurs, as shown in Figure 2.13.

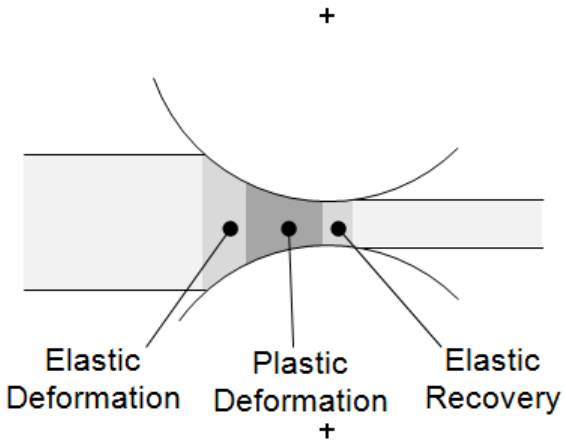

Figure 2.13: Strip Deformation Zones

2.5.2 Strip Deformation Stress

Assuming no strip tension, the minimum normal pressure that needs to be applied to the strip to cause deformation is equal to the compressive yield stress. This has been approximated to 1.155 times the tensile yield stress, σ_{yield} (Nadai, The Forces Required for Rolling Steel Strip Under Tension, 1939). If we take into account the longitudinal stress due to strip tension at the entry of the roll bite, σ_1, then the minimum roll pressure σ_{min} at the entry of the roll bite is:

$$\sigma_{min} = 1.155\sigma_{yield} - \sigma_1 \quad 2.20$$

A similar calculation also applies at the exit of the roll bite.

2.5.3 Von Kármán Approach

One of the most widely used models of pressure distribution was developed by noted aerodynamicist Theodore von Kármán who used a differential equation to model the pressure along the arc of contact (Kármán, 1925).The model is based on the equilibrium forces applied to a slab of metal undergoing plastic deformation between two rollers.

The Von Kármán approach starts by considering a vertical element of the strip between the roll bite entrance and plane of the neutral points (Mukerjee, 1973), as shown in Figure 2.14.

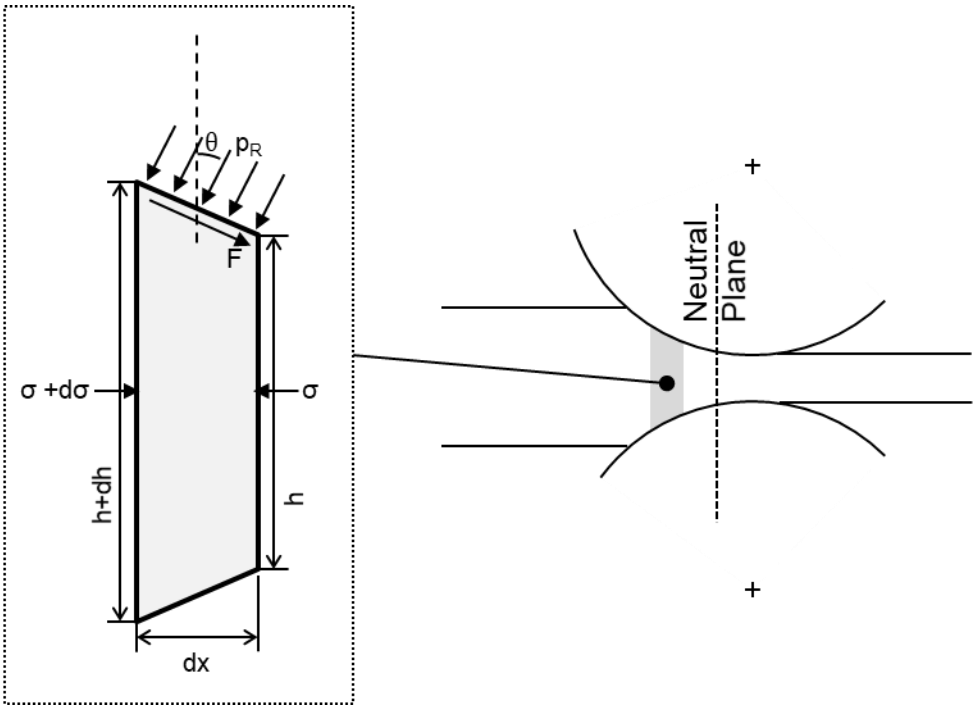

Figure 2.14: Vertical Strip Element used in Von Kármán Formulation

Where σ and $\sigma+d\sigma$ represent the compressive stresses applied to either side of the element. The radial pressure applied by the roll to the strip is p_R at an angle θ which is dependent on the position of the element in the roll bite. This can be converted to radial roll force P_R simply by multiplying by the area of the end of the element:

$$P_R = p_R \frac{dx}{\cos\theta} \quad 2.21$$

The tangential force acting on the end of the element is represented by F. This force can be calculated in terms of p_R using the coefficient of friction μ:

$$F = \mu p_R \frac{dx}{\cos\theta} \quad 2.22$$

The horizontal components of the forces given in Equations 2.21 and 2.22 respectively are given below:

$$P_{R,x} = p_R \tan\theta \, dx \quad (2.23)$$

$$F_x = \mu p_R dx \quad (2.24)$$

These forces can be balanced with the horizontal forces due to the compressive stresses to give:

$$2p_R \tan\theta \, dx - 2\mu p_R dx = (\sigma + d\sigma)(h + dh) - \sigma h \quad (2.25)$$

Then by treating the product of the infinitesimal increments as insignificant and using the product rule we can simplify the equation to:

$$2p_R dx(\tan\theta - \mu) = d(\sigma h) \quad (2.26)$$

We can then calculate the vertical components of the forces given in Equations 2.21 and 2.22 respectively:

$$P_{R,z} = p_R dx \quad (2.27)$$

$$F_z = \mu p_R \tan\theta \, dx \quad (2.28)$$

Equation 2.27 can be substituted into 2.26 to give:

$$2P_{R,z}(\tan\theta - \mu) = d(\sigma h) \quad (2.29)$$

This can be rearranged using the factor rule to give Equation 2.30:

$$P_{R,z}(\tan\theta - \mu) = d\left(\frac{\sigma h}{2}\right) \quad (2.30)$$

The vertical force $F_{R,z}$ can be calculated from the vertical pressure p using the following relationship:

$$P_{R,z} = p_R \frac{dx}{\cos\theta} \cos\theta = p dx \quad (2.31)$$

Substituting this into Equation 2.30 gives:

$$p(\tan\theta - \mu)dx = d\left(\frac{\sigma h}{2}\right) \quad (2.32)$$

A similar analysis can be completed for an element between the neutral plane and exit of the roll bite, the only difference being that the direction of the tangential frictional force is reversed, due to the opposite direction of the slip. This results in the following equation:

$$p(\tan\theta + \mu)dx = d\left(\frac{\sigma h}{2}\right) \quad (2.33)$$

Combining Equations 2.32 and 2.33 results in:

$$p(\tan\theta \pm \mu)dx = d\left(\frac{\sigma h}{2}\right) \quad (2.34)$$

From Figure 2.14 it can be seen that:

$$\tan\theta = \frac{1}{2}\frac{dh}{dx} \quad 2.35$$

Substituting this in and rearranging slightly gives:

$$p\left(\frac{1}{2}\frac{dh}{dx} \pm \mu\right) = \frac{d\left(\frac{\sigma h}{2}\right)}{dx} \quad 2.36$$

The total vertical force acting on the element can be found by combining the component due to the radial force of the roll with that from the friction, Equations 2.28 to give 2.31:

$$F_z + P_{R,z} = \mu p_R \tan\theta\, dx + p dx \quad 2.37$$

Simplifying using Equation 2.31 and rearranging to give a value for the total pressure:

$$\frac{F_z + P_{R,z}}{dx} = p(\mu\tan\theta + 1) \quad 2.38$$

Next Tresca's criteria for plastic yield is considered:

$$\sigma_{max} - \sigma_{min} = \sigma_{yield} \quad 2.39$$

Where σ_{max} is the maximum principal stress, σ_{min} the minimum principal stress and σ_{yield} the yield stress, in this application this is the constrained yield stress of the strip. It is assumed that the vertical stress, from Equation 2.38, is the maximum and the horizontal stress, σ, is the minimum, this results in the following relationship

$$p(\mu\tan\theta + 1) - \sigma = \sigma_{yield} \quad 2.40$$

Substituting this into Equation 2.36 and rearranging gives:

$$p\left(\frac{1}{2}\frac{dh}{dx} \pm \mu\right) = \frac{d\left\{\frac{[p(\mu\tan\theta + 1) - \sigma_{yield}]h}{2}\right\}}{dx} \quad 2.41$$

It is assumed that due to the relatively small angle of contact commonly seen in cold rolling that:

$$\mu\tan\theta \cong 0 \quad 2.42$$

This leaves the following differential equation, widely called Von Kármán's Equation:

$$0 = \frac{d\left[\frac{h}{2}(p - \sigma_{yield})\right]}{dx} - p\left(\frac{1}{2}\frac{dh}{dx} \pm \mu\right) \quad 2.43$$

This is a key result used in the formulation of many models of cold rolling.

2.5.4 Solutions to Von Kármán's Equation

A number of authors have presented solutions to Von Kármán's equation based upon various assumptions. Tselikov (Tselikov, 1939) made the assumption that θ is constant and took the value of half the angle of entry to the roll bite. This allowed a form of Von Kármán's equation that can be directly integrated. Smith (Underwood, 1950) assumed a parabolic, rather than circular, arc of contact. The equation used for this was:

$$\frac{h}{2} = \frac{1}{2}\left[h_1 + d\left(\frac{x}{L}\right)^2\right] \quad 2.44$$

Where *h* is the strip thickness, h_1 is the exit strip thickness, *x* the distance from the exit plane, *d* is the draft and *L* is the projected contact length. Differentiating this expression gives:

$$\frac{1}{2}\frac{dh}{dx} = \frac{dx}{L^2} \quad 2.45$$

Rearranging Equation 2.44 gives:

$$h = h_1 + d\left(\frac{x}{L}\right)^2 \quad 2.46$$

Putting the Equations 2.45 and 2.46 into Von Kármán's Expression, Equation 2.43, yields:

$$0 = \frac{d\left\{\frac{1}{2}\left[h_1 + d\left(\frac{x}{L}\right)^2\right](p - \sigma_{yield})\right\}}{dx} - p\left(\frac{dx}{L^2} \pm \mu\right) \quad 2.47$$

This can then be differentiated and rearranged to give:

$$\frac{d\left(\frac{p}{\sigma_{yield}}\right)}{d\left(\frac{x}{L}\right)} = \frac{\frac{2d}{h_2}\left(\frac{x}{L} \pm \frac{pL\mu}{\sigma_{yield}d}\right)}{1 + \frac{dx^2}{h_2 L^2}} \quad 2.48$$

Trinks (Trinks, 1937) presented a graphical solution to this equation in the form of a number of curves, this allows the average rolling pressure and peak pressure to be easily ascertained for a range of rolling conditions.

Nadai (Nadai, The Forces Required for Rolling Steel Strip Under Tension, 1939) considered the effect of strip tensions and made assumptions of constant μ, constant τ_{xz} and μ proportional to slip velocity. The last of these assumptions was based upon hydrodynamic lubrication with constant oil film thickness and viscosity. The constant viscosity assumption is questionable due to the changes in the lubricant caused by the pressures and temperatures seen in the roll bite.

2.5.5 Orowan Approach

The previous approaches have all assumed homogeneous compression of the strip. Orowan (Orowan, 1943) developed an approach that discarded this assumption.

The model starts by considering expressions developed by Prandtl (Prandtl, 1923) for a strip deformed between two parallel plates. This gives the following expressions for vertical pressure *σ*, horizontal pressure *q* and shear stress *τ*:

$$\sigma = \frac{\sigma_{yield}}{h}x + C \quad 2.49$$

$$q = \frac{\sigma_{yield}}{h}x - \sigma_{yield}\sqrt{1 - \frac{4z^2}{h^2}} + C \quad 2.50$$

$$\tau = -\frac{\sigma_{yield}}{h} z \qquad 2.51$$

Where *h* is the distance between the plates, *x* and *z* are the horizontal and vertical directions respectively and *C* is the constant of integration. This assumes the shear (friction) stress is maximum. If σ drops to zero at the edge of the plate, where $x = \pm L$ then Equation 2.49 can be rearranged to obtain the constant of integration:

$$C = \pm \frac{L\sigma_{yield}}{h} \qquad 2.52$$

This results in the stresses shown in as shown in Figure 2.15.

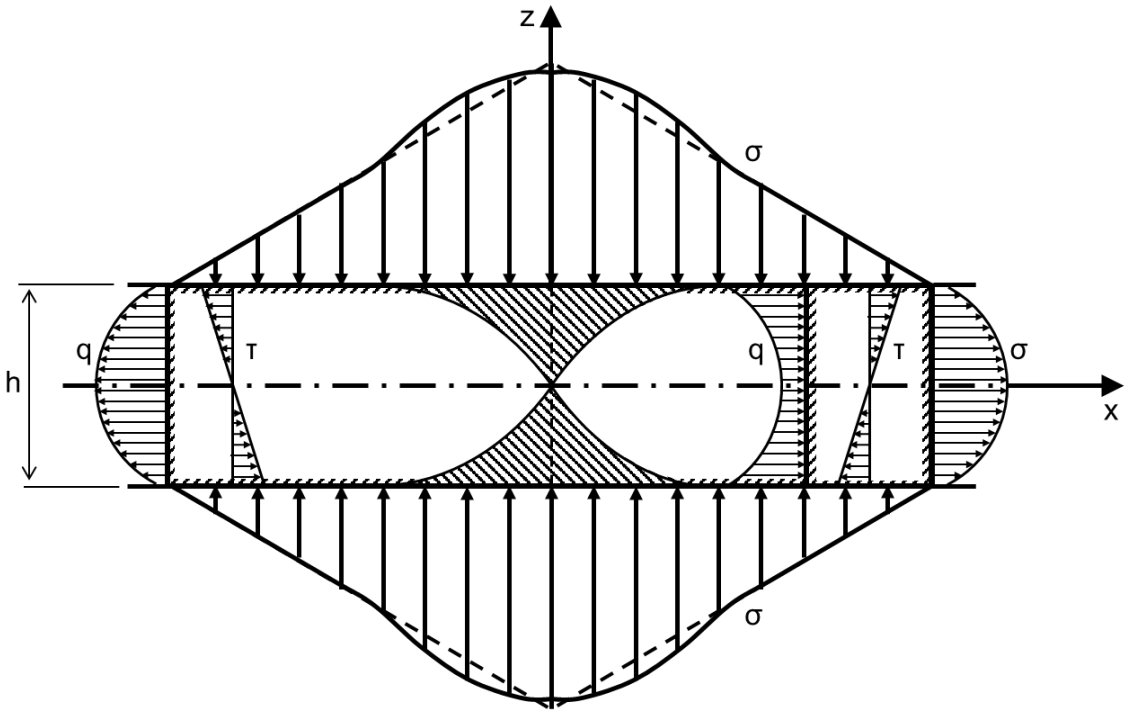

Figure 2.15: Pressures in Compressed Plastic Strip, Reproduced from (Roberts W. L., 1978).

Orowan applied this to cold rolling using an extension to Prandtl's work developed by Nadai (Nadai & Wahl, Plasticity: Mechanics of the Plastic State of Matter, 1931). Here the strip is compressed between two plates each rotated by a small angle θ away from the axis of the strip, as shown in Figure 2.16 .

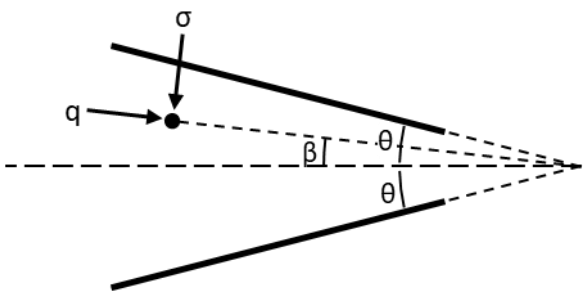

Figure 2.16: Pressures in Compressed Plastic Strip

For flow towards the apex this resulted in the following equations:

$$q = \sigma - \sigma_{yield}\sqrt{1 - \frac{\beta^2}{\theta^2}} \quad 2.53$$

$$\tau = \frac{\sigma_{yield}\beta}{2\theta} \quad 2.54$$

The equations shown so far apply for sticking friction. In order to adapt these for the sliding case Orowan made the assumption that values for *h* and θ could be chosen so that the shear stress τ at the surface equalled $\mu\sigma$ instead of $\sigma_{yield}/2$, as shown here:

$$\mu\sigma h^* = \frac{\sigma_{yield}}{2}h \quad 2.55$$

$$\mu\sigma\theta^* = \frac{\sigma_{yield}}{2}\theta \quad 2.56$$

Where *h** and θ*** are the values chosen to fulfil the above criteria. These values can then be substituted in place of *h* and θ into Equations 2.53 and 2.54 to give:

$$q = \sigma - \sigma_{yield}\sqrt{1 - \left(\frac{2\mu\sigma}{\sigma_{yield}}\right)^2\left(\frac{\beta}{\theta}\right)^2} \quad 2.57$$

$$\tau = \frac{\mu\sigma\beta}{\theta} \quad 2.58$$

The next step is to consider a vertical element of the strip bounded by surfaces *A* and *A'*. As mentioned earlier Orowan's approach doesn't assume homogeneous compression of the strip, this vertical element can have arbitrary shape.

The horizontal forces acting on surfaces A and A' are given by F and $F - \frac{dF}{d\theta}d\theta$ respectively. The horizontal component of the normal force σ acting on the end of the element is given by $2\sigma R\sin\theta \cdot d\theta$ and the horizontal component of the frictional drag τ is $\pm 2\tau R\cos\theta \cdot d\theta$ where *R* is the roll radius. Balancing all of these horizontal forces gives:

$$\frac{dF}{d\theta} = (\sigma\sin\theta \pm \tau\cos\theta)D \quad 2.59$$

Where *D* is the roll diameter. The variables used in Orowan's formulation are shown in Figure 2.17.

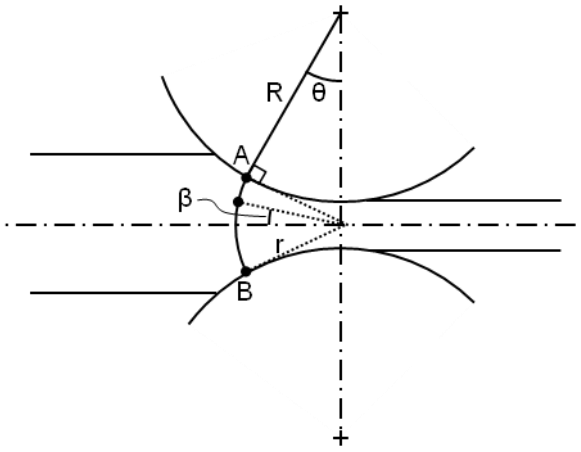

Figure 2.17: Variables used in Orowan Formulation

The length of an element of the arc AB is $rd\beta$ where

$$r = \frac{h}{2\sin\theta} \tag{2.60}$$

Therefore the area of this element for a unit width is given by

$$dA = \frac{h}{2\sin\theta}d\beta \tag{2.61}$$

The component of the horizontal force *dF* that acts across this element is a combination of the contribution from the radial pressure σ and shear stress τ. The contribution from the radial pressure is:

$$q\cos\theta\, dA = q\cos\theta\frac{h}{2\sin\theta}d\beta \tag{2.62}$$

Substituting in q from Equation 2.57 then integrating between the limits $\beta = -\theta$ *to* $+\theta$ gives the contribution of the horizontal force F made by the radial pressure F_q:

$$F_q = 2\int_0^{\theta}\cos\beta\frac{h}{2\sin\theta}\left[\sigma - \sigma_{yield}\sqrt{1-\left(\frac{2\mu\sigma}{\sigma_{yield}}\right)^2\left(\frac{\beta}{\theta}\right)^2}\right]d\beta \tag{2.63}$$

$$F_q = \frac{h\sigma}{\sin\theta}\int_0^{\theta}\cos\beta\, d\beta - \frac{h\sigma_{yield}}{\sin\theta}\int_0^{\theta}\left[\sqrt{1-\left(\frac{2\mu\sigma}{\sigma_{yield}}\right)^2\left(\frac{\beta}{\theta}\right)^2}\right]d\beta\cos\beta\, d\beta \tag{2.64}$$

$$F_q = h\sigma - \frac{h\sigma_{yield}}{\sin\theta}\int_0^{\theta}\left[\sqrt{1-\left(\frac{2\mu\sigma}{\sigma_{yield}}\right)^2\left(\frac{\beta}{\theta}\right)^2}\right]\cos\beta\, d\beta \tag{2.65}$$

Where σ_{yield} is the yield stress. We can simplify by using the following substitutions:

$$b = \frac{2\mu\sigma}{\sigma_{yield}} \tag{2.66}$$

$$w = \frac{1}{\sin\theta}\int_0^{\theta}\left[\sqrt{1 - b^2\left(\frac{\beta}{\theta}\right)^2}\right]\cos\beta\, d\beta \quad 2.67$$

This results in:

$$F_q = h\sigma - h\sigma_{yield}w \quad 2.68$$

Next the contribution to the horizontal force made by the shear stress F_τ is considered.

$$\tau \sin\beta\, dA = \frac{\mu\sigma}{\theta}\beta\sin\beta\frac{h}{2\sin\theta}d\beta \quad 2.69$$

Integrating this by parts results in:

$$F_\tau = \pm 2\frac{\mu\sigma h}{2\theta\sin\theta}\int_0^{\theta}\beta\sin\beta\, d\beta = \pm h\mu\sigma\left(\frac{1}{\theta} - \frac{1}{\tan\theta}\right) \quad 2.70$$

Finally combining Equations 2.68 and 2.70 gives the total horizontal force:

$$F = F_\tau + F_q = h\sigma - h\sigma_{yield}w \pm h\mu\sigma\left(\frac{1}{\theta} - \frac{1}{\tan\theta}\right) \quad 2.71$$

For values of $\mu < 0.2$ and $\theta < 10°$ which are typical of cold rolling, Orowan stated that F_τ is around 1% of $h\sigma$ and can therefore be neglected. This leads to the following simplification:

$$F = h\left(\sigma - \sigma_{yield}w\right) \quad 2.72$$

Substituting this value for q, along with $\tau = \mu\sigma$ due to slipping friction, into Equation 2.59 gives:

$$\frac{dF}{d\theta} = D\left(\frac{F}{h} + \sigma_{yield}w\right)(\sin\theta \pm \mu\cos\theta) \quad 2.73$$

This is Orowan's model. The model requires the calculation of the pressure distribution and the integration of the subsequent curve. This makes the model onerous, and consequently a number of attempts have been made to approximate and thereby simplify the model. Bland and Ford (H. Ford, 1951) formulated an approximation which has since found widespread use.

2.5.6 Bland and Ford Approximation

Bland and Ford (H. Ford, 1951) used the differential equation (Equation 2.59) developed by Orowan thereby adopting the small angle assumption (Lenard, 2013). Taking this equation but representing the shear stress by $\sigma\mu$ and using the deformed roll radius R' in place of the deformed roll diameter we get.

$$\frac{dF}{d\theta} = 2\sigma R'(\sin\theta \pm \mu\cos\theta) \quad 2.74$$

They also assumed that the roll pressure is equal to the stress in the vertical direction. This assumption was considered to result in very small error due to the small angles involved. This resulted in the following closed-form solution presented below. Roll force P_r calculated using this technique is given by:

$$P_r = 2\sigma_{\text{yield}} R' \left\{ \int_0^{\theta_n} \frac{h}{h_1} e^{\mu H} d\theta + \int_{\theta_n}^{\theta_1} \frac{h}{h_0} e^{\mu(H_0 - H)} d\theta \right\} \quad 2.75$$

Where $\theta_n$the angular position of the neutral point, θ_1 the angular distance at the entry to the roll bite, *H* is calculated from the equation below and h_1 is this value at the entry to the roll bite:

$$H = 2\sqrt{\frac{R'}{h_1}} \tan^{-1}\left(\sqrt{\frac{R'}{h_1}}\theta\right) \quad 2.76$$

And the angular distance at the entry to the roll bite θ_1 is:

$$\theta_1 = \sqrt{\frac{h_0 - h_1}{R'}} \quad 2.77$$

The position of the neutral point θ_n is calculated from:

$$\theta_n = \sqrt{\frac{h_1}{R'}} \tan\frac{H_n}{2} \sqrt{\frac{h_1}{R'}} \quad 2.78$$

Where H_n is:

$$H_n = \frac{H_0}{2} - \frac{1}{2\mu} ln\left(\frac{h_0}{h_1}\right) \quad 2.79$$

Sims (Sims, 1954) developed a model using a similar approach which is not detailed here.

2.6 Roll Stress

As with the contact length, the Hertzian assumption of an elastic cylinder on plate (modelled as a cylinder of infinite radius) can be used to obtain a value for the maximum stress in the contact, as given in Equation 2.80 (Hertz, 1896).

$$\sigma_{max} = 0.798 \sqrt{\frac{f}{2R\left(\frac{1-\upsilon_1^2}{E_1} + \frac{1-\upsilon_2^2}{E_2}\right)}} \quad 2.80$$

Where σ_{max} is the maximum stress, *f* is force per unit width, *R* is the roll radius, *v* is the Poisson's ratio and *E* the Young's modulus, with subscripts *1* and *2* denoting the cylinder and plate respectively. This value assumes an elliptical stress distribution, with the maximum at the centre of the contact.

Although the maximum value and distribution of stress across the contact are of great interest in rolling, also of interest is the distribution of stress within the roll. This is important for roll design to ensure adequate roll life and reduce degradation

For simplicity the analysis has used the stick-slip stress distributions given in Equations 2.17 and 2.19 although as recognised earlier in this chapter, these represent significant simplifications of the distributions seen in real world rolling. Figure 2.18 shows the definitions used in the following analysis.

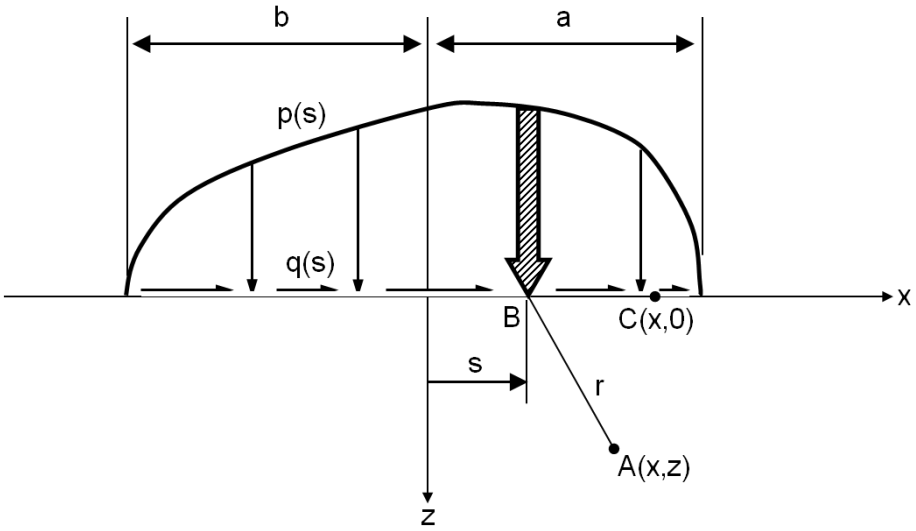

Figure 2.18: Schematic of Variables used in the Calculation of Hertzian Stress Distribution, redrawn from (Johnson, 1987).

In this analysis the stress distribution is symmetrical therefore *a=b*. The orthogonal normal and shear stresses in the x-z plane can be calculated from classical elastic mechanics (Johnson, 1987) and are given in Equations 2.81, 2.82 and 2.83.

$$\sigma_x(x,z) = -\frac{2z}{\pi}\int_{-L/2}^{L/2}\frac{p_z(s).(x-s)^2}{[(x-s)^2+z^2]^2}ds - \frac{2}{\pi}\int_{-L/2}^{L/2}\frac{p_x(s).(x-s)^3}{[(x-s)^2+z^2]^2}ds \quad 2.81$$

$$\sigma_z(x,z) = -\frac{2z^3}{\pi}\int_{-L/2}^{L/2}\frac{p_z(s)}{[(x-s)^2+z^2]^2}ds - \frac{2z^2}{\pi}\int_{-L/2}^{L/2}\frac{p_x(s).(x-s)}{[(x-s)^2+z^2]^2}ds \quad 2.82$$

$$\tau_{xz}(x,z) = -\frac{2z^2}{\pi}\int_{-L/2}^{L/2}\frac{p_z(s).(x-s)}{[(x-s)^2+z^2]^2}ds - \frac{2z}{\pi}\int_{-L/2}^{L/2}\frac{p_x(s).(x-s)^2}{[(x-s)^2+z^2]^2}ds \quad 2.83$$

Into these equations we can substitute the relationships for normal and tangential stress, Equations 2.17 and 2.19, and normalise with respect to the contact width a by substituting in $x/a = i$, $z/a = j$ and $s/a = t$ to get:

$$\sigma_x(i,j) = -\frac{4p_n}{b\pi^2}[jI_{x1} + \mu I_{x2}(\xi) + \mu I_{x3}(\xi)] \quad 2.84$$

$$\sigma_z(i,j) = -\frac{4p_n j^2}{b\pi^2}[jI_{z1} + \mu I_{z2}(\xi) + \mu I_{z3}(\xi)] \quad 2.85$$

$$\tau_{xz}(i,j) = -\frac{4p_n j}{b\pi^2}[jI_{xz1} + \mu I_{xz2}(\xi) + \mu I_{xz3}(\xi)] \quad 2.86$$

Where,

$$I_{x1} = \int_{-1}^{1}\frac{\sqrt{1-t^2}(i-t)^2}{[(i-t)^2+j^2]^2}dt \quad 2.87$$

$$I_{x2}(\xi) = \int_{-1}^{1-2\xi}\frac{\sqrt{1-t^2}(i-t)^3}{[(i-t)^2+j^2]^2}dt \quad 2.88$$

$$I_{x3}(\xi) = \int_{1-2\xi}^{1}\frac{\left[\sqrt{1-t^2}-\sqrt{\xi^2-(\xi+t-1)^2}\right](i-t)^3}{[(i-t)^2+j^2]^2}dt \quad 2.89$$

$$I_{z1} = \int_{-1}^{1} \frac{\sqrt{1-t^2}}{[(i-t)^2+j^2]^2}\,dt \qquad 2.90$$

$$I_{z2}(\xi) = \int_{-1}^{1-2\xi} \frac{\sqrt{1-t^2}(i-t)}{[(i-t)^2+j^2]^2}\,dt \qquad 2.91$$

$$I_{z3}(\xi) = \int_{1-2\xi}^{1} \frac{\left[\sqrt{1-t^2}-\sqrt{\xi^2-(\xi+t-1)^2}\right](i-t)}{[(i-t)^2+j^2]^2}\,dt \qquad 2.92$$

$$I_{xz1} = \int_{-1}^{1} \frac{\sqrt{1-t^2}(i-t)}{[(i-t)^2+j^2]^2}\,dt \qquad 2.93$$

$$I_{xz2}(\xi) = \int_{-1}^{1-2\xi} \frac{\sqrt{1-t^2}(i-t)^2}{[(i-t)^2+j^2]^2}\,dt \qquad 2.94$$

$$I_{xz3}(\xi) = \int_{1-2\xi}^{1} \frac{\left[\sqrt{1-t^2}-\sqrt{\xi^2-(\xi+t-1)^2}\right](i-t)^2}{[(i-t)^2+j^2]^2}\,dt \qquad 2.95$$

From σ_x, σ_z and $\tau_{xz}$the two principal stresses can be calculated using the well know formulas, Equations 2.96 and 2.97.

$$\sigma_{1,xz} = \frac{\sigma_x+\sigma_z}{2} + \sqrt{\left(\frac{\sigma_x-\sigma_z}{2}\right)^2+\tau_{xz}^2} \qquad 2.96$$

$$\sigma_{2,xz} = \frac{\sigma_x+\sigma_z}{2} - \sqrt{\left(\frac{\sigma_x-\sigma_z}{2}\right)^2+\tau_{xz}^2} \qquad 2.97$$

In order to draw a picture of the stress conditions within the roll this set of equations must be solved for each point in the x-z plane. To demonstrate the form of the various stress distributions these equations were solved using values for stick-slip ratio and friction coefficient of ξ=0.2 and, μ=0.3. As only the shape of the distributions is of interest at this stage the stresses have been normalised. Calculating such a large set of equations by hand is both impractical and unnecessary, instead a computer script was written to solve these. Contour plots of the results are given in Figure 2.19 with a contour interval of 10%. Positive normal stress represents tension and positive shear stress is in positive x-direction, the direction of rolling.

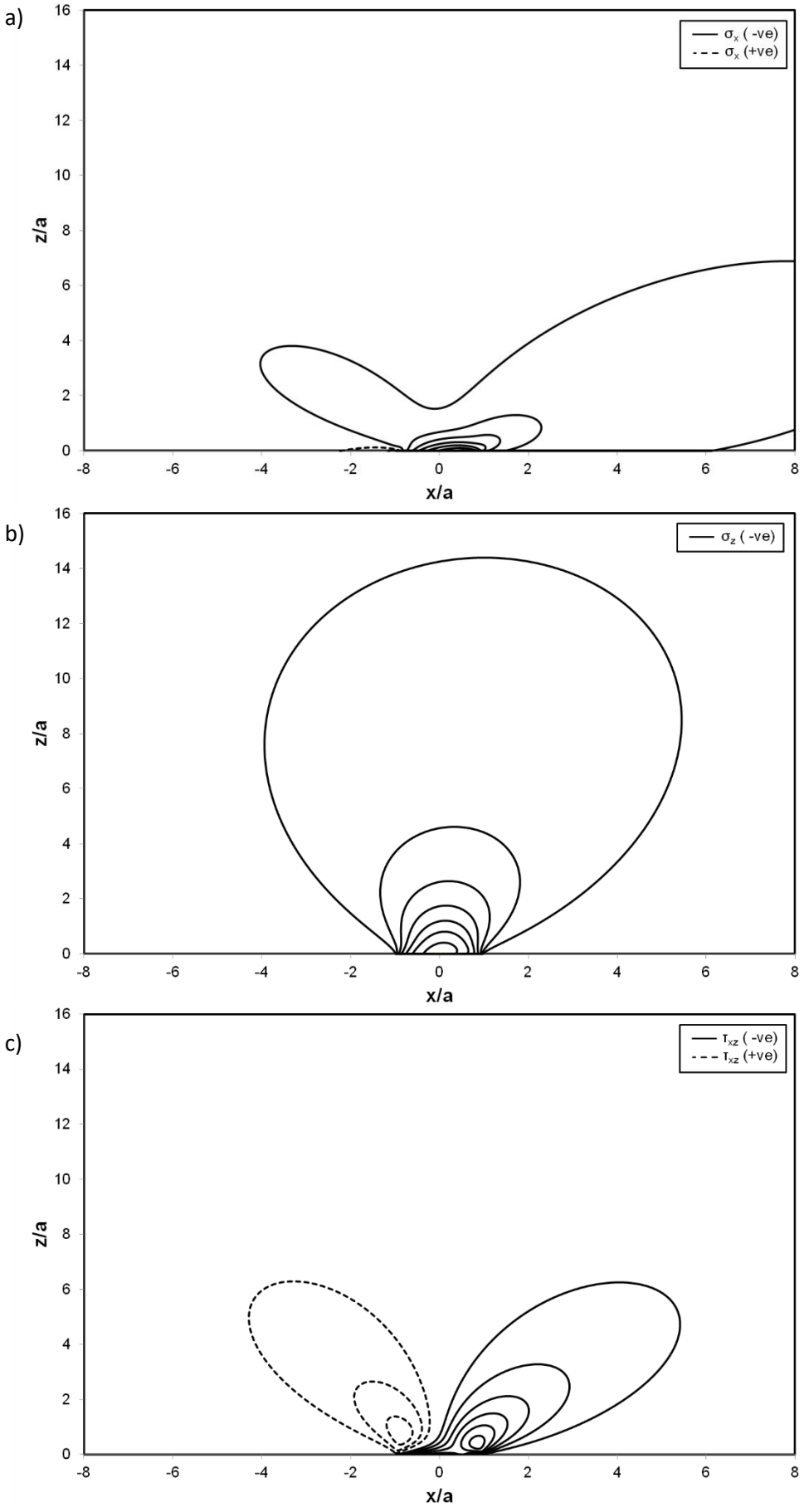

Figure 2.19: Stress distribution patterns with ξ=0.2, μ=0.3, peak stresses have been normalised to unity and contours are drawn at 10% intervals a) σ_x b) σ_z c) τ_{xz}

The average of each stress type in the z direction (from z/a of 0 to 16) is of particular interest later in this thesis. The average of the values plotted in Figure 2.19 are shown in Figure 2.20.

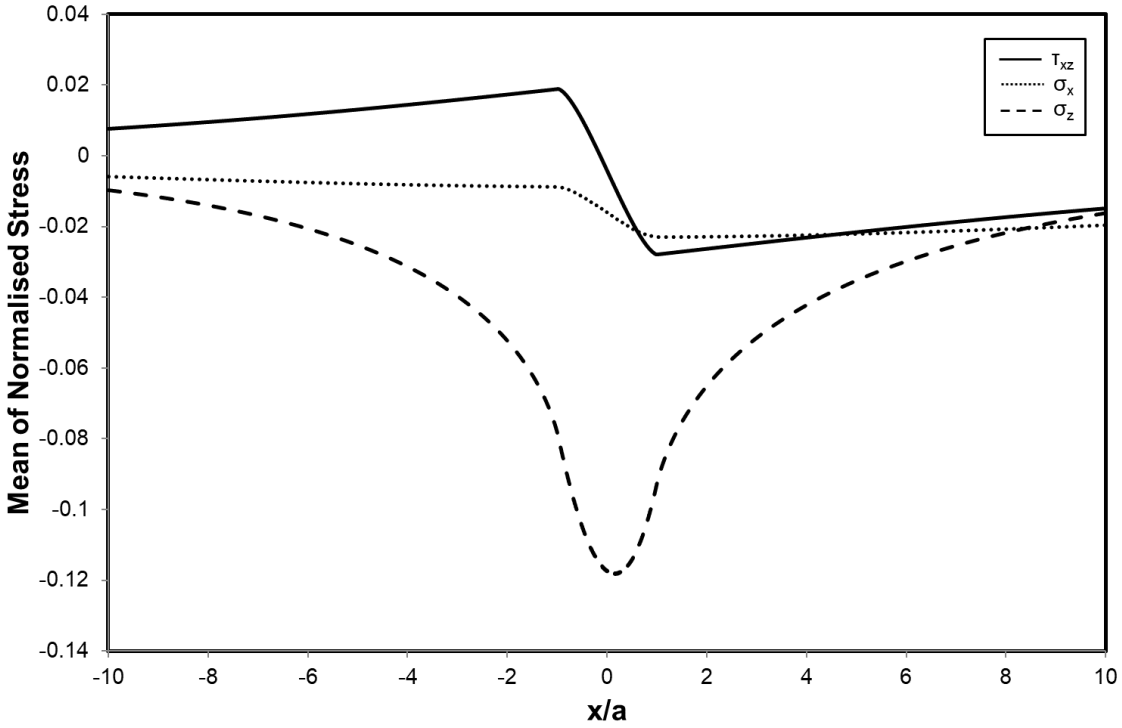

Figure 2.20: Mean of normalised stresses in the z-direction.

The shear stress switches sign in the contact patch, while the normal stress in the z direction shows only compression as expected. The normal stress also varies continuously to form a dip, no sharp changes are seen unlike with the shear stress.

2.7 Roll Bending

In typical mill construction the work rolls are held in bearings at either end, but the strip is rolled across the centre of the roll barrel. This means as well as deformation of the roll radius, the roll will bend along its axis, as shown in Figure 2.21. This can make it hard to ensure the correct strip thickness, and cause inconsistent wear. Backup rolls can be used to reduce this. Roll *Crowning* or *Cambering*, the practice of giving the roll surface a slight curve, can also be used to compensate for this effect. It is especially important for rolls with a low aspect ratio, a long axial length to barrel diameter, for high rolling pressures or for applications where a consistent transverse profile of the strip is important.

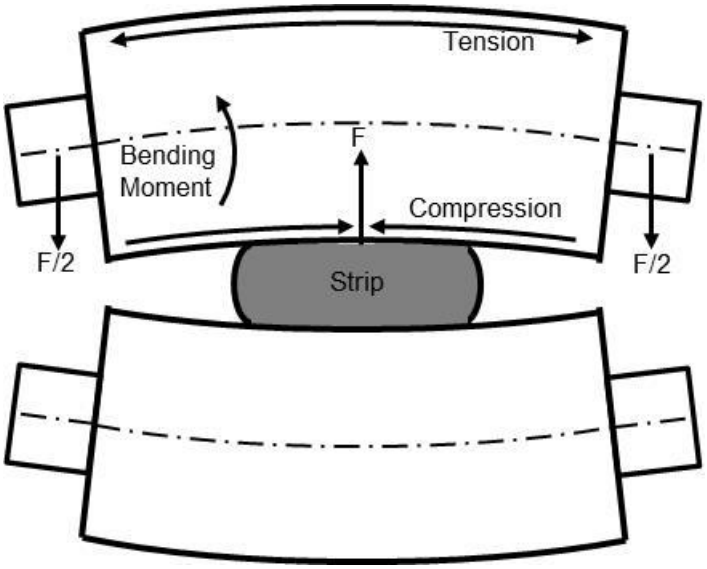

Figure 2.21: Schematic of Roll Bending (Roberts W. L., 1969).

Maximum roll deflection, Δ, occurs at the centre of the roll. Rowe (Rowe, 1977) calculated this to be:

$$\Delta = \frac{PL_y{}^2(5L_y + 24c)}{6\pi E D^4} + \frac{PL_y}{2\pi G D^2} \qquad 2.98$$

Where *P* is the uniform rolling force across the roll, L_y is the centre to centre distance between the bearings, *c* is the half the bearing width, *E* is the Young's Modulus, *G* the shear modulus and *D* the roll diameter. The augend in this equation results from the bending stresses while the addend results from the shear stresses.

2.8 Rolling Lubricants

The following section discusses lubricants and the lubrication methods used in cold rolling.

2.8.1 Why use Lubricant?

The key purpose for using rolling lubricant is to reduce the rolling force required for strip deformation. This reduces the energy consumption of the mill. Rolling force is reduced by controlling the friction in the roll bite. In doing so it also results in several added benefits. Reducing the rolling force makes attaining the required strip flatness easier. It also reduces stress and wear of the roll. As shown earlier there is relative velocity between the strip and roll, which results in frictional stresses. This friction combined with the plastic deformation of the strip results in heat generation. In addition to the lubricating effects of the lubricant it also acts as a coolant, reducing both the roll and strip temperatures. Finally by forming a coating on the recently reduced strip the lubricant prevents oxidisation and corrosion (Roberts W. L., 1978). Correct use of rolling lubricant is therefore important.

A better understanding of rolling lubricant conditions and the associated frictional characteristics enable better operation of rolling facilities, aid mill design and provide better information to input into mathematical and computational models. More effective and efficient use of lubricant can also enable economies by reducing the quantities required.

2.8.2 Types of Lubricant and Properties

Lubricants are most commonly applied as aqueous emulsions, known as rolling solutions, with oil concentrations varying between 3 and 15% (Roberts W. L., 1969). The oil is made by combining a base oil with a selection of lubricant additives, emulsifiers, defoamers, antioxidants and rust inhibitors (Roberts W. L., 1969) (Dubey, Sharma, Shishodia, & Sekhon, 2005).

2.8.3 Lubrication Systems

The lubricant is applied on the entry side of the mill. There are a number of approaches for applying the lubricant, typically they fall into one of two categories *direct application* and *recirculation*.

In direct application systems the lubricant is applied once and then discarded. This can be either applied as a neat oil spray, an emulsion premixed using a metering system or an emulsion applied through separate water and oil supply systems. When an emulsion the oil "plates-out" on the strip and roll. When pure oil is used the spray is typically a fine mist created using an atomizer, such as a Grammer or electrostatic oiler (Roberts W. L., 1978). This approach can apply a lubricant film layer on the strip with much greater uniformity than the plate out approach.

Recirculation systems apply the lubricant in copious amounts but recapture and reuse the excess to reduce costs and waste. Recirculation requires much more stable lubricant emulsions. The oil must remain emulsified for the time taken to recirculate the lubricant, while in direct application systems it only needs for the time taken to apply the emulsion

In some cases the lubricant may already be present on the strip from previous processes in the manufacturing line, such as pickling. Recirculated rolling lubricant may also be used to lubricate the bearings although normally only in cluster mills.

2.8.4 Lubrication Regimes

Cold rolling is thought to exhibit a range of lubrication regimes depending upon the lubricant and rolling conditions. Hydrodynamic lubrication occurs when two surfaces are fully separated by a lubricant layer which is several times greater than the roughness of the surfaces. This can either be achieved hydrostatically by entrapping the lubricant, or more commonly by the wedge effect where the viscosity of the lubricant combined with the relative motion of the two surfaces causes a buildup of lubricant layer thickness. This happens for higher viscosity lubricants, high sliding speeds and relatively low loads. Such lubrication conditions are rarely seen in cold rolling and only occur at very high rolling speeds and low reductions (Halmos, 2005).

For higher loads the higher shear stress causes a pressure increase. This increased pressure causes significant elastic deformation of the metal surfaces a regime known as Elastohydrodynamic Lubrication (EHD or EHL) (Halmos, 2005). At even higher pressures this can result in Plastohydrodynamic (PHD) lubrication, plastic deformation of the surfaces. EHD and PHD occur with very thin films or mixed lubrication. Mixed lubrication is where there is no continuous film and the load is supported by a combination of asperity contact and lubricant pockets.

Boundary Lubrication occurs where a thin layer of lubricant physically adheres to the surfaces due to molecular or chemical forces, this results in much thinner films and higher frictions than

those seen in EHD. Unlike hydrodynamic or EHD lubrication where the bulk lubricant properties such as viscosity are the key characteristic, here the chemical properties of the lubricant are more important.

Initially it was believed that boundary lubrication was ubiquitous for all types of rolling and for this reason many rolling models assumed a constant coefficient of friction. However it was realised that both the viscosity of the lubricant and rolling speed influenced the frictional conditions in the roll bite. This has led to the proposition that hydrodynamic effects are taking place. Despite this even at very high speeds it is still widely thought unlikely that the fluid film is continuous in nature and therefore not fully hydrodynamic.

More recently Micro-Plasto-Hydrodynamic Lubrication (MPH) theory has been developed to better explain the lubricant conditions between asperity contacts where the workpiece is plastically deforming (Sutcliffe, Surface Finish and Friction in Cold Metal Rolling, 2002) (Laugier, et al., 2014). This theory states that it may be possible to generate a very thin film even in the contact areas of mixed lubrication. This works on the idea that lubricant is entrapped in pockets between the roll and the strip. As the reduction due to plastic deformation of the strip reduces the volume of these pockets the lubricant is pressurised. Eventually the lubricant reaches a sufficient pressure to escape resulting in a thin local lubricant layer.

2.8.5 Lubrication Characterisation

Initially rolling lubricants were characterised by their effective viscosity, obtained by multiplying the viscosity of water by a factor based upon the concentration of oil, an approach most notably adopted by Albert Einstein in his doctorial thesis (Einstein, 1906). However it was shown that this does not adequately explain the behaviour of the emulsion in the roll bite (Wilson, Sakaguchi, & Schmid, A Dynamic Concentration Model for Lubrication with Oil-in-Water Emulsions, 1993).

Subsequently a different approach known as the ‘Plate-Out’ theory was developed and used by a number of authors (Dubey, Sharma, Shishodia, & Sekhon, 2005). It was found that even a small increase in oil content resulted in a substantial increase in the film thickness in the roll bite. In contradiction of the plate-out theory it was shown that when the supply of emulsion to the roll bite was limited, oil droplets where forced out of the contact resulting in a thin film composed only of water residue (Wan, Kenny, & Spikes, 1984).

Current thinking is based on the concept of ‘Dynamic Concentration’ (Wilson, Sakaguchi, & Schmid, A Dynamic Concentration Model for Lubrication with Oil-in-Water Emulsions, 1993). This theory predicts that the higher viscosity of oil in comparison to water causes it to be favourably entrained in the roll bite. This predicted that increased oil concentration, but also droplet size, result in thicker oil films. It has however been observed that at higher rolling speeds large oil droplets do not enter the contact zone due to the flow of expelled water. This results in only the small droplets near the roll and strip surfaces being drawn into the roll bite.

As neither fully hydrodynamic assumption nor a single friction coefficient could be used to create an adequate model for any rolling conditions an approach based upon two frictional characteristics of the lubricant was adopted. In this approach a lubricant is empirically evaluated to give two frictional characteristics, typically denoted K_1 and K_2 (Roberts W. L., 1969, p. 323). These can then be used to calculate the friction coefficient for a given rolling speed, roll diameter

and draft. The coefficient can even be adjusted for different work roll roughness's using this approach.

Although lubricant is often applied as an emulsion, its concentration will vary across the roll bite. As previously highlighted at the entry to the roll bite the strip is moving slower than the roll. This has the effect of drawing in the more viscous oil and forcing out the water in the emulsion, Figure 2.4. This results in the concentration of oil in the roll bite being much higher than the applied emulsion

2.8.6 Lubricant Solidification

The contacts under consideration have both very high loads, enough to plastically deform metal, and potentially geometrically constrained lubricant pockets. This may result in very high lubricant pressures and possibly even lubricant solidification. This is where the lubricant can no longer be adequately described as a liquid, the viscosity will lose its importance and the stresses and flow within the lubricant are defined by its solid properties. This happens when the lubricant is compressed above its glass transition pressure causing an amorphous structure to be frozen into the lubricant preventing the molecules from moving freely (Jacobson, 1991). The required pressure for solidification increases with increased temperature.

The bulk modulus of the lubricant increases steeply with compression and it has been shown that "at pressures above the solidification pressure the bulk modulus is about ten times larger than at ambient pressure" (Jacobson, 1991). It is clear that some consideration should therefore be given to whether the lubricant has solidified when studying in detail the lubricant properties of a given rolling contact**.**

2.9 Existing Roll Bite Measurement Techniques

The nature of the rolling interface makes in-situ measurements difficult. Roll bite length was measured by Orowan (Orowan, 1943) using a 2-high mill to roll brass and steel strip. The mill was quickly stopped and the shape of the partially rolled strip studied. With this approach a noticeable bump was observed in the roll bite when rolling brass. This corresponded to a pressure peak part way through the roll bite as proposed by Orowan. Using this technique, it was relatively straightforward to determine the entry to the roll bite, due to the clear angle induced in the strip, however the exit point was much harder to ascertain, making accurate determination of the roll bite length impossible. This method is also unsuitable for measurements in an industrial setting.

Video of strip during rolling was taken and used to assess the length of the roll bite arc by Kobasa and Schultz (Kobasa & Schultz, 1968) as shown in Figure 2.22. This technique meant that the zones of elastic deformation and recovery, in addition to the zone of plastic deformation, could be observed.

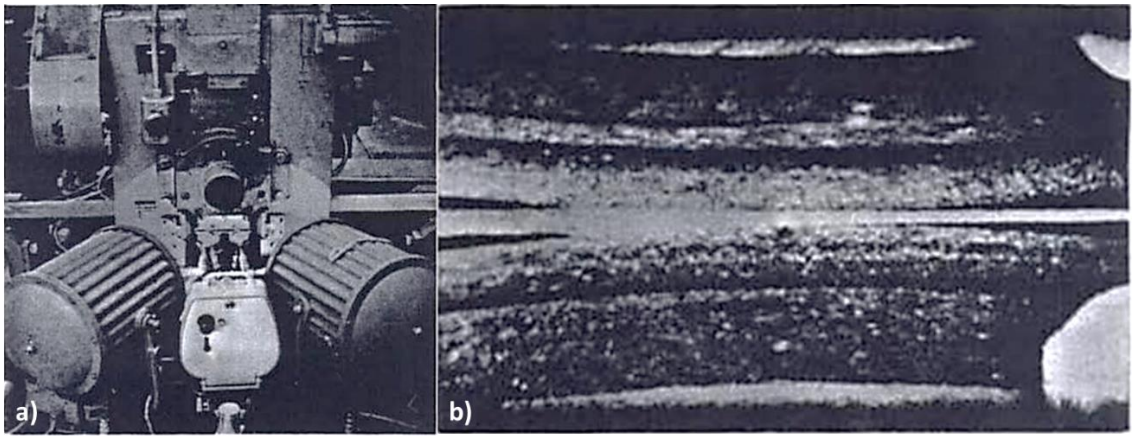

Figure 2.22: High Speed Camera recording of Roll Bite by Kobasa and Schultz a) Video Equipment Used b) Side View of the Roll Bite (Kobasa & Schultz, 1968).

The pressure distribution acting on a roll surface has been the subject of many studies using a pressure pin technique, first developed by Siebel and Lueg (Seibel & Lueg, Untersuchungen über die Spannungsverteilung im Walzspalt [Investigations into the Distribution of Pressure at the Surface of the Material in Contact with the Rolls], 1933) and later refined Van Rooyen and Backofen (Van Rooyen & Backofen, 1957), as shown in Figure 2.23. This involves attaching a pin or cone onto a pressure transducer, and mounting this within the roll so that the pin is exposed to the rolling interface. This requires modification of the rolling surface and therefore results in marking of the rolled product. Using a similar radial pin technique, but including either a lateral force transducer or oblique pin, allows for the frictional stress profile on the roll bite to be recorded (Van Rooyen & Backofen, 1957) (Matsuoka & Motomura, 1968) (Liu, Tieu, Wang, & Yuen, Friction Measurement in Cold Rolling, 2001). An example of such a setup is shown in Figure 2.24.

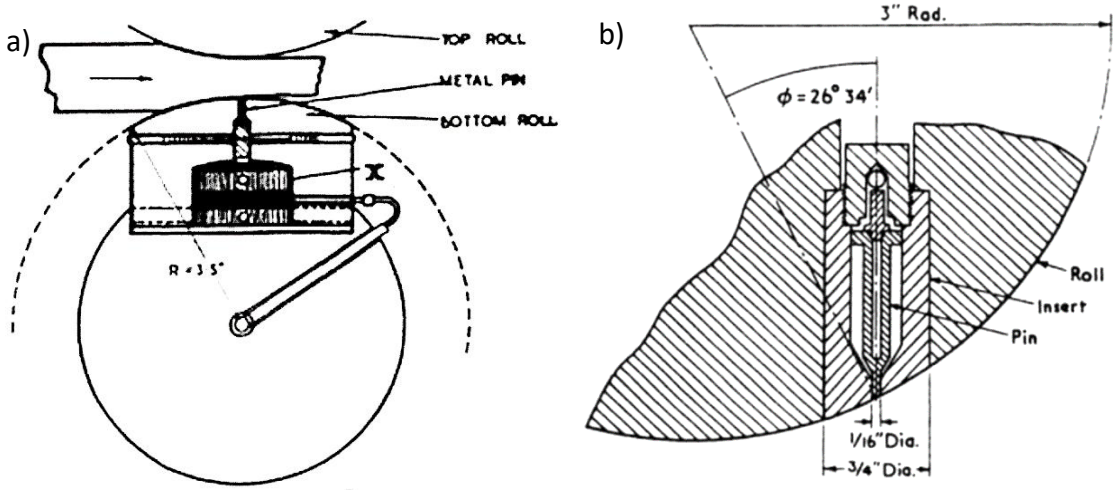

Figure 2.23: Pressure Pin Technique a) Developed by Seibel and Lueg **(Seibel & Lueg, Untersuchungen über die Spannungsverteilung im Walzspalt [Investigations into the Distribution of Pressure at the Surface of the Material in Contact with the Rolls], 1933)** b) Refined by Van Rooyen and Backofen (Van Rooyen & Backofen, 1957).

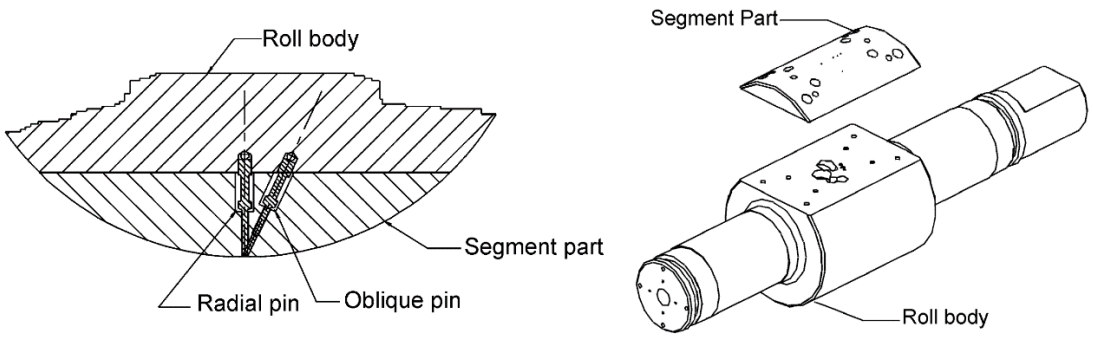

Figure 2.24: Radial and Oblique Pin Technique employed by Liu et. al. (Liu, Tieu, Wang, & Yuen, Friction Measurement in Cold Rolling, 2001).

Various instrumentation approaches have been attempted which have the aim of sensing stress in the roll, as shown in Figure 2.25. These typically use resistance strain gauges although piezoelectric elements have also been applied. These can be placed either in internal voids within the roll, or on the side of the roll outside of the roll bite. Both these approaches require the peak and surface stress to be extrapolated.

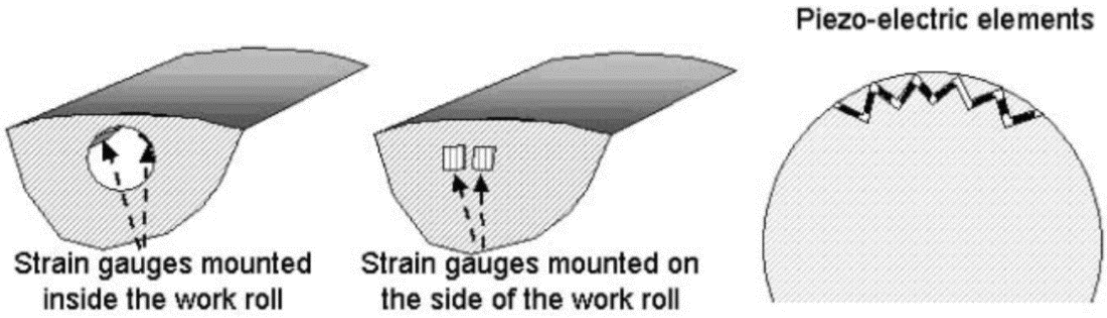

Figure 2.25: Strain Gauge and Piezo Techniques (Jeswiet, Arentoft, & Henningsen, 2006).

Strain gauges can also be used in conjunction with roll inserts designed to deform in a known manner. One such example is the 'Portal Frame Sensor' as shown below in Figure 2.26. The two legs of the frame are instrumented with strain gauges and deform under stress. The nature of this deformation can be detected by the strain gauges and the normal and friction forces inferred. As with the pin technique this still requires significant modification of the roll, and subsequently marks the strip. The rolling face of this sensor type is much larger than the roll bite contact length. Although this means it will not have the resolution achievable with the pin technique, it will also cause less disruption to the rolling interface.

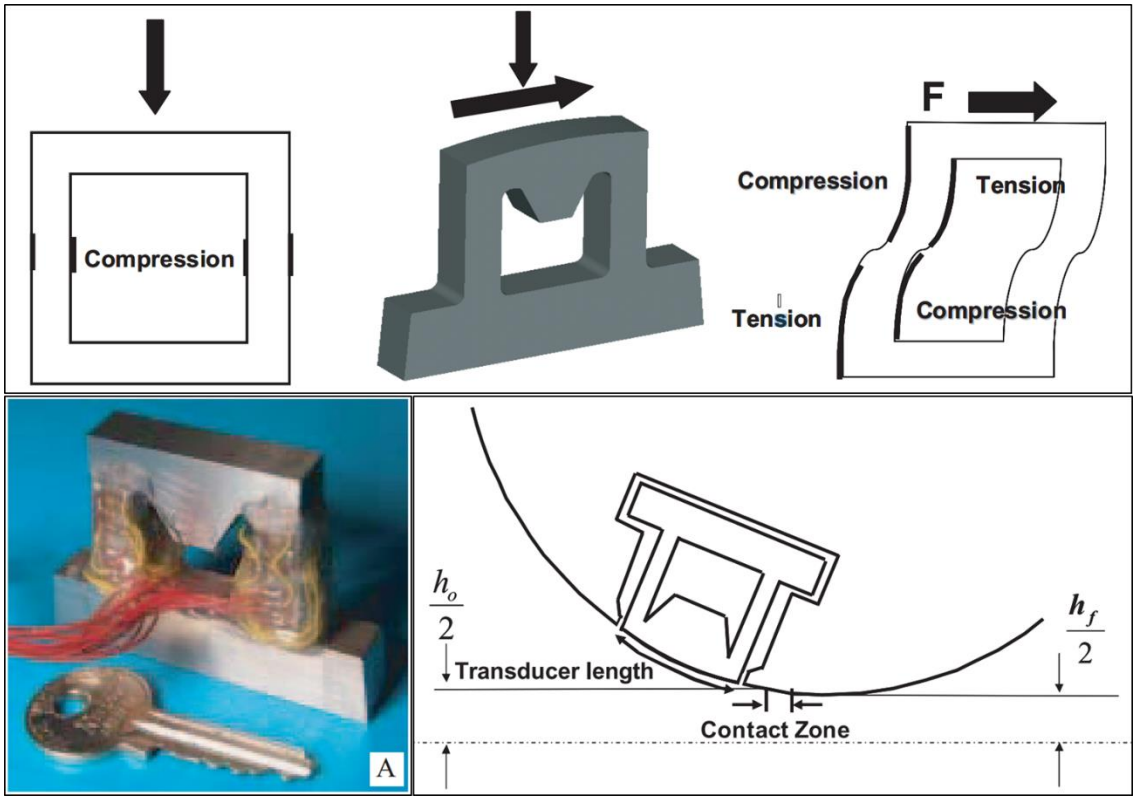

Figure 2.26: A Portal Frame Sensor developed by Henningsen et. al. (Henningsen, Arentoft, & Wanheim, 2006).

No studies have yet measured the roll bite lubricant film thickness in-situ. Several techniques have been employed in other applications which may be applicable to cold rolling. These include optical florescence (Ford & Foord, Laser-based Fluorescence Techniques for Measuring Thin Liquid Films, 1978) (Cameron & Gohar, Optical Measurement of Oil Film Thickness under Elasto-hydrodynamic Lubrication, 1963), capacitive (Grice N. , Sherrington, Smith, O'Donnell, & Stringfellow, 1990) and resistive (Palacio & Bhushan, Surface potential and resistance measurements for detecting wear of chemically-bonded and unbounded molecularly-thick perfluoropolyether lubricant films using atomic force microscopy, 2007) approaches. Work jointly performed between the University of Sheffield and the University of Bristol used ultrasonic techniques to measure the lubricant films in a range of engineering components including hydrodynamic bearings (Dwyer-Joyce, Harper, Pritchard, & Drinkwater, 2006) and mechanical seals (Reddyhoff, Dwyer-Joyce, & Harper, A New Approach for the Measurement of Film Thickness in Liquid Face Seals, 2006).

2.10 Conclusions

It has been shown in this chapter that the theory behind cold rolling is well developed, with numerous authors having established models which can be used to estimate most key rolling parameters including friction, interface normal and shear stress, contact size, slip, strip and roll velocity and strip reduction. Experimental work has been completed that demonstrates the validity of these models under laboratory conditions. There is a benefit in measuring many of these parameters on real-world rolling mills to provide inputs to these models, allow tailoring of the models to specific rolling mills and materials, and therefore enable a more precise understanding and control of the rolling process.

Modern rolling mills are well instrumented and many of the parameters of interest are recorded as a matter of course. However, measurements taken on industrial mills are normally recorded away from the roll bite, such as strip entry and exit tensions, roll normal force and roll torque. These measurements therefore only infer the roll bite condition. Few direct measurements of the roll bite are taken and no technology exists to measure some parameters, such as lubricant film thickness.

The lubrication conditions of the interface are important for efficient mill operation and product quality. These conditions are complex and highly dependent on a range of factors including rolling parameters, strip surface roughness, lubricant formulation, emulsion percentage and application method. All of these parameters, and their interactions, must be understood in order to effectively emulate a specific rolling case. This makes modelling of the interface a complex and involved process. Models do not exist that make case-by-case modelling practical for commercial applications. A more reliable approach would be to measure rather than model the lubricant conditions.

Of the measurement options for studying the roll bite that do exist, few are industrially applicable. This has limited these measurements of the roll bite to the research environment. Rolling mill development and process monitoring would therefore benefit from in-situ measurements which could enable more precise monitoring and control of the rolling conditions.

3 Ultrasonic Waves in Elastic Media

This chapter gives an overview of the mathematical models that describe the behaviour of ultrasonic waves in elastic media and at the interface between acoustically dissimilar materials. These are presented due to their importance in developing measurements introduced later in this thesis. The mathematical models presented can be traced back to Newton and Hooke in the 17th century. Only a concise introduction, covering the aspects required in this thesis, is given here.

3.1 Definition of Ultrasound

The electromagnetic spectrum varies from radio waves and infrared, through visible light to ultraviolet, gamma rays and x-rays. The sound spectrum draws a neat parallel to this. The audible range of sound wave frequencies, called sonic waves, can be thought of as the equivalent of visible light. The frequency, or pitch, of a sound wave is the equivalent of colour and the amplitude is the equivalent of luminosity. As with electromagnetic waves, human senses only detect a certain range of sound wave frequencies. Although this range is impressive, covering several orders of magnitude, it still only represents a fraction of the full spectrum. Frequencies below the lower cut-off of normal human hearing, 20Hz, are referred to as infrasound. Such waves are the staple of seismologists. Ultrasound is defined as those waves with a frequency above 20 kHz, the limit of normal human hearing. Above 1GHz sound waves enter the hypersonic regime. Unlike electromagnetic waves sound requires an elastic medium such as a liquid or a solid to propagate.

Wave frequency can be translated into wavelength through the speed of sound of the material carrying the wave, using the relationship given in Equation 3.1.

$$\lambda = c/f \tag{3.1}$$

A sound wave will interact with physical features differently depending upon whether that feature is approximately the same size as the wavelength (or a multiple thereof), sub-wavelength or significantly larger. Therefore the frequency of the wave used must be suited to the size of the feature being inspected. The frequency range normally employed in ultrasonic Non-destructive Testing (NDT) and thickness gauging is 100 kHz to 100 MHz. There are a plethora of reasons why values in this range are used, from the practicality of generating these frequencies to attenuation issues at higher frequencies. It is worth noting the physical characteristics of such frequencies. In a common engineering material such as steel, with an assumed speed of sound of 5880m/s, wave frequencies of 0.1-100MHz translate to wavelengths of 58.8mm-58.8µm.

3.2 Ultrasonic Wave Basics

The following section outlines the basic concepts of ultrasonic wave propagation.

3.2.1 Modes of Ultrasonic Wave

Waves are an oscillatory pattern of particle motion that maintains its shape while propagating through a medium in a stable manner. In gases sound only travels as a simple pressure wave, however in solids the molecule structures can support vibrations in other directions. This allows a number of different types oscillation pattern to be maintained. The manner of these oscillations and their relationship to the wave propagation is described as the waves mode.

Surface or Rayleigh waves have an elliptical particle motion and travel across the surface of a material. Their depth of penetration is approximately equal to one wavelength. Plate waves such as Lamb and Love waves have a complex vibration occurring in materials where the thickness is less than the wavelength of ultrasound introduced into it (Modes of Sound Wave Propagation, n.d.).

The most common methods of ultrasonic examination utilize either longitudinal waves or shear waves. The longitudinal wave is a compression wave in which the particle motion is in the same direction as the propagation of the wave. This forms a pressure wave made of successive compressions and rarefactions. Compression is the point when the most force is being applied to a molecule and rarefaction is the point when the least force is applied. The shear wave is a wave motion in which the particle motion is perpendicular to the direction of the propagation. These two wave modes are shown in Figure 3.1.

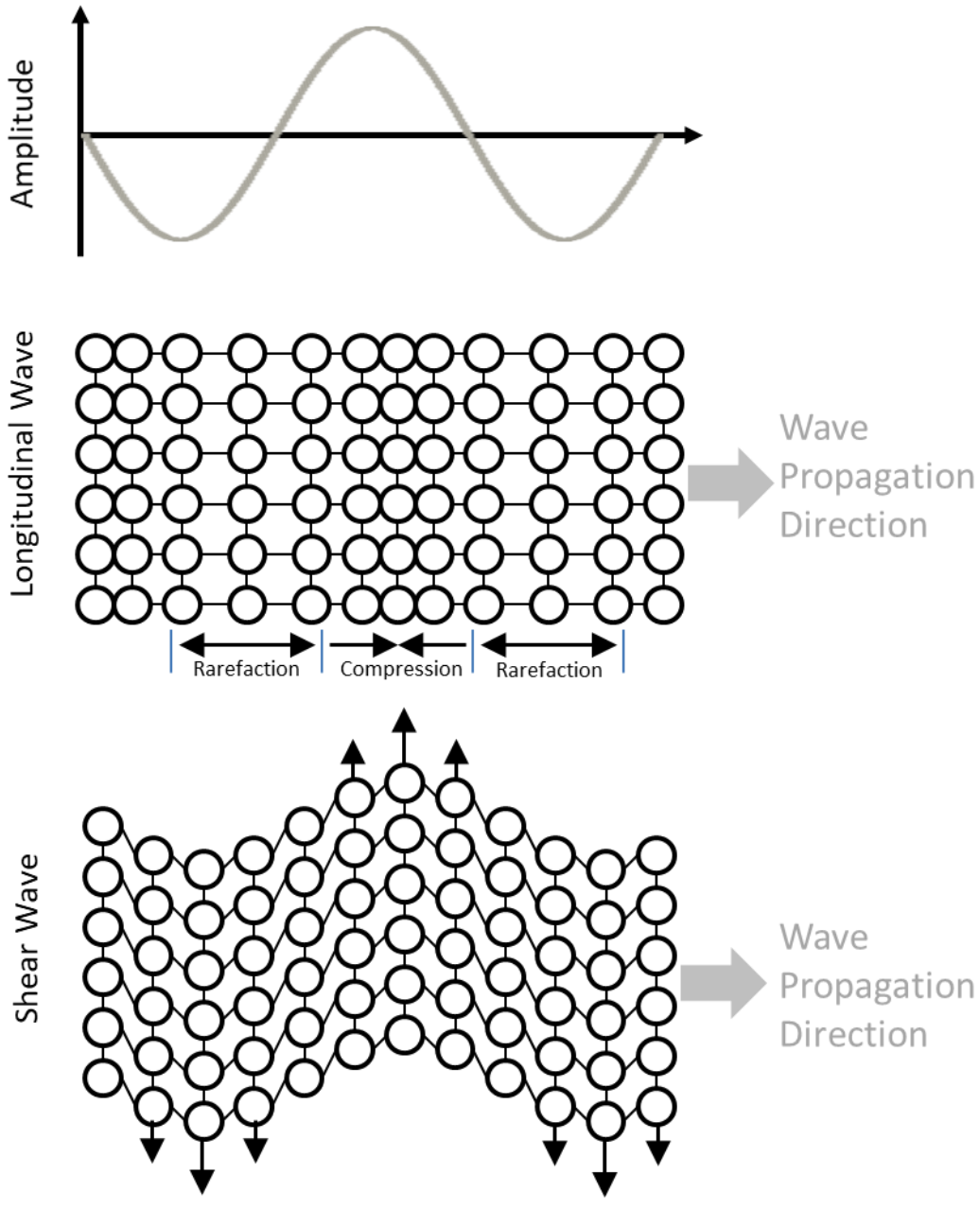

Figure 3.1: Particle and Wave Motion for Longitudinal and Shear Waves.

3.2.2 Speed of Propagation

The speed of propagation, more commonly referred to as the acoustic velocity or speed of sound (SoS for short) is the speed at which a sound wave travels through a medium. This speed is defined by a number of properties including the wave mode, frequency and material properties. The material properties of interest in liquids are the elasticity and density with the addition of shear modulus for some wave types in solids.

Elasticity is the material property which describes how much a material will change in volume for a given change in the pressure applied to it. This is also known as the compressibility and is characterised by the bulk modulus of elasticity (which is the inverse of compressibility). At the particle level, a rigid material's atoms and/or molecules have strong forces of attraction to each other. These forces act like springs and determine how quickly the particles return to their original positions. Particles that return to their resting position quickly are able to vibrate at higher speeds (The Speed of Sound in Other Materials, n.d.). Therefore, sound travels faster through mediums with higher stiffness (like steel) than it can through solids which have lower stiffness (like rubber).

The higher the density of a material, the more mass it has per unit volume. In most cases this higher mass is due to larger molecules. A material with larger molecules will transmit sound slower. This is because the particles have more inertia, due to their greater mass, and are less responsive to the movement of neighbouring particles (Henderson, n.d.). They have a lower acceleration for same the force applied by the neighbouring element. This means that the wave will travel at a slower rate in a denser material with the same elastic properties (The Speed of Sound in Other Materials, n.d.). It is commonly incorrectly stated that sound waves travel faster in solids than gases due their higher density, in fact it is due to the lower elasticity which dominates over the higher density change which has the opposite effect of decreasing the acoustic velocity.

Temperature has an effect in the speed of sound due to the temperature dependence of density and elasticity. This effect is typically much more marked in gases and liquids than solids.

3.2.3 Plane Waves

Pure longitudinal or shear waves are 1 dimensional. This means that longitudinal waves only produce deformations in the propagation direction, the effect of Poisson's ratio is ignored. This approximation holds true where propagation can be treated as 1 dimensional, such as in the case of a longitudinal wave travelling down a thin rod (diameter<wavelength). For plane longitudinal and shear waves the speed of sound in a solid can be calculated using the following relationships (Bray & Stanley, 1996) which are only dependent on the elasticity and density of the material, as described above.

$$c_{L,Solid} = \sqrt{\frac{E}{\rho}} \tag{3.2}$$

$$c_{S,Solid} = \sqrt{\frac{G}{\rho}} \tag{3.3}$$

Where *c* is the speed of sound, subscripts *L* and *S* denote Longitudinal and Shear respectively, *E* is Young's Modulus of Elasticity, ρ is the density and G is the shear modulus. Using typical values for steel (E=210GPa, G=80GPa, ρ=7800kg/m^3) gives $c_{L,Solid}$ of 5189m/s and $c_{S,Solid}$ of 3202m/s.

As liquids do not support a shear load to the same extent as solids, they also don't support shear waves, only longitudinal waves can travel a significant distance within a liquid. The speed of sound of a longitudinal plane wave within a liquid is given in Equation 3.4.

$$c_{L,Liquid} = \sqrt{\frac{B}{\rho}} \tag{3.4}$$

Where B is the bulk modulus of the liquid.

3.2.4 Bulk Waves

The above equations describe plane waves, however in some applications of ultrasound this 1 dimensional approximation doesn't hold. In particular, the propagation of a wave through a bulk material, known as a bulk wave. Ideal bulk waves emanate from a point source.

Shear results in no volumetric change, and so Poisson's ratio has no effect. The speed of a bulk shear wave is therefore the same as in the plane wave case, Equation 3.3. A longitudinal wave however will also produce transverse (or shear) deformations governed by Poisson's ratio. Here the effect of Poisson's ratio must be taken into account. This results in the following relationship for the speed of sound (Bray & Stanley, 1996):

$$c_{BL,Solid} = \sqrt{\frac{B + \frac{4}{3}G}{\rho}} \tag{3.5}$$

Where c_{BL} is the speed of sound of a bulk longitudinal wave. Bulk and shear modulus can be converted to Young's modulus and Poisson's ratio using the following relationships:

$$E = 2G(1 + \upsilon) \tag{3.6}$$

$$E = 3B(1 - 2\upsilon) \tag{3.7}$$

Where υ is Poisson's ratio. Combining Equation 3.5 with these relationships gives the alternative form:

$$c_{BL,Solid} = \sqrt{\frac{E(1-\upsilon)}{\rho(1+\upsilon)(1-2\upsilon)}} \tag{3.8}$$

By comparing Equations 3.2 and 3.8 for steel with a Poisson's ratio of $\upsilon = 0.3$, we can see the bulk longitudinal wave is 34.6% faster than the equivalent plane wave. Example speeds of sound for a number of materials are given in Table 3.1.

	Speed of Sound (m/s)		
Material	**Plane Longitudinal**	**Plane Shear**	**Bulk Longitudinal**
Steel	5190	3230	5900
Copper	3670	2260	4700
Aluminium	5090	3130	6320
Fused Quartz	5300	3520	5570

Table 3.1: Speed of Sound for a range of Materials (Bray & Stanley, 1996).

3.2.5 Dispersion

When referring to the speed of sound so far it has been assumed the speed is constant for all frequencies of wave. However in some materials the speed of sound is frequency dependent (Cobus, Ross, Scanlon, & Page, 2007). The speed of a specific frequency can be described by its *phase velocity*, this is the velocity at which a set point of constant phase travels through a medium.

For most ultrasonic applications it is assumed that all the frequencies in a wave have the same phase velocity. However some materials, known as *dispersive* materials, have frequency dependent phase velocities. The link between the frequency and phase velocity is known as the mediums *dispersion relationship*. The materials studied in this thesis are treated as non-dispersive, they have the same phase velocity for all frequencies.

A wave packet may be made up of a number of frequencies of differing phase velocities. The overall velocity of the wave packet is called the *group velocity.*

3.2.6 Refraction

A wave passing between acoustically dissimilar materials will experience a change in phase-velocity. For oblique waves this change in phase velocity causes a change in the propagation direction of the wave, an effect known as refraction. For a simple plane interface between two materials the relationship between incident and refracted wave propagation directions is governed by Snell's Law, Equation 3.9.

$$\frac{\sin\theta_1}{\sin\theta_2} = \frac{c_2}{c_1} \qquad 3.9$$

Where θ_1 and θ_2 are the angle of incidence and refraction respectively, and c_1 and c_2 the speed of sound in the materials either side of the interface, as shown in Figure 3.2.

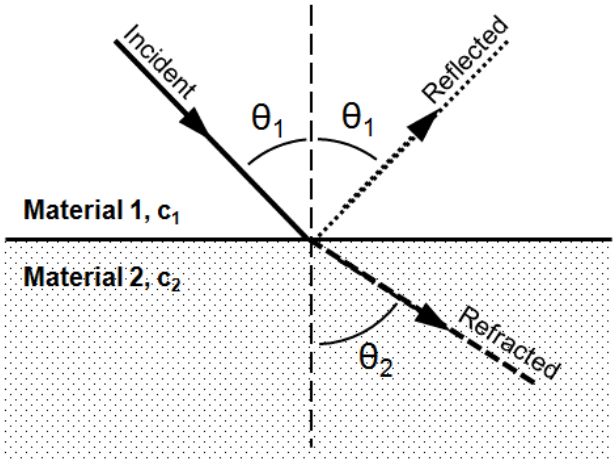

Figure 3.2: Variables used in Snell's Law.

3.2.7 Attenuation

The attenuation of an ultrasonic wave occurs due to three effects: *Absorption*, *Scattering* and *Beam Spread*. Absorption is the conversion of acoustic energy to other forms of energy, commonly the conversion to thermal energy caused by the viscosity of a material. Scattering is the reflection of the wave away from the direction of wave propagation, meaning it is not captured by the receiving element. This can be caused by particulate in a liquid, or grain boundaries in alloyed metals. Beam Spread is the divergence of an ultrasonic wave as it propagates through a medium, this reduces the intensity of the wave.

Attenuation can be modelled using the following exponential equation (Attenuation of Sound Waves, n.d.)

$$A = A_0 e^{-\alpha x} \qquad 3.10$$

Where A is the amplitude, A_0 is the initial amplitude, x is the path length and α is the attenuation coefficient. The attenuation coefficient is normally in Nepers per metre, this can be converted to decibels per metre by dividing by 0.1151.

3.2.8 2D Approximations

The descriptions of waves so far have assumed that they propagate as a 1 dimensional entity. Real world wave propagation is much more complex than this with spreading of the wave in directions other than its nominal direction of propagation.

Huygens principle states that wave-fronts can in fact be decomposed into a collection of point sources, each the origin of a spherical, expanding, wave (Shull & Tittmann, 2002). These will constructively and destructively interfere to create an interference pattern. This results in a wave-front as shown in Figure 3.3.

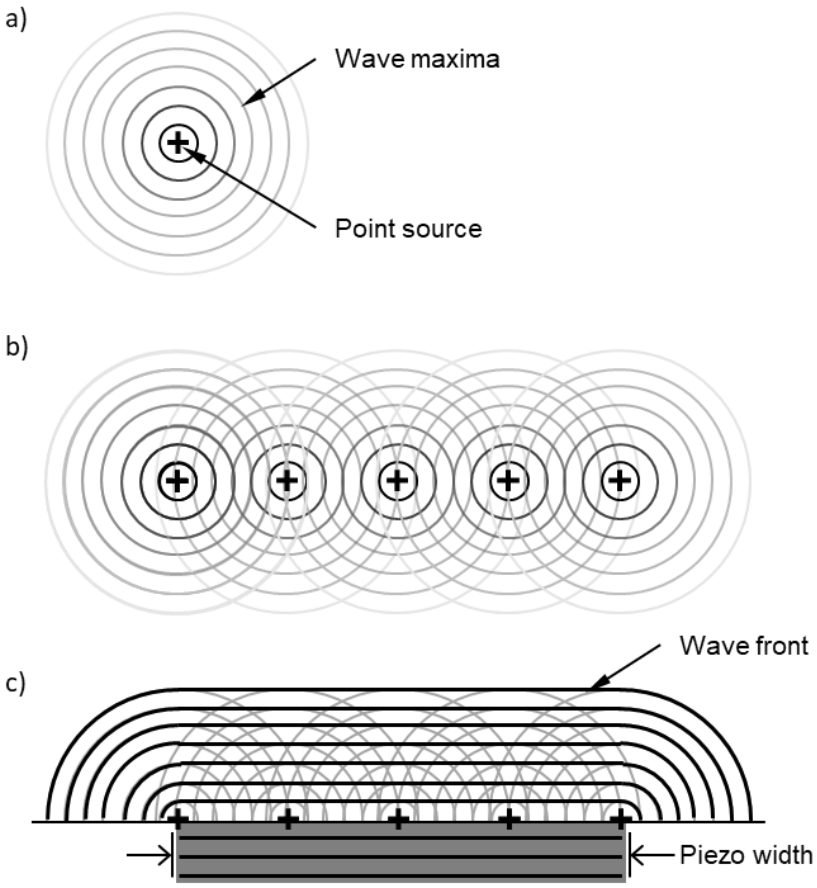

Figure 3.3: Wave front constructed using the Huygens-Fresnel principle a) Point Source b) Multiple Point Sources c) Plate Source.

These concepts can be expanded to model a wave in 3 dimensions. The complexity of this makes it impractical for most applications, more commonly a representative 2 dimensional model is taken instead. The most common approach to modelling a wave in 3 dimensions is numerically using finite element simulations. Rarely are waves modelled in 3 dimensions outside of this.

3.3 Ultrasonic Wave Equations

As described above ultrasonic waves are a form of mechanical oscillation. The following section introduces the basics of oscillations, the wave equation and the interaction of an ultrasonic wave with an ideal interface.

3.3.1 Oscillations

The most basic form of oscillation is simple undamped harmonic motion. The rules governing this can be derived from Hooke's law (Cheeke, 2012) (Ensminger, Ultrasonics: Data, Equations and Their Practical Uses, 2008), Equation 3.11:

$$F = -ku \tag{3.11}$$

and Newton's second law of motion, Equation 3.12:

$$F = m\frac{d^2u}{dt^2} \tag{3.12}$$

Where *F* is force, *k* is stiffness, *u* is extension and *m* is mass. Combining the two gives the following:

$$\frac{d^2u}{dt^2} + \frac{k}{m}u = 0 \qquad 3.13$$

For reasons that will be seen later, here we substitute the following:

$$\omega_0^2 = k/m \qquad 3.14$$

This results in:

$$\frac{d^2u}{dt^2} + \omega_0^2 u = 0 \qquad 3.15$$

This is the equation of motion for a simple harmonic oscillator. This has the general solution:

$$u = A_1 cos\omega_0 t + A_2 sin\omega_0 t \qquad 3.16$$

Which can be converted to:

$$u = Asin(\omega_0 t + \varphi_0) \qquad 3.17$$

We can take the relationship between linear and angular frequency:

$$\omega_0 = 2\pi f_0 \qquad 3.18$$

Replacing f with $1/T_0$, where T_0 is the time period of the wave:

$$\omega_0 = \frac{2\pi}{T_0} \qquad 3.19$$

Multiplying both sides by t:

$$\omega_0 t = \frac{2\pi t}{T_0} \qquad 3.20$$

Then the numerator and denominator of the right hand side are multiplied by c:

$$\omega_0 t = \frac{2\pi ct}{cT_0} \qquad 3.21$$

The distance travelled *x*, which can be calculated from the wave speed *c* and the time elapsed *t*:

$$x = ct \qquad 3.22$$

Substituting this in gives

$$\omega_0 t = \frac{2\pi x}{cT_0} \qquad 3.23$$

Replacing cT_0 with the wavelength λ according to the following equation:

$$\lambda_0 = cT_0 \qquad 3.24$$

Gives

$$\omega t = \frac{2\pi x}{\lambda_0} \quad 3.25$$

Finally it is useful to substitute in the wavenumber k, which is defined as:

$$k = \frac{2\pi}{\lambda_0} \quad 3.26$$

To give:

$$\omega_0 t = kx \quad 3.27$$

Substituting this into Equation 3.17 gives:

$$u = Asin(kx + \varphi_0) \quad 3.28$$

Finally a frame of reference is chosen so that the initial phase angle is zero ($\varphi_0 = 0$) giving:

$$u = Asin(kx) \quad 3.29$$

This is the equation for a fixed oscillator.

3.3.2 1D Wave Equation

One dimensional wave motion can be described by a second order partial differential equation, first developed by Jean le Rond d'Alembert in 1746 (Cheeke, 2012).

$$\frac{\partial^2 u}{\partial x^2} = \frac{1}{c^2}\frac{\partial^2 u}{\partial t^2} \quad 3.30$$

This has the general solution, known as d'Alembert formula, of:

$$u = A_1 f(x - c_0 t) + A_1 f(x + c_0 t) \quad 3.31$$

Substituting this into Equation 3.29 gives

$$u = Asin(k(x - ct)) \quad 3.32$$

Knowing $\omega = kc$ leaves us with

$$u = Asin(kx - \omega t) \quad 3.33$$

Note that $sin(kx - \omega t)$ is a wave while $sin(\omega t)$ is not, this is a fixed oscillator. It is more convenient for mathematical manipulation to represent this as a complex exponential, this is the notation most commonly used in physics and engineering literature.

Using Euler's identity

$$e^{ix} = \cos x + i \sin x \quad 3.34$$

And taking the complex conjugate results in:

$$u(x,t) = Ae^{i(\omega t - kx)} \quad 3.35$$

It follows that the wave pressure is given by (Mukdadi):

$$P(x,t) = P_m e^{i(\omega t - kx)} \quad 3.36$$

Where P_m is the amplitude of the pressure, this is for a wave travelling in the positive *x* direction, for a wave travelling in the opposite direction we get.

$$P(x,t) = P_m e^{i(\omega t + kx)} \quad 3.37$$

3.3.3 Reflection from an Ideal Interface

The nature of ultrasound is such that when it reaches an interface between two acoustically dissimilar materials, some of the wave will be reflected while some will be transmitted. The proportion of a wave reflected and transmitted by an interface can be quantified in the form of reflection and transmission coefficients.

$$P_R = RP_I \quad 3.38$$

$$P_T = TP_I \quad 3.39$$

Where *T* is the transmission coefficient, *R* is the reflection coefficient and *P* is the pressure with subscripts R, T and I representing reflected, transmitted and incident respectively.

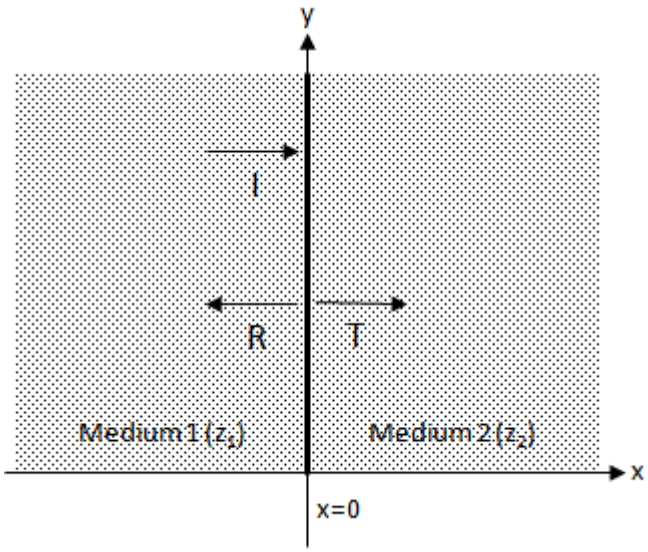

Figure 3.4: Wave Reflection from a Simple Interface.

Representing the incident, reflected and transmitted waves using Equation 3.36 and 3.37 gives:

Incident wave:

$$P_I = P_m e^{i(\omega t - k_1 x)} \quad 3.40$$

Reflected wave:

$$P_R = P_m R e^{i(\omega t + k_1 x)} \quad 3.41$$

Transmitted wave:

$$P_T = P_m T e^{i(\omega t - k_2 x)} \quad 3.42$$

Where the subscripts 1 and 2 represent the materials either side of the interface. As the two surfaces are in perfect contact then there must be a continuity of pressure and velocity. For continuity of pressure at the interface:

$$P_1 = P_2 \tag{3.43}$$

For the incident, reflected and transmitted waves this gives:

$$P_I + P_R = P_T \tag{3.44}$$

Combining Equations 3.40, 3.41, 3.42 and 3.34 gives:

$$P_m e^{i(\omega t - k_1 x)} + P_m R e^{i(\omega t + k_1 x)} = P_m T e^{i(\omega t - k_2 x)} \tag{3.45}$$

Taking the origin of the interface at $x = 0$ the above equation simplifies to:

$$P_m e^{i(\omega t)} + P_m R e^{i(\omega t)} = P_m T e^{i(\omega t)} \tag{3.46}$$

Dividing through by $P_m e^{i(\omega t)}$ yields:

$$1 + R = T \tag{3.47}$$

This equation assumes an ideal plane wave travelling perpendicular to the interface, an ideal interface and only models the interface in 1 dimension. As such it neglects any other wave modes (such as surface waves) that may be generated in a real interface.

Continuity of particle velocity, which should not be confused with the wave velocity, gives:

$$v_I - v_R = v_T \tag{3.48}$$

Where v_I , v_R and v_T are the particle velocity components due to the incident, reflected and transmitted waves respectively. It should be noted that unlike the pressure terms in Equation 3.44 the direction of the waves matter. We then introduce the following definition of acoustic impedance:

$$z = P/v \tag{3.49}$$

z is the acoustic impedance, *P* is the amplitude of the sound pressure and *v* is the particle velocity. Combining 3.48 and 3.49 gives:

$$\frac{P_I}{z_1} - \frac{P_R}{z_1} = \frac{P_T}{z_2} \tag{3.50}$$

Note the different acoustic impedance values used dependent upon which side of the interface the waves are. This simplifies to:

$$\frac{P_I - P_R}{z_1} = \frac{P_T}{z_2} \tag{3.51}$$

Substituting in Equations 3.40, 3.41 and 3.42 leaves:

$$\frac{P_m e^{i(\omega t - k_1 x)} - P_m R e^{i(\omega t + k_1 x)}}{z_1} = \frac{P_m T e^{i(\omega t - k_2 x)}}{z_2} \tag{3.52}$$

Again taking $x = 0$ we get:

$$\frac{P_m e^{i(\omega t)} - P_m R e^{i(\omega t)}}{z_1} = \frac{P_m T e^{i(\omega t)}}{z_2} \tag{3.53}$$

This simplifies to:

$$\frac{1-R}{z_1} = \frac{T}{z_2} \tag{3.54}$$

Combining and solving the simulations equations 3.47 and 3.54 we get

$$\frac{1-R}{z_1} = \frac{1+R}{z_2} \tag{3.55}$$

Rearranging we can get reflection coefficient in relation to the acoustic dissimilarity of the interface materials:

$$R = \frac{z_2 - z_1}{z_2 + z_1} \tag{3.56}$$

A similar approach can be used to get the transmission coefficient:

$$T = \frac{2z_2}{z_2 + z_1} \tag{3.57}$$

3.4 Thin Film Measurement Techniques

The measurement of thin interfacial layer thickness is important in a range of applications. In addition to the roll bite lubrication being studied in this thesis, lubricant films are found in a variety of tribological applications. The thickness of lubricant films has a significant effect on the performance, efficiency and life of many machine components. Such films often have thicknesses of micron or sub-micron scale.

Several techniques are available to measure these thin films; however each has its associated limitations. The most common techniques currently in use are those based on optical fluorescence (Ford & Foord, Laser-based fluorescence techniques for measuring thin liquid films, 1978) or interferometry (Cameron & Gohar, Optical Measurement of Oil Film Thickness Under Elastohydrodynamic Lubrication, 1963). Although accurate, these methods require a transparent window to be set into the surfaces either side of the liquid layer. Other available techniques work by measuring the resistance (Palacio & Bhushan, Surface potential and resistance measurements for detecting wear of chemically-bonded and unbounded molecularly-thick perfluoropolyether lubricant films using atomic force microscopy, 2007) or capacitance (Grice N. , Sherrington, Smith, O'Donnell, & Stringfellow, 1990) across the liquid layer. This requires the media either side of the thin layer to be both conductive and electrically insulated from each other.

Distance measurement using a sound wave's *Time-of-Flight (TOF)* has long been used in many sectors of engineering and is well understood. For very thick liquid layers (of the order of mm) the liquid layer thickness can be determined by measuring the time difference between two reflected pulses, one each from the near and far interfaces of the layer. By taking this time difference and with knowledge of the speed of sound, the thickness of the layer can be calculated. This typically reaches a limit as the layer thickness falls below a few hundred microns (>> Wavelength, λ). The decreasing time difference between the returning pulses means that they begin to overlap in the time domain and an accurate measurement of the time of flight between them cannot be made. As the lubricant films observed in tribological applications are typically on the micron or sub-micron scale, TOF measurements are therefore normally

unfeasible. To overcome this, two novel ultrasonic techniques have been developed which aim to accurately measure the thickness of these thin films. One method is based on the amplitude of the reflected pulse, known as the *Spring Model* approach (Dwyer-Joyce, Drinkwater, & Donohoe, The Measurement of Lubricant Film Thickness using Ultrasound, 2003). The other method uses the resonant frequency of the oil film and is known as the *Film Resonance* method (Dwyer-Joyce, Drinkwater, & Donohoe, The Measurement of Lubricant Film Thickness using Ultrasound, 2003).

The film resonance method, also called the resonant dip technique, is suitable for thinner layers than the Time-of-Flight technique, typically around 30-900µm (≈ Wavelength, λ). Here the film is forced by the incident wave to resonate at a frequency corresponding to it's thickness. This resonant frequency is observed as a dip in the frequency spectrum of the reflected wave. The thickness can therefore be measured by measuring this resonant frequency.

For very thin layers around <50µm (< Wavelength, λ), the frequency of the resonance becomes too high to be measured using standard NDT frequencies. The layer appears as a single reflector with a single reflection. The proportion of the wave reflected depends on the stiffness of this layer which is a function of its thickness. The layer thickness can therefore be ascertained from the amplitude of the reflected wave.

As well as the layer thickness the recorded amplitude of the reflected wave also depends on a combination of the attenuation within the inspected material and the sensor and instrumentation characteristics. Both the attenuation and behaviour of the hardware will change with temperature, so it is common when using an amplitude based measurement to either have some method of referencing against a known condition, such as a film of known thickness, or an air interface.

Figure 3.5 shows a summary of the responses from of each of the measurement types (*Time of Flight, Frequency* and *Amplitude)* for different thicknesses of embedded layer.

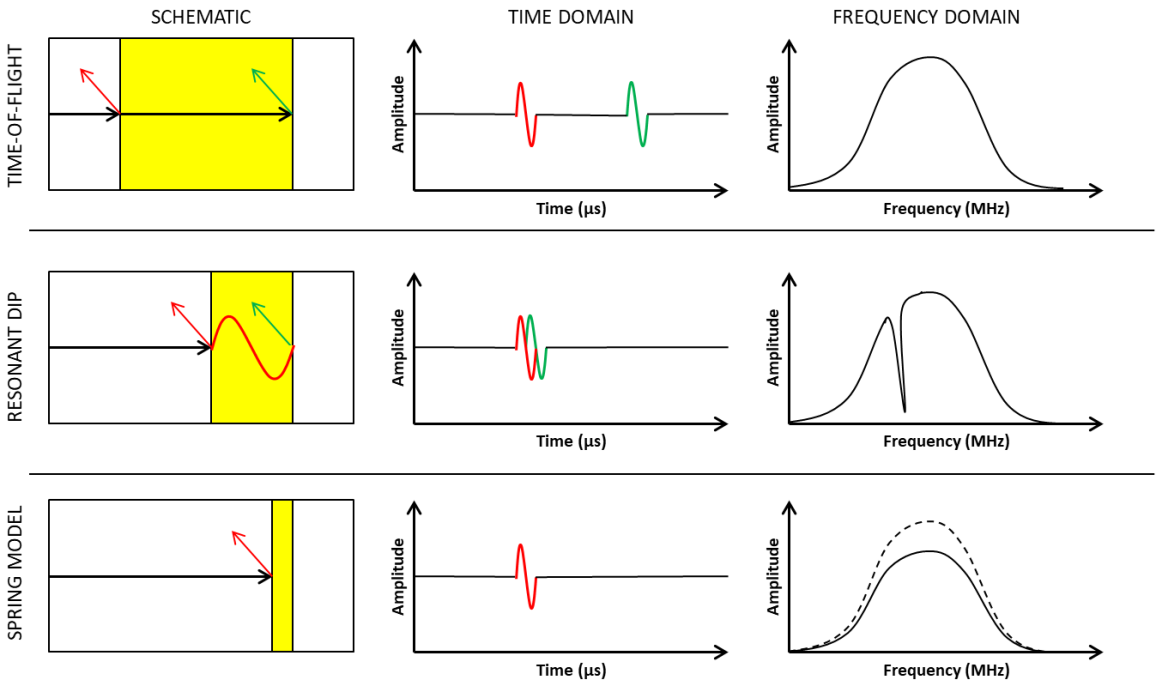

Figure 3.5: Summary of Embedded Layer Ultrasonic Measurement Techniques.

The advantage of these ultrasonic measurements over the equivalent optical or electrical techniques lies in their non-invasive nature. In many applications an ultrasonic sensor can be bonded to the outside of a component with minimal alteration to the part and a sound wave transmitted through to the interface of interest. This also maintains the running surfaces ensuring no disruption to the liquid layer being observed.

3.5 Reflections from an Embedded Layer

The theory covering the response of an embedded layer to incident ultrasound is well understood (Kraütkramer & Kraütkramer, 1977) and is presented for both the resonant dip and spring model regimes below. All equations presented are 1-dimensional, they assume perpendicular incidence waves and infinite interfaces.

3.5.1 Thin Film - Spring Model

When the wavelength of the incident ultrasonic pulse is large in comparison to the thickness of the liquid layer, then the layer can be thought of as a unique reflector. The properties of this interface will depend both on the properties of the embedded layer as well as the materials on either side.

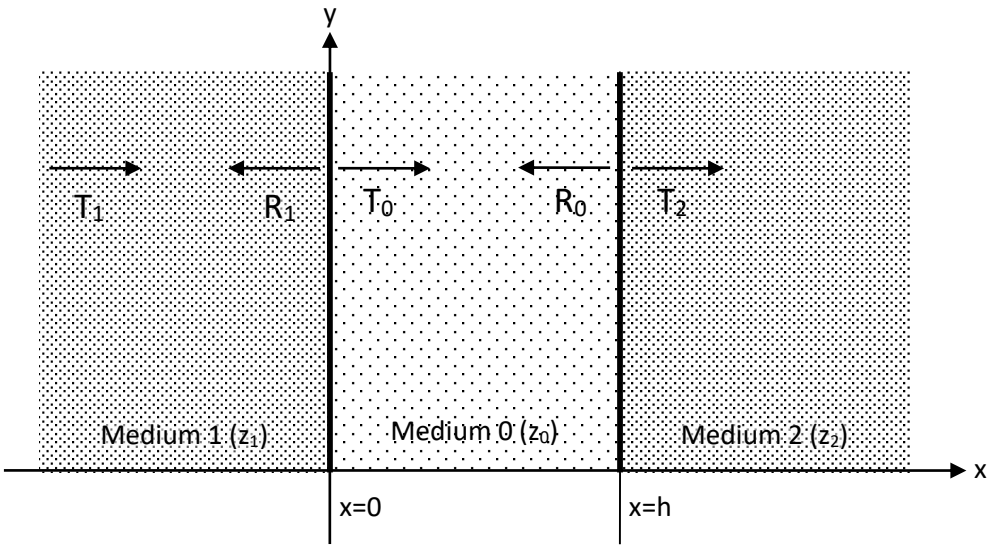

Figure 3.6: Wave Reflection from a Thin Embedded Layer.

Taking Equation 3.35 we can substitute in the following relationship for wave number:

$$k = \omega/c \tag{3.58}$$

To get:

$$u(x,t) = Ae^{i(\omega t - \omega x/c)} \tag{3.59}$$

For simplicity we omit the term $e^{i\omega t}$. We will also assume an incident wave amplitude of unity. The displacements in the two mediums either side of the interface therefore become:

$$u_1(x) = e^{-i\omega(x/c_1)} + R_1 e^{i\omega(x/c_1)} \tag{3.60}$$

$$u_2(x) = T_2 e^{-i\omega(x/c_2)} \tag{3.61}$$

We can then differentiate with respect to *x* to give:

$$u_1'(x) = -\frac{i\omega}{c_1}(e^{-i\omega(x/c_1)} - R_1 e^{i\omega(x/c_1)}) \quad 3.62$$

$$u_2'(x) = -\frac{i\omega}{c_2} T_2 e^{-i\omega(x/c_2)} \quad 3.63$$

This is equivalent to strain. We can therefore apply the stress strain relationship:

$$u'^{(x)} = \varepsilon_x = \frac{\sigma_x}{E} \quad 3.64$$

Where ε is the strain, σ is stress and *E* is Young's modulus. To give the stress in each medium:

$$\sigma_1(x) = -\frac{i\omega}{c_1} E_1(e^{-i\omega(x/c_1)} - R_1 e^{i\omega(x/c_1)}) \quad 3.65$$

$$\sigma_2(x) = -\frac{i\omega}{c_2} E_2 T_2 e^{-i\omega(x/c_2)} \quad 3.66$$

Next we can substitute in the acoustic impedance using the following relationship.

$$E = zc \quad 3.67$$

And cancelling the speed of sound terms to give:

$$\sigma_1(x) = -i\omega z_1\left(e^{-i\omega x/c_1} - R_1 e^{i\omega x/c_1}\right) \quad 3.68$$

$$\sigma_2(x) = -i\omega z_2 T_2 e^{-i\omega x/c_2} \quad 3.69$$

Assuming the interfaces between materials 1→0 and 0→2 are perfectly bonded with negligible mass then continuity of stress and displacement apply:

$$\sigma_1(x) = \sigma_2(x) = \sigma_0(x) \quad 3.70$$

Tattersall modelled the interface such that "the interfacial forces are represented by a density of springs between the two media". As such stress at the boundaries of layer 0 can be modelled by:

$$\sigma_0(x) = K(u_2(x) - u_1(x)) \quad 3.71$$

Where *K* is the embedded layer stiffness. This equation is similar to Hooke's law although in this case the layer stiffness is in terms of stress over layer thickness, rather than force over thickness, and is typically quoted in units of GPa/µm.

$$\sigma_0(x) = K(T_2 e^{-i\omega x/c_2} - (R_1 + 1)e^{-i\omega x/c_1}) \quad 3.72$$

Taking x=0

$$-i\omega z_2 T_2 = K(T_2 - R_1 + 1) \quad 3.73$$

Then rearranging:

$$-i\omega z_1(1 - R_1) = K(T_2 - R_1 + 1) \quad 3.74$$

Solving these equations simultaneously for *R:*

$$R_1 = \frac{z_2 - z_1 + i\omega(z_1 z_2/K)}{z_2 + z_1 + i\omega(z_1 z_2/K)} \quad 3.75$$

With ω being the angular frequency of the wave. From Equation 3.75 we can separate the real and imaginary parts by multiplying by the complex conjugate of the denominator. This gives us the magnitude of the reflection coefficient vector $|R|$ and its angle to the real axis. This angle is the same as the phase shift. Equation 3.76 gives the magnitude, this has also been simplified by presuming identical material on either side of the interface.

$$|R| = \frac{1}{\sqrt{1 + (2K/\omega z)^2}} \quad 3.76$$

Therefore, by measuring the reflection coefficient, and provided with the acoustic impedance of the surrounding material and wave frequency, the layer stiffness *K* can be calculated.

To calculate the layer thickness the stiffness is then related to the layer thickness by modelling the layer as an elastic spring (Dwyer-Joyce, Drinkwater, & Donohoe, The Measurement of Lubricant Film Thickness using Ultrasound, 2003) and substituting in speed of sound *c* and density ρ values for bulk modulus *B* based upon the Newton-Laplace formula, a rearrangement of Equation 3.4:

$$B = \rho c^2 \quad 3.77$$

This then returns the relationship given in equation below:

$$K = \frac{\rho c^2}{h} \quad 3.78$$

With ρ the layer density, *c* the speed of sound in the layer and *h* the layer thickness. This equation is often combined with the Equation 3.76 so that the film thickness may be calculated in one step from the reflection coefficient. This method is suitable only for very thin layers which can be treated as quasi-static. Figure 3.7 shows how, using the spring model, the reflection coefficient varies against *kh* in a typical steel-oil-steel system.

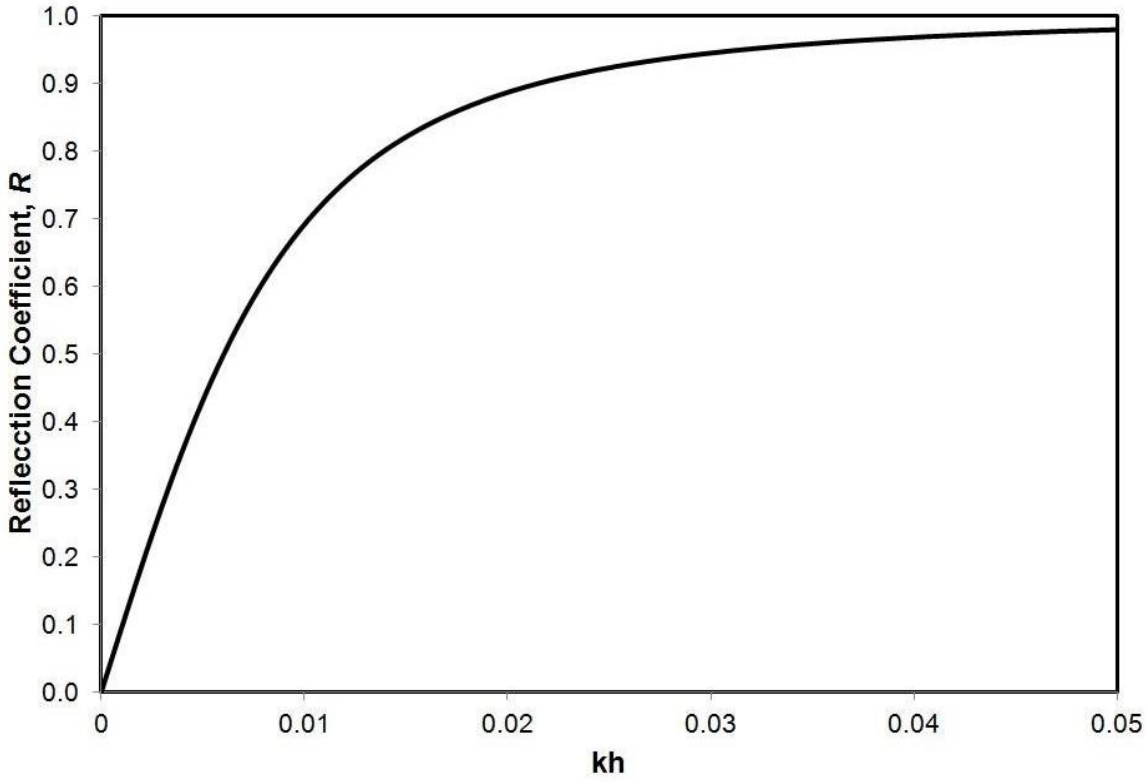

Figure 3.7: Reflection coefficient variation against *kh*, as calculated using the Spring Model.

Figure 3.8 shows example reflection coefficient values for various film thickness and frequency values for an oil layer embedded between identical steel interfaces.

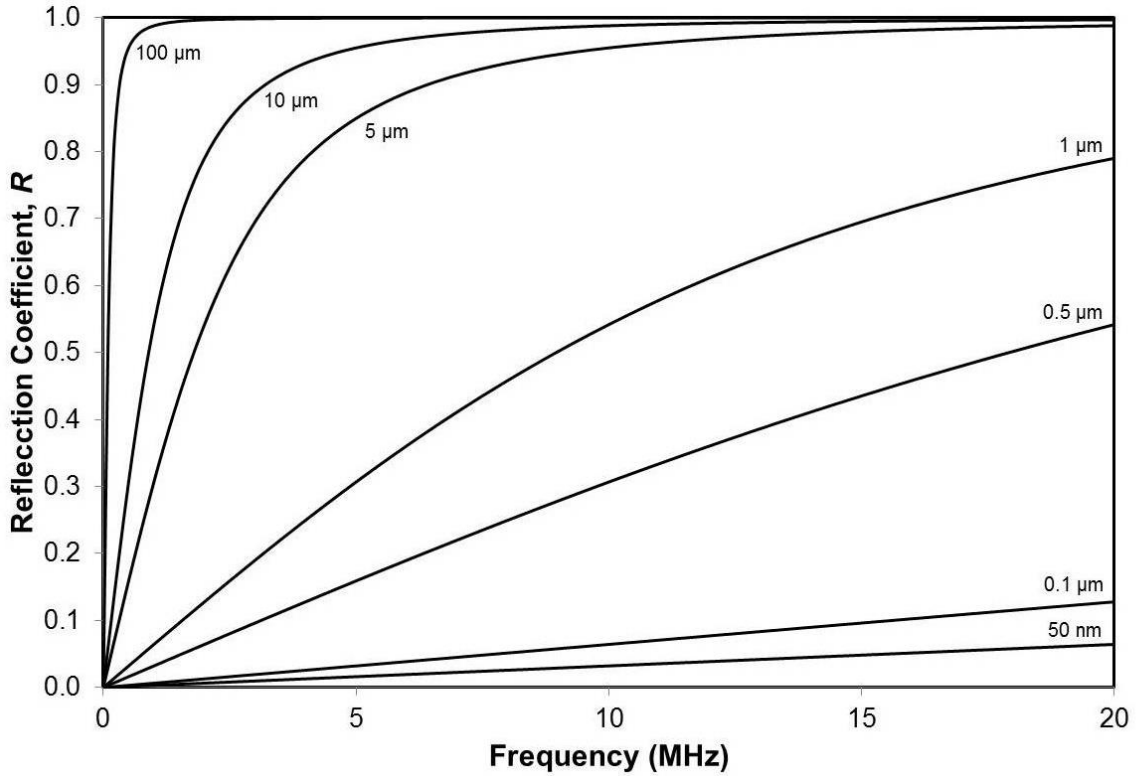

Figure 3.8: Reflection coefficient against frequency for a typical Steel-Oil-Steel System (z = 46MRayls, ρ = 880kg/m^3, c = 1415 m/s*).*

The measurement of the reflection coefficient loses accuracy as the value approaches 0, due to noise, and 1 as the method becomes over sensitive. The minimum and maximum measurable film is therefore dependent upon frequency of the wave used. It can be seen from the figure that for a 10MHz sensor the measurable range of film-thicknesses are approximately 50nm to 10um, although this will be dependent upon the accuracy with which the reflection coefficient can be measured.

3.5.2 Thin Film – Resonance Technique

Assuming the material either side of the layer is identical ($z_1 = z_2 = z$) the following impedance ratio can be taken, Equation 3.79.

$$n = \frac{z}{z_0} \tag{3.79}$$

Here Z_0 denotes the acoustic impedance of the embedded layer. The manner in which the waves from each interface interfere is governed by the thickness of the layer and the ultrasonic wavelength in the layer material. This relationship is given Equation 3.80 (Krautkrämer & Krautkrämer, Ultrasonic Testing of Materials, 1977).

$$R = \sqrt{\frac{\frac{1}{4}\left(n - \frac{1}{n}\right)^2 \sin^2 \frac{2\pi h}{\lambda}}{1 + \frac{1}{4}\left(n - \frac{1}{n}\right)^2 \sin^2 \frac{2\pi h}{\lambda}}} \tag{3.80}$$

Where h is the layer thickness and λ wavelength in the layer. The sine functions make this expression periodic. This is best demonstrated by plotting the reflection coefficient against the normalised quantity kh, where k is the wavenumber, Figure 3.9.This shows the results calculated for an example steel-oil-steel system.

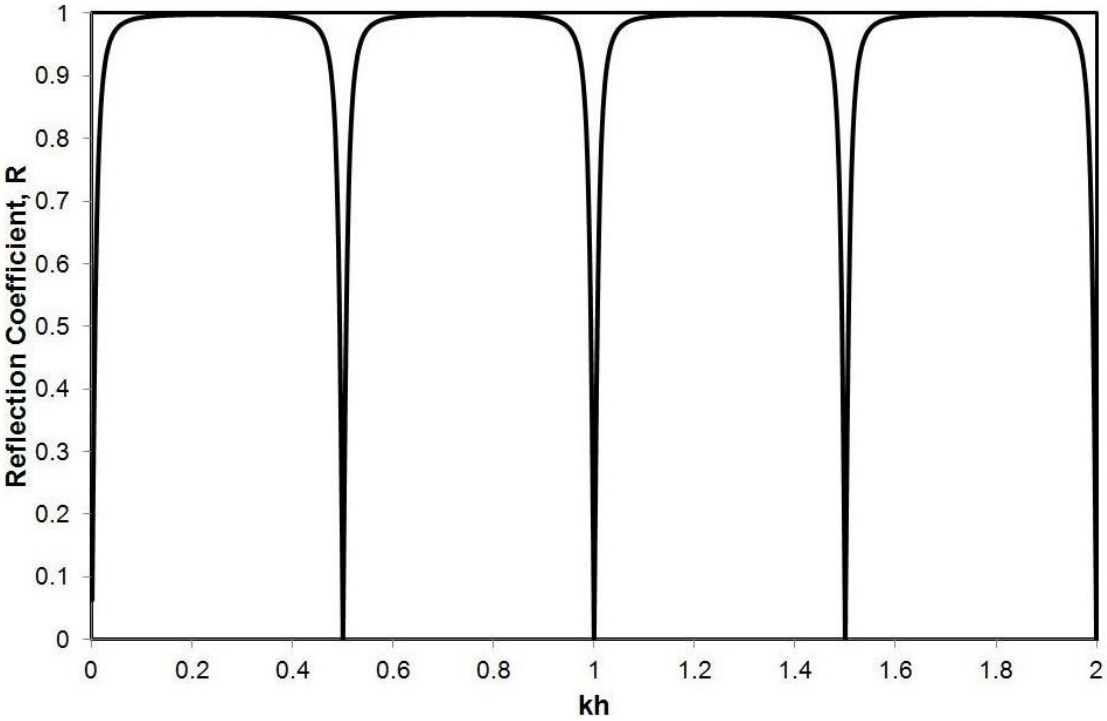

Figure 3.9: Reflection coefficient Vs. normalised quantity *kh*, calculated using Equation 3.80.

Periodic minima of *R* can clearly be seen. In fact each minima occurs at definite number of half wavelengths. This corresponds to resonance occurring within the layer. The frequency of this resonance can be calculated using Equation 3.81 (Banks, Oldfield, & Rawding, Ultrasonic Flaw Detection in Metals; Theory and Practice, 1962).

$$f_m = \frac{cm}{2h} \tag{3.81}$$

Here f_m is the resonant frequency of the layer, *c* the speed of sound in the layer and *m* the mode of resonance. Pialucha & Cawley have proved this relationship numerically (Pialucha & Cawley, 1994). This is the key equation for the film resonance technique. The reflected pulse will exhibit a dip in the response at the resonant frequency. Therefore, by measuring the frequency of this dip, and provided with the speed of sound in the material, the layer thickness *h* can be calculated. We can see from the formula that the thinner the liquid layer, the higher the resonant frequency. Above certain frequencies, typically 60MHz for a good quality steel but as low as 10MHz for cast iron, the use of ultrasound becomes problematic due to attenuation. This puts a limit on the thinnest layers measureable using this method.

3.5.3 Mixed Mode Interface

The previous sections detailed the response from a continuous embedded layer. In many engineering applications boundary or mixed mode lubrication is exhibited, a combination of part asperity contact and part lubricant layer.

The following diagrams show exaggerated plots of the surface profile of a pre-hot-rolled strip. These measurements were taken using a needle profilometer. The diagram shows how the asperity contacts are interspersed with lubricant pockets, even with no separation between the surface mean lines.

Cold rolling exhibits boundary or mixed-mode lubrication depending upon the parameters used. The stiffness of the interface is a combination of the solid and liquid components. To illustrate this Figure 3.11 shows schematics of two example interfaces where *A* is the apparent area of contact, A_R is the real area of contact, *V* is the lubricant volume and *h* is the mean film thickness.

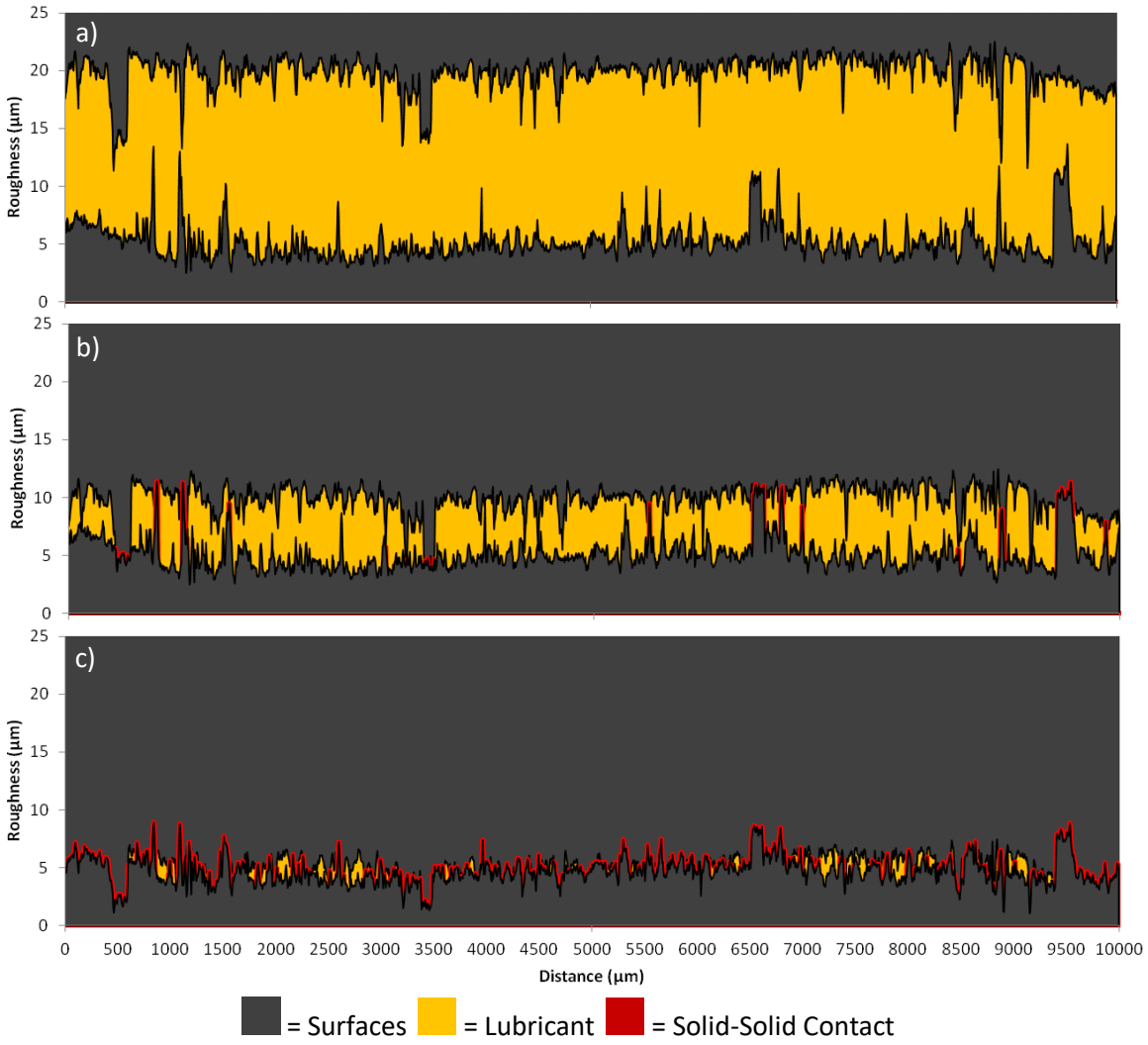

Figure 3.10: Example Surfaces in Mixed Mode Contact with an R_a of 1.04µm a) Separated Surfaces b) 5µm separation between mean lines c) 0µm separation between mean lines.

Equation 3.78 shows that Bulk Modulus and film thickness can be used to calculate the layer stiffness. It can be seen in these diagrams that for a simple triangular model of the roughness the mean film thickness can be calculated from Equation 3.82:

$$h = \frac{V}{A} \qquad 3.82$$

This is the average film thickness across the apparent area of contact, and not just the lubricated sections. As the real area of contact (the asperity to asperity contact) increases, the volume of liquid per unit area of the interface decreases, as shown in Figure 3.11b. This results in the mean film thickness decreasing, and therefore means it is not necessary to account for the real area of contact. The same applies to stiffness of the liquid component of the interface.

For asperity contact Kendall and Tabor (Kendall & Tabor, 1971) concluded that a given contact stiffness can be achieved with a single large area of contact, or with a number of smaller contact areas spaced apart. As with the liquid stiffness, the solid stiffness of the interface is treated as an average over the apparent area of contact, rather than being considered at each asperity contact.

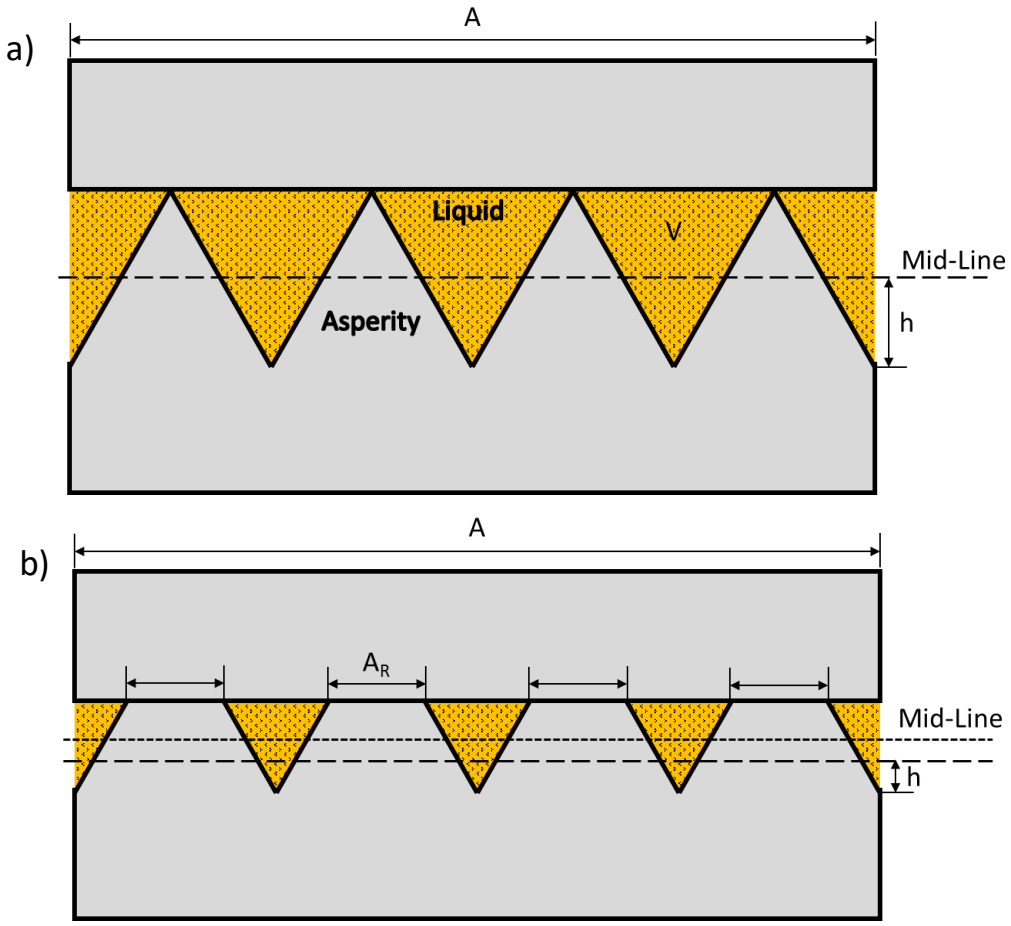

Figure 3.11 Schematics of Example Interfaces a) Triangular Roughness b) Increased Contact.

The stiffness of each component can be treated as two springs in parallel, as shown in Figure 3.12

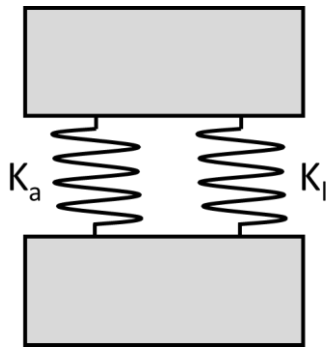

Figure 3.12 Components of Interface Stiffness.

The equivalent spring constant of two springs in parallel is just the summation of the two individual spring constants. The interface stiffness of a mixed mode interface is therefore the summation of the stiffnesses resultant from the solid and liquid components, as given in Equation 3.83

$$K_{Total} = K_{Liquid} + K_{Solid} \tag{3.83}$$

This will be true for both normal and shear stiffnesses

$$K_\sigma = (K_a)_\sigma + (K_l)_\sigma \quad 3.84$$

$$K_\tau = (K_a)_\tau + (K_l)_\tau \quad 3.85$$

Where the subscripts σ and τ denote normal and shear respectively with the subscripts a and l the contributions from the asperity and liquid parts of the contact. The normal and shear stiffnesses can be calculated using Equation 3.76 from the longitudinal and shear wave reflection coefficients respectively.

As, by definition, a liquid does not support a shear load it also does not transmit a shear wave. The shear stiffness at the liquid part of the interface is only due to liquid viscosity and can be treated as negligible, $(K_l)_\tau \approx 0$. For this reason, the shear stiffness seen by a shear wave reflected from a mixed mode interface will only result from the asperity contact:

$$K_\tau = (K_a)_\tau \quad 3.86$$

Mindlin (Mindlin, 1949) was able to relate the shear to normal stiffness by treating the contact regions as elastic uncoupled circular Hertzian contacts, there are other versions of this relationship which vary depending upon the assumed surface geometry. The outcome was Equation 3.87.

$$K_\tau / K_\sigma = 2(1-\nu)/(2-\nu) \quad 3.87$$

Where ν is Poisson's ratio. For steel ($\nu = 0.3$) this gives a ratio of 0.824. By combining this with Equation 3.84 the normal stiffness only from the solid contact can be calculated.

The stiffness measured by a longitudinal wave will have both solid and liquid components. The stiffness only due to liquid can therefore be calculated from the difference between the total longitudinal stiffness, and the normal stiffness from the solid contact alone and calculated from the shear stiffness, Equation 3.88.

$$(K_l)_\sigma = K_L - K_S/0.824 \quad 3.88$$

Where K_L is the stiffness measured with a longitudinal wave and K_S is the stiffness measured with a shear wave. The next step is to calculate the film thickness by combining Equations 3.78 and 3.88 to give:

$$h = \frac{B}{K_L - K_S/0.824} \quad 3.89$$

The final step is to combine Equation 3.76 for the shear and longitudinal cases with Equation 3.89 to give:

$$h = \frac{B}{f\pi\left[\left(z_L\sqrt{\left(\frac{1}{R_L}\right)^2 - 1}\right) - \left(z_S\sqrt{\left(\frac{1}{R_S}\right)^2 - 1}\right)\Big/0.824\right]} \quad 3.90$$

Where subscripts *L* and *S* denote longitudinal and shear respectively.

3.5.4 Asperity Stiffness Models

Several models have been developed to estimate asperity stiffness, these will prove useful in verifying the results gained from the ultrasonic method. For example Greenwood & Williamson

(Greenwood & Williamson, 1966) propose a simple asperity model for solid stiffness, Equation 3.91.

$$K_{a,\sigma} = p/r_{RMS} \quad 3.91$$

This treats the asperities as elastic hemispheres, with the stiffness $K_{a,\sigma}$ related to normal pressure p and the root mean square surface roughness r_{RMS}.

3.6 Conclusions

A number of conclusions can be drawn from the theory presented in this chapter. Firstly, it is shown that the proportion of an ultrasonic wave reflected from an ideal interface is dependent on the acoustic impedances of the materials on either side of that interface.

If a thin continuous layer, such as a lubricant film, is introduced between the two surfaces of an interface, then the proportion of an ultrasonic wave reflected by that interface is dependent on the stiffness of the layer, the acoustic impedance of the materials on either side of it and the incident wave frequency. This stiffness is a function of the layer thickness and its bulk modulus. Therefore, knowledge of the layer bulk modulus, the acoustic impedance of the surrounding material, the layer ultrasonic reflection coefficient and the wave frequency used to measure it, can be used to calculate the interfacial layer thickness.

A mixed mode interface such as that seen in a cold rolling roll bite, is made up of a combination of both solid asperity contact, and a thin fluid film. The overall interface stiffness can be ascertained from the proportion of a longitudinal wave reflected by that interface. The stiffness of the solid-to-solid contact alone can be determined from the proportion of a shear wave reflected. The fluid layer stiffness is the difference between these two values. This fluid layer stiffness can be converted to film thickness via the material properties and wave frequency as described before.

This technique offers a way to measure the thickness of a thin interfacial film using longitudinal and shear ultrasonic waves. This forms the basis of the film thickness measurements put forward in this thesis. The technique has the advantage that it allows for measurement of an otherwise inaccessible interface, but its accuracy is dependent on good knowledge of several material properties.

4 Acoustoelastic Effect

The following chapter describes *Acoustoelasticity*, the stress dependence of the acoustic wave velocity in an elastic media. If a material is subjected to a stress, the velocity of an acoustic wave passing through that material will change depending on the wave mode and both the magnitude and orientation of the applied stress. This stress dependence stems from the relationship between the speed of an acoustic wave and the properties of the material in which it is propagating, such as its density and elasticity. When a material is subject to a stress these properties change which in turn alters the speed at which sound propagates through it.

4.1 Literature Review

Acoustoelasticity has been the subject of previous research. The effect is slight with large stresses required in order to produce a small relative change in the acoustic velocity, making measurement of the effect difficult. Crecraft (Crecraft, 1967) gives a summary of different methods that have been employed to measure the effect.

Cauchy (Cauchy, 1829) developed a theory for acoustoelasticity which superimposed a continuum model for infinitesimal disturbances onto an elastic material. Cauchy's theory of small deformations is restricted to elastically deformed medium and the theory breaks down if the material becomes plastic or if the amplitude of the disturbance becomes too large.

Murnaghan (Murnaghan, 1951) extended this theory to cover finite deformations. This was achieved through two revisions to Cauchy's work on infinitesimal deformations. Firstly, the comparatively larger deformations mean then the initial and final coordinates are no longer treated as interchangeable. Secondly, the strain energy terms were expressed in terms of the initial or final coordinates independently. Murnaghan introduced three Third Order Elastic (TOE) constants (l, m and n) for an isotropic body in addition to the second order coefficients (λ and μ) also known as Lamé constants. The application of Murnaghan's finite theory to the propagation behaviour of acoustic waves in an elastically deformed material was completed by Toupin and Bernstein (Bernstein, 1961). They also show how the measured acoustoelastic effect can be used to determine the TOE constants for an isotropic material.

The theory of acoustoelasticity was extended to orthotropic media by Pao and Gamer (Gamer, 1985). Hughes and Kelly (Kelly, 1953) derived expressions for the speed of elastic waves in a stressed solid using Murnaghan's theory. The effect of compressive stresses and hydrostatic pressure on polystyrene, Pyrex glass, and iron was investigated and velocities of longitudinal and shear waves determined as a function of stress.

The technique used by Hughes and Kelly lacked precision and a modification of this method by Bergman and Shahbender (Bergman & Shahbender, 1958) enabled a better sensitivity. The modified method transmitted a reference pulse through an ultrasonic delay line set to give the same delay as the specimen in the unstressed state. Comparison of the offset between the reference and measurement pulses yielded the change in Time-of-Flight. Another similar technique called the pulse superposition method was also developed which uses the principle of matching the pulse repetition frequency (PRF) to an integral multiple of the travel time of a single pulse. This allows the series of received pulses to arrive in phase. The transit time can be determined from the PRF, the echo number, and averaging from the number of readings.

Egle and Bray (Bray D. M., 1976) measured the acoustoelastic and TOE constants for rail steel using longitudinal waves. The method employed contact transducers for the generation and reception of longitudinal waves. The acoustoelastic constants for the change in wave speed in five directions were determined. The sing-around, resonant frequency and pulse overlay technique were compared and it was found that the latter yielded most consistent results. Measured values of the acoustoelastic constants were found to be consistent with the predictions of Hughes and Kelly (Kelly, 1953).

Fukuoka and Toda (Toda, 1977) determined the acoustoelastic constants for aluminium, pure iron, and copper using shear transducers as transmitter and receiver and also employing the sing-around technique. Their results demonstrated that, for aluminium and pure iron, ultrasonic velocity for shear waves varies linearly to the applied stresses and for copper this relation is parabolic.

The acoustoelastic change in the speed of sound manifests itself as a change in the Time-of-Flight (ToF) of an ultrasonic wave passed through the material under stress in comparison to the unstressed state. The ToF is therefore the means by which the stress in a component is inferred. However the acoustoelasticity is not the only effect that causes a change in ToF of a wave in a stressed component. The applied stress can result in compression, expansion or deflection of the inspected material. This can change both the ultrasonic path length and, due to the change in volume of the material, the density. These effects must therefore also be considered when attempting to measure stress using a ToF technique.

4.2 Deflection Effect

The effect of deflection on the ToF is a simple relationship. The change in path length of the wave caused by the deflection can be related to the ToF via the speed of sound in the material, as shown in Equation 4.1.

$$\Delta t_{\delta} = \frac{2\delta}{(c_{xx})_0} \tag{4.1}$$

Where Δt_{δ} is the change in ToF due to deflection alone, δ is the deflection of the workpiece and $(c_{xx})_0$ is the unstressed speed of sound of a longitudinal wave in the direction of the stress. The numerator has been multiplied by two to account for the back and forth transit of the wave. A similar relationship applies for shear waves by substituting in the appropriate unstressed speed of sound for the a shear wave polarisation $\left(c_{xy}\right)_0$ or $(c_{xz})_0$.

The two primary effects that combine to alter a sound waves velocity, are the *Density Effect* and the *Elasticity Effect* as described below.

4.3 Density Effect

The velocity of a longitudinal ultrasonic wave is dependent on a material's density and elasticity, as given by the Newton-Laplace Equation, see Equation 4.2

$$c_{xx} = \sqrt{\frac{E(1-\upsilon)}{\rho(1+\upsilon)(1-2\upsilon)}} \tag{4.2}$$

Where *c* is the speed of sound, *E* is the Young's modulus, υ is Poisson's ratio and ρ the density. Sound will travel at a slower rate in the denser object than a less dense object if they have the same elastic properties. A substance that is denser per unit volume has more mass per unit volume. Usually this greater mass is the result of larger molecules. A larger molecule has greater inertia which causes it to react more slowly to the vibration of adjacent particles. This results in slower propagation of a sound wave passing through the material.

The effect of stress on density can be seen using Hooke's law in three dimensions, given in the below equations:

$$\begin{aligned}\sigma_x &= \frac{1}{E}\left[\varepsilon_x - \nu(\varepsilon_y + \varepsilon_z)\right] \\ \sigma_y &= \frac{1}{E}\left[\varepsilon_y - \nu(\varepsilon_x + \varepsilon_z)\right] \\ \sigma_z &= \frac{1}{E}\left[\varepsilon_z - \nu(\varepsilon_x + \varepsilon_y)\right]\end{aligned} \quad 4.3$$

Where σ denotes stress, ε the strain and υ the Poisson's ratio. If a material is strained in any axis the other two axes will change dependent upon Poisson's ratio υ. This results in an overall volume change, and as mass is conserved this will result in a net change in the material density proportional to the change in volume, as described in the relationship below.

$$\rho = M/V \quad 4.4$$

Where ρ is the density, *M* the mass and *V* the volume. The volume under pressure can be calculated from:

$$V_p = V_0\left(\frac{d_0 - \delta}{d_0}\right) \quad 4.5$$

Where V_0 and V_p are the initial and deformed volumes respectively, d_0 is the initial length of the material in the direction of the applied pressure and δ is the deflection resulting from the pressure. This assumes that the material only deforms in the direction of the applied pressure. Combining Equations 4.4 and 4.5 we get the density under pressure:

$$\rho_p = \rho_0\left(\frac{d_0}{d_0 - \delta}\right) \quad 4.6$$

Where ρ_0 and ρ_p are the initial density and the density under pressure respectively. Combining Equations 4.2 and 4.6 and rearranging to get the speed of sound:

$$(c_{xx})_p = \sqrt{\frac{E(1-\upsilon)}{\rho_0\left(\frac{d_0}{d_0 - \delta}\right)(1+\upsilon)(1-2\upsilon)}} \quad 4.7$$

The Time-of-Flight is then gained by dividing the ultrasonic path length by the speed of sound.

$$ToF_p = 2d_0 \Big/ \sqrt{\frac{E(d_0 - \delta)(1-\upsilon)}{\rho_0 d_0(1+\upsilon)(1-2\upsilon)}} \quad 4.8$$

The change in the time of flight is the difference between the ToF in the stressed and unstressed states.

$$\Delta t_\rho = ToF_p - ToF_0 \tag{4.9}$$

Combining Equations 4.8 and 4.9 gives the change in ToF of a longitudinal wave due to the density change of the material alone, Equation 4.10.

$$(\Delta t_{xx})_\rho = \frac{2d_0}{\sqrt{\frac{E(d_0-\delta)(1-\upsilon)}{\rho_0 d_0(1+\upsilon)(1-2\upsilon)}}} - \frac{2d_0}{(c_{xx})_0} \tag{4.10}$$

A similar approach can be used to get the change in ToF for a shear wave travelling in the direction of the stress. In this case the velocity of a shear wave is dependent on the material's density and shear modulus, as given by Equation 4.11.

$$c_{xy} \text{ or } c_{xz} = \sqrt{\frac{G}{\rho}} \tag{4.11}$$

Where *G* is the Shear Modulus. Substituting this in place of Equation 4.2 and repeating the above derivation yields the following expression for ToF change of a shear wave due to the density change of the material alone.

$$\left(\Delta t_{xy}\right)_\rho = \frac{2d_0}{\sqrt{\frac{G(d_0-\delta)}{\rho_0 d_0}}} - \frac{2d_0}{\left(c_{xy}\right)_0} \tag{4.12}$$

4.4 Elasticity Effect

At a particle level a rigid material is characterized by atoms and/or molecules with strong forces of attraction and repulsion to each other. These forces can be thought of as springs between the particles. The stiffness of these springs represents the materials elasticity. This stiffness, or elasticity, controls how quickly particles that are displaced from their resting positions return to these positions. Particles that return to their resting position quickly are ready to move again more quickly, and thus they can vibrate at higher speeds. Therefore, sound can travel faster through mediums with higher elastic properties (like steel) than it can through solids like rubber, which have lower elastic properties. The following section describes this in more detail, and shows how an applied stress can change a material's elasticity and result in a change in the speed of sound.

The elasticity of a material is dependent on the stress-strain relationship. When an object is loaded axially then the stress is described by:

$$\sigma = \frac{F}{A} \tag{4.13}$$

σ < 0 = Compressive Stress
σ > 0 = Tensile Stress

Where σ is the stress, F is the force and A is the area. The stress-strain relationship for most engineering materials is imagined as a linear relationship to simplify the mathematics behind engineering equations. However for acoustoelasticity it is the nonlinear characteristics that are of importance. Any nonlinearity of the stress-strain relationship results in a variation of the elasticity under an applied stress. This nonlinearity appears as the higher order terms in the Taylor series expansion of the constitutive law, Equation 4.14, using a strain energy approach.

$$\sigma_{ij} = \frac{\partial U}{\partial \varepsilon_{ij}} \tag{4.14}$$

Where *U* is the strain energy and ε is the strain. The Taylor series expansion of this is:

$$U = C^{(0)} + C_{ij}^{(1)}\varepsilon_{ij} + \frac{1}{2}C_{ijkl}^{(2)}\varepsilon_{ij}\varepsilon_{kl} + \frac{1}{6}C_{ijklmn}^{(3)}\varepsilon_{ij}\varepsilon_{kl}\varepsilon_{mn} \ldots \tag{4.15}$$

Where the *C* terms are the elastic tensors of different degrees. The first order term can represent residual stresses. The variation of elasticity under stress arises from the non-linearity of the stress-strain relationship. As stated above the second order terms and above of the Taylor series expansion are normally neglected as they greatly complicate the mathematics while having little effect. However, when studying the acoustoelastic effect these terms must be retained.

In order to understand the origin of the higher order terms in the stress-strain relationship we need to first consider the interatomic forces that produce this relationship. Here we consider the covalent bonds of an isotropic crystalline metal. The interatomic bond energy is a balance between their electrostatic attraction as calculated between two ions using Coulomb's law, and the repulsion of their nuclei here given in Born's repulsive energy form, Equations 4.16 and 4.17 respectively (Stobbe, 2005).

$$U_a = \frac{q^2}{4\pi\epsilon_0 r} \tag{4.16}$$

$$U_r = \frac{q^2 r_0^{n-1}}{4\pi\epsilon_0 n r^n} \tag{4.17}$$

Here U_a is the attractive energy, U_r is the repulsive energy, *r* is the interatomic spacing, r_0 is the equilibrium atomic bond length, *q* the fundamental charge, ϵ_0 the permittivity in a vacuum and *n* is the Born exponent, a large power that is typically gained experimentally and normally in the range 6 to 12 (a value of 12 was used to plot Figure 4.1). To get the force from these equations we simply differentiate with respect to *r*. The energies calculated from Equations 4.16 and 4.17 along with the calculated force are given in Figure 4.1.

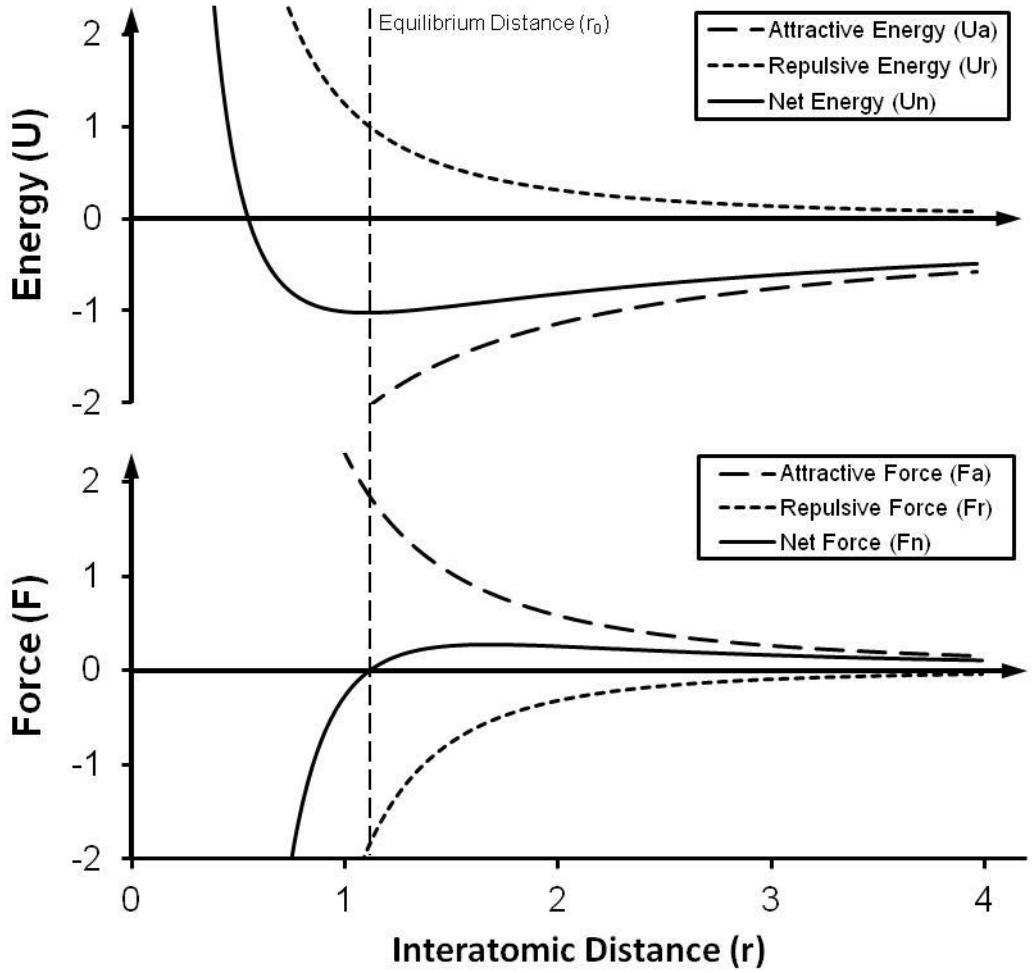

Figure 4.1: Potential Energy Well and Atomic Separation Force.

The attractive and repulsive forces balance to give a net force which varies with interatomic distance. It is the gradient of this curve that defines the materials elasticity. In an unstressed state the atoms in the material settle at an equilibrium interatomic distance. This is the point at which the attractive and repulsive forces balance to give zero net force. When the material is stressed, the applied force shifts this balance and changes the interatomic spacing. For small forces the relationship between applied force and interatomic spacing can be assumed to be linear. However as can be seen in Figure 4.1 the net force curve is not linear with interatomic distance and so for larger applied forces the linear approximation is no longer accurate.

The above Figures and Equations relate to Ionic bonds. For metals and their alloys, metallic bonds are more commonly found. These bonds give an energy curve that is very similar to that shown in Figure 4.1, and can be described by the relationship in Equation 4.18 (Ashby & Jones, 1996).

$$U = \frac{A}{r^m} + \frac{B}{r^n} \qquad 4.18$$

Where the first addend encapsulates the attractive energy, the second addend the repulsive energy, the constants (*A*, *B*, *m* and *n*) depend upon the particular bond, and *n* is greater than *m*.

4.4.1 Third Order Elastic Constants (TOEC)

Third order elastic constants were introduced to describe the nonlinear stress-strain model. For an isotropic solid there are 2 Second Order Elastic Constants (SOEC) and 3 Third Order Elastic Constants (TOEC) needed to describe and define the properties of the material. The second order elastic constants are often known as the Lamé constants λ and μ and the third order constants are given the convention *l, m* and *n*. These constants can then be related to acoustic velocity for a given stress, this is the basis of the acoustoelastic measurement. Inversely it is possible to determine the TOEC experimentally by measuring the velocity of longitudinal and shear acoustic waves through a material with varying orientation and stress.

4.4.2 Acoustoelasticity

If we consider two types of acoustic waves, longitudinal and shear, and consider two directions of propagation, parallel and perpendicular to stress, then we can start to consider what effect stress on acoustic wave velocity will have.

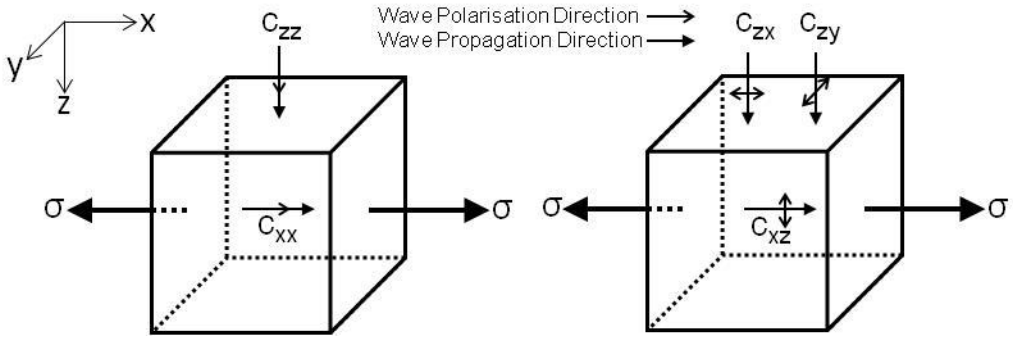

Figure 4.2: Wave Type and Polarisation Notation with Reference to the Direction of Stress.

The equations for the acoustic velocity of each of these wave types and orientations with stress have already been derived and are shown below. Equation 4.18 gives this relationship for a longitudinal wave travelling parallel to the applied stress:

$$\rho_0 c_{xx}^2 = \lambda + 2\mu + \frac{\sigma}{3B}\left[2l + \lambda + \frac{\lambda+\mu}{\mu}(4m + 4\lambda + 10\mu)\right] \qquad 4.18$$

Where ρ_0 denotes unstressed density, c_{xx} is the speed of sound, the first subscript denoting wave propagation direction, the second subscript denoting the polarisation direction. σ is the uniaxial stress and B is the bulk modulus. The second order elastic constants are given by λ, μ and the third order constants are given by *l, m* and *n*. Equation 4.19 gives the relationship for a longitudinal wave travelling perpendicular to the stress.

$$\rho_0 c_{yy}^2 \text{ or } \rho_0 c_{zz}^2 = \lambda + 2\mu - \frac{\sigma}{3B}\left[2l - \frac{2\lambda}{\mu}(m + \lambda + 2\mu)\right] \qquad 4.19$$

Equation 4.20 gives the relationship for a shear wave with polarisation perpendicular to the stress travelling parallel to the stress.

$$\rho_0 c_{xy}^2 \text{ or } \rho_0 c_{xz}^2 = \mu + \frac{\sigma}{3B}\left[m + \frac{\lambda n}{4\mu} + 4\lambda + 4\mu\right] \qquad 4.20$$

Equation 4.21 gives the relationship for a shear wave with polarisation parallel to the stress travelling perpendicular to the stress.

$$\rho_0 c_{yx}^2 \text{ or } \rho_0 c_{zx}^2 = \mu + \frac{\sigma}{3B}\left[m + \frac{\lambda n}{4\mu} + \lambda + 2\mu\right] \quad 4.21$$

Equation 4.22 gives the relationship for a shear wave with polarisation perpendicular to the stress travelling perpendicular to the stress.

$$\rho_0 c_{yz}^2 \text{ or } \rho_0 c_{zy}^2 = \mu - \frac{\sigma}{3B}\left[m - \frac{\lambda + \mu}{2\mu} n - 2\lambda\right] \quad 4.22$$

It is also useful to note that the bulk modulus can be calculated from the SOEC as shown in Equation 4.23.

$$B = \lambda + \frac{2}{3}\mu \quad 4.23$$

A number of previous studies have determined the SOECs, TOECs and densities for a range of steels. Some of these values, along the bulk modulus calculated using Equation 4.23 are given in Table 4.1.

	Steel, unspecified (Allen & Sayers, 1984)	StE 355 (Lüthi, 1990)	StE 42 (Si-Chaib, Menad, Djelouah, & Bocquet, 2001)	DIN 22NiMoCr37 (Si-Chaib, Menad, Djelouah, & Bocquet, 2001)	E 295 (Si-Chaib, Menad, Djelouah, & Bocquet, 2001)	Low Carbon Steel (Muir, 2009)	Rail Steel (Bray D. M., 1976)	Nickel-Steel S/NTV (Crecraft, 1967)
λ (GPa)	112.8	109	110.4	109.1	110	111	115.8	109.0
μ (GPa)	83.4	82	81.4	81.9	83	82.1	79.9	81.7
l (GPa)	-429.6	-192	-48.3	-196.4	-251	-461.0	-248	-56
m (GPa)	-664.4	-565	-501	-520.2	-519	-636.0	-623	-671
n (GPa)	-643.5	-724	-639.6	-656.5	-656	-708.0	-714	-785
ρ (kg/m^3)	7900	7790	7800	7850	7800	7800	7800	-
B (GPa)	168.4	163.7	164.7	163.7	165.3	165.7	169.1	163.5
α_{xx}*	-3.046	-2.066	-1.359	-1.746	-1.781	-2.978	-2.517	-2.629

*Calculated from Equation 4.32

Table 4.1: SOEC, TOEC and Density for a Number of Steels.

The values for the first steel listed in Table 4.1 where used to calculate the relative change in the speed of sound when a material is under tension for both longitudinal and shear waves propagating both parallel and perpendicular to the direction of the stress. These values show that the wave types relating to Equations 4.18 to 4.21 have a decreasing wave velocity with increasing tensile stress, while the wave polarisation relating to Equation 4.22 is the only one which has an increasing wave velocity with increasing tensile stress. The relative change in the speed of sound for each wave type in a material experiencing a tensile stress are plotted in Figure 4.3.

The figure shows that a longitudinal wave propagating in the direction of stress has the largest variation of acoustic velocity, followed by a shear wave travelling perpendicular to the direction of stress but polarised in the direction of stress. It is also interesting to note that the acoustic velocity of a shear wave travelling and polarised perpendicular to the stress direction will increase with tensile stress.

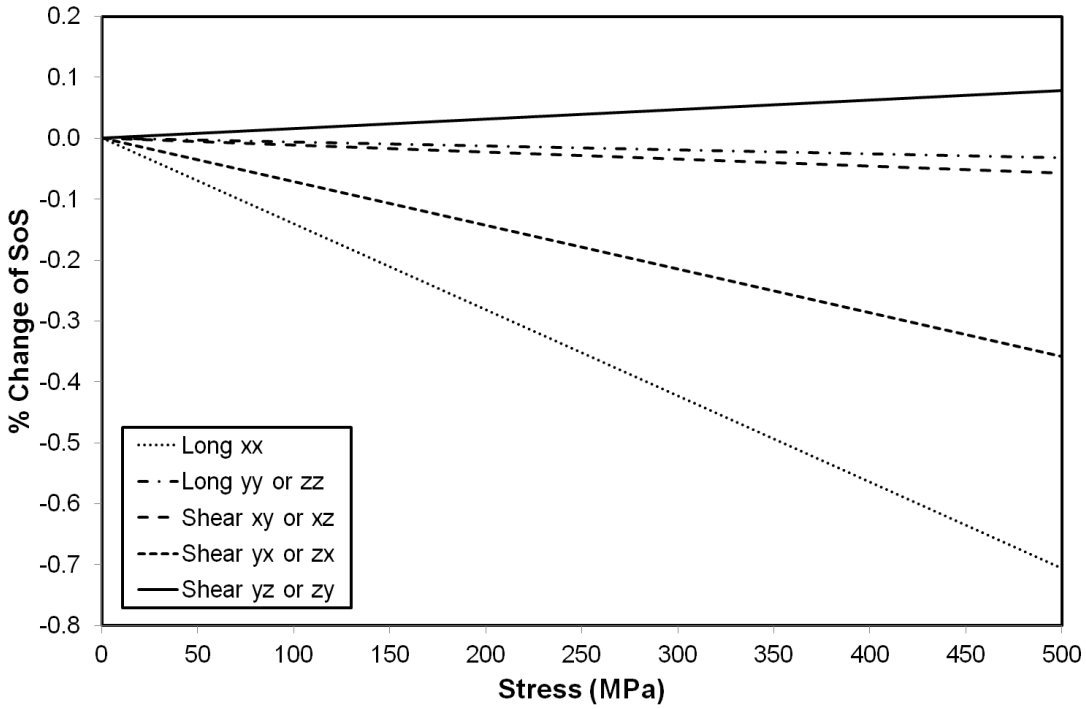

Figure 4.3: Percentage change in Speed of Sound for Various Wave Types and Polarisations in a Standard Steel subjected to Tensile Stress in the x-direction.

Figure 4.3 shows that over the range of stresses calculated the various equations can be approximated as linear. The relationship between stress and the change in a materials time of flight can be characterised by the acoustoelastic constant. This can be derived from the TOEC as shown below.

For uniaxial stress acting in the x-direction (σ_x), as shown in Figure 4.2 the triaxial principal strains are given by:

$$\varepsilon_x = \varepsilon \tag{4.24}$$

$$\varepsilon_y = \varepsilon_z = -\nu\varepsilon \tag{4.25}$$

Where ε_x, ε_y and ε_z are the components of strain in the x, y and z directions respectively and ν is Poisson's ratio. From this and Equations 4.18 to 4.22 the speed of sound with respect to strain can be calculated (Bray D. M., 1976).

$$\rho_0 c_{xx}^2 = \lambda + 2\mu + [4(\lambda + 2\mu) + 2(\mu + 2m) + \nu\mu(1 + 2l/\lambda)]\varepsilon \tag{4.26a}$$

$$\rho_0 c_{yy}^2 = \rho_0 c_{zz}^2 = \lambda + 2\mu + [2l(1 - 2\nu) - 4\nu(m + \lambda + 2\mu)]\varepsilon \tag{4.26b}$$

$$\rho_0 c_{xy}^2 = \rho_0 c_{xz}^2 = \mu + [4\mu + \nu(n/2) + m(1 - 2\nu)]\varepsilon \tag{4.26c}$$

$$\rho_0 c_{yx}^2 = \rho_0 c_{zx}^2 = \mu + [(\lambda + 2\mu + m)(1 - 2\nu) + (n\nu/2)]\varepsilon \tag{4.26d}$$

$$\rho_0 c_{yz}^2 = \rho_0 c_{zy}^2 = \mu + [(\lambda + m)(1 - 2\nu) - 6\nu\mu - (n\nu/2)]\varepsilon \quad 4.26e$$

Following from this we can calculate the change in time of flight using the method developed by Chen et. al. (Chen, Mills, & Dwyer-Joyce, 2015) and detailed below. The speed of sound in the unstrained state is given by:

$$\rho_0 (c_{xx})_0^2 = \lambda + 2\mu \quad 4.27$$

Where $(c_{xx})_0$ is the unstrained longitudinal speed of sound in the x-direction. Next by differentiating Equation 4.26a we get:

$$\rho_0 (c_{xx})_P d(c_{xx})_P = [2(\lambda + 2\mu) + (\mu + 2m) + \nu\mu(1 + 2l/\lambda)]\mathrm{d}(\varepsilon_x)_P \quad 4.28$$

If the change in the speed of sound is small the following assumption can be made.

$$\rho_0 (c_{xx})_P (c_{xx})_0 \approx \rho_0 (c_{xx})_0^2 = \lambda + 2\mu \quad 4.29$$

Dividing Equation 4.28 by 4.29 gives the change in the speed of sound in relation to the strain.

$$\mathrm{d}(c_{xx})_P/(c_{xx})_0 = \left[2 + \frac{(\mu + 2m) + \nu\mu(1 + 2l/\lambda)}{\lambda + 2\mu}\right]\mathrm{d}(\varepsilon_x)_P \quad 4.30$$

This can be rearranged to leave the right hand side of this equation dependant on material properties alone. It is useful to substitute the term α_{xx} in place of these properties.

$$\alpha_{xx} = 2 + \frac{(\mu + 2m) + \nu\mu(1 + 2l/\lambda)}{\lambda + 2\mu} \quad 4.31$$

Where α_{xx} is the acoustoelastic constant for a longitudinal wave propagating in the x-direction. Substituting into Equation 4.30 and rearranging yields:

$$\alpha_{xx} = \frac{\mathrm{d}(c_{xx})_P/(c_{xx})_0}{\mathrm{d}(\varepsilon_x)_P} \quad 4.32$$

From Equation 4.32 we can get the change in speed of sound for a given change in the strain.

$$\Delta c_{xx} = \alpha_{xx}(c_{xx})_0 \Delta\varepsilon_x \quad 4.33$$

Taking the change in the speed of sound as:

$$\Delta c_{xx} = (c_{xx})_0 - (c_{xx})_P \quad 4.34$$

And the change in the strain as:

$$\Delta\varepsilon_x = -(\varepsilon_x)_P \quad 4.35$$

Combining Equations 4.33 to 4.35 gives the change of speed of sound with the change in the strain.

$$(c_{xx})_P = (c_{xx})_0(1 - \alpha_{xx}\Delta\varepsilon_x) \quad 4.36$$

The change in time of flight caused by the change in speed of sound due to stress alone can be calculated from the difference between the time-of-flight of the stressed and unstressed states, Equation 4.37.

$$(\Delta t_{xx})_{\mathrm{E}} = \frac{2d_0}{(c_{xx})_0} - \frac{2d_0}{(c_{xx})_P} \tag{4.37}$$

Substituting in Equation 4.36 and rearranging results in:

$$(\Delta t_{xx})_{\mathrm{E}} = \frac{2d_0}{(c_{xx})_0}\left(\frac{-\alpha_{xx}\Delta\varepsilon_x}{1-\alpha_{xx}\Delta\varepsilon_x}\right) \tag{4.38}$$

It is useful to substitute the deflection in the place of the strain. The deflection, δ, is given in terms of strain by the following

$$\delta = \Delta\varepsilon_x d_0 \tag{4.39}$$

This gives the change in Time-of-Flight due to the acoustoelastic effect alone, in terms of the deflection, acoustoelastic constant, initial length and unstressed speed of sound.

$$(\Delta t_{xx})_{\mathrm{E}} = \frac{-2d_0\alpha_{xx}\delta}{(c_{xx})_0(d_0-\alpha_{xx}\delta)} \tag{4.40}$$

This gives the change in Time-of-Flight due to the acoustoelastic effect alone in terms of the deflection, acoustoelastic constant, initial length and unstressed speed of sound of a longitudinal wave. The effect is slight, resulting in a 0.05% increase in the speed of sound within a typical steel for a compressive load of 100MPa. Because the acoustoelastic constant is just an expression of material properties, the same equation can be applied to a shear wave by substituting in the shear speed of sound and acoustoelastic constant, α_{xy}.

4.4.3 Other Effects

As well as stress induced acoustoelasticity, density and deflection there are other factors that can affect the acoustic wave velocity. These include residual stress in the material and processing anisotropy. Anisotropy is a result of how the material is processed and is likely to occur in cold rolled due to the distortion of the material grain structure that it induces. Residual stresses can remain in the material after processing and affect the acoustic velocity of the material following the same principle as applied stress. It should be noted that the theory for acoustoelasticity defined above is for an isotropic solid only.

4.5 Time of Flight

The change in Time-of-Flight due to stress is the summation of the three effects described above, the deflection of the material and the change in speed of sound due to density and elasticity effect.

$$\Delta t = \Delta t_\rho + \Delta t_\delta + \Delta t_E \tag{4.41}$$

Substituting in the relationships for this as given in Equations 4.1, 4.10 and 4.40 gives:

$$\Delta t_{xx} = \frac{2d_0}{\sqrt{\frac{E(d_0-\delta)(1-\upsilon)}{\rho_0 d_0(1+\upsilon)(1-2\upsilon)}}} + \frac{2\delta - 2d_0}{(c_{xx})_0} - \frac{2d_0\alpha_{xx}\delta}{(c_{xx})_0(d_0-\alpha_{xx}\delta)} \quad 4.42$$

Using the corresponding terms for shear waves yields the shear equivalent:

$$\Delta t_{xy} = \frac{2d_0}{\sqrt{\frac{G(d_0-\delta)}{\rho_0 d_0}}} + \frac{2\delta - 2d_0}{(c_{xy})_0} - \frac{2d_0\alpha_{xy}\delta}{(c_{xy})_0(d_0-\alpha_{xy}\delta)} \quad 4.43$$

Using representative values for steel, as given in Table 4.2, the change in time of flight expected for a longitudinal ultrasonic pulse travelling through 70mm of steel a range of stresses was calculated. The results are plotted in Figure 4.4, which shows a stack of the change in time-of-flight due to the various effects.

Density (kg/m^3)	7900
Initial Length (m)	0.035
Poisson's Ratio	0.3
Speed of Sound (m/s)	5996.19
Acoustoelastic Constant	-3.046
Youngs Modulus (GPa)	211
Unstressed ToF (µs)	11.67

Table 4.2: Example Material Properties for Steel used in Acoustoelastic Calculations.

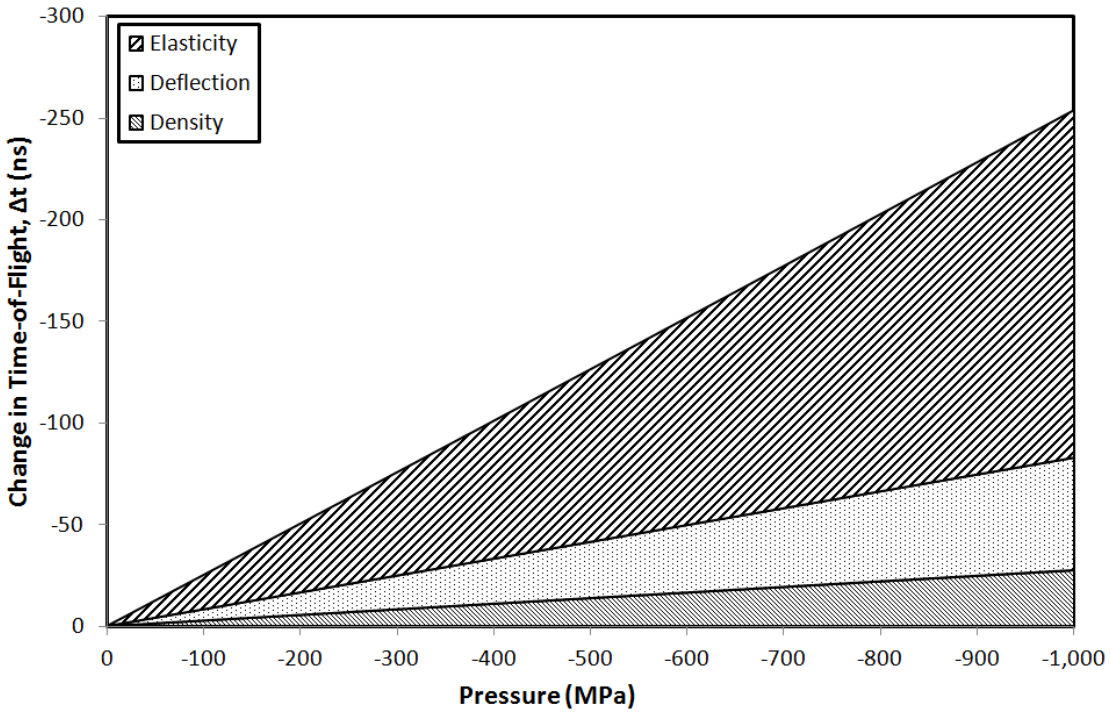

Figure 4.4: Longitudinal Change in Time of Flight against Pressure for values in Table 4.2. The absolute Time of Flight when unstressed is 11.67µs.

It is clear from the above figure that acoustoelasticity has the largest influence; however, neither the density or deflection effects are negligible in comparison.

4.6 Time of Flight Measurement Techniques

In order to measure the effects mentioned above it is necessary to ascertain the speed of sound with a high degree of accuracy. To calculate the speed of sound the time of flight of an ultrasonic wave through the material must be measured. The path length is then divided by this transit time to yield the speed of sound. The ToF is measured by taking the time difference between multiple reflections within a material. For the time of flight value to be accurate a consistent point on each returned pulse must be taken. There are a number of methods for doing this as shown in Figure 4.5 and outlined in the following sections.

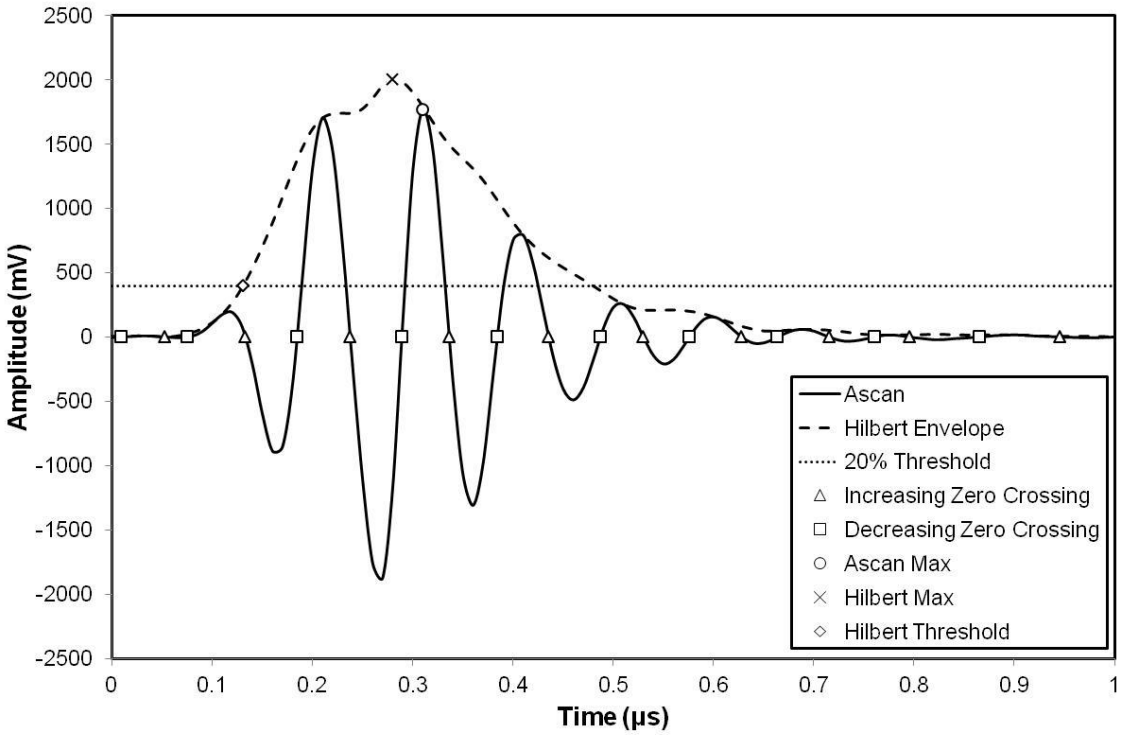

Figure 4.5: Methods of Time-of-Flight Measurement.

4.6.1 Maximum Peak Detection

Conceptually the simplest approach to detect the time of a reflection is to take the maximum peak of the reflection. Providing that successive returned pulses have the same shape the difference in time between the maximum peaks will give a measurement of the ToF. In some cases the returned pulse is inverted and a maximum peak must be compared to the subsequent minimum dip. In practical applications this approach is limited. In some cases the shape of the reflected pulse means that another peak is close in amplitude to the maximum peak. Therefore a small change in amplitude, such as that caused by noise, can cause the peak chosen as the maximum to jump. This approach is also affected by phase change within the reflections. If no interpolation is performed the peak time measurement has the same resolution as the sampling rate. To increase this resolution a peak fitting algorithm can be applied. Using this type of algorithm increases the computational load and such algorithms are still susceptible to noise. Implementing this detection technique in software is straightforward, but a hardware implementation of a peak detection algorithm is more complex.

4.6.2 Threshold

A widely used approach is to take the time of a threshold crossing. This approach is favoured in some applications because of its ease of implementation in hardware, by use of a simple comparator. As subsequent reflections drop in amplitude a fixed value threshold would trigger on a different point on each pulse. This problem can be tackled in two ways. One approach which is again straightforward to implement in hardware is to employ a non-linear amplifier, such as a log-amp, to amplify the signal. This amplifies the signal in such a manner that ensures that the lower end values are disproportionally enlarged. This distortion of the signal means that the offset in the threshold point resulting from a drop in signal amplitude is not removed, however it is reduced. The second approach is to scale the threshold proportionality to the pulse amplitude. This in essence combines the maximum detect and threshold methods, and providing only the pulse amplitude changes, and not pulse shape, this will remove the offset error. Any threshold method applied to the waveform is susceptible to errors introduced by a phase change.

4.6.3 Zero Crossing

The zero crossing technique is a particular form of threshold which looks for points in the waveform that cross the X-axis. By taking the zero crossing points any amplitude change in the pulse doesn't have any effect. The zero crossing is where the curve is steepest and can be approximated to a straight line in the vicinity of the axis. Linear interpolation can therefore be used to increase the resolution of the measurement by up to 2 orders of magnitude. This approach is still affected by a change in phase. It can be implemented in hardware in a similar way to the standard threshold technique.

4.6.4 Analytic Representation

All of the techniques outlined above rely on picking a consistent point on the waveform which is dependent on its shape. Their accuracy is vulnerable to changes in the pulse shape, such as those caused by phase changes in the pulse. To remove the effect of the phase the analytic signal is taken. This gives a 'envelope' of the signal amplitude accounting for both the real and imaginary parts. It is calculated by first using a Hilbert transform to reconstruct the imaginary component from the recorded signal. Then the analytic signal is gained by taking the square root of the sum of the squares of both the real and imaginary components. An example analytic signal can be seen in Figure 4.6.

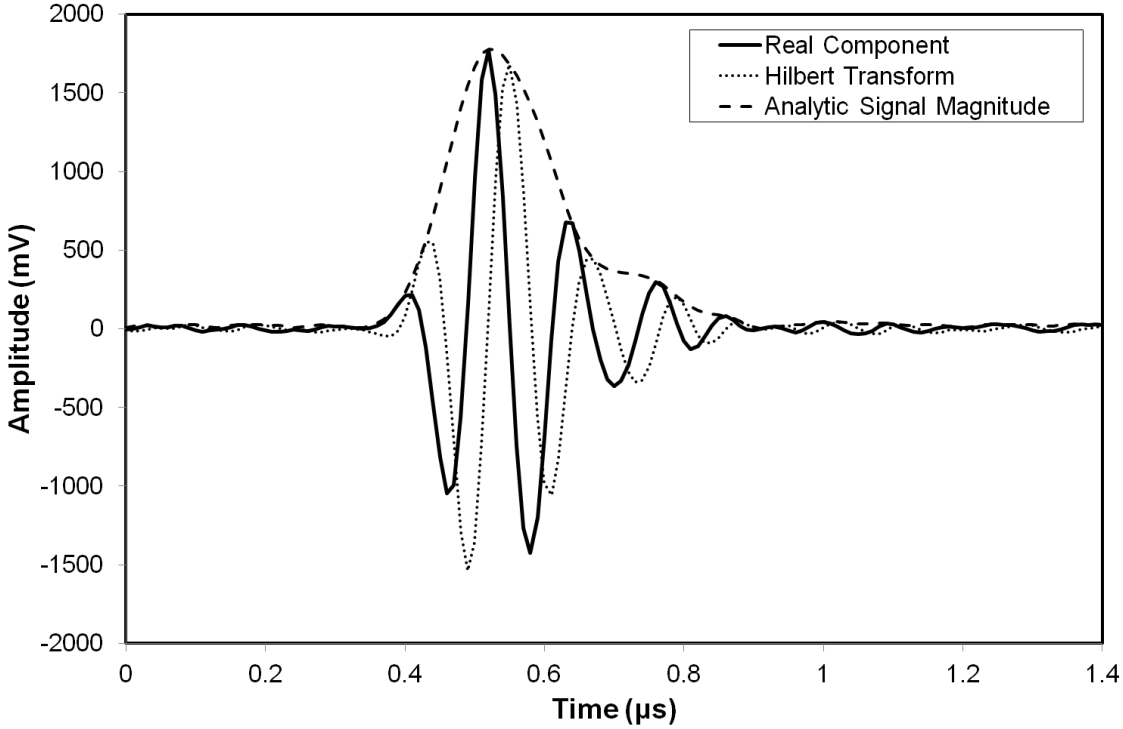

Figure 4.6: Example Analytic Signal.

Both the peak and threshold techniques can be applied to the analytic signal to yield the pulse time, however unlike when applied to the raw signal, the result is not susceptible to changes in the pulse phase. The additional functions come at a significant computational cost which makes this method unsuitable for real-time high-speed measurements, however it can be applied in post processing of the data. Also the method assumes only a single signal is in each data window. Alternatively cross-correlation algorithms can be used which locate subsequent reflections as entities, rather than via a single point.

4.7 Stress Induced Refraction

The above analysis demonstrates how induced stress will cause a change in the speed of sound of a material. A non-uniform stress field will therefore produce a similar non uniformity in the speed of sound of a material. As shown in Chapter 3 a wave passing between mediums with a different speed of sound will be refracted, as governed by Snell's Law. This calculation is adequate for a simple discontinuity in the speed of sound between two distinct mediums, however the effect on wave trajectory across a sound gradient, like that seen in a stressed part, requires a more in-depth analysis.

Previous work has been carried out studying the acoustic ray trajectory across speed of sound gradients in non-destructive testing (Ben-Benjamin & Cohen, 2015) (Wang, Takatsubo, Toyama, Akimune, & Zhao, 2006), the atmosphere for the purposes of noise control in the discipline of civil engineering (Keith Wilson, 2003) (Reynolds, 1874) (Rayleigh, 1912) and ocean acoustics, for applications such as sonar (Duda, 2005). The gradients in these scenarios are predominantly caused by temperature and pressure variations. The underlying wave bending effect is the same as that seen in ultrasonic waves travelling through a medium with non-uniform speed of sound.

4.7.1 1D Speed of Sound Gradient Propagation Model

To quantify the wave bending effect, it is easiest to start with a simple case of a 1 dimensional gradient in the speed of sound, and considering the propagation the ultrasonic wave as a ray. Then starting with Snell's law (§3.2.6) Equation 4.44.

$$\frac{\sin\theta_1}{\sin\theta_2} = \frac{c_2}{c_1} \tag{4.44}$$

This can be rearranged to give:

$$\sin^{-1}\left(\frac{c_1 \sin\theta_1}{c_2}\right) = \theta_2 \tag{4.45}$$

This allows the refracted angle to be calculated for a simple interface between two materials which can each be characterised by a constant speed of sound. This will now be extended to account for a linearly changing speed of sound within the second material.

A 1 dimensional gradient in the speed of sound can be described by a simple linear relationship as follows:

$$c(x) = c_1 + ax \tag{4.46}$$

Where a is the gradient and x is the distance in the x-direction. Here it has been assumed the speed of sound in the second material matches the first material at the interface, then linearly varies the further from the interface. varies Substituting Equation 4.45 in place of c_2 in Equation 4.46 gives:

$$\sin^{-1}\left(\frac{c_1 \sin\theta_1}{c_1 + ax}\right) = \theta(x) \tag{4.47}$$

Assuming that the wave originates at the origin, the distance travelled by the wave in the y-direction can be calculated from the following:

$$y(x) = \frac{x}{\tan(\theta(x))} \tag{4.48}$$

Using Equations 4.47 and 4.48 the path of the ray can be plotted. Ray paths have been calculated for a number of material speed of sound arrangements, as shown in Figure 4.7. These have been calculated for an incident wave at 15° to the direction of the gradient. For this plot the speed of sound in every arrangement starts at 6000m/s and drops to 2000m/s, accordingly the final angle of each ray is the same. The profile of the speed of sound varies between arrangements, this results in different ray offsets in the Y-direction, and also different ray path lengths.

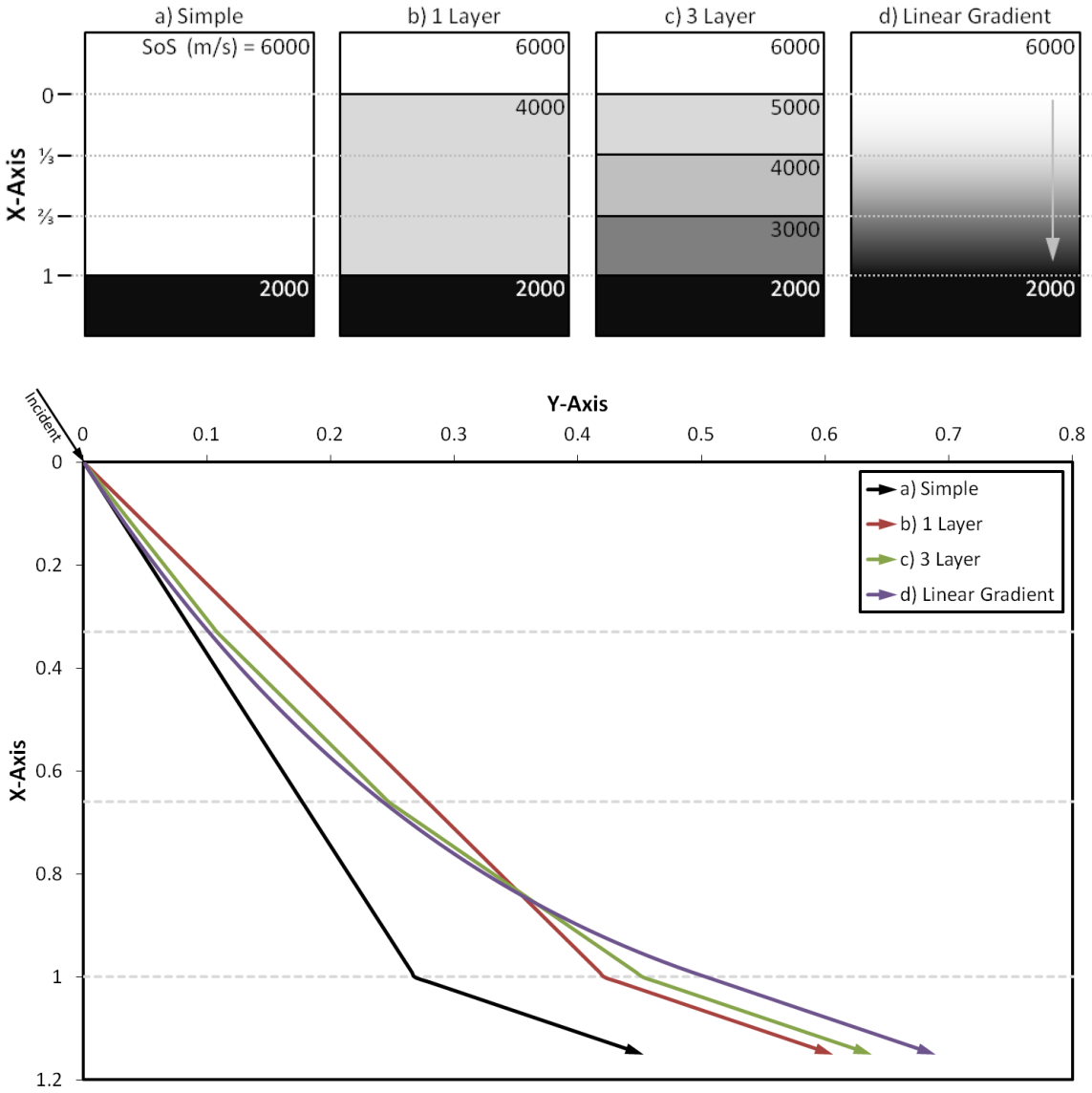

Figure 4.7: Ray Path for 15° Incident Angle and Various Speed of Sound Gradients.

Figure 4.8 shows another set of profiles, this time the speed of sound both starts and finishes as 6000m/s. The impact of each gradient profile with respect to the unchanged state can clearly be seen. Again the final refracted angle in all cases is the same, equal to the incident angle, but the Y-offset and ray path length varies. It should also be noted that as well as the difference in ray path length, there is also a difference in the average speed of sound. The combination of these two factors means that the Time of Flight for each ray path is also different.

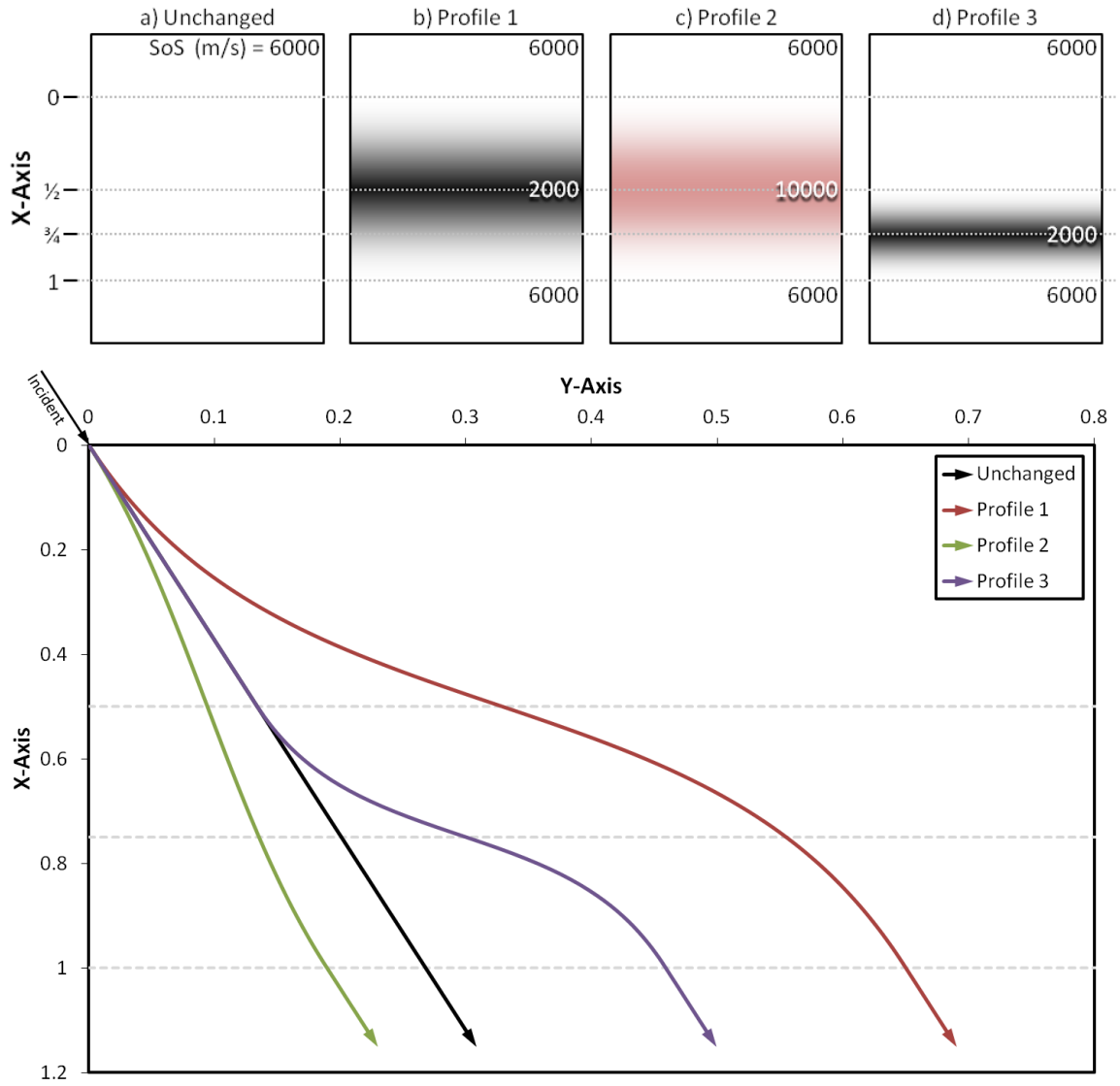

Figure 4.8: Ray Path for 15° Incident Angle and Various Speed of Sound Gradients.

From the above analysis it is clear that a non-uniform speed of sound will result in an alteration of the ultrasonic ray path, and both the magnitude of the change, and distance over which it occurs are important. It has already been shown that stress in a part can cause a change in the speed of sound due to acoustoelasticity. Therefore stress in a part can also result in an alteration in the ultrasonic ray path.

4.7.2 2D Speed of Sound Gradient Propagation Model

The 1D approximation demonstrates the effect, however in order to quantify the effect in a rolling contact a 2D model is required. Such a model could be developed analytically, however this would be complex and unwieldy to adapt to different speed of sound profiles. Instead a numerical approach was adopted. This method is shown below.

The model was implemented as a script in NI LabVIEW. The purpose of the model is to demonstrate the ultrasonic ray path across a material with a known speed of sound profile. In a stressed component this profile could be gained through modelling of the acoustoelastic effect as shown earlier. As such the model starts with a surface giving the speed of sound profile, as

represented by a magnitude array. An example array is shown in Figure 4.9, this has a simple radial profile to the speed of sound.

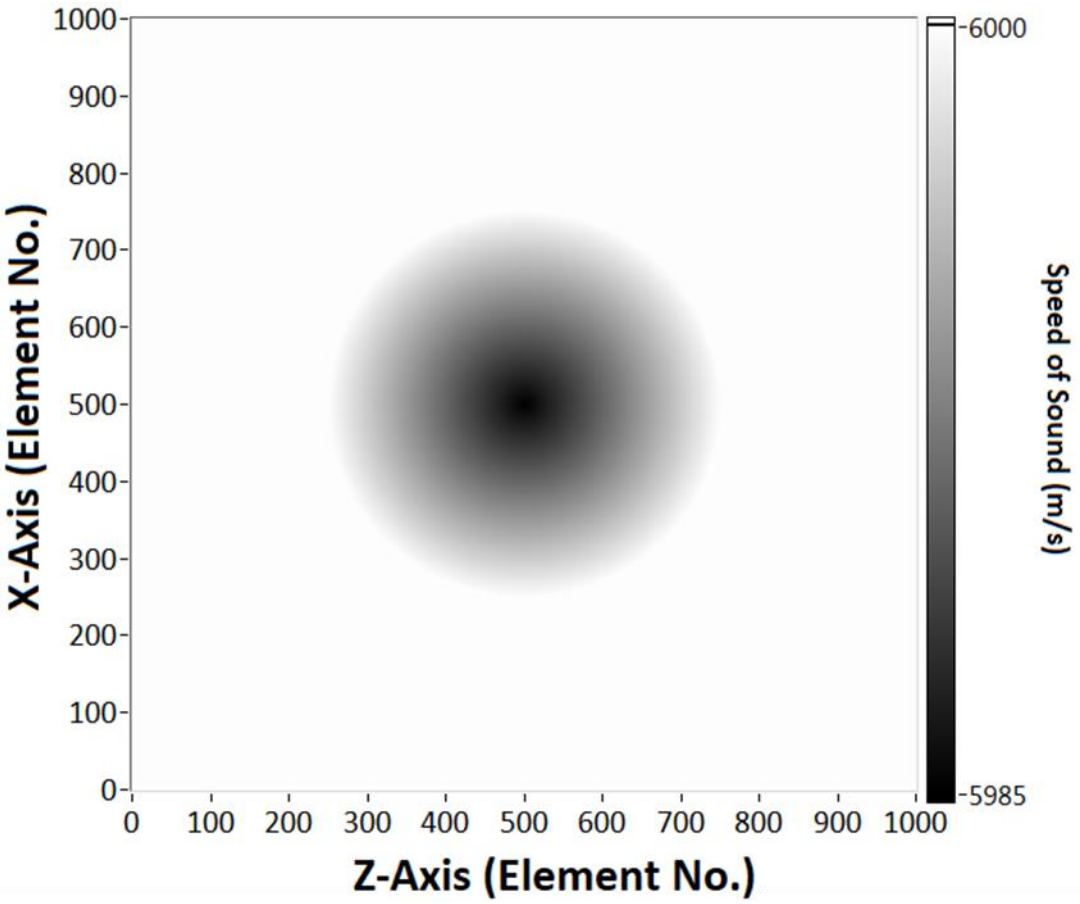

Figure 4.9: Speed of Sound Array, X and Z axis are in array elements.

The next step is to differentiate this array in both X and Z directions in order to get the gradient of the speed of sound in each direction. With the X and Z components the slope of the surface at each point, and the direction of this slope with respect to Z-axis, can be calculated using the following relationships.

$$\left|g_{Surface}\right| = \sqrt{g_x^2 + g_z^2} \tag{4.49}$$

$$\theta_{Surface} = \tan^{-1}(g_z/g_x) \tag{4.50}$$

Where g_x, g_z and $g_{Surface}$ are the magnitude of the gradients in the X-direction, Z-direction and surface respectively and $\theta_{Surface}$ is the angle of the surface gradient with respect to the Z-axis. It should be noted that in this simple model the ray is always assumed to be progressing in the positive Z direction as such $\theta_{Surface}$will always take values $-\pi/2 < \theta_{Surface} < \pi/2$, and where g_z is negative then $g_{Surface}$ is taken to be negative. Where both g_x, g_z are zero, then $\theta_{Surface}$ is also defined as zero. The results of these are shown in Figure 4.10 and Figure 4.11.

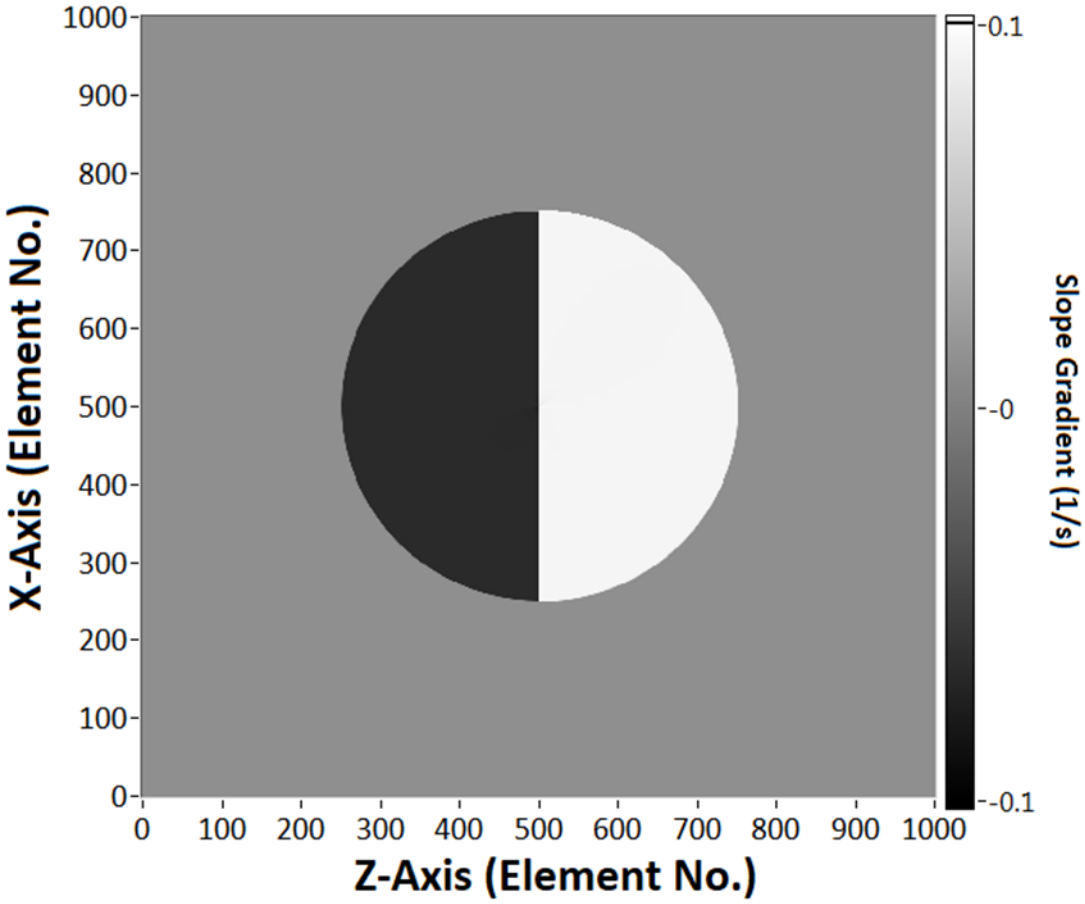

Figure 4.10: Gradient of Slope for the Array in Figure 4.9.

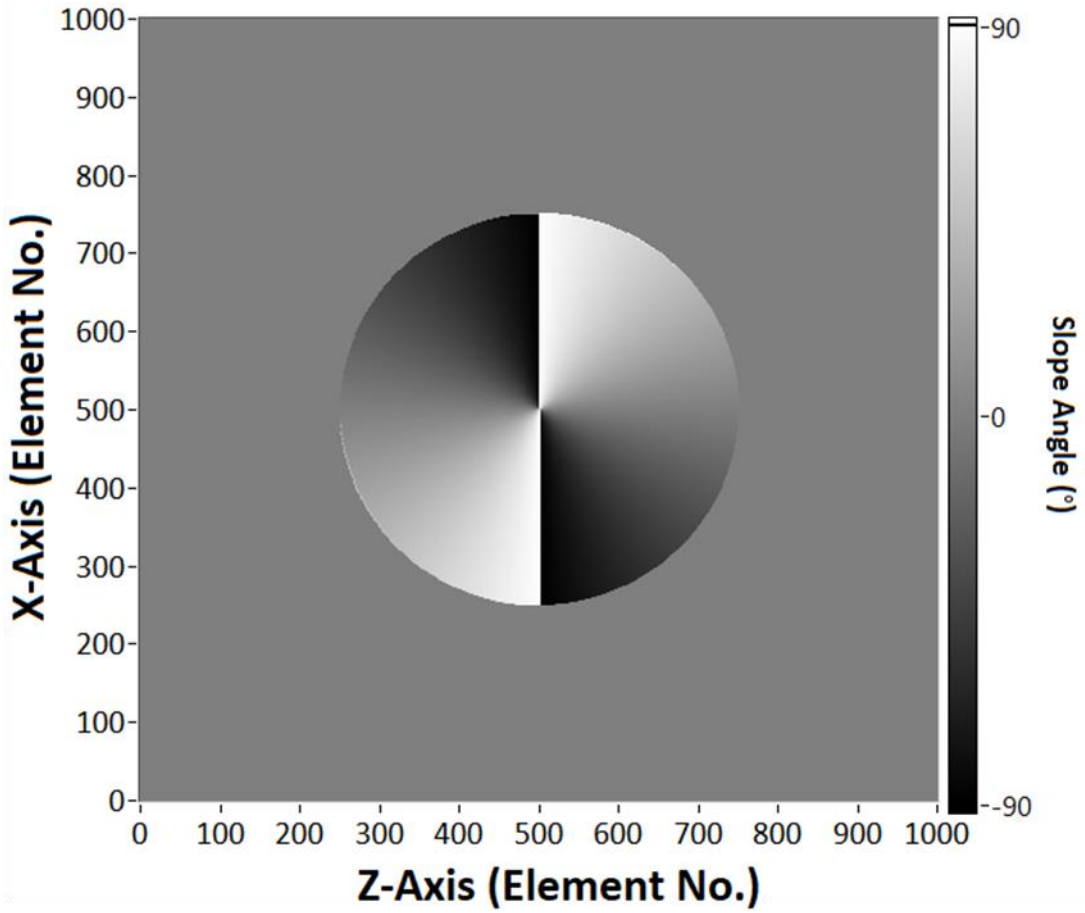

Figure 4.11: Angle of Slope with respect to Z-axis for the Array in Figure 4.9.

This means that each point in array has a value for c, g and $\theta_{Surface}$. With this information it is now possible to trace ray paths through this field. Each element in the array is treated as a separate interface to which Snell's law can be applied. Figure 4.9 to Figure 4.11 show unscaled arrays. The scale of these is set by assigning an element spacing. For demonstration purposes the element spacing is set to 10m which magnifies the effect of the ray steering. A ray is introduced at the left hand side of the arrays (as shown in the figures above, z = 0), with a defined x-coordinate and a starting angle (in this case the angle is set to 0). The difference between the ray angle and the slope angle is calculated to give the ray incident angle (θ_1). The speed of sound array is used to get an initial speed of sound (c_1) and the gradient of the slope is added to this to give an exit speed of sound (c_2). These values can then be used in Snell's law to give an exit angle (θ_2). This angle is then used to calculate the direction of the ray and either the next element it will encounter, or the next line adjoining elements. This gives a new set of x and y coordinates and angle θ_{Ray}. The values for the next element are then taken and the process is then repeated. If the ray encounters a line adjoining elements then the values are taken by interpolating between the two elements. This process is shown in Figure 4.12.

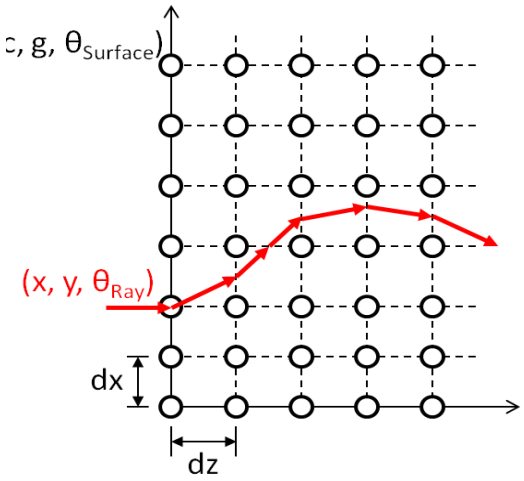

Figure 4.12: Ray Propagation through Grid.

The path length can be calculated by summing the lengths of each ray iteration, and the ToF can be calculated by dividing the individual line lengths by the speed of sound at each point before summing. The ray iterations are repeated until either the x or y coordinate of the ray is outside the bounds of the array. By overplotting many rays, each starting with a different x-offset a picture of the ray propagation through the array being studied can be drawn, as shown in Figure 4.13 for the arrays given in Figure 4.9 to Figure 4.11. As expected this shows a clear lensing effect with the rays defocusing as they encounter the slower speed of sound. If we invert the speed of sound array, so that the maximum and minimum values are now reversed, we see the opposite, a focusing effect, Figure 4.14.

.

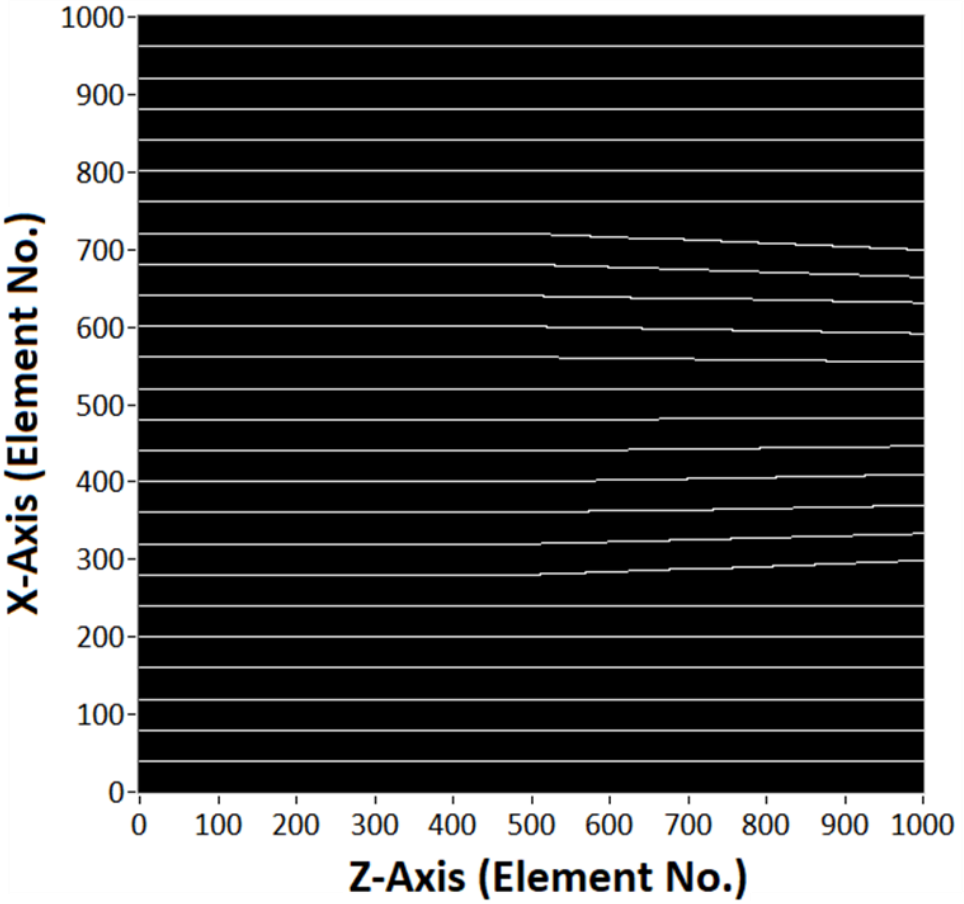

Figure 4.13: Calculated Ray Paths for Array in Figure 4.9.

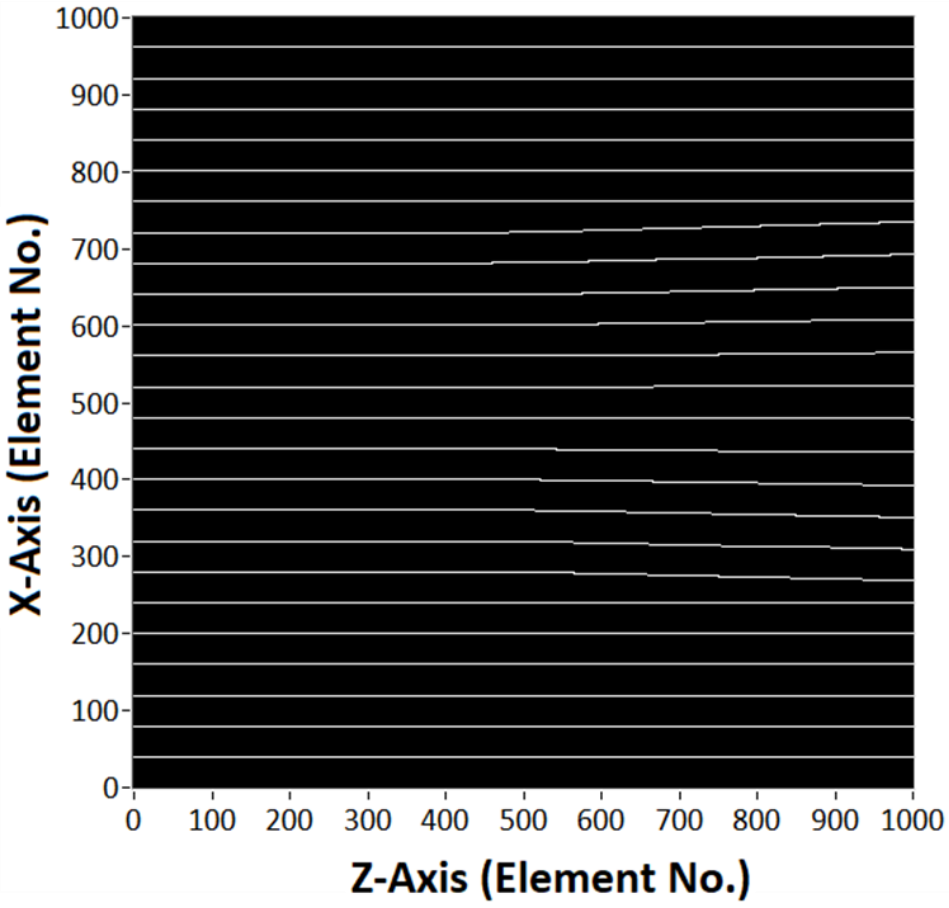

Figure 4.14: Calculated Ray Paths for Inverted Speed of Sound Array.

As information regarding the ray path and ToF can be calculated at every point it is possible to crudely simulate the propagation of a wave through the medium. This is achieved by simulating a number of rays emanating from each starting element, with the each ray having a different starting angle, as shown in Figure 4.15. This is similar to Huygens principal as introduced in Chapter 3.

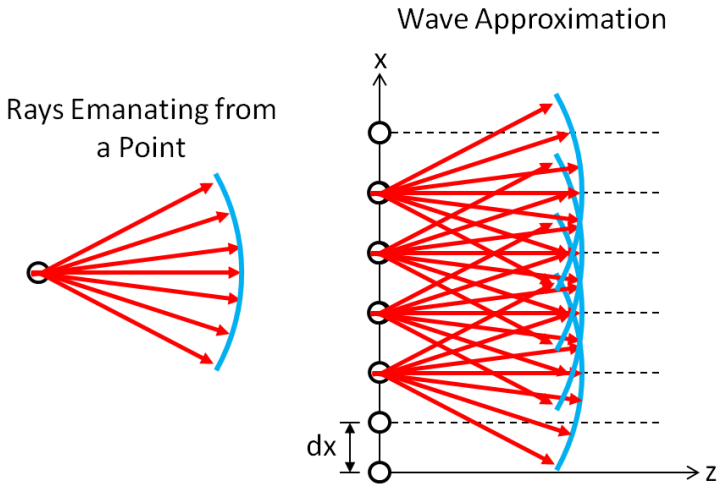

Figure 4.15: Wave Approximation using Multiple Rays.

This is completed for a large number of rays (in the simulations below 40,000 rays where used). A simulated wave is then propagated through the medium by stepping the wave along each ray based upon the ToF at each point. The amplitude of the overlapping rays is summed for each ToF step of the simulated wave. Figure 4.21 shows such a wave simulation, this is a composite image showing the wave every 0.5µs.

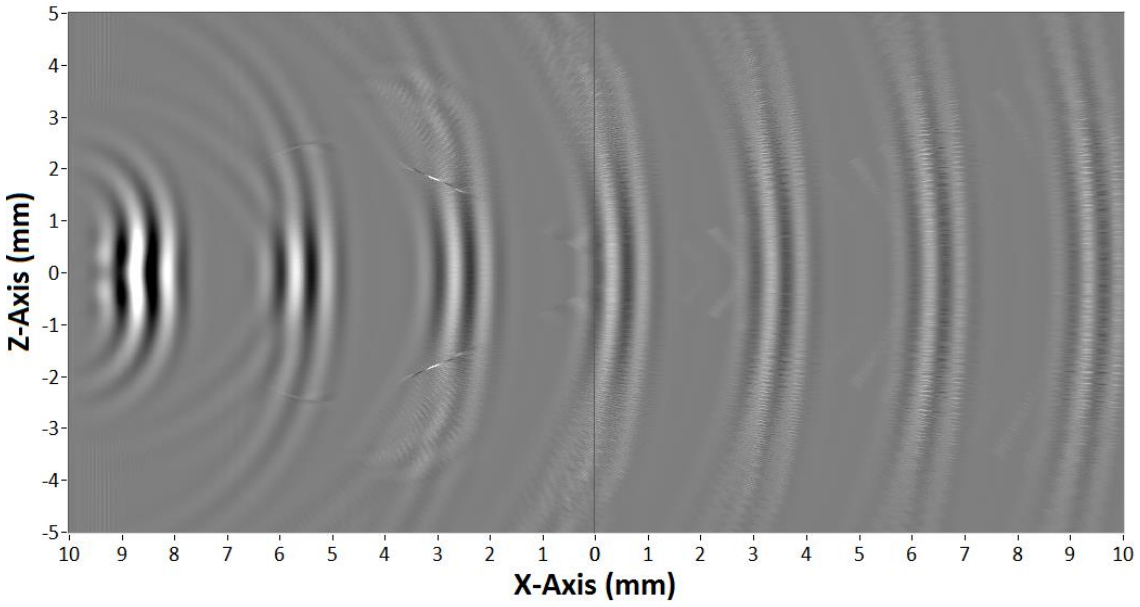

Figure 4.16: Wave Propagation Simulation, comprising of the wave every 0.5µs for the Speed of Sound array shown in Figure 4.9.

4.8 Acoustoelastic Beam Steering in a Cold-Rolling Contact

Now that the beam steering effect due to speed of sound gradients has been demonstrated, the next step is to investigate the effect of this in a cold-rolling contact, due to acoustoelasticity. As has already been shown the acoustoelastic effect is slight, with large stresses resulting in a small change to the speed of sound. In cold rolling the contact pressure is relatively high and it is hypothesised that in and around the contact this results in a non-uniform speed of sound profile which results in beam steering around the contact. In order to estimate the magnitude of the effect in cold rolling, a representative rolling case, given Table 4.3, has been modelled and the acoustoelastic effect along with ultrasonic ray paths through the contact have been modelled.

Strip Entry Thickness (mm)	2.8
Strip Exit Thickness (mm)	2.154
Strip Width (mm)	100
Elongation (%)	30
Roll Bite Length (mm)	13.464
Roll Diameter (mm)	391
Rolling Force (tonne)	67.5
Slip (%)	3.7
Entry Tension (tonne)	0.55
Exit Tension (tonne)	1.3

Table 4.3: Example Cold Rolling Parameters.

The stress pattern for a representative rolling case was calculated using the approach presented in §2.6. The first step from the data in Table 4.3 was to calculate the friction coefficient of the contact. This can be calculated from Equation 4.51 (Liu, Tieu, Wang, & Yuen, Friction Measurement in Cold Rolling, 2001).

$$S_f = \frac{R'}{h_1}\left(\frac{\theta}{2} - \frac{\theta^2}{4\mu}\right)^2 \qquad 4.51$$

Where θ is the roll bite entry angle, R' is the deformed roll radius, μ is the Coulomb friction coefficient, h_1 is the strip exit thickness and S_f is the forward slip. Taking values given above with a deformed roll radius of **280.6mm**, calculated from Equation 2.7, and a roll bite entry angle of **0.06889rad**, calculated geometrically, this equation gives a friction coefficient of **0.0674**. This resulted in the stress field as shown in Figure 4.17.

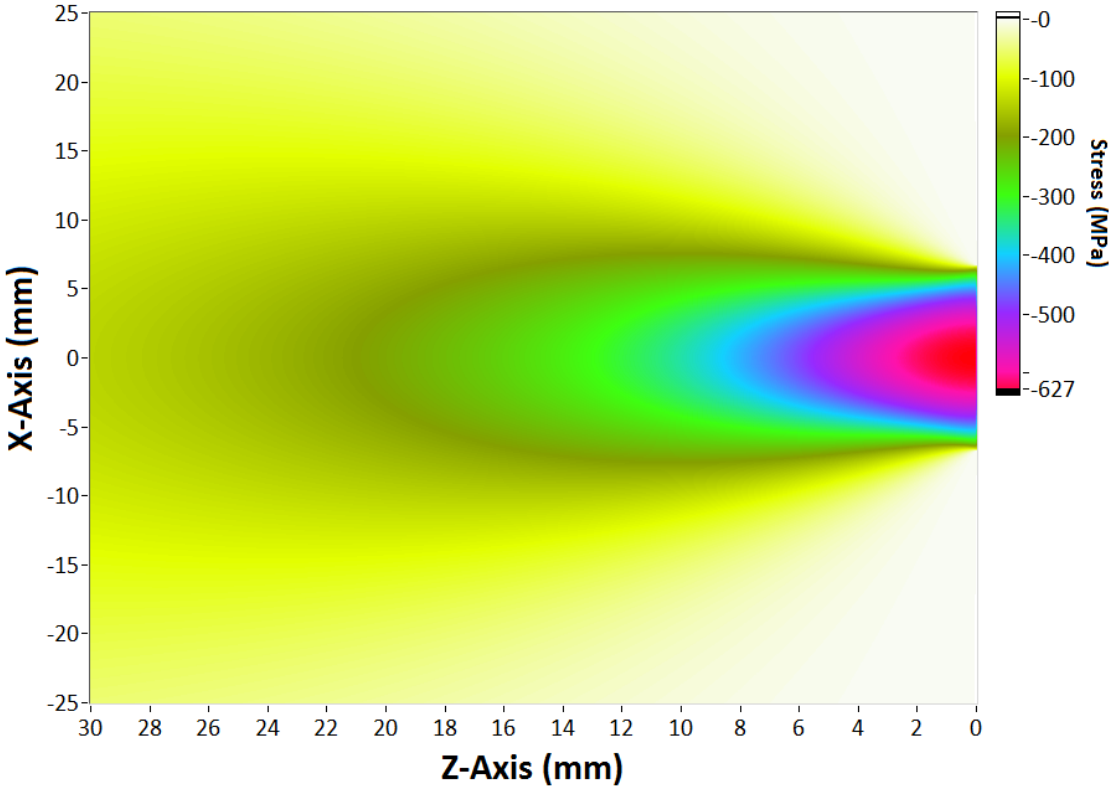

Figure 4.17: Stress (σ_{zz}) Calculated for Representative Rolling Case, Table 4.3.

As with the previous analysis a wave propagating in the Z-direction will be calculated. The average stress across the Z-direction from 0 to 30mm is plotted in Figure 4.18. This gives an indication of the average stress encountered by an ultrasonic wave travelling across the Z-direction, without accounting for any beam steering. Only the stress in Z-direction has been calculated as this is the primary direction of the wave propagation and will have the largest effect

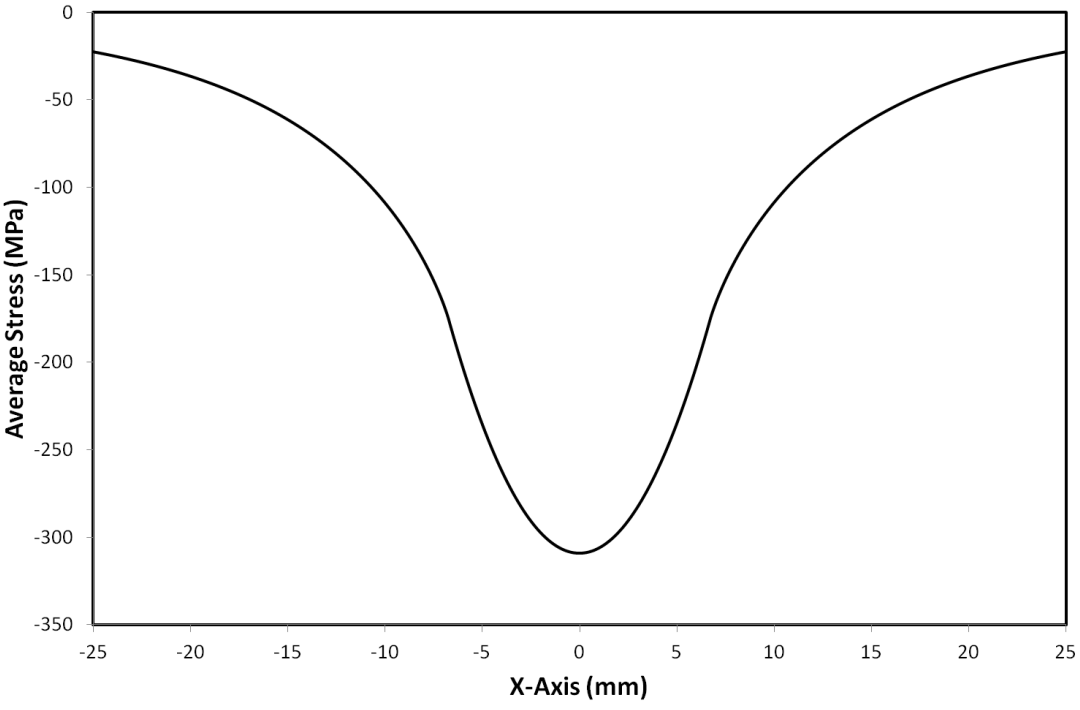

Figure 4.18: Average of Stress in Z-Axis Direction of Figure 4.17.

The stress array was then converted to a speed of sound array via the acoustoelastic equations. The parameters for steel in Table 4.2 where used. This resulted in the speed of sound field shown in Figure 4.19.

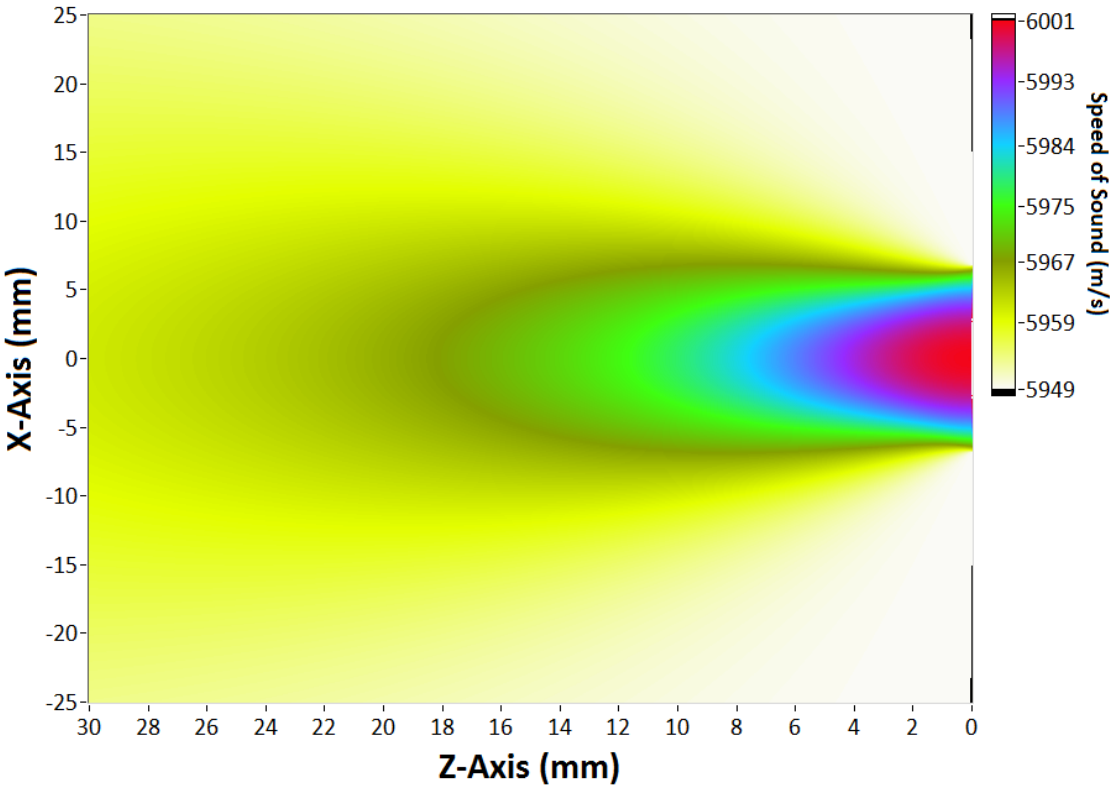

Figure 4.19: Cold Rolling Contact Speed of Sound Array.

The average speed of sound in the Z-direction, and the corresponding Time-of-Flight, are plotted in Figure 4.20 and Figure 4.21. The magnitude of the ToF change is large relative to the digitisation rate of current high frequency ultrasonic systems and should be measurable.

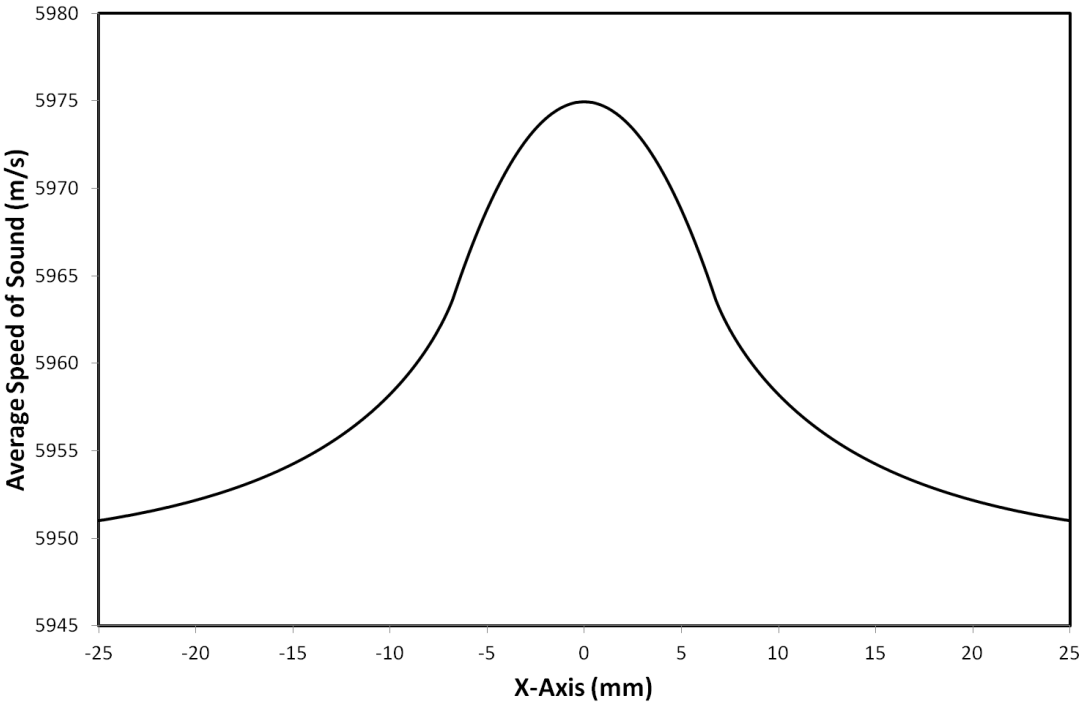

Figure 4.20: Average of Speed of Sound in Z-Axis Direction.

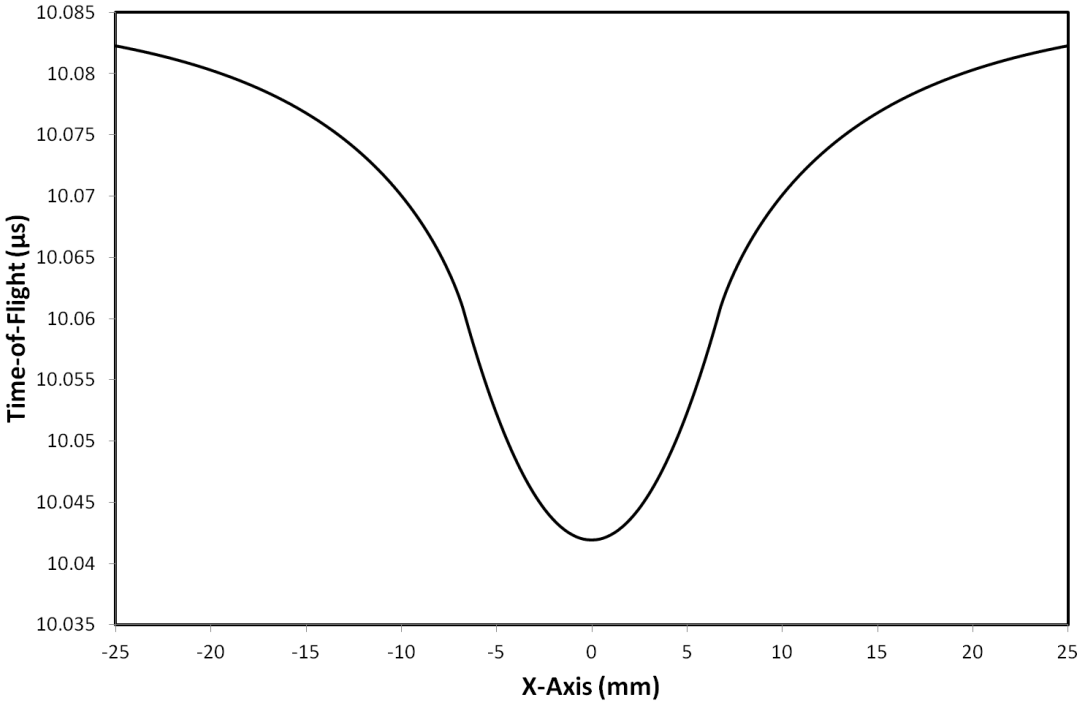

Figure 4.21: Time of Flight based upon Speed of Sound in Figure 4.20.

The approach shown in §4.7.2 was then adopted. The gradients in the X and Z directions and the surface gradient and direction with respect to the X-axis are shown in Figure 4.22 to Figure 4.25.

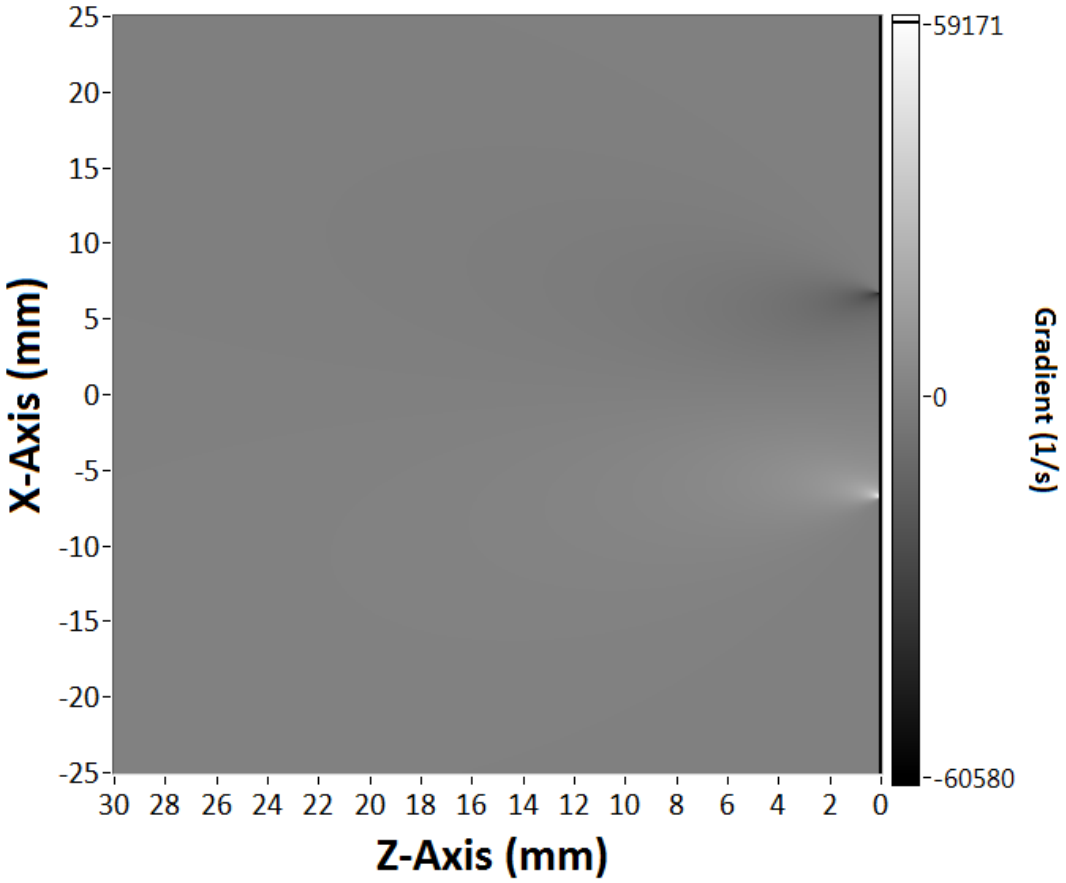

Figure 4.22: Gradient in the X-Direction.

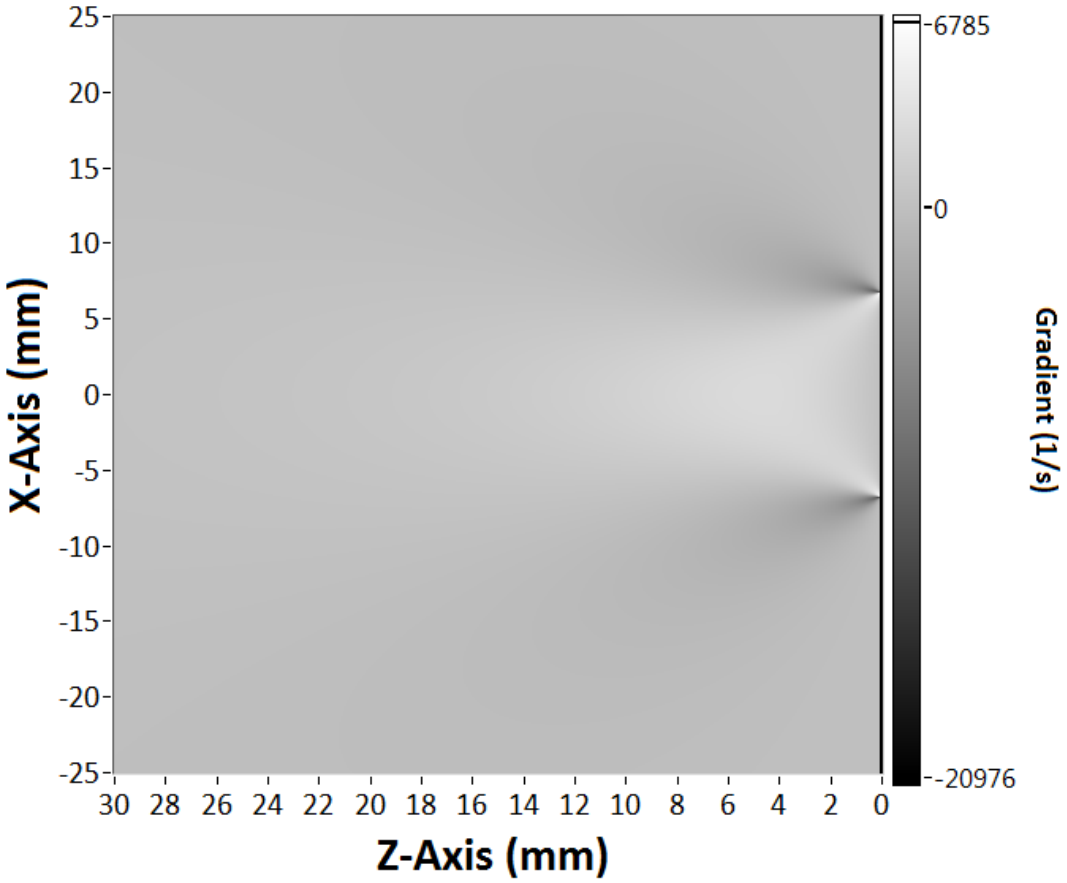

Figure 4.23: Gradient in the Z-Direction.

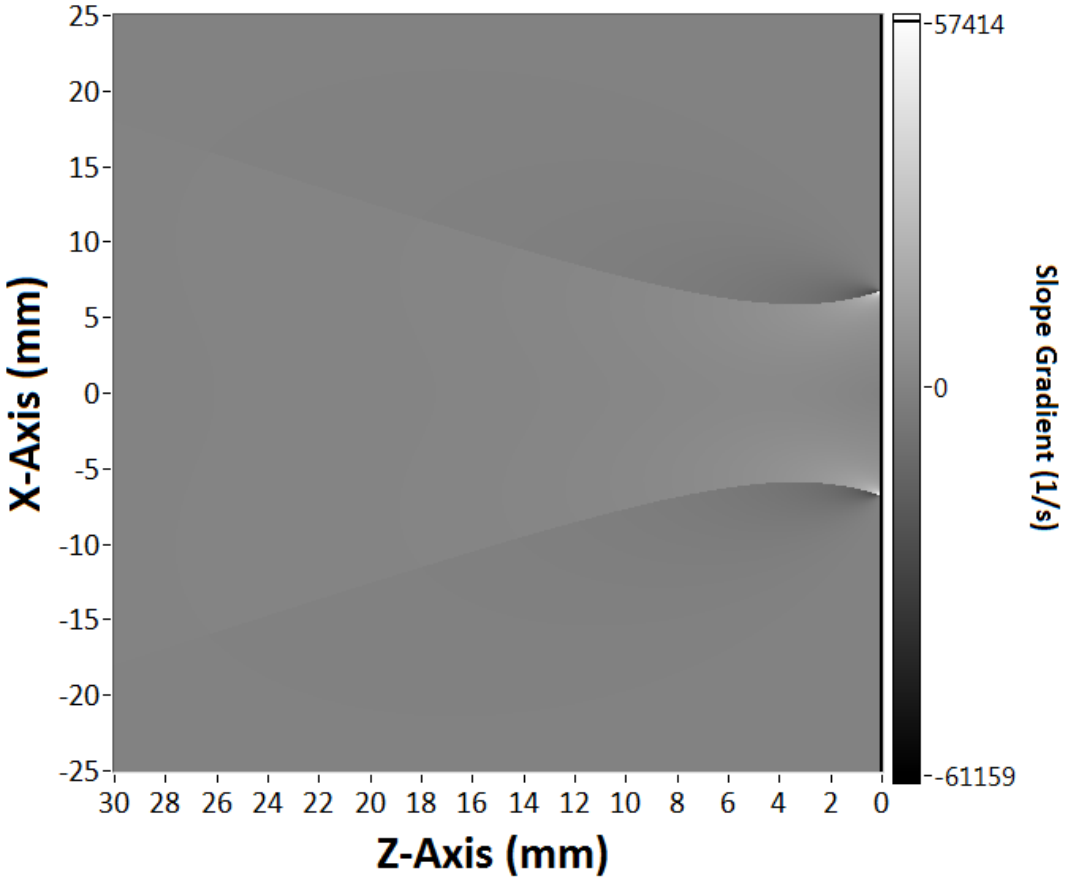

Figure 4.24: Gradient of Slope.

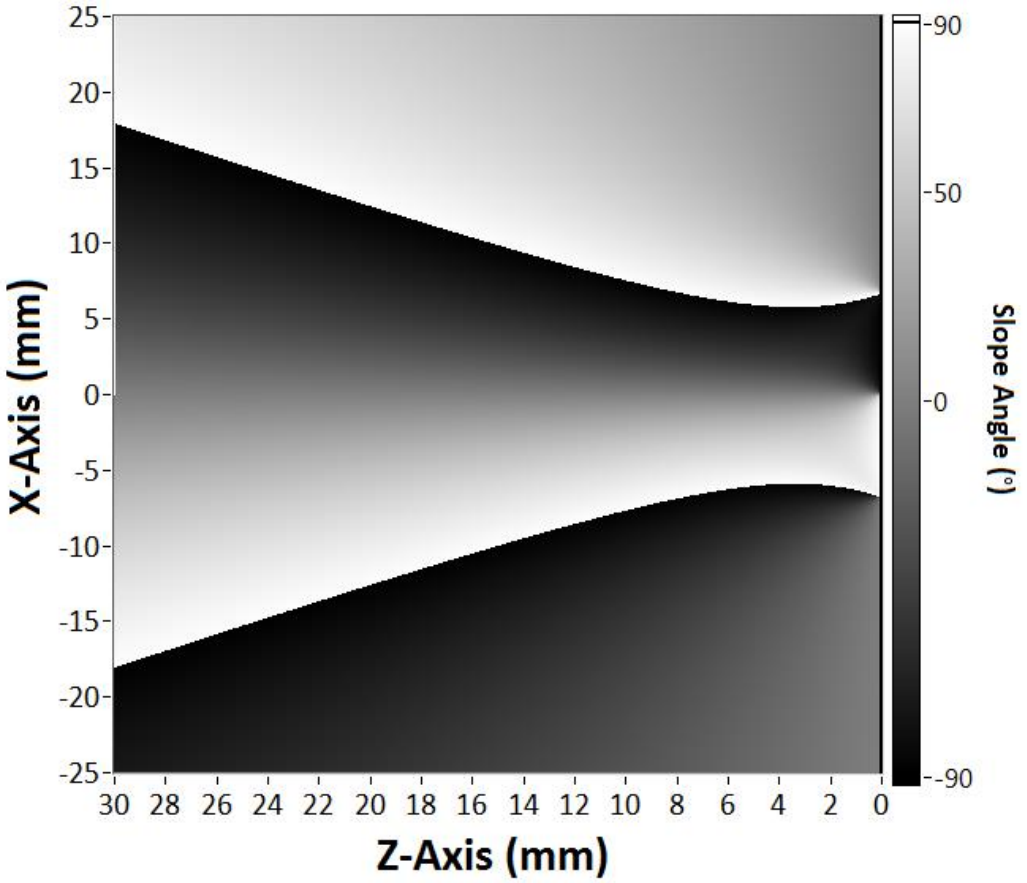

Figure 4.25: Direction of Slope relative to Z-Axis.

The results show two points of high gradient can be observed at the entry and exit to the contact. The paths for a set of normally incident rays across this field are shown in Figure 4.26. The rays incident to the contact surface and subsequently reflected from the surface are plotted side by side to show the complete ray path of a wave reflected from the surface.

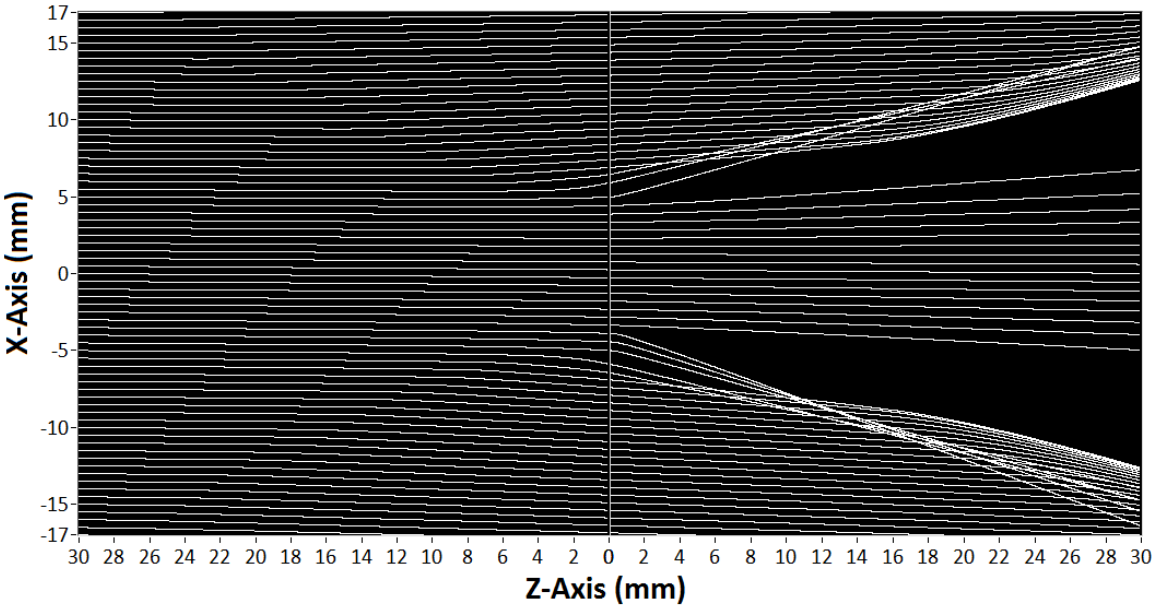

Figure 4.26: Incident and Reflected Ray Paths.

The figure shows a lensing effect occurs, with the rays being steered away from the contact due the higher speed of sound induced by the stress in the contact. In particular this happens near

to the entry and exit of the roll bite. This is due to the zones of high speed of sound change which were noted above. Also the angle of the gradient relative to the incoming beam angle results in an exaggerated beam deflection at these points. This is because as the angle of the slope deviates from the angle of the beam, it is refracted more, due to the relationship in Snell's Law. It is for the same reason that the rays travelling straight towards the centre of the contact deviate much less. That is because although they see a similar change in speed of sound magnitude, the slope of this is aligned much more closely to the beam direction.

Individual rays give an indication of the path an ultrasonic wave would take, but it is harder to ascertain the focusing effect of this, and the resultant wave intensity. To achieve this a large number of rays were introduced to the model (1000 per mm in the x-axis). These where introduced not just at element locations, but also at intervals between elements. The number of rays at each point in the array was summed. When plotted in an intensity plot this gives an indication of the ray intensity. It should be noted that this doesn't account for the different ToF's of each ray and so doesn't consider time varying or destructive interference effects.

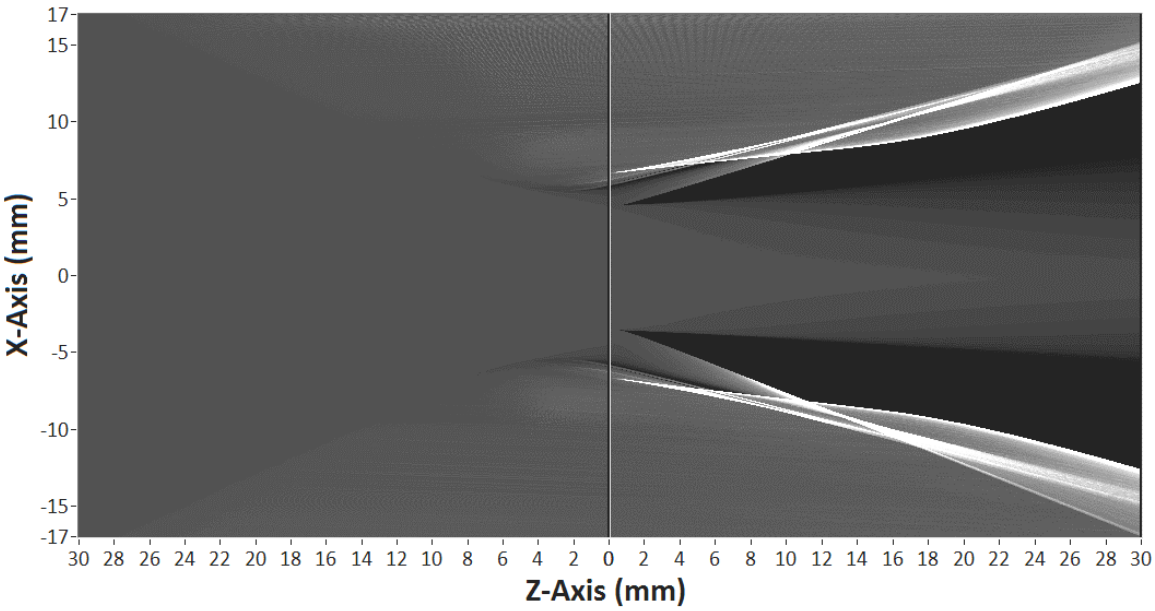

Figure 4.27: Incident and Reflected Ray Intensity.

Propagation of a wave using the same technique as shown in Figure 4.16 from a 2mm simulated transducer over the entry to the roll bite, and in the centre of the roll bite are shown in Figure 4.28 and Figure 4.29. These wave propagation plots are made by overlaying the waves at 1µs intervals.

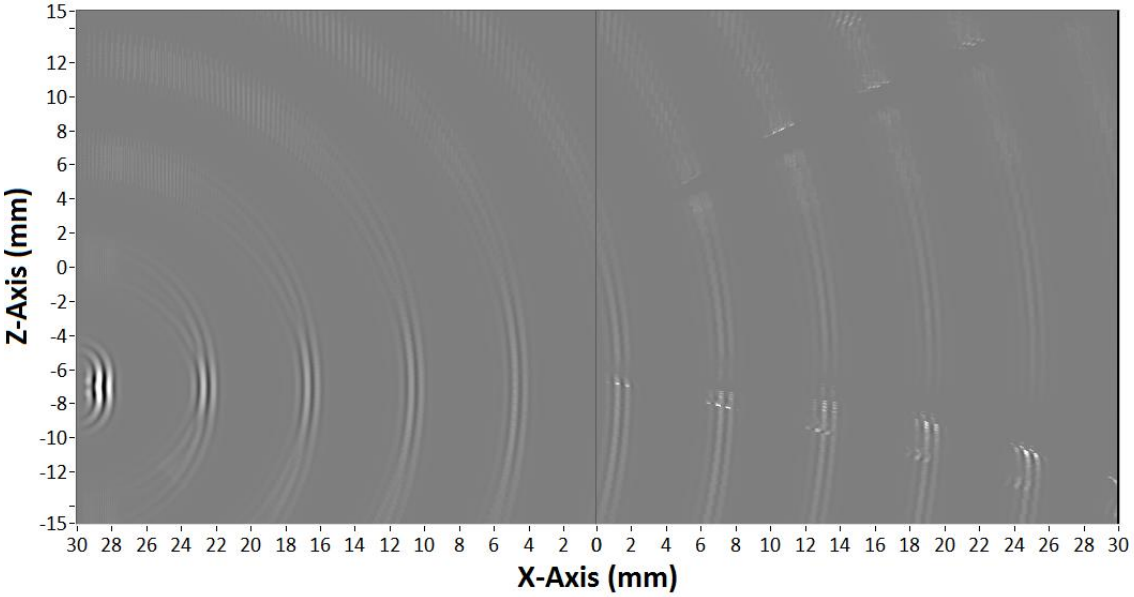

Figure 4.28: Wave at 1µs Intervals from 2mm transducer over the entry to the Roll Bite.

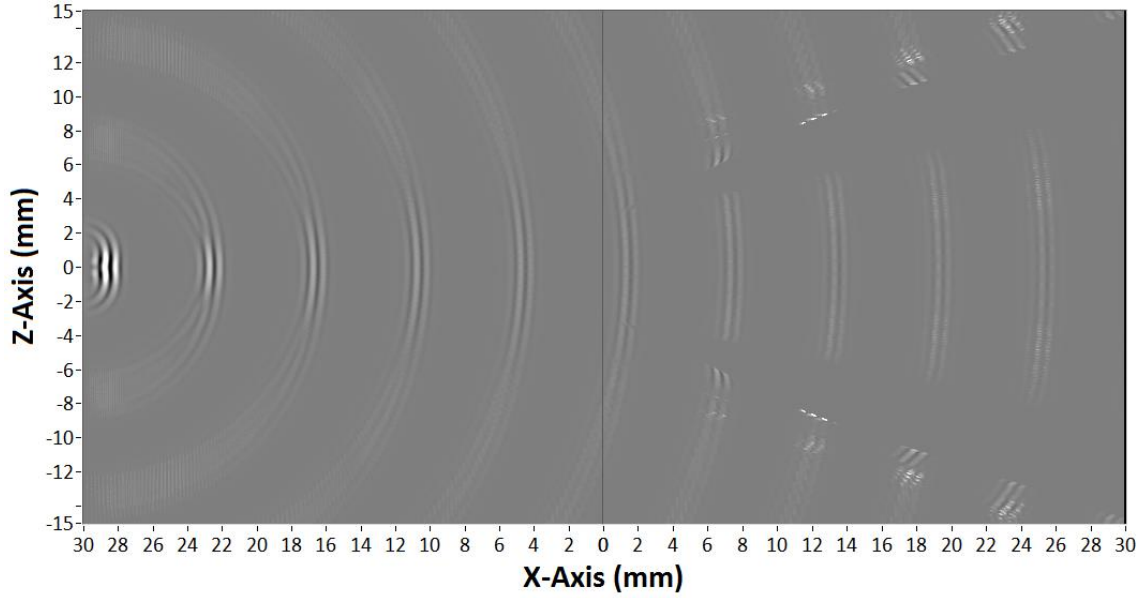

Figure 4.29: Wave at 1µs Intervals from 2mm transducer over the centre of the Roll Bite.

From the wave propagation models it was possible to calculate what the signal received at the simulated transducer would be. This is achieved by summing the amplitude of all the rays reaching the simulated sensor for each time step. This results in a plot of amplitude against time, an A-scan. By incrementally offsetting the simulated transducer location a set of A-scans can be produced and combined to form a B-Scan. In Figure 4.30 the B-Scan calculated for all rays emanating from simulated transducer is presented. Figure 4.31 shows the result when only considering those rays which return to the coordinates covered by the transducer. The first of these figures shows a clear interference pattern. This occurs as there are essentially two offset waves returning to the transducer, which move relative to each other across the roll bite. The first of these waves is the sum of the reflections which are only slightly deflected, while the second wave is the result of waves deflected at the entrance and exit to the roll bite which have a larger ToF. As this figure shows the result from all the returning rays it is not representative of the B-scan that would be captured by a transducer. In the real case only those waves returning to the transducer would be recorded, as shown in the second plot, Figure 4.31. This shows two

'dead spots' between -11 to -8 and 8 to 11 on the X-axis. These occur because all of the rays emanating from the transducer are steered away in, resulting in no energy being received at the transducer. It still shows interfering waves at the extremes of the X-axis, although the wave returning in the centre of the roll bite is undisturbed.

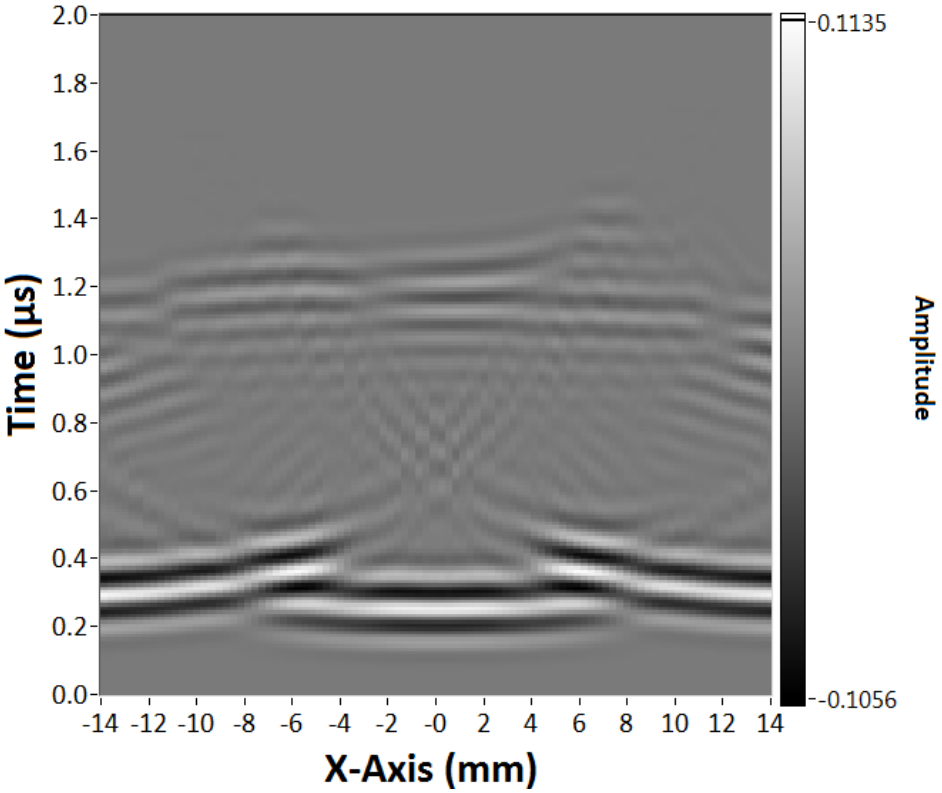

Figure 4.30: Simulated B-Scan.

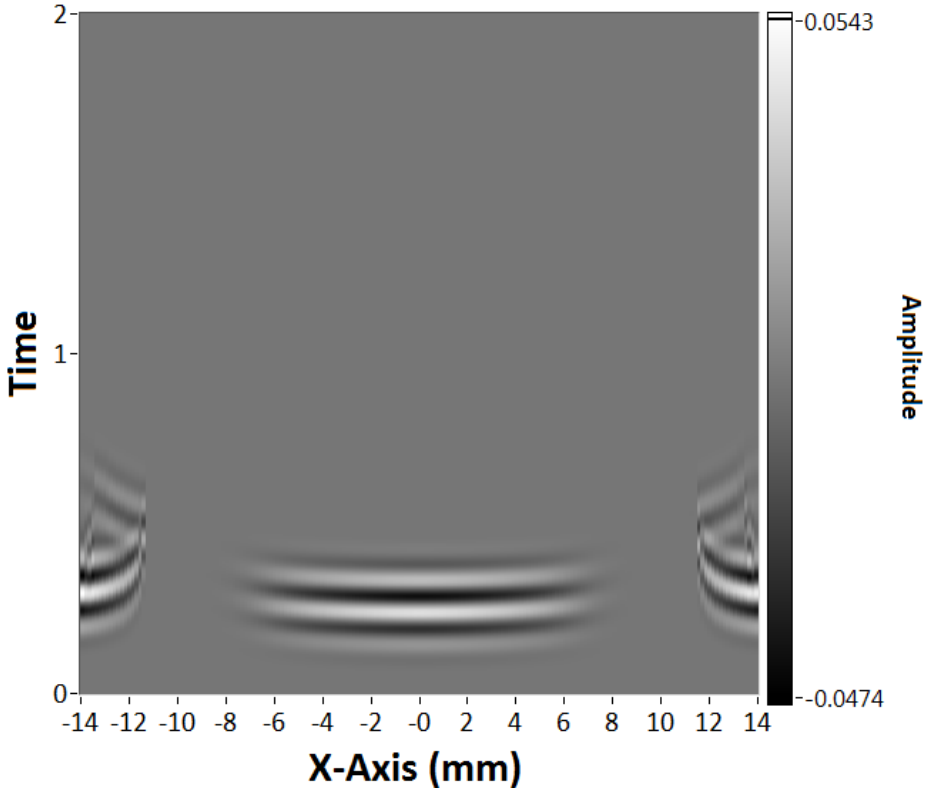

Figure 4.31: B-Scan accounting for sensor width.

It should be noted that there are several limitations and assumptions relating to the ray tracing approach adopted. It takes no account of frequency effects. For the simulated waves the rays spread out the further they travel. The lower density of rays with increasing distance from the transducer means the method becomes less accurate the further from the transducer. The rays are assumed to only originate from one point, effects such as diffraction are ignored. The beam spread is defined by the angular spacing of the rays, and this may not represent actual beam spread. The resolution of the speed of sound array and number of rays has a direct influence on the accuracy of the model.

4.9 Conclusions

The work in this chapter demonstrates that the acoustic velocity of a material is dependent upon its stress state. Unlike with more traditional ultrasonic measurements It is clear that the large stresses seen in cold rolling mean that this acoustoelastic effect has a non-negligible influence on the ultrasonic wave propagation. This can be used beneficially to measure the stress within the roll during rolling.

This is achieved by measuring the time of flight of an ultrasonic pulse passing through a material and relating this to the average stress across the pulse path through the materials acoustoelastic constant. The time-of-flight measurement method proposed is not just effected by a materials acoustoelasticity, but is also sensitive to changes in the material density and surface deflection. The relative magnitude of each of these has been shown to conform to a set ratio dependent upon the propagation material properties. Elasticity is the dominant effect for the roll steel considered, although neither the density or deflection effects are negligible.

The magnitude of localised stresses within the roll that result from a typical roll-strip contact, and their gradients, are sufficient to induce noticeable refraction of an ultrasonic wave. This alters the propagation path of an ultrasonic wave travelling into or away from the contact. This is especially prominent at pinch-points found at the entry and exit of the roll bite. This beam steering must be considered when taking measurements of highly loaded contacts using ultrasound. It may also be possible to use this to offer additional insights into the stress conditions within the roll in the vicinity of the roll bite contact**.**

5 Ultrasonic Transducers

Key to any ultrasonic measurement is the ability to receive, and in some cases generate, ultrasonic signals. The following chapter gives an introduction to the current ultrasonic transducer technologies used to achieve this. It covers transducers based both upon commonly used piezoelectric technologies, as well as non-piezoelectric devices. The piezoelectric effect is explored in some detail. The influence of the transducer characteristics on the ultrasonic beam shape are also explored.

5.1 Active and Passive Ultrasonics

When an ultrasonic wave travels through, or emanates from, a system under inspection, information relating to that system is encoded into the wave. This information may manifest itself in many different aspects of the wave such as its amplitude, frequency content and propagation speed. If this information is extracted from the wave it can then be related back to the originating effect. This is the basis for all ultrasonic measurements.

In some applications the ultrasonic wave is produced in the system under inspection as the by-product of the process being inspected. It is possible to record the acoustic output of the system and look for certain acoustic signatures which related the mechanisms that resulted in these emissions. This approach is used to measure crack growth, stress fracture and the degradation of rolling element bearings and is known as *Acoustic Emissions (AE)* or *Passive Ultrasonics*. Acoustic Emission techniques have the limitation that they often require a process to begin failing in order for waves to be emitted, it is not possible to predict failure in advance of this. The nature of the emissions are also very specific to a particular system. The signals received must therefore be interpreted with consideration to the system, which often requires the acoustic signals produced by the failures modes of interest to be profiled for each system to be inspected. This is done by destructive testing which can be both expensive and time consuming, and must be repeated if there are any changes in the system.

An alternative approach is to induce an ultrasonic wave in the system for the purpose of taking a measurement. This methodology is known as *Active Ultrasonics*. A wave is generated using a transducer, passes through the medium of interest, and is then captured using a receiver. In some cases the transducer/receiver are the same device. Because the ultrasonic signal is being artificially generated the wave characteristics can be tuned to suit the measurement being taken. Unlike acoustic emissions, active ultrasonics has the advantage that an unchanging part can be inspected, and properties measured before failure. It is the active ultrasonic approach which is used in this thesis.

In both active and passive ultrasonics it is necessary for the hardware employed to capture and process the wave, only in active ultrasonics is it also necessary for this hardware to generate a wave. Accordingly, the hardware cost and complexity in active ultrasonic systems is typically higher than passive systems.

The waves used for active ultrasonic measurements typically take the form of a short pulse. This is because a pulse of this form can contain a broad range of frequencies, and is also easier to differentiate in the time-domain, especially where a number of pulses are transmitted or received in short succession. Continuous single frequency waves and more exotic coded pulse

trains have also been used in a number of applications, however these are not considered as part of this work.

Transducers are used to convert the mechanical energy of the ultrasonic wave to electrical energy, and vice-versa. This is useful as electrical signals are more easily captured, conditioned and processed than their ultrasonic equivalents. Common mechanisms used by transducers include lasers, electromagnetism and piezoelectricity.

5.2 Non-Piezoelectric Transducers

The most common approaches to generating ultrasonic waves that do not use piezoelectric elements are (EMAT) and laser induced ultrasound.

EMAT transducers generate an ultrasonic field through the action of a magnetic field induced in the inspected material. A permanent magnet, or pulsed electromagnet, produces a vertically polarised magnetic field which penetrates the inspection material. An alternating current is then passed through a coil located in this magnetic field, and in close proximity to the surface of the inspection material. This generates an eddy current field and an associated Lorentz Force in the material, which produces an ultrasonic wave (EMAT Technology, n.d.). When used on a Ferro-Magnetic material this effect is enhanced by the Magnetostrictive Principle (Electro Magnetic Acoustic Transducers, n.d.). Ultrasonic waves can be detected using the reverse of this process.

Because the ultrasonic wave is generated directly in the material the surface finish, which would have a significant effect on a wave transmitted into the material from a external transducer, is not an issue when using EMATs. EMATs do require high voltages to achieve the same strength of ultrasonic signal as would be achieved via a piezoelectric contact transducer. The signal-to-noise ratio (SNR) observed when using EMATs is less than that observed for contact transducers. The instrumentation used with EMATs is also more expensive than contact transducers, prohibitively so in some cases.

Laser induced ultrasound uses modulated laser pulses to thermally expand or ablate the surface of the material to be inspected (Krishnaswamy, 2003). The optical power of the laser is absorbed by the material and is converted to heat. This leads to a localised but rapid temperature increase in the material. If the material is acting in the thermoelastic regime (the laser power is insufficient to melt or ablate material) the rapid expansion of the material results in an ultrasonic wave. If the absorbed laser power is high enough to melt the material and lead to plasma formation, then an ultrasonic wave is generated via momentum transfer due to material ejection.

Waves generated by laser are typically measured using optical approaches (Krishnaswamy, 2003). This is advantageous because it allows both the generation and reception of the ultrasound to be non-contact. If a light beam is shone on the surface experiencing ultrasonic perturbations, then the intensity of the reflected light can change due to ultrasound inducing changes in the refractive index of the medium, and this can be monitored directly using a photo-detector. Ultrasonic motion on the surface of the material can also change the phase of the reflected light. Because the phase of a single light beam cannot be measured directly commonly an optical interferometer is used. Optical detection sensitivity is an order of magnitude poorer than contact transducers (Krishnaswamy, 2003).

5.3 Piezoelectric Transducers

The most common way ultrasonic waves are generated is by using piezoelectric materials. This work exclusively uses piezoelectic materials to both generate and receive ultrasonic pulses. Typical characteristics of these transducers are explored in the rest of this chapter.

Unlike both laser and EMAT transducers, which generate ultrasonic waves in the material under inspection, in piezoelectric transducers the wave originates in the transducer itself. This must then be transmitted to the inspected material. Piezo transducers therefore require contact with the inspected piece. Piezoelectric transducers are by far the most widely used transducers due to their relative simplicity, robustness, low cost and ease of implementation. There are many variants and manufacturers of Commercial-off-the-Shelf (COTS) piezoelectric transducers, some examples of typical transducers can be seen in Figure 5.1.

Figure 5.1: Typical Ultrasonic Contact Transducers (Olympus, n.d.).

5.3.1 Transducer Construction

Most piezoelectric transducers follow a similar construction as shown in Figure 5.2. The active element in this figure is the piezoelectric material. More detail on the elements shown in this Figure are given below.

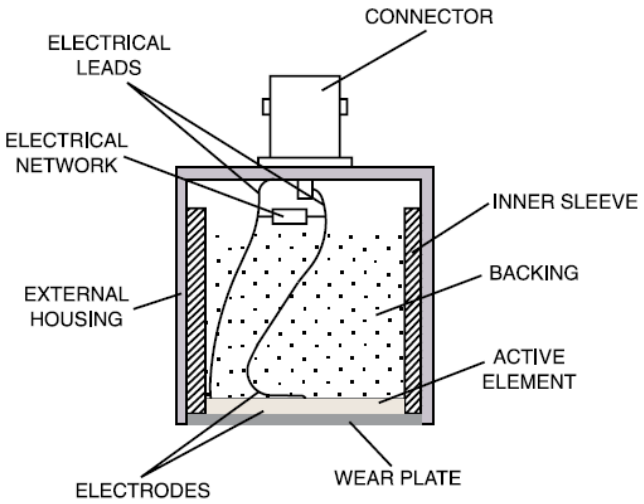

Figure 5.2: Typical Ultrasonic Transducer Construction (Olympus NDT, 2006).

5.3.2 Electrical Network and Cabling

Various elements are included in the transducer in order to allow an electrical connection to be made to the piezo element. These include internal wiring, electrical matching network and

connector. These elements must be suitable to carry ultrasonic signal frequencies. Although the internal wiring is relatively short the effect of electromagnetic interference must also be considered.

The transducer electrical impedance affects its noise performance, driving response, bandwidth and sensitivity (Svilainis & Dumbrava, Evaluation of the ultrasonic transducer electrical matching performance, 2007). It should therefore be matched to the impedance of the pulser output. In some cases this can be achieved by adjusting the impedance at the pulser end although normally the pulser will have a fixed output impedance. Instead a matching network is often used in the transducer to fine tune the transducer characteristics. This is important in order to maximize the efficiency of the power transfer to the piezo element, and so achieve better signal-to-noise ratio (Garcia-Rodriguez, et al., 2010). This is particularly important for transducers with high impedance elements. Matching networks become less important when using lower impedance transducers because the losses are less.

5.3.3 Backing

The backing material behind the piezo element has a great influence on signal. It serves two functions. Firstly it provides damping of the transducer, increasing the bandwidth resulting in higher sensitivity across a wider range of frequencies. Secondly it dissipates the wave propagating from the rear of the piezo, so that this is not confused with the response from the wave emanating from the front of the transducer. In order to allow the rear facing wave to transmit into the backing material its acoustic impedance should be similar to that of the piezo element. This can conflict with the need for the material to be relatively dense to provide damping. Tungsten loaded epoxy is commonly used as this has preferable damping and absorption material properties while still being easy to manufacture.

5.3.4 Front Face

The front face of the transducer is the face through which the ultrasonic wave propagates. As such the design of this face is important for the operation of the transducer.

In its most basic form this face can just be a protective layer between the piezo element and the inspection material, called a *Wear Face*. This ensures the fragile piezo is protected during use, especially where the transducer is being moved across the material surface, which may result in scratching of the transducer face. It is also possible to modify the design of the front face to the benefit of the ultrasonic measurement.

The closer the acoustic impedance of the piezo and the inspection material are, the more efficient transmission of ultrasound will be. Because it is rarely possible to select either the piezo or inspected material impedance for this purpose, instead the transmission efficiency can be increased by adding a *Matching Layer* between the piezo and material which has an intermediate acoustic impedance. The ultrasonic wave will reverberate within the matching layer producing a train of overlapping waves propagating out of both sides of the layer into the piezo and the inspection material. If the thickness of the matching layer is the same as a quarter of the ultrasonic wavelength then successive pulses emanating from the front of the layer into the inspection material will constructively interfere, resulting in greater transmission (Whittingham & Martin, 2010). Simultaneously the waves travelling into the piezo will

destructively interfere, reducing their detrimental effect on the measurement. A matching layer made to this thickness is referred to as a *quarter wave plate*.

As mentioned earlier the front face can incorporate a length of material which acts as a *delay line*. This offsets the measurement face which can make features close to the inspection material surface easier to resolve. Delay lines can also be contoured to the inspected surface to ensure better contact and improve the transmission across the transducer front face interface. Shaping the front face can also distort the ultrasonic beam. This can be used advantageously to focus the beam and reduce the measurement spot.

5.3.5 Transducer Configurations

Transducers can be arranged in many ways. As piezoelectric transducers can both send and receive waves it is common for a single transducer to be used to do both. In order for this to work it is necessary for the induced wave to return back to the originating transducer, this is achieved by reflecting the wave from a suitable surface. Hence this configuration is referred to as *pulse-echo*. This has the advantage that it only requires a single transducer and access to one side of the inspected material. It is only applicable where the material geometry allows an echo to return to the transducer. The hardware used for this must be able to switch between pulse generation and reception modes fast enough to capture the returning wave.

Where the material geometry, or attenuation makes a pulse-echo configuration unviable, a *through-transmission* configuration can be employed. This involves a separate transmission and reception transducer mounted on either side of the inspected piece. This has the advantage of allowing the transmission and reception transducers to be specialised for their separate roles which can give a higher Signal-to-Noise ratio (SNR), this is helped by the typically shorter ultrasonic wave path. The hardware can be simpler than in a Pulse-Echo setup as the generation and reception systems are kept separate. However it has the cost of an additional transducer and requires access to both sides of the work-piece.

A compromise between the above two configurations is *Pitch-Catch*. This is where a wave is reflected from a surface, like in a Pulse-Echo setup, but is received on a different transducer to the one that generated the wave. Again this requires suitable geometry, but allows for separate transmission and reception systems.

5.3.6 Transducer Types

Transducers can be tailored to suit particular measurements and applications in a number of ways. This has resulted in a range of transducer variants.

Contact Transducers: Contact transducers are single element transducers, which usually generate a longitudinal wave. They are the simplest form of transducer and are intended for direct contact with a test piece.

Delay Line Transducers: Delay line transducers are single element contact transducers which incorporate a short piece of material (normally plastic or epoxy) in front of the transducer. Delay lines offer improved resolution of flaws very near to the surface of a part and allow thinner range and more accurate thickness measurements. Delay lines can be contoured to match the surface geometry of a part. They can also be used in high temperature applications to offset the temperature sensitive transducer from a hot inspection face.

Immersion transducers: These are single element longitudinal wave transducers, whose wear face is impedance matched to water. They are designed to use water as both a couplant and delay line and hence have waterproof casings. Immersion transducers are ideal for use in scanning applications. Immersion transducers can also be focused.

Dual Element Transducers: These utilize separate transmitting and receiving elements in the same transducer casing and normally mounted on separate delay lines. The elements are angled slightly towards each other to bounce a signal off the backwall of a part in a V-shaped signal path. This configuration improves near surface resolution. The crossed beam design provides a pseudo focus that makes dual element transducers more sensitive to echoes from irregular reflection faces. They therefore find use when measuring faces that have corrosion and pitting.

Wedge (or Angle Beam) Transducers use the principles of refraction and mode conversion to produce shear, longitudinal and surface waves in the test material. This is achieved by having a wedge mounted on the front face of the excitation transducer so that the incident wave is not normal to the surface of the inspected material. Common use for angle beam transducers is in weld inspection.

Sensor Arrays: These are simply a collection of individual elements arranged either in a 1D or 2D pattern. This allows 2D and 3D scans to be constructed.

Phased Array: These are specialised arrays that allow for the flexibility to individually select which elements to use to generate and receive the ultrasonic wave. This allows elements to be pulsed in such a way as to cause multiple beam components to combine with each other to build up a single wave front travelling in the desired direction (beam steering). Similarly, the receiver function can be used with the principal of superposition to combine the input from multiple elements into a single presentation, this can emulate focusing. Because phasing technology permits electronic beam shaping and steering, it is possible to generate a vast number of different ultrasonic beam profiles from a single probe assembly, and this beam steering can be dynamically programmed to create electronic scans. The potential disadvantages of phased array systems are a higher cost and a requirement for more highly skilled operators.

5.3.7 Coupling

A couplant material is used to remove any air from the interface between the transducer and the inspection material, which is introduced due to the microstructure of the two contacting surfaces. The acoustic impedance of air is much lower than that of the sensor and if it isn't displaced it will cause considerable loss in transmission (Theobald, n.d.). Couplants come in many forms, some examples of which follow.

Liquid: Liquid couplants are used with immersion type or water jet/bubbler probes. Water is most common although Propylene Glycol has the advantage that it will not cause corrosion of the measurement surface. Liquid couplants give a consistent coupling however their low viscosity means they have a tendency to drip, run out or dry up with time. Liquid couplants are not suitable for shear waves

Gel: Is generally better for rougher surfaces. Typically this is a specialist ultrasonic gel or glycerine. Many gel type couplants are water based and will dry out over time, particularly

around the edge of the sensor. More viscous gels can be used to transmit shear waves. The transducer must be mechanically held when using gel based couplants.

Grease: Has a much higher viscosity than gels or liquids and due to this a high application force is required on the sensor to remove any trapped air. Grease offers better long-term stability than gels or liquids but slightly reduced transmission efficiency in comparison to liquids/gels.

Bonding: The sensor can be physically attached to the measurement surface with an adhesive. Because the sensor is mechanically secured the sensor does not need to be held. This also helps damp the sensor response. Bonding is ideal for applications where the sensor will not be removed or where absolute stability in the coupling or sensor position is needed.

Solid Couplants: Typically these are elastomer compounds which are sometimes integrated into ultrasonic transducer itself. They avoid the drawbacks of wet couplants such as time variability, drying up, varying transmission performance properties. These compounds can have a relatively high attenuation and are less effective at excluding air in the transducer-inspection material interface. This makes them less efficient than liquids, gels or bonding. Solid couplants are used for applications such as roller probes.

5.4 Piezoelectricity

The *piezoelectric effect* is the property of some materials to generate electrical charges when subjected to pressure, the term coming from the Greek work *piezein* meaning to press (Piezo, 2015). The converse of this effect also applies with electrical fields causing deformation of the material. Although this is technically the *inverse piezoelectric effect*, in practice the term piezoelectric effect is used interchangeably to refer to both processes. It is these two effects that enable the reception and transmission of ultrasonic waves.

The piezoelectric effect was first discovered in 1880 by brothers Jacques and Pierre Curie. Famously Pierre would later discover Radium with his wife Marie (Technical Publication TP-238 Piezoelectricity). The first use of a piezo material to generate ultrasound in an engineering application, and the birth of modern ultrasonics, can be traced to Paul Langevin in 1916. In response to the outbreak of World War I, and the threat posed by submarines, a range of submarine detectors were developed. Langevin developed an idea proposed by Constantin Chilowsky (Graff, 1981) of echo-ranging and he constructed an underwater ultrasonic source from a quartz element sandwiched between steel plates to achieve this. This pioneering work was continued by Alfred Loomis and Robert Wood (Wood & Loomis, 1927) who, after hearing of Langevin's work, teamed up with a number collaborators and released a variety of papers looking into the chemical aspects and biological effects of intense ultrasound.

There are a number of naturally occurring piezo materials. A large amount of development was carried out on quartz due to its use in radio communication (Technical Publication TP-238 Piezoelectricity). It was realised that the mechanical resonance of the material could be used as a method for frequency control. While quartz has excellent chemical stability, for ultrasonic applications its sensitivity is limited. It was discovered that metallic oxides demonstrated a comparable chemical stability, but with much higher sensitivity. A discussion on the various piezo materials is covered in the next section.

The piezoelectric effect results from the deformation of a piezoelectric material's crystal structure. This deformation leads to a redistribution of the charges within the material and a net charge at the surfaces of the material. The difference in the net charge at opposing sides of the crystal creates a potential difference. This change in structure, and corresponding potential difference, is shown in Figure 5.3 for a lead or barium latticed piezoelectric ceramic.

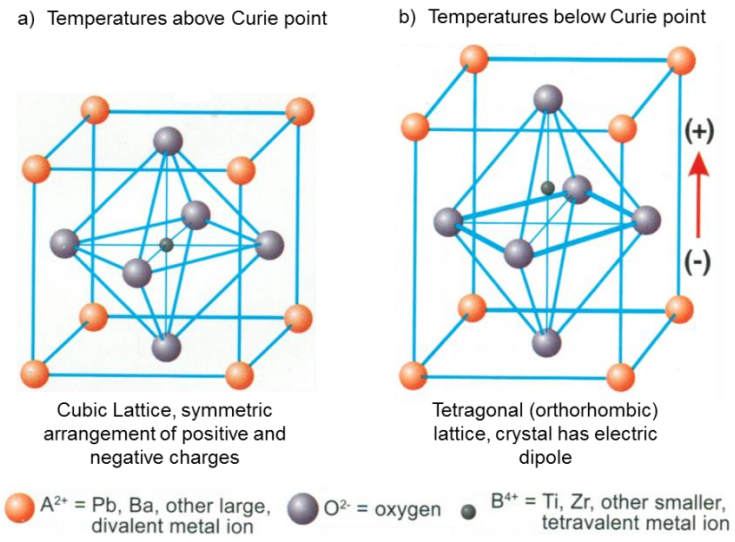

Figure 5.3: Crystal Structure of a Traditional Piezoelectric Ceramic, reproduced from (APC International Ltd., 2002).

At a sufficiently high temperature a phase change occurs in the material which removes this structure and therefore the piezoelectric properties of the material. The temperature is known as the Curie temperature after the discoverers of piezoelectricity.

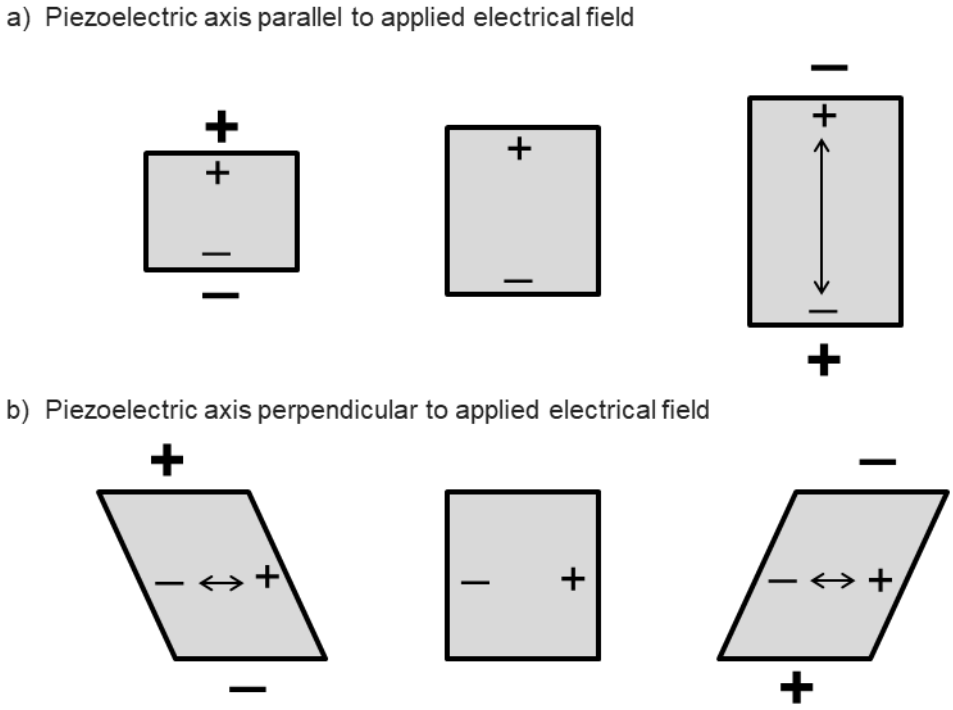

Figure 5.4: Reverse Piezoelectric Effect for Two Crystal Orientations.

By altering the orientation of the applied electrical field relative to the crystal orientation it is possible to produce various strain conditions in the crystal. An electrical field applied parallel to the piezoelectric axis will produce elongation or shortening along the axis dependant on the field polarity as shown in Figure 5.4 a). If the electric field is applied perpendicular to the piezoelectric axis, a shear motion is induced as shown Figure 5.4 b). These two orientations correspond to elements which produce Longitudinal and Shear waves respectively.

Longitudinal and shear elements can therefore be produced by cutting piezo elements from a larger crystal that have orientations with respect to the polarisation axis as shown in Figure 5.4.

5.4.1 Piezo Materials

Early studies into piezoelectricity concentrated on quartz. In order to produce transducers from quartz, suitably large single crystals have to be grown and cut. These manufacturing limitations, and the limitation they placed on element sensitivity (Silk, 1984), lead to the development and adoption of a range of alternative materials.

The development of piezo materials beyond quartz relied on the discovery of *Ferroelectricity* (Technical Publication TP-238 Piezoelectricity). This refers to the property of certain piezoelectric materials to have their electric polarization, and therefore piezoelectric properties, aligned by placement in a large electric field. This process of aligning the polarisation is known as *Poling* and typically takes place using a field of the order of several thousand volts per cm. By poling at temperatures above the Curie point the resistance to polarisation is reduced.

Sodium Potassium Tartrate (more widely known as Rochelle or Seignette salt) was observed to demonstrate ferroelectric properties and was the first such material to find a use generating ultrasound. Rochelle salt showed far greater sensitivity than quartz albeit with much reduced temperature resistance.

Around 1940 Arthur von Hippel and co-workers at Massachusetts Institute of Technology recognized the ferroelectric nature of the refractory material Barium Titanate $BaTiO_3$ (Technical Publication TP-238 Piezoelectricity). This marked the next step in material development as Barium Titanate was usable up to temperatures of 120°C, an increase compared to Rochelle salt. The use of ceramics also carried the benefit of allowing element shapes and sizes which were unfeasible with single crystals.

The temperature constraint imposed by Barium Titanate was relaxed in the 1950's with the discovery of the piezoelectric and ferroelectric nature of Lead Metaniobate $PbNb_2O_6$ and Lead Titanate Zirconate $Pb(Zr_xTi_{x-1})O_3$. Lead Titanate Zirconate, typically abbreviated to PZT, has now found widespread use and forms the basis for most ultrasonic transducers in engineering use today.

In addition to the ceramics mentioned so far, piezo polymers such as Polyvinylidene fluoride (PVDF) have also found some use. Unlike the crystal structure of quartz or piezoceramics, polymers exhibit piezoelectricity due to the attraction and repulsion of their intertwined long-chain molecules (Bauer & Bauer, 2008). Piezo polymers are limited due to a much lower operating temperature, typically <50°C. However there are a couple of key

advantages over piezoceramic materials. They are flexible, allowing for them to be fitted to a curved surface, or for focusing. Their acoustic impedance is also much lower than piezoceramics allowing for better matching to human tissue and water, impedance matching is discussed in more detail later in this chapter. These properties mean PVDF transducers have found use both in medical applications as well as for hydrophones (RP Acoustics, n.d.).

5.4.2 Piezo Manufacture

Piezoelectric products are made in single layer (monolayer) and multilayer configurations dependent upon the end application. Monolayer elements are manufactured in a number of steps, requiring numerous heating, grinding and machining processes as follows (Manufacturing Tutorial) (Piezo-ceramic Manufacturing Process - Proven Expertise in Piezo-ceramic Manufacturing, n.d.) (Piezo Elements Made by Pressing Technology, n.d.).

1. **Raw Materials:** Firstly the raw materials in oxide form are sourced. For PZT this is a combination of PbO, TiO_2, ZrO_2 and any dopants. These are weighed to a specified formulation and mixed.
2. **Pre-Sintering (Calcination):** The mixed materials are heated to around 75% of the sintering temperature (~900°C) to induce a solid state reaction between the oxides, a process known as calcination. This also removes any organics, water or other volatiles left after mixing (Kin, Lee, Shrout, & Venkataramani, 1991) and reduces the final sintering shrinkage (Krsmanovic, November 2009).
3. **Ball Milling:** The calcinated material is ground to a powder of a defined grain size using a ball mill. The coarseness will influence the final material density and the presence of internal voids. This powder is then used to create a highly homogeneous suspension by mixing with an organic vehicle (a liquid used to 'carry' the mixture). A glassy binder such as *lead borosilicate or* lead(II) oxide (Dargie, Harris, White, Atkinson, & Sion, 1998) is also introduced to allow the mixture to be formed into the desired shape
4. **Granulation (Spray Drying):** The suspension is granulated by spray drying which yields powder suitable for pressing.
5. **Pressing:** The powder is compacted using a hydraulic press to form a compact of the desired shape. This is normally a disc or plate which is slightly oversize to take into account contraction during the subsequent sintering, or with excess material to allow the sintered part to be machined to size.
6. **Binder Burn Out:** The organic compounds in the binder material, additives and remaining solvents are then removed by very slowly heating to a temperature of around 500 to 700°C, where the organic compounds decompose and evaporate.
7. **Sintering:** At this point the ceramic is referred to as being in its *green state*, i.e. before sintering. In order for the ceramic grains to grow and merge thus developing the materials polycrystalline ceramic structure the fired parts need to be heated to a temperature above 1000°C and in some cases up to approximately 1300°C. The resulting material is a solid ceramic with a high density. The properties of this material will be dependent upon the temperature ramp rates, holding time and the sintering atmosphere. Sintering leads to approximately 15 to 30 % (Piezo Elements Made by Pressing Technology, n.d.) shrinkage by volume.
8. **Machining:** To ensure dimensional accuracy and surface finish the sintered part is machined by one or more processes including lapping, grinding and cutting. The surface roughness will be dependent upon the grain size of the milled powder mixture.

9. **Electrode Application (Metalising):** Electrical connections are then made by applying electrodes to the part. More details on this are given on page 117.
10. **Polarisation (Poling):** The ceramic piezoelectric properties are then achieved by *poling*. This process aligns the grain dipoles. The dipoles in a piezo ceramic element are aligned by applying a high DC electrical field (2-3kV/mm) to the external electrodes at elevated temperatures (80 to 140°C) for a period of 1-10 minutes. The dipoles more closely aligned with the electric field expand at the expense of those that are not aligned, and the ceramic lengthens in the field direction. Once the field is removed there is a bias of the dipoles locked in the alignment direction. Due to the high voltages involved poling must be performed in an isolation medium, typically a silicone oil bath (Wersing & Lubitz).
11. **Inspection:** After poling the components are inspected and various mechanical and electrical parameters measured such as capacitance, dielectric loss and mechanical strain level (stroke).

5.4.3 Piezoelectric Constants

A number of constants are used to define the piezoelectric properties of a material. As a piezo-material is anisotropic, these constants are directionally dependent, and therefore have different values and formulations dependent on their orientation in comparison to the piezoelectric axis. Different works define the orientation of the piezo electric axis differently. Most commonly for quartz the piezoelectric axis is orientated parallel to the X-axis (Standards on Piezoelectric Crystals, 1949), while in works on ceramic materials such as PZT typically follow IEEE 176 -1987 (ANSI/IEEE 176-1987 - Standard on Piezoelectricity, 1987) where the Z-axis is orientated to the piezoelectric axis, although this standard has now been withdrawn.

The most commonly used constants are presented below, where the direction of positive polarisation coincides with the Z-axis. Direction X, Y, or Z is represented by the subscript 1, 2, or 3, respectively, and shear about one of these axes is represented by the subscript 4, 5, or 6, respectively.

Piezoelectric Charge Constant, d

The piezoelectric charge constant is the amount of charge (due to polarisation) generated per unit of stress applied to the material, is represented by *d* and typically has units SI units of CN^{-1} and is defined by:

$$Q = dF \tag{5.1}$$

Where *Q* is the charge generated and *F* is the force applied. As the reverse piezoelectric effect applies it also represents the strain experienced by the piezoelectric material per unit of electrical field applied. The first subscript of *d* indicates the direction of polarization generated or the direction of the applied electrical field. The second subscript is the direction of the applied stress or the induced strain. For example d_{33} is either the induced charge in the Z-direction per unit of stress applied in the Z-direction or is the strain induced in the Z-direction per unit of electrical field applied in the Z-direction. This is important for Longitudinal sensors. Similarly d_{15} is either the induced charge in X-direction per unit of shear stress applied about the Y-direction or is the strain induced in the Y-direction per unit of electrical field applied in the X-direction, an important consideration for Shear sensors.

Piezoelectric Voltage Constant, g

The piezoelectric voltage constant is the electrical field generated by a piezo per unit of stress applied to the material. It is denoted by *g* and has SI units of VmN^{-1}.

$$d = g\varepsilon_r\varepsilon_0 \qquad 5.2$$

Where d is the piezoelectric charge constant, ε_r is the relative permittivity and ε_0 is the permittivity of free space (= 8.85×10^{-12} F/m). The first subscript to *g* indicates the direction of the electric field generated in the material, while the second subscript is the direction of the applied stress. The strength of the induced electric field produced in response to an applied physical stress is the product of the stress and *g*. The sensor output voltage is obtained by multiplying the electric field by the thickness of the ceramic between the electrodes (Piezo Systems Inc., 2011). Therefore the value of *g* is important for assessing a material's suitability for sensing. Reversely the g value also gives the mechanical strain experienced by a piezoelectric material per unit of electric displacement applied.

Permittivity, ε

The permittivity, or dielectric constant, *ε* for a piezoelectric material is the dielectric displacement per unit electric field, ε^T is the permittivity at constant stress. The first subscript of ε denotes the direction of the dielectric displacement, while the second subscript is the direction of the electric field.

Elastic Compliance, s

Elastic compliance *s* is the strain produced in a piezoelectric material per unit of stress applied. It is in units of m^2N^{-1}. The first subscript denotes the direction of strain while the second is the direction of stress. For subscripts 11 and 33 this is the reciprocal of Young's modulus. The superscript D indicates the compliance under a constant electric displacement, and the superscript E indicates the compliance under a constant electric field.

Electromechanical Coupling Factor, k

The electromechanical coupling factor *k* is one indicator of the effectiveness with which a piezoelectric material converts between electrical and mechanical energy.

$$k^2 = \frac{M}{T} \qquad 5.3$$

Where *M* is the stored mechanical energy and *T* is the total stored energy. The first subscript of *k* denotes the direction of the electrodes, the second subscript denotes the direction of the mechanical energy. A high *k* value indicates efficient energy conversion, however this does not account for dielectric or mechanical losses. Taking the efficiency as the ratio of the useable energy delivered by the piezo element to the total energy taken up by the element, well designed systems can exhibit efficiencies that exceed 90% (APC International Ltd., 2002). Some piezo element geometries have special expressions of *k*. For a thin disc the planar coupling factor k_p is used. For a disc or plate with a large width large relative to its thickness, the thickness coupling factor k_t is used. This is a specific version of k_{33}, which is the corresponding factor for longitudinal vibrations of a thin rod of the same material.

Mechanical Quality Factor, Q_m

The mechanical quality factor Q_m, the inverse of the mechanical loss factor, is the ratio of the energy supplied per cycle to the energy dissipated per cycle and gives a measure for the sharpness of the resonance peak of the response in the frequency domain. It can be computed from:

$$Q_m = \frac{f_p^2}{2\pi f_s Z_s C\left(f_p^2 - f_s^2\right)} \qquad 5.4$$

Where f_p is the parallel resonance frequency, f_s is the series resonance frequency, *C* is the capacitance and Z_s is the impedance at resonance.

Dielectric Loss Factor, tan(δ)

The efficiency of a transducer depends on the dielectric losses as well as the mechanical losses and coupling factor. The dielectric loss, *tan(δ)* is calculated from the tangent of the loss angle *δ*. Ceramics with a low *tan(δ)* should be used for transducers which are run continuously at high power levels.

Frequency Constant, N

The frequency constant, *N,* describes the relationship between a dimension of the piezo element and the corresponding unrestrained resonant frequency, using the following relationship:

$$f_s = N/x \qquad 5.5$$

Where x is the dimension, N is the frequency constant and f_s is the unrestrained resonant frequency. The frequency constant varies depending upon element geometry, polarisation and oscillation direction. Examples include N_P the frequency constant for the planar surface oscillation of a round disk, N_1 the frequency constant for the transverse oscillation of a slim rod polarized in direction 3, N_3 the frequency constant for the longitudinal oscillation of a slim rod polarized in longitudinal direction, N_5 the frequency constant for the thickness oscillation of a thin plate and N_t the frequency constant for the thickness oscillation of a thin plate polarized in the thickness direction.

Values of the properties described above for PZT-5A1 are given in Table 5.1.

Lead Zirconate-Titanate Type PZT5A1		
Electrical – Low Field		
Relative Permittivity, $\varepsilon_{r\ 33}^{T}$	1875	-
Dielectric Loss, $\tan\delta$	0.02	-
Dielectric Constant, ϵ_r (Banks, Oldfield, & Rawding, Ultrasonic Flaw Dectection in Metals: Theory and Practice, 1962)	1500	
Resistivity (at 25°C), ρ el	10^{12}	Ωm
Electro-Mechanical		
Coupling Factor, k_p	0.62	-
Coupling Factor, k_{15}	0.69	-
Coupling Factor, k_{31}	-0.34	-
Coupling Factor, k_{33}	0.67	-
Coupling Factor, k_t	0.45	-
Charge/Strain Constant, d_{33}	$409x10^{-12}$	CN^{-1} or mV^{-1}

Charge/Strain Constant, d_{31}	-176x10^{-12}	
Charge/Strain Constant, d_h	58x10^{-12}	
Voltage/Stress Constant, g_{33}	25.7x10^{-3}	VmN^{-1}
Voltage/Stress Constant, g_{31}	-11x10^{-3}	
Voltage/Stress Constant, g_h	3.6x10^{-3}	
Piezoelectric Constant of Deformation, h_{33} (Banks, Oldfield, & Rawding, Ultrasonic Flaw Dectection in Metals: Theory and Practice, 1962)	1.8x10^9 to 4.6x10^9	Vm^{-1}
Frequency Constant, N_p	2000	Hz.m
Frequency Constant, N_1	1370	
Frequency Constant, N_3	1410	
Frequency Constant, N_S	1465	
Frequency Constant, N_C	930	
Frequency Constant, N_t	1940	
Quality Factor, Q_m	60	-
Mechanical		
Compliance, $S^E{}_{33}$	17.2x10-^{12}	m^{2}N^{-1}
Compliance, $S^E{}_{11}$	16.7x10^{-12}	
Compliance, $S^E{}_{12}$	-5.2x10^{-12}	
Compliance, $S^D{}_{33}$	9.4x10^{-12}	
Compliance, $S^D{}_{11}$	15x10^{-12}	
Compliance, $S^D{}_{12}$	-7.1x10^{-12}	
Compliance, S_{66}	43.7x10^{-12}	
Acoustic Impedance, Z (Banks, Oldfield, & Rawding, Ultrasonic Flaw Dectection in Metals: Theory and Practice, 1962)	22.5x10^6	kgm^{-2}s^{-1}
Density, ρ	7750	kgm^{-3}
Young's Modulus, E (Banks, Oldfield, & Rawding, Ultrasonic Flaw Dectection in Metals: Theory and Practice, 1962)	5.85x10^{11}	Nm^{-2}
Maximum Operating Temperature, T_{Max} (Banks, Oldfield, & Rawding, Ultrasonic Flaw Dectection in Metals: Theory and Practice, 1962)	290	ºC
Curie Temperature, T_C	370	
Time Stability		
Coupling Factor, k_p	-0.40	% change per decade
Capacitance, *C*	-1.60	
Frequency, f	0.20	

Table 5.1: Material Properties for PZT-5A1 (Morgan Technical Ceramics Electroceramics).

5.4.4 Element Shape

As shown by the frequency constant a piezo element's frequency is dependent on its thickness. The relationship between frequency and thickness for thin disc oscillating and polarised axially and made of a common Piezoceramic (PZT-5A1) is shown in Figure 5.5.

Figure 5.5: Frequency Vs. Thickness Relationship for PZT-5A1, N_p = 2000Hz·m.

Figure 5.5 is based upon a thin disc whose diameter is much greater than its thickness. This assumes a single mode of resonance within the piezo element. However, depending upon the elements shape, it is possible for more than one mode to be excited.

The responses from two shear sensors with different aspect ratios are shown in Figure 5.6 and Figure 5.7. One sensor was a flat plate (0.2 x 2 mm) while the other was square in cross section (1 x 1mm). The sensors were bonded on steel blocks and the response shows two reflections from the far side of each block. The reflections for the plate sensor are clear, with sharp responses, and only one apparent mode of resonance which equates to the frequency that would be expected given the piezo thickness. The response for the square cross section sensor looks significantly different. The response consists of a package of distinct sharp peaks rather than the smoother joined peaks seen in the flat plate response.

For clarity a single reflection for the square cross section sensor has been plotted in Figure 5.8. The plot shows that the reflection is built up of multiple higher frequency pulses with consistent spacing. This implies that there are in fact two modes of resonance. When the cross sectional dimensions of the piezo are considered the two modes of resonance can be explained. The time period between the high frequency pulses is approximately 0.45us, this is a frequency of 2.22 MHz. As we can see from Figure 5.5 this equates to a thickness of 0.9mm, and so would correspond to the thickness resonance of the element. The results of a Fast Fourier Transform performed on the window shown in Figure 5.8 is plotted in Figure 5.9 along with the frequency spectrum for a reflection from the flat plate element. The square section element shows multiple resonant harmonics in comparison to the single peak seen in the flat plate sensor. This clearly demonstrates the importance of considering not just the thickness, but also the lateral dimensions of the element used in a transducer.

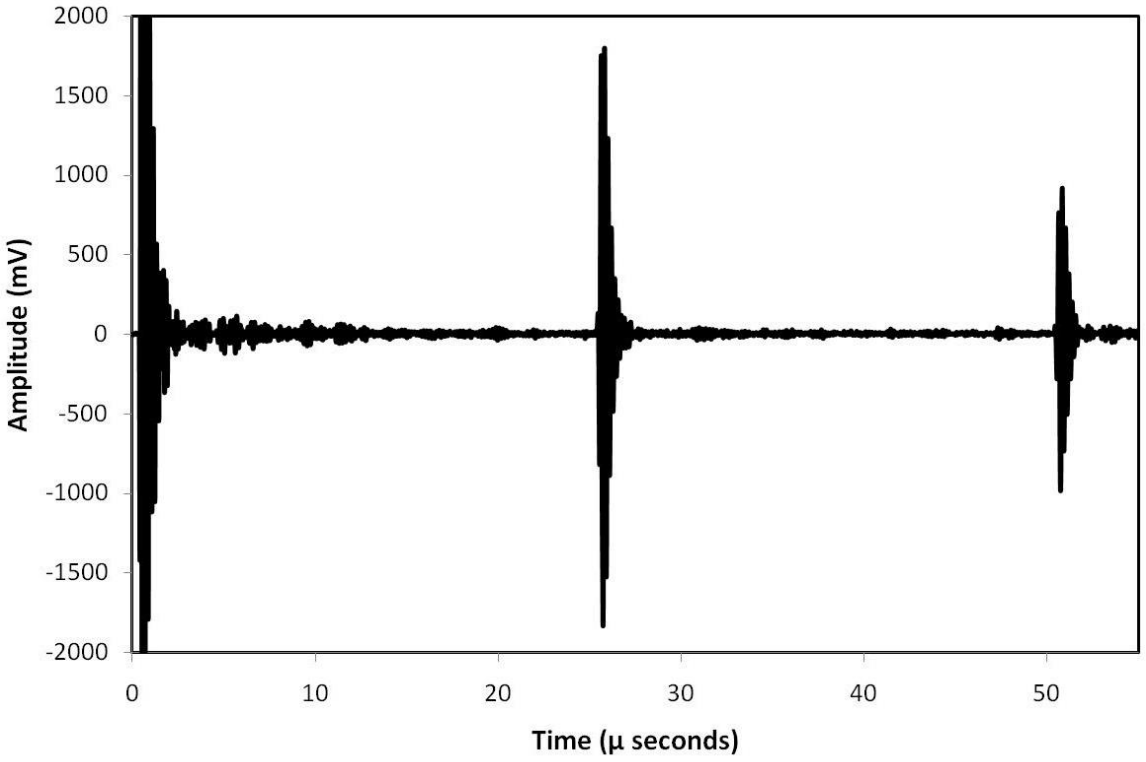

Figure 5.6: Shear Sensor Response with an Aspect Ratio of ~10:1.

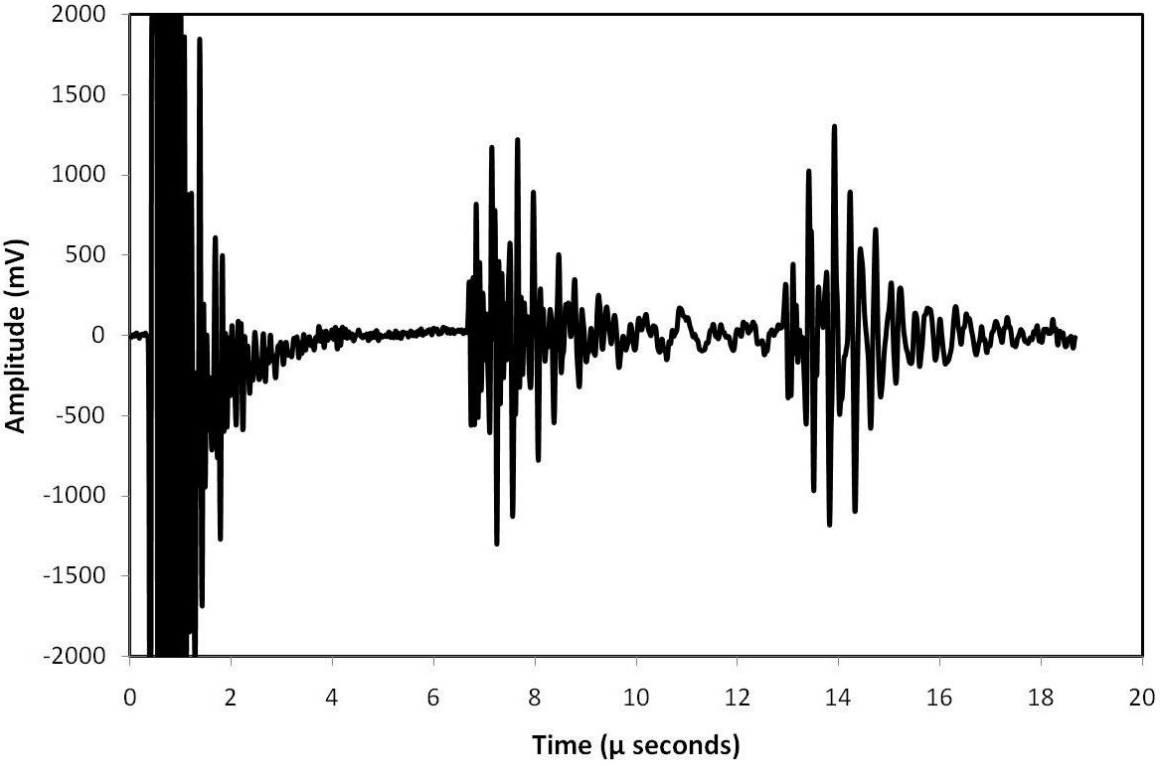

Figure 5.7: Shear Sensor Response with and Aspect Ratio of ~1:1.

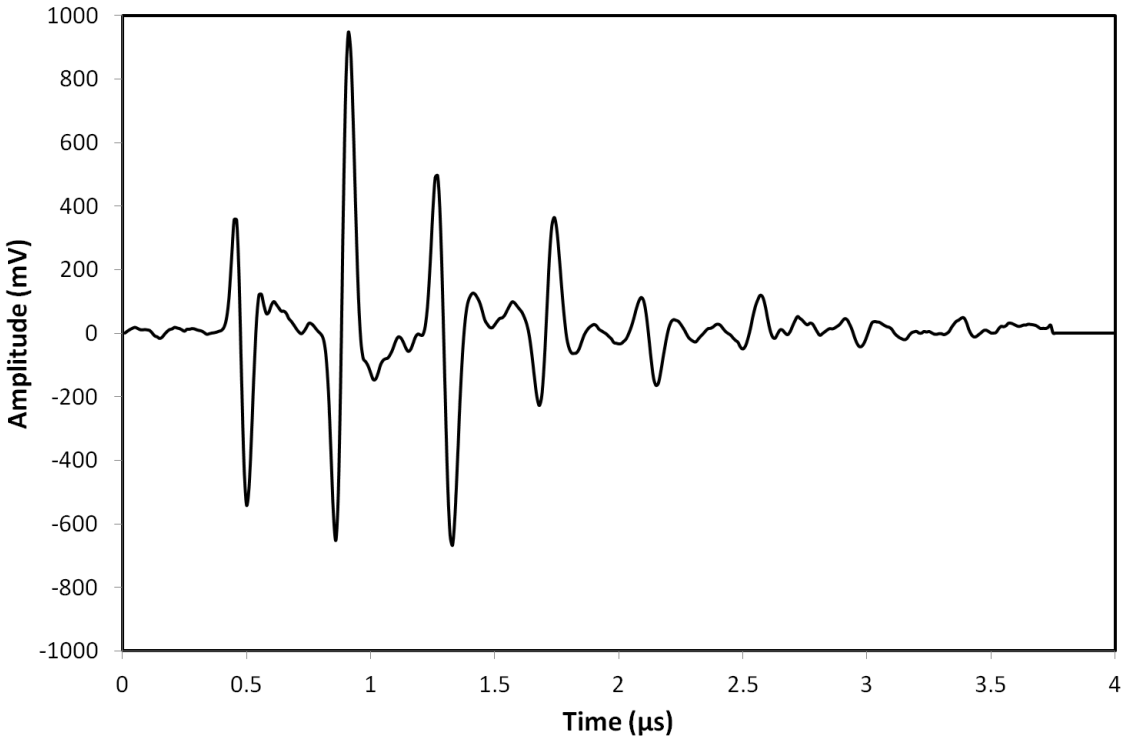

Figure 5.8: Single Shear Wave Reflection from Square Cross Section Sensor.

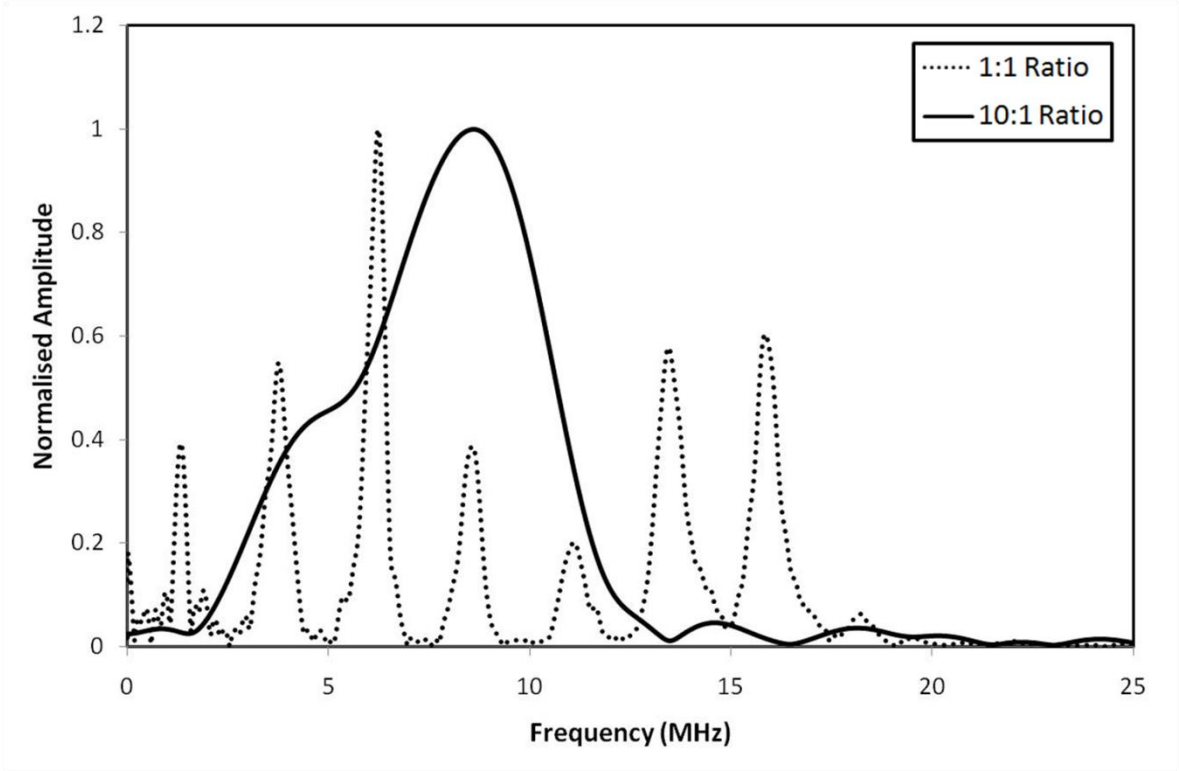

Figure 5.9: Shear Sensors Frequency Response.

5.4.5 Electrodes

In order to induce and measure electrical fields in a piezo element, electrodes must be mounted on either side. These electrodes come in a variety of forms, materials and manufacturing techniques (Morgan Technical Ceramics, n.d.). Key design considerations are electrode bond strength, thickness and solderability. When soldering to the electrodes it is essential that the

piezo does not exceed it's Curie temperature. As well as the piezoelectric effect, piezoceramics also have a pyroelectric effect. Heating of the piezo during the soldering process can therefore cause a significant build-up of charge, the piezo should be soldered in short-circuit conditions. Where an electrode is unsuited to soldering the electrical connections can be made either via a conductive adhesive or mechanical clamping. The electrode material and thickness will define the deposition methods that can be used. Electrode deposition techniques are typically split into two types, thin and thick film.

Thick-Film Electrodes

These are in the region of 3 to 10 µm and are applied to the piezo ceramic by screen printing. After careful cleaning, the components are applied with a conductive electrode paste, typically a noble metal such as silver. Silver and palladium alloys are also commonly used. The electrode paste is fired at a temperature between 600-800 °C depending on the material. This then forms a conductive layer with a good adhesion to the ceramic and results in relatively robust electrodes to which wires can directly be soldered. This method can leave small air pockets between the piezo material and electrode, reducing the ultrasonic transmission. Silver dissolves in standard solders, therefore high silver content solder is normally used to reduce absorption of the electrodes when soldering. In order to create separate ground and positive electrodes an electrode pattern is created by laser cutting the coating.

Thin-Film Electrodes

Physical vapour deposition (sputtering) can be used to create much thinner electrodes. This results in electrode thicknesses in the range of 1 µm down to a few 100 nm, with less air gaps in comparison to the screen printing method. Sputtering can be used with a range of electrode materials including Gold-Nichrome, Nichrome, Silver and Aluminium. The technique involves creating positive ions in an inert gas. The material to be used for the electrode is struck by these ions and broken up into a fine spray that covers the piezo. The electrode shape is defined by masking of the defined area. Shear elements must be metalised in the polarized state and are generally manufactured with thin-film electrodes. Nickel electrodes can be chemically plated or evaporated. Due to the thinness of this electrode type, and the materials involved, wicking of the electrode during soldering is an issue. Therefore, for evaporated electrodes conductive epoxies are typically used.

5.4.6 Element Excitation

In order to produce an ultrasonic wave, the piezo element must be excited using an electrical signal. This excitation signal can take many forms as follows.

Spike Pulse: A spike pulser generates a pulse with a very fast rise time and an exponential decay. The pulse shape is adjusted by altering the pulse energy and damping. The fast rise time results in a broadband pulse, making this pulse type suitable for high-frequency transducers (Olympus).

Square Wave/Top Hat: A square wave pulse has controlled rise and fall times. The pulse can either be a bipolar square wave cycle, or a unipolar half cycle (also called a "Top-Hat" pulse). The pulse frequency is matched to the transducer resonant frequency to increase the pulse energy transferred to the transducer. The potential pulse energy gained by using a frequency matched square wave as opposed to a spike excitation is shown in Figure 5.10. Although the hardware required to generate a square wave pulse is more complex than for spike pulsers, they are now more commonly available.

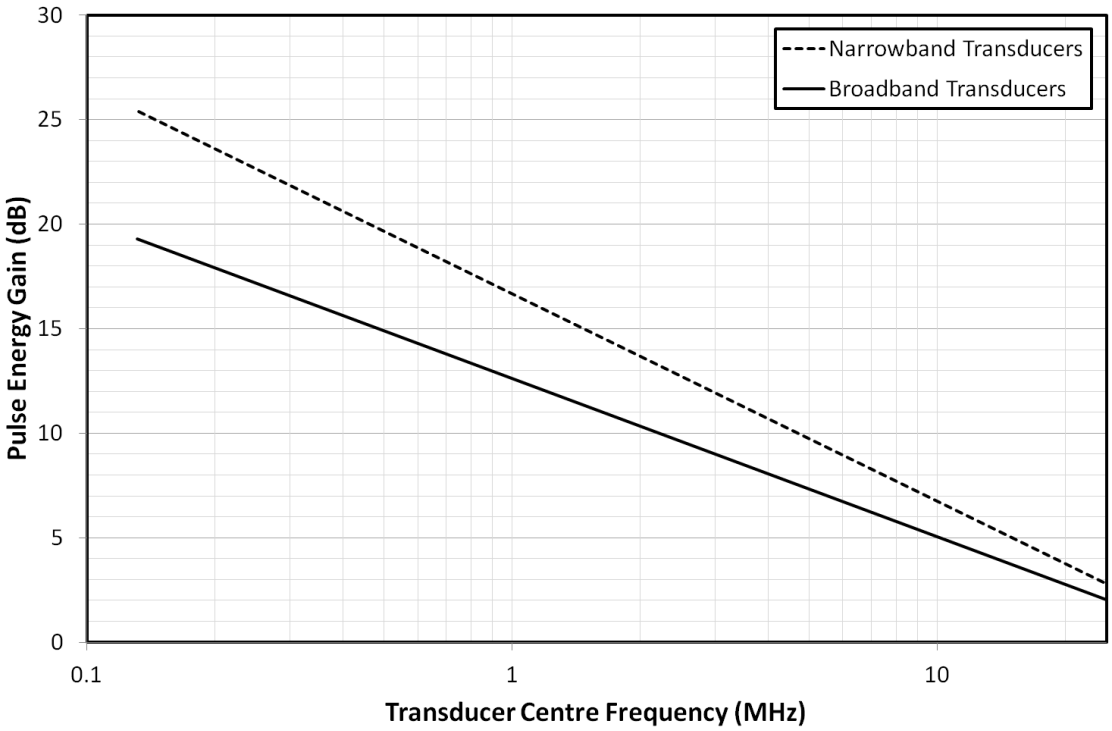

Figure 5.10: Potential Pulse Energy Gain using a Tuned Square Wave Excitation Pulse in comparison to a Spike Pulse, reproduced from (Olympus).

Encoded Pulses: The transducer can be excited by a train of pulses in a defined pattern, such as a Golay code (Challis & Ivchenko, 2011). This can be used to increase the energy transmitted by the sensor, or aid with the detection of a returning signal.

Continuous Wave: Unlike the excitation methods discussed above, which rely on discrete pulses, continuous wave excitation continuously transmits and receives. While pulses are broadband, continuous wave systems use single frequency sine waves. This approach can enable Doppler measurements, but because there is no way of ascertaining when a captured wave originated, it cannot be used to work out the location of any the reflections via time-of-flight.

Chirp: More exotic continuous waves such as 'Chirps' can be used to encode the outgoing wave with certain characteristics by modulating its frequency. This is done in order to study a wider range of frequencies and enable temporal measurements.

In all cases the excitation wave amplitude (voltage) will affect outgoing wave amplitude. The excitation voltage should not exceed the voltage acceptable to the sensor or this may damage the piezo element. Some of the common excitation pulse shapes are as follows.

5.5 Beam Shape

The ultrasonic wave emanating from the front of the transducer changes in intensity and shape as it travels away from the transducer. As was shown in §3.2.8 the wave emitted by a transducer can be thought of as being built up of collection of spherical waves interfering with each other, and originating at every point on the transducer face. If the transducer was infinitely wide this would result in a flat plane wave. However, the finite width of transducers results in this non-uniform sound field. It is important to consider the effect of this on measurements taken using the wave.

5.5.1 Near Field

Close to the face of a transducer an interference pattern occurs. This is referred to as the transducer *Near-Field* or *Fresnel Zone*. The difficultly in interpreting measurements in this zone mean that it is avoided where possible. The area beyond this effect is called the *Far-Field* or *Fraunhofer Zone*. The interference pattern is related to the wavelength and piezo element size, the pattern of interference maxima for two spherical waves is shown in Figure 5.11.

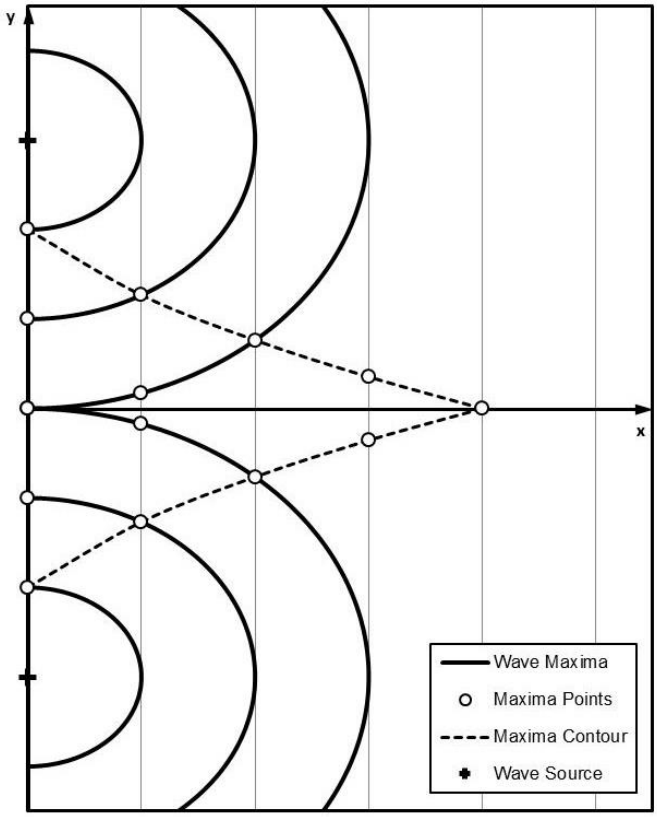

Figure 5.11: Interference Maxima (Krautkrämer & Krautkrämer, 1977).

The distance from the transducer that the transition from near to far field occurs can be approximated for circular elements using the following equation:

$$N = \frac{D^2 - \lambda^2}{4\lambda} \qquad 5.6$$

Where *N* is the near field length, *D* the transducer diameter and λ the wavelength. This equation assumes a circular transducer. This equation is often quoted with the wavelength term neglected from the numerator, this is a simplification made when the wavelength is small compared to the element width.

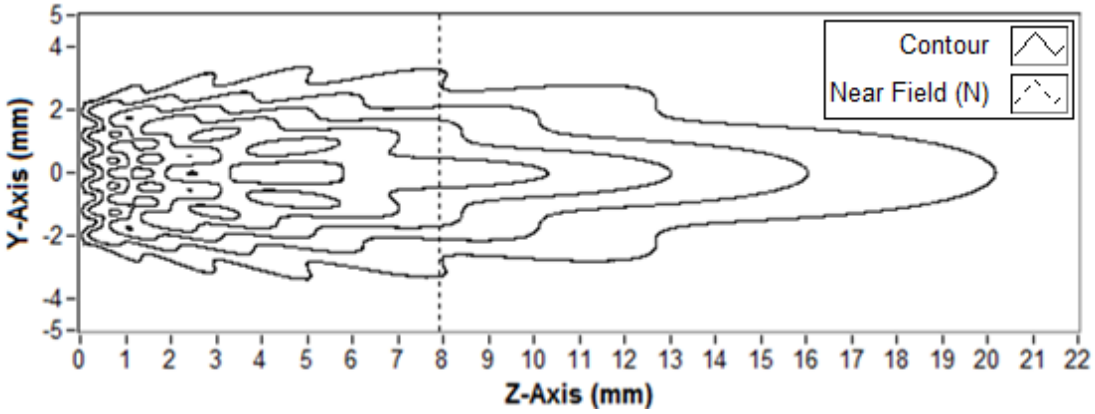

Figure 5.12: Beam Intensity Profile in Steel, Longitudinal, 7.88MHz, 5mm Width, N = 7.95mm.

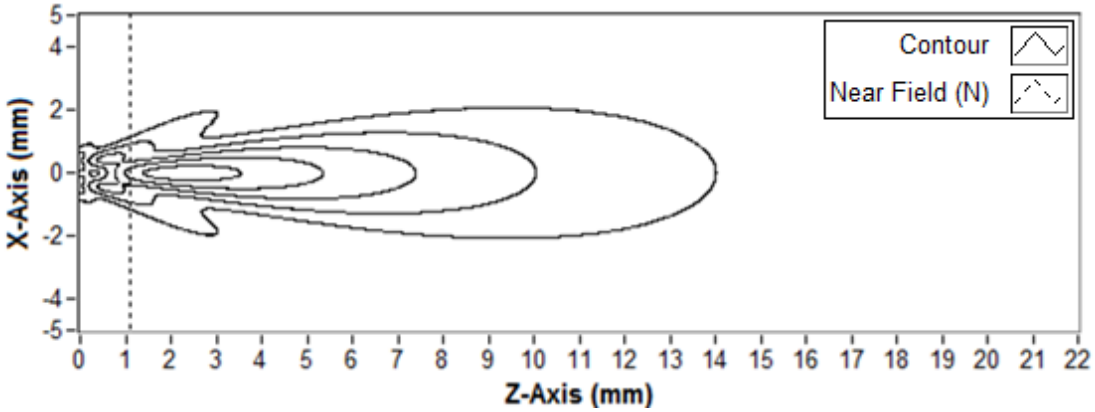

Figure 5.13: Beam Intensity Profile in Steel, Longitudinal, 7.88MHz, 2mm Width, N = 1.11mm.

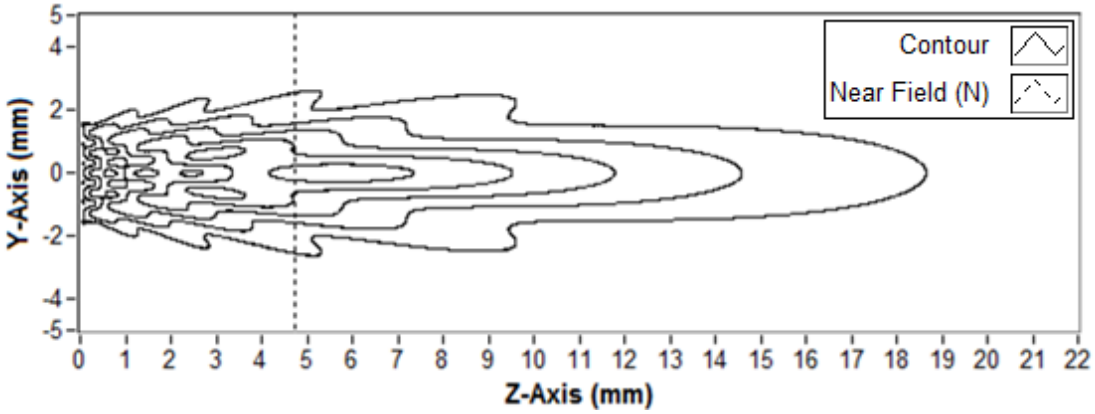

Figure 5.14: Beam Intensity Profile in Steel, Shear, 5.32MHz, 3.5mm Width, N = 4.76mm.

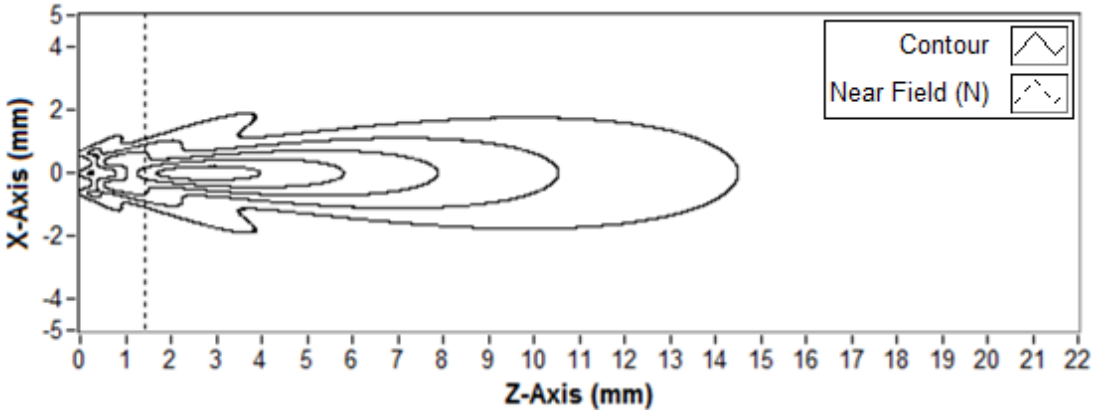

Figure 5.15: Beam Intensity Profile in Steel, Shear, 5.32MHz, 2mm Width, N = 1.45mm.

The ultrasonic beam pattern for a range of transducer frequencies and diameters were calculated using a specially written software based upon the Huygens-Fresnel principle. These are plotted in Figure 5.12 to Figure 5.15. The pattern was calculated for an ultrasonic beam travelling in a steel block. Interference patterns for shear and longitudinal waves were approximated by adjusting the speed of sound to 3315m/s and 6050m/s respectively. The plots show a cross section of the ultrasonic intensity of the beam through the propagation axis. Contours represent points of equal ultrasonic intensity and are equispaced on the intensity scale. The near field distances calculated from Equation 5.6 are also plotted.

The wider elements show clear grid like interference patterns in front of the element. These are much less pronounced in the thinner elements. The main ultrasonic beam spreads out in a much more regular pattern after it has passed through the near-field, hence why measurements are preferred in this zone. A number of 'lobes' can also be observed coming off the sides of the main beam.

The pressure profile along the central beam axis *P(R)* for these circular elements can be described by Equation 5.7 (Silk, 1984)

$$P(R) = \left| P(0) 2 sin \left[\frac{\pi}{\lambda} \left(\sqrt{\frac{D^2}{4} + R^2} - R \right) \right] \right| \qquad 5.7$$

Where $P(0)$ is the initial pressure, λ is the wavelength, D is the element diameter and R is the distance from the transducer. A plot of this profile in steel for some representative element values is plotted in Figure 5.16.

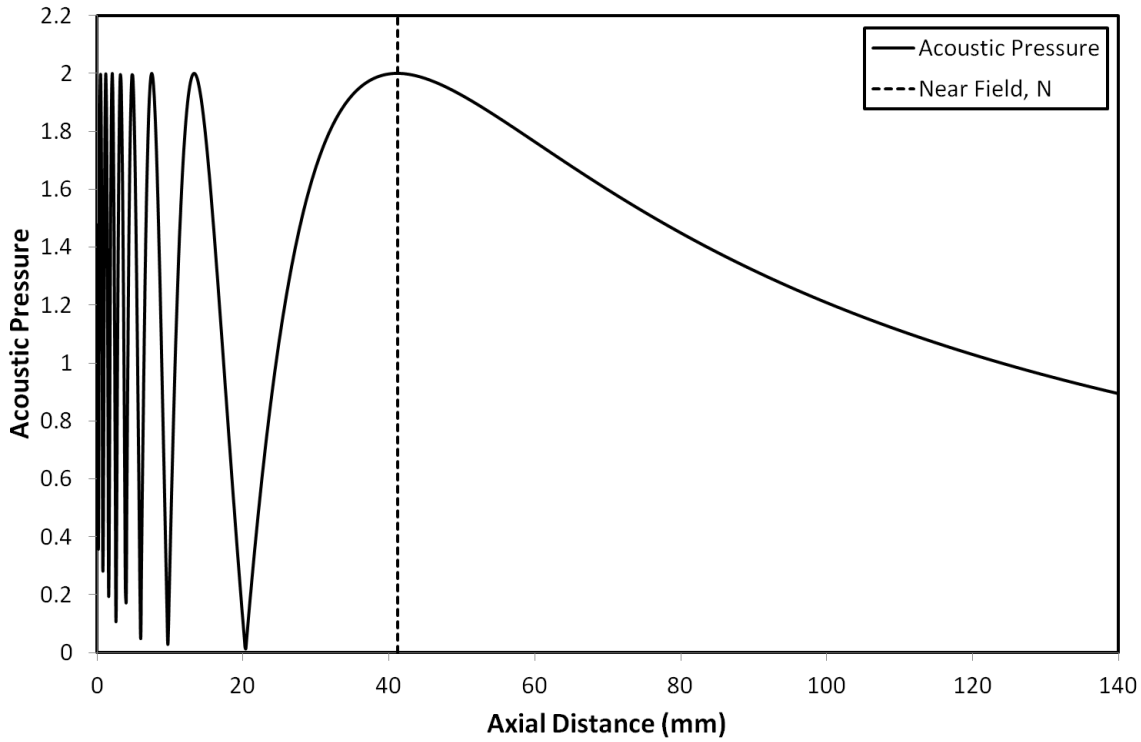

Figure 5.16: Acoustic Pressure on Axis of Piezo Element, P(0) = 1, Steel, 10MHz, D = 10mm, N = 41.17mm.

This clearly shows how the near-field is defined as the distance of the last pressure maximum from the element on the propagation axis.

5.5.2 Rectangular Elements

The profiles presented so far have been for circular elements, however often rectangular elements are used. This change in geometry results in a beam profile which unlike a circular transducer lacks axial symmetry (Ocheltree & Frizzell, 1989). The 3-dimensional pressure profile in relation to the centre of the element is given by Equation 5.8 (Silk, 1984):

$$P(\gamma_1, \gamma_2, R) = P(R) sinc\left(\frac{\pi D_1}{\lambda} sin\gamma_1\right) sinc\left(\frac{\pi D_2}{\lambda} sin\gamma_2\right) \quad 5.8$$

Where D_1 and D_2 are the side lengths of the elements, γ_1 and γ_2 are angles from the beam centreline, R is the distance from the element centre and λ is the wavelength. The "sinc" function is an abbreviation for the "sine cardinal", a function found commonly in signal processing. As can be seen from Equation 5.8 the radiation pattern from a rectangular element is not axially symmetrical. Counter intuitively the pattern is wider in the narrower piezo direction. A 3-dimensional view of the radiation pattern for a rectangular element, without secondary lobes, is shown in Figure 5.17.

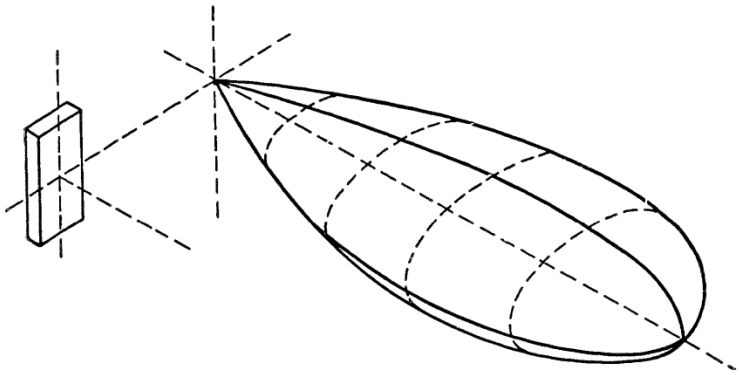

Figure 5.17: Rectangular Element Radiation Pattern. Secondary Side Lobes exist but are hidden for this plot. Side Ratio 2:1, $D_1/\lambda \approx 4$, $D_1/\lambda \approx 2$ reproduced from M.G. Silk (Silk, 1984).

The near field for a rectangular transducer can be calculated by adjusting Equation 5.6 with a dimensionless factor *k*, as shown in Equation 5.9 (the equation has been simplified by removing the λ^2 term).

$$N = k\frac{a^2}{4\lambda} \quad 5.9$$

Where *a* is the longer element side. For a circular, plane transducer this factor is k = 1. For a square element k = 1.35, a line source of length 2a has k = 0.988 and for an element with a side ratio of 0.5 then k = 1.014 (Schlengermann).

5.5.3 Beam Spread

Once the ultrasonic wave is into the Far-Field it can be treated as a single beam which slowly diverges as shown in Figure 5.18, and can also be seen in the intensity profile plots presented previously, particularly in Figure 5.13 and Figure 5.15.

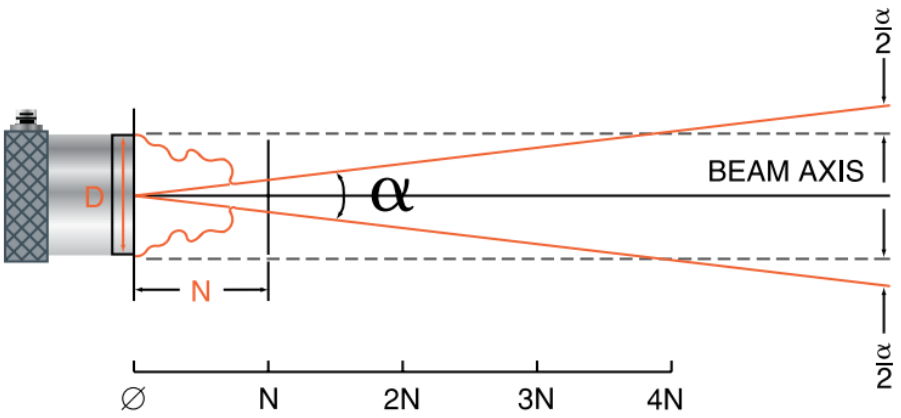

Figure 5.18: Ultrasonic Beam Spread, reproduced from (Olympus NDT, 2006).

The beam divergence does not have a distinct boundary, instead it is defined with reference to the peak pressure value. The -6 dB intensity points are the most common measurement of the beam edge. The beam spread angle as measured at the -6 dB points is given by Equation 5.10 (Olympus NDT, 2006):

$$\sin(\alpha/2) = \frac{0.514c}{fD} \qquad 5.10$$

Where α is the angle spread between the -6dB points, D is the element diameter, f is the transducer frequency and c is the speed of sound in the material. Beam spread results in reduced signal amplitude and increased measurement spot size with distance.

5.5.4 Focusing

The effects of beam spread can be reduced by focusing the ultrasonic beam. In the same way that a lens focuses light to a focal point at a set distance from the lens, by shaping the front face of the transducer it is possible to achieve a similar effect with an ultrasonic beam, as shown in Figure 5.19.

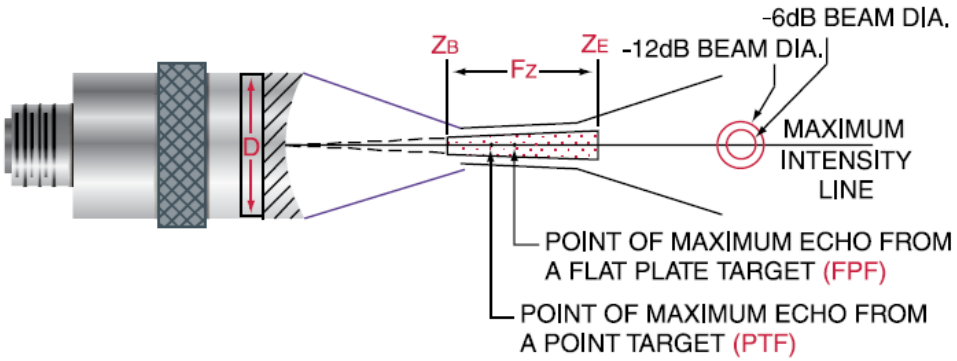

Figure 5.19: Beam Focusing Zone, reproduced from (Olympus NDT, 2006).

Where Z_B is the beginning of the focal zone, F_z is the focal zone, Z_E is the end of the focal zone and D is the element diameter. The ultrasonic beam can be focused to a point by using a spherical focusing. It can also be focused to a line, known as cylindrical focusing. The names of the types of focusing come from the shape of the faces used to create them.

5.6 Conclusions

In ultrasonics the transducer used to convert electrical signals to ultrasonic waves and back is key to the quality of the measurement. Ultrasonic transducers have been developed over a number of years and have found widespread use in traditional non-destructive testing applications, such as handheld thickness gauging and crack detection, as well as medical imaging, such as pregnancy scans. Transducers commercially available today are therefore normally tailored towards these applications.

Piezoceramic technologies form the basis of most ultrasonic transducers, although EMAT and laser induced ultrasonic technologies are found in research applications. Piezoceramic devices are a mature technology and most follow similar design concepts. Piezoceramics are suitable for industrial ultrasonic applications due to their proven consistency, relatively high conversion efficiency, robustness, low cost and ease of use. For these reasons piezoceramics have been chosen for the proposed roll bite measurements. However, unlike either EMAT of laser induced ultrasound, piezoceramic technologies have the disadvantage of requiring physical coupling to the inspected piece.

A huge range of piezoceramic materials and element configurations are available, each with differing characteristics. These attributes are quantified by a wide range of material parameters, and their suitability is dependent upon application specific requirements. For this work a PZT (lead zirconate titanate) has been selected as this represents a good balance between sensitivity and temperature stability across the range of temperatures expected in operation.

Despite developments in transducer design, amplitude measurement repeatability using piezoceramics is still limited by the sensor coupling. This work will circumvent current coupling limitations, such as signal variation and time/temperature stability, by permanently bonding the piezo elements to the part to be inspected. This will deliver good coupling efficiency, stability and repeatability.

Element geometry has a large effect on the form of the ultrasonic beam produced. This will be considered when selecting the transducers used in order to ensure sufficient measurement special resolution, element frequency, beam spread and nearfield length.

6 Instrumentation and Experimental Setup

The following chapter details the experimental setup used to gather the data presented in later chapters. This includes details of the rolling mills used, methods of installation, ultrasonic pulse generation, data acquisition hardware, strip materials and lubricants.

6.1 Rolling Mills

The rolling experiments were performed on two rolling mills, a small pilot mill based at the University of Sheffield, UK, and a semi-industrial pilot mill based at ArcelorMittal's research campus in Maizières-lès-Metz, France.

6.1.1 Sheffield Pilot Mill

The small pilot mill in Sheffield was used for feasibility level work to demonstrate the proposed methods. The relatively low cost of instrumenting the mill and performing tests enabled fundamental proof-of-concept work to be carried out, de-risking the work before implementation was carried out on a setup more representative of the industrial case. The mill used was a Hille 25 two-high cold rolling mill, shown in Figure 6.1.

The Sheffield pilot mill is relatively small with rolls of 111mm in diameter. The mill was hand fed, and therefore there was no tension applied to the strip. The maximum rolling force of the mill is 250kN, although no direct measurement of load was employed. Specific figures relating to the mill specifications are given in Table 6.1.

Roll Diameter	111 mm
Load Capacity	250 kN
Maximum rolling speed	76 mm/s
Roll gap	<10 mm
Strip width	<80 mm

Table 6.1: Sheffield Mill Specifications

6.1.2 ArcelorMittal Semi-Industrial Mill

Upon completion of the proof-of-concept stage, testing was moved to the semi-industrial pilot mill as shown in Figure 6.2. This mill had been used in a previous European Commission project (A. Fouratier, F. Geißller, G. Endemann and B. Schmidt, 2002) and as part of this was modernised in 1995.

The mill is capable of both two-high (just work rolls) and four-high configurations (work rolls and backup rolls). The two high configuration was used in these tests. The work roll had a diameter of 386mm and a barrel width of 300mm, other details are included in Table 6.2 .

Roll Diameter	386 mm
Load Capacity	1.96 MN
Maximum rolling speed	1500 m/min
Roll gap	0.05 to 4mm
Strip width	50 to 200mm

Table 6.2: ArcelorMittal Mill Specifications

The rolling force is applied via a hydraulic screw. The stand has two 300 kW drives. There is a matching coiler/uncoiler pair, each of 110 kW, with tension bridles of 70kW capable of providing

tensions of 4216 Kg at 100m/min to 222 Kg at 1500m/min. The strip does not pass through the roll bite horizontally, and it makes an angle of 0.7° with the horizontal at the roll bite entry.

Figure 6.1: Hille 25 Pilot Mill.

The lubricating system consists of both a *Direct Application* (DA) and *Recirculated* (RE) circuit. The DA circuit is made up of 2 tanks of 100l with temperature control and agitation, 2 centrifugal pumps capable of $1m^3/h$ at 10 bar, 2 volumetric pumps capable of $1m^3/h$ at 10 bar and 4 heads with transverse flow. The RE circuit has 2 tanks of 2000l with temperature control and agitation, 2 pumps delivering $18m^3/h$ at 10 bar and 4 heads. These systems allow a range of lubrication conditions seen in industrial applications to be emulated. In addition to the lubricating system there is a separate water cooling system made of one centrifugal pump providing $50m^3/h$ at 10 bar with two heads.

During the initial tranche of testing a periodic fluctuation in the rolling force was recorded by the mill control system. Several possibilities for this were investigated however the problem was not entirely resolved. A suspected reason was an imbalance in the mass of the roll due to the modifications made to accommodate the sensors, as described later in this chapter. To minimise this effect and maintain safety the top rolling speed was limited to 300m/min. Following a

change in instrumentation technique for the second round of testing the maximum rolling speed was increased to 1200m/min.

Figure 6.2: ArcelorMittal Pilot Mill and Control Room.

6.2 Data Acquisition Equipment

A typical setup for an ultrasonic pulse-echo system, such as that designed and built for testing, is shown in Figure 6.3. Selection of the components that are used to fulfil the various roles in this system must not only be informed by measurement performance, but also application specific requirements including, environmental conditions, cost and integration limitations.

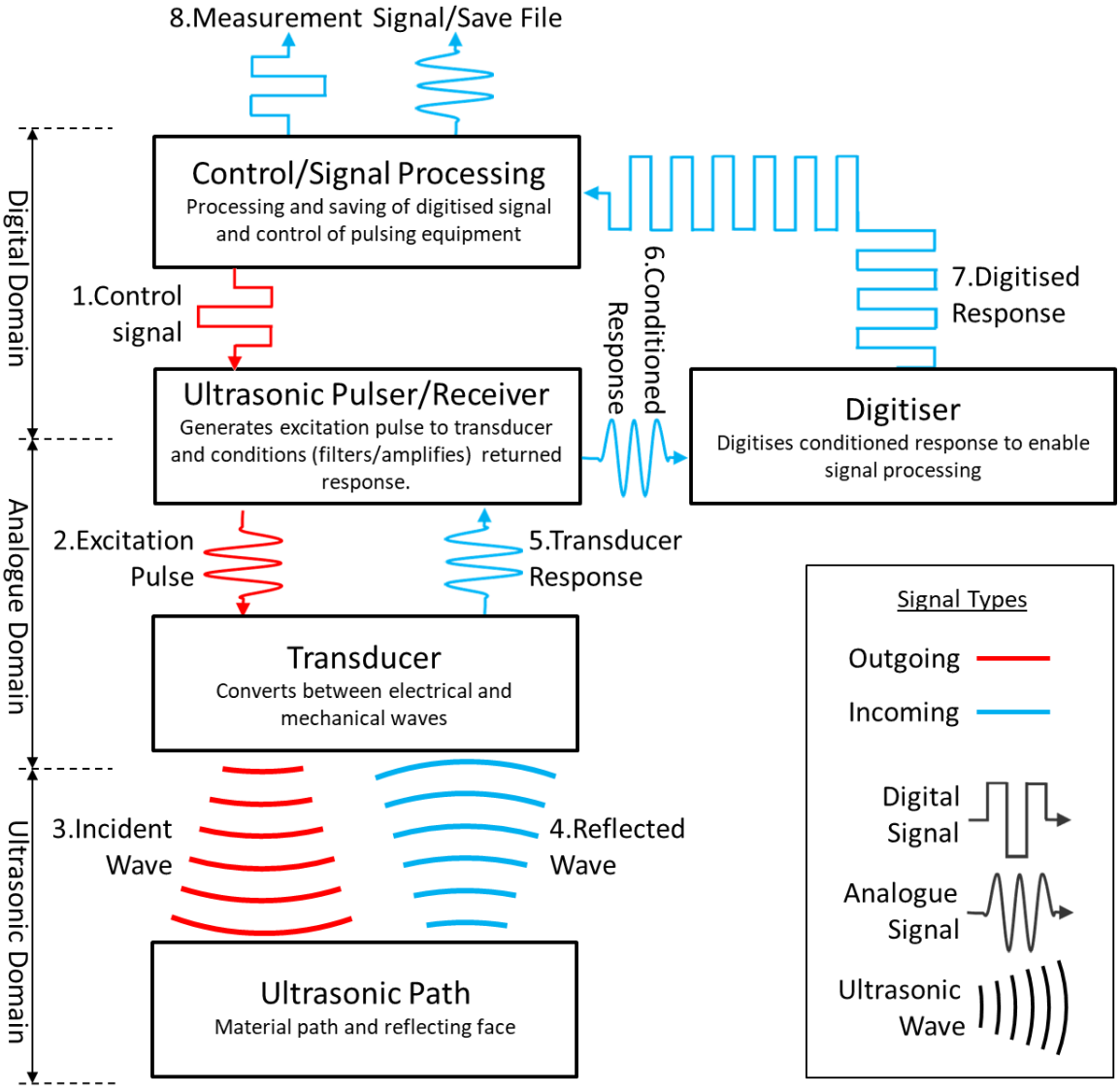

Figure 6.3: Schematic of a Typical Ultrasonic System.

Figure 6.3 shows that the system must handle and convert between electrical digital, electrical analogue and mechanical (ultrasonic) signals. The Signal Processing, Ultrasonic Pulser/Receiver (UPR) and Digitiser elements are normally built into a single unit, to which an application specific transducer is attached.

A schematic of the elements which made up the data acquisition system for the semi-industrial pilot mill are shown in Figure 6.4, and detailed in the following sections. This system was developed during feasibility testing on the Sheffield mill. The figure shows the plug approach for sensor instrumentation, other approaches were also used and these are detailed later in this chapter. The other elements of the system remained consistent throughout the testing performed.

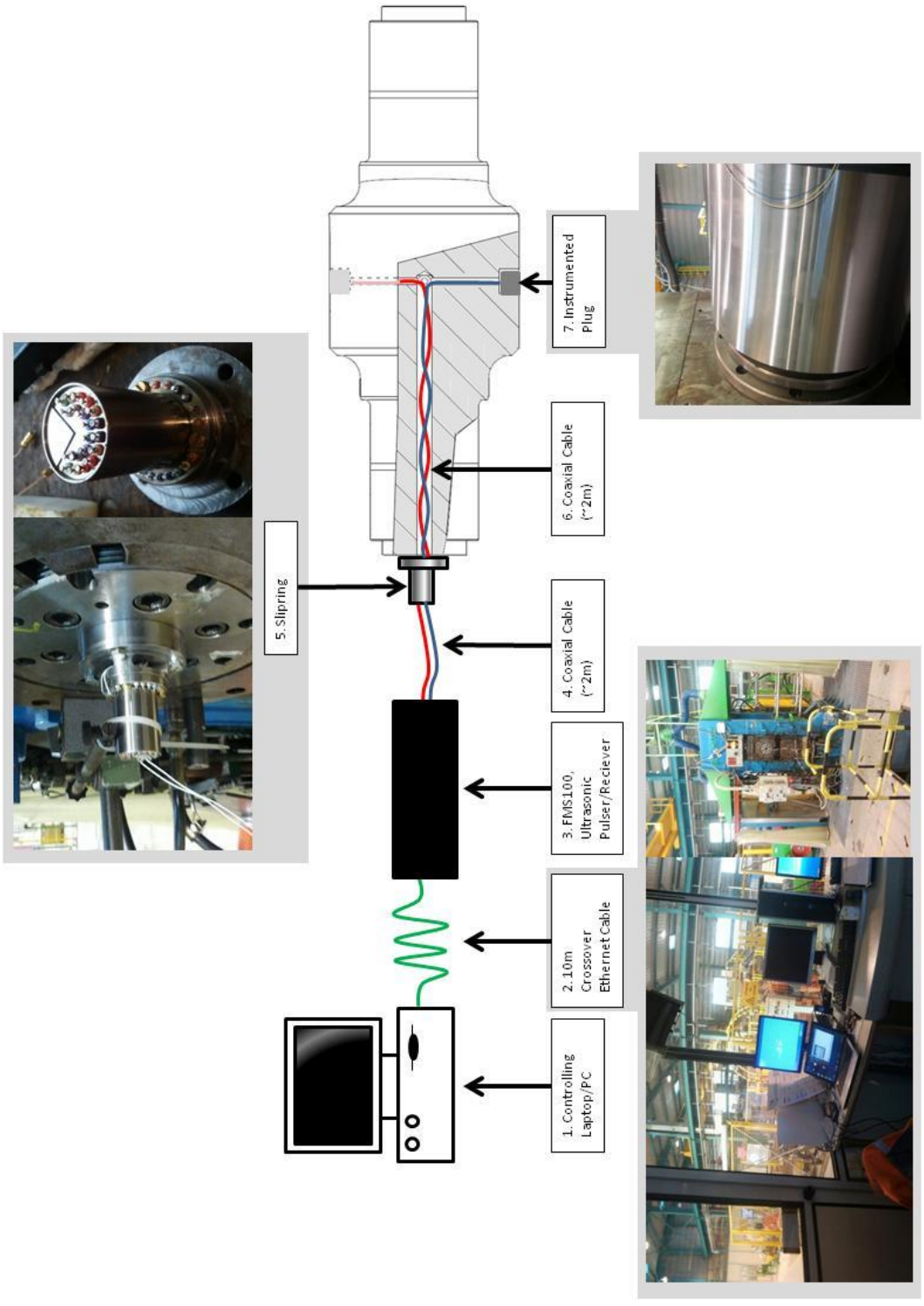

Figure 6.4: Data Acquisition Setup.

6.2.1 Ultrasonic Pulsing, Receiving and Digitising Hardware

The UPR and digitisation equipment selected was the FMS100 supplied by Tribosonics Ltd, which is shown as item 3 in Figure 6.4. This takes the form of specialist ultrasonic PCI cards mounted within an industrial PC chassis. The specifications of this equipment are given in Table 6.3.

FMS-100 UPR	
Switched Input Impedance	50/100/200/500R (50 ohm used)
Input Attenuator	0/-20/-40 dB
Input Preamp	+20dB
Receiver Gain	+90 dB
-6dB Bandwidth	0.1 to 25 MHz
Bandpass Filters	0.5/1/2.5/5/10/15 MHz (10 MHz used)
TCG	16 Points 10ns Time Resolution 80dB Total Correction 0-40dB/µs Slope Range
Dynamic Range	>80dB
Channel Crosstalk Isolation	>80dB
Receiver Noise	1.3nV/√Hz to 2nV/√Hz
Pulser Output	-20V to -350V Inverted 'Top-Hat'
Rise and Fall Times	5ns ± 1ns
Pulse Width	10ns to 2µs in 10ns Steps
Global PRF	100 kHz max.
FMS-100 Digitiser	
Sampling Frequency	100 MHz
Resolution	12bit
Analogue Bandwidth	25MHz
Noise	60dB SNR
Gates	6 Real Time in Hardware
Software	Bespoke NI LabVIEW code

Table 6.3: Ultrasonic Equipment Specification.

Many of the hardware settings are adjustable. The *Pulse Repetition Frequency* (PRF) is the rate at which ultrasonic pulses are sent out. The system is capable of 100kHz global PRF which is split between the number of channels in use, so 2 channels will have a maximum PRF of 50kHz, 3 channels have a maximum of 33.3kHz and so on. The hardware switches between pulsing and receiving modes, it cannot do both simultaneously. This means that it is necessary to pulse, switch to receiving mode and wait for the response, before switching back to send another pulse. This limitation can be overcome by using separate pulsing and receiving transducers, which would mean the hardware does not need to switch. The length of the ultrasonic path and the speed of sound of the transit material define the minimum length of this wait. The maximum achievable PRF is therefore a function of the hardware capability, number of sensors and ultrasonic transit time.

As the sensor is mounted within the roll it will rotate past the contact spot with each roll revolution. The amount of time it will spend over the contact is a function of the contact size and rolling velocity. Using a representative contact length of 5mm, Figure 6.5 shows the number of data points measured across the contact for various PRFs.

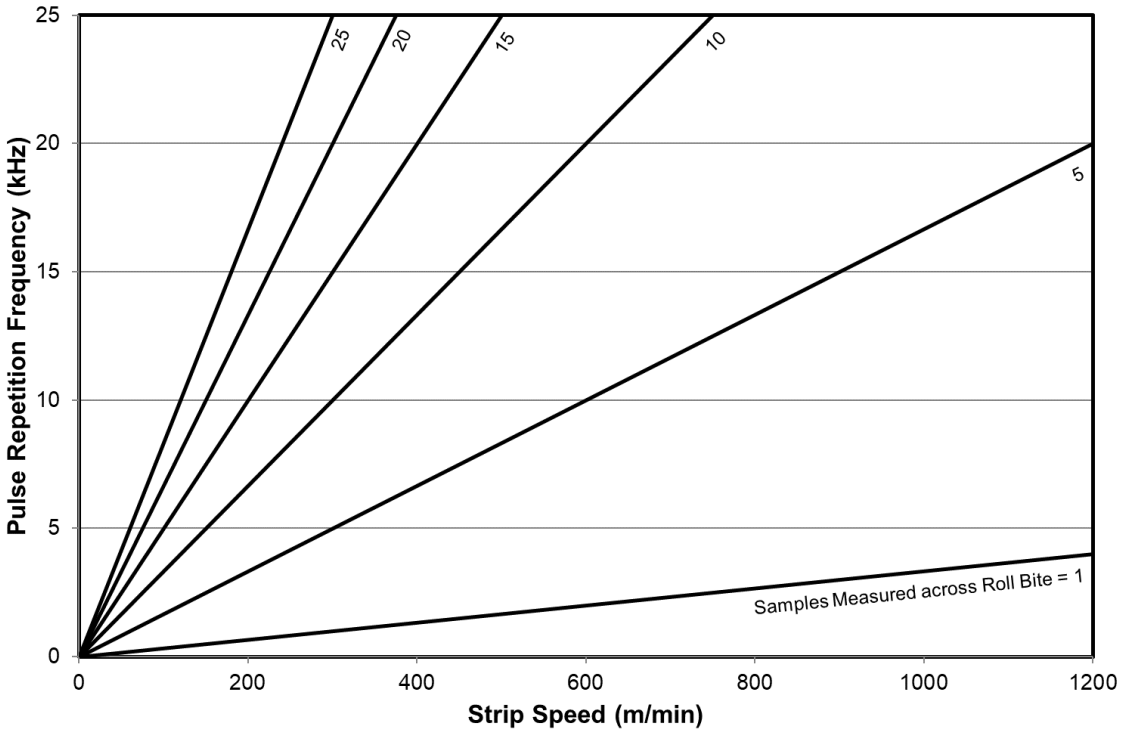

Figure 6.5: Required Pulse Repetition Rate at different Strip Speeds, contact size 5mm.

The range of strip speeds shown in Figure 6.5 are the same as those used in testing on the semi-industrial pilot mill. The Sheffield mill had a maximum rolling speed of 4.56m/min, so the PRF was much less of a concern. Industrial rolling mills can operate at much higher speeds than those tested in this thesis, and this may require pulsed repetition at much higher rates, possibly outside of the capabilities of currently available equipment.

There are several approaches that could be adopted to overcome this. A continuous wave rather than pulsed approach could be adopted, for which the measurement rate becomes the digitisation rate. Alternatively, by triggering the excitation pulse relative to the roll position, exact locations across the roll bite could be measured.

The *Sampling Frequency* is the rate at which the returning waveform is digitised. In signal processing, the Nyquist rate (Chen C. T., 2001) defines a lower boundary of the sampling rate required for alias-free signal digitising. This stipulates a sampling rate of greater than twice the highest frequency component of the waveform. This represents a theoretical ideal, a more commonly used rule of thumb when dealing with pulse based ultrasonic signals is to use a digitising rate at least a factor of ten greater than the wave centre frequency. For example a 100MHz digitiser is required to capture at a high enough resolution to reconstruct a 10MHz pulse.

In order to match the returned signal amplitude to the digitiser range the incoming signal is amplified prior to digitisation. This is done in two stages, firstly the signal passes through a fixed preamplifier, then a variable *Gain* amplifier. Amplification only ensures the best use of the digitiser resolution, reducing quantization error. As it also amplifies any noise, there is no gain in the signal to noise ratio (SNR). Improved signal to noise ratio is achieved by increasing the incident wave amplitude, and by removing sources of electromagnetic interference (EMI)

through adequate screening of the electronics and cabling.

The *Wave Frequency* is predominantly defined by the transducer, however is also affected by the excitation pulse frequency. The excitation pulse takes the form of an inverted 'Top-hat' signal which can be approximated as half a cycle. Therefore for best efficiency the pulse width (or period) should be set to half the transducer's centre frequency. This means energy is transferred to the transducer at its natural resonant frequency. This can increase the signal amplitude by 12 dB or more compared to a spike pulse of the same amplitude (Olympus).

6.2.2 Software

The software to control the data acquisition hardware was custom written in National Instruments LabVIEW. Software to provide basic control of the pulsing/receiving hardware had already been written and where possible this was adapted. The completed software was capable of saving the raw data to disk while also processing the data in real-time, including the calculation of the signal Fast Fourier Transform (FFT), reflection coefficient and interface stiffness. By performing some basic processing in real-time the signals could be analysed and verified during testing, reducing the risk of incorrect hardware setup and poor data. More complex analysis of the signals was later performed on the recorded data using separate software, again written in LabVIEW. The interface for the FMS100 software used to configure the hardware can be seen in Figure 6.6 and the acquisition interface can be seen in Figure 6.7.

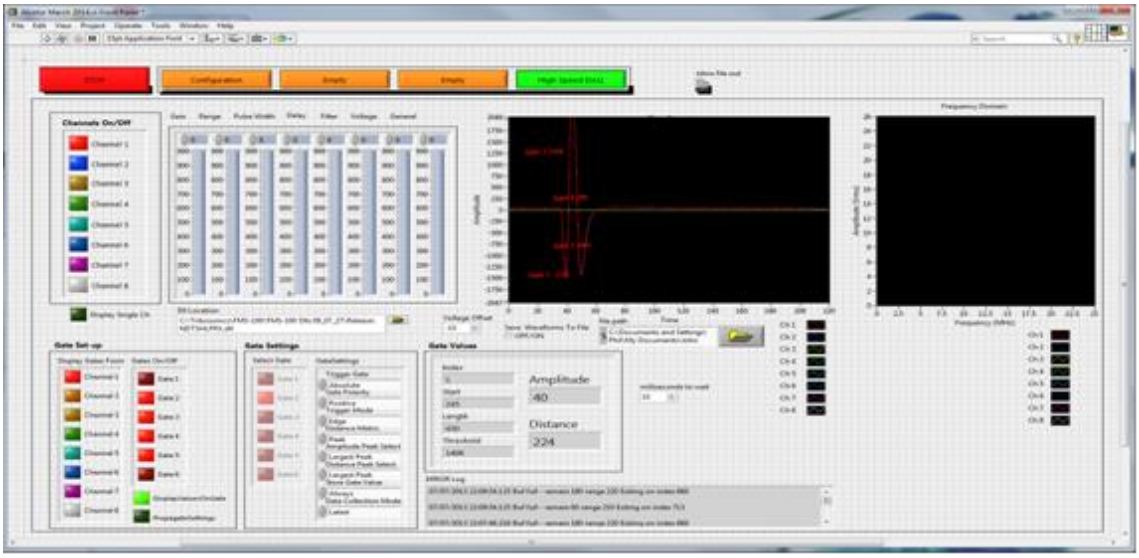

Figure 6.6: FMS100 Software Configuration Interface.

Data was saved as TDMS (Technical Data Management System) file type. Although proprietary to National instruments this data format can be opened in a range of industry standard applications, including Matlab and Microsoft Excel, via associated plugins and import tools. TDMS files combine binary data which has the advantage of small file size and quick read/write speeds with an XML header giving them the ability for stored data to be easily identified, opened and edited.

In order to capture at the necessary speed the hardware buffered multiple pulse responses before passing these into software. This data was then parsed into the individual responses,

processed and saved to file. With data rates in the order of 20MB/s memory management was important to ensure no data was lost.

In its editable form the data acquisition software required an instance of LabVIEW to be installed on the data acquisition machine, and therefore an appropriate software licence. This was acceptable for testing performed at the University of Sheffield who hold the appropriate licences. For external implementations, such as the industrial testing, the software as exported as a stand-alone executable file. This required LabVIEW Run-Time, but no license. Both implementations were widely tested and the demonstrated functionality was identical for both.

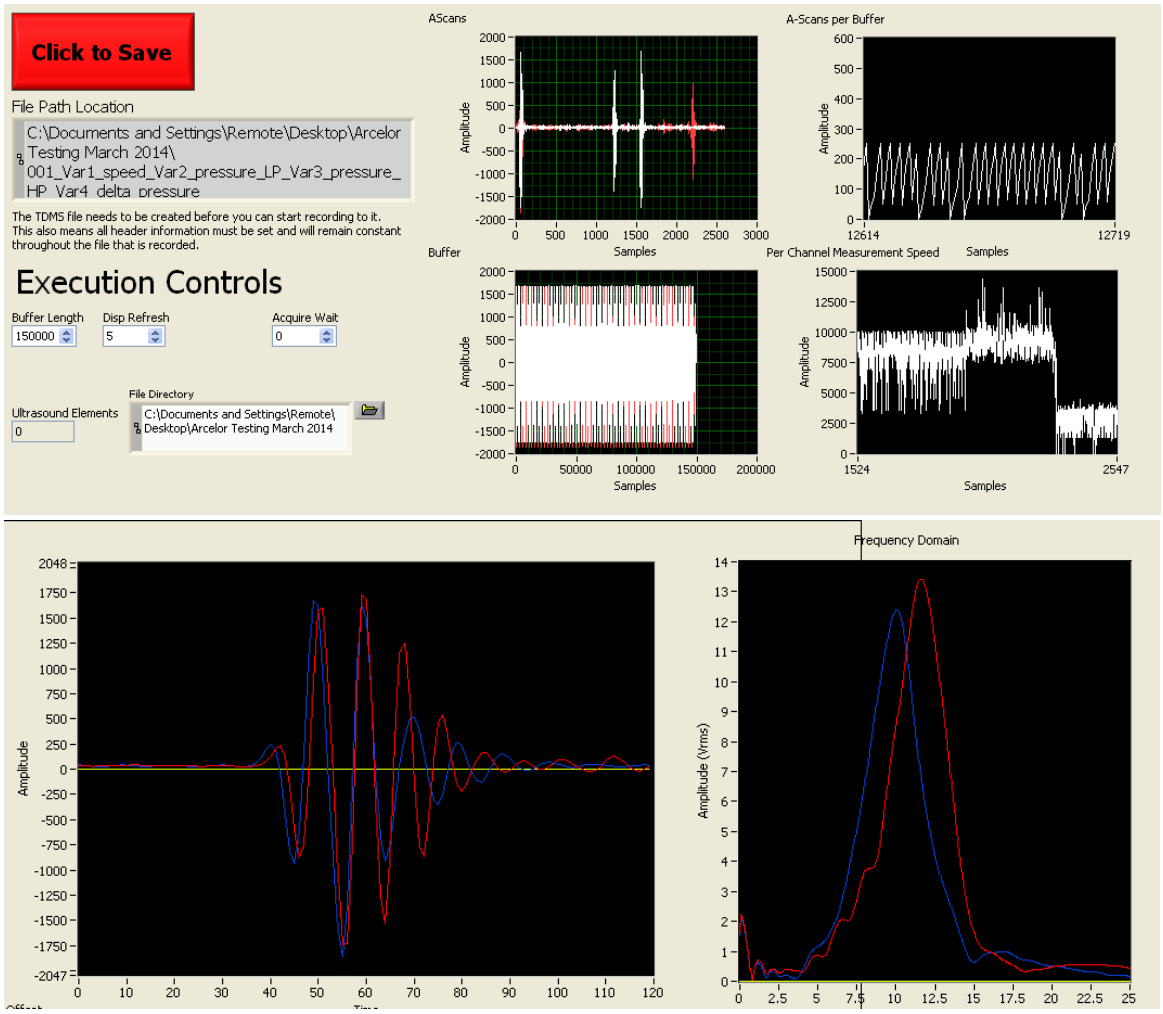

Figure 6.7: Data Acquisition Software Acquisition Interface.

6.2.3 Control Hardware

Due to safety concerns, and the spray emanating from the lubricating and cooling systems, no access was allowed to the space surrounding the mill while it was running. The acquisition hardware was enclosed within a metallic box to protect it from lubricant spray as well as to reduce the effect of EMI. A laptop located in the mill control room was connected to the hardware via an Ethernet cable and Windows Remote Desktop was used to control the software running locally on the acquisition hardware. This also allowed for data to be extracted and post-processed during testing so that the validity of the data could be verified.

6.2.4 Cabling

The length of cable used can have a detrimental effect on the integrity of the signal transmitted. Cables cause signal attenuation that increases with length. Attenuation is highly dependent on signal frequency, with higher frequencies being more readily attenuated. The cable capacitance causes it to act like a low pass filter, the lower the capacitance of the cable, the better it performs at higher frequencies. Cables can also pick up electromagnetic interference. For these reasons, and others, cable lengths should be kept to a minimum, and the cable selection should be appropriate for the system.

As shown in Figure 6.4 approximately 4 metres of coaxial cable was used between the FMS100 and transducers for each sensor. To reduce EMI these cables were wrapped in a metallic mesh which was grounded to the box containing the FMS100.

The cable capacitance can be calculated from the following equation (Chapter 4 - Capacitance per Unit Length, n.d.)

$$\frac{C}{l} = \frac{2\pi k \epsilon_0}{\ln(b/a)} \qquad 6.1$$

Where C is the cable capacitance, l is the cable length, k is the relative dielectric constant of the insulator, ϵ_0 is the permittivity of free space, b is the insulation radius and a is the inner conductor radius. The cable used has a polyethylene insulator with dimensions and values given in Table 6.4.

Inner Conductor Radius, a	0.2286 mm
Insulation Radius, b	0.7747 mm
Dielectric Constant of Insulator, k	2.3
Permittivity of Free Space, ϵ_0	8.854×10^{-12} F/m (Calvert & Farrar, 1999)
Calculated Capacitance, C	104.84 pF/m
Measured Capacitance, C	102.36 pF/m

Table 6.4: Cable Capacitance Calculations.

The cable inductance can be calculated from the following equation (Chapter 5 - Inductance, n.d.)

$$\frac{L}{l} = \frac{\mu_0}{2\pi} ln \frac{b}{a} \qquad 6.2$$

Where L is the inductance and μ_0 is the permeability of free space. The values for cable used are given in Table 6.5.

Inner Conductor Radius, a	0.2286 mm
Insulation Radius, b	0.7747 mm
Permeability of free space, μ_0	$4\pi \times 10^{-7}$ H/m
Calculated Inductance, L	0.244 µH/m
Measured Inductance, L	0.252 µH/m

Table 6.5: Cable Inductance Calculations.

The inductance and capacitance can be used to calculate the wave velocity factor, this is the speed of propagation down the cable comparative to the speed of light in a vacuum, and is given in Equation 6.3 (Fonseca, Santos, & Montenegro, 2007).

$$v_{Factor} = \frac{1}{c_{Light}\sqrt{LC}} \qquad 6.3$$

Where v_{Factor} is the velocity factor as a percentage of c_{Light} the speed of light in a vacuum (2.9979x10^{8}m/s). Taking the measured values in Table 6.4 and Table 6.5 the velocity factor is **65.79%**. This equates to a transit time, and therefore signal delay, of **5.07ns per meter**. This is important due to cable reflections.

As shown in §3.3.3 when an ultrasonic signal meets the interface between materials with different acoustic impedances, part of the signal will transmit, and part will reflect. Similarly, an electrical signal will reflect from the joint at the end of the cable based upon the electrical impedance mismatch. When the excitation pulse reaches the transducer some of the electrical wave is reflected back towards the pulser based upon the impedance mismatch between the sensor and cable. A similar reflection occurs when the excitation reflection returns to the pulsing hardware. When successive reflections reach the transducer they will drive it in the same way as the initial excitation pulse, with each excitation having a delay corresponding to the transit time. These additional excitations can have the effect of increasing the number of sensor oscillations, the sensor 'ringing', which extends the length of the pulse. Where cable lengths are very long, these additional reflections can even generate distinct pulses.

The cable length between the pulser and transducer is 4 metres giving a round trip transit time of **40.56ns**. The frequency of excitation pulse reflections is the reciprocal of this, **24.65MHz**. This is unlikely to cause an issue with the sensor frequencies used in this study, which were 10MHz resonant frequency and below. It is necessary to know the cable impedance in order to ascertain the likely reflection amplitudes, this can be calculated from Equation 6.4 (Fonseca, Santos, & Montenegro, 2007).

$$Z_{Cable} = \sqrt{\frac{L}{C}} \qquad 6.4$$

Where Z_{Cable} is the electrical impedance of the cable. Using the values for inductance and capacitance stated earlier gives a cable impedance of **49.62 ohms**, well within the manufacturers stated impedance of 50±2 ohms. The pulser hardware has 50 ohm termination so reflections from this are likely to be minimal. A 50 ohm terminator could be added to the transducer end of the cable to reduce the reflection amplitude, however this may have the side effect of reducing echo amplitude and shape.

6.2.5 Slip Ring

The signals needed to be extracted from the rotating roll to the stationary data acquisition equipment. Wireless extraction of the signals was proposed. However, the digitisation and data transfer rates required to transmit the raw ultrasonic signals are beyond what is technically feasible using commercially available wireless technologies. Also the need to excite the sensor with high voltage pulses makes this an unsuitable method unless the pulser is located local to

the sensor, on the roll. A more straightforward approach is the use of a slip ring. Slip rings can be susceptible to noise, both induced by the slip ring itself, as well as picked up from radiated emissions. For the feasibility testing performed in Sheffield a coaxial liquid metal slip ring was used (Mercotac 630). Being coaxial and having liquid metal contacts meant the noise picked up by the slip ring was minimal. This was mounted to the mill stand using the custom mounting shown in Figure 6.8. It can also be seen on the figure that provision was made for the fitting of an encoder, however this was not used in testing.

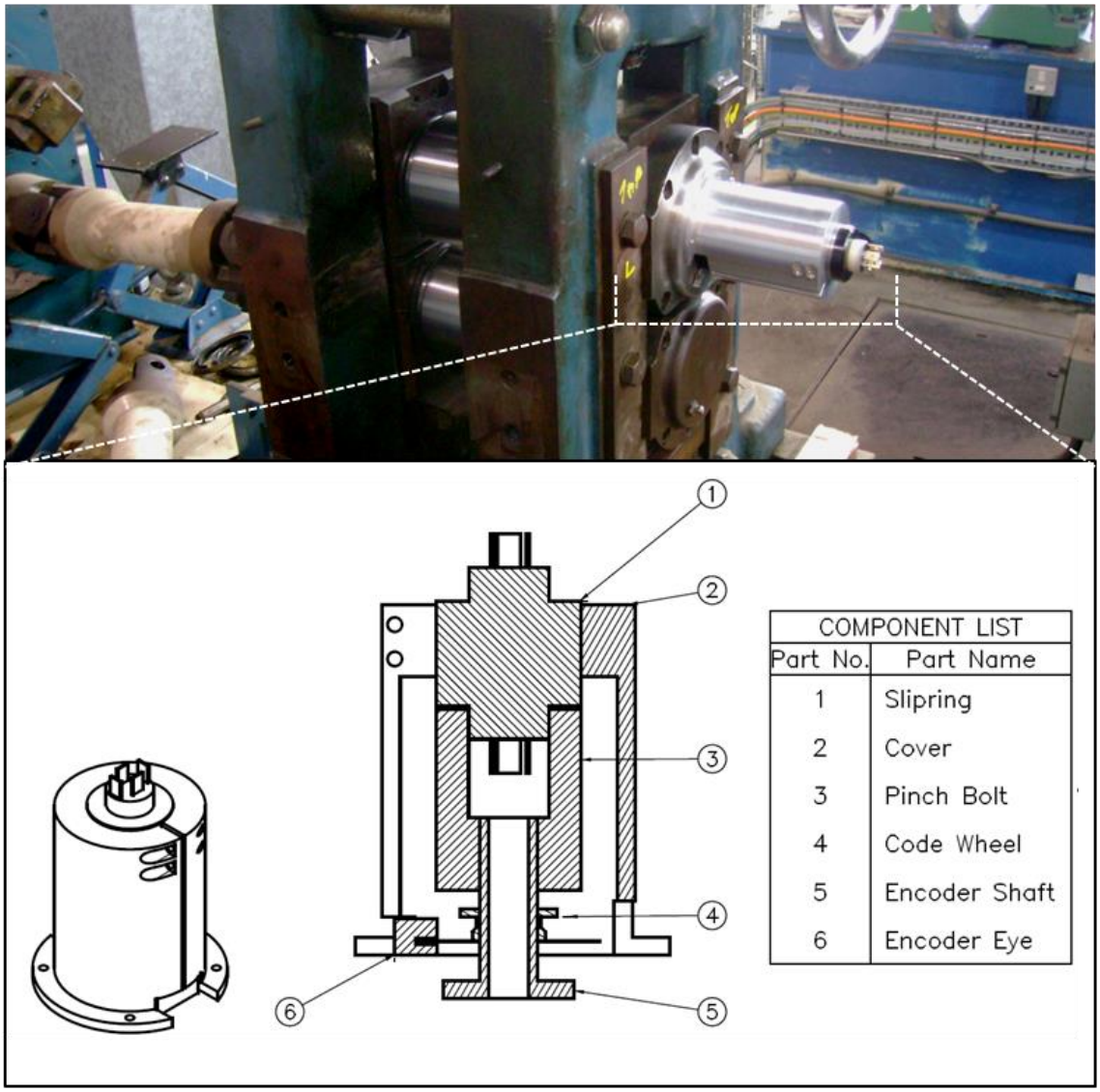

Figure 6.8: Sheffield Pilot Mill Slip Ring Mounting.

This slip ring had a limited maximum rotation speed (300RPM), a limited number of channels and containing mercury. For the semi-industrial pilot testing a high quality traditional brush type slip ring was selected (Michigan Scientific SR20). The specifications for both slip rings are given in Table 6.6. To understand the effect of these different slip ring types testing was carried out to assess their performance (the results of which are presented in §7.4).

	Mercotac 630	Michigan Scientific SR20
Conductors	6	20
Voltage Range AC/DC	0 to 250 V	-
Current Capacity	-	500mA
Max. Frequency	100 MHz	-
Contact Resistance	<1mΩ	100mΩ
Max. RPM	300	1200
Operating Temp. Range	-29 to 60°C	-40 to 121°C
Typical Rotation Torque	700 gm-cm	-
Circuit Separation	>25 MΩ	-

Table 6.6: Slip Ring Specifications.

Due to the concerns of the system susceptibility to external noise the data acquisition equipment was shielded in a metal box, this also provided protection from the mill cooling and lubricant spray. The wires between the box and slip ring were fed through a grounded metal sheath.

6.2.6 Mill Variables

In addition to the ultrasonic data other variables relating to the mill operation were recorded by the mill control system. The system was developed by iba AG and the data was saved as .iba data type, a proprietary format. The following variables were recorded:

- Velocity (m/min)
- Elongation (%)
- Strip Entry Thickness (mm)
- Strip Exit Thickness (mm)
- Strip Entry Tension (kgF/mm^2)
- Strip Exit Tension (kgF/mm^2)
- Rolling Load (Tonnes)
- Slip (%)
- Emulsion Concentration (%)
- Strip Width (mm)
- Lubricant Temperature (^{0}C)

Third-party software was used to export this data into Matlab and NI LabVIEW formats so that it could be combined with the ultrasonic data for post processing.

6.2.7 Other Measurements

As shown in § 3.5.3 the ultrasonic theory used to calculate film thickness is dependent upon material properties, specifically the density and speed of sound. An accurate estimation of these properties is therefore essential for accurate results. These properties are temperature dependent and so this must be taken into account. The mill acquisition system measured lubricant temperature, but there was no direct measurement of roll temperature. In the 'Roll-Slice" implementation described later in this chapter a 4-wire Resistance Temperature Detector (RTD) was installed along with the ultrasonic sensors, however this was not used. It was judged from the experience of the mill operators that the high thermal inertia of the roll was likely to mean that any temperature fluctuations of the bulk roll material would be negligible.

The roughness of the rolls and strip plays an important role in cold rolling. The following surface parameters where used to define the surface finish during the various tests:

- R_a – A common roughness parameter. It gives the arithmetic average of the absolute value of the deviations from the mean-line of the surface.
- R_{RMS} – Similar to Ra except that average of the profile height deviations from the mean line is calculated from the root mean square
- R_{Pc} – Is a count of the number of peaks. This number is scaled to give the equivalent number of peaks over 10mm. A peak is defined as a deviation from the mean-line which exceeds a threshold value, and is separated from other peak values by a valley which drops below another threshold.
- R_{sk} - Is a measure of the degree of skew. This is calculated from the symmetry of peaks and valleys around the mean-line. Negative values of R_{sk} show a skew upward relative to the average line.

The R_a, R_{Pc} and R_{sk} were measured for both work rolls on the semi-industrial pilot mill. These measurements were achieved by taking a cast of the roll surface, as shown in Figure 6.9, and then analysing this cast using a profilometer.

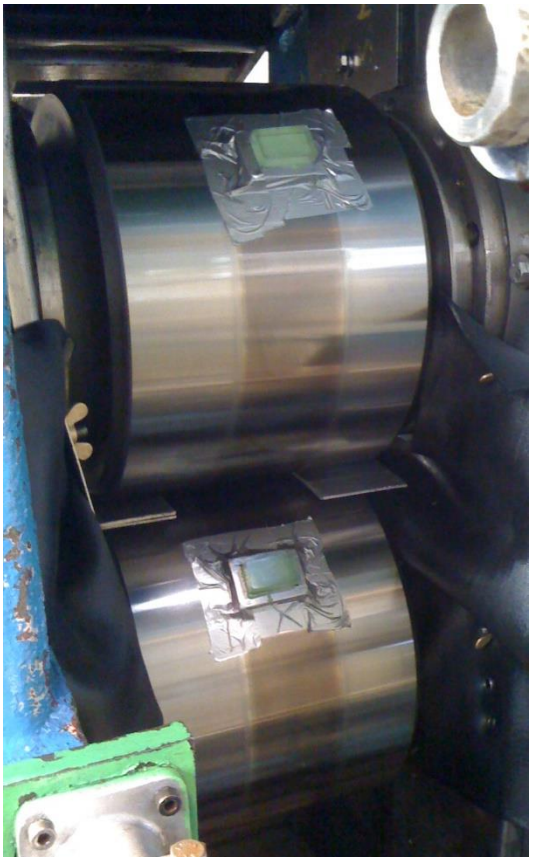

Figure 6.9: Roughness Castings of Mill Surface.

The R_a was measured for the strip both before and after rolling on the semi industrial mill. The R_a and R_{RMS} of the strip were measured after rolling in the Sheffield testing. Strip surface measurements were taken with a needle profilometer.

6.3 Ultrasonic Transducers

The sensor used were operated in Pulse-Echo configuration, acting pulse transducer and receiver. The sensors used in all experiments were simple piezoceramic elements. The elements used differed from more conventional transducers in several key areas. Conventional transducers typically have a number of backing layers behind the piezo. They are then coupled to the transmission material using a liquid such as water or an ultrasonic gel. This type of transducer is typically quite expensive, large and fragile.

The bare elements to be used here are instead bonded directly to the surface of the transmission material using a strain gauge adhesive. The adhesive acted to both couple the sensors to the material and to damp the response, reducing ringing and increasing sensor bandwidth. Bonding meant that these sensors could not be removed and reused, however the lower cost comparative to the conventional transducers means they could be treated as a consumable. By directly bonding the elements to the surface it was not possible to add a focusing layer. Without focusing, the sensors typically have a resolution comparable to their size. The sensors varied in size, however it was possible to use elements as small as 2-3mm in width. Piezo coating technologies which work on a similar principle were also considered, but were deemed to add an unnecessary level of complication and expense for this application.

6.3.1 Longitudinal and Shear Elements

Two types of sensors were used, these produced shear and longitudinal waves. The construction of both sensor types is very similar, the key difference being the piezo poling direction used. The material used in both types of sensors is PZT-5A1, a commonly used piezo-ceramic. This material offers a high sensitivity, but has a limited temperature range. The longitudinal sensors had screen printed silver electrodes, as opposed to the shear transducers which had gold sputtered electrodes.

The two sensor types where used in order to measure the shear and longitudinal stiffness of the interface. Longitudinal wave reflection from a mixed mode interface is a function of both solid and liquid stiffness. Shear waves on the other-hand will only transmit across a solid interface, not a fluid. It was therefore the aim to exploit a combination of the sensor types to provide a more complete picture of the solid and liquid components of a mixed mode interface, as described in §3.5.3.

6.3.2 Transducer Frequency Selection

The selection of the sensor frequency is a function of a number of considerations. Manufacturability, attenuation, expected interface dimensions, fluid film thickness, digitisation rate and pulser/receiver bandwidth must all be considered.

It is important to select a sensor with a centre frequency suitable for measuring the expected range of film thicknesses. The two main techniques used in ultrasonic thin film measurement are the spring model and resonant dip techniques, these are covered in greater detail in §3. Typically the resonant technique is used in the measurement of thicker films (>100um) while the spring technique is used for much thinner films. It is useful to note that a single sensor can be used for both techniques. Each sensor however will have a blind spot between these techniques in which the film thickness cannot be accurately measured. The range of thicknesses covered by this blind spot will be dependent on the sensor frequency. Therefore by using two

sensors of differing frequencies this blind spot can be covered. To avoid the need for multiple frequencies of sensor a suitable frequency sensor must be specified so that the full range of expected film thicknesses can be covered by one technique. Previous experience pointed to sensors of around 5-10MHz centre frequency. To give some idea as to the range of film thicknesses measureable using the spring model and this frequency of sensor, a 10MHz sensor is theoretically good from 50nm to 5 um. A lower frequency sensor will shift this window upwards, covering thicker films. For the Sheffield pilot testing element frequencies of 2.5, 5, 10 and 12MHz were trialled. From this testing 10 MHz longitudinal elements were selected for the industrial testing.

The lack of understanding relating to ultrasonic behaviour of shear waves in a mixed mode contact made prediction of the necessary shear sensor centre frequency more difficult, as the shear sensor was not intended to measure the fluid film and so was not selected on the basis of film thickness. For the Sheffield pilot tests 5 MHz shear sensors were used as they were the only sensors available at the time of installation. Following this 10MHz shear sensors were sourced and a mixture of 5 and 10 MHz elements where used.

Attenuation of an ultrasonic wave is dependent on the transmission material, path length and the frequency of the wave. A longer path length will result in greater attenuation, and thus poorer signal. This needed to be balanced with a requirement for a thicker transmission material for several reasons. The material needs to be of sufficient thickness to ensure that enough support is given to the rolling face. Also if the sensor is too near the measured interface then the incident wave or transducer ring-down will interfere with the reflected waves, making them hard to separate. There are also other undesirable effects related to operating the sensing interface within the near-field zone of the sensor, these will further complicate accurate measurement.

Higher frequency waves suffer from greater attenuation. The distance which the ultrasonic wave had to travel between the sensor and the rolling interface was varied from 10 to 40 mm depending upon the installation approach. Previous work had shown that attenuation of a 10 MHz wave over this distance in the roll material was unlikely to be an issue.

6.3.3 Sensor Robustness

The simplicity of the sensors made them relatively robust and simple to install. The elements used start as larger discs or plates of thickness typically under 1mm (this is dependent on the frequency of the sensor). These were then cut into strips down to minimum of 2mm wide. Reducing the size of the sensor has an associated effect on the amplitude of the transduced pulse, and the size of the induced electric signal from the received pulse. Previous applications using strips of this size have proved that such an effect is not prohibitive to the operation of the sensor/transducer.

The sensors began to degrade during the industrial testing using the roll-slice approach described later. Particular issues arose with the longitudinal sensors. Once testing was completed and the segment removed from the roll it was clear that the sensors and epoxy backing had become detached from the roll. The reason for this is likely to have been due to the ingress of rolling lubricant, some of which was at elevated temperatures of 50^{o}C. The lubricant destroyed the adhesive causing the sensors to debond. Testing using the plug instrumentation approach did not suffer from these issues as no lubricant was able to ingress to the sensors.

6.4 Strip Material

For the feasibility testing in Sheffield short mild steel strips were used. Before testing these samples were hot rolled to bring them down to a thickness suitable for the mill. Because the pre-rolling was performed hot the surface was left fairly rough. The surface profile of a short section of the rolled strip is given in Figure 6.10. The roughness parameters of this surface are **R_a = 1.178** and **R_{rms} = 1.635.**

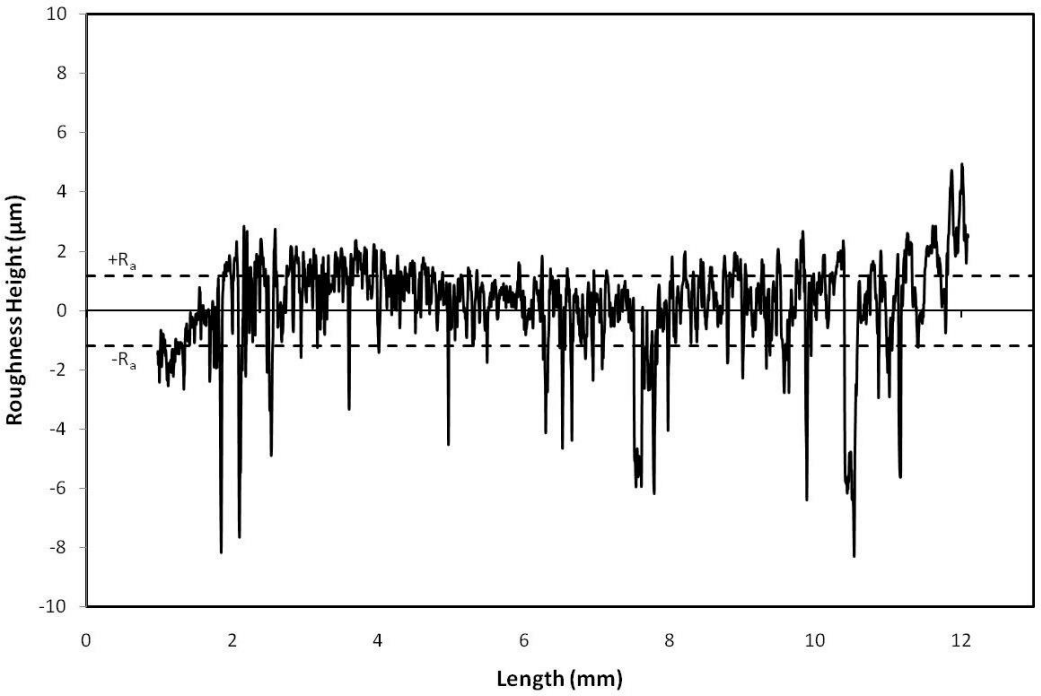

Figure 6.10: Rolled Strip Surface Profile

The R_a values measured before and after rolling for a number of the strip coils used in testing are given in Table 6.7.

Strip Coil No.	Material	R_a Before Rolling (µm)	R_a After Rolling (µm)
1	DD14	0.995	0.551
4	DD14	0.905	0.554
5	DD14	0.755	-
6	DD14	0.844	0.510
7	DD14	-	0.544
8	DD14	1.015	0.483
9	DD14	0.967	0.531
10	DD14	-	0.548
11	DD14	0.940	0.571
12	DD14	0.877	-
13	DD14	0.916	0.762
14	DD14	-	0.543
15	DD14	0.975	0.769
16	DD14	1.046	0.939
17	ARCELOR06	0.166	0.240

Table 6.7: Strip Roughness Measurements, Before and After Rolling.

For the semi-industrial pilot tests two soft grades of Interstitial Free (IF) steel was used, each of a different thickness. The thicker strip (2.78mm) was made of **DD14 Steel** as defined in EN 10111:2008 (BS EN 10111:2008 - Continuously Hot Rolled Low Carbon Steel Sheet and Strip for Cold Forming. Technical Delivery Conditions, 2008). This has a minimum yield strength of **170 to 290 MPa** and a maximum tensile strength of **380 MPa**. The thinner strip (0.75mm) was made ArcelorMittal 06, the equivalent of **DC06** (ArcelorMittal, 2016) as defined in EN 10130:2006 (BS EN 10130:2006 - Cold Rolled Low Carbon Steel Flat Products for Cold Forming. Technical Delivery Conditions, 2006). This has a maximum yield strength of **180 MPa**, a lower limit yield strength for design purposes of **120 MPa** and a tensile Strength of **270 to 350 MPa**. The material compositions of the strips are given in Table 6.8.

Material	C (%)	Mn (%)	P (%)	S (%)	Si (%)	Al (%)
DD14	≤0.080	≤0.35	≤0.025	≤0.025	-	≥0.02
ArcelorMittal 06 (ArcelorMittal, 2010)	≤0.02	≤0.25	≤0.02	≤0.02	≤0.02	≥0.01

Table 6.8: Strip Material Compositions.

6.5 Lubricants and Properties

A range of lubricants, and emulsion concentrations were use. Feasibility testing at Sheffield, and the first phase of testing on the semi-industrial pilot mill both used *Henkel Gerolub 5525*. The second phase of semi-industrial test used *Fuchs 812 TCC*, *Fuchs K2* and *Quaker HV2*.

For the Sheffield testing lubricant was brushed onto the strip neat before rolling. On the semi-industrial mill lubricant was applied via one or both lubricant circuits. The differences in the lubrication circuit application techniques are shown in Figure 6.11.

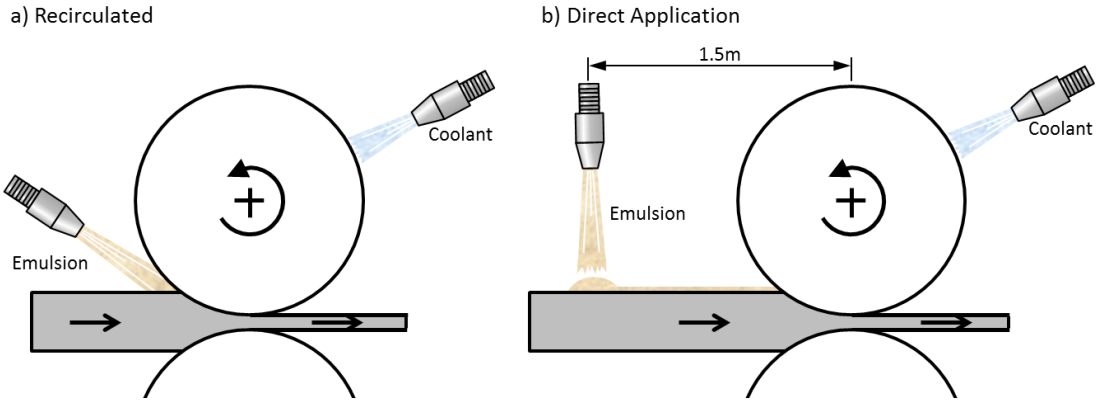

Figure 6.11: Lubricant Application Arrangements.

The recirculated emulsion concentration was monitored throughout testing and was in the range of 1.95% to 2.25%. The particle size for the Fuchs 812TCC emulsion was measured on two occasions as 3.4µm and 4.8µm, and for the Quaker HV2 emulsion was 6.9µm.

Data on the speed of sound of Gerolub 5525 for a range of temperatures and pressures was measured in a previous study and is shown in Figure 6.12 (Bouscharain & Vergne, Etude D'huiles de Laminage sous Hautes Pressions [Study of Rolling Oils under High Pressures], 2010).

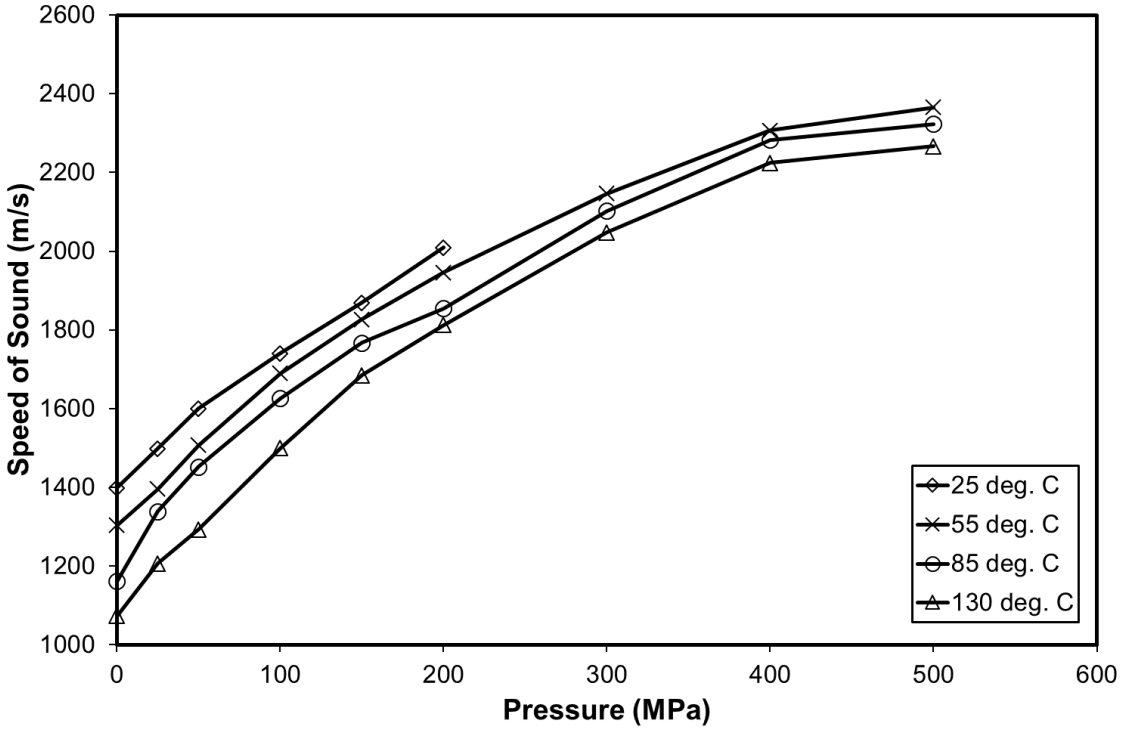

Figure 6.12: Speed of Sound Vs. Pressure for Gerolub 5525

The density of Gerolub 5525 at 20°C is given in the range 914 to 924 kg/m^3 (Henkel Limited, 29-11-2013)**.** The mean value of **919 kg/m^3** was assumed. For lubricant film thickness calculation, the bulk modulus is required. Although not measured explicitly, this can be calculated from the speed of sound against pressure data and the density using Equation 3.4. Using the data in Figure 6.12 and the density at atmospheric pressure the bulk modulus for a range of pressures was calculated and plotted in Figure 6.13.

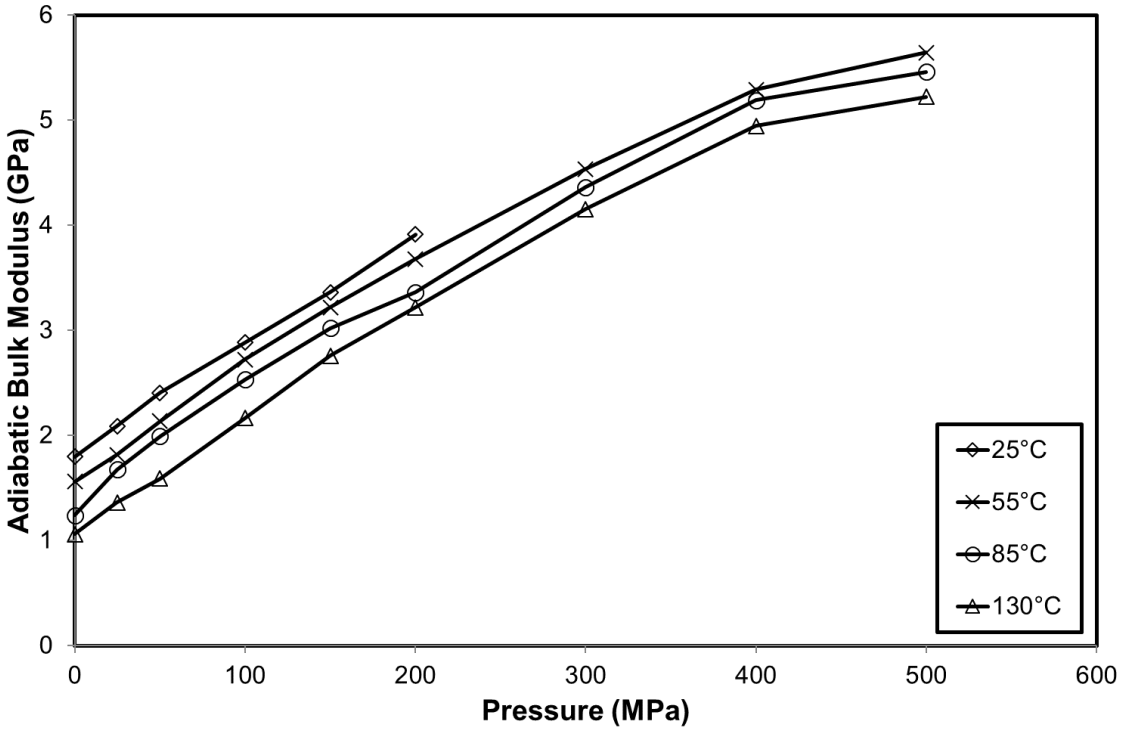

Figure 6.13: Bulk Modulus Vs. Pressure for Gerolub 5525

The same density was used for all of the datasets, regardless of temperature and pressure. The error in the bulk modulus from this assumption will be low, as density changes little with pressure and temperature and the change in speed of sound dominates the relationship given in Equation 3.4.

A 2-dimensional quadratic polynomial fit of the form shown below in Equation 6.5 was applied to the experimental data in Figure 6.13 to yield an expression giving bulk modulus in terms of pressure and temperature.

$$B = a + bP + cT + dP^2 + ePT + fT^2 \qquad 6.5$$

Where B is the bulk modulus, P is the pressure in MPa, T is the temperature in °C and a, b, c, d, e, f are the polynomial coefficients. For Gerolub 5525 the polynomial coefficients are given in Table 6.9:

a	b	c	d	e	f
1.948	1.231×10^{-2}	-7.763×10^{-3}	-8.576×10^{-6}	4.767×10^{-6}	4.360×10^{-6}

Table 6.9: Polynomial Coefficients for Bulk Modulus of Gerolub 5525.

This relationship across the range of experimental values has been plotted as a surface in Figure 6.14.

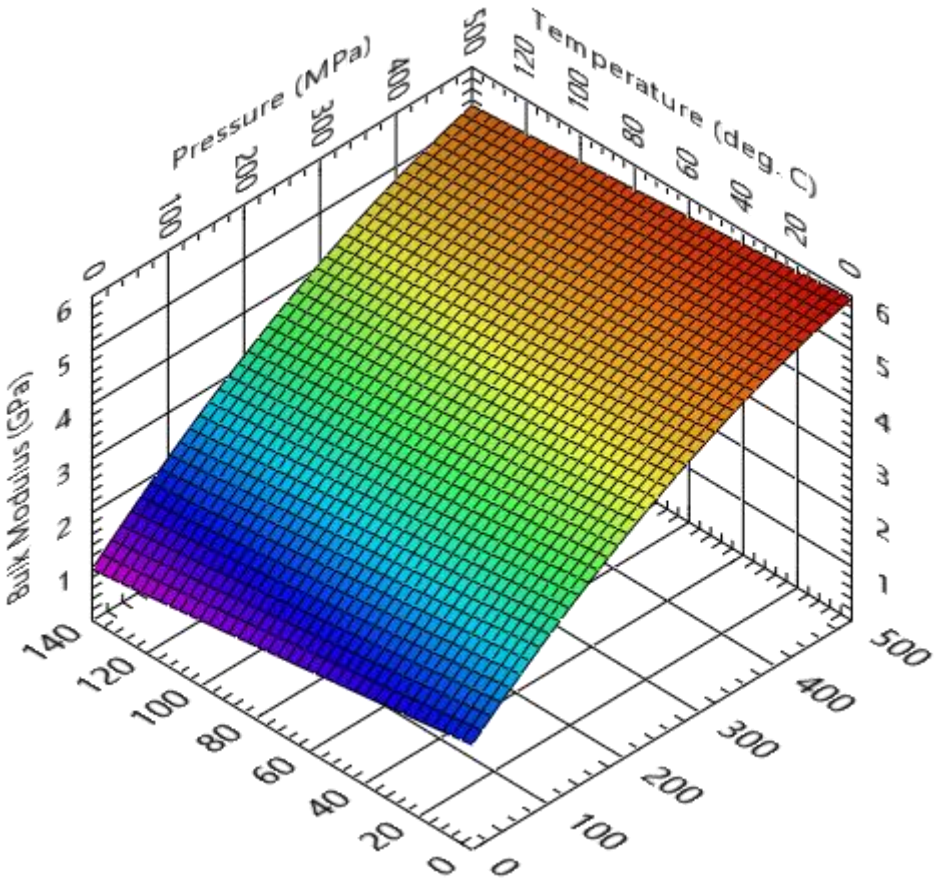

Figure 6.14: Relationship for Bulk Modulus against Temperature and Pressure for Gerolub 5525.

Neither the bulk modulus nor speed of sound data was available for the other lubricants used. Dynamic viscosity data against temperature at ambient pressure, had been determined in a

separate study (Bouscharain & Vergne, Comportement Rhéologique D'huiles de Laminage sous Hautes Pressions [Rheological Behaviour of Rolling Oils under High Pressure], 2013) and is presented in Figure 6.15. Also the viscosity against pressure relationships at 55°C are given in Figure 6.16.

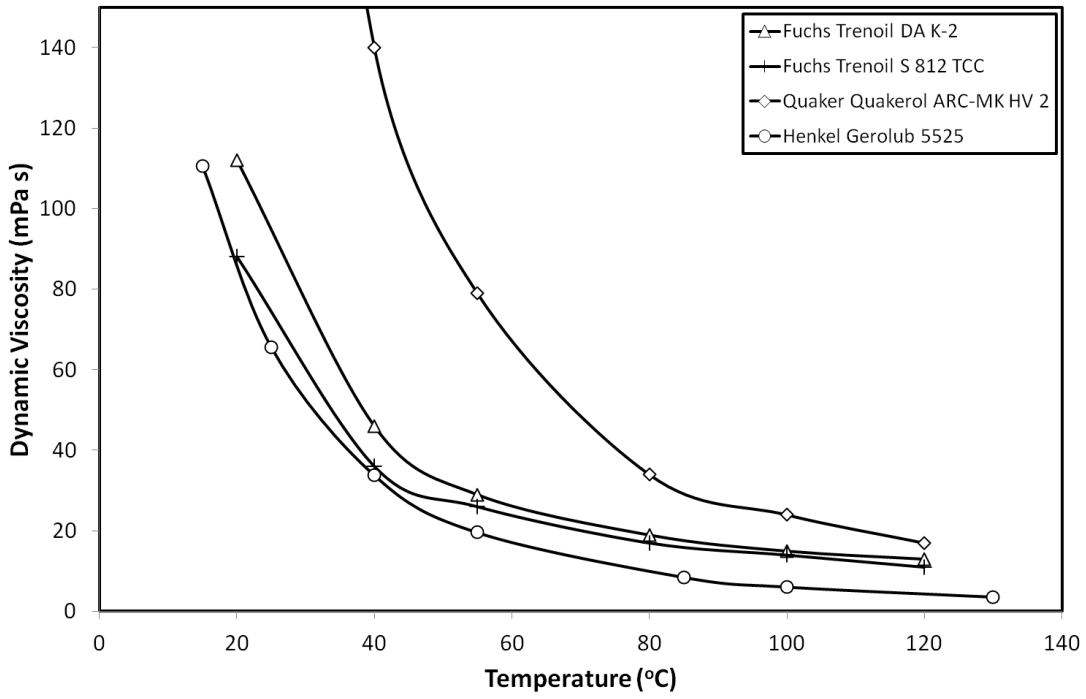

Figure 6.15: Dynamic Viscosity Vs. Temperature for Rolling Lubricants (Bouscharain & Vergne, Comportement Rhéologique D'huiles de Laminage sous Hautes Pressions [Rheological Behaviour of Rolling Oils under High Pressure], 2013).

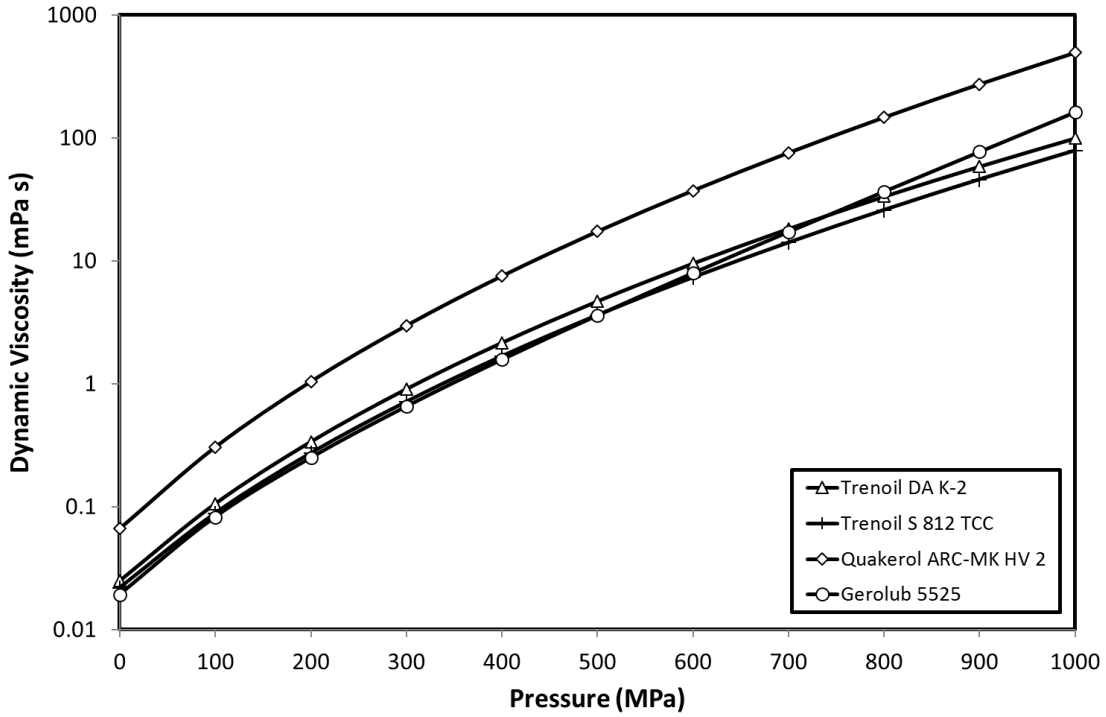

Figure 6.16: Dynamic Viscosity Vs. Pressure for Rolling Lubricants (Bouscharain & Vergne, Comportement Rhéologique D'huiles de Laminage sous Hautes Pressions [Rheological Behaviour of Rolling Oils under High Pressure], 2013).

The viscosity for the lubricants at 55°C are given for ambient pressure in Table 6.10 (Bouscharain & Vergne, Comportement Rhéologique D'huiles de Laminage sous Hautes Pressions [Rheological Behaviour of Rolling Oils under High Pressure], 2013).

Lubricant	Dynamic Viscosity @ 55°C (mPa.s)
Gerolub 5525	19.6
Trenoil K2	29 ±1.2
Trenoil 812	26 ±1.2
Quaker HV2	79 ±1.3

Table 6.10: Rolling Lubricants Dynamic Viscosity at 55°C (Bouscharain & Vergne, Comportement Rhéologique D'huiles de Laminage sous Hautes Pressions [Rheological Behaviour of Rolling Oils under High Pressure], 2013).

During the measurement of the oil viscosity (Bouscharain & Vergne, Comportement Rhéologique D'huiles de Laminage sous Hautes Pressions [Rheological Behaviour of Rolling Oils under High Pressure], 2013), solidification of the lubricants was observed at higher pressures. The solidification point was not the primary aim of the study and so was not measured with a high resolution. Table 6.11 shows the approximate solidification pressures recorded.

The pressures were measured to the nearest 100MPa, with the exception of the 25°C Gerolub measurement which had a resolution of 50MPa. Despite the poor resolution, this data still gives an indication of the solidification pressure magnitude and clearly shows how the solidification pressure increases significantly with increased temperature. The pressures seen are comparable to those seen in rolling, so there is a strong possibility that lubricant solidification occurred in at least some of the rolling conditions tested.

	Approximate Solidification Pressure (MPa)			
Temp. (°C)	Gerolub 5525	Trenoil K2	Trenoil S812 TCC	Quakerol HV2 DA
25	150	-	-	-
40	-	200	300	200
55	400	-	-	-
75	-	600	700	500

Table 6.11: Approximate Lubricant Solidification Pressures.

6.6 Work Roll Instrumentation

Instrumentation of the ultrasonic sensors onto the mill proved to be the largest technical challenge in this work. Two key concerns where the effect of the instrumentation method on the surface finish of the strip and the on the stiffness of the roll. To overcome these concerns several methods were considered, such as coupling the sensors to the external of the work roll, however it was decided that the most effective approach would be to mount the sensors inside one of the work rolls facing radially outwards. By instrumenting the roll in this manner the sensors swept across the contact spot as the roll revolves, thus allowing a profile across the contact to be recorded. As the sensing face was exposed to air with each revolution it also offered the possibility to retake the reference value used in the ultrasonic calculations. This offered greater resilience to changes in the conditions over time, such as fluctuations in roll temperature or roll wear.

In the scope of the work presented here only the upper work roll was instrumented. However, in future it may also be of interest to instrument the bottom work roll so that the interfaces on either side of the strip can be studied simultaneously. For the semi-industrial mill used there is a slight asymmetry between the two interfaces as the strip enters the roll bite at a slight angle of 0.7^{o} to the horizontal, the difference between these interfaces may be of interest. By instrumenting both rolls simultaneously it may also be possible to perform through transmission measurements, where a signal is transmitted from one roll and received in the other. This could yield additional data to verify the reflection based measurements.

Four approaches of sensor implementation were trialled. These were *Transition-Fit Plug*, *Roll Segment*, *Shrink-Fit Plug and Press-Fit Plug*. For each method the effect on the strip surface finish was evaluated, and some methods proved more suitable than others, the results of this are reported below. Modifications, especially where this required removal of material from the roll were kept to a minimum to reduce any effect on the overall stiffness of the roll. In all methods implemented the wires were extracted via a central axial hole into the roll. The material removed at this position would have the least effect on roll bending as this region is under the least stress, as see in Figure 2.21. The radial holes through which wires were fed were kept to a minimum diameter and drill symmetrically in the roll to maintain the balance of the roll. The relative proportion of material removed was higher for the smaller pilot mill rolls which had a smaller diameter, however this testing was performed at lower pressures.

6.6.1 Transition-Fit Plug

The first implementation was in the Sheffield pilot mill. The sensors were mounted onto plugs that were then fitted into holes machined into the roll. The plugs were fitted in such a way that the sensors were sealed inside of the roll facing outwards. This means the ultrasonic pulse is transmitted through the plug to the rolling interface. The plugs were equispaced around the diameter of the roll and lay in the same axial plane, as shown in Figure 6.17. While there is space for additional plugs, only 6 were installed to ensure that the amount of material did not unduly effect the stiffness of the roll, especially considering that all the plug holes are on the same plane.

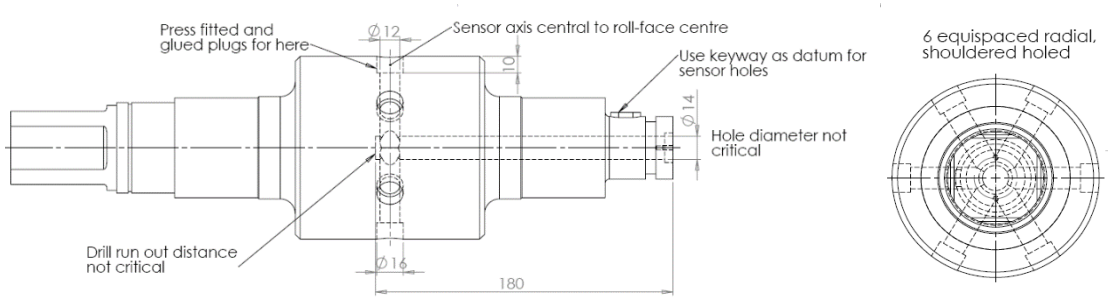

Figure 6.17: Sheffield Work Roll Design

Wires attached to the sensors were fed out through a hole running axially along the roll, and exited through the non-driven end of the roll to the data acquisition equipment via a slip ring. Initially the intention was to make these modifications to an existing work roll, however the hardness of the roll caused problems in machining the roll. Figure 6.18 shows an attempt to drill a hole for the plugs into a spare roll taken from the Sheffield mill, a depth of only around 10mm could be achieved.

The hardness of this roll was around **500HV** (Vickers Hardness). This proved too hard to machine either using standard Steel-Cobalt tools or specialist Tungsten-Carbide bits. The problem was compounded by the length of the axial hole required to extract wires from the sensors (~180mm).

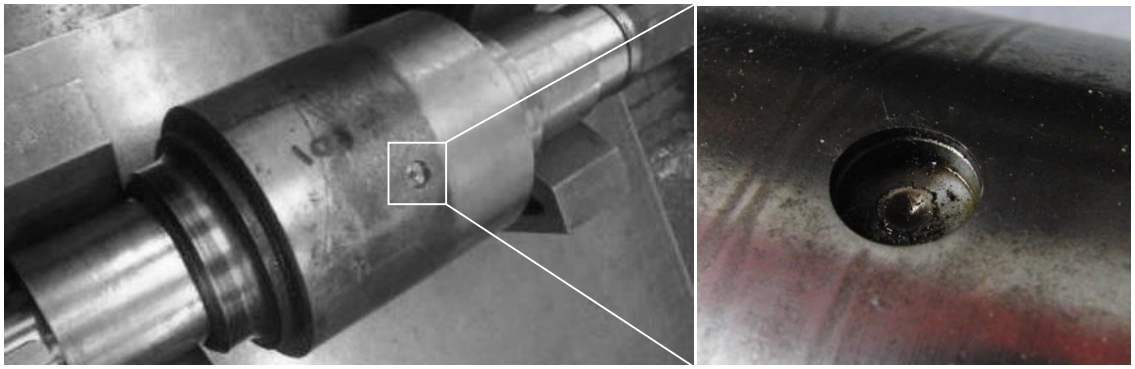

Figure 6.18: Attempted Drilling of Sheffield Mill Roll

As the roll was relatively small it was decided that the easiest approach was to manufacture a new roll. A roll was machined from stock bar of steel (**EN31**). The new roll raw material and an existing roll are shown in Figure 6.19.

Figure 6.19: New Roll Stock Material and Existing Work Roll

The bar had been annealed to improve machinability. Holes for the plugs and wire routing were drilled. These consisted of 6 stepped radial holes one for each plug, and a central axial hole that met at the intersection of the radial holes. The length of the axial hole used to extract the wires was non-trivial and required an extended drill bit. Once machining was completed the rolling surface was induction hardened by Flame Hardeners Ltd. in Sheffield, UK to a hardness of approximately **850 HV**. The depth of this hardened layer graduated to the hardness of the bulk material over an estimated depth of around 5mm. The process also hardened the roll necks either side of the rolling face which insert into the bearings, to **210 HV**. Figure 6.20 shows the machined and hardened roll.

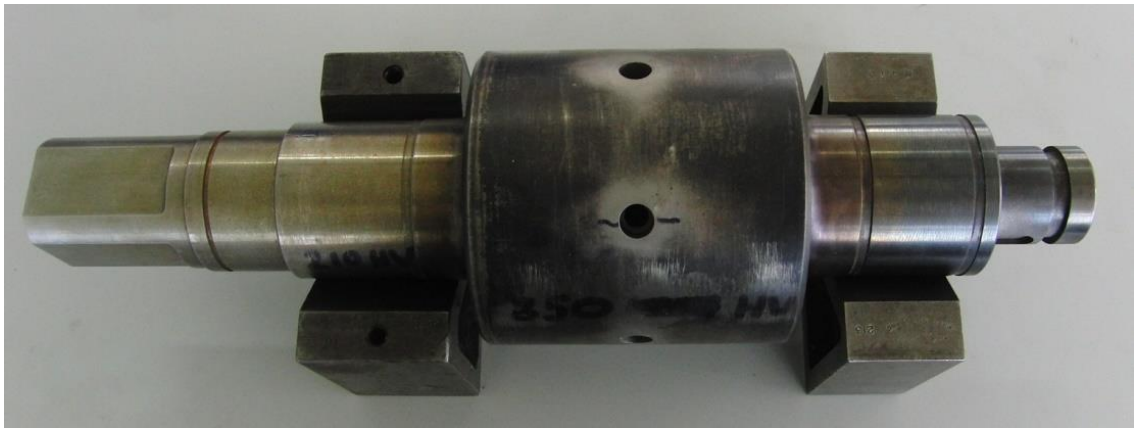

Figure 6.20: Machined and Hardened Roll.

The sensor plugs were made of silver steel. The sensors were attached to the plugs using a high temperature strain gauge adhesive. This required curing at elevated temperatures (~140°C) for around 2 hours. The sensors installed on each plug are given in Table 6.12, although with a photo of an instrumented plug.

	Sensor 1	Sensor 2
1	10 MHz Long.	5 MHz Shear
2	10 MHz Long.	5 MHz Shear
3	12 MHz Long.	2.5 MHz Shear
4	10 MHz Long.	-
5	5 MHz Shear (orientated Axially)	-
6	5 MHz Shear (orientated Tangentially)	-

Table 6.12: Sensors fitted to Sheffield Pilot Mill Plugs.

Wires were soldered onto the sensors and then coated in an epoxy putty for protection and to provide some strain relief from the cables. Figure 6.21 shows the plugs and roll just before the plugs were fitted. The plugs have a diameter of **11mm** and were hardened to approximately **800 to 830 HV**.

There were several options in how to secure the plugs into the roll. It would be possible to weld the plugs in place, however the heat seen by the sensor during this may have damaged the piezoelectric material. As the predominant force seen by the plugs was the normal force into the roll it was decided that a simple transition-fit would suffice. The plugs were hand-pushed into the roll and a low viscosity bearing retaining compound (Loctite 603) was used to fix them into place. The purpose of the compound was only to stop the plugs coming loose during testing, not to bear the rolling load. This was supported by steps in the radial holes of the roll, which formed shoulders on which the plug sat. The plugs were machined slightly oversize so that they sat proud of the roll surface when fitted.

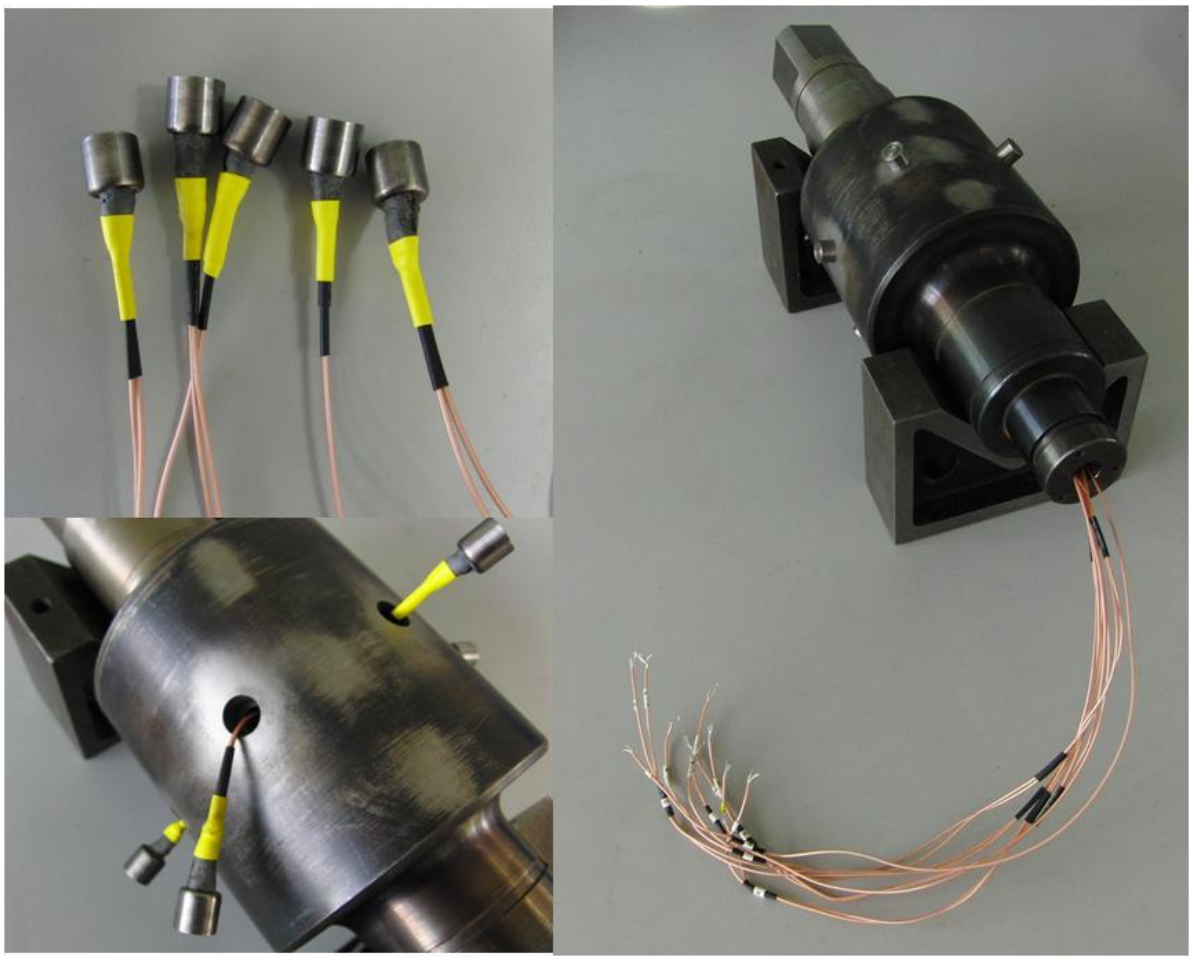

Figure 6.21: Roll and Instrumented Plugs.

Once the plugs were secured the final step was to ensure the surface finish and cylindricity of the roll. This was achieved by grinding the roll surface and plugs using a cylindrical grinder. This left a smooth finish suitable for rolling, with the plugs barely distinguishable from the roll, Figure 6.22. The rolling surface was ground to a surface roughness of approximately **R_a = 1µm**, although this wasn't explicitly measured.

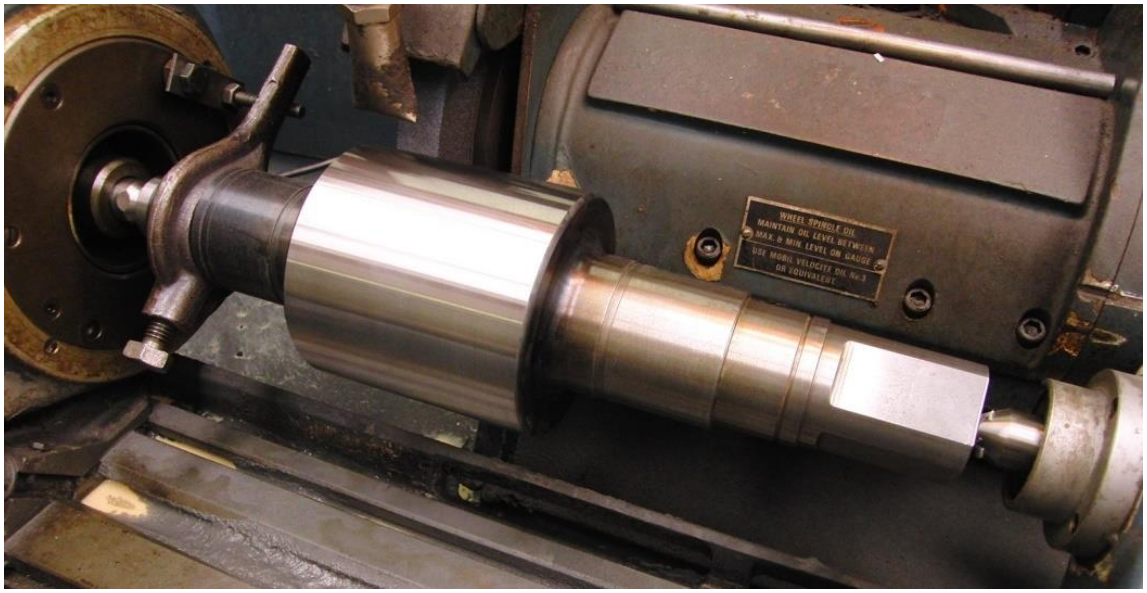

Figure 6.22: Work Roll After Grinding

The details of both the plug and roll material chemical composition are given in Table 6.13. The existing work rolls were still used for the bottom work roll. These were made from hardened steel, and although the precise details of the material are unknown, the new roll was surface hardened to the same hardness as the existing rolls and ground to the same diameter to maintain symmetry.

	C	Si	Cr	Mn
EN31 (Roll)	1.0%	0.20%	1.40%	0.50%
Silver Steel (Plug)	1.0%	0.30%	0.40%	0.35%

Table 6.13: Roll and Plug Material Compositions

The strip being rolled was made of mild steel. As such the primary interface observed by the ultrasonic sensors was that between the silver steel plug and the mild steel strip.

It was convenient to manufacture a roll for the relatively small Sheffield mill, and this had the added benefit of allowing greater freedom of design. It is also however important to consider the feasibility of implementing the technique in an industrial application. In such a situation the manufacture of a new roll is likely to be unfeasible, and alternative methods to fit the sensors to existing rolls must be evaluated.

This plug approach had the disadvantage of marking the strip as shown in Figure 6.23. At first it was unclear if these were marks due only to the gap between the plug and strip, or if plug deformation had left a protrusion on the surface. A surface profile was taken as shown in Figure 6.24 using a needle profilometer. This clearly shows that the plug had deformed relative to the roll leaving a protrusion on the strip. The strip marking means this method is unlikely to be acceptable in industrial rolling where strip surface finish is highly controlled. If this approach was installed on in a multi-stand mill it may be possible to remove the defect as the strip passes through latter stands.

The deformation of the plug also has implications for measurement accuracy. The load isn't being equally shared between the roll and plug, so the rolling load and lubricant film may not be representative of that seen without a plug.

Figure 6.23: Plug Mark on Strip

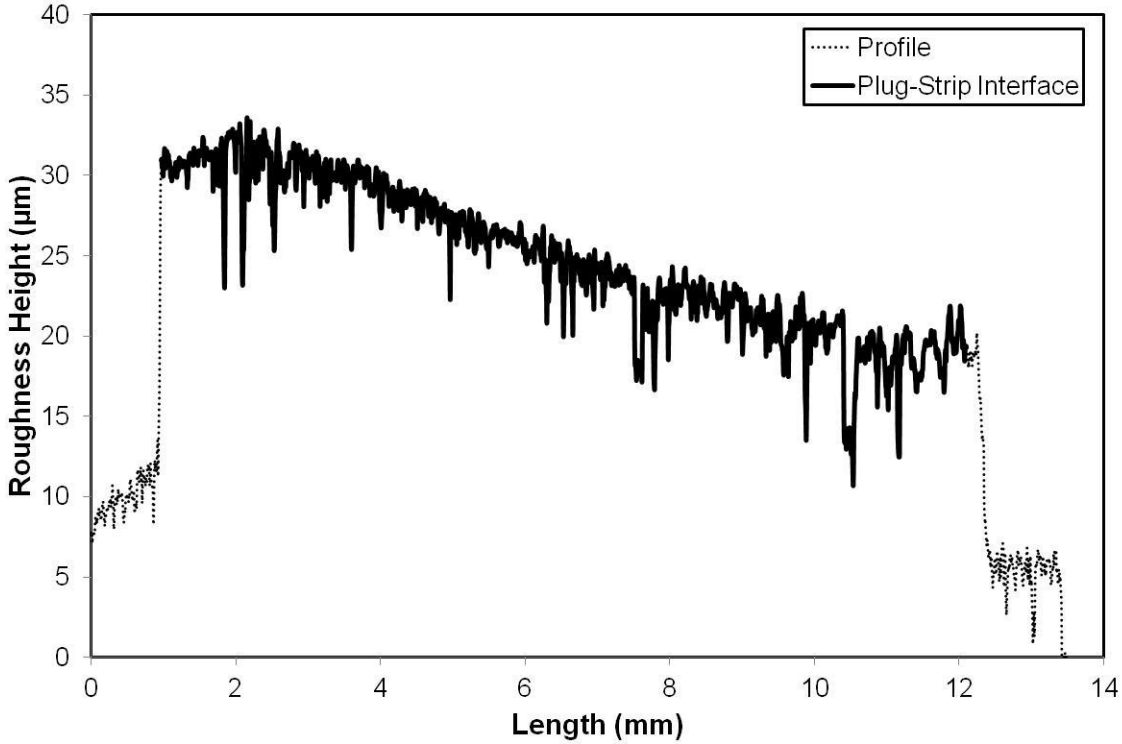

Figure 6.24: Strip Protrusion Profile

6.6.2 Roll Segment

For the first implementation on the Semi-Industrial pilot mill a different technique was developed to install the sensors. The technique required a segment to be cut from the work roll, a replacement part machined, instrumented and then attached with mechanical fasteners in place of the removed section. This method meant the segment, unlike the plugs, could be easily removed allowing access to the sensors in order to change or repair them. A similar approach had been previously adopted for another project so a roll with a segment removed had already been prepared. Only a new segment needed to be manufactured to accommodate the ultrasonic sensors, photos of the parts are shown in Figure 6.25, and a drawing of these parts is shown in Figure 6.26.

Figure 6.25: a) Modified Roll b) Manufactured Segment.

A replacement half-moon was manufactured from **EN31** grade steel by ArcelorMittal. This was heat treated from an initial hardness of **217HV** to **560HV** to match that of the roll surface. A shallow slot was machined in the flat face of the segment to allow for the sensors. As with the Sheffield mill an axial hole was drilled along the roll to allow for the extraction of the wires from the sensors. These were taken to the non-driven end of the roll and through the slip ring described earlier.

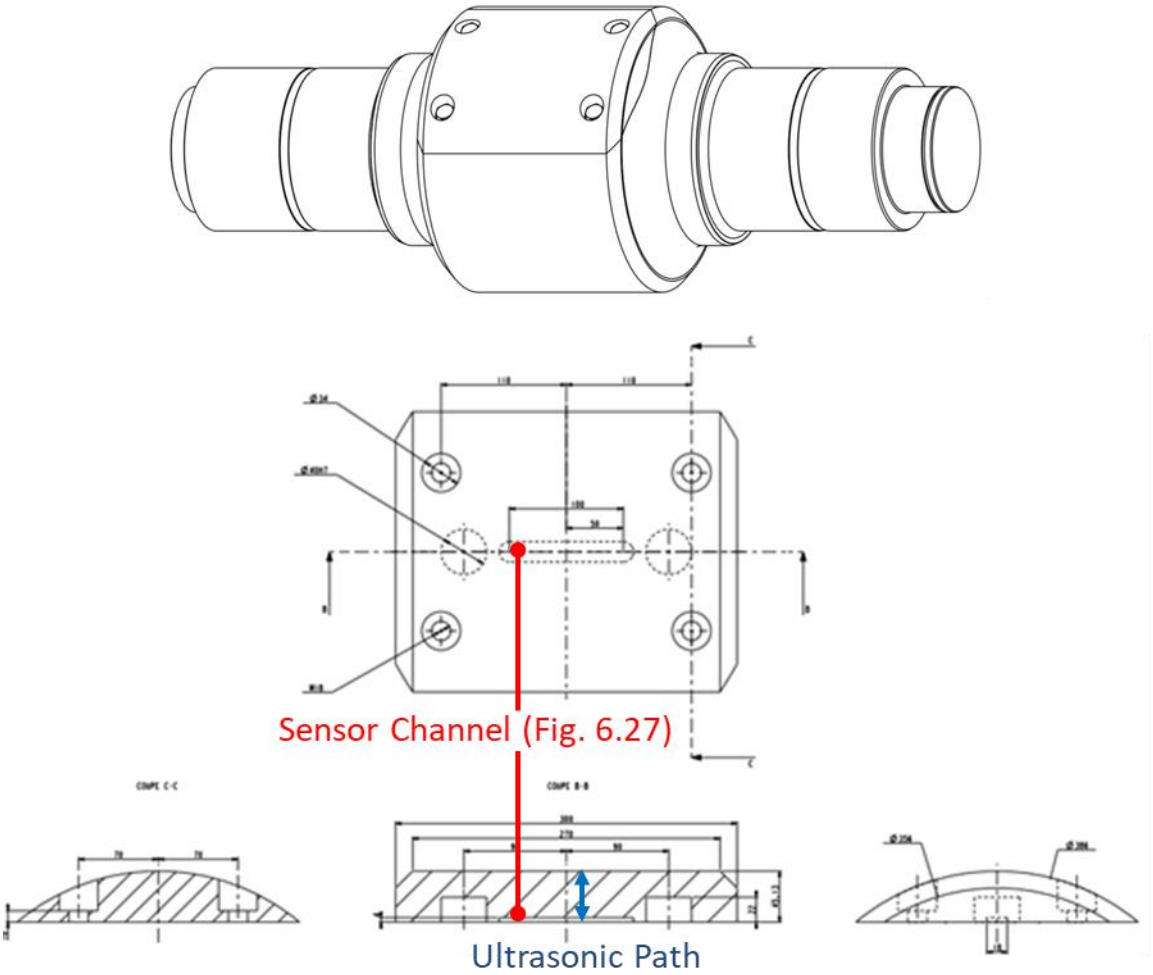

Figure 6.26: Roll Segment and Assembly Drawing.

The segment was instrumented with 8 ultrasonic sensors (4 x 10 MHz longitudinal, 2 x 10 MHz shear, 2 x 5 MHz shear) as shown in Figure 6.27. The sensors where spaced in 10mm intervals. Upon installation sensor 2 (10MHz Longitudinal) was damaged and showed greatly reduced response. The active area of the sensors was assumed to be same as positive sensor electrode. This was **2mm x 5mm** for the longitudinal sensors and **2mm x 3.5mm** for the shear sensors**.**

Number	1	2	3	4	5	6	7	8
Type	Shear	Long.	Shear	Long.	Shear	Long.	Shear	Long.
Freq. (MHz)	5	10	5	10	10	10	10	10

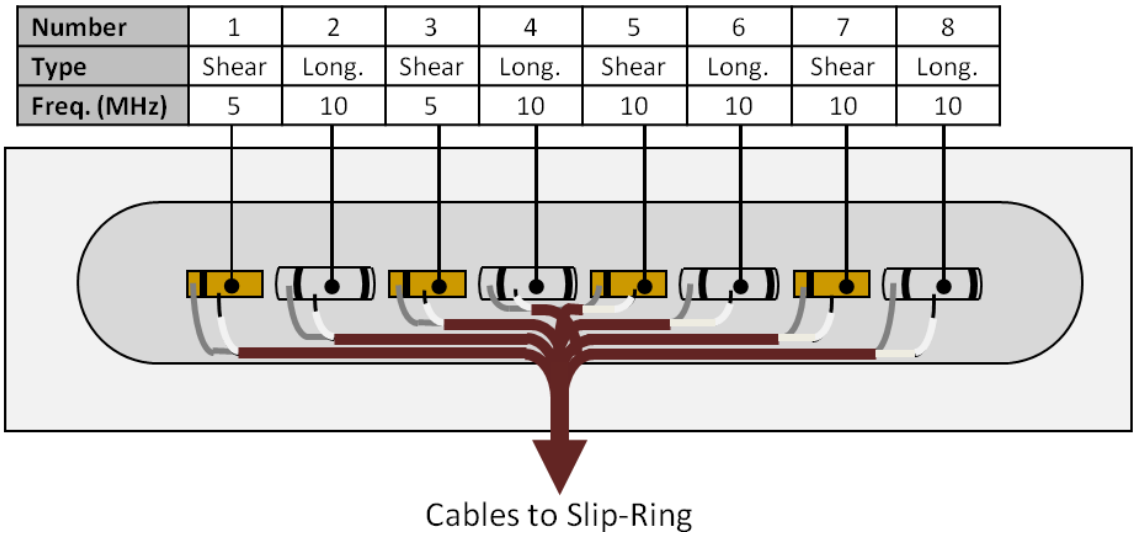

Figure 6.27: Sensor Arrangement on Roll Segment.

The sensors were attached using the same adhesive used in the Sheffield testing. The surface was 'keyed' first using some abrasive paper to enable the adhesive to adhere to the surface, hence the marking seen on the surface in Figure 6.28. Thin coaxial cable (1.27mm diameter) was soldered directly to the sensors and then the sensors and cable were coated in an epoxy to provide protection and strain relief. In addition to the ultrasonic sensors a 1kΩ platinum RTD was also potted in the epoxy, although this was not used during testing.

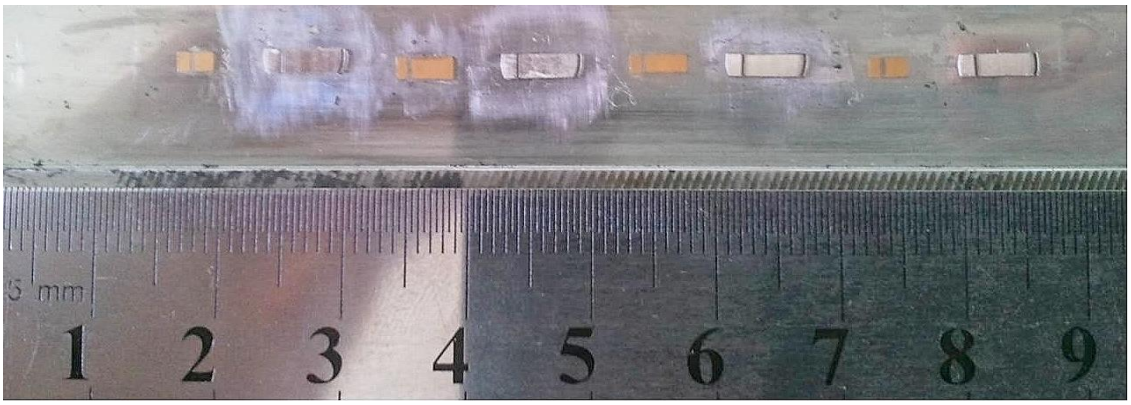

Figure 6.28: Sensors Installed in Slot with Ruler for Scale.

The roughness of the roll segment surface, and the lower work roll for comparison, was recorded at various points throughout the testing. These values are given in Table 6.14. The surface roughness decreased slightly between the measurement taken before rolling and the first reading taken after rolling had commenced. It remained reasonably consistent throughout the rest of the testing. The roughness of the upper and lower rolls was comparable.

		Upper Roll			Lower Roll		
Strip Coil No.	Material	R_a (µm)	RPc	Rsk (µm)	R_a (µm)	RPc	Rsk (µm)
Before Rolling	-	0.634	107	-0.36	0.588	104	-0.22
After Coil 4	DD14	0.568	93	-0.46	-	-	-
After Coil 6	DD14	0.556	97	-0.38	-	-	-
After Coil 8	DD14	0.54	85	-0.51	-	-	-
After Coil 9	DD14	0.542	89	-0.45	-	-	-
After Coil 10	DD14	0.562	85	-0.39	0.534	82	-0.38

Table 6.14: Roll Roughness Measurements, After Rolling Various Strips.

Again, like with the transition-fit plugs this technique had the disadvantage that it will leave marks in the strip. This makes it unsuitable for industrial rolling applications. During the first phase of testing a periodic oscillation was measured in the roll force. The reason for this was never conclusively proved, however it was suspected that replacing the removed part of the roll with a new part, and drilling the wire routing holes had lead to an imbalance in the roll. These oscillations limited the maximum safe speed at which the mill could be run.

6.6.3 Shrink-Fit Plug

Following successful instrumentation of both pilot and semi-industrial mills, it was planned to instrument a work roll for an industrial cold rolling reversing mill based at ThyssenKrupp Rasselstein GmbH in Neuwied, Germany. Like the Sheffield implementation the intention was to instrument a plug which would then be fitted to the roll, however unlike the Sheffield approach the plug would be shrunk fit using liquid nitrogen, rather than transition-fit. As before radial and axial holes were required in the roll to extract the cabling.

The roll being used in this application was an existing roll taken from the mill. Modification of the roll was carried out by METHU Belgium BVBA in Evergem, Belgium. As described earlier the drilling of hardened work roll material can be problematic. As well as difficulties in the actual drilling, the process was also risky due to the high residual surface stresses. This can cause cracking of the roll material. The residual stresses can also lead to drill-drift making maintaining the required accuracy difficult. During use the work roll is subject to large bending loads, increasing the chance of breaking the roll, especially at the hole edges.

To reduce these risks a worn work roll was selected. The hardened surface layer had been worn and the exposed surface was therefore softer. It was also decided that only a single plug would be inserted into the roll. Manufacture of the roll was successful and the prepared work roll is shown in Figure 6.29.

Figure 6.29: Prepared Industrial Cold Rolling Reversing Mill Work Roll.

Separately from the work completed in this thesis ArcelorMittal carried out testing to determine the amount of shrinkage required, and to assess the effects on the rolled strip. It was determined that an interference of at least **0.1%** as measured at room temperature is required. Compression tests where undertaken to determine the necessary shoulder size to prevent the plug shifting and marking the strip. It was determined that the ratio of the shoulder surface to the plug face should be **≥98%** to result in no marking of the strip from compressive loads up to 600MPa. The plug and hole dimensions used are given in Table 6.15.

	Diameter (mm)
Plug	79.97
Cooled Plug	79.81
Work Roll Hole	79.89
Cable Hole	14.00

Table 6.15: Plug and Hole Diameters.

The sensor and plug assembly process, along with the final plug, are shown in Figure 6.30. Two sensors, a shear and a longitudinal, were installed in each plug and two plugs were instrumented.

Figure 6.30: Shrink-Fit Plug.

To avoid surface damage to the strip and backup roll the plug was manufactured from roll material with comparative hardness as the bulk roll surface. This was DHQ3 (Steinhoff, 2008) a common cold rolling steel grade supplied by Steinhoff GmbH & Cie. OHG in Dinslaken, Germany. The plugs were temperature hardened before being machining to size. As before the sensors were attached to the plug with a strain gauge adhesive. Unlike before a special protective housing was mounted over the sensors to protect them and the soldered connection. In the first iteration this housing was back filled with epoxy to secure the wires. This sensor and housing assembly protruded from the plug surface and was designed to fit into the hole drilled in the roll for wire extraction.

To gain the required shrinkage amounts the plug was cooled with liquid nitrogen. There was concern that the temperatures seen by the sensor during the freezing of the plug for assembly may cause the material to degrade, or mechanical failure of the sensor housing and wiring components. To assess the effect of this, benchtop testing was carried out on the sensors and plugs. Both the disassembled components (wires, bare sensor, connector and soldered wires) and the assembled sensors were frozen by submersing them in a bath of liquid nitrogen, Figure 6.31. This meant the sensor was directly immersed in liquid nitrogen. The response from the assembled sensors was monitored throughout as the plugs where frozen, and the disassembled sensors where checked before and after.

The sensors on both of the instrumented plugs functioned at these temperatures and when they were returned to room temperature, seemingly without any ill effects. This implied no permanent damage was caused to the sensor, adhesive or housing materials by the extremes in

temperature. Following the successful tests the plugs were then taken to the roll manufacturer for assembly in the roll.

Figure 6.31: Shrink-Fit Plug and Components in Liquid Nitrogen at ~-194°C

The response from the sensors was monitored as the plugs where frozen in preparation for installation. At some point during freezing the sensors on both plugs failed. The nature of the sudden loss of signal from the sensors pointed to a failure in the electrical connection, rather than material degradation. There was no apparent damage to the external wiring, and the weakest point in the electrical path to the sensors inside the housing is the solder connection from the wires to the piezo element electrodes. It was suspected that this was the point of failure. The plugs had previously passed temperature testing in Sheffield, however the cause of failure may have been the repeated thermal cycling. It may also have been due to damage during transit to the roll manufacturer. The soldered connections were coated by epoxy which has a different thermal coefficient of expansion to the sensors and solder. This may have contributed to the fracture of the soldered joint.

A second attempt was made with a new design of housing. The new housing still enclosed the sensor elements, and provided strain relief to the cabling, but this time left a volume of free air around the solder connections. This second set of plugs also failed, this time due to a failure in

the bond between the protective backing epoxy and housing, the failed part is shown in Figure 6.32.

Figure 6.32: Failed Frozen Shrink-Fit Plug, Second Design

A third iteration was designed to be substantially more robust than the previous plugs, addressing the issues seen in the previous two iterations. Schematic drawings of both of the failed plug designs, the points of failure and the proposed third iteration are shown in Figure 6.33.

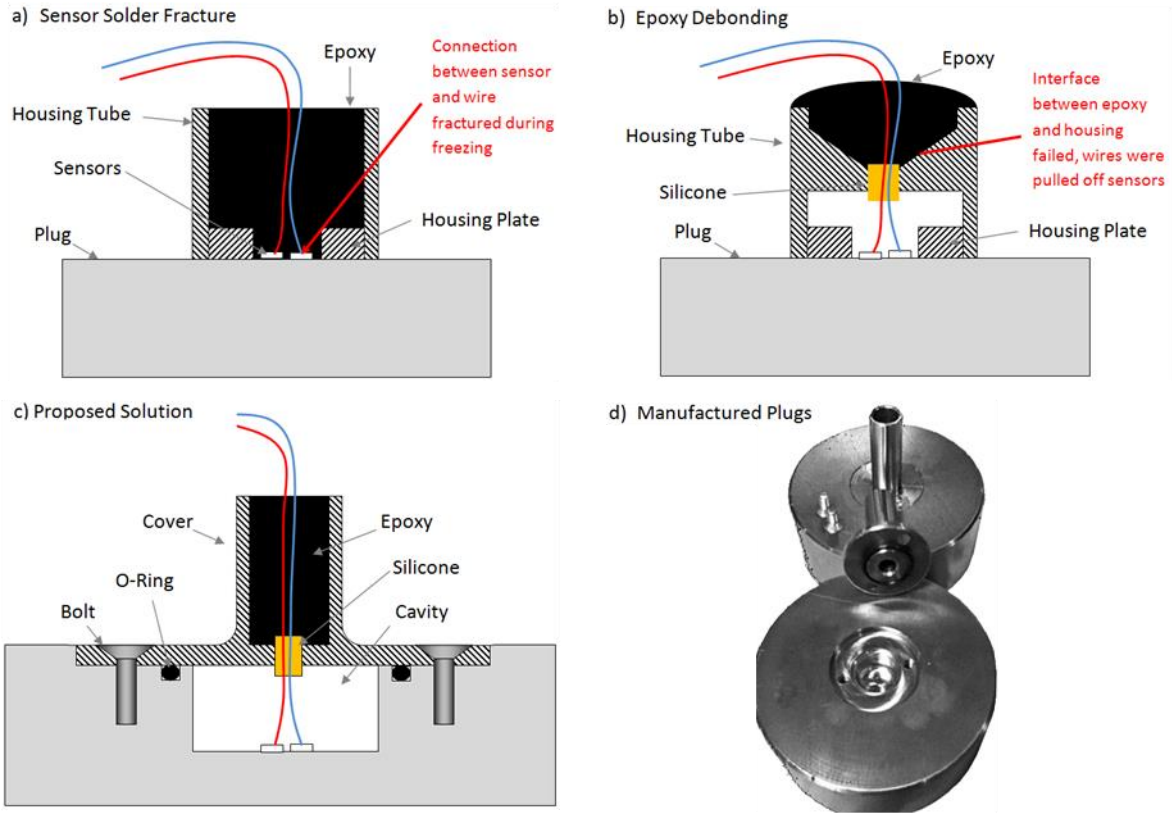

Figure 6.33: Plug Failures and Proposed Solution.

The third iteration plug design was manufactured, however the parts were lost in transit from the manufacturer. The previous two sensor iterations meant that instrumentation of the roll had taken longer than planned, meaning there was limited time left on the project. This

combined with long lead times on replacement parts and limited remaining opportunities to complete the testing at the industrial site it was decided to stop the industrial testing at this stage.

6.6.4 Press Fit Plug

With the industrial testing cancelled it was decided to complete testing of representative industrial conditions on the semi-industrial pilot mill. Again it was decided to attempt the plug technique, although this time to avoid the issues seen with the industrial implementation the plugs were press fit, rather than freeze shrunk.

Two plugs were instrumented. Before grinding the plugs were simple cylinders 40mm diameter and 40mm high. A 5mm recess of 16mm diameter was machined into one end face to accommodate the sensors. Each plug was instrumented with a 10MHz shear and a 10MHz longitudinal sensor. The polarisation of the shear sensor relative to the plug was unknown during installation. However by cutting the sensors from the same shear crystal, but perpendicular to each other, it was possible to ensure perpendicular shear wave orientations were installed on each sensor. The longitudinal elements were 1.4 x 5.75mm, and the shear sensors were 1.4 x 5mm and 1.4 x 3.6mm. The difference in shear sensor size arose from the need to cut perpendicular elements from the same 5x5mm piezo material. A magnified view of the installed piezo elements can be seen in Figure 6.34.

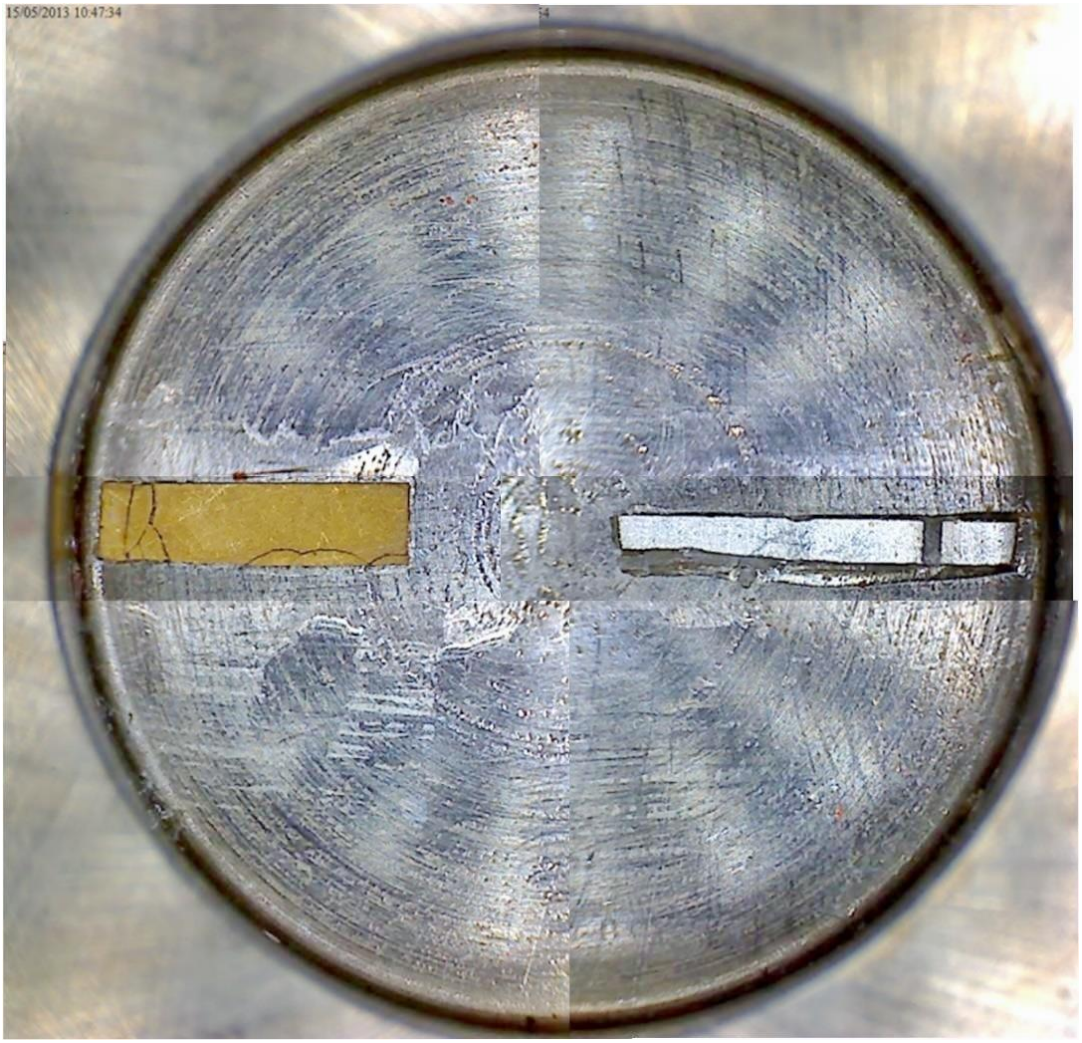

Figure 6.34: Magnified View of the Piezo Elements in a Plug, a Composite of Multiple Images.

The shear sensor on the left of Figure 6.34 shows some cracking. This occurred due to the clamping force applied during bonding. The cracked electrode was re-joined using solder and the sensor showed no ill effects from this.

After the sensors were installed wires were attached and then fed through a small retaining part. This part offered strain relief, and ensured that the wires came out centrally from the plug. The retaining part and wires were then epoxied in place. A plug at the various stages of instrumentation can be seen in Figure 6.35.

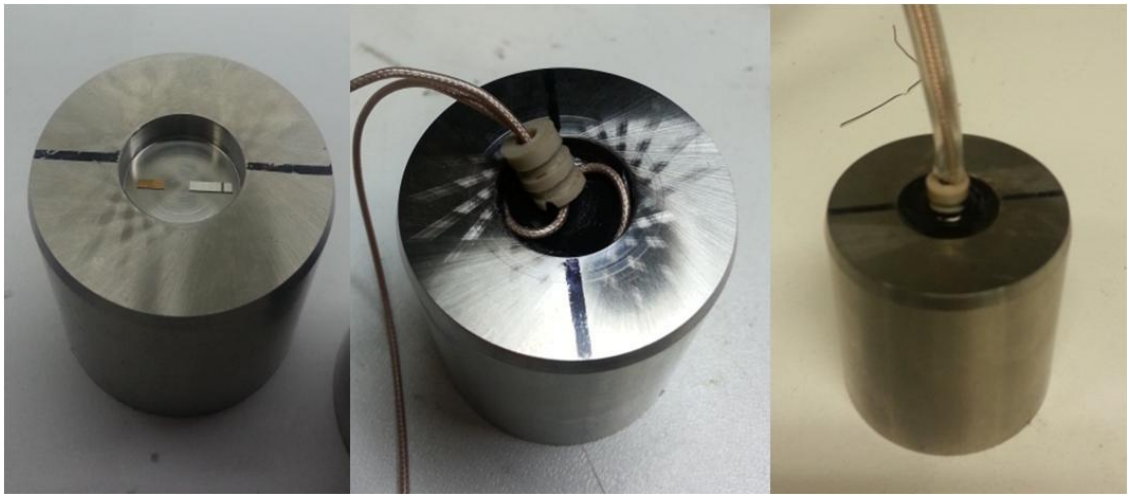

Figure 6.35: Press-Fit Plugs at various Stages of Manufacture.

Applying epoxy directly to the back face of the sensor had the effect of damping the response, resulting in a shorter pulse, as shown in Figure 6.36. This makes it possible to resolve pulses that occur closer in the time domain.

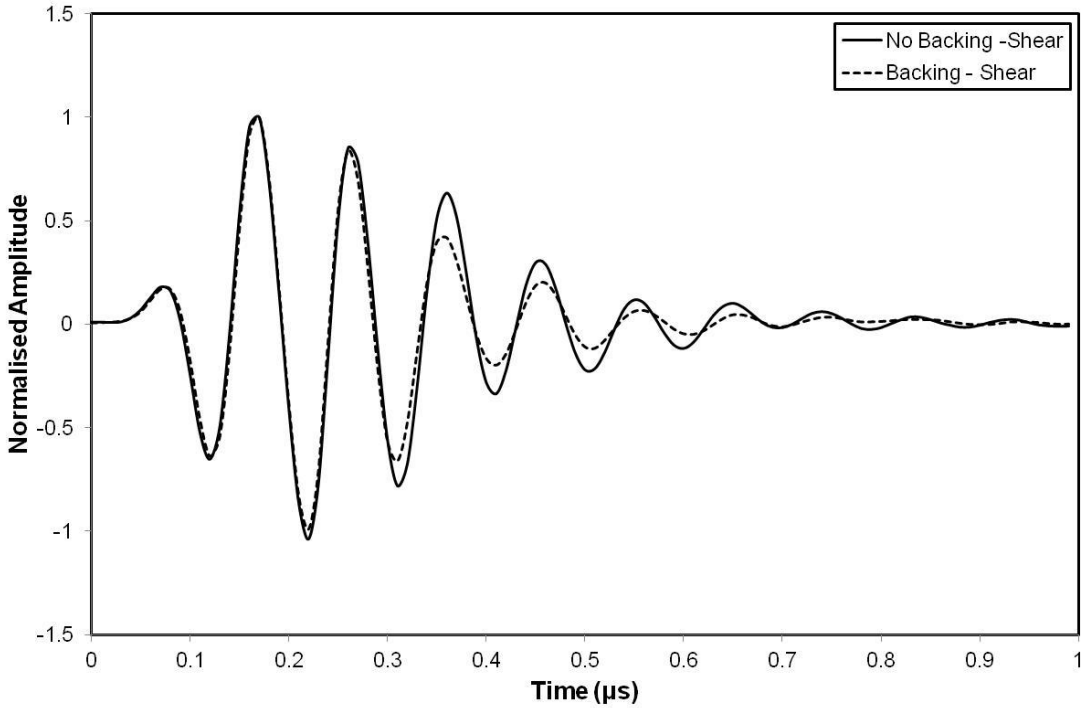

Figure 6.36: Shear Sensor Reflections with and without Sensor Backing.

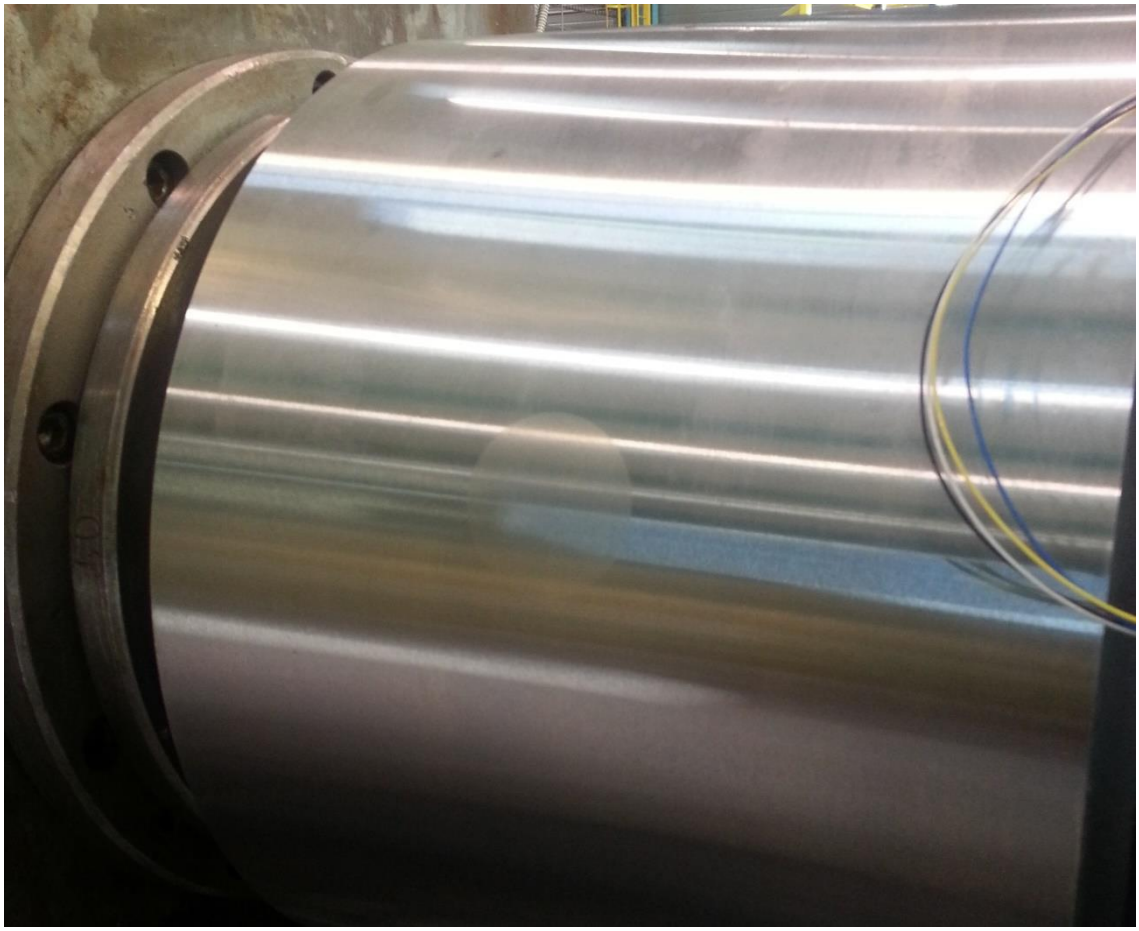

Figure 6.37: Instrumented Roll showing barely perceptible Plug.

Once assembled the plugs were press fit into the roll which was then ground. A plug after installation and grinding in the roll is shown in Figure 6.37. The first attempt to fit the plugs failed when the wiring from the plugs was trapped inside the roll, and severed between the plug and shoulder on which it was design to rest. A repeat set of plugs as made, this time with more rigid wiring. The second attempt to install the plugs was successful.

Apart from the plug, the rest of the experimental setup was the same as used in the Roll-Segment approach. The use of small plugs, as opposed to the segment technique resolved the roll oscillation issues and testing was completed at speeds up to 1200mpm.

6.7 Test Conditions

Once the plug was fitted a number of rolling conditions were tested. Strip thickness, strip material, rolling speed, elongation and lubrication conditions were all varied. A summary of the complete tests are given in Table 6.16.

Three different rolling lubricants were trialled: *Fuchs 812 TCC*, *Fuchs K2* and *Quaker HV2*. The lubricants were applied either directly to the strip (direct application) and/or sprayed into the roll bite (recirculated). The emulsion percentage was monitored throughout. A new strip coil was used with each test, with the exception of Test 15 in which the remainder of the coil from Test 8 was used.

Test No.	Strip Thick. (mm)	Material	Rolling Speed (m/min)	Elong. (%)	Lubrication Conditions		Lubricant Temp. (°C)
					Direct Application	Recirculated	
1	2.8	DD14+Ti	25 to 500	30%		812 2%	50
2	2.8	DD14+Ti	25 to 400	30%	K2 20%	812 2%	-
3	2.8	DD14+Ti	300	30%	K2 0 to 20%	812 2%	-
4A	0.75	ARCELOR06	25 to 500	30%		812 2%	50
4B	0.75	ARCELOR06	25 to 500	30%	K2 20%	812 2%	-
5A	0.75	ARCELOR06	400	30%	K2 0 to 20%	812 2%	-
5B	0.75	ARCELOR06	25 to 500	30%	K2 100%		60
6	2.8	DD14+Ti	25 to 400	30%	K2 100%		60
7	2.8	DD14+Ti	100	5 to 40%	K2 100%		60
8	0.75	ARCELOR06	100	5 to 40%	K2 100%		60
9	0.75	ARCELOR06	25 to 1200	30%	K2 100%		40
10A	0.75	ARCELOR06	25 to 500	30%	HV2 100%		40
10B	0.75	ARCELOR06	25 to 500	30%	HV2 100%		60
11	2.8	DD14+Ti	25 to 400	30%	HV2 100%		60
12	0.75	ARCELOR06	25 to 1200	30%	HV2 100%		40
13	2.8	DD14+Ti	25 to 500	30%		HV2 2%	50
14A	0.75	ARCELOR06	100	5 to 50%	HV2 100%		60
14B	0.75	ARCELOR06	500	5 to 30%	HV2 100%		60
15	0.75	ARCELOR06	50	11 to 50%	K2 100%		60

Table 6.16: Semi-Industrial Pilot Mill Test Conditions.

6.8 Conclusions

In this chapter a system capable of performing the proposed ultrasonic measurements has been developed and successfully implemented within both a pilot and semi-industrial mill.

To achieve this a measurement system was put together including ultrasonic hardware, control software, signal extraction and transducers. The resolution of this system across the roll bite is dependent upon the pulse repetition frequency and rolling speed. At a rolling speed of 500 m/min, the assembled system is capable of performing 15 measurements on 4 sensors across an assumed contact length of 5mm. Custom software was written which was capable of saving the full time-domain responses to file at the full measurement rate.

To extract the signals, wiring and a slip ring were selected. A liquid metal (mercury) slip ring was used on the pilot rig due to its low rotational speed. A high quality brush-type slip ring was necessary during the semi-industrial trials due to the larger rolling speeds. Both slip rings were selected to introduce the minimum level of noise into the ultrasonic signals. The cable length between the pulser and transducer was 4 metres giving a round trip transit time of 40.56ns. The frequency of excitation pulse reflections is the reciprocal of this, 24.65MHz. It is not expected that either of these values represents an issue to the measurements to be taken.

The effective instrumentation of the roll is a key technical challenge in implementing the proposed ultrasonic measurements. To ensure a consistent coupling it was decided to develop a method of affixing the transducer directly to the roll material. The chosen method had to

balance the ease and robustness of instrumentation while minimising the effect that any roll modifications have on the strip-roll interface of interest.

An installation approach based upon removing a segment from the roll and instrumenting and reattaching a replacement was trialled. This approach was advantageous in allowing for ease of instrumentation and access to sensors. However, it is suspected this approach resulted in a misbalance in the roll. This resulted in vibration, especially at higher rolling speeds, and meant the maximum rolling velocities that could be tested were limited, and the rolling loads inconsistent compared with an unmodified roll. It was therefore concluded that this technique was unsuitable without further modification.

Several installations were attempted using variations of a plug insertion technique. In this approach a hole was drilled in the roll and plugged with an instrumented plug. Such plugs were successfully installed in both the pilot and semi-industrial mills using transition and press fits respectively. This method provided a robust way to mount sensors. Several attempts were also made to shrink-fit a plug in place using liquid nitrogen, but these failed. While the sensors were shown to survive, the wiring and associated solder joints became brittle and broke during freezing. This technique therefore requires further design consideration and testing before it is viable.

All of the techniques trialled allowed for a full sweep across the roll bite to be taken with each revolution, and this allowed for a profile of the contact to be recorded. While acceptable for research applications the methods are likely to be too invasive for practical implementation in industrial environments, requiring heavy modification of the roll and resulting in marking of the rolled strip. Further work should be completed to identify a more suitable method for wider adoption.

7 Preliminary Testing

In preparation for testing on the semi-industrial pilot mill a number of preliminary tests were run. The purpose of these was to quantify a number of measurement variables, tune the data acquisition approach and verify where possible the measurement method.

7.1 Thin Film Measurement Techniques

The first experiment that was completed aimed to verify the thin film measurement techniques. The embedded liquid layer reflection coefficient is key to the measurement of the roll bite interface and is used in both the spring model and film resonance methods. To calculate this first an ultrasonic pulse is reflected with air in place of the interfacial layer. This gives a reference signal. The interfacial layer is then introduced and a second measurement taken. By comparing the change in signal between these two measurements the effect on amplitude solely due to the layer can be calculated.

7.1.1 Experimental Setup

The greatest difficulty in testing the thin film measurement techniques is in accurately producing thin-films of a known thickness. In this experiment an oil layer was created between two flat faces. One of these faces was then moved, and the distance of this movement measured by displacement sensors. From this the change in film thickness was inferred. The resulting incremental change in oil layer thickness was measured using the ultrasonic methods. This only allowed comparison of relative values and not absolute values due to an undefined zero-point.

A range of flat thin liquid layers were created using the rig shown in Figure 7.1. This consists of pucks made of either steel or aluminium. One puck is fixed to a base and one is movable and attached to a fine-threaded stage. A thin interfacial layer was created by introducing liquid in-between the two mating faces of the pucks and was held in place by surface tension. The thickness of this layer was manually adjusted using the stage. Two types of displacement sensor, a capacitive sensor and laser interferometer, were used to measure the movement of the movable puck. The capacitive sensor used was an ADE Technologies 2805 non-contact capacitive sensing head and was attached to an ADE 4810 gauge. The device converts displacement to a voltage output that was captured via a PC. A Zygo laser interferometer was used, the output of which was recorded using the same PC as the capacitive sensor. The setup of the capacitive sensor simply required it to be located within a few millimetres of the rear face of the moving sample. The laser interferometer was setup to reflect off of the same face.

The ultrasonic sensor was mounted on the back of the fixed puck. The mating face of the fixed puck was smaller (5mm in diameter) than the mating face on the moving side. The portion of the faces which contacted and formed the liquid layer was therefore 5mm in diameter. This arrangement is shown in the schematic in Figure 7.1. The reason only a small diameter face was used to create the liquid layer was that this reduced the normal force required to create very small layer thicknesses. Because the liquid layer was on 5mm in diameter it was smaller than the ultrasonic beam. However, it is easily distinguishable in the time domain from the other faces in the ultrasonic beam path, and appears as a separate pulse.

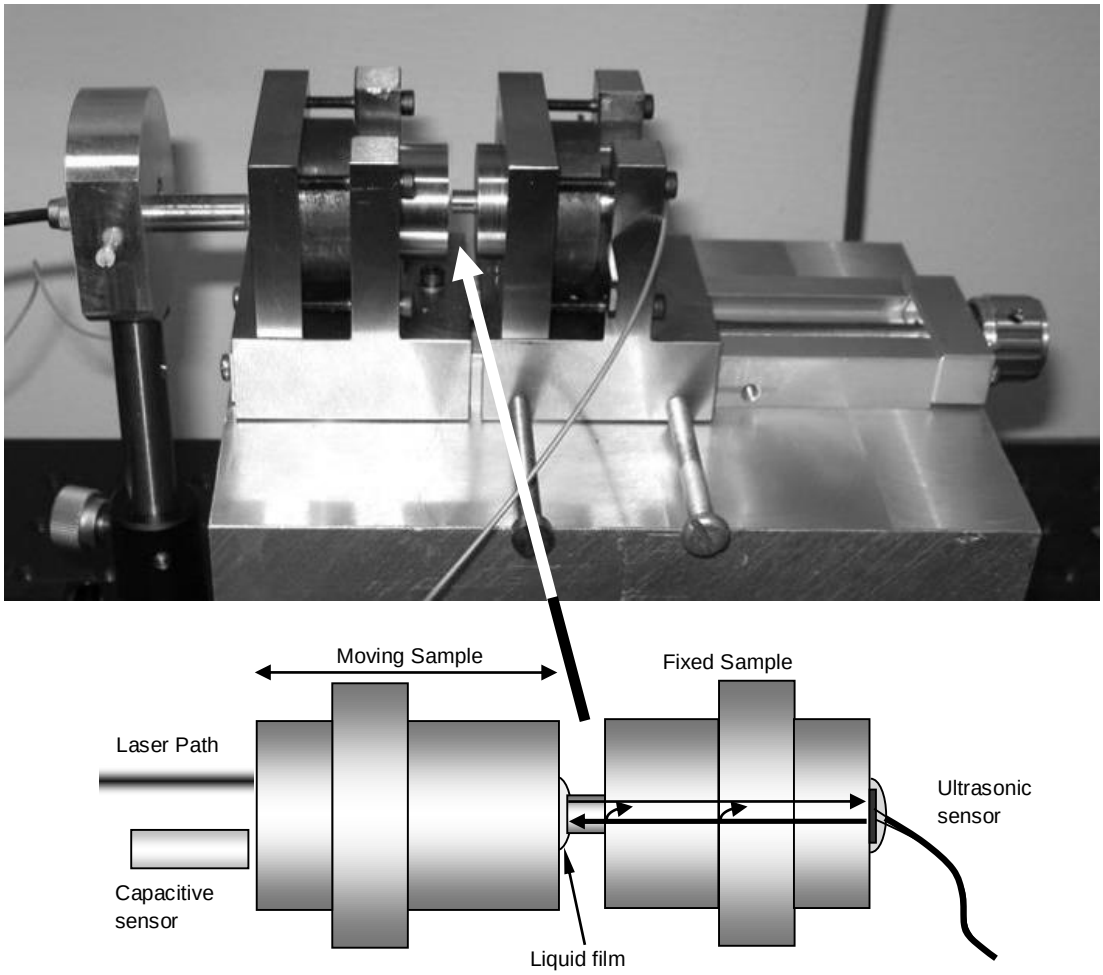

Figure 7.1: Photograph and Schematic of Thin Film Test Apparatus.

The thinner range of films being measured was in the micron range, this is of a similar magnitude to the surface roughness of the liquid faces. For this reason, two surface finishes were used, a polished finish and a ground surface. These were profiled using a stylus profilometer. Profile measurements were taken across the face both horizontally and vertically with respect to the sample orientation during testing. R_a and R_q values for these faces are given in Table 7.1.

	Displacement Puck				Fixed Puck			
	Ground		Polished		Ground		Polished	
	Hori.	Vert.	Hori.	Vert.	Hori.	Vert.	Hori.	Vert.
R_a (µm)	0.28	0.275	0.309	0.292	0.237	0.281	0.304	0.342
R_q (µm)	0.37	0.341	0.527	0.35	0.285	0.374	0.382	0.411

Table 7.1: Surface Roughness Values for Puck Liquid Faces.

All the surfaces show low roughness parameter values of around 0.3µm. The surface profiles taken showed the fixed side was noticeably convex with a deviation of ~1.5µm between its highest and lowest points. This was caused by the inaccuracies in polishing such a small face. This curvature was corrected for in the roughness parameter calculations by approximating it to a parabolic curve. The inaccuracy in this approximation may explain the slightly higher roughness measurements seen in the polished surface compared to the ground surface.

One potential source of error with this validation work is the difference in the type of measurement taken by the ultrasonic and displacement sensors. The ultrasonic sensor gives an absolute value of the layer thickness, while the other sensors measure the relative displacement of one of the faces. Therefore, in order to tie the two sets of results together a common point must be found. A zero point was created by bringing the two faces into contact with no liquid film. However, this does not necessarily give a conclusive value for zero film thickness. The roughness of the two surfaces means that on a microscopic scale there will still be gaps between asperities. Liquid in these gaps could still be detected by the ultrasonic sensor and recorded as a thin film. Applying a greater force to clamp the two samples together would reduce the size of these gaps, and therefore the associated zero error, however this may also deform the samples affecting both the validity of the displacement measurement and the parallelism of the two faces. It is recognised that this offset error may have introduced a systematic error in the results.

7.1.2 Ultrasonic Pulsing & Receiving Instrumentation

The same ultrasonic pulser/receiver hardware as described in §6 was used to generate and digitise the ultrasonic signals. Negative top hat signals of magnitude 50V were used in the following tests. To get the best response the excitation signal width was matched to the centre frequency of the various transducers used. Only longitudinal bond-on piezo elements were used. These had a nominal centre frequency of 10 MHz. These provided useful energy between 6 and 14 MHz. The element is bonded to the transmission material using a standard strain gauge adhesive, the same as for the industrial testing. The elements were disc shaped with a diameter of 7 mm. The sensing area was an average over approximately the same size as the sensor.

The returned signal was amplified then digitized at 100MHz. The digitised signal was then passed to a PC. Most of the processing was done at this point in real-time using bespoke software. Frequency spectra were calculated using a Fast Fourier Transform (FFT).

7.1.3 Liquids and Materials

Both water and oil were used to create the thin layers. The material properties, specifically speed of sound and density, of these liquids were determined by experiment. Tabulated material properties for aluminium and steel were used (Banks, Oldfield, & Rawding, Ultrasonic Flaw Detection in Metals; Theory and Practice, 1962). All properties were taken at 20^{o}C and are given in Table 7.2.

	Density, ρ (kg/m^3)	Speed of sound, c (m/s)	Acoustic Impedance, z (MNs/m^3)
Distilled Water	998.2032 (+/- 0.01)	1482.36	1.48
Light Oil	879.885 (+/- 0.05)	1415.1	1.25
Steel	7700	5850	45.05
Aluminium	2810	6360	17.90

Table 7.2: Thin Film Test Material Properties.

7.1.4 Film Resonance Method

The frequency domain plots for reflected pulses from a range of water film thicknesses and an air interface are shown in Figure 7.2. The associated reflection coefficients are plotted in Figure 7.3 with the frequency spectra over-plotted with an arbitrary scale in order to show the pulse bandwidth. Outside of the sensor bandwidth noise will dominate over the signal of interest and

the results become meaningless. This is demonstrated by the R>1 peaks seen in Figure 7.3 which are just noise artefacts. The resonant dips can clearly be observed with respect to the reference.

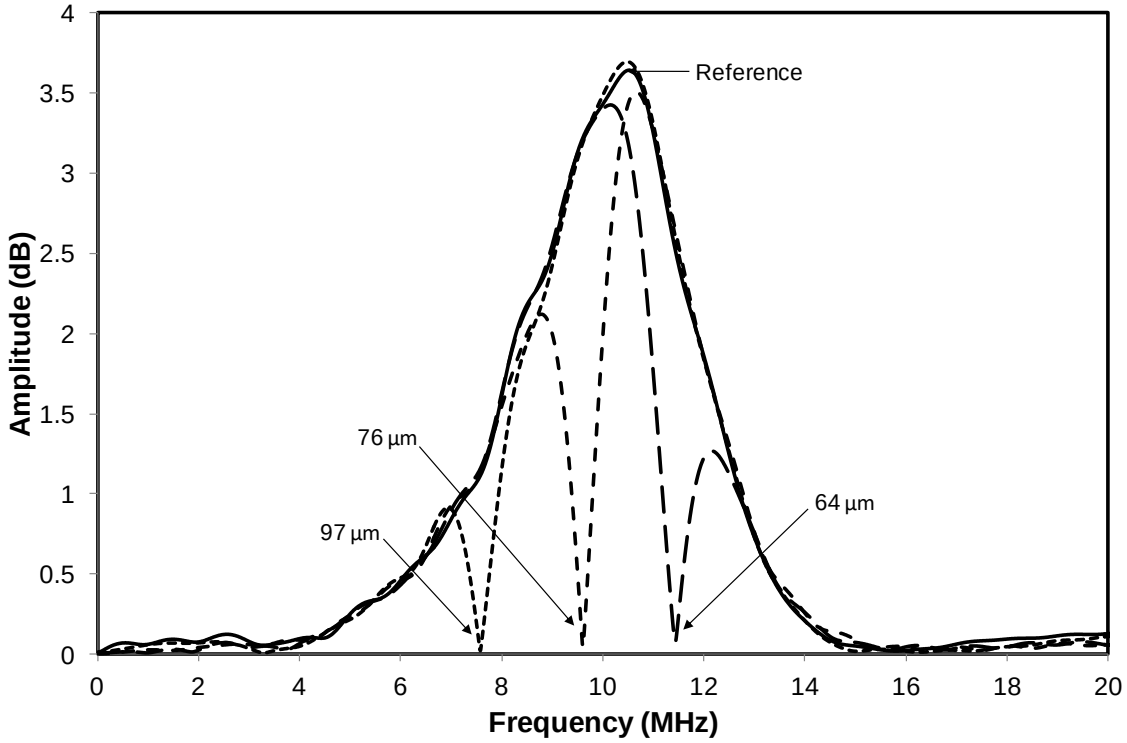

Figure 7.2: Frequency Spectra for the Reference Reflection and three Water Film Thicknesses.

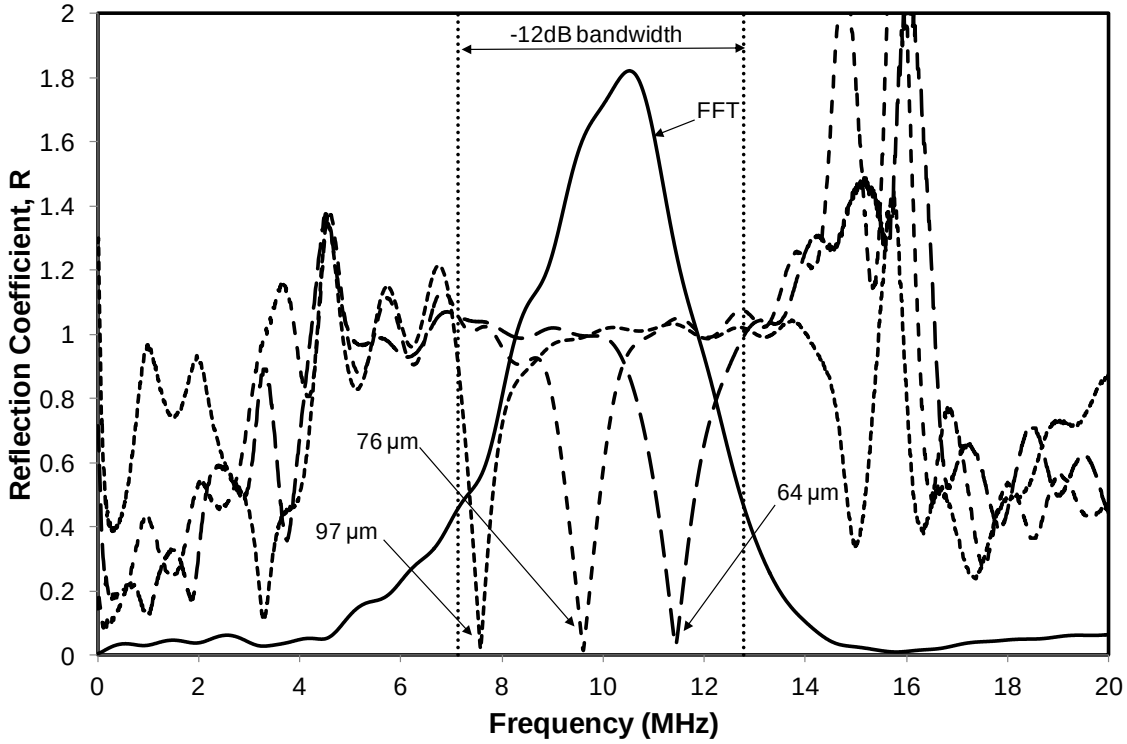

Figure 7.3: Reflection Coefficient for the Reference Reflection and three Water Film Thicknesses. The Reference Frequency Spectra has been over-plotted on an arbitrary scale.

The film thickness can be calculated from the frequency of a resonant dip and its mode. For greater resolution a peak fitting algorithm was used to calculate the dip frequencies. When multiple dips were present the value of the dip closest to the pulse centre frequency was used

as this represents the dip with the best signal to noise ratio. A comparison plot between the laser interferometer and resonant technique for a water layer can be seen in Figure 7.4. The results appear consistent regardless of the surface finish used.

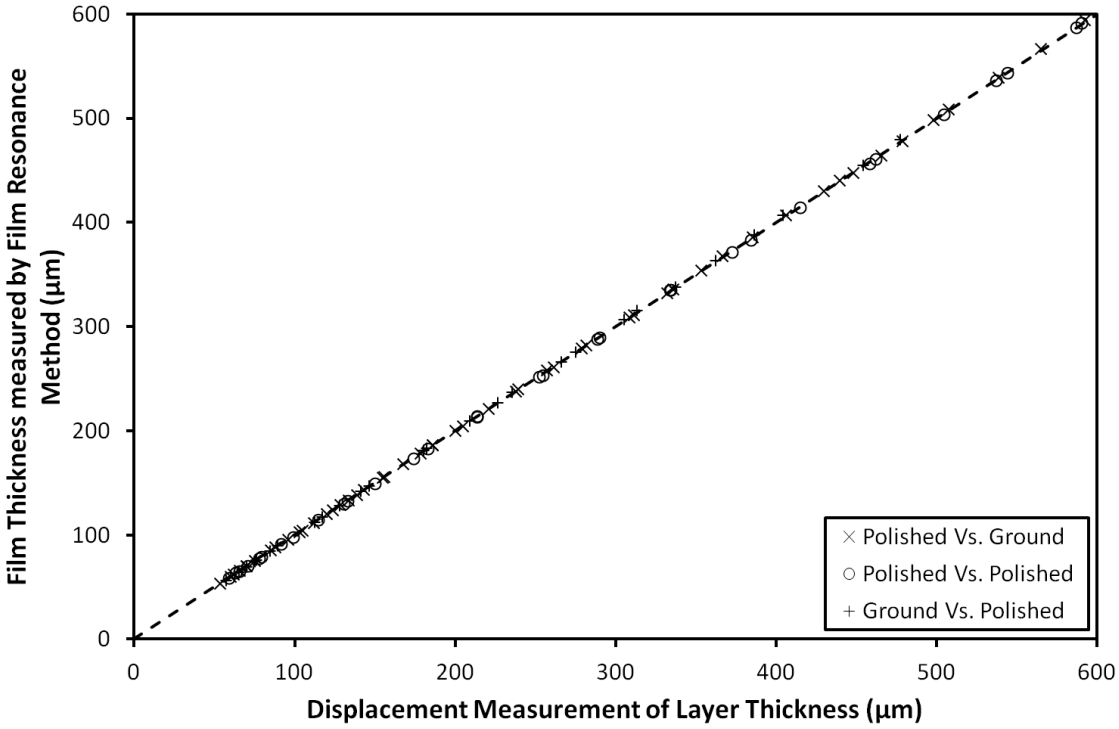

Figure 7.4: Comparison of Film Thickness Measured using Film Resonance and Laser Interferometer for different puck surface finishes.

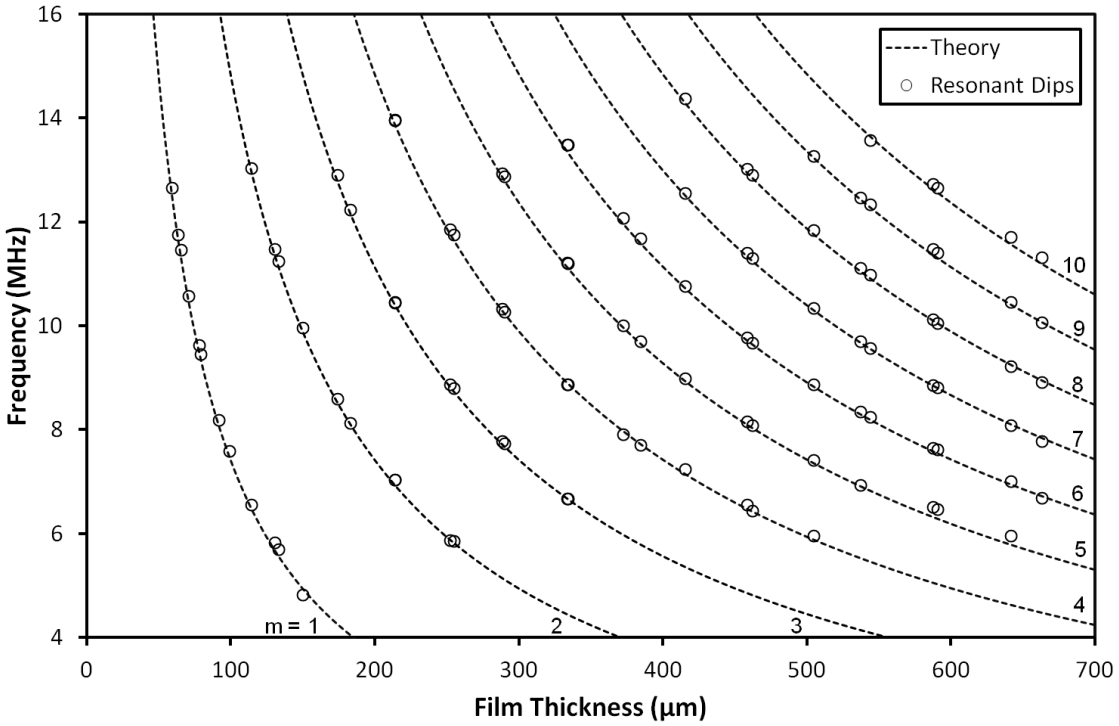

Figure 7.5: Film Resonance Modes for Water Layers and Polished Puck Faces.

These results show a very strong correlation. Results taken using oil as the layer liquid showed similar correlation. Figure 7.5 shows the resonant dips recorded compared to the theoretical

values calculated using Equation 3.81, demonstrating good correlation across a range of film thicknesses, resonant frequencies and modes.

7.1.5 Spring Model

As the liquid film was reduced to much thinner thicknesses, a clear reduction in the returned pulse amplitude with decreasing film thickness was observed. The frequency spectra in Figure 7.6 show this reduction in amplitude for a number of film thicknesses.

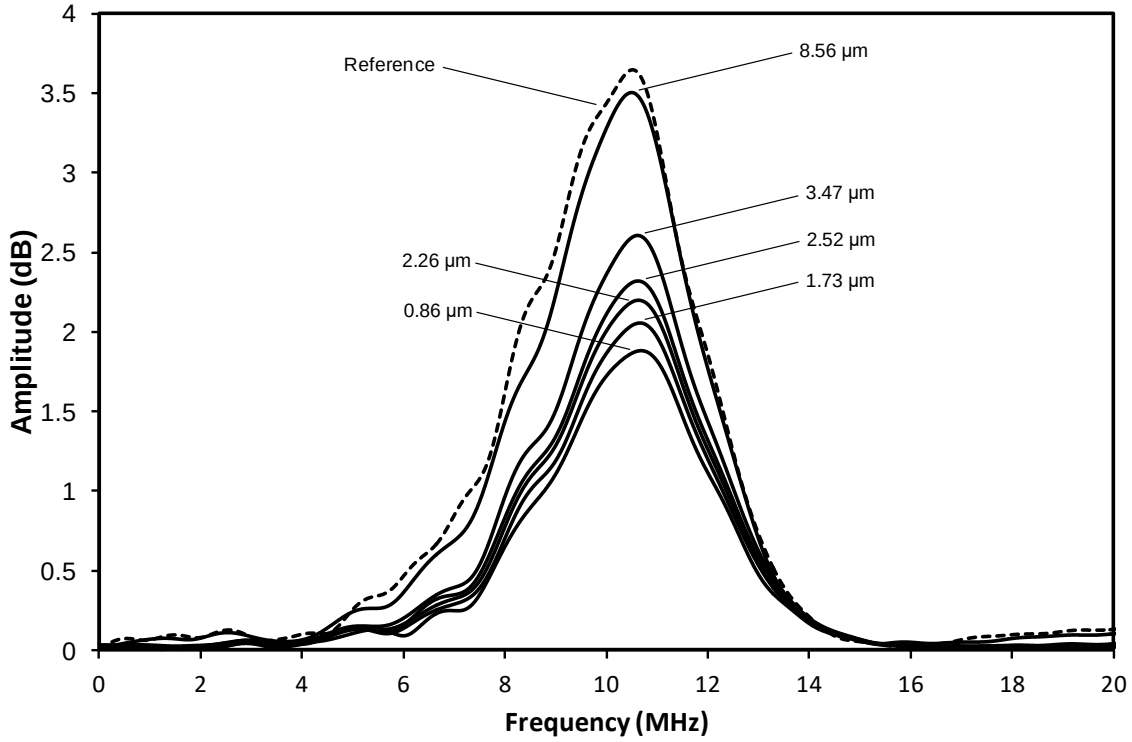

Figure 7.6: Frequency Spectra for a range of Thinner Water Films.

The reflection coefficient spectra are given in Figure 7.7. Again the reference FFT has been overlaid in order to show the pulse bandwidth. Within this bandwidth the reflection coefficient shows an approximately linear frequency dependent response.

The reflection coefficient is then used to calculate the film thickness for every frequency within the sensor bandwidth. The average of these over the bandwidth was then calculated to give a final value of film thickness.

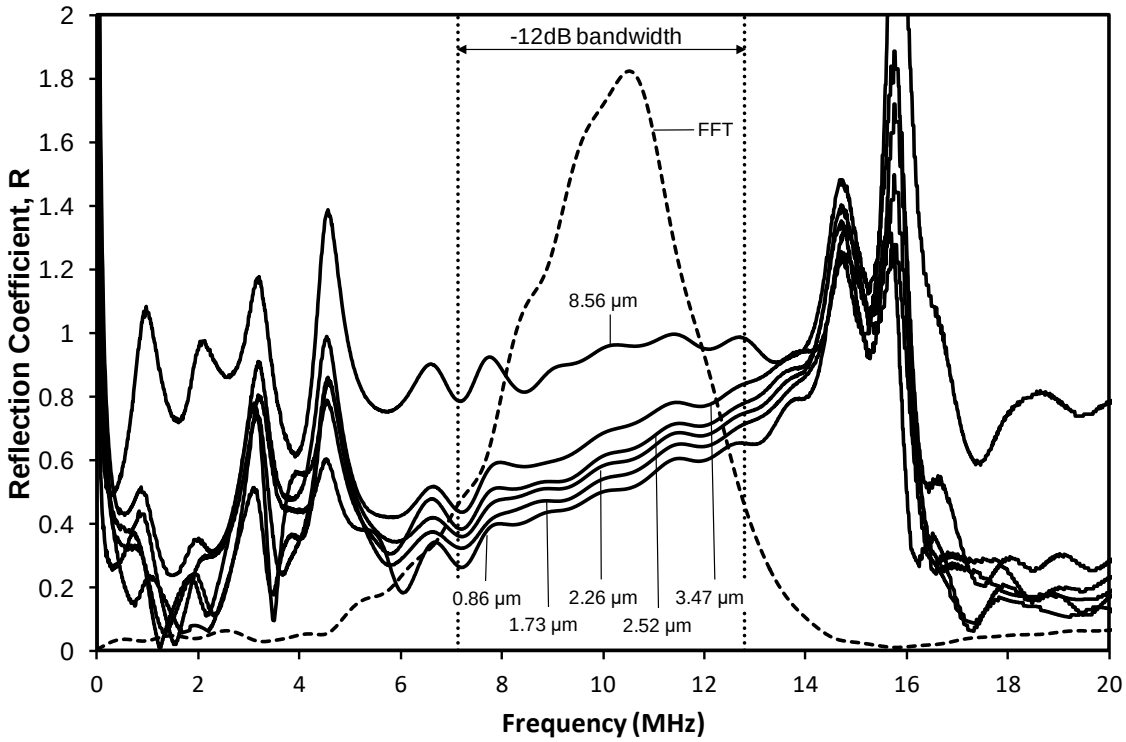

Figure 7.7: Reflection Coefficient for a range of Thinner Water Films. The Reference Frequency Spectra has been over-plotted on an arbitrary scale.

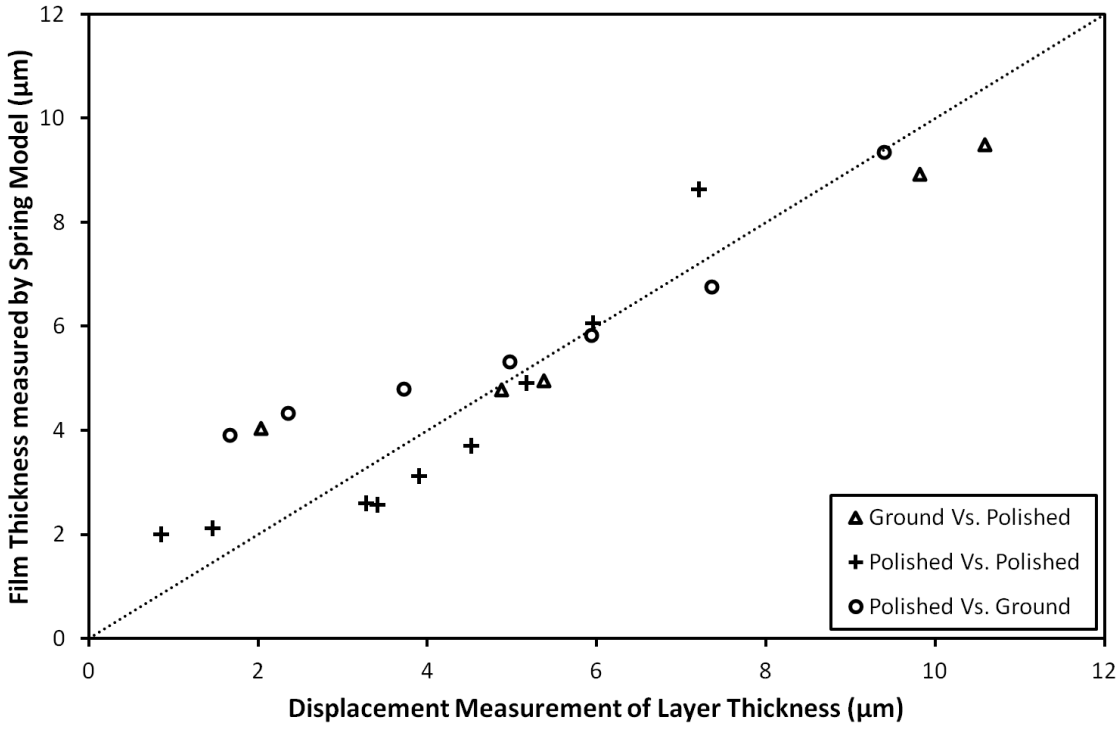

Figure 7.8: Comparison of Film Thickness Measured using Spring Model and Laser Interferometer for different puck surface finishes.

Figure 7.8 compares the spring model and laser interferometer results for the different surface finishes with water as the liquid film. Multiple results were taken and showed repeatability. Figure 7.8 shows the general agreement between the spring model and the laser interferometer readings. The results measured reached a lower limit at a thickness comparable to the combined

surface roughness of the two faces. It must also be remembered that as previously described there are potential errors due to incorrect zeroing, which could explain any offset.

7.1.6 Thin Film Validation Discussion and Conclusions

A large range of films were measured for a number of surface finish combinations, surface geometries and liquid layer materials. The thinnest films measured in this experiment using the film resonance method were ~30 µm. Using the spring model, films up to ~11µm were measured.

The results from the film resonance method showed a very strong correlation to the calibrated standards, and this provides a good validation of the technique. The accuracy appeared unaffected either by the liquid used or the surface finishes tested. This also shows robustness in the method. The technique was consistent throughout all the tests performed. This technique relies on frequency rather than amplitude. The key benefit of this over the amplitude dependant spring model is that the reference is not required for film thickness calculation. Therefore, no error is introduced by reference drift. If multiple modes are present, then the mode number can be calculated. However, if only one resonant dip has been observed within the bandwidth the mode number must be assumed, which may lead to an erroneous reading.

The generation of static thin oil films of a known thickness proved challenging, and most likely source of error in this work. This is especially apparent when the film is of the order of the surface roughness of the bounding faces. It was demonstrated that the minimum measureable film for the spring model is limited to the point of contact between the opposing faces. As soon contact occurs the interface stiffness has a contribution from asperity contact. The surface roughness therefore introduces an interesting problem in quantifying film thickness, as a non-continuous liquid film is still present even after contact has occurred. Any distortion of the pucks could potentially lead to discrepancies between the displacement of the moving face, and the actual film thickness created. This may be caused by incorrect securing of the puck in the rig, or by the forces required to displace the liquid when creating thinner films.

In each ultrasonic technique either resonant frequency or reflection coefficient are being measured, and not film thickness directly. Therefore, there is the potential for error in the relationships used to convert these values into film thickness. In particular, the material properties of the thin layer and its surrounding materials play an important role and the accuracy of these properties will have a direct effect on the accuracy of the film thickness measurement. These properties will be affected by temperature. This experiment was performed in a temperature controlled room, held at a constant 19.8°C. The density of the liquids in this experiment were calibrated in a specialist laboratory to an estimated uncertainty ±0.010 kg m^{-3} for the water and ±0.050 kg m^{-3} for the oil. The speed of sound was measured to 1 decimal place. Temperature effects were therefore minimal.

The speed of sound in the liquid is the only material property required for the film resonance technique. It is a relatively straightforward calibration test to measure this over a range of temperatures. Thereby a speed of sound calibration curve can be produced to compensate for any temperature effects. However, it is often much less practical to measure the liquid temperature of thin films in the components where they are formed. The liquid temperature can normally be estimated quite accurately in static components of uniform temperature,

however it is much harder for an accurate estimation when a temperature gradient is present, or the system is dynamic.

The spring model relies on the density and speed of sound of the liquid as well as the acoustic impedance of the surrounding material. Again these can be calibrated for temperature using simple benchtop tests, as before the challenge comes in the accurate measurement of the temperature in-situ. Accurate temperature estimation there presents a significant challenge in the application of both techniques.

7.2 Acoustoelastic Constants

As shown in §4 the stress in the roll material can be measured through the speed of sound. This changes with stress due to the acoustoelastic effect. In order to relate the change in the speed of sound to stress, the acoustoelastic properties of the material must be understood. Testing was completed to measure these properties in the material used for the press fit plugs installed as part of the industrial testing.

7.2.1 Experimental Setup

A load was applied to a plug which was identical to the plugs installed in the work roll. This plug was instrumented with 10 MHz shear and longitudinal sensors. As the load was increased the time of flight was calculated be measuring the time difference between two successive ultrasonic reflections.

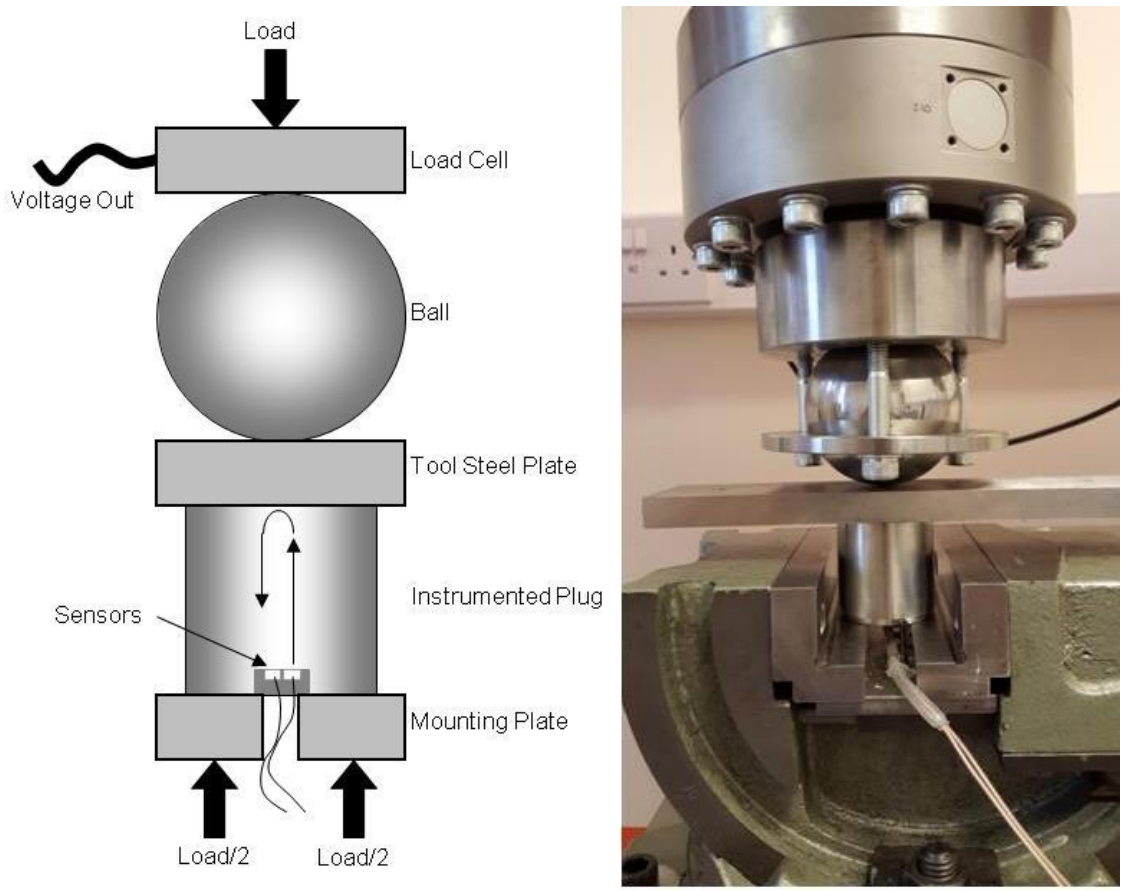

Figure 7.9: Schematic and Photo of Plug Loading Test Setup.

It was important that the plug was loaded evenly to ensure a uniform compression. In order to achieve this, the load had to be applied normal to the surface of the plug. Any misalignment in

the loading would result in shear or non-uniform stresses. This was achieved by loading the plug via a ball as shown in Figure 7.9. This accounted for any misalignment in the rig and ensured that no shear loading was transmitted to the instrumented plug. A tool steel plate was placed between the ball and plug to ensure that the plug was not loaded just at the point of the ball contact. The load was applied by a hydraulic ram and measured using a load cell. This test equipment was provided by Tribosonics Ltd., Sheffield, UK.

On the opposite side of the plug to the loading ball the annular face surrounding the sensors was supported on a mounting plate. This was the same manner that the plug was supported when it was mounted in the roll. By using a plug and loading conditions representative of those seen in the final application the results gained should emulate those seen in the rolling mill implementation.

7.2.2 Results

The measured change in Time-of-Flight (ToF) for both the shear and longitudinal waves as the plug was loaded is shown in Figure 7.11. The compressive stress plotted was calculated using the cross sectional area of the plug and the load measured from the rig load cell. The negative change in time-of-flight corresponds to a reduction, and the negative stress represents compression.

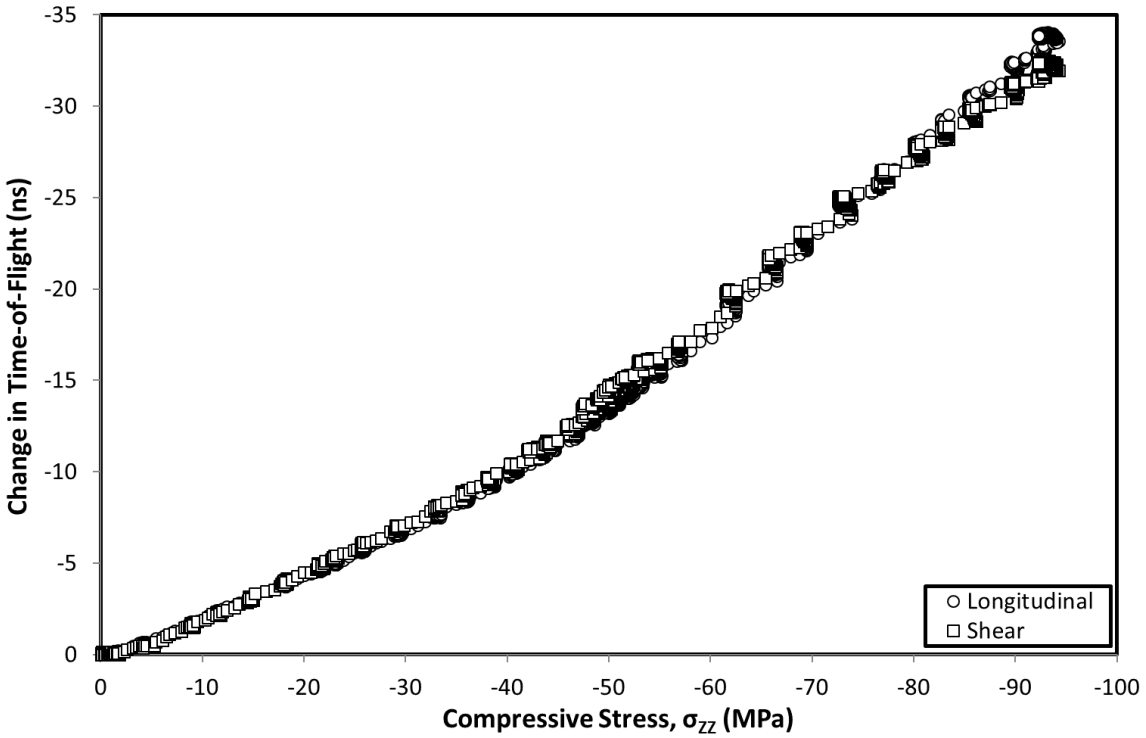

Figure 7.10: Measured change in Time-of-Flight against Compressive Stress. The ultrasonic path length is 70±0.1mm and the absolute unstressed Time-of-Flights are Longitudinal = 11.66µs and Shear = 21.54µs.

It was expected that both plots would be linear, however the figure shows that both datasets appear to consist of two linear sections. The plots transition between these at around ~-45 MPa. The plots show a very similar change in the time-of-flight.

From this the apparent speed of sound was calculated by dividing the ultrasonic path length (twice the plug length) by the time-of-flight. This speed of sound calculation doesn't account for the plug deformation. In this case the deformation will result in a slight shortening of the plug, and therefore an over-prediction in the value of the speed of sound. The values gained for the data in Figure 7.10 are plotted in Figure 7.11.

Again a slight increase in the data gradient is seen at ~-45 MPa. However unlike in Figure 7.10 there is a difference in magnitude between the longitudinal and shear results. This is due to the differing speed of sound of the two wave types.

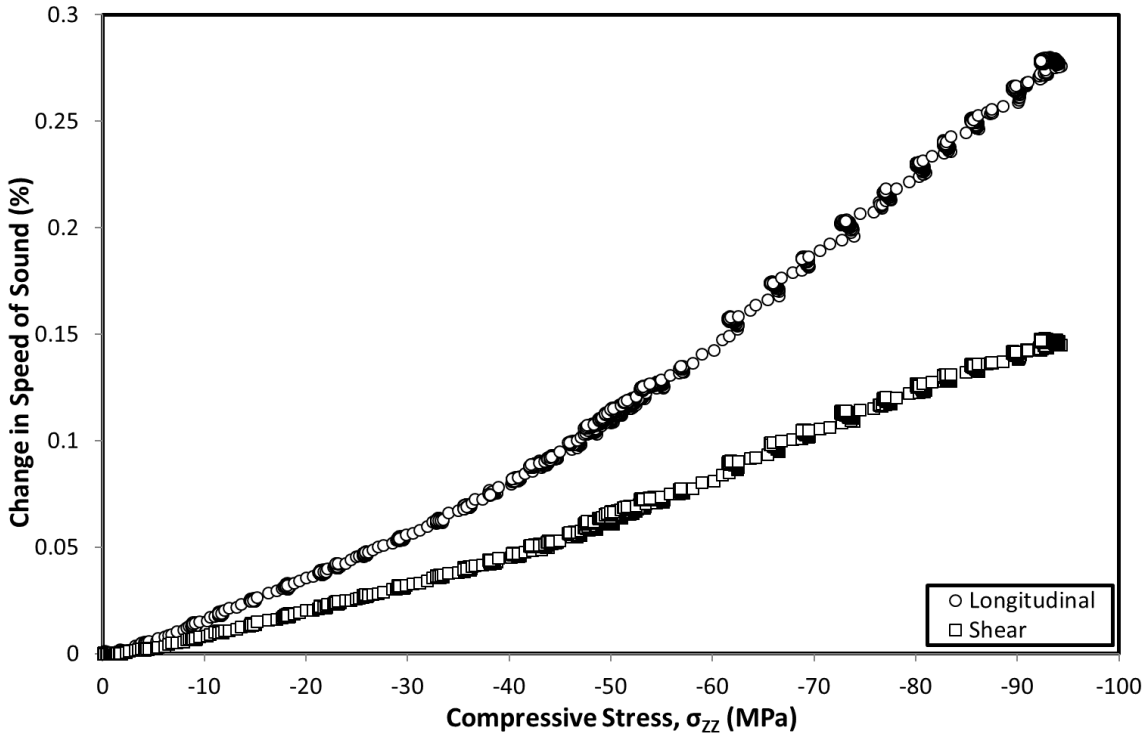

Figure 7.11: Percentage change in the apparent Speed of Sound against Compressive Stress.

Figure 7.12: 10.137mm diameter indentation left by loading ball in the Tool Steel plate.

When the test was disassembled it was observed that the loading ball had deformed the tool steel plate that was used to transmit load to the plug. This indentation is shown in Figure 7.12.

It is suspected that this plastic deformation happened at higher loads although this is not expected to have affected the acoustoelastic measurement.

The gradient above ~-45 MPa for both Figure 7.10 and Figure 7.11 appears to have a linear trend, but with a non-zero intercept. Non-uniform stress within the plug has been identified as the most likely source for this unexpected behaviour. The calibration assumes an ideal plane stress being applied through the plug. The whole of the top face of the plug is loaded, however the bottom face of the plug is only supported at its shoulders and not directly behind the sensors, due to the gap in the plug mounting plate required to extract the sensor cables as shown in Figure 7.11. Therefore, the stress does not transmit from the bottom to top faces of the plug in direct alignment with the ultrasonic path. Additionally, the rig will only have a finite stiffness, there will be some deformation of the rig and sample holder which will increase with higher loading. This means at higher loads the plane stress assumption is likely to be invalid. Because of this only data for the initial linear section of the graph was used to calculate the relationship between stress and acoustic velocity.

In cold rolling compressive stresses of up to several hundred MPa are expected. Only using the data for compressive stresses up to 45MPa to determine the acoustoelastic relationship means that the results potentially need to be extrapolated to stresses up to an order of magnitude higher. This could be a source of error, however, it was demonstrated in §4.5 and shown in Figure 4.4, that the stress to Time-of-Flight change is expected to remain linear up to at least 1GPa therefore the extrapolation is expected to hold.

The change in time-of-flight and speed of sound, along with linear trend lines and equations, are plotted in Figure 7.13 and Figure 7.14.

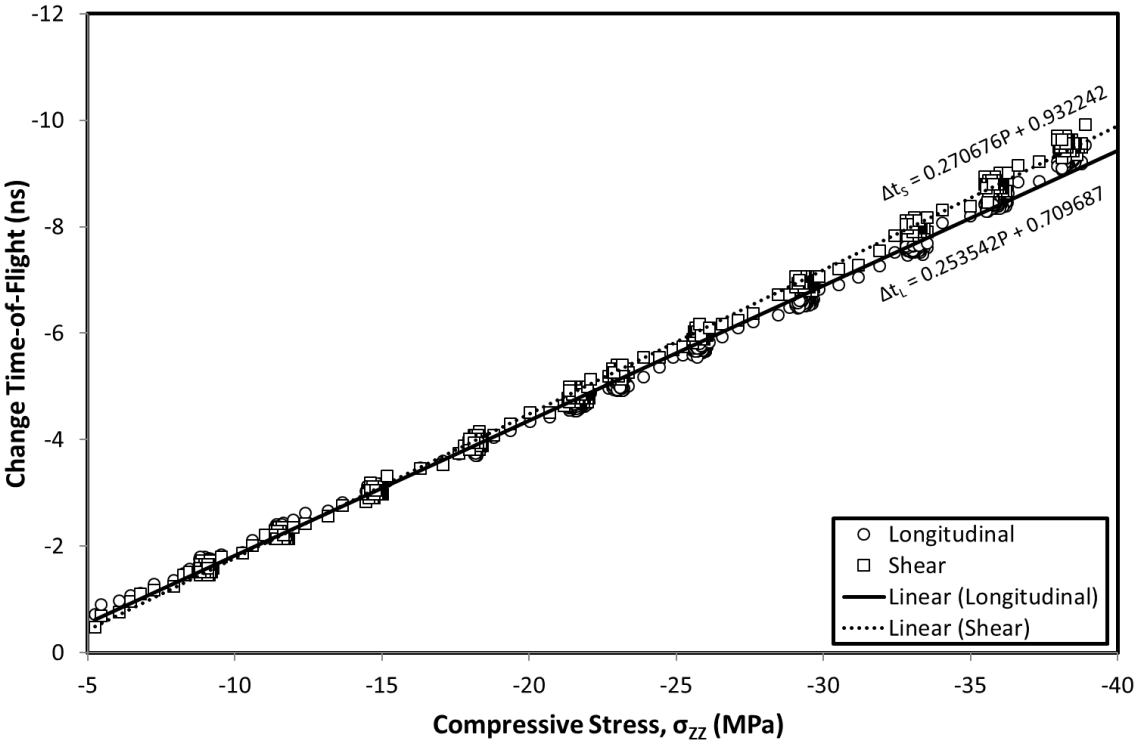

Figure 7.13: Measured change in Time-of-Flight against Compressive Stress, -5 to -40 MPa.

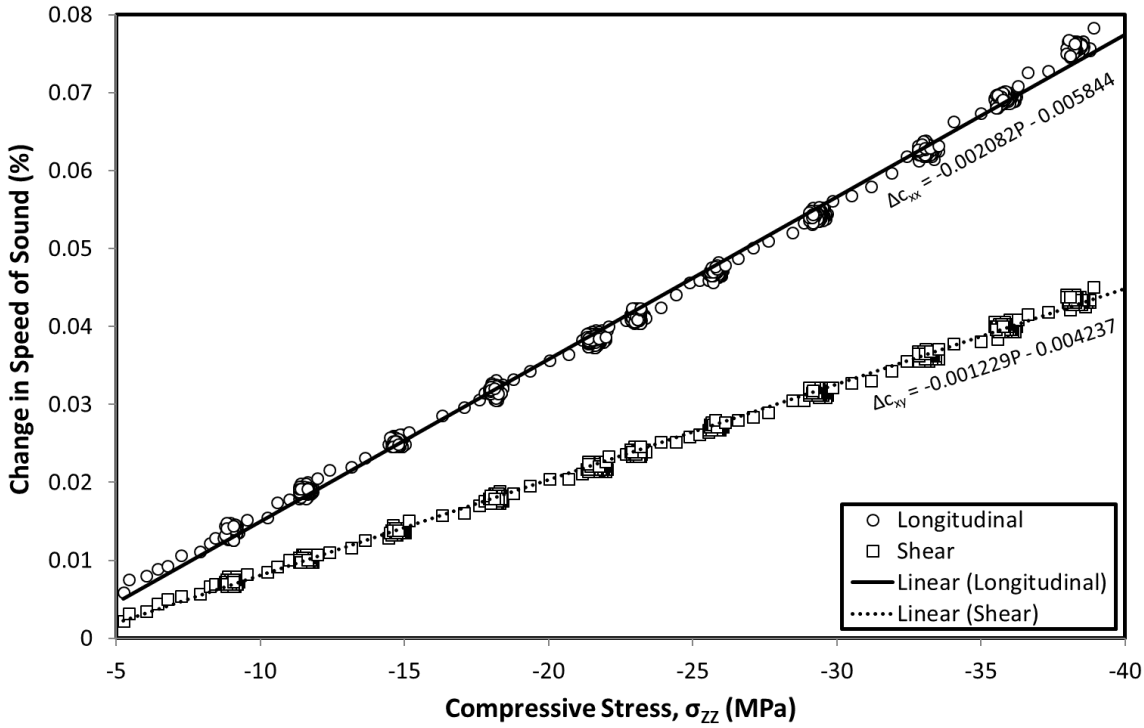

Figure 7.14: Percentage change in the Speed of Sound against Compressive Stress, -5 to -40 MPa.

While it would be expected that the trends pass through the origin, their equations show that they have a slight offset. This is likely to be due to the system settling as the load is initially applied, the results below -5 MPa have therefore been ignored. The offsets have been discarded and only the slope of the trend line has been used to quantify the relationship between the load and the speed of sound.

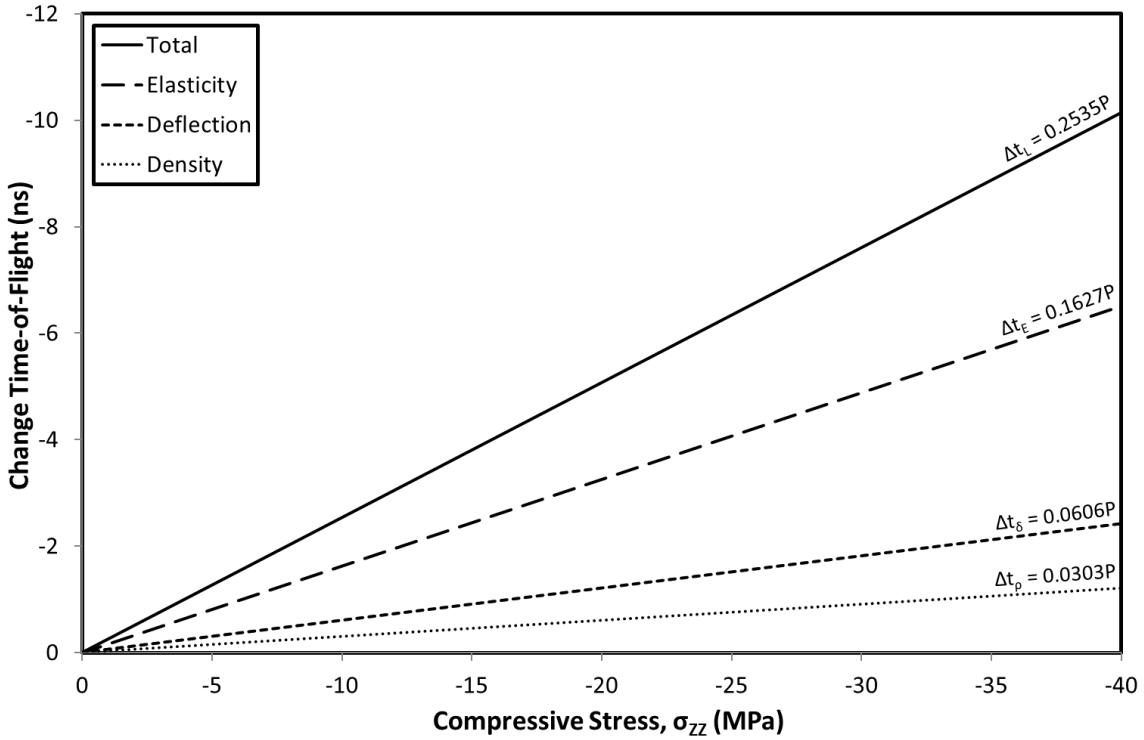

Figure 7.15: Contributions to the change in Time-of-Flight for a Longitudinal Wave.

Knowing the stress and cross sectional area it was possible to calculate the strain and therefore the deflection of the plug. This allowed the contributions of both the density and plug deflection to the change in ToF to be calculated using the equations in §4. The difference between measured change in ToF and the combined density and deflection effects was assumed to be solely down to the acoustoelastic effect. The results of these calculations for both the shear and longitudinal results and are plotted in Figure 7.15 and Figure 7.16.

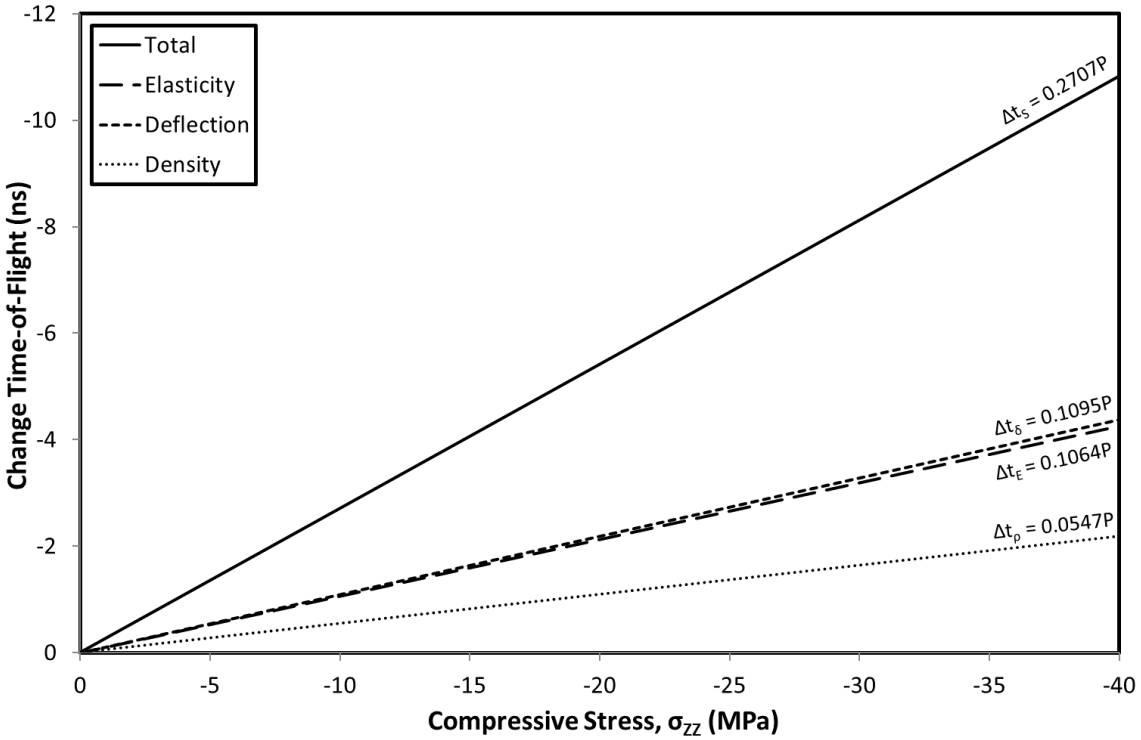

Figure 7.16: Contributions to the change in Time-of-Flight for a Shear Wave.

Table 7.3 shows the contribution of each effect as calculated from the equations in Figure 7.15 and Figure 7.16. Also stated is the back calculated acoustoelastic constant calculated from Equation 4.40.

	Density		Deflection		Elasticity		Total		
	ns/MPa	%	ns/MPa	%	ns/MPa	%	ns/MPa	%	α
Long.	0.0303	11.95	0.0606	23.91	0.1627	64.18	0.2535	100	-2.685
Shear	0.0547	20.21	0.1095	40.45	0.1064	39.31	0.2707	100	-1.757

Table 7.3: Contributions of Density, Deflection and Elasticity to the change in Time-of-Flight.

7.2.3 Acoustoelastic Testing Discussion and Conclusions

The value for the longitudinal acoustoelastic constant compares well with those found in literature, as shown in Table 4.1. Also the ratio of the contributions from the deflection and elasticity effects compare favourably with those found in previous studies (Chen, Mills, & Dwyer-Joyce, 2015). No equivalent values for the shear waves were found, and no previous study appears to have accounted for the effect of density.

The data used (Figure 7.13) to calculate the contributions to the change in time-of-flight and acoustoelastic constants demonstrated excellent linearity. The square of Pearson's correlation coefficient is **0.9971** and **0.9984** for the longitudinal and shear data respectively. The

combination of good data correlation, and consistency with literature values, gives confidence that the results reported are accurate.

A number of potential sources of error were identified in this testing. Some plastic deformation of a loading plate was observed, although it is not thought that this will have affected the acoustoelastic results. The inability to support the entire bottom face of the plug, due to the presence of the sensors and the need to extract cabling, may have resulted in some bending of the plug. This meant that only the results for compressive stress up to -40 MPa were used for the calculation of the acoustoelastic constants. The peak stresses seen in cold rolling are likely to be multiple times this magnitude, and so the acoustoelastic relationship will have to be extrapolated beyond that measured. Because the relationship is linear this extrapolation should be valid, however the error is likely to increase with greater extrapolation. The ultrasonic waves were digitised with a 10 ns time-step. This is large in comparison to the measured time-of-flight changes. The resolution was increased beyond that of the digitiser using the time-of-flight interpolation methods discussed in §4.6, these represent another potential source of error.

7.3 Cable Length

Some simple bench top tests were performed to quantify the effect of cable length on the ultrasonic signal. The response of an ultrasonic sensor connected to an Ultrasonic Pulser-Receiver (UPR) via various extension cable lengths was recorded.

7.3.1 Experimental Setup

The same cable and longitudinal piezo element type that were used in the final instrumentation were tested. The sensor was mounted on a steel block ~13mm thick. A schematic of the test setup can be seen in Figure 7.17, with the returned ultrasonic responses in Figure 7.18. The responses in Figure 7.18 show the remnants of the excitation pulse followed by 4 successive reflections within the sample block, and the associated frequency spectra in Figure 7.19.

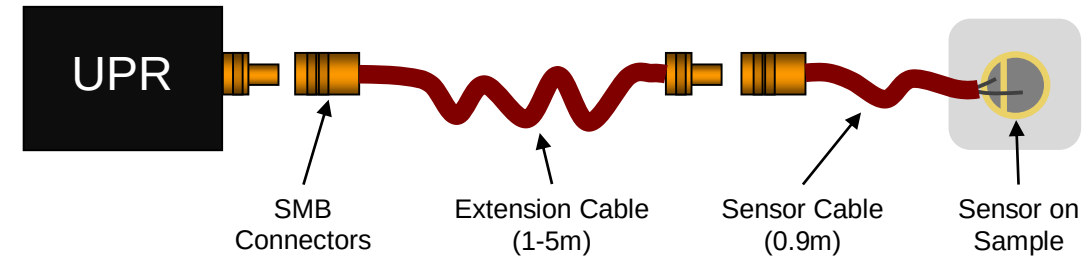

Figure 7.17: Cable Length Test Setup.

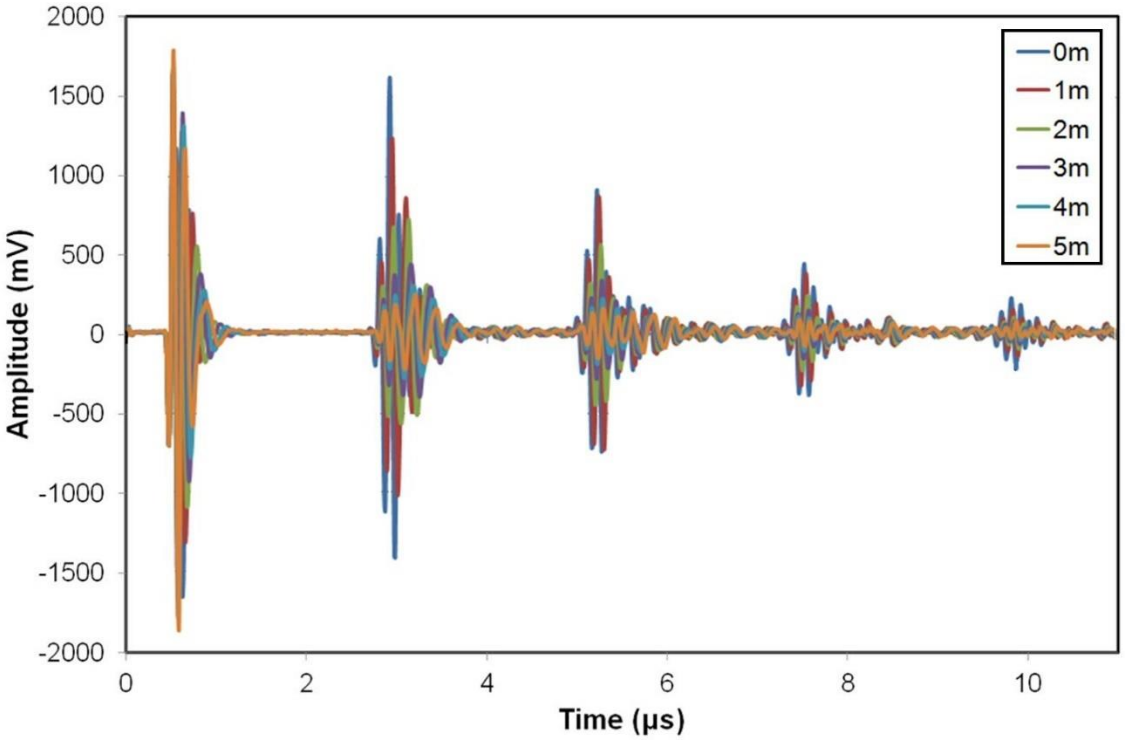

Figure 7.18: Ultrasonic Responses with Various Extension Cable Lengths.

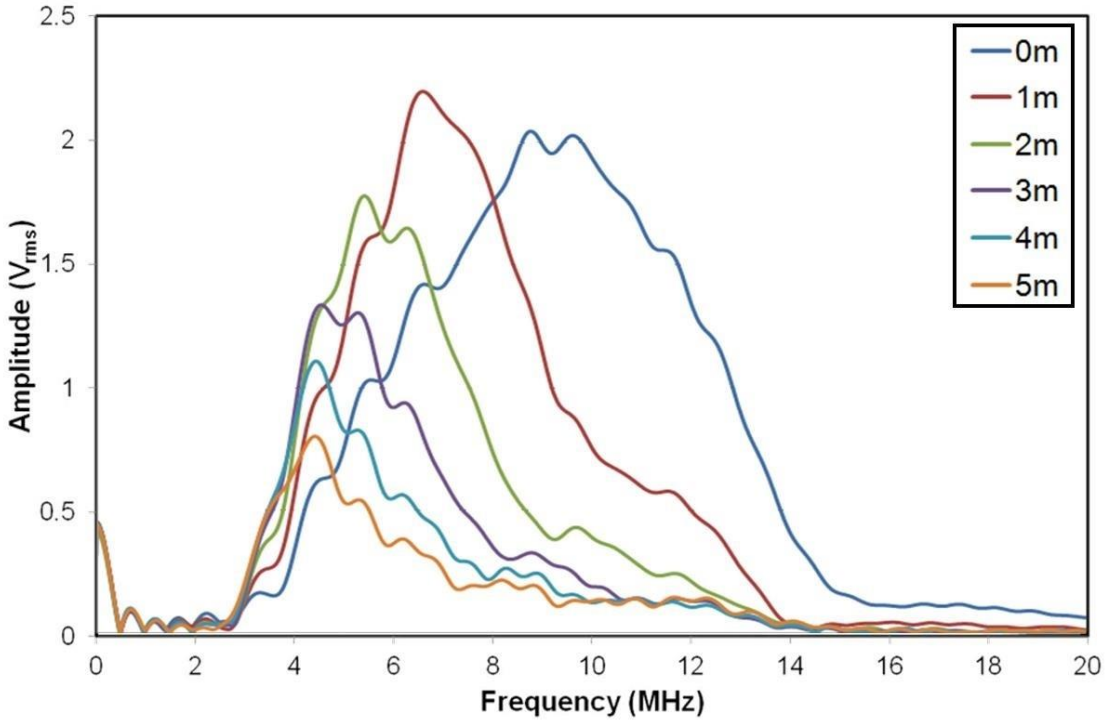

Figure 7.19: Cable Length Test Response Frequencies.

7.3.2 Cable Testing Discussion and Conclusions

The successive reflections decay as expected due to signal attenuation and beam spread. When comparing equivalent reflections between the different cable length setups it is clear that the increased cable length results in a drop in signal amplitude, approximately 3dB per additional metre of cable. It also shows an attenuation in higher signal frequencies and a corresponding drop in the peak frequency. This manifests itself as a flattening of the signal, with duller rising and falling edges. This is likely to be an effect of the additional capacitance of the cable.

As well as the attenuation of the signal as it travels down the cable, the presence of different lengths of the cable will result in different electrical characteristics of the system. This may cause the efficiency of energy transmission from the UPR to the piezo to change and thus reduce the initial excitation pulse, and conversely reduce the proportion of the reflected wave that is converted back into electrical energy and received by the UPR.

This test setup does not account for effects introduced by any assembly differences in the various extension cables, such as the assembly of the connectors. Also an additional connector pair is introduced between the 0m case and all other readings. The significant change in the frequency spectrum between the 0m and 1m cases may be partially the result of this.

It is clear from these tests that the amount of cable used should be kept to a minimum to maintain signal integrity. Although increased amplification can be used to offset the reduced signal amplitude, albeit at the cost of a reduced signal to noise ratio, the frequency dependant attenuation is less practical to compensate for.

7.4 Slip Ring Noise

In addition to the cabling it was also important to ensure that the slip ring used was suitable for transmitting ultrasonic signals. Some benchtop testing was completed to ensure the Signal-to-Noise Ratio (SNR) of the ultrasonic signal was not significantly affected by the presences of the slip ring when it rotates.

7.4.1 Experimental Setup

The rotating side of a Michigan Scientific SR20 slip ring was mounted in a lathe along with an ultrasonic sensor bonded to a plain steel block. The stationary side was connected to the same UPR and cabling that was to be used in the rolling tests. The peak-to-peak amplitude of an ultrasonic reflection across the steel block was recorded as the slip ring was spun up to 2000RPM in incremental steps. A minimum sample of 4000 reflections at each speed was recorded and the maximum, minimum and standard deviation of the peak to peak amplitude at each speed was calculated.

7.4.2 Results

The peak-to-peak results against rotational speed from this testing are plotted in Figure 7.20. Also on this plot are lines showing the mean peak-to-peak amplitude when the lathe was stationary before and after the test was run. The distribution is described by the standard deviation relative to the mean, the maximum and the minimum values. The standard deviation of the peak-to-peak amplitude across these speeds is plotted in Figure 7.21.

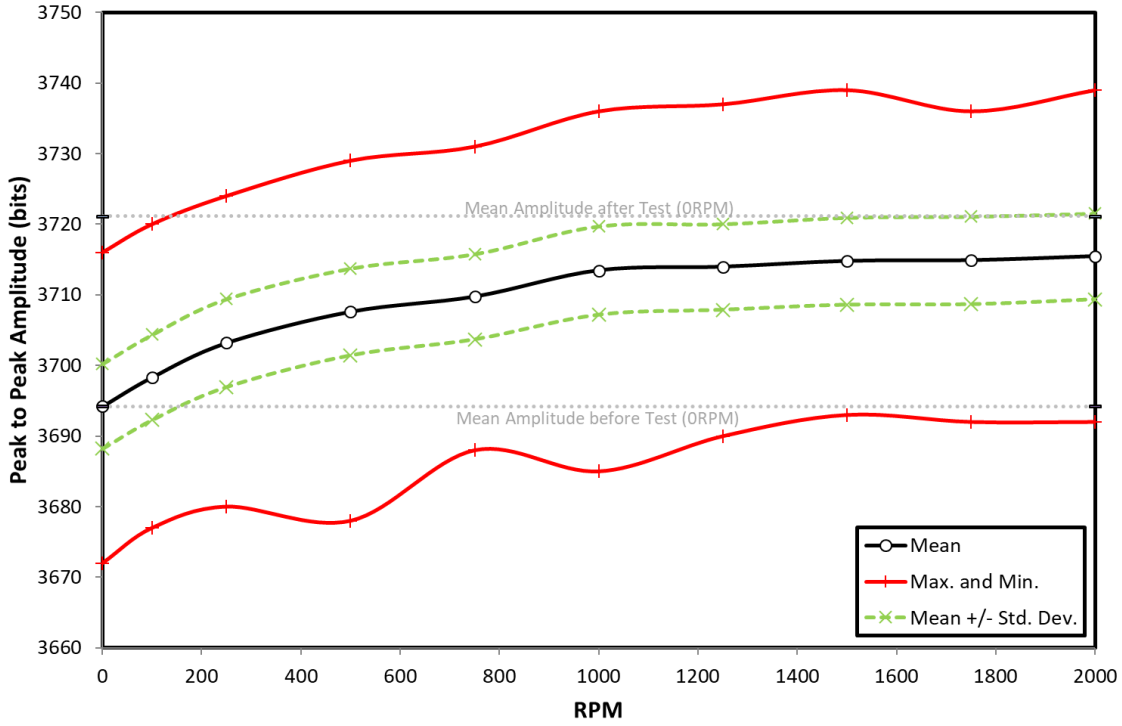

Figure 7.20: Change in Peak-to-Peak Amplitude for Mich. Sci. SR20 at Various RPM.

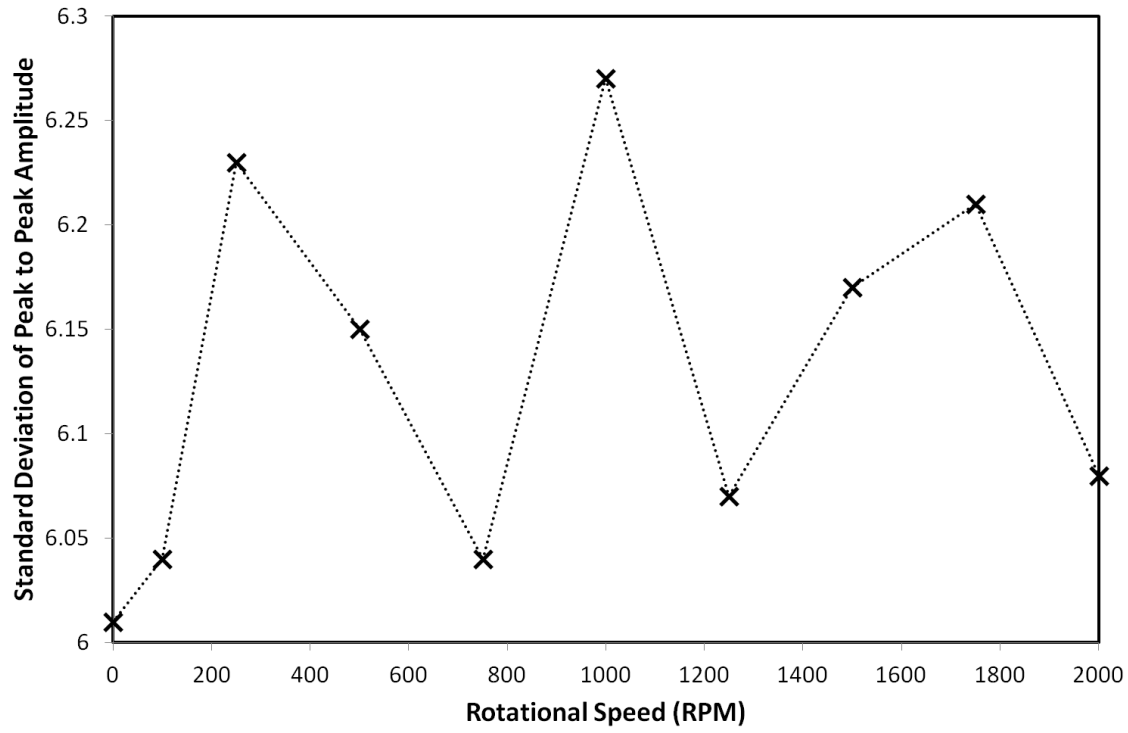

Figure 7.21: Standard Deviation of Peak-to-Peak Amplitude for Mich. Sci. SR20 at Various RPM.

The mean increased slightly (0.57%) between the initial stationary value and the value at 2000RPM. It remained at a higher value once lathe was stopped. This implies that the increase was not due to the rotational velocity, but a related effect which altered the slip rings electrical characteristics, such as heating, or the slip ring wearing in. Once the slip ring had been left for a period of time the peak to peak amplitude returned to its initial value, implying the former, previous studies have shown that slip ring heating due to frictional losses can be significant

(Magnussen, Nordlund, Châtelet, & Sadarangani). The standard deviation values are consistent and do not show any correlation to the rotational speed. This shows that the noise performance of the slip ring is independent of the rotational speed across the range tested.

Onsite tests were also performed to estimate the signal-to-noise ratio in the actual application environment. Tests were completed with a single shear and longitudinal transducer and with the roll stationary. Results were recorded using a Panametrics 5072R pulser combined with a Tektronics oscilloscope. For the Mercotac slip ring on the Sheffield rig the signal amplitude of **34mV** was recorded with baseline noise of **2mV** giving a Signal-to-Noise Ratio (SNR) of **17:1**.

For the Michigan Scientific slip ring on the semi industrial pilot mill the signal amplitude recorded with the FMS100 was around **1800 bits** with a standard deviation of **45 bits** giving a SNR of **40:1**. Some noise parasites were noticed when other machinery in the test area was turned on. The level of parasitic interference observed was not deemed significant enough to cause a problem during testing. When the mill was rotating (400m/min) the noise displayed a slight periodic variation, with each period corresponding to one rotation. This variation was very slight (<1%).

7.4.3 Slip Ring Testing Discussion and Conclusions

Testing on the level of noise of the system, including slip ring, has demonstrated that it is acceptable for the planned testing. The noise was recorded on the final test arrangement and was shown to be independent of rotational speed, a key concern. The SNR can further be improved by more shielding of the data acquisition hardware, cabling and slip ring. It can also be further mitigated in post processing through averaging and signal filtering.

7.5 Sensor Temperature Dependence

Temperatures seen by the sensor during testing may result in material degradation reducing its sensitivity. In §6.6.3 the piezo element was cooled using liquid nitrogen to demonstrate its survival during the freezing of the plug for assembly. The sensor may also see elevated temperatures due to heating in the roll, and the application of heated lubricant.

The PZT-5A1 piezo material used has a stated operating temperature of 290^{o}C (Banks, Oldfield, & Rawding, Ultrasonic Flaw Detection in Metals; Theory and Practice, 1962), and a curie temperature of 370^{o}C (Morgan Technical Ceramics Electroceramics). This makes it suitable for the cold rolling temperatures expected for both pilot and industrial testing. Piezo materials capable of withstanding higher temperatures (up to ~500^{o}C) are available; these may be of interest for hot rolling applications.

Despite the fact that the piezo material being used is known to survive up to the planned temperatures, it is still important to understand how the response of the material will change with temperature. Any temperature dependant effects have the potential to invalidate reference measurements taken at a different temperature. Therefore temperature profile testing was completed on the sensors to understand this.

7.5.1 Experimental Setup

The instrumented roll-slice shown in §6.6.3 was used to record a sensor temperature profile. The roll segment was instrumented with thermocouples and placed in an oven. This was then heated to 110^{o}C while the ultrasonic peak-to-peak amplitude was recorded. As described earlier

the selected sensor type was bonded directly to a surface using a strain gauge adhesive. This adhesive is rated for continuous use at temperatures down to –269°C and up to 250°C.

7.5.2 Results

The results for the longitudinal and shear sensors are shown in Figure 7.22 and Figure 7.23 respectively.

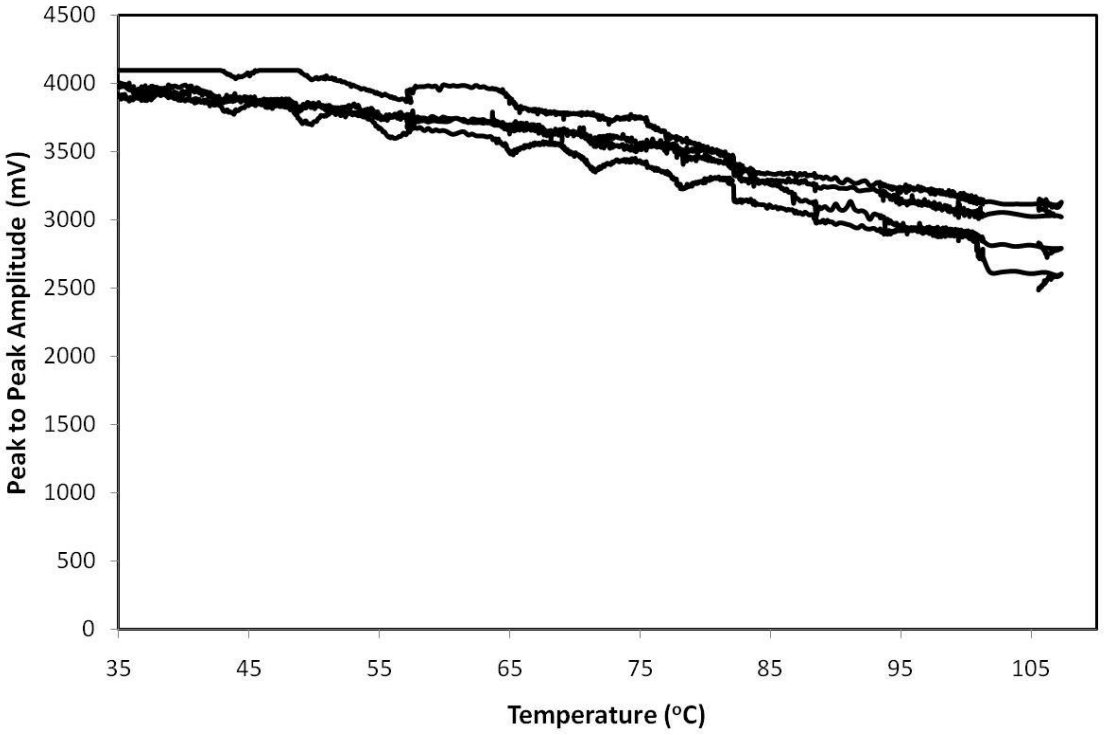

Figure 7.22: Longitudinal Response against Temperature for 10 MHz sensors.

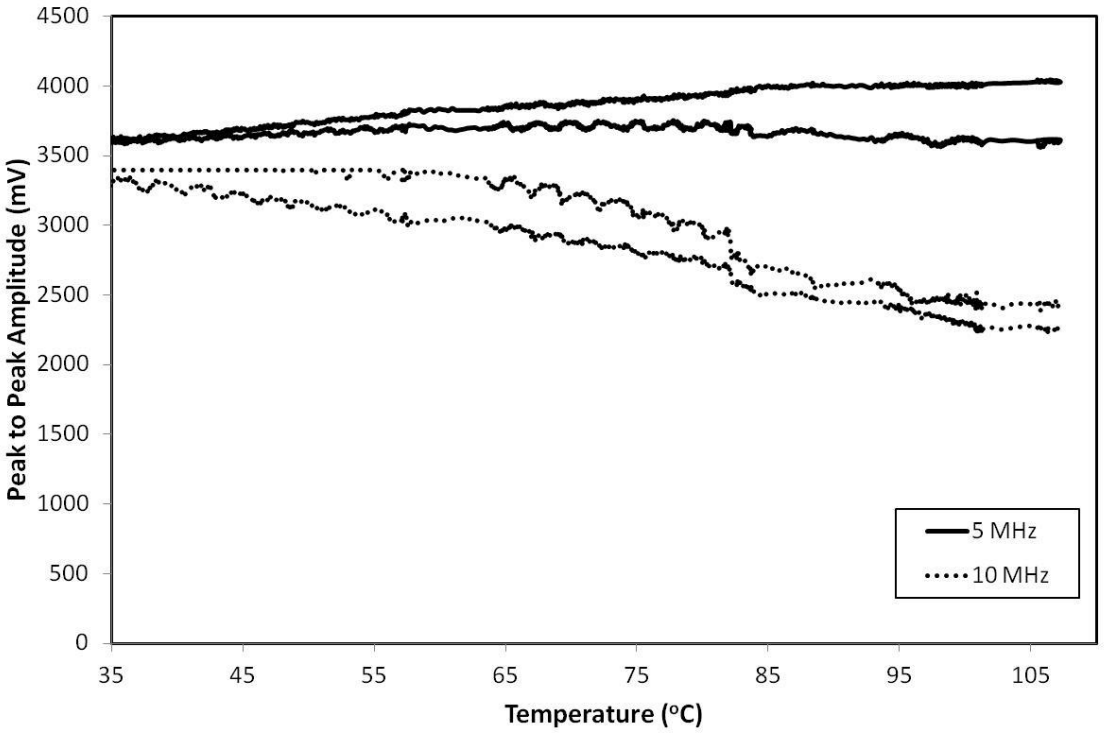

Figure 7.23: Shear Response against Temperature for 5 MHz and 10 MHz sensors.

7.5.3 Temperature Profiling Discussion and Conclusions

As expected the response from the majority of the sensors drops with increased temperature. With the exception of the 5 MHz shear sensors which increase slightly with temperature. The cause of this has not been identified, however this result is observed on both 5 MHz sensors that were tested. The digitiser had a maximum range of 4096, and it can be seen that one of the 5 MHz shear sensors swamps the digitiser at higher temperatures.

Some sections of the curves show a periodic variation. This is due to phase shift of the signal. As only the real amplitude of the signal is measured, and the imaginary part of the signal is not accounted for, phase variations may result in a slight change in the peak-to-peak magnitude.

The change in the peak-to-peak amplitude of the signal is the result of the combined effects of adhesive relaxation, piezo material sensitivity and material attenuation. The measurement approach taken accounts for all of these and therefore the results presented are representative of the changes that will be seen in the final testing. The absolute value does not drop significantly enough within the expected temperature range to represent a problem to the measurements being taken. The reduction in amplitude can be mitigated by increasing the signal amplification. However, this result reinforces the need to record any reference measurements at temperature to cancel out any effects of temperature variation during the testing.

7.6 Cold Rolling Pilot

To test the measurement feasibility an initial pilot test program was completed on a pilot mill. The purpose of this testing was to prove the concept of the proposed measurements, inform the data acquisition setup, provide data for development of the data processing algorithms and thus de-risk the work before implementation was carried out on a semi-industrial mill. An overview of this testing is given below.

7.6.1 Experimental Setup

The experimental setup for the pilot mill is described in greater detail in §6, with the mill detailed in §6.1.1 and the instrumentation carried out in the manner described in §6.6.1.

The pilot mill is relatively small so to ensure the strip to be rolled did not damage the rolls, plugs or mill the strip was annealed before rolling. The mill was hand fed and lubricant was applied by brushing the strip before insertion.

The small roll diameter resulted in a small roll bite length, and correspondingly a small sensing area. A larger roll bite would be preferable in giving a greater resolution to the roll bite. To aid this a large strip thickness and reduction were used. The mill would not bite the strip when samples were >5mm, so initial samples were prepared by hot rolling until an acceptable strip thickness was found, this was ~4mm. Each strip sample was approximately 200mm long and fed through the mill in multiple passes, the roll separation being reduced each time to yield the same reduction.

The instrumentation broadly performed as expected, with only a couple of points for consideration for the semi-industrial implementation. As noted in §6.6.1 the plug technique resulted in marking of the strip. This implied that either the plug was deforming more than the surrounding roll material, that the plug was being pushed into the roll due to inadequate support, or a combination of both effects. For the industrial testing roll material was used to

manufacture the plug, and the plugs were significantly larger with more supporting material. Marking of the strip is unacceptable in industrial rolling and so this is an important result when considering the industrial adoption of the technology.

The UPR had a Pulse Repetition Frequency (PRF) of 20 KHz with an excitation pulse amplitude of ~150 V. The UPR has an input attenuator and a fixed 20 dB preamp, in addition to this the UPR variable gain amplifier was set in the range of 20-30 dB and was varied between sensors to ensure a consistent response.

7.6.2 Ultrasonic Response

A typical A-Scan from an instrumented plug would be expected to feature an initial pulse followed by a number of repeated reflections from the interface being studied. This was observed for both the longitudinal and shear sensors tested, but for the purposes of this study only the first reflection from the plug-strip interface was considered.

Figure 7.24 shows the first reflection from a longitudinal sensor. This shows a distinct signal, approximately 0.4 μs in duration, which implies good damping and signal bandwidth.

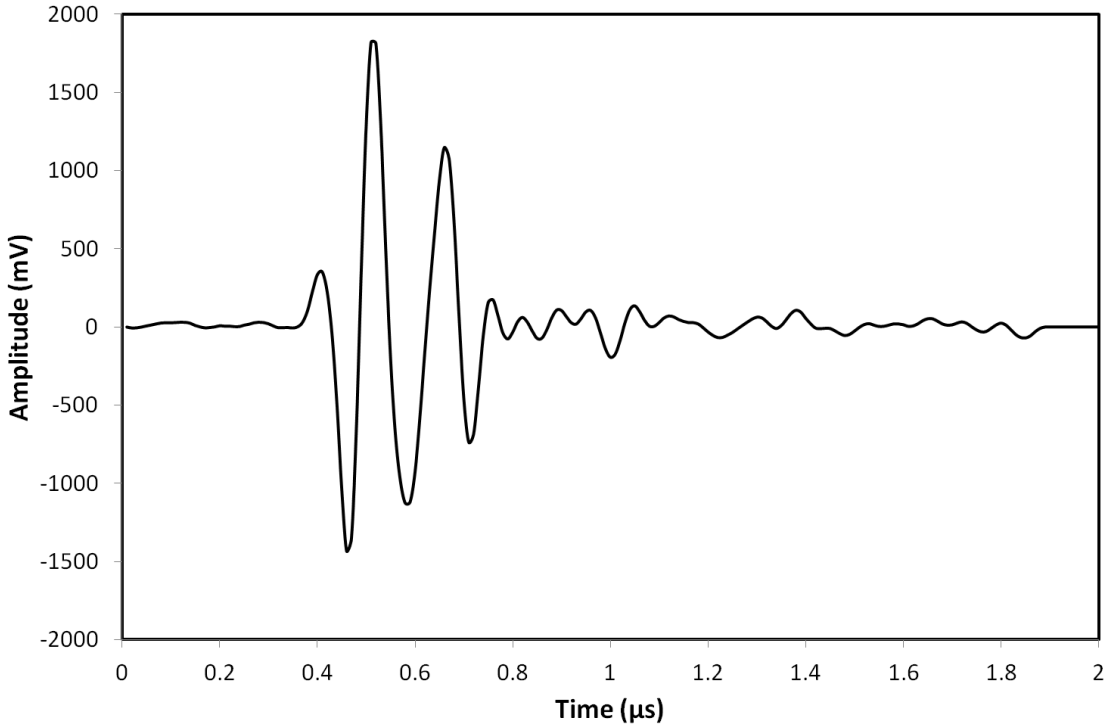

Figure 7.24: Longitudinal Sensor Reflection.

The response from one of the shear sensors is shown in Figure 7.25. The sensor exhibited multimode resonance as described §5.3.4. The plug method of installation made removing the shear piezo and changing it to a more suitable element impractical. Instead feasibility testing proceeded with this sensor and a new sensor with different dimensions was used for the semi-industrial testing, which resolved this issue. Figure 5.6 and Figure 5.7 show the responses from the semi-industrial and pilot mill shear sensors.

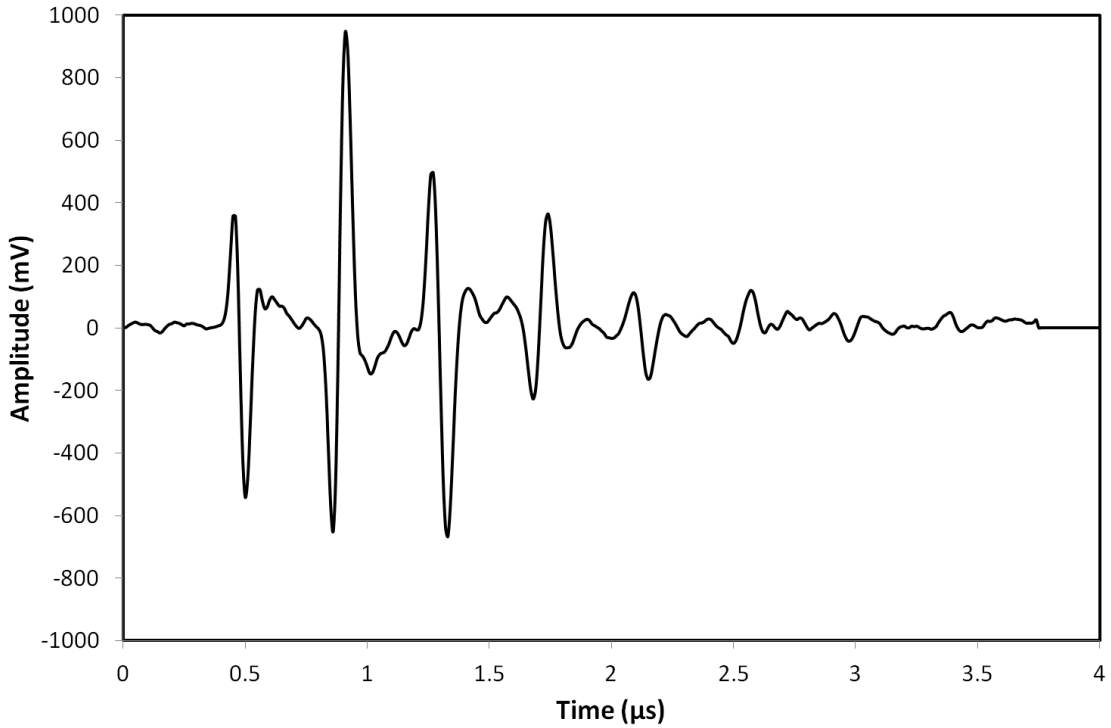

Figure 7.25: Shear Sensor Reflection.

Once the response of the elements had been verified the next step was to ensure that the rolling interface could be measured. Figure 7.26 shows the response of the longitudinal sensors first as the plug face is exposed to air as a reference, then when it was in contact with the strip in the roll bite contact. Figure 7.27 shows the surfaces that the pulses in Figure 7.26 reflected from.

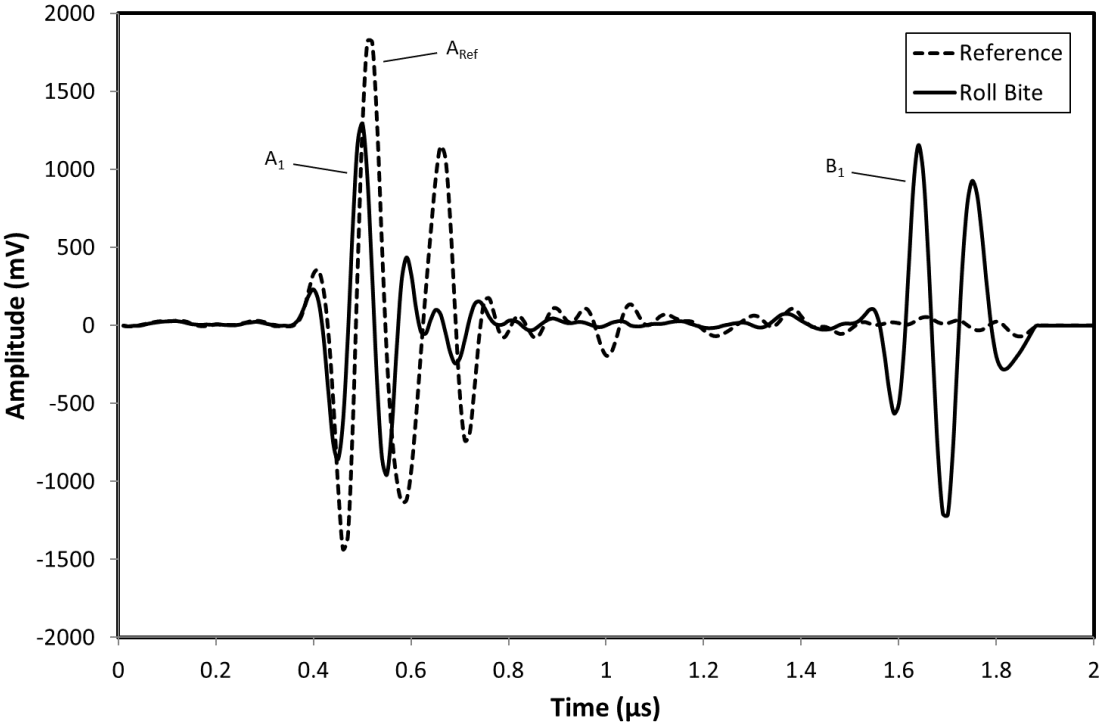

Figure 7.26: Longitudinal Response in the Roll Bite.

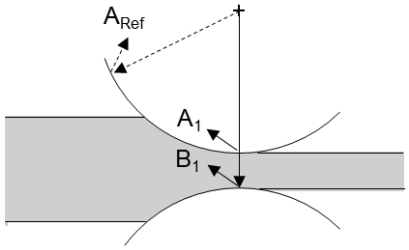

Figure 7.27: Reflecting Surfaces in Roll Bite.

The response taken when the sensing face was exposed to air showed a single clear reflection from the interface, as expected. As the sensing face begins to come into contact with the strip the amplitude of this initial reflection begins to reduce as some of the wave is transmitted into the strip. A second distinct pulse also begins to appear. The first larger pulse corresponds to the plug-strip interface. By taking time difference between this and the successive pulse, and using a tabulated value for the speed of sound in mild steel, it could be calculated that the second pulse occurred from an interface approximately 3.34mm further on from the plug-strip interface. This is consistent with the interface between the bottom roll and strip. In addition to the change in amplitude the signals also show a slight phase-shift between the first reflection of the reference (A_{ref}) and the signal in the roll bite (A_1). This phase shift is caused by the presence of the thin lubricant film in the roll bite, as reported by Reddyhoff et. al. (Reddyhoff, Kasolang, & Dwyer-Joyce, The Phase Shift of an Ultrasonic Pulse at an Oil Layer and Determination of Film Thickness, 2005). In addition to the phase-shift there is also the potential for the presence of the lubricant film to alter the frequency content of the pulse reflected from the lubricated layer, as shown in §3.5.2, which can also lead to a change in pulse shape.

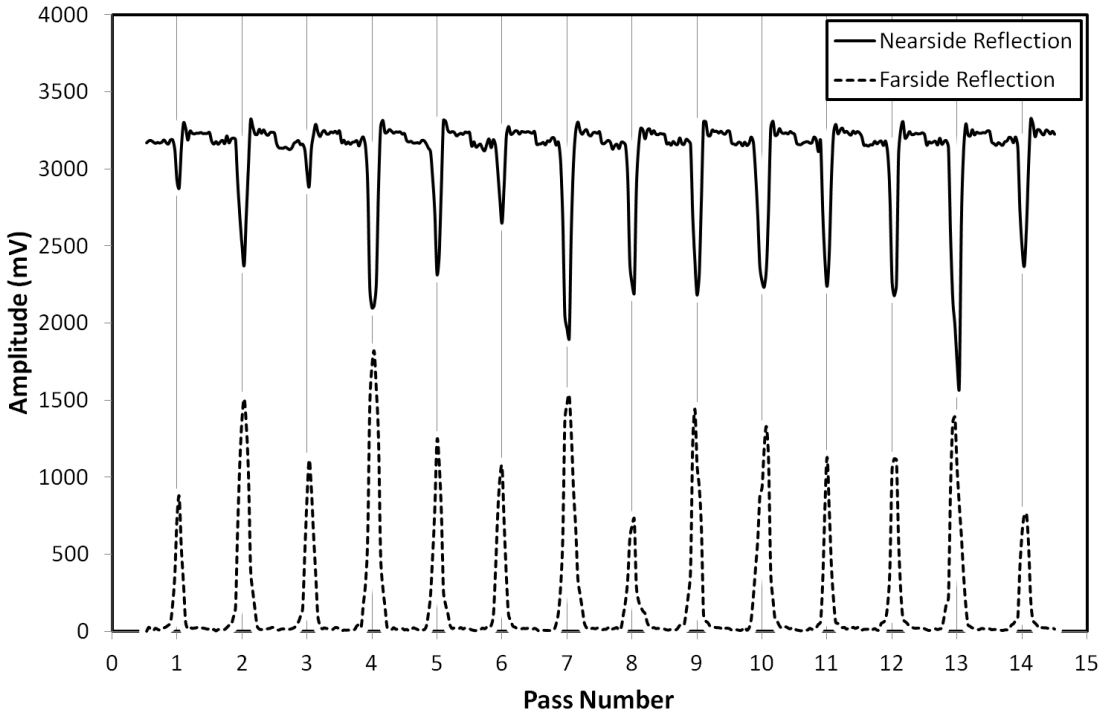

Figure 7.28: Peak-to-Peak Amplitude of Top and Bottom Strip Interfaces for Multiple Passes.

With the sensing face fully in contact with the strip the initial pulse amplitude reached a minimum and the pulse from the far side of the strip increased to a maximum. The peak-to-peak amplitude of these two pulses for a number of successive strip passes can be seen in Figure 7.28.

The figure shows symmetry between the reduction in the nearside reflection, A_1, and the subsequent increase in the farside reflection, B_1, for a given pass. There did not however appear to be any correlation between the amplitude changes seen in successive passes, despite the rolling conditions being nominally the same. The mill reduction is adjusted manually via a screw, the accuracy of which is unknown. It was likely that the reduction applied varied significantly between passes.

As a clear reflection was received from both the top and bottom interfaces it may be possible to simultaneously measure the interface on either side of the strip. This would potentially capture any asymmetric effects. However, as no reference is possible for the far interface using the pilot mill setup this analysis is not trivial. As the pulse from the far strip interface passes through the near interface twice this also has to be accounted for, and is beyond the scope of this thesis. The rest of the interface analysis concentrates only on the pulses returned from the top interface.

7.6.3 Reflection Coefficient

The reflection coefficient can be calculated from the peak to peak value of the returned pulse, however this is susceptible to peak detection and phase shift errors. These can be avoided by studying the pulse in the frequency domain. A Fast Fourier Transform (FFT) was used to convert the ultrasonic response from the time to frequency domain and the amplitude spectrum for the longitudinal sensor is shown in Figure 7.29. A clear reduction in the pulse amplitude across a range of frequencies can be seen when in contact with the roll bite. This indicates some of the wave has been transmitted through the interface.

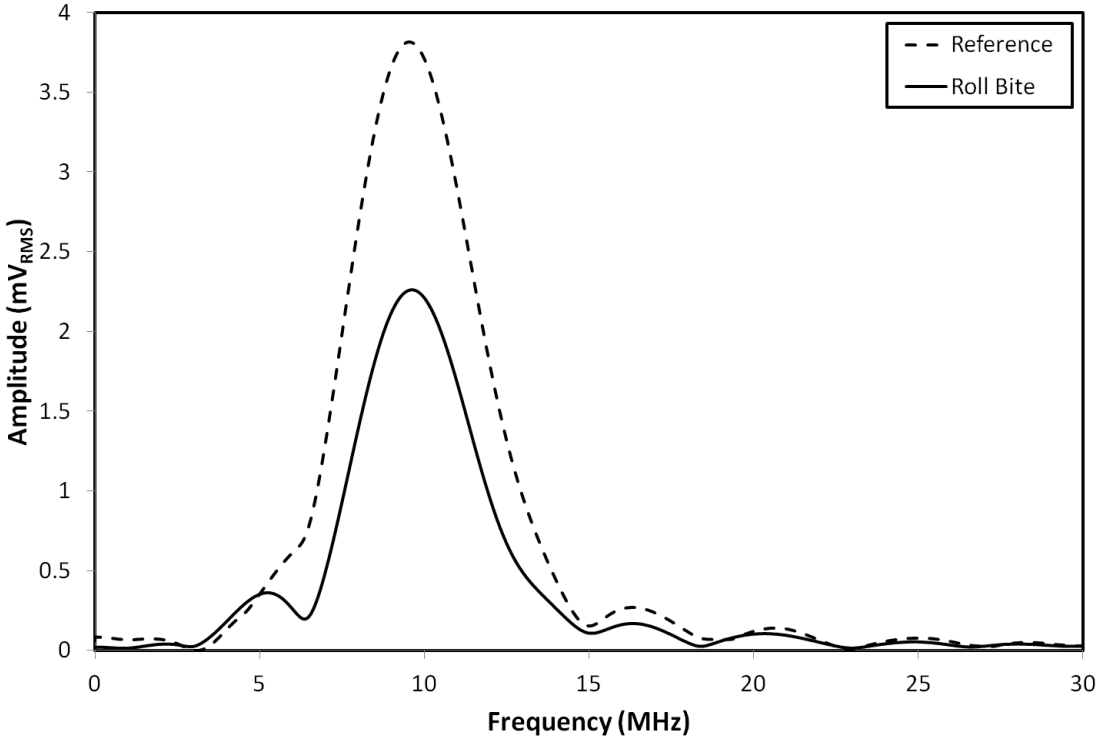

Figure 7.29: Frequency Spectrum of Longitudinal Reflections.

7.6.4 Stiffness

Dividing the roll bite FFT by the reference FFT gives the reflection coefficient over a range of frequencies. By using a reference any attenuation effects in the material are cancelled out. Figure 7.30 shows the reflection coefficient for the data plotted in Figure 7.29. In Figure 7.30 the pulse amplitude spectrum has been overplotted to show the frequencies where the most energy is, this corresponds to the highest signal-to-noise ratio.

Using these values for the reflection coefficient and a tabulated value for the acoustic impedance of steel (z = 46 MRayls) in Equation 3.76 the stiffness was calculated and has been plotted in Figure 7.31.

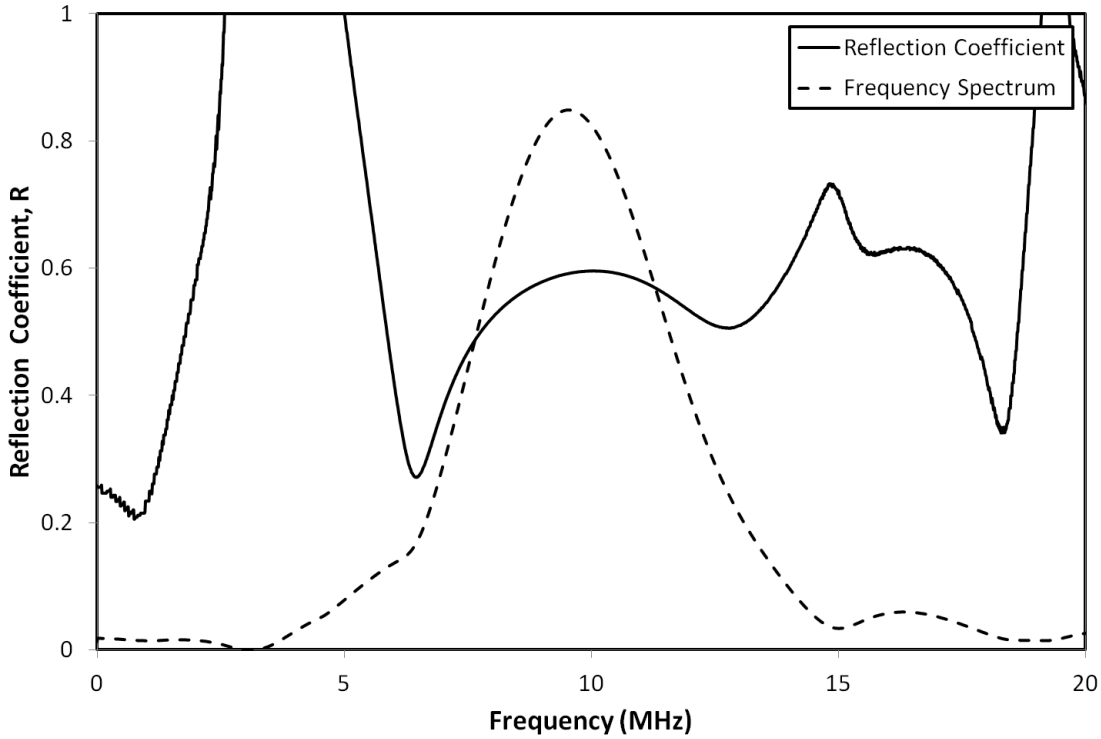

Figure 7.30: Reflection Coefficient against Frequency, the Pulse Amplitude Spectrum over plotted with an Arbitrary Scale

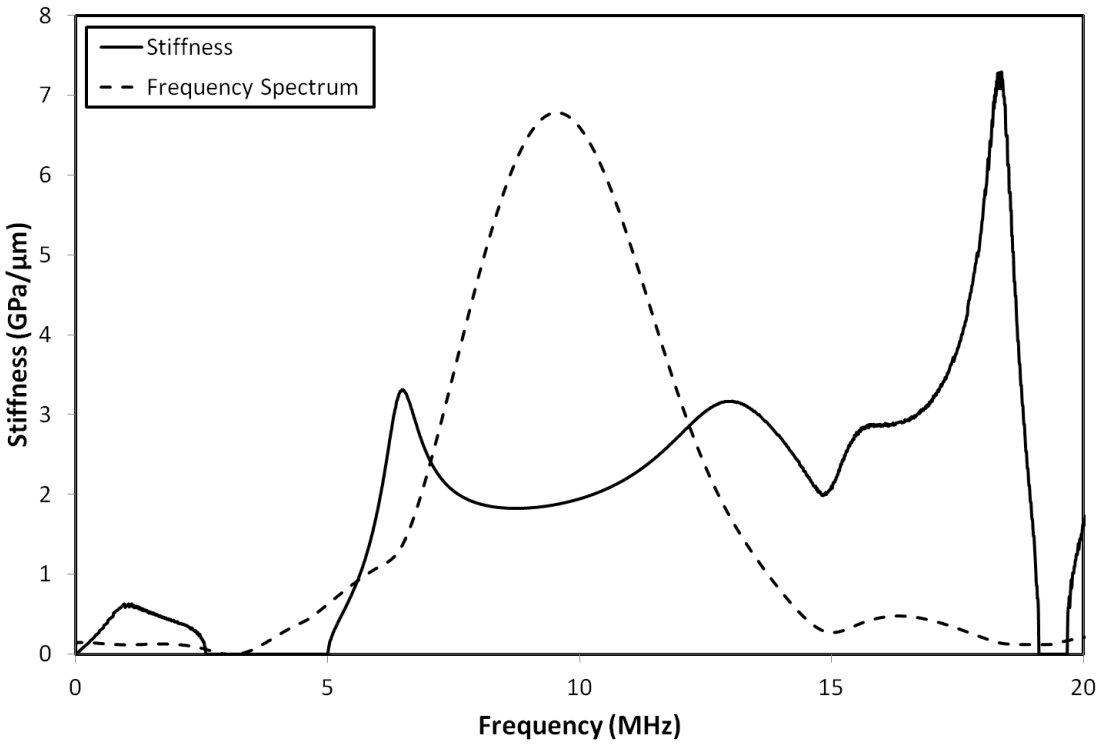

Figure 7.31: Stiffness against Frequency, the Pulse Amplitude Spectrum over plotted with an Arbitrary Scale.

Results were taken and the stiffness calculated for both lubricated and non lubricated cases. The longitudinal stiffnesses for two measurements of each case are shown in Figure 7.32.

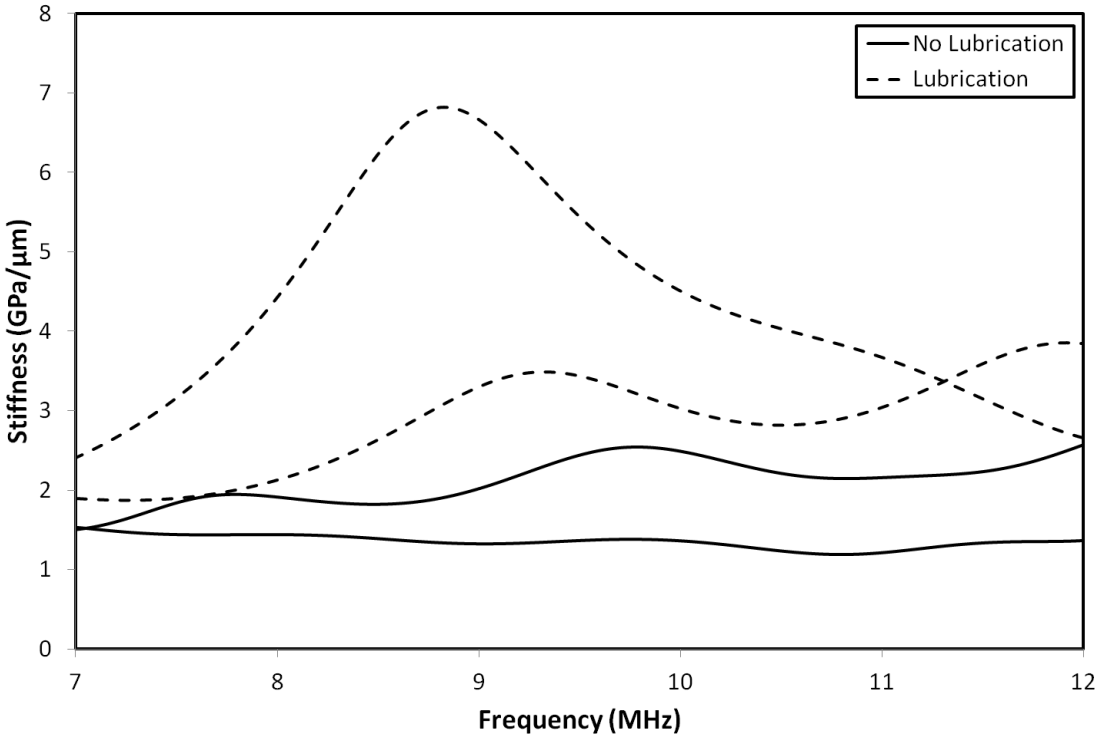

Figure 7.32: Longitudinal Stiffness for both Lubricated and Non-lubricated Interfaces.

The lubricated cases can clearly be seen to have a higher stiffness than the non-lubricated cases. This is expected because the longitudinal stiffness represents total stiffness of the interface, due to both the asperity contact and lubricant in the interface. However both cases showed a large variation in the stiffness measured. Comparing the results of the non-lubricated stiffness to the stiffness predicted by Greenwood & Williamson's (Greenwood & Williamson, 1966) elastic hemisphere asperities model also gives a good correlation, the model giving a stiffness of **1.72 GPa/µm** and the experiments an approximate value of **1.5 to 2.3 GPa/µm** at the pulse centre frequency, 10 MHz.

Although the shear response was not as normally expected, due to the multimode resonance, it was still possible to extract some useful data. A second reflection from the far strip-roll interface was not clearly observed, however may have been obscured by the initial reflection due to its extended pulse length. Figure 7.33 shows the interface stiffness calculated from shear response, using the same technique described above.

This time it can be seen that the lubricated and non-lubricated cases have similar shear stiffness. This is expected because liquids do not support a shear force, therefore they do not contribute to the shear stiffness, so the shear sensor should only represent the solid stiffness which is the same in both cases.

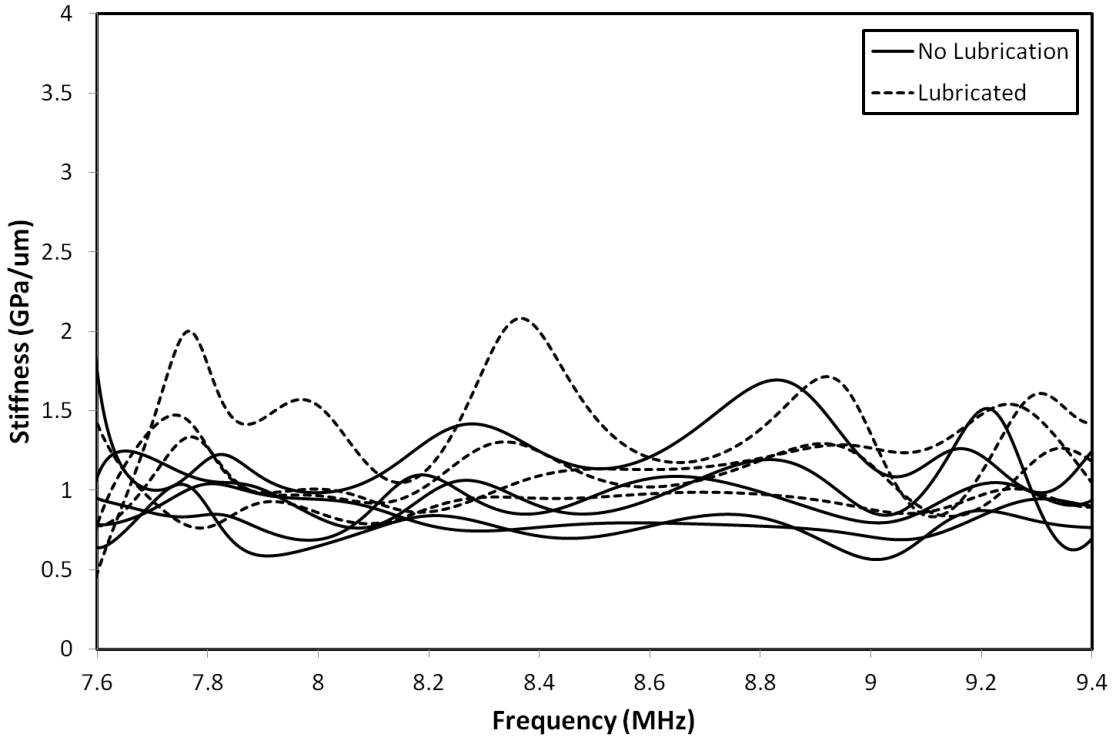

Figure 7.33: Shear Stiffness for both Lubricated and Non-lubricated Interfaces.

The lubricant stiffness can be calculated by taking the difference between the total and solid stiffness. In order to do this the shear stiffness must first be converted to an equivalent normal stiffness using Equation 3.85, Poisson's ratio was taken as 0.3.

Using Equation 3.87 the film thickness can be measured. Approximate values for the lubricated stiffness at 9 MHz from the above plots where taken to be 3 GPa/µm for the longitudinal and 1 GPa/µm for the shear measurement. Combining this with an assumed bulk modulus of 1.8 GPa

(taken for the lubricant at atmospheric pressure and 25°C from Figure 6.13), yields a film thickness of **1.008µm**. This is in the region of film thicknesses expected based on the combined roughness of the two interface surfaces (~1µm).

Although the above film thickness calculation uses only approximate values, with large uncertainties, the values are representative of those observed during testing. The agreement between the resultant film thickness value and that expected from the surface roughness's gave a good degree of confidence that similar measurements could be taken on the semi-industrial mill.

7.6.5 Strip Thickness and Plug Deformation

The reflections from the near and far interfaces of the strip allowed for the Time-of-Flight (ToF) across both the plug and strip to be extracted, as shown in Figure 7.34. By combining the ToF with a tabulated value for the speed of sound in mild steel (5800 m/s) the strip thickness could be measured.

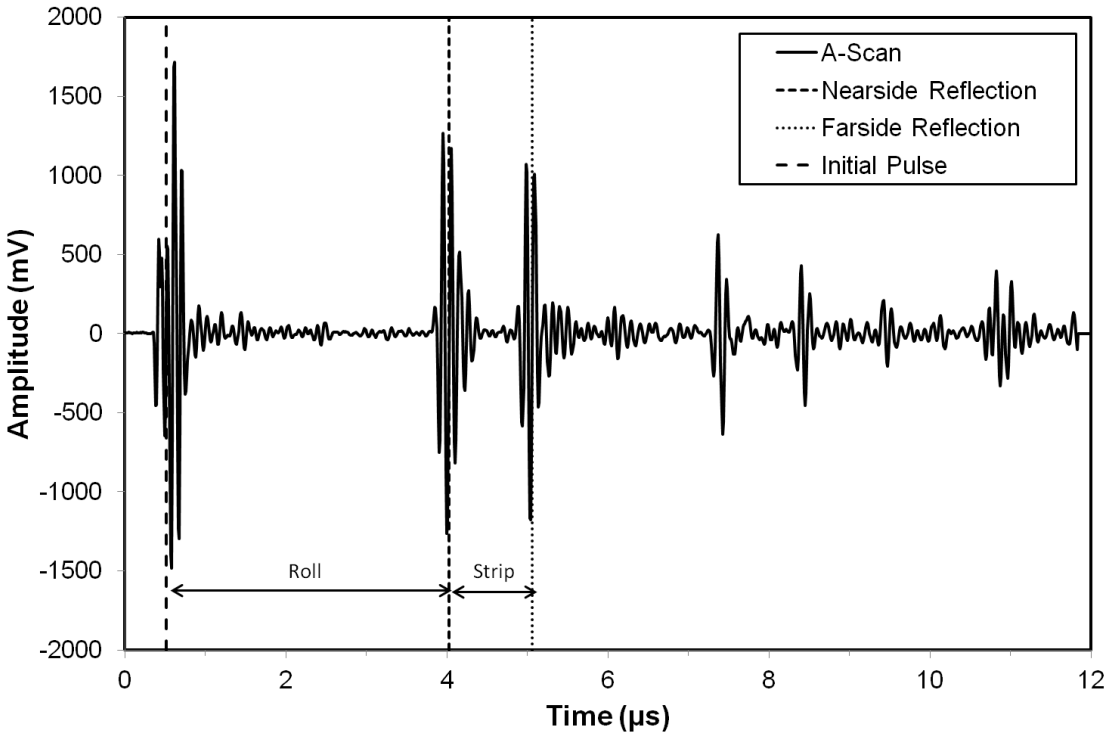

Figure 7.34: Ultrasonic Response showing the Reflections from the Near and Far Strip Interfaces.

A plot of the results for the strip thickness calculation for 14 consecutive passes is given in Figure 7.35. The strip thickness for each pass, calculated from the average of the 5 most central data points, is plotted in Figure 7.36. The gradual reduction of the strip can clearly be seen.

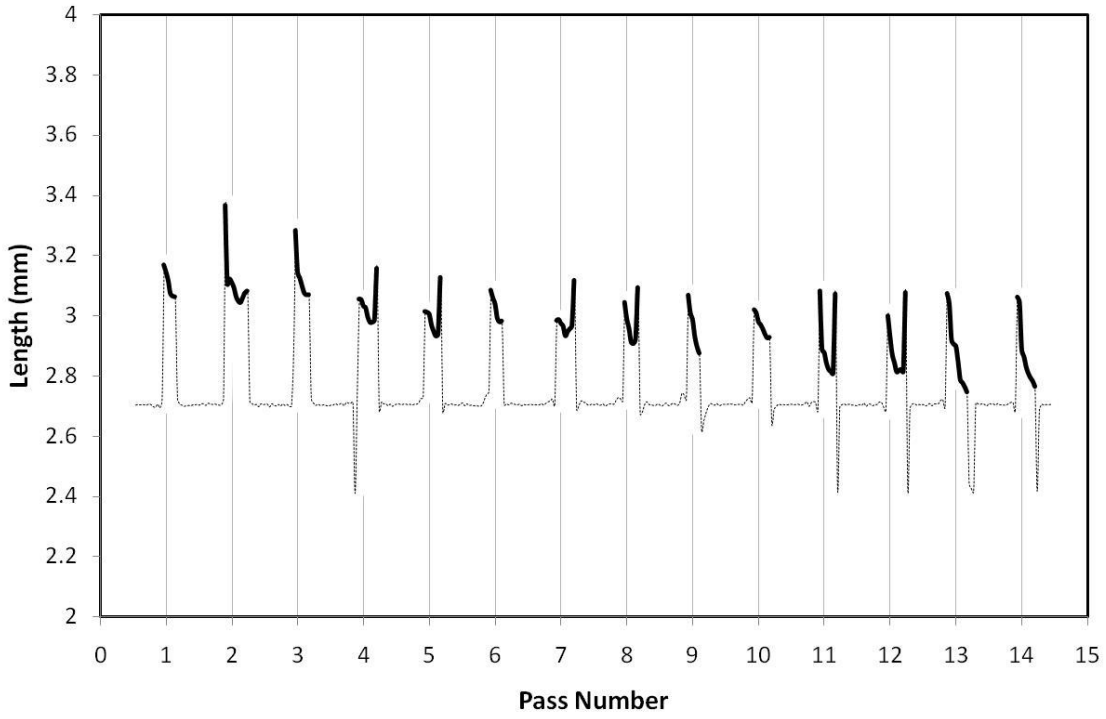

Figure 7.35: Strip thickness Measured from the ToF for Consecutive Passes of the same Strip.

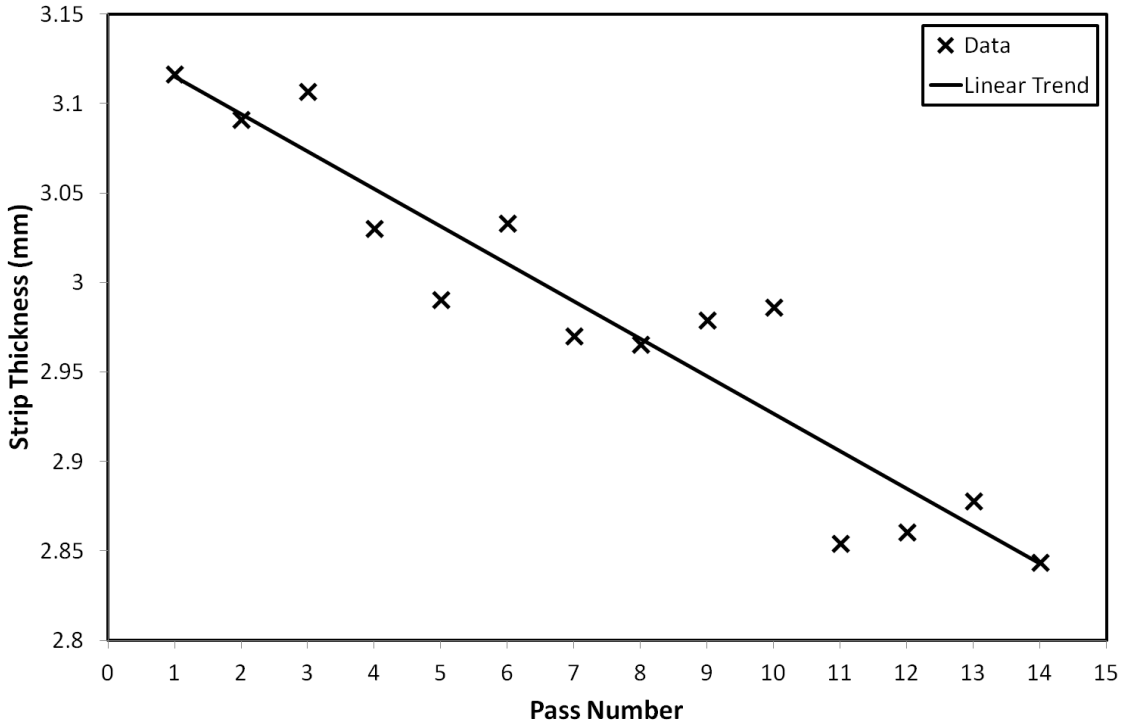

Figure 7.36: Strip Thickness for Multiple Consecutive passes of the Strip, calculated from the average of the centre 5 points across the Roll Bite.

The trend line in this plot is the equivalent of a 20.9 µm reduction per pass. The mill was set to have a consistent reduction of 25 µm. It is clear from these results that the multiple passes are not consistent. It is suspected this is due to inaccuracies in the mill when setting the reduction.

A similar approach was taken to measure the ToF across the plug during rolling. A plot for the same 14 consecutive passes is given in Figure 7.37.

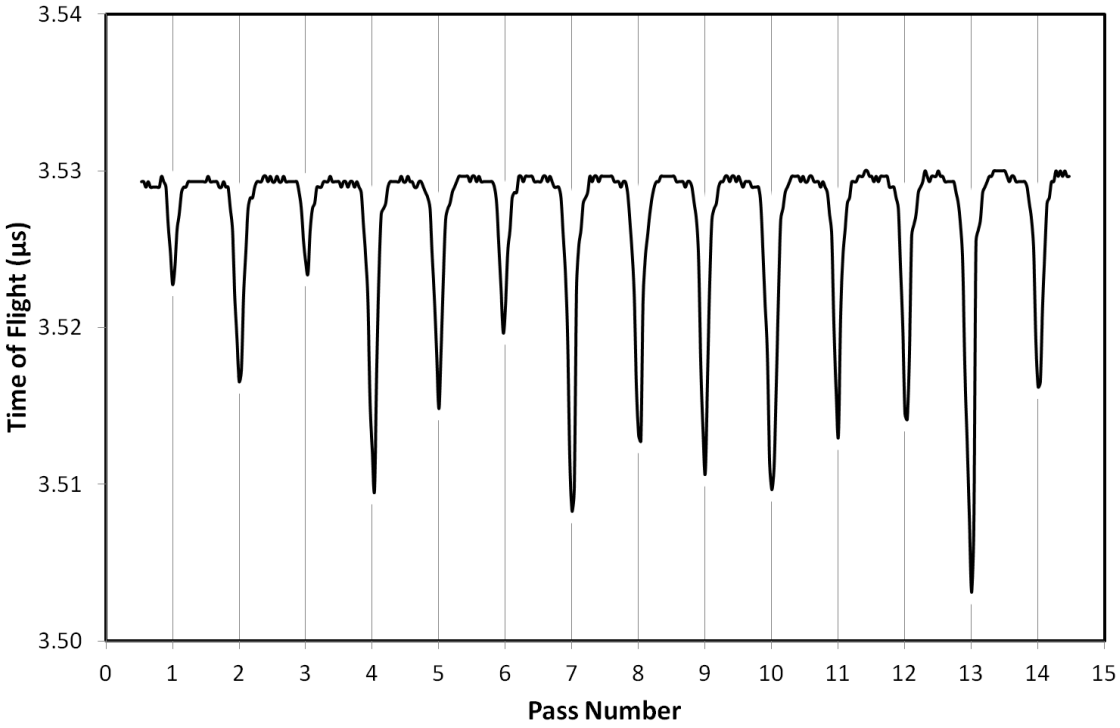

Figure 7.37: Plug ToF for Multiple Consecutive passes of the Strip.

Acoustoelastic material properties were not available for the plug material. Additionally, as demonstrated by the strip indentation, it was known that the plug deformed inconsistently with the roll. Therefore, the acoustoelastic calculations where not performed on the plug ToF data. However, this data does demonstrate the ability to measure the ToF to nanosecond accuracy.

7.6.6 Pilot Testing Discussion and Conclusions

The results from the pilot mill were promising, demonstrating in principal the measurement of lubricant film thickness, strip thickness and plug Time-of-Flight. The testing gave the opportunity to learn about limitations in the measurements and highlighted areas which can be improved upon for the semi-industrial testing.

The lubricant film thickness measurements showed that reasonable values for stiffness could be measured for both the longitudinal and shear waves, and that these could be used to calculate realistic values for the lubricant film thickness in the interface. A clear difference could be measured between lubricated and unlubricated interfaces. Processing of the results demonstrated the need for accurate material properties to be understood in order for the calculations to yield reliable film thickness results. Based on this the materials used for the plugs in the semi-industrial tests were acoustically profiled to give the relevant material properties, as shown in §8.

It was shown that the size of the roll bite contact relative to the sensing area is of great importance. In the preliminary testing the rolls were of a relatively small diameter, and the mill has a small rolling force. In the semi-industrial mill both the rolling force and roll diameters will be larger. This will result in a larger contact area, meaning higher resolution measurements of the interface can be captured across the roll bite. An additional improvement made to the

instrumentation for the semi-industrial test setup which will improve the resolution was to decrease the sensor size, and therefore the reduce the size of the sensing area relative to the contact size.

The lack of mill instrumentation made verification of the measured results difficult. In particular, the inability to measure rolling force and elongation. As well as being unable to measure it, the setting of the reduction was inaccurate causing errors when comparing the results. This led to these additional signal feeds being recorded along with the ultrasonic data in the semi-industrial tests.

The lack of strip tensioning due to the pilot mill being hand fed resulted in inconstant entry of the strip, and limited the variety of rolling cases that could be tested. This was remedied in the semi-industrial testing through the use of tension devices and coilers/uncoilers installed on the mill.

A number of improvements were also made to the acquisition software following the pilot testing. The software was adapted to record at higher speeds. It was also adapted to be able to process sample results in real-time to reduce the amount of post-processing required and aid troubleshooting.

Finally, the pilot testing demonstrated how the design of the plug implementation left noticeable marks on the strip after rolling. It is suspected that this occurred due to the plug having inadequate supporting material for the rolling loads used, causing the plug to withdraw into the roll. The design of the plugs used was investigated because of this and changed for the semi-industrial tests following this discovery. Larger plugs with a greater amount of support from the roll were used to reduce the effect.

7.7 Conclusions

A number of experiments have been presented in this chapter, each with the aim to de-risk semi-industrial pilot testing by quantifying or validating a different aspect of the proposed measurements. This will provide material property inputs to the mathematical models and allow the data acquisition approach to be fine-tuned.

Tests were completed comparing the ultrasonic spring model and resonant dip thin film measurement techniques to a calibrated laser interferometer. The thinnest films measured using the film resonance method were ~30 µm and films up to ~11µm were measured with the spring model. The results from the film resonance method showed a very strong correlation to the calibrated measurement. There was slightly more scatter in the spring model results, however it still showed good correlation. As the roll bite is a mixed mode interface under normal operation, it is expected that the lubricant films present will be of the order of the interface combined surface roughness. These will therefore fall within the spring model measurement window rather than the resonant dip regime.

A value of -2.685 was measured for the longitudinal acoustoelastic constant. This compares well with equivalent values found in literature. The measured value for the shear acoustoelastic constant was -1.757. The maximum stress for which reliable data was recorded was ~40 MPa. It is assumed that this relationship can be extrapolated to reach the stress magnitudes seen in cold

rolling. Also the loaded specimen was assumed to be in plain compression however the support of the loaded part may have allowed it to bend and so result in a more complex stress pattern.

Testing was performed to understand the effect of the cabling and slip ring on the signal. This showed that increased cable length results in a drop in signal amplitude, by approximately 3dB per additional metre of cable. It also shows an attenuation in higher signal frequencies and a corresponding drop in the peak frequency. It is clear from these tests that the amount of cable used should be kept to a minimum to maintain signal to noise ratio.

The slip rings were tested in the rolling mill environments to estimate the signal-to-noise ratio (SNR) in the final application. Results for the Mercotac slip ring on the Sheffield pilot mill gave a SNR of 17:1. For the Michigan Scientific slip ring on the semi industrial pilot mill the SNR recorded was 40:1. Tests were also run with the Michigan Scientific slip ring to see it's stability across a range of rotational speeds. A slight change in amplitude was observed as the slip ring was spun, however it is believed this is due to slip ring heating, and not directly due to the rotational velocity. This showed that the noise performance of the slip ring is independent of the rotational speed across the range tested.

The sensors used on the roll segment instrumentation were temperature profiled. These are the same element types as later used on the plugs inserted into the semi-industrial mill. The amplitude response of all the sensors, except for the 5 MHz shear sensors, dropped with increased temperature. This change in amplitude is the result of the combined effects of adhesive relaxation, piezo material sensitivity and material attenuation. Regular referencing during testing is required in order to reduce or remove the effects of these.

Initial pilot mill testing was performed in Sheffield with positive results. It demonstrated the plug instrumentation method and the principal of measuring lubricant film thickness, strip thickness and plug time-of-flight. The small roll bite contact size, lack of strip tensioning, limited lubricant application options and no precise rolling force or strip reduction control limited the pilot testing to proof-of-concept.

8 Ultrasonic Signals, Geometry and Material Properties

The following chapter covers the ultrasonic signals recorded during testing and the measurements made of the material properties and geometries, including the strip thickness and roll bite length.

8.1 Ultrasonic Signals

The following analysis shows the signals received from the instrumented plugs installed in the semi-industrial pilot mill. In total three plugs where instrumented with a longitudinal and shear sensor each. Two of these plugs where installed in a work roll while the third was used for bench top testing.

8.1.1 Longitudinal Response

The longitudinal A-scan recorded from a plug prior to rolling has been plotted in Figure 8.1. A number of successive reflections can be clearly seen, with a consistent spacing and gradual decay in amplitude. These are successive echoes of the same pulse as it travels back and forth along the length of the plug, with the drop in amplitude a result of attenuation in the material and losses at the reflecting surfaces. The clarity of these pulses shows the good operation of the sensor.

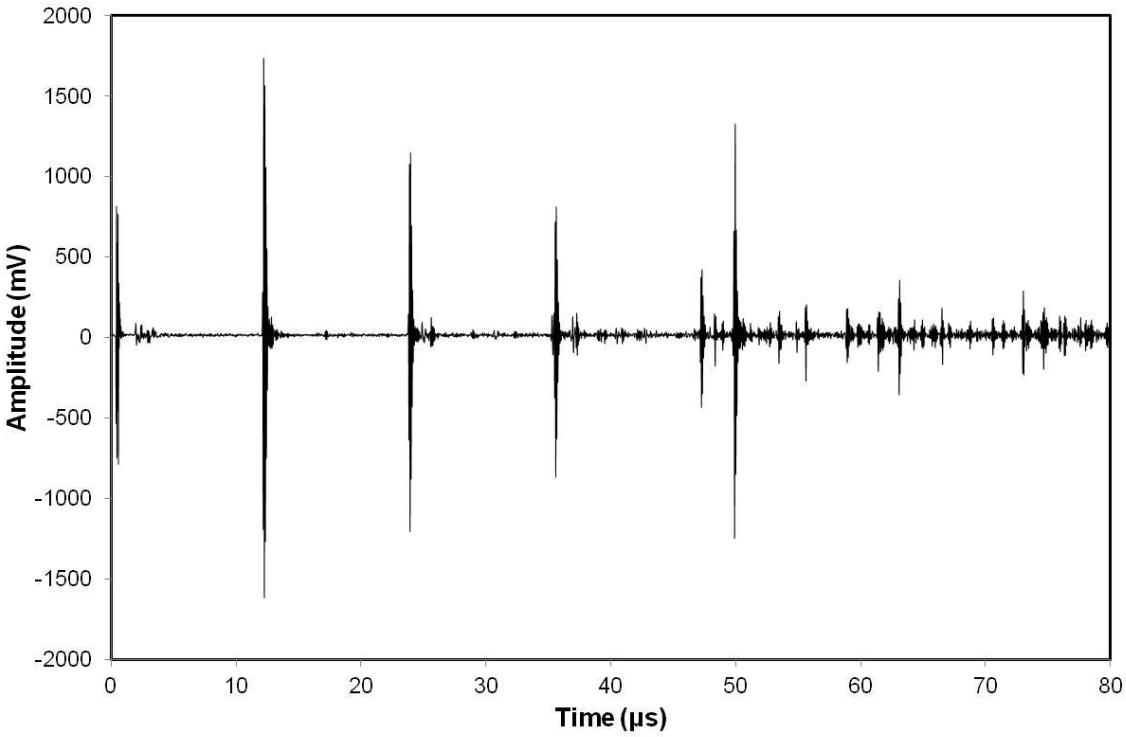

Figure 8.1: Plug 2 Longitudinal Sensor A-Scan.

At 50 µs a pulse is observed with timing and amplitude inconsistent with the decaying internal plug reflections. This A-Scan was recorded while the data acquisition hardware was connected to both the shear and longitudinal sensors. These two sensors were excited alternately with a pulse repetition frequency of 20 kHz, which corresponds to pulse separation time of 50 µs. The enlarged pulse is the result of crosstalk between the channels causing a proportion of the excitation pulse sent to the shear sensor to be detected on the longitudinal channel. This pulse

is omitted from the following analysis, only reflections corresponding to internal plug reflections are considered.

To inspect the consistency of the sensors on the two plugs installed in the work roll, the first reflections for both have been overplotted in Figure 8.2. The two responses show a good consistency, with near identical pulse shapes.

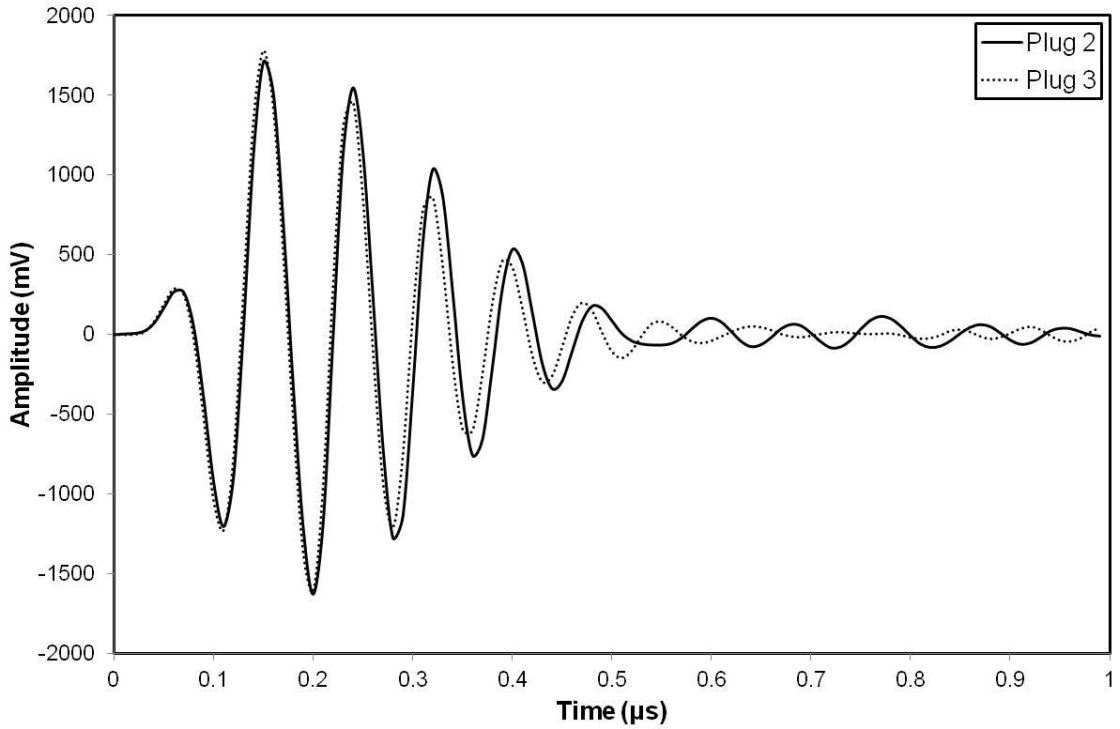

Figure 8.2: Installed Plugs Longitudinal Sensor First Reflections.

The frequency content of the reflections was calculated using a Fast Fourier Transform (FFT) and the frequency magnitude spectrum is plotted in Figure 8.3.

The frequency content distribution for both sensors form smooth peaks as expected. Again the sensors show strong similarity as implied by the comparable time-domain responses. There are a number of standards, such as ASTM E1065 (Standard Guide for Evaluating Characteristics of Ultrasonic Search Units, 2014) and BS EN 12668-2 (Characterization and verification of ultrasonic examination equipment - Probes, 2010), which specify measurements to characterise the frequency response of ultrasonic transducers. These standards use a peak or centre frequency as the transducer nominal frequency, and calculate the range of frequencies with useful energy by taking a threshold relative to the peak amplitude. Normally the selected threshold is either -6 dB or -12 dB. For the readings reported here -12 dB levels have been selected. As described in §5 piezo elements have a resonant frequency defined by their thickness. The sensors used were specified to be 0.2 mm thick, which corresponds to a centre frequency of 10 MHz, the manufacturing tolerance was ±0.05 mm. The frequency measurements for all three plugs are given in Table 8.1. These show good consistency, the centre frequencies observed are higher than expected, but are within range of the manufacturing tolerance.

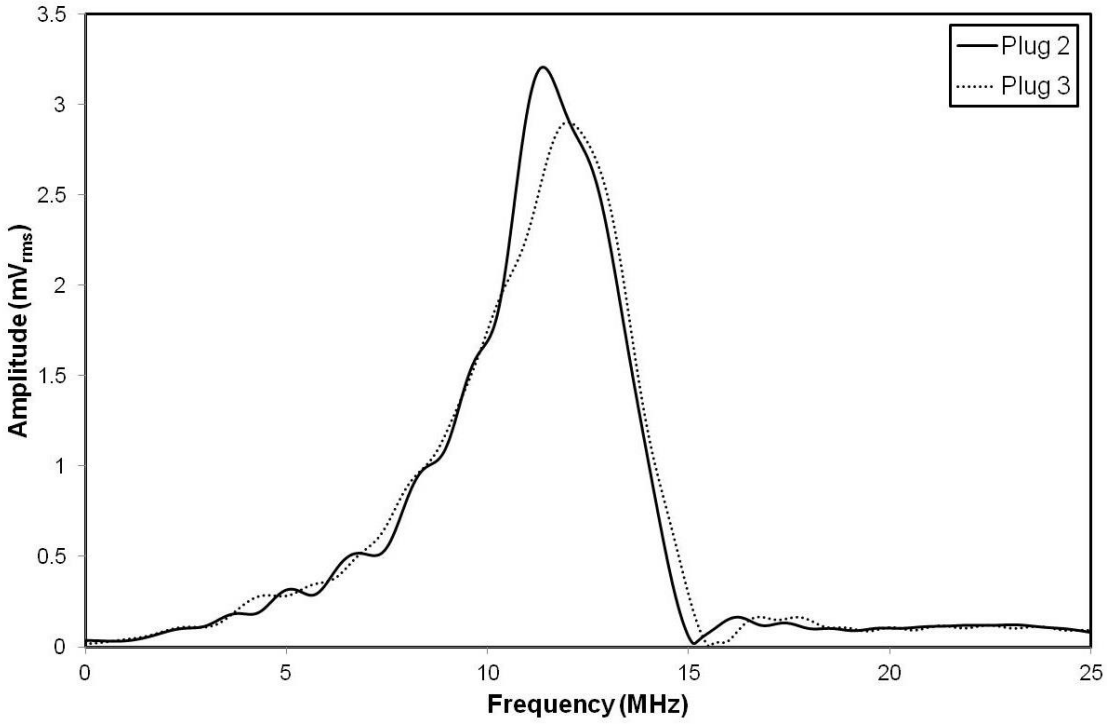

Figure 8.3: Plug Longitudinal Sensors Frequency Content.

	Longitudinal		
	1	2	3
Centre Frequency (MHz)	13.211	12.781	13.245
Peak Frequency (MHz)	12.3	11.37	11.99
-12dB Lower Freq. (MHz)	8.15	7.963	7.608
-12dB Higher Freq. (MHz)	14.123	14.192	14.501
-12dB Bandwidth (%)	45.2	48.7	52.0

Table 8.1: Plug Longitudinal Sensor Characteristics.

The excitation pulse was a negative unipolar square wave. As the pulse is only unipolar it can be approximated as half a cycle, and the resonant excitation pulse width for a given transducer can be calculated from Equation 8.1.

$$t_p = \frac{1}{2f} \qquad 8.1$$

Where t_p is the excitation pulse width, and f is the sensor resonant frequency. For a 10 MHz transducer the ideal excitation pulse width is 50 ns. However the pulse shape will distort as it propagates through the cabling, and the damping, electrical characteristics and manufacturing variability of the sensor mean that the pulse width generated by the system must be tuned to give the optimal sensor response. It is also possible to drive a sensor off resonance, however this will greatly reduce the efficiency of the sensor.

The successive longitudinal internal reflections recorded from plug 2 have been aligned and overplotted in Figure 8.4. The pulses maintain a similar shape, but as expected slowly decrease in amplitude due to attenuation effects.

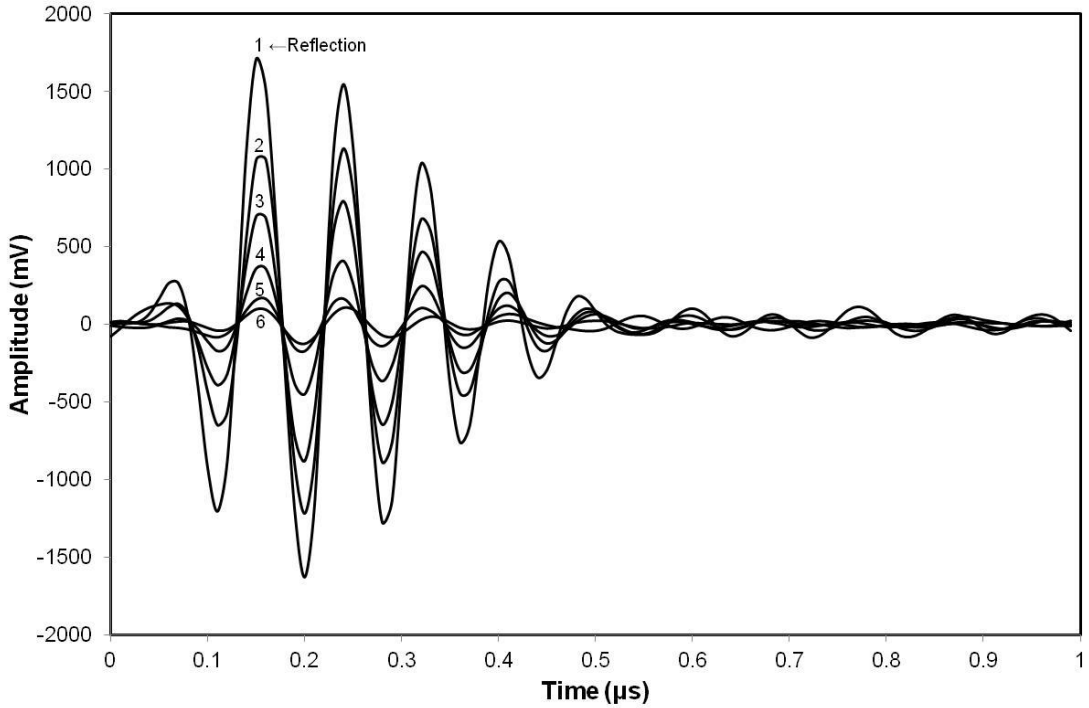

Figure 8.4: Plug 2 Longitudinal Sensor Reflections.

The time interval between each reflection and the average of these are given in Table 8.2. These were calculated by cross correlating each pulse with the following pulse.

Reflections	1->2	2->3	3->4	4->5	5->6	Average
Time (µs)	11.62051	11.67000	11.67000	11.7197	11.62030	11.6601

Table 8.2: Longitudinal Reflection Intervals.

From the geometry of the plug the ultrasonic path length was measured using digital callipers to be **70±0.1 mm**. Taking this and the average ToF as given in Table 8.2 the bulk longitudinal speed of sound for the material was calculated to be **6003.38 m/s**.

The frequency content for the successive reflections is plotted in Figure 8.5. The first four reflections show good consistency, with only the amplitude changing, and no appreciable shift in frequency. The last two reflections show complicated profiles as the signal level is comparable to the background noise and likely to be subject to interference.

The successive reflections are of interest as they could be used to gain greater sensitivity. With each successive reflection the pulse has passed through material and interacted with the interface an additional time. This effect in isolation increases the sensitivity of a time-of-flight measurement by a multiple of the reflection number (the second reflection has twice the sensitivity, the third has three times and so on), and the sensitivity of measurement of the reflection coefficient of the interface is raised to the power of the reflection number (for example the second reflection gives a measurement of R^2, the third R^3 and so on). This additional sensitivity must however be balanced against the drop in signal amplitude which makes the signal-to-noise ratio less favourable. It is also necessary to wait for the reflection of interest to be received before sending the next excitation pulse, the longer wait time required in order to capture a later pulse will also limit the maximum pulse repetition rate that can be used.

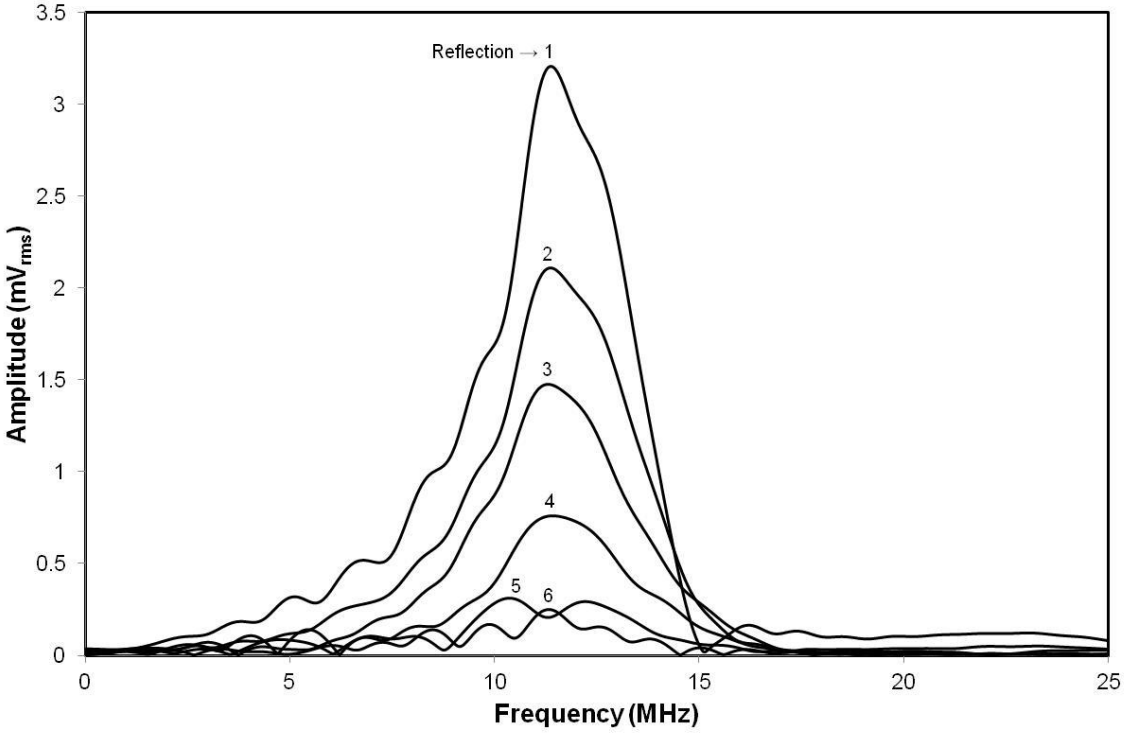

Figure 8.5: Plug 2 Longitudinal Sensor Frequency Content.

8.1.2 Shear Response

As with the longitudinal sensor the A-scan for the shear sensor on the same plug has been plotted in Figure 8.6. It is noticeable that the reflections occur at larger intervals than with the longitudinal sensor, this is due to the slower speed of sound of shear waves in comparison to longitudinal waves.

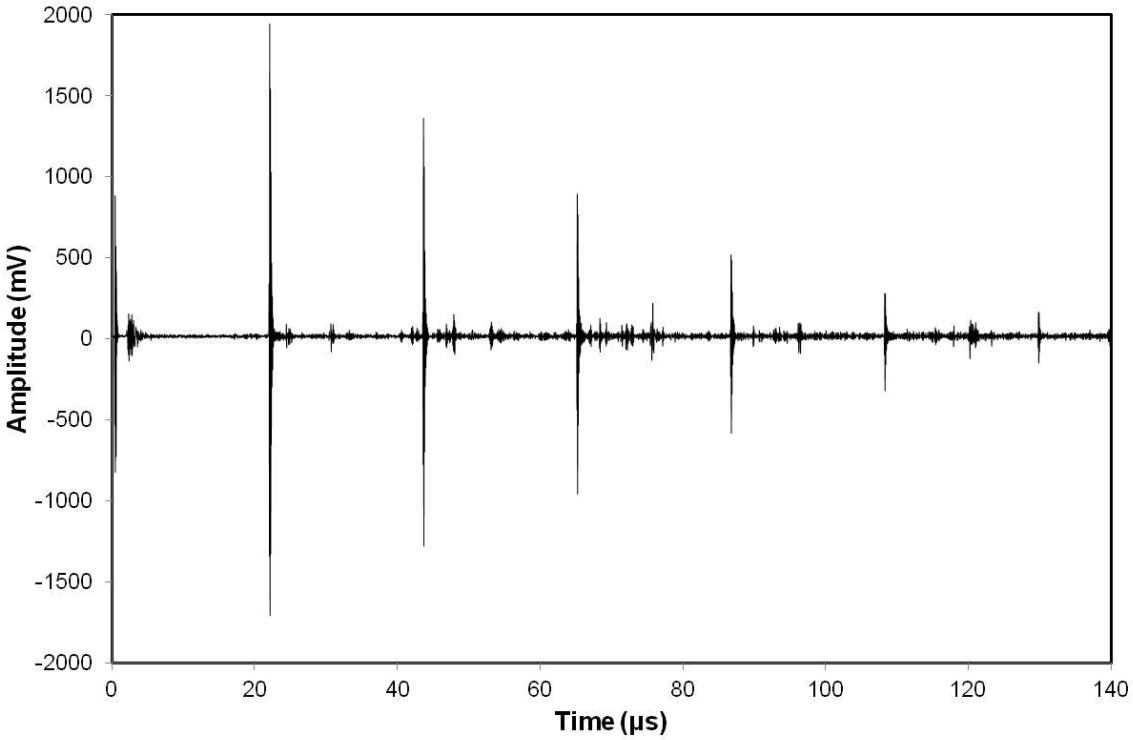

Figure 8.6: Plug 2 Shear Sensor A-Scan.

As before a small pulse is observed at 50 µs, however in this case the pulse amplitude is much reduced in comparison to the internal plug reflections. The first reflections for the two plugs installed in the roll have been plotted in Figure 8.7. Again the sensors show good similarity.

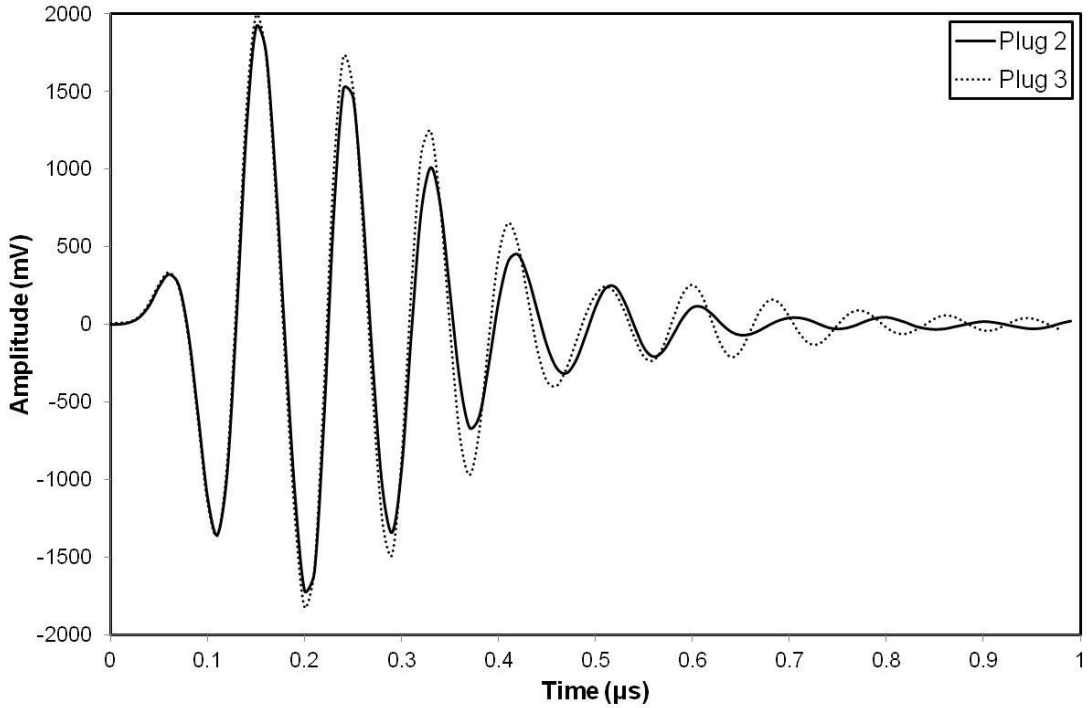

Figure 8.7: Plug Shear Sensor First Reflections.

The frequency distributions of the reflections shown in Figure 8.7 are given in Figure 8.8. The shear responses have clean frequency peaks. The frequency measurements for all three plugs are given in Table 8.3. These show good uniformity and are comparable to the results from the longitudinal sensors.

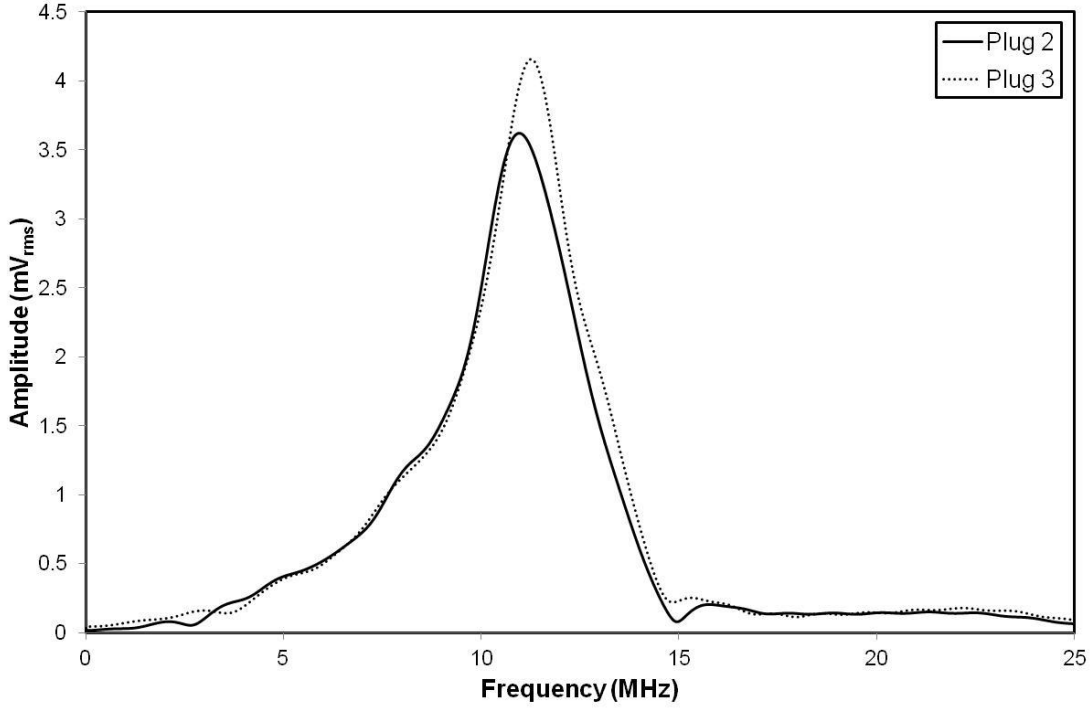

Figure 8.8: Plug Shear Sensors Frequency Content.

	Shear		
	1	2	3
Centre Frequency (MHz)	10.397	10.554	10.738
Peak Frequency (MHz)	11.04	10.96	11.26
-12dB Lower Freq. (MHz)	7.181	7.454	7.713
-12dB Higher Freq. (MHz)	13.612	13.655	13.762
-12dB Bandwidth (%)	61.9	58.8	56.3

Table 8.3: Plug Shear Sensor Characteristics.

The successive shear wave reflections have been over plotted in Figure 8.9. The time of flight between each subsequent reflection was calculated and is presented in Table 8.4.

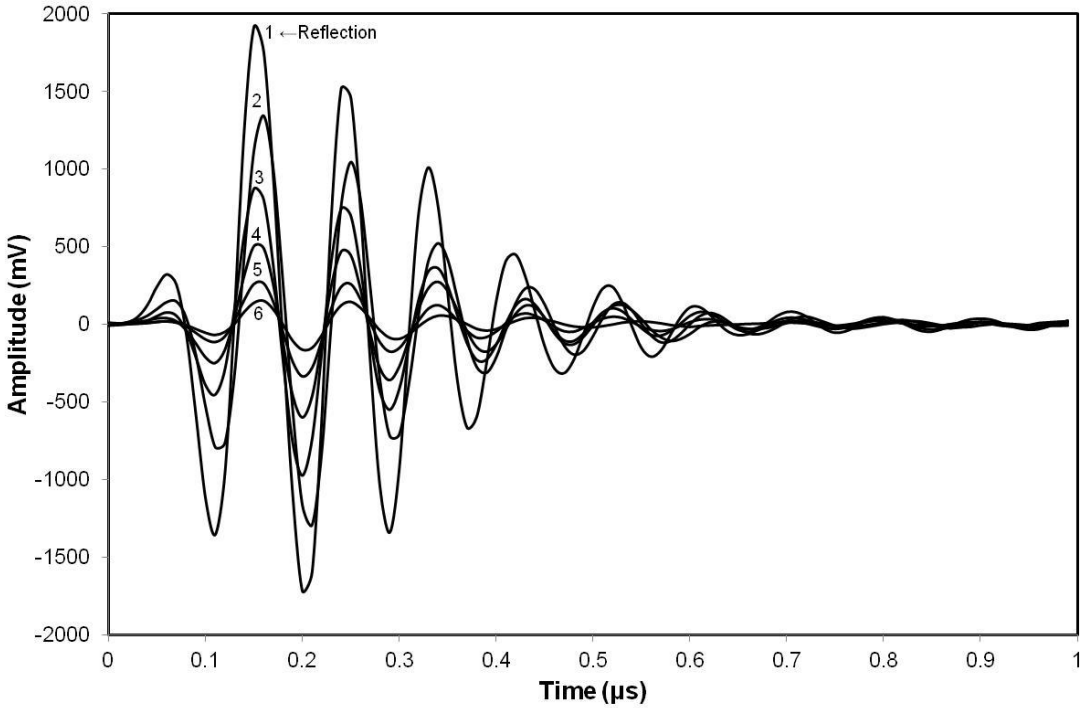

Figure 8.9: Plug 2 Shear Sensor Reflections.

Reflections	1->2	2->3	3->4	4->5	5->6	Average
Time (µs)	21.544	21.256	21.540	21.540	21.540	21.542

Table 8.4: Shear Reflection Intervals.

Again an ultrasonic path length of **70±0.1 mm** was taken and from the average ToF given in Table 8.2 the shear speed of sound was calculated to be **3249.47 m/s**.

The frequency content for the successive reflections is plotted in Figure 8.10. For this sensor the first five reflections show good consistency, with only the amplitude changing. There is a slight drop in the peak frequency between the first and second reflection.

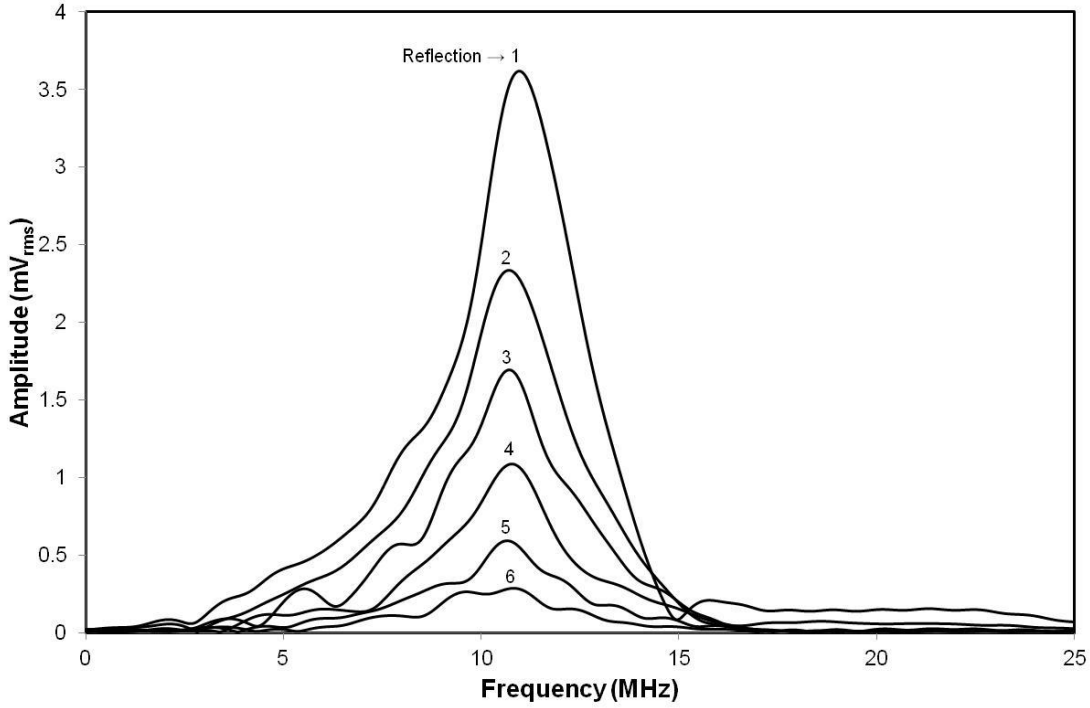

Figure 8.10: Plug 2 Shear Sensor Frequency Content.

8.2 Plug Material Properties

Assuming an isotropic material, and using the ultrasonically measured values of the longitudinal and shear speed of sounds, it is possible to calculate a number of plug material properties of interest.

8.2.1 Density

For many of the following calculations the density of the material is needed. This was calculated by weighting the plug and dividing by the volume. From its geometry the plug volume was calculated to be **4.918x10^{-5} m^3** and it was weighed at **383.310 g** giving a density of **7794.02 kg/m^3.** This compares well to tabulated values for the density of stainless steel (7850 kg/m^3 (Metals and Alloys - Densities, n.d.)).

8.2.2 Poisson's Ratio

The Poisson's ratio can be calculated using Equation 8.2 (Olympus NDT, 2006).

$$\upsilon = \frac{1 - 2(c_S/c_L)^2}{2 - 2(c_S/c_L)^2} \qquad 8.2$$

Where υ is Poisson's Ratio, c_S is the shear wave speed of sound and c_L is the longitudinal speed of sound. Using the measured values for speed of sound results in a Poisson's Ratio of **0.293.** This agrees well with tabulated values of Poisson's ratio in steel which is commonly taken as 0.3.

8.2.3 Young's Modulus

Young's Modulus of Elasticity can be calculated from the longitudinal speed of sound, density and the Poisson's ratio, the relationship is given in Equation 8.3 (Olympus NDT, 2006) which is a rearrangement of Equation 3.8.

$$E = \frac{{c_L}^2 \rho (1+\upsilon)(1-2\upsilon)}{(1-\upsilon)} \quad 8.3$$

Where *E* is the Young's Modulus and ρ is the density. Taking a tabulated value for the density of steel at results in a bulk modulus of **212.69 GPa**. A typical value used for stainless steel is 211 GPa.

8.2.4 Lamé Constant

The first Lamé constant, another elastic modulus, is calculated from Equation 8.4 (Brown)

$$\lambda = \rho({c_L}^2 - 2{c_S}^2) \quad 8.4$$

For the plug steel measured this is **116.31 GPa**.

8.2.5 Shear Modulus

The shear modulus, equivalent to the 2nd Lamé constant μ in a solid, can be calculated from the shear speed of sound and density, Equation 8.5 (Olympus NDT, 2006) which is a rearrangement of Equation 3.3.

$$G = {c_S}^2 \rho \quad 8.5$$

Where *G* is the shear modulus. This results in a value of **82.30 GPa** which is slightly higher than tabulated values for stainless steel, 77.2 GPa (Modulus of Rigidity of some Common Materials, n.d.) .

8.2.6 Bulk Modulus

The bulk modulus is a product of the density, shear and longitudinal acoustic velocities, the relationship of these is given in Equation 8.6 (Brown).

$$B = \rho\left({c_L}^2 - \frac{4{c_S}^2}{3}\right) \quad 8.6$$

For the measured steel this gives **171.18 GPa**. Again this is higher than typical values for steel which are in the range 156 to 165 GPa (Metals and Alloys - Bulk Modulus, n.d.).

8.2.7 Acoustic Impedance

The acoustic impedance introduced in §3 can also be defined in terms of the longitudinal bulk velocity and density, see Equation 8.7 (Krautkrämer & Krautkrämer, 1977).

$$z = \rho c_L \quad 8.7$$

Which yields a value of **46.791 MRayls** (x10^6 kg/m^{2}s). Most tabulated values for steel are in the region of 46 MRayls. The calculations were completed for all three plugs and the results presented in Table 8.5. As the material is the same for each plug an average has been taken of each of the properties. The slight variability between the plugs can be explained by differences introduced by the hardening of the steel, and error in the speed of sound measurement due to the variation in plug length caused by machining inaccuracies.

	Plug 1	Plug 2	Plug 3	**Average**
Longitudinal Speed of Sound (m/s)	6008.21	6003.44	5964.68	**5992.11**
Shear Speed of Sound (m/s)	3257.69	3249.47	3235.99	**3247.72**
Density, ρ (kg/m^3)	7794.02			**7794.02**
Poisson's Ration, ν	0.292	0.293	0.291	**0.292**
Young's Modulus, E (GPa)	213.59	212.69	211.05	**212.44**
Shear Modulus, G (GPa)	82.71	82.30	81.62	**82.21**
Bulk Modulus, B (GPa)	171.07	171.18	168.47	**170.24**
Lamé Constant, λ (GPa)	115.93	116.31	114.06	**115.43**
Long. Acoustic Impedance, z_L (MRayls)	46.828	46.791	46.489	**46.703**
Shear Acoustic Impedance, z_s (MRayls)	25.391	25.326	25.221	**25.313**

Table 8.5: Plug Material Properties.

Table 8.6 gives literature values for the shear speed of sound and longitudinal speed of sound and attenuation coefficient. The values calculated in Table 8.5 compare well with these. The attenuation coefficient is estimated in the following section.

	Mild Steel (Bacon & Jarvis, n.d.)	**Tool Steel (Hardened)** (Bacon & Jarvis, n.d.)	**Stainless Steel** (Bacon & Jarvis, n.d.)
Long. SoS (m/s)	5960	5874	5980
Shear SoS (m/s)	3235	3179	3297
Long. Atten. (neper/m)	-	4.94 (@10 MHz)	-

Table 8.6: Example Steel Material Properties.

8.2.8 Attenuation

The ultrasonic attenuation between two points in a material is described in Equation 3.10. This equation has been adapted to enable the attenuation coefficient to be measured in the pulse echo setup used in the plug. This requires the proportion of the ultrasonic signal transmitted into the sensor with each successive reflection to be accounted for. This is achieved using the plug-to-sensor reflection coefficient, as shown in Equation 8.8.

$$A_2 = RA_1e^{-\alpha 2d} \tag{8.8}$$

Where A_1 and A_2 are the amplitude of the first and second reflections respectively, d is the plug length, R is the plug-to-sensor reflection coefficient and α is the attenuation coefficient. Rearranging gives the attenuation coefficient as:

$$\alpha = \frac{1}{2d} ln\left(\frac{A_1R}{A_2}\right) \tag{8.9}$$

This follows the same form as the equation used in ASTM C1332 (Standard Test Method for Measurement of Ultrasonic Attenuation Coefficients of Advanced Ceramics by Pulse-Echo Contact Technique, 2013). The amplitude of successive reflections in the plug are plotted in Figure 8.11 and Figure 8.13 for the longitudinal and shear sensor respectively. Some of the reflections show a slight asymmetry about the x-axis. To correct for this the peak to peak amplitude of each reflection has been extracted. This peak to peak amplitude has then been plotted equally about the x-axis. For some reflections the slight offset between the raw data and the centralised peak to peak values can be seen. An exponential curve was then fitted to the peak to peak values to quantify the signal decay.

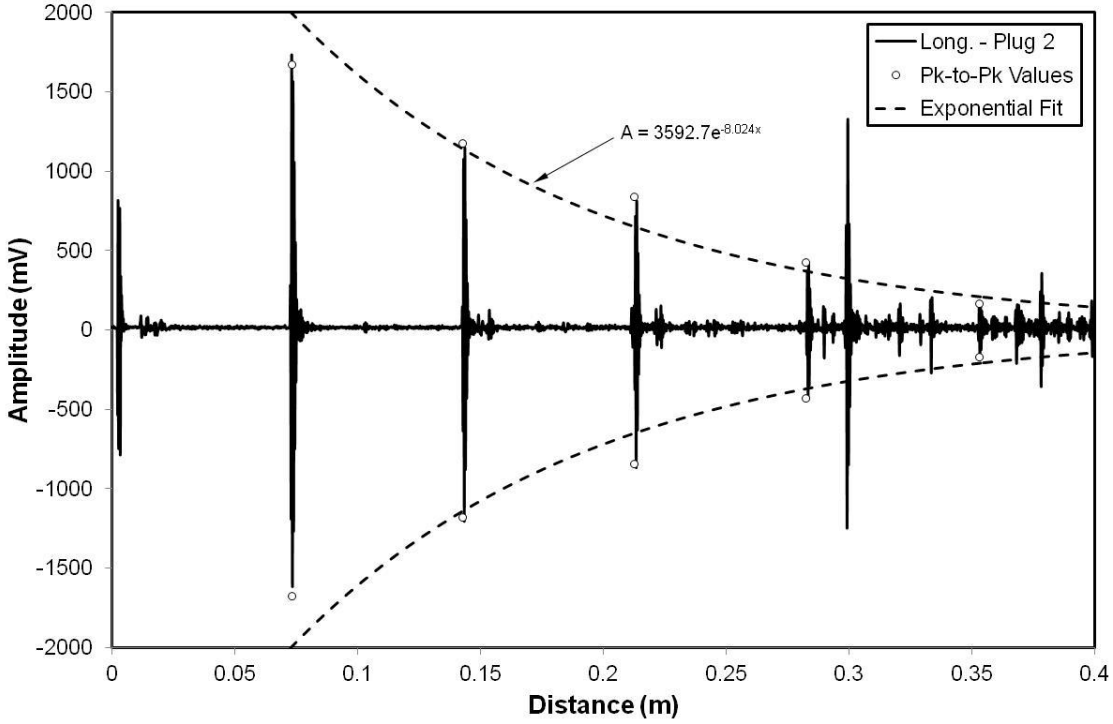

Figure 8.11: Plug 2 Longitudinal Reflections and Exponential Envelope.

Reflection	1	2	3	4	5	6	**Average**
Long. FFT Mag. @ 11.3 MHz	3.208	2.112	1.475	0.759	0.310	0.251	-
Atten. Coeff. (Neper/m)	-	-20.06	-20.90	-16.54	-13.24	-23.01	**-18.75**
Long. Pk to Pk	3344	2353	1678	855	336	233	-
Atten. Coeff. (Neper/m)	-	-21.01	-21.20	-16.40	-12.69	-20.80	**-18.42**

Table 8.7: Plug 2 Longitudinal Attenuation Calculations.

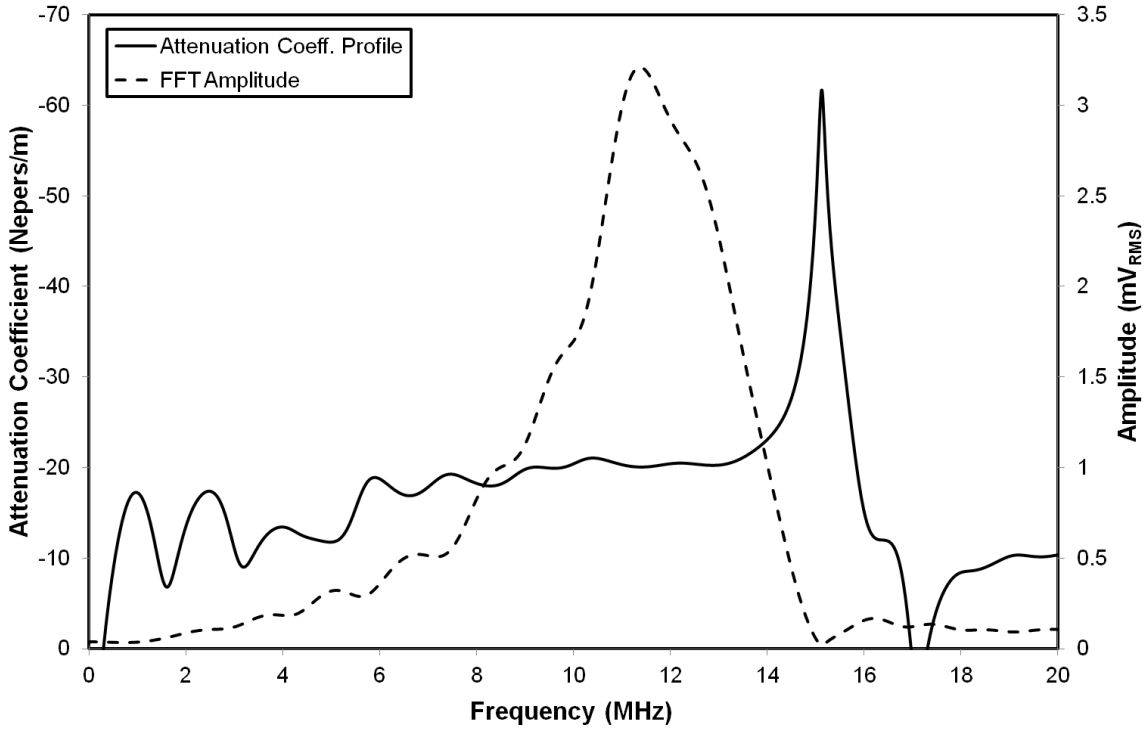

Figure 8.12: Plug 2 Longitudinal Attenuation Spectrum.

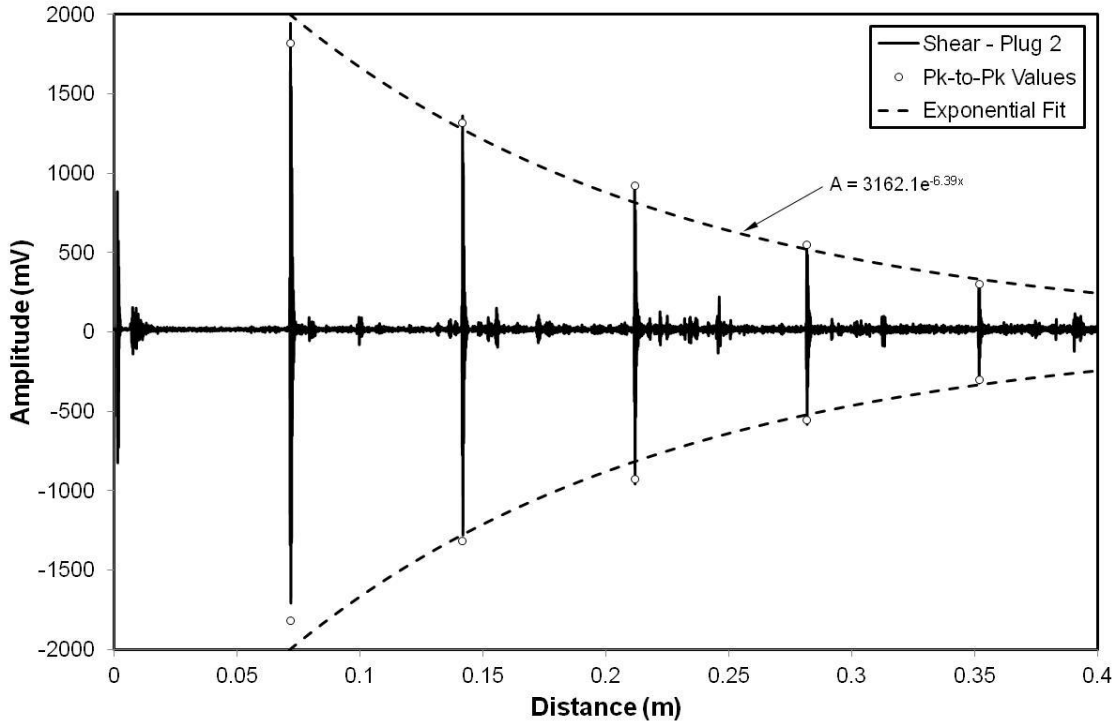

Figure 8.13: Plug 2 Shear Reflections and Exponential Envelope.

Reflection	1	2	3	4	5	6	**Average**
Shear FFT Mag. @ 10.7 MHz	3.619	2.337	1.695	1.089	0.595	0.287	-
Atten. Coeff. (Neper/m)	-	-19.78	-21.44	-19.71	-17.39	-15.61	**-18.79**
Shear Pk to Pk	3638	2633	1849	1100	602	315	-
Atten. Coeff. (Neper/m)	-	-21.41	-20.98	-18.61	-17.41	-16.78	**-19.04**

Table 8.8: Plug 2 Shear Attenuation Calculations.

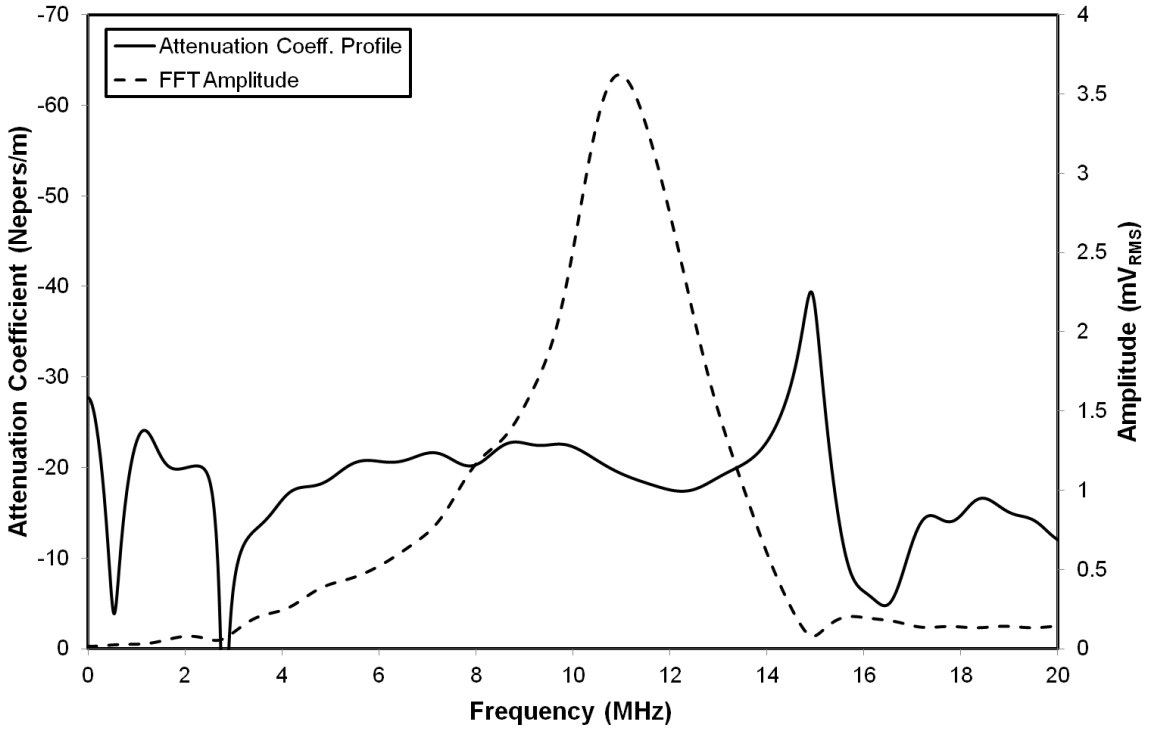

Figure 8.14: Plug 2 Shear Attenuation Spectrum.

The attenuation coefficient was calculated in two different ways. In the first approach the peak to peak amplitudes of the successive reflections were taken and put into equation 8.9. The reflection coefficient was calculated from Equation 3.56 using an acoustic impedance for the sensor (PZT-5A) of 33.7 MRayls (NDT Resource Center, n.d.) and plug of 46.703 MRayls. This gave a reflection coefficient of -0.1617.

The other approach used the reflection amplitudes across a range of frequencies to calculate attenuation coefficient spectra. These were calculated by FFT and are shown in Figure 8.5 and Figure 8.10. The FFT magnitude was divided by √2 before calculating the attenuation coefficient in order to convert the RMS values shown to peak values. The results of these methods for both the longitudinal and shear waves are given in Table 8.7 and Table 8.8, with the attenuation spectra given in Figure 8.12 and Figure 8.14. The frequency magnitude spectra are also included in the figures to indicate the signal strength at each frequency. I can be seen that at frequencies with low energy, the poorer signal-to-noise ratio results in erroneous results. An example of this can be seen in the peak at 15 MHz in Figure 8.12. Here the attenuation shows a sharp peak at the same point where the frequency spectrum in the plot shows very little energy.

The attenuation coefficient values using either calculation method are similar and are comparable for both wave types, in the range of 18 to 19 Nepers/m. The peak to peak attenuation values of **-18.42 Nepers/m** and **-19.04 Nepers/m** for the longitudinal and shear results respectively equate to -160.00 dB/m and -165.38 dB/m. There is a small amount of discrepancy between the reflection amplitudes and the exponential fit. This may be caused by any nonlinearity in the ultrasonic measurement system, possible sources of which include the hardware amplifier and the piezo element response.

8.3 B-Scans

An A-Scan presents the received ultrasonic amplitude over time. The later in time a reflection is received, the deeper in to a material the reflecting face is. This approach can therefore be used to give a 1 dimensional view through the roll, roll bite and strip. As the roll turns, the sensor sweeps across the roll bite and successive A-Scans can be stacked up to create a 2 dimensional section view of the roll bite. This is referred to as the B-Scan.

8.3.1 Simple Geometrical Model

In order to understand and validate the roll bite section image created by the B-Scan, first a simple geometrical model of the rolls and strip has been developed. Equations 8.10 to 8.13 describe the top and bottom roll surfaces and the top and bottom surfaces of the strip respectively.

$$z_{Top} = \sqrt{R^2 - x^2} \tag{8.10}$$

$$z_{Bottom\ Roll} = 2R + h_1 - \sqrt{R^2 - x^2} \tag{8.11}$$

$$z_{Strip\ Top} = \begin{cases} R - \dfrac{h_0 - h_1}{2}, & x \le x_1 \\ \sqrt{R^2 - x^2}, & x_1 < x \le x_2 \\ R, & x_2 < x \end{cases} \tag{8.12}$$

$$z_{Strip\ Bottom} = \begin{cases} R + h_1 + \dfrac{h_0 - h_1}{2}, & x \le x_1 \\ 2R + h_1 - \sqrt{R^2 - x^2}, & x_1 < x \le x_2 \\ R + h_1, & x_2 < x \end{cases} \quad 8.13$$

Where R is the roll radius, h_0, h_1 are the strip entry and exit thicknesses and x_1, x_2 the roll bite contact entry and exit locations. The entry and exit points are given in Equations 8.14 and 8.15.

$$x_1 = -\sqrt{R^2 - \left(R - \frac{h_0 - h_1}{2}\right)^2} \quad 8.14$$

$$x_2 = 0 \quad 8.15$$

Figure 8.15 shows the schematic using these Equations and the values given in Table 8.9. These are representative of a typical rolling scenario. Note the top and bottom work rolls have been inverted, this has been done to make the vertical axis ascending and therefore match with the ultrasonic results presented later.

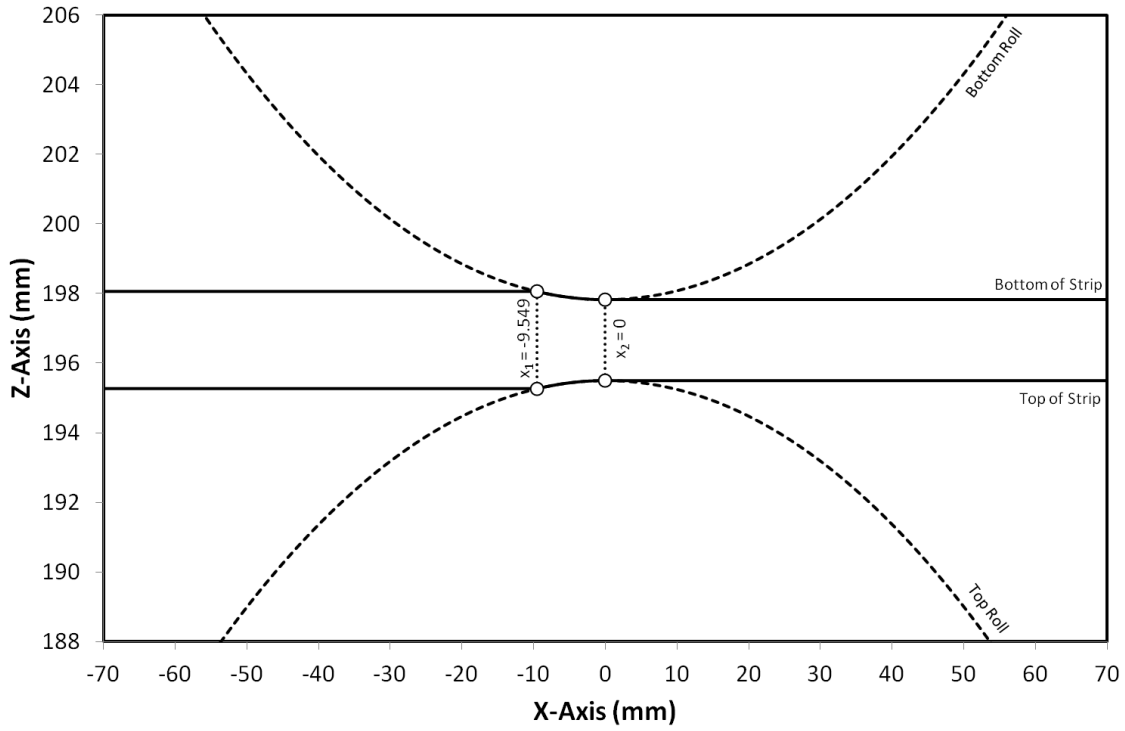

Figure 8.15: Schematic of Rolls and Strip.

Roll Radius, R	195.5 mm
Plug Length	35mm
Entry Thickness, h_0	2.8mm
Elongation, el%	20%
Steel SoS	5992.11 m/s
Lubricant SoS	1800 m/s

Table 8.9: Geometric Model Values.

These equations form a simplified model with no roll deformation and no elastic relaxation of the strip after rolling. The origin was taken as the centre of the top roll with the positive X-axis

in the direction of rolling, and the positive Z-axis pointing downwards following the line connecting the centres of the top and bottom rolls.

Figure 8.15 shows the schematic using Cartesian coordinates. The sensors are mounted within the roll, and rotate around a central axis. The roll schematic has therefore been converted into polar coordinates, as this is what the response from the sensor translates into. The converted schematic is given in Figure 8.16. The angle is zeroed around the Z-Axis and the radial distance is taken from the centre of the top roll.

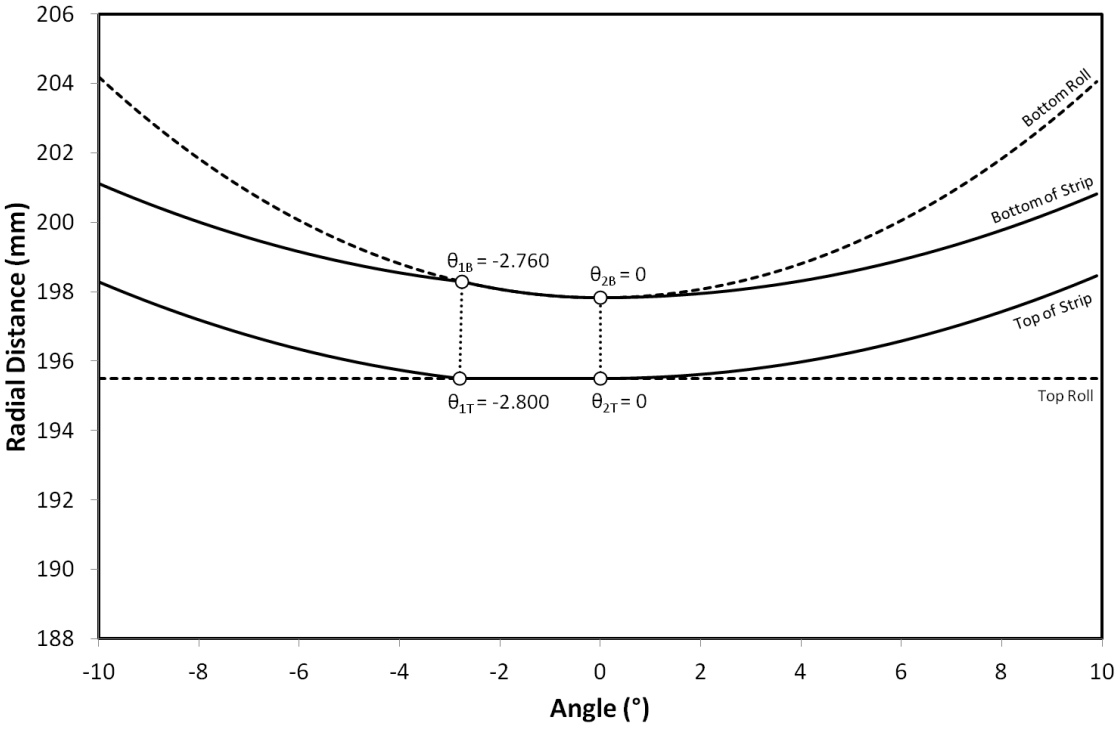

Figure 8.16: Schematic of Rolls and Strip Translated to Polar Coordinates.

Converting to polar values has the effect of warping the picture so that the strip bows away from the sensor the further it is from the roll bite centre as shown in Figure 8.16. The top roll surface is now represented as a straight line of a fixed distance, as the length between the sensor and roll surface remains unchanged across the roll bite.

The final step in presenting this model in a form that is consistent with the ultrasonic results is to convert the Z-axis from distance to ultrasonic Time-of-Flight. This is achieved using the speed of sound of the various layers. For this purpose, the gaps between the strip and roll were assumed to be lubricant filled, and the rolls and strip were assumed be made of identical steel. The values used for the speed of sound are given in Table 8.9. The Time-of-Flight adjusted plot is presented in Figure 8.17. This plot is similar to Figure 8.16, however the slower speed of sound in the lubricant has increased the ToF through the lubricant layers relative to the steel parts. This has distorted the areas outside of the roll bite.

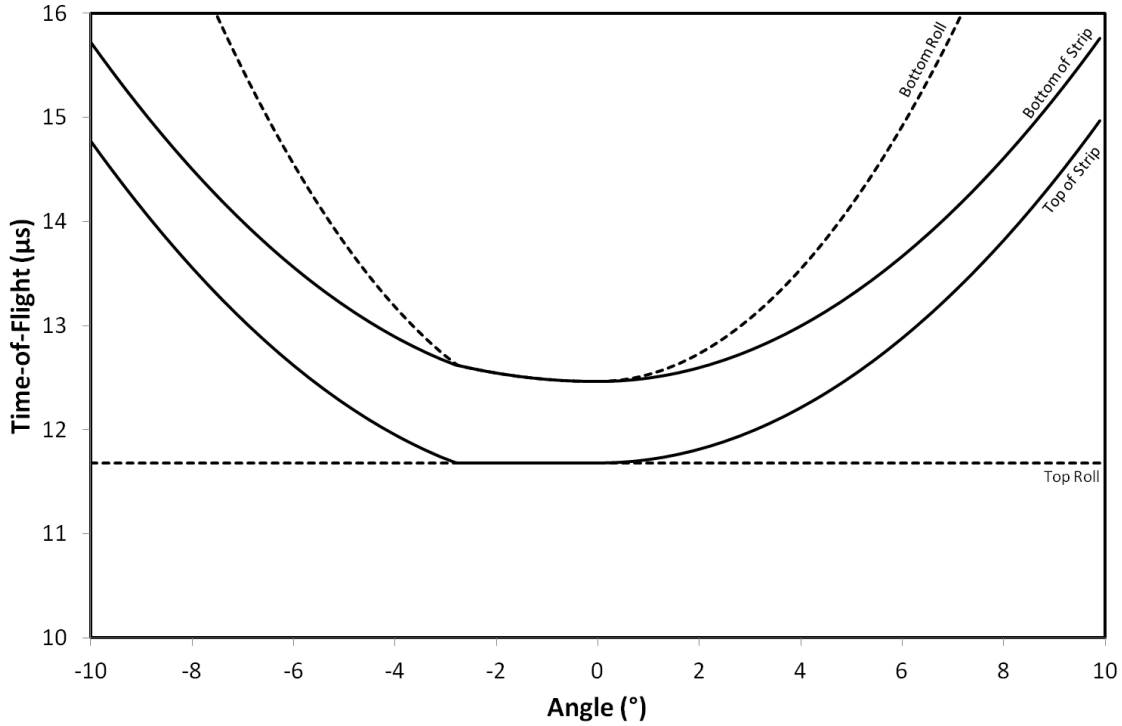

Figure 8.17: Rolling Schematic Adjusted for Time-of-Flight.

8.3.2 B-Scan Plots

B-Scans for the shear and longitudinal transducers are plotted in Figure 8.18 and Figure 8.19 respectively. These were recorded at a rolling speed of 100mpm, entry strip thickness of 2.8mm, 30% elongation, and with pure K2 oil at 60°C used as the lubricant.

By viewing the data in Figure 8.18 as a 3 dimensional image as opposed to a 1 dimensional A-Scan, a number of features are highlighted that may otherwise have been obscured. The drop in the roll surface reflection across the roll bite can be clearly observed. A number of additional reflections (labelled B_1, B_2, B_3) can also be seen, these interfere with the main reflection from the roll surface (labelled A_1), especially at the entrance and exit to the roll bite. It is clear from the B-Scans that these additional reflections have a large effect on the response. The source of these additional reflections is not immediately clear. Similar reflections are seen in the shear results plotted in Figure 8.19, albeit spaced further apart due to the lower speed of sound.

To allow the additional reflections to be viewed with greater clarity the roll surface reflection was removed from the B-Scans to leave just the additional reflections, these are plotted in Figure 8.20 and Figure 8.21. This was achieved by subtracting a reference, an A-Scan captured with the sensors pointing outside of the roll bite, from all subsequent A-Scans. As the amplitude of the response varies across the roll bite, the reference was scaled to account for this based upon the maximum value in each A-Scan. As the pulse shifts during rolling, due to the acoustoelastic effect and deformation of the roll, it was also necessary to apply a small offset to the reference before it was subtracted, the values used for these offsets are given in Figure 8.22.

The method is not perfect in isolating the additional reflections, especially in the roll bite where the shape of the roll surface reflection changes from the reference, however it is still useful in extracting the general form of the reflections.

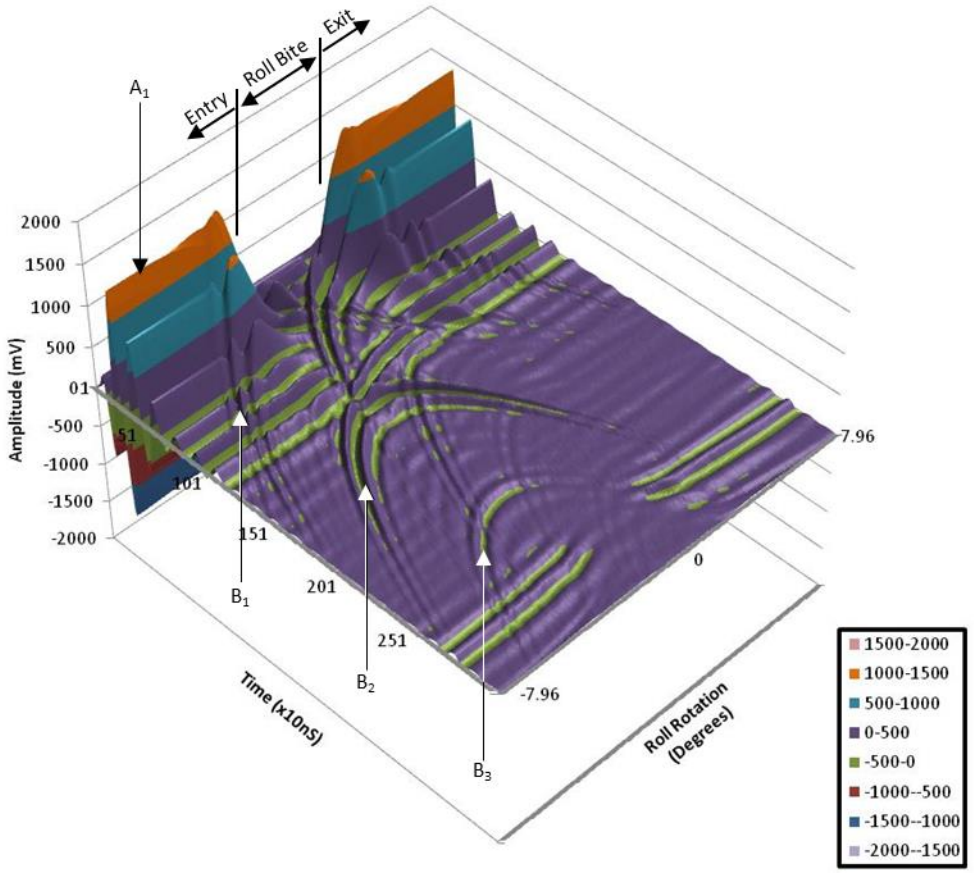

Figure 8.18: Longitudinal B-Scan.

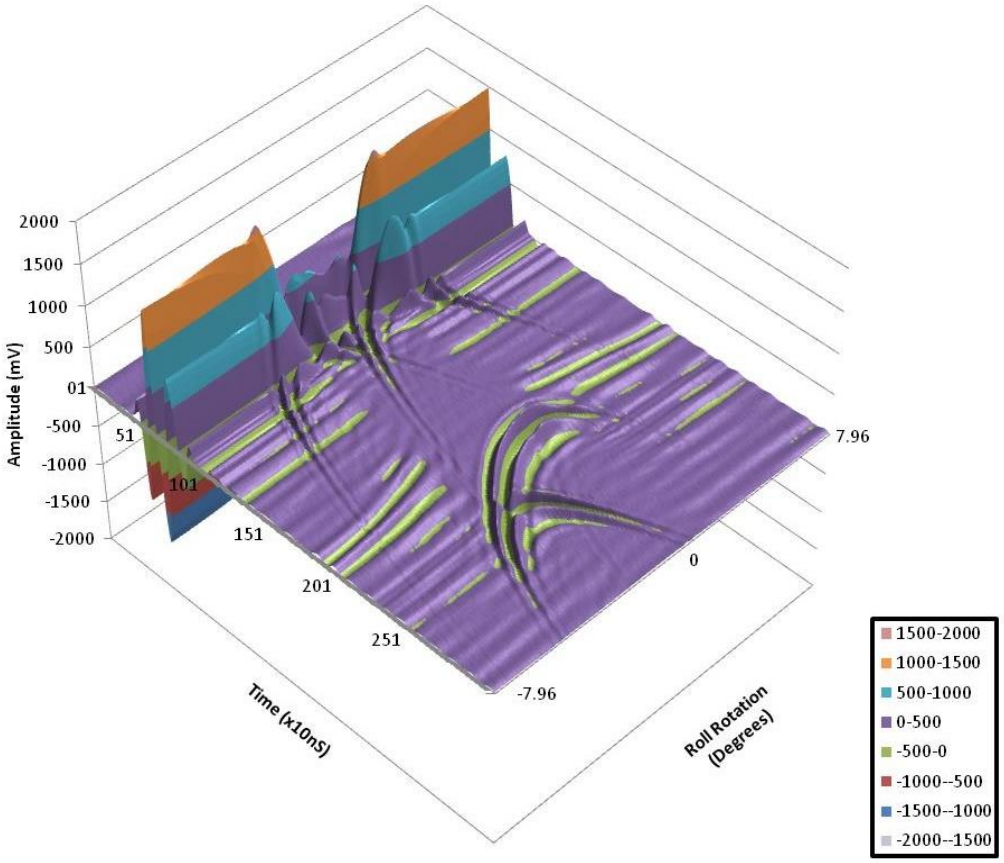

Figure 8.19: Shear B-Scan.

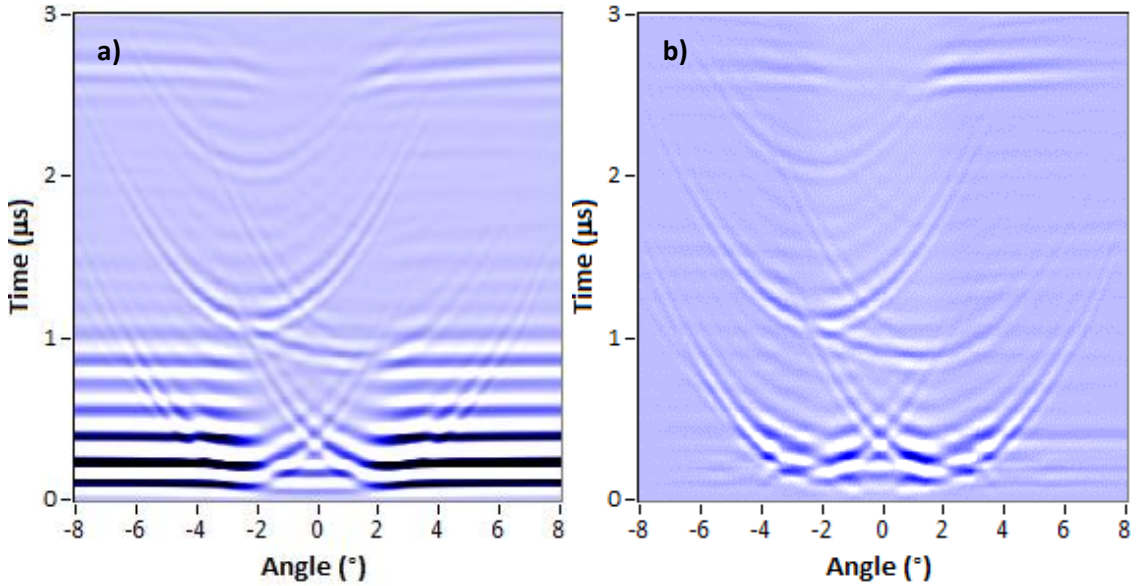

Figure 8.20: Longitudinal B-Scan with a Delay of 12 µs a) Raw b) With Reference Subtracted.

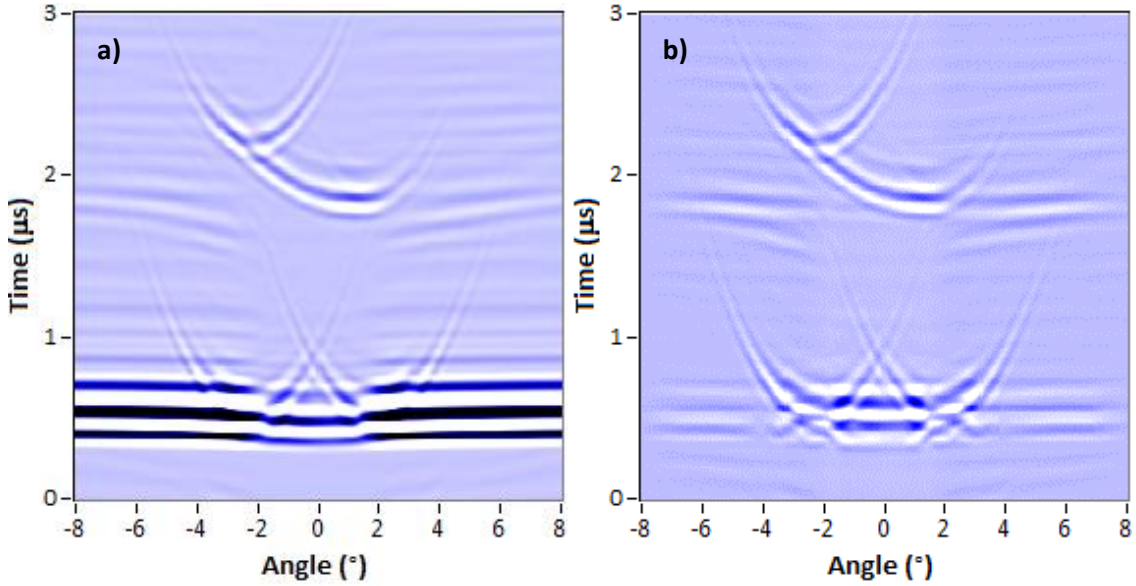

Figure 8.21: Shear B-Scan with a Delay of 21.5 µs a) Raw b) With Reference Subtracted.

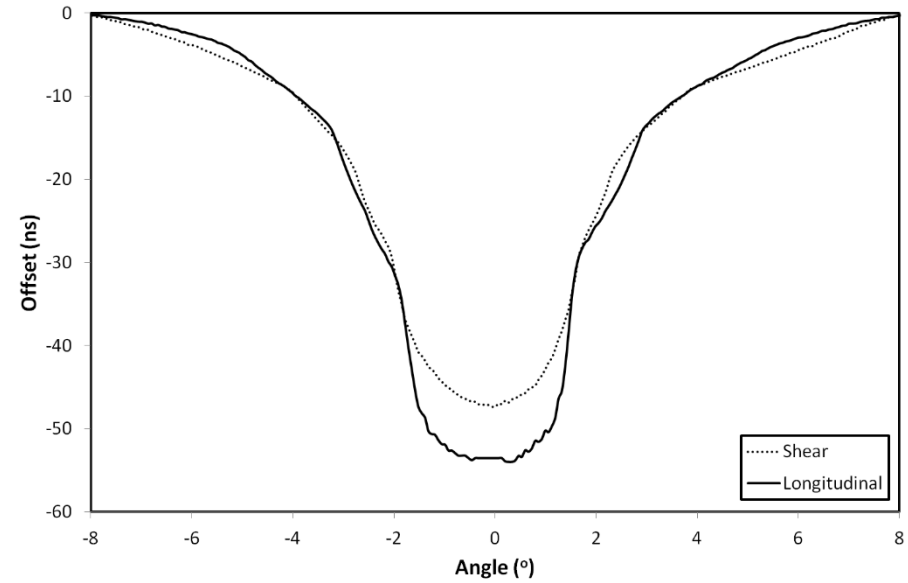

Figure 8.22: Reference Offsets.

8.3.3 B-Scan Reflections

In Figure 8.23 the strip surfaces calculated from the simple geometrical model, Figure 8.17, are plotted over the B-Scan. This shows that a clear reflection corresponding to the far side of the strip can be observed. Therefore it should be possible, knowing the speed of sound in strip, to measure the strip thickness by taking the difference in time-of-flight between the reflection from the top and bottom surfaces of the strip.

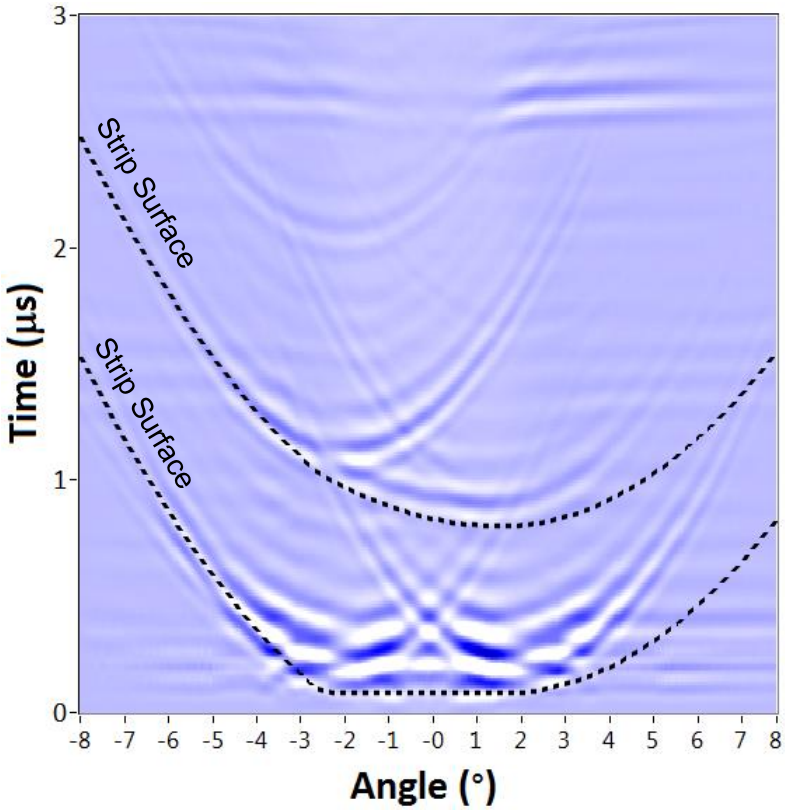

Figure 8.23: Longitudinal B-Scan Over-Plotted with the Calculated Strip Surfaces.

This plot still shows a number of waveforms of unknown origin. The model presented so far has assumed a point sensor, and that ultrasound only propagates in 1 dimension directly out from the sensor (in the direction of the Z-axis). This ignores the possibility for beam deflection or spread.

The earlier analysis on acoustoelasticity (§4.8) showed that this assumption may be inaccurate. The analysis showed the loading conditions experienced in cold rolling results in a lensing effect with concentrated beams emanating from the entry and exit to the roll bite. The Time-of-Flight to the entrance and exit points of the roll bite have been plotted onto the Time-of-Flight adjusted roll and strip schematic, and are shown in Figure 8.24. The roll, strip and lubricant have been coloured for clarity.

The ToF to the exit and entry shown in Figure 8.24 are for a beam that hasn't travelled perpendicular to the sensor, but at an angle. This means that although these beams have only travelled within the roll, the received response occurs later in time than the surface of the top roll. It should be noted that although the interfaces shown in Figure 8.24 do account for the change in strip thickness, they do not account for deflection of the work rolls. This could be accounted for by assuming a deflected roll radius (*R'*) in the roll bite, such as that shown in Figure

2.3, and including this value in place of R between $x_1 < x \leq x_2$ for Equation 8.10 to Equation 8.13. This has not been done here as the deflections would be too small to be apparent and add little to the following analysis.

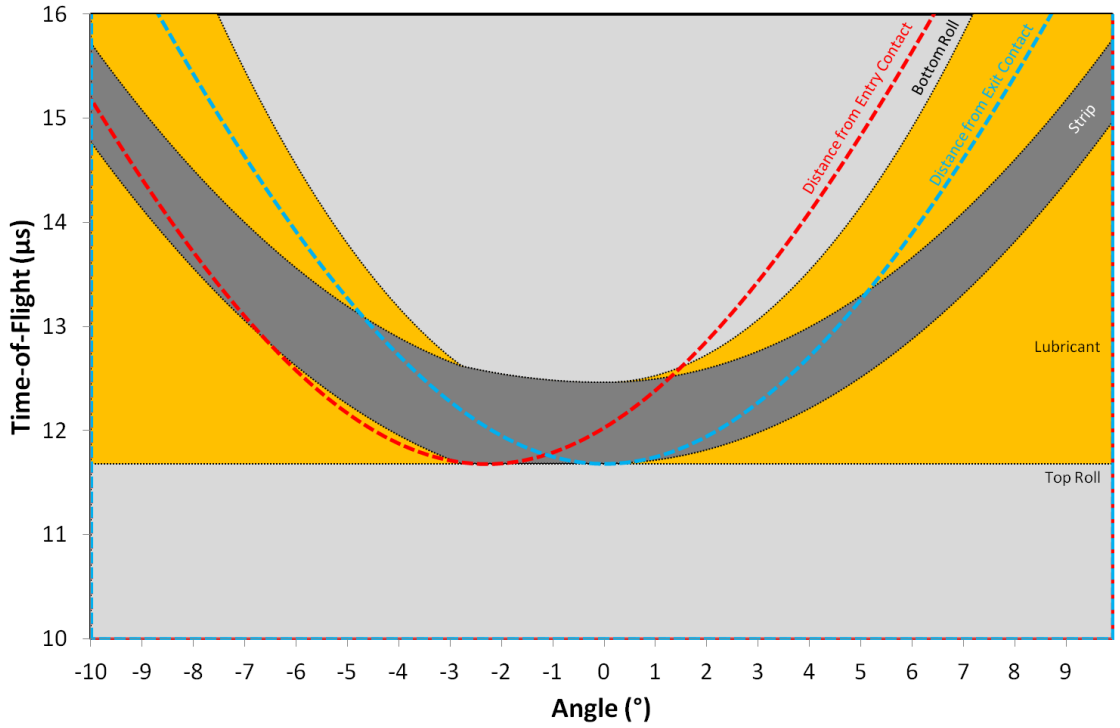

Figure 8.24: Roll Bite Schematic with the Time-of-Flight to the Roll Bite Exit and Entry Over-Plotted.

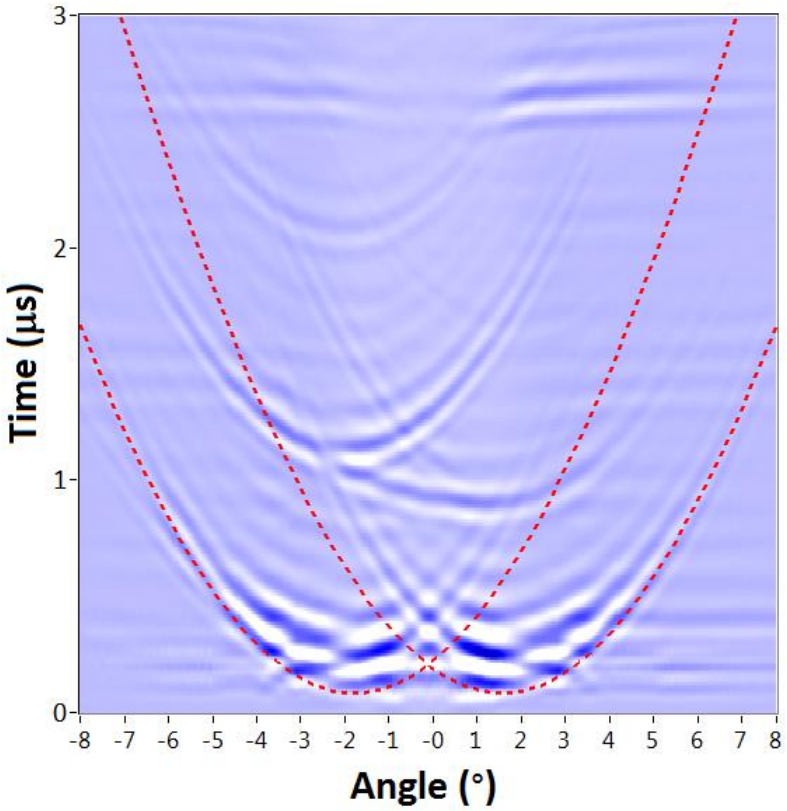

Figure 8.25: Longitudinal B-Scan with Time-of-Flight to Entry and Exit Contact Points Over-Plotted.

These values have been plotted onto the B-Scan, Figure 8.25. The reflection shapes match up well with the reflections seen at the entrance and exit of the roll bite. There are also repeat reflections that are offset by the strip thickness.

The variation in ToF for the waves received from the contact points varies dependent on the length of the plug. The shape of the Time-of-Flight offset for various plug lengths are shown in Figure 8.26.

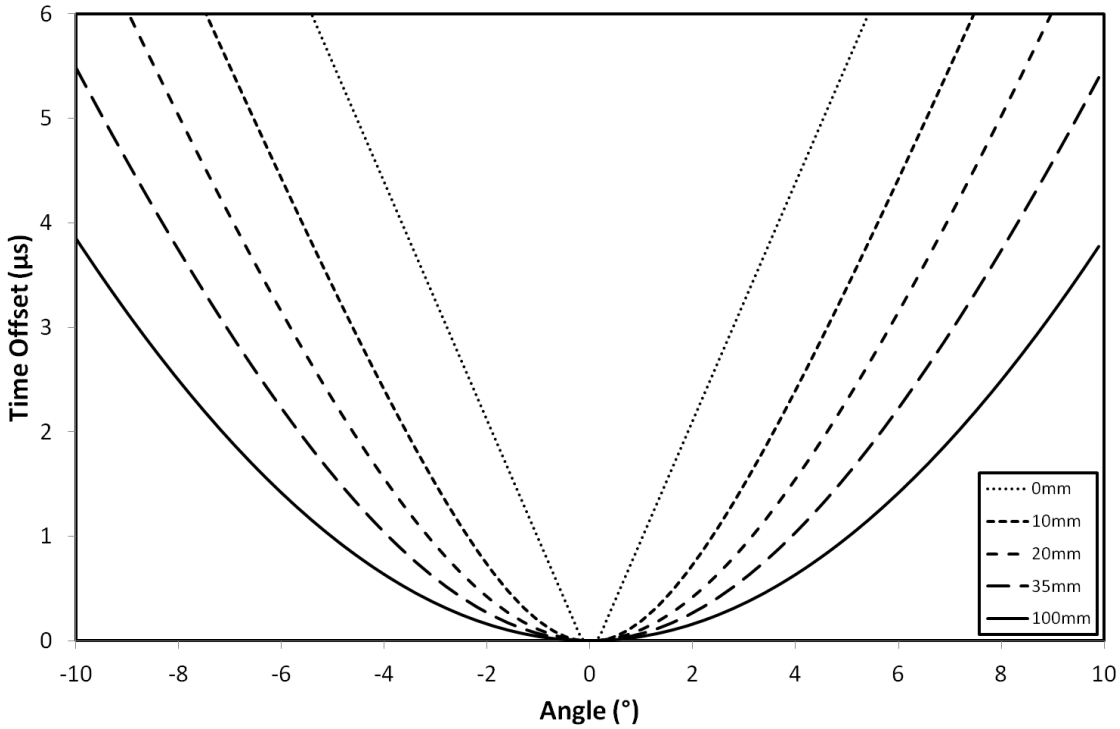

Figure 8.26: Time-of-Flight to Entry and Exit Contact Points for Longitudinal Wave and Various Plug Lengths.

8.4 Roll Bite Width

For a given position of the sensor, the reflection coefficient was computed from the FFT for the first reflected pulse and a reference signal. The reference was a signal measured outside of the roll bite, when the plug is exposed to an air interface. The reflection coefficient is obtained as the ratio between these two signals.

As the roll rotates and the ultrasonic sensor passes across the rolling interface, a profile of the reflected pulse amplitude can be built up, see Figure 8.27. An amplitude drop was observed, as expected, due to the ultrasonic wave being transmitted through the rolling interface, and therefore a smaller proportion of the wave being reflected.

On the left part of the curve reflection coefficient values are close to 1. This means that most of the incident signal is reflected back to the transducer. Then, the response drops with a linear gradient to a value of around 0.1 to 0.2. At this stage, the sensor beam is facing the roll bite and the returned signal is reduced. Finally, the reflection coefficient increases linearly to reach the initial value close to 1 as the sensor leaves the roll bite. The actual location of the entry and exit of this roll bite occurs at some point along these two slopes.

Although they have no effect on the measurement being taken, it is interesting to note that peaks with a reflection coefficient of >1 can be observed near to the entry and exit of the roll bite, as shown in Figure 8.27. These peaks occur in the same position relative to the roll bite entry and exit, regardless of roll bite width or rolling conditions and correspond to the constructive interference experienced from the unexpected waves shown in Figure 8.18 and Figure 8.19.

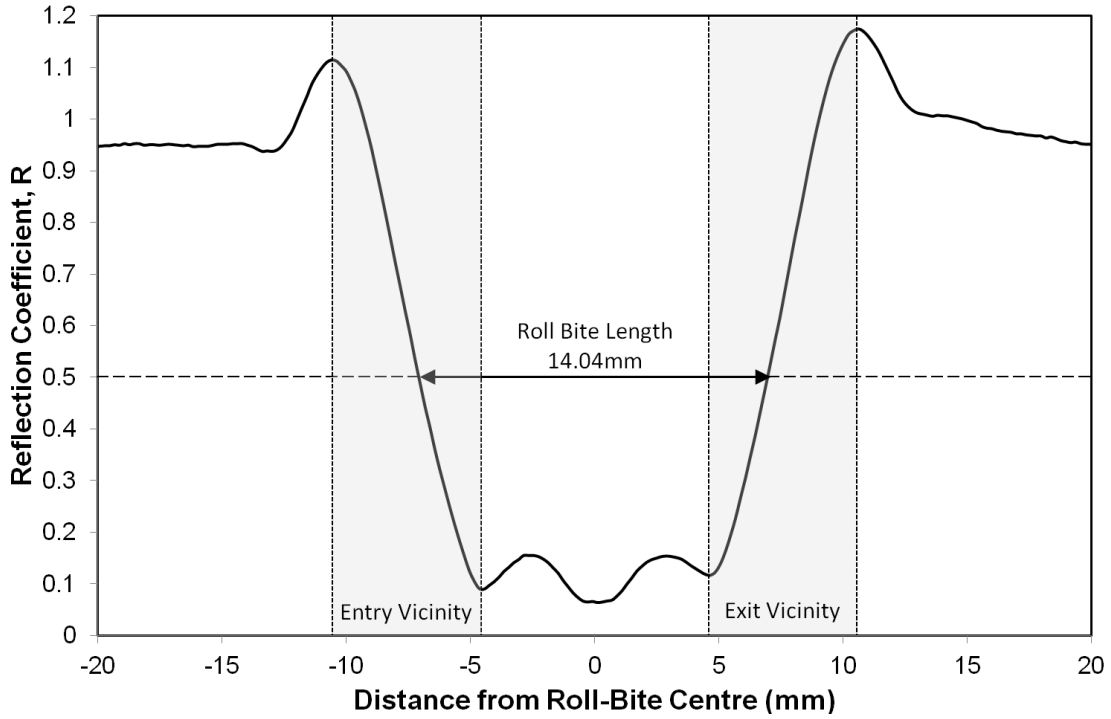

Figure 8.27: Reflection Coefficient Profile across Roll Bite.

Reflection coefficient profiles corresponding to several strip elongation values are plotted in Figure 8.28. It can be seen from the Figure that different rolling conditions result in different roll bite widths. The strip elongation is a function of the strip reduction. Geometrically a greater reduction would be expected to have a wider roll bite width. A larger strip elongation induces a larger roll-bite length for two reasons. The first reason is geometrical, the arc of the roll intercepted by the strip becomes larger as the strip elongation increases. The second is due to the larger rolling load inducing roll deformations leading to a larger contact length.

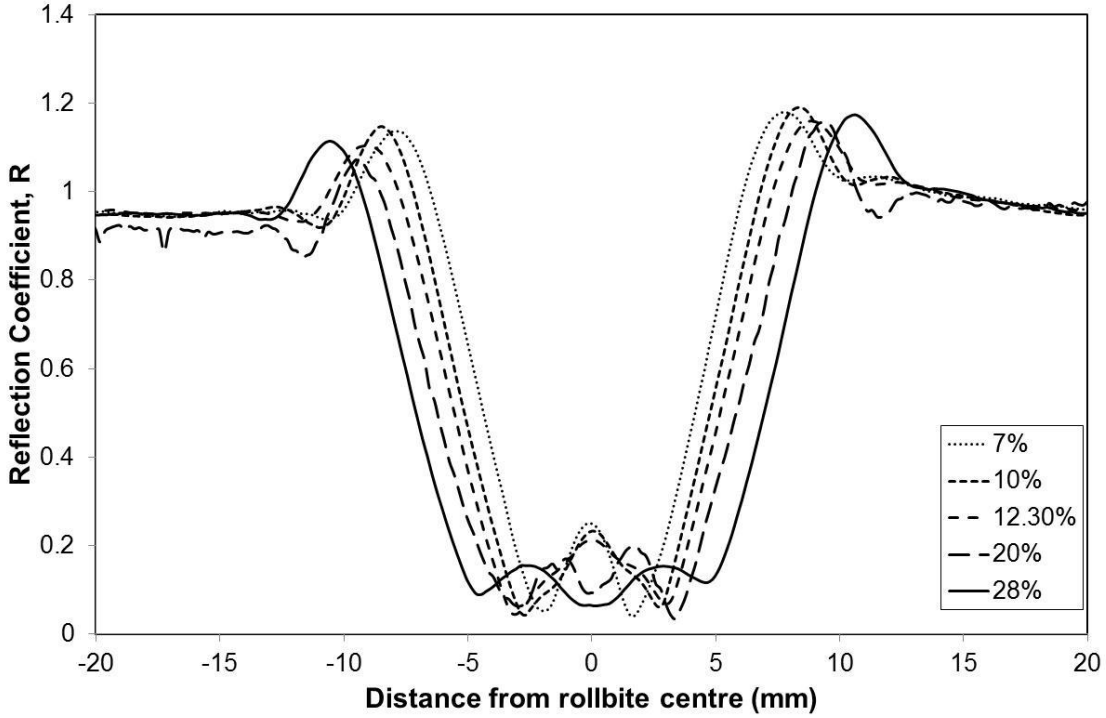

Figure 8.28: Longitudinal Response for Various Strip Elongations.

The roll-bite length can be estimated by measuring the distance between the entry and exit slopes of the graph. This is done by measuring points of equal value on the reflection coefficient profile. Figure 8.29 shows the calculated roll bite width for different reflection coefficient threshold values from the shear and longitudinal responses for the different elongation cases.

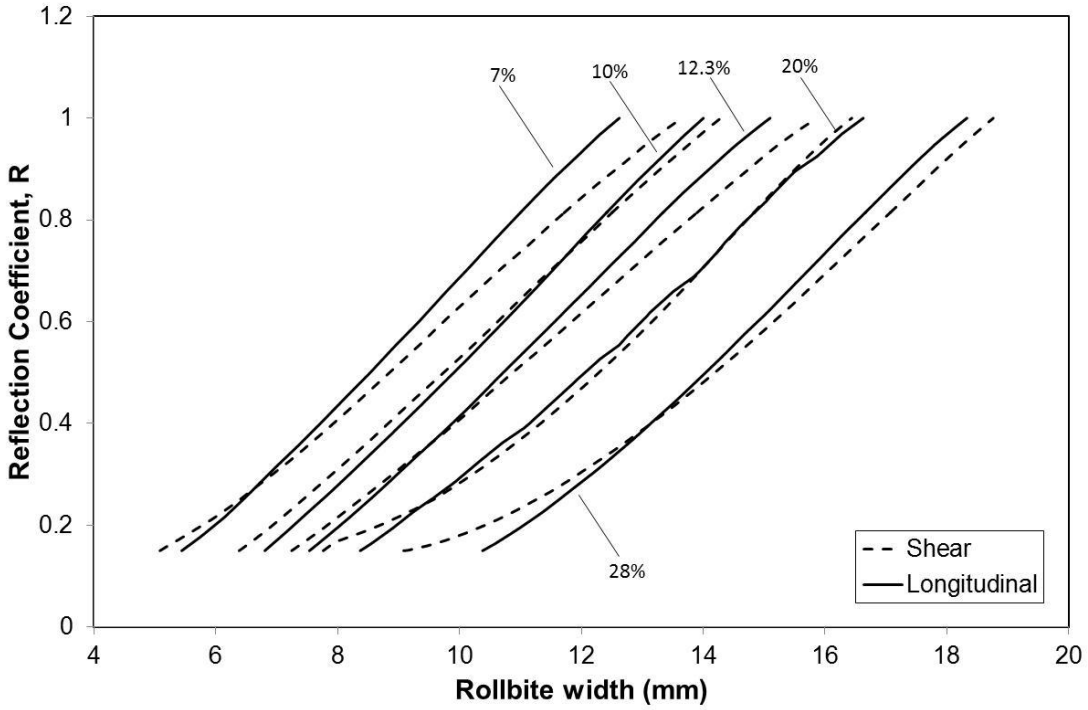

Figure 8.29: Reflection Coefficient Threshold against Calculated Roll Bite Width.

As shown in Figure 8.30 the sensing spot is averaged across the sensor width, in this case approximately 2mm. This is significant with respect to the roll bite length, but still smaller than

the roll bite width in all test conditions presented. It is because of this that the response changes with a linear gradient into and out of the roll bite. The actual location of the entry and exit of this roll bite occurs at some point along this slope, this was assumed to be the midpoint (R = 0.5).

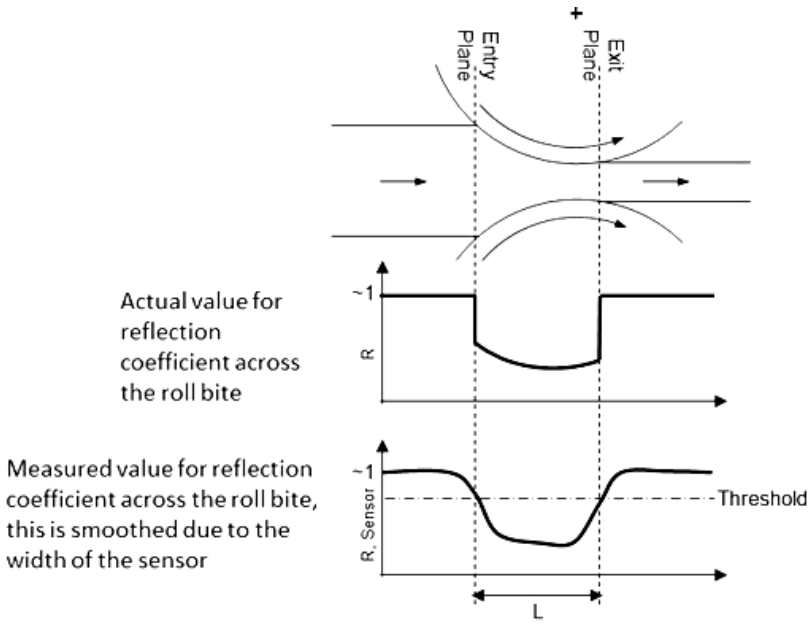

Figure 8.30: Reflection Coefficient Smoothing due to Sensor Width.

The roll bite width for the test cases given in Table 6.15 were measured ultrasonically using a threshold of 0.5. The results for tests with varying rolling speed are plotted in Figure 8.31 and those with varying elongation are plotted in Figure 8.32.

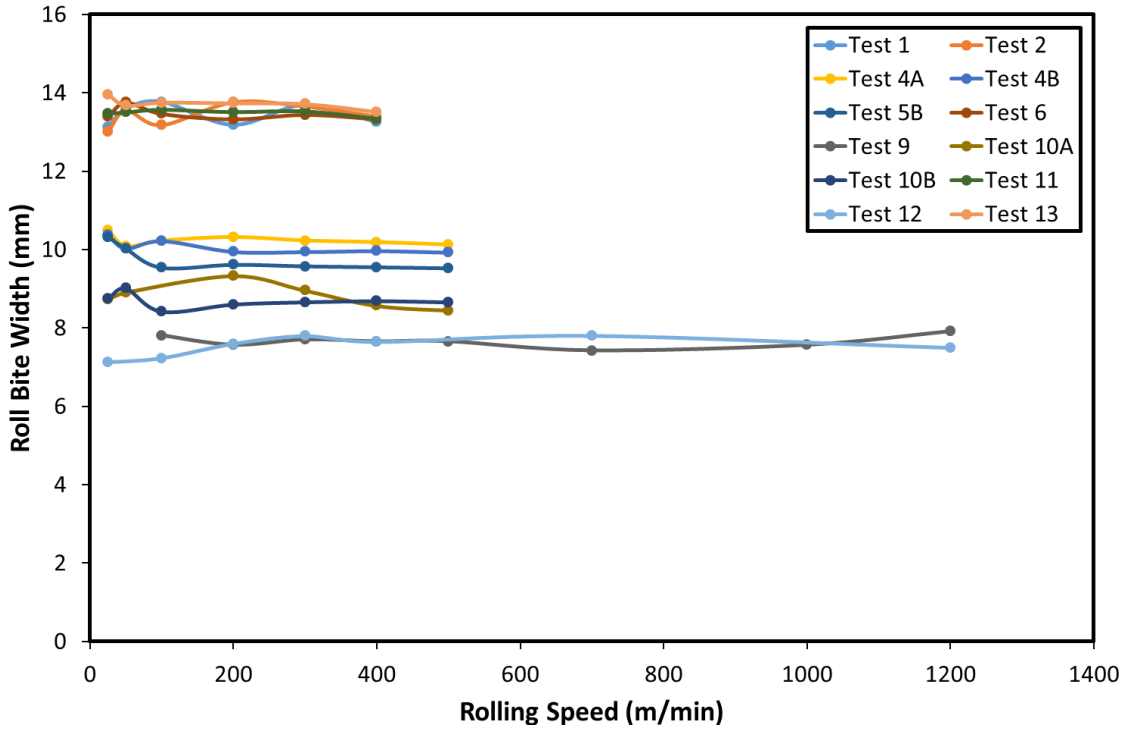

Figure 8.31: Roll Bite Width for Test Conditions with varying Rolling Speed.

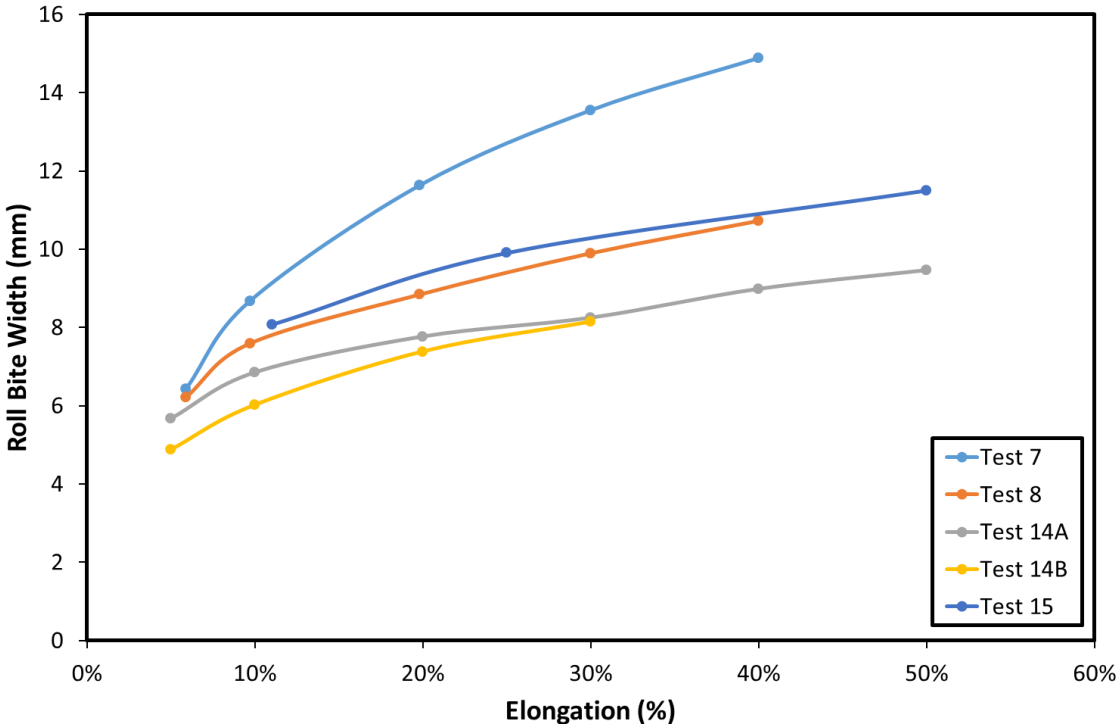

Figure 8.32: Roll Bite Width for Test Conditions with varying Strip Elongation.

It is clear from the plots that the roll bite width remains constant with rolling speed. The tests completed with the thicker strip have a larger roll bite width (~13.5mm), as would be expected. The results for the thicker strip are consistent regardless of lubrication conditions. The measured contact widths for the thinner strip are smaller. While they are also constant with rolling speed, they do demonstrate some variation with lubrication conditions. Tests with higher emulsion percentages and more viscous oils show small contact sizes. This can be explained by the reduced rolling load that is required.

The roll bite width changed for tests with varying strip elongations, again this was expected. Greater elongation resulted in larger roll bite widths, with the thicker strip demonstrating a larger roll bite width for a given elongation, as dictated by the geometry of this case.

To verify the results gained from measuring the roll bite width ultrasonically, the results where compared with those predicted by simple geometry, as given in Equation 8.16.

$$L = \sqrt{R(h_0 - h_1)} \qquad 8.16$$

Where L is the roll bite length, R is the roll radius, h_0 and h_1 are the entry and exit strip thicknesses respectively. The results from both the ultrasonic testing and those calculated from the above equation compare favourably. The results for two entry strip thickness across a range of elongations are plotted in Figure 8.33. The roll bite width predicted by simple geometry is slightly larger than the measured value, especially for smaller elongations.

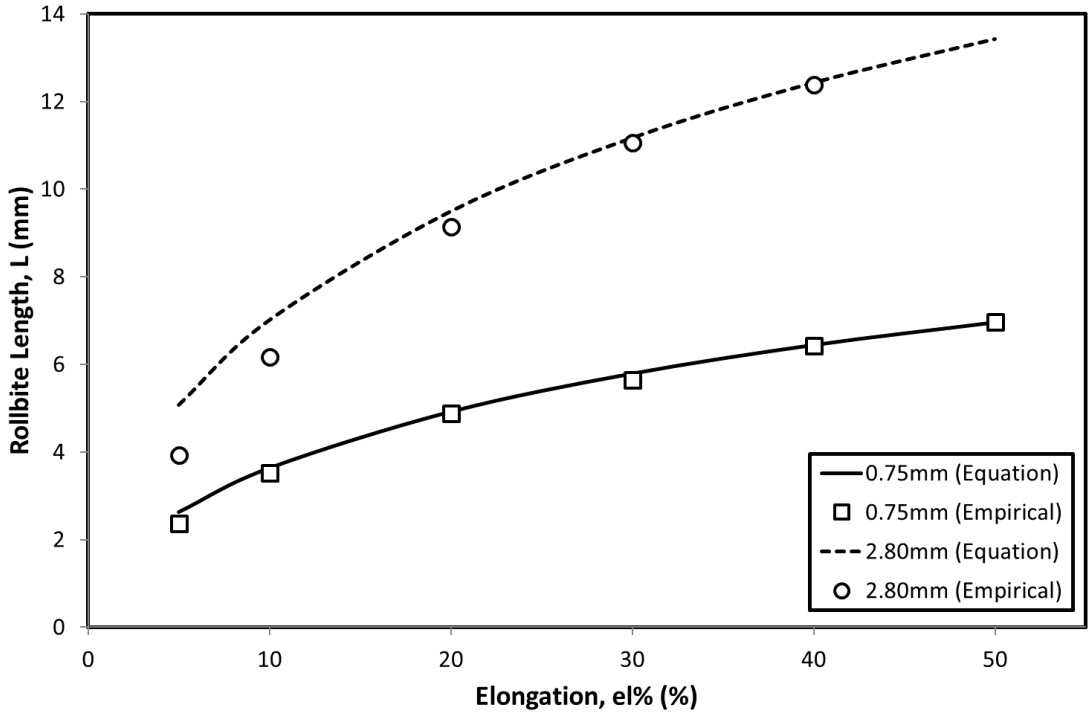

Figure 8.33: Calculated (Equation 8.16) and Measured Roll Bite lengths for 0.75mm and 2.8mm strip thicknesses with various elongations.

8.4.1 Dynamic Measurements

The contact width was also determined continuously while strip elongation was increased during rolling. The variation observed in the transient regime is plotted in Figure 8.34 along with strip elongation.

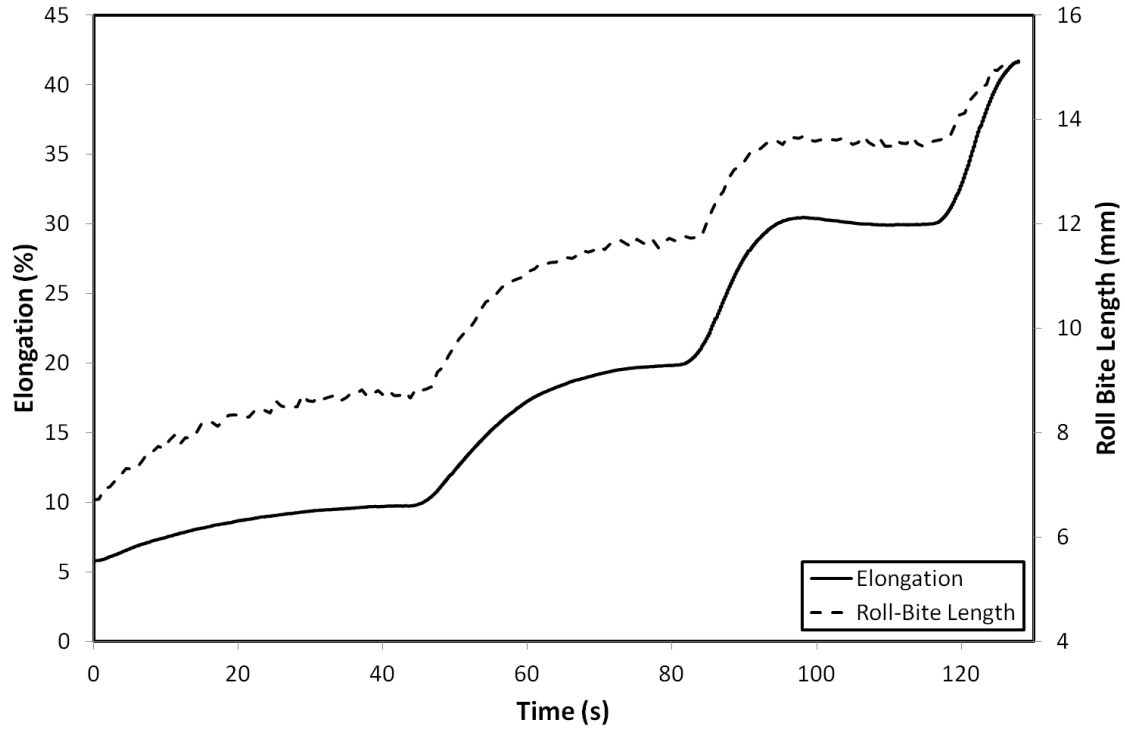

Figure 8.34: Contact Width Measured Ultrasonically in the Transient Regime and Elongation Measured by the Mill Coiling System.

These two curves exhibit the same pattern, with strip elongation increasing from 5% to 40%, while contact length varies from 6.7mm to 15.1mm, demonstrating how such measurements can be taken dynamically.

8.5 Strip Thickness

The A-Scan in Figure 8.35 shows a train of returned pulses from the roll bite of the Sheffield pilot mill. A pulse voltage of 150 V was used, with a gain in the range of 20-30 dB. This graph presents a number of reflections from different interfaces, with the time difference between the pulses being the result of the respective differences in wave path length and propagation material speed of sound. When the sensing face is outside of the roll bite, only reflections coming from the roll surface are observed. However, as this figure shows, when the sensing face is in the roll bite reflections are received from both the upper and lower faces of the strip.

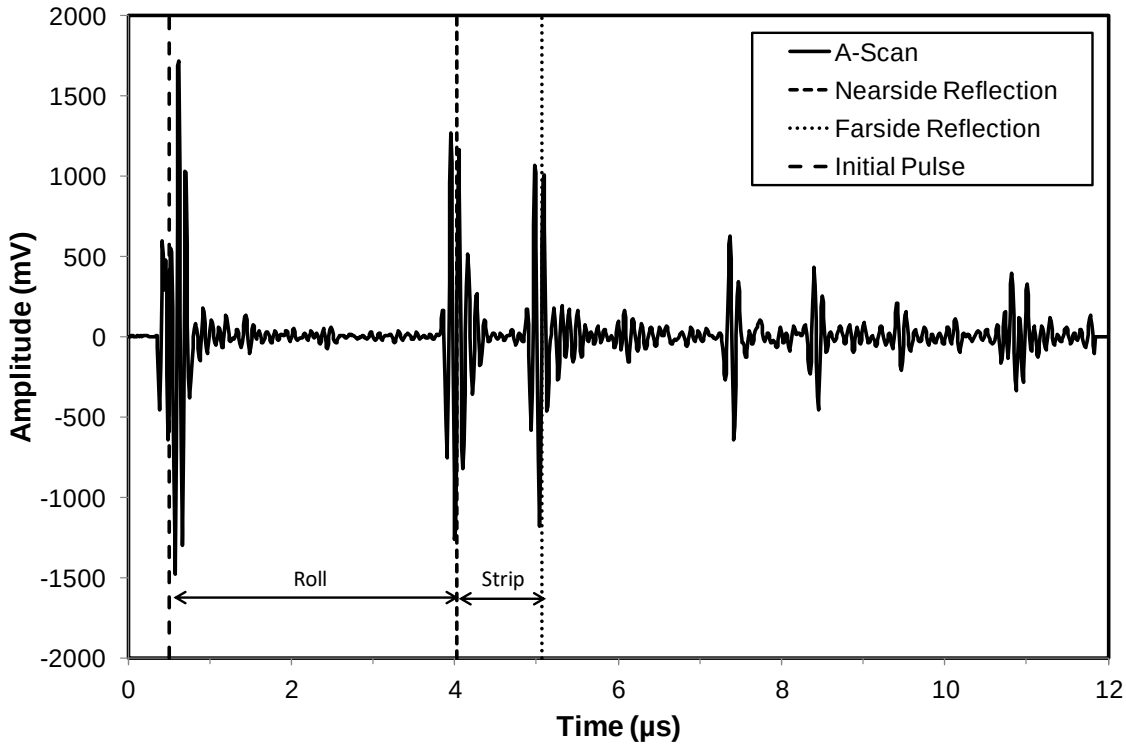

Figure 8.35: Pilot Mill AScan from the Roll Bite.

When the sensing surface is in the roll bite, the signal amplitude of the first roll reflection also decreases. The difference in Time-of-Flight (ToF) between the various pulses can be used to measure distance via the speed of sound in the transmission media. For example, the difference between the reflections from the nearside and farside of the strip enable the measurement of the strip thickness.

8.5.1 Strip Thickness Measurement Method

For the time of flight value to be accurate a consistent point on each returned pulse must be taken. The simplest approach to time a returning pulse is to take a threshold value, but a change in pulse amplitude will affect the accuracy of this. Another approach is to select the maximum peak. However, when there are two peaks that are close in amplitude a small change in amplitude (such as that caused by noise) can cause the algorithm to jump from one peak to another. Simple peak location detection has a resolution the same as the sampling rate. This can be increased by fitting a curve to the peak to interpolate between samples. This method is more

complicated, computationally expensive, prone to inaccuracies and heavily affected by noise. Alternatively, cross-correlation algorithms can be used which locate the pulse as a whole entity, rather than a single point. However, these are more complex, require greater processing of the captured data and a consistent signal shapes.

Instead the ToF was determined with a zero-crossing method. This consisted of measuring the intersection of the response with the horizontal axis at a point between a selected peak and the following minima. To ensure a consistent zero-crossing was selected the first positive-to-negative zero crossing after the threshold peak was then selected. The threshold that was applied was scaled based upon the maximum waveform value. This went some way to reducing errors caused by amplitude changes, although was not infallible. Figure 8.35 shows the points described above.

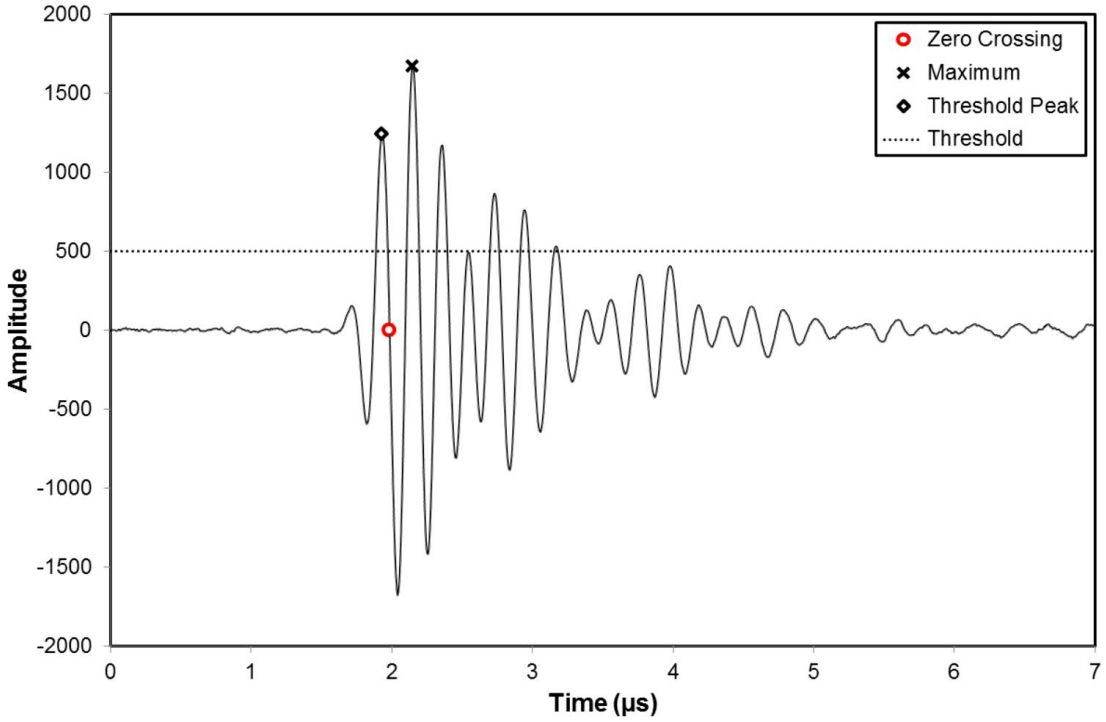

Figure 8.36: Pilot Mill AScan from the Roll Bite.

As the slope of the data at a zero crossing is nearly linear, and it has a steep gradient, it is possible to interpolate between data points either side of the zero crossing to increase the resolution. The same zero-crossing approach was applied to both the first and second reflections and the difference in the time between these was taken as the ToF. This relies on at least two clear reflections being observed.

The time difference obtained with zero-crossing is not only due to the distance between the top and bottom part of the strip (it's thickness), it is also affected by phase shift and the acoustoelastic effect. Indeed, when a reflection occurs at a contact between two components both the amplitude and the phase are affected by contact conditions (Reddyhoff, Kasolang, & Dwyer-Joyce, The Phase Shift of an Ultrasonic Pulse at an Oil Layer and Determination of Film Thickness, 2005). Therefore, phase shift induces a variation of the signal shape which may give inaccurate measurements with ToF. However, measurement error due to phase variations observed in experimental measurements were small compared to the overall strip thickness and therefore neglected in this study.

Acoustoelasticity, as described in §4, describes a change in the speed of sound in a material under stress. Any change in the sound speed results in a different ToF, and therefore an error in the thickness calculation. However, in the present case, the effect is only slight and the error it will induce is likely to be very small (<1%) and so again it has been disregarded.

8.5.2 Strip Thickness Results

For the results presented here the strip thickness is computed from signals measured with shear sensors. As shear waves travel at approximately half of the speed of longitudinal waves, it is possible to gain almost twice the resolution in strip thickness using the same digitising rate. The speed of sound for bulk shear waves in the plug when the material is unloaded is 3252.68 m/s

The strip thickness obtained from experimental measurement using two sensors for the rolling conditions in Table 8.10 is plotted in Figure 8.37.

Entry Strip Thickness, h_0 (mm)	Elongation, el. (%)	Entry Strip Tension, σ_1 (MPa)	Exit Strip Tension, σ_2 (MPa)	Rolling Velocity, V_R (m/min)	Rolling Force, F_y (N/mm)	Forward Slip, S_F (%)
2.8	29.7	44	117	22.5	6138	4.3

Table 8.10: Test Conditions for Strip Thickness Measurements.

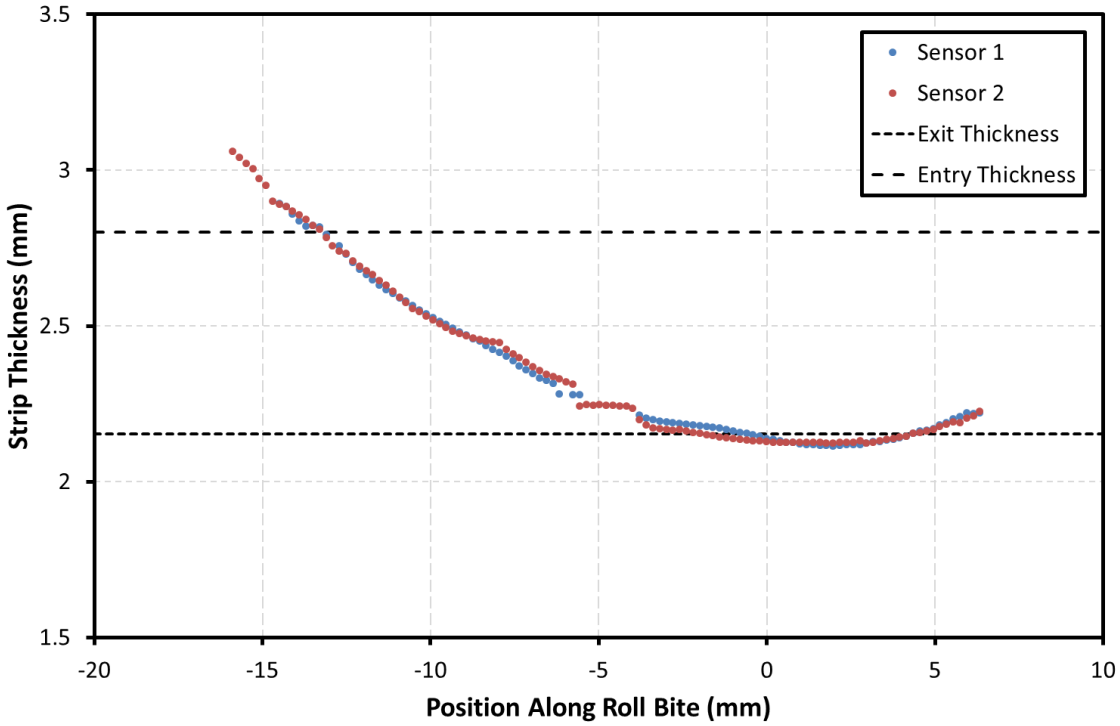

Figure 8.37: Ultrasonic measurement of Strip Thickness Profile from two Shear Sensors.

The measured profile gives the correct trend of decreasing strip thickness across the roll bite, and the strip thickness magnitudes report seem reasonable. The results appear to give an initial strip thickness in excess of the entry strip thickness according to Table 8.10. The reason for this is that the ultrasonic beam spreads as it propagates through a material, and the wave at the extremes of the beam is travelling at an angle to the primary beam direction. This means that while the sensing spot may appear to be outside of the roll bite, some of the signal at the extreme of the ultrasonic beam is returning from the roll bite. This signal will be travelling at an

angle, so when passing through the strip will have a longer path length than the thickness of the strip, thereby explaining this erroneous reading.

By measuring the roll bite length for this test condition using the reflection coefficient curve as described earlier a length of 14.04 mm is obtained.

8.5.3 Limits of Strip Thickness Measurement

Two entry strip thicknesses where trialled, 2.8 and 0.75 mm. During these tests it was noticed that for the thinner strip the ultrasonic pulses reflected from the top and bottom of the strip overlapped in the time-domain. The strip thickness at which the pulses begin to overlap can be calculated from Equation 8.17.

$$h = \frac{cl}{2} \qquad 8.17$$

Where *h* is the strip thickness, *c* the speed of sound in the strip and *l* the pulse length in the time domain. Figure 8.38 and Figure 8.39 show the first reflections for the two wave types in the testing performed, these along with Equation 8.17 where used to calculate the values given in Table 8.11. This gives the minimum strip thickness that can be measured with each sensor type without the pulses overlapping in the time-domain. This is important because overlapping pulses will result in interference, distorting the pulse shape and disrupting the strip thickness measurement.

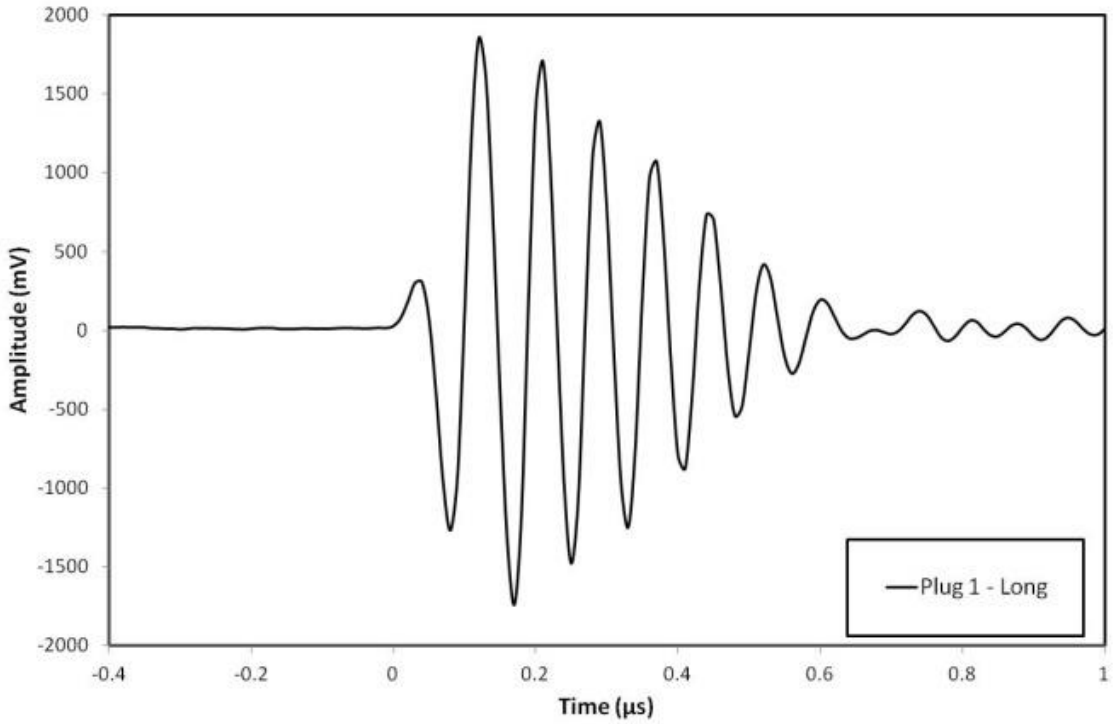

Figure 8.38: First Reflection for Longitudinal Sensor.

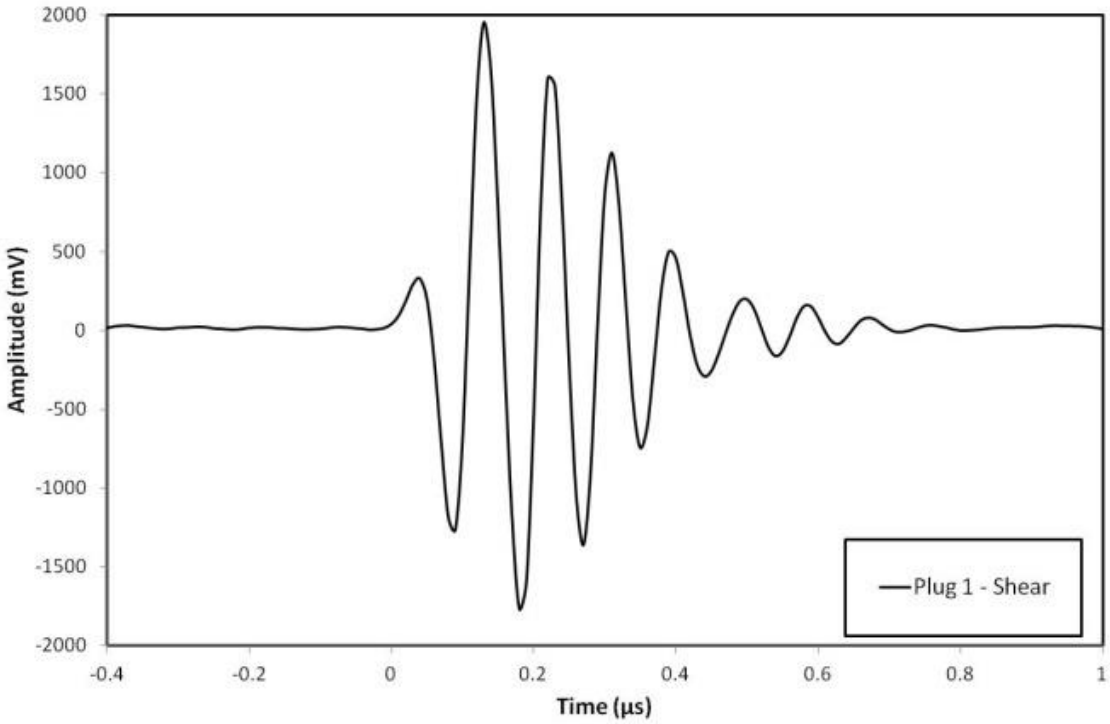

Figure 8.39: First Reflection for Shear Sensor.

Wave Type	Speed of Sound (m/s)	Pulse Length (µs)	Min. Strip Thickness (mm)
Longitudinal	5994.85	0.5	1.499
Shear	3251.16	0.4	0.650

Table 8.11: Pulse Lengths and Equivalent Strip Thicknesses.

Both 2.8mm and 0.75mm thick strip was used during testing. It can be seen from Table 8.11 that the longitudinal sensor cannot be used for the thinner strip. To change this limitation, it can be seen that the pulse length would need to be altered as it would be impractical to specify a different strip speed of sound. Equation 8.18 shows the variables which influence the pulse length.

$$l = \frac{n}{f} \qquad 8.18$$

Where *l* is the pulse length, *n* is the number of cycles of the pulse and *f* is the pulse centre frequency. Therefore by reducing the number of cycles, or increasing the sensor frequency, a thinner strip could be measured. The number of cycles in a signal is dependent on a few factors. This includes the signal used to excite the sensor. In order to reduce the pulse length this should tend towards an impulse. The number of cycles in the signal is then dependent on its damping, the rate at which the sensor response dies down after excitation (often referred to as the sensor 'ringing', analogous to a musical bell). The damping is controlled by the mechanical constraint of the sensor. Better damping curtails the sensors response resulting in fewer cycles, and this can be achieved by mechanically clamping the sensor, or applying mass to the sensor faces. In practice this is often achieved by applying a tungsten loaded epoxy to the back of the sensor, or by bonding the front face of the sensor onto the inspected part.

8.6 Conclusions

The assembled ultrasonic measurement system, and plug instrumentation method, have both been successful, yielding good ultrasonic signals. Data has been recorded while the mill has been running, and ultrasonic signals across the roll bite captured. A comparison between equivalent sensors installed on different plugs shows a very good consistency.

The data recorded as the mill was running has been used to create B-Scan plots. These show an unexpected ultrasonic response. In addition to expected reflections from the roll surface, and far side of the strip, the B-Scans have also shown secondary waves which appear to be associated with the roll bite entry and exit points. These waves appear to interfere with the roll surface reflection in and around the roll bite entry and exit. This may cause disruption to data recorded at these points.

A variety of roll plug material properties have been measured using the measured longitudinal and shear speed of sound in conjunction with the materials density. This has yielded the Poisson's ratio, Young's modulus, Lamé constant, shear modulus, bulk modulus and acoustic impedance. In addition, an amplitude measurement was used to measure the material attenuation. All the values gained are reasonable when compared to literature values.

Roll bite widths in the region of 5 to 15mm have been measured. The roll bite width has been shown not to vary significantly with rolling speed, but does vary with strip elongation. The results gained agree well with the contact length estimated from simple geometry. The method was successful for both thin (0.75mm) and thicker (2.8mm) strip. The measurements can be taken dynamically as the roll speed is changed.

An approach for measuring the strip thickness profile across the roll bite, during rolling, has been demonstrated. The measured strip profile presented gives a trend of decreasing strip thickness as expected. The strip thickness magnitudes reported seem reasonable. There is some discrepancy as results appear to give an initial strip thickness in excess of the entry strip thickness. It is thought this is due to the ultrasonic wave not travelling perpendicular through the strip and thereby experiencing a long path length. The minimum strip thickness that is measureable has been shown to be dependent upon the ultrasonic pulse length and the material acoustic velocity. For the sensors installed in this study it was calculated that the longitudinal sensor could measure a thickness down to 1.499 mm, and the shear sensor down to 0.65 mm.

9 Roll Bite Interface Measurements

The following chapter presents the results gained from measurements of the rolling interface, specifically measurements of interface stiffness and lubricant film thickness. The results shown were processed from data recorded on an Arcelor-Mittal semi-industrial pilot mill in Maizières-lès-Metz. The results in this chapter were all captured using sensors mounted on a press fit plug fitted to the upper work roll, as described in §6.6.4, with test conditions described in Table 6.15.

9.1 Surface Roughness

When studying the roll bite interface the strip and roll roughness's are a key parameter. These were measured at intervals throughout testing. These values are reported in Table 9.1. The roll roughness did not change significantly throughout the test program. The strip roughnesses were only measured after rolling, no equivalent measurements were taken on the unrolled strip. There was a noticeable difference in the roughness of the two strip materials rolled with the thicker DD14+Ti strip (measured after test 2) exhibiting a higher roughness than the thinner ARCELOR06 strip (measured after tests 5, 12 and 14).

	Surface	R_a (µm)	R_z (µm)	R_{max} (µm)	R_t (µm)	R_{Pc}	R_{sk}
After Test 2	Top Roll	0.618	4.389	5.114	5.434	89	-0.42
	Bottom Roll	0.614	4.413	5.16	5.422	103	-0.28
	Test 2 Strip	1.505	9.653	12.09	12.5	75	-0.09
After Test 5	Top Roll	0.617	4.621	5.841	5.841	92	-0.34
	Bottom Roll	0.651	4.567	5.494	5.917	103	-0.18
	Test 5 Strip	0.101	1.136	1.36	1.481	-	-
After Test 11	Top Roll	0.577	4.065	4.823	4.991	73	-0.33
	Bottom Roll	0.563	4.204	4.882	5.194	75	-0.53
After Test 12	Top Roll	0.563	4.194	4.811	5.186	83	-0.53
	Bottom Roll	0.569	4.309	5.395	5.801	72	-0.25
	Test 12 Strip	0.189	1.4	2.596	2.683	3.5	-1.05
After Test 14	Top Roll	0.543	4.022	4.849	5.136	67	-0.48
	Bottom Roll	0.535	3.697	4.481	4.849	71	-0.26
	Test 14 Strip	0.079	0.915	1.219	1.271	-	-2.41

Table 9.1: Roll and Strip Roughness Measurements taken at Intervals during Testing.

A combined surface roughness value for the top roll and strip was calculated. The roughness values from Table 9.1 where converted to RMS using the relationship $r_{rms} = 1.11\mathrm{r}_a$. This conversion is only an approximation and assumes a sinusoidal surface profile. These values where then added in quadrature to get a combined surface roughness, these values are reported in Table 9.2.

	Top Roll		Strip		Combined
Test No.	R_a (µm)	R_{RMS} (µm)	R_a (µm)	R_{RMS} (µm)	R_{RMS} (µm)
2	0.618	0.680	1.505	1.656	**1.790**
5	0.617	0.679	0.101	0.111	**0.688**
12	0.563	0.619	0.189	0.208	**0.653**
14	0.543	0.597	0.079	0.087	**0.604**

Table 9.2: Combined Roughness Measurements for Top Roll and Strip.

9.2 Ultrasonic Data Capture and Processing

Each sensor was excited with a pulse at a Pulse Repetition Frequency (PRF) of 7.5 kHz or 9 kHz depending upon the test. For each excitation, the time-domain sensor response was recorded. Only a short window in the time domain was captured, as defined by a time delay from the sensor excitation, and a window length (also known as the range). The captured window was adjusted to ensure that the first returning pulse reflected from the roll-strip interface was recorded.

9.2.1 Data Capture

The data was captured using a specialist PCI card (Tribosonics RapiDAQ) which buffered the captured data locally on the card memory. Each buffer was then transferred to the PC memory via the PCI interface for processing and storage. It was necessary to transfer data using this buffering approach due to throughput limitations of the PCI interface.

Example responses for a buffer of one longitudinal and one shear sensor can be seen in Figure 9.1a. This buffer captured two revolutions of the roll, and therefore two passes of the roll bite. The amplitude axis represents digitiser bits (12-bit digitiser). While this could be converted to a voltage based upon the digitiser range, it is necessary to consider the amplification applied and the electrical characteristics of the sensor, cabling and data-acquisition system in order to yield a meaningful value. As the results are normalised in the later analysis this is of little value and the data has been left in its original bit format.

Figure 9.1b shows a zoomed view of the data from just one roll bite pass. The individual ultrasonic reflections can now be seen, and a clear change in amplitude is observed between the reflections inside and outside of the roll bite. It should be noted that the data shown in Figure 9.1a and Figure 9.1b doesn't represent a continuous recording of time, there is a delay between the successive responses. The length of these gaps are constant and depend upon the PRF and captured window length.

Once a buffer of data was received, it was then broken down into its constituent time domain responses (A-Scans). Figure 9.1c shows two example A-Scans from outside and inside the rollbite. Each A-Scan was then processed to produce a single reading of interfacial stiffness, stress or strip thickness depending upon the algorithm used. To extract interfacial stiffness the wave amplitude for a certain frequency must be calculated. This is done in the frequency-domain. The frequency-domain response is calculated by applying a Fast Fourier Transform (FFT) to the time-domain response. Examples of the frequency spectra for the A-Scans in Figure 9.1c are shown in Figure 9.1d.

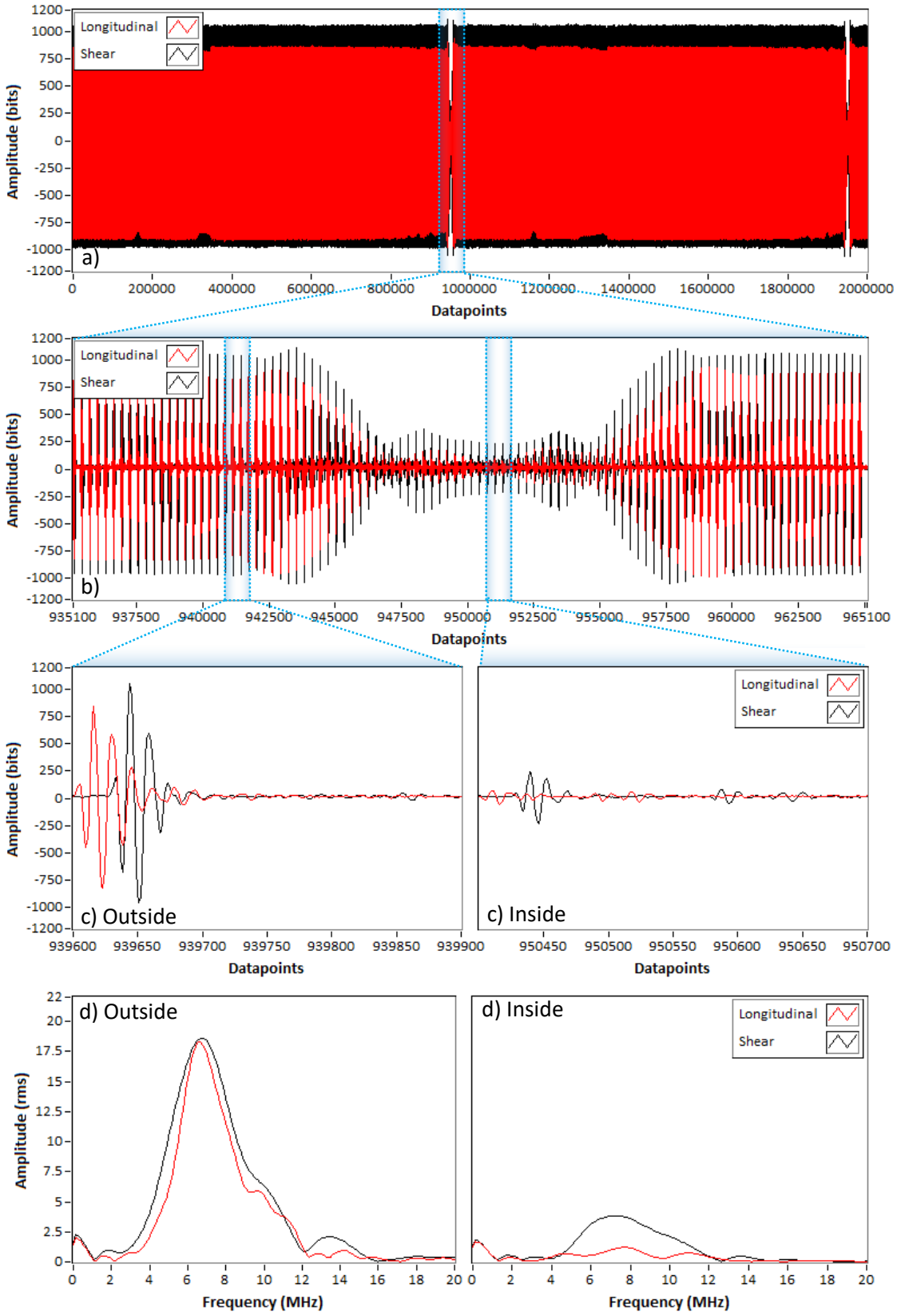

Figure 9.1: Ultrasonic data showing a) Data Buffer b) Responses across the Roll Bite c) A-Scans from Outside and Inside the Roll Bite d) Frequency Spectra of A-Scans Outside and Inside the Roll Bite.

9.2.2 Signal Amplitude – Frequency Approach

The resolution of an FFT is dependent upon the length (number of data points) and resolution of the time-domain data, as defined in Equation 9.1:

$$N = \frac{f_s}{\Delta f} \qquad 9.1$$

Where N is the number of time-domain samples, f_s is the sampling frequency and Δf is the FFT resolution. The A-Scans shown in Figure 9.1c are 300 points long and recorded at 100 MHz. An FFT on this data will therefore have a resolution 333.3̇ kHz.

It is possible to decrease the frequency step of the FFT, and therefore create an apparent increase in resolution, by zero-padding the time domain data. This involves adding zero values to the end of the data to increase the number of samples put into the FFT. As can be seen from Equation 9.1 for a fixed sampling frequency an increase in N will result in a decrease in Δf. Normally the amount of zero padding is selected to give a waveform with a length equal to a power of two. This is to enable the use of more efficient FFT algorithms. However in this testing the processing was performed post capture and computational efficiency was less of a concern. Instead the amount of zero-padding has been selected to yield a set frequency resolution (100 kHz). This is to allow comparisons at the same frequencies between the various sensors and tests, even where the time-domain capture length may be different. Although the FFT produced is of a finer frequency step it doesn't actually increase the true resolution. Zero-padding is in essence a form of interpolation which just more clearly defines the underlying Sinc function.

Once the FFT had been calculated the change in amplitude at a set frequency was recorded. The frequency that displayed the maximum energy when the interface was subject to air was selected, as this represents the frequency with the best Signal-to-Noise Ratio (SNR). In the case of the data shown in Figure 9.1 the amplitude at 6.5 MHz was used. The amplitude of the FFT at 6.5 MHz for all of the data in Figure 9.1a is plotted in Figure 9.2. The two passes of the roll bite in this data are clearly visible. Dips can also be seen in this plot at around datapoints 1100 and 4500. As these are only observed in the longitudinal response it is likely that they correspond to liquid on the surface of the roll, possibly the points on the roll at which coolant is sprayed.

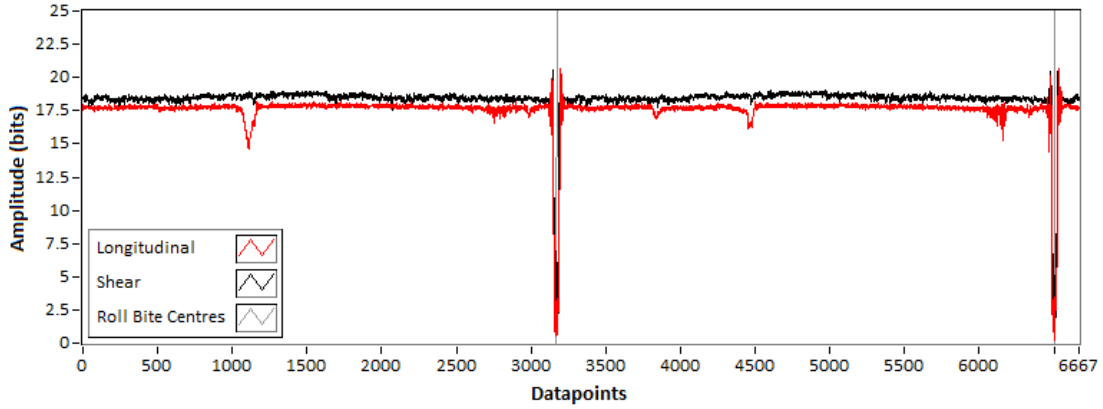

Figure 9.2: Amplitude at 6.5 MHz for each A-Scan displayed in Figure 9.1a.

By cropping the data to just the first roll bite pass, we can see the form that the amplitude of the ultrasonic response takes, as shown in Figure 9.3. This plot also shows the roll bite centre

and width calculated using the approach described in §8.4 for both the shear and longitudinal responses.

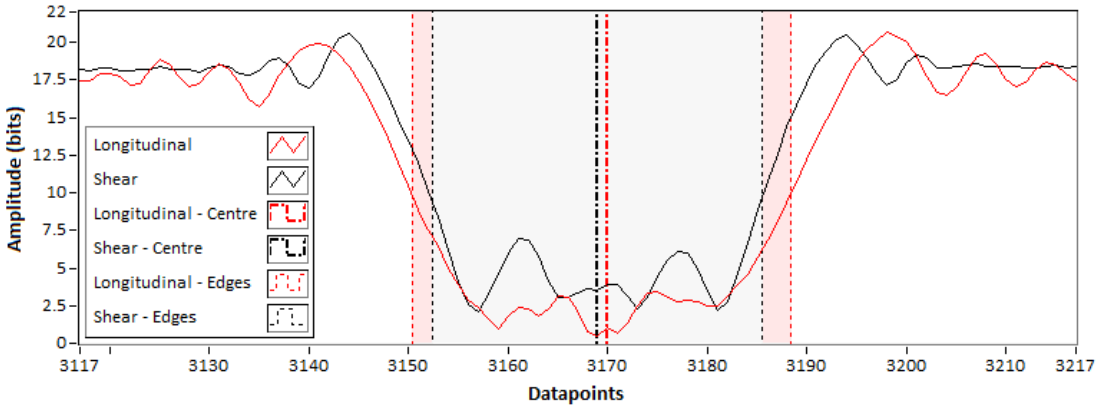

Figure 9.3: Amplitude at 6.5 MHz across Roll Bite.

Within each dataset the centre of every roll bite pass was located and the data was cropped around these points. This yielded a set of equivalent A-Scans for each successive roll bite pass. Knowing the time separation between each roll bite centre also allowed the rotational speed of the roll to be calculated. This speed was compared to the rolling speed recorded separately by the mill control system, to help verify the data had been recorded correctly. The amplitude profiles for multiple passes of the roll bite under the same conditions at four different rolling speeds are given in Figure 9.4.

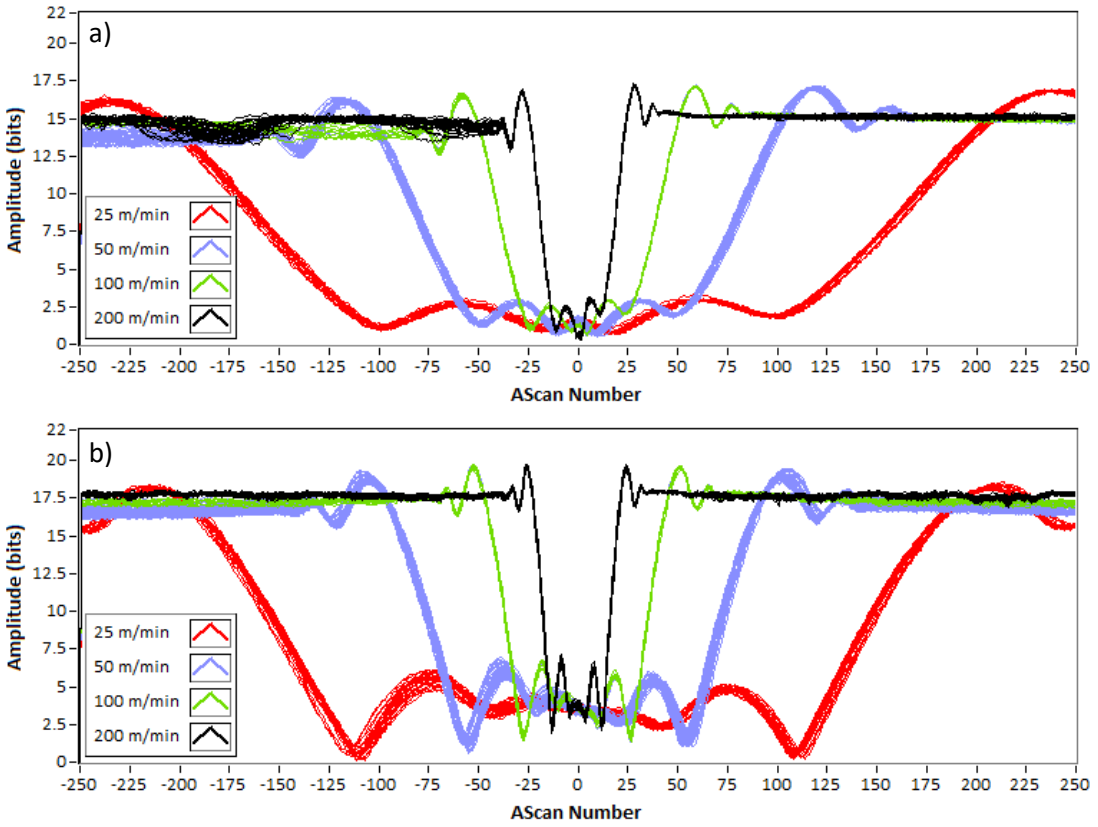

Figure 9.4: Amplitudes for Multiple Passes across Roll Bite and 4 different Rolling Speeds a) Longitudinal Response at 6.8 MHz b) Shear Response at 7.2 MHz.

The Figures show that the data received for successive passes had a good consistency at each test condition. A fixed PRF was used throughout these tests, meaning that more A-Scans were recorded across the roll bite at slower speeds. In Figure 9.4 this has the effect of stretching the roll bite profile as the amount of roll rotation occurring between each A-Scan reduces.

9.2.3 Signal Variation

To quantify the variation between roll bite passes equivalent A-Scans both at a point outside of the roll bite, and at the centre of the roll bite, were compared at a rolling speed of 50 m/min. The mean, standard deviation and 99% certainty boundaries were calculated at each point across the A-Scan to see it there were any points that showed particular variation. The 99% certainty was calculated by assuming the results were normally distributed and multiplying the standard deviation by 2.326. The results of this for a shear sensor are plotted in Figure 9.5.

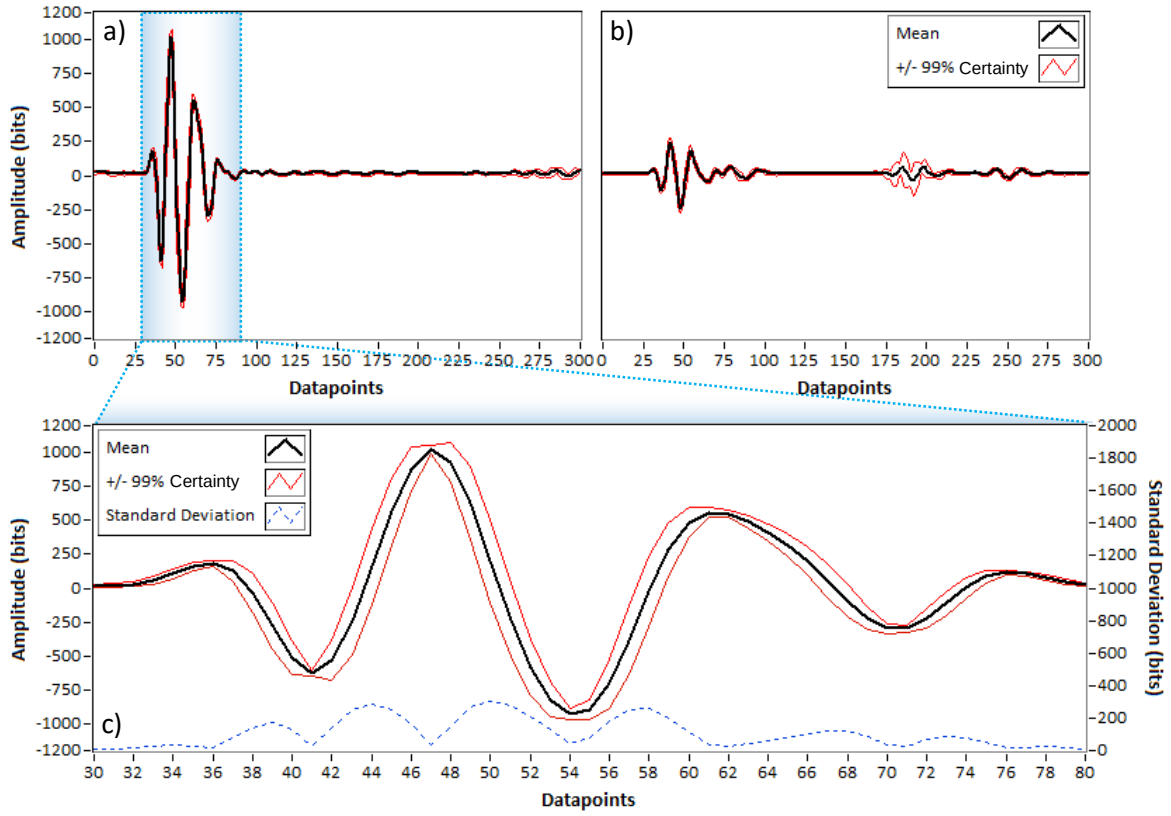

Figure 9.5: Shear Sensor A-Scan Variation for Multiple Passes a) Outside Roll Bite b) Inside Roll Bite c) Zoomed View of First Reflection Outside Roll Bite.

In Figure 9.5 the second reflection of the A-Scan inside the roll bite (Figure 9.5b starting at datapoint 175) shows the most variation. This reflection corresponds to the far side of the strip. The pulse returning from this interface will have reflected from the bottom strip interface and passed through the top strip interface twice. Any changes in either of the strip interfaces will have an effect on the returned signal, and as these effects are compounding, the reflection is very sensitive which results in the fluctuations seen. This is an important consideration in assessing the applicability of ultrasonics as an in-situ strip thickness measurement technology. Apart from this reflection the rest of the A-Scans in Figure 9.5a and Figure 9.5b show a regular level of variation likely to be the result of consistent background noise. Figure 9.5c shows a close up view of the first reflection outside of the roll bite. The variation seen is lowest for the parts

of the signal which have the least gradient. This can be explained by the pulse shifting in the X-axis. The timing accuracy of the pulse trigger electronics and digitiser is significantly better than the level of variation seen, so it is likely this variation is actually a signal phase shift. This could possibly be due to a change in the bulk speed of sound in the roll/plug material due to heating as the test was running. The variation in the timing of the pulse will not affect any amplitude measurements being taken, but may affect any thickness, deflection or stress measurements, which all rely on an accurate measurement of time.

9.3 Interference Effects

A shear sensor B-Scan, for the same data as shown in Figure 8.19 is plotted in Figure 9.6. This was made by averaging multiple passes of the roll bite at a rolling speed of 50 m/min.

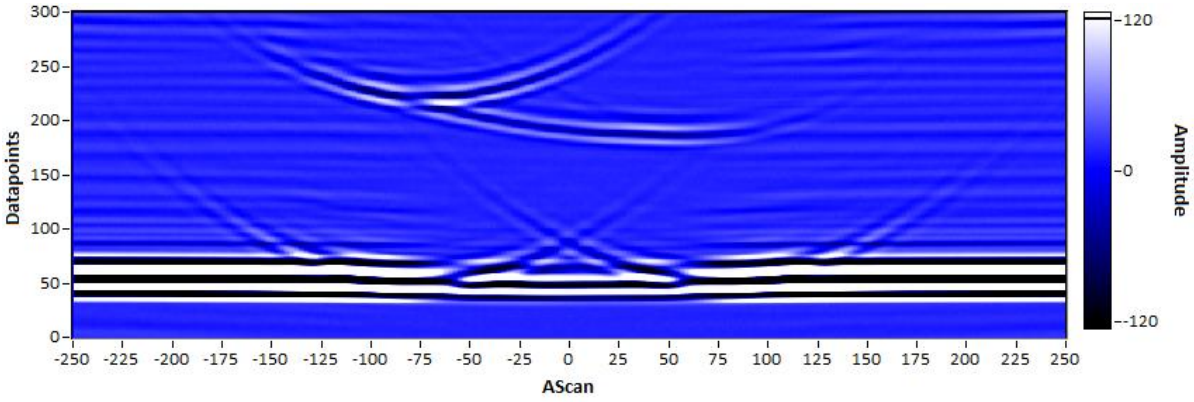

Figure 9.6: B-Scan of Roll Bite with Rolling Speed of 50m/min.

A spectrogram was created from the data in Figure 9.6. Each A-Scan was cropped to the first 140 points to remove the reflection seen from the far side of the strip. An FFT was performed on each A-Scan in turn. The frequency spectrum from a reference pulse was then subtracted. This reference spectrum was taken from an A-Scan recorded outside of the roll bite. This gave a set of frequency spectra which show only the change in frequency amplitude compared to the reference spectrum. Finally the data was normalised with respect to the maximum value to create the spectrogram plotted in Figure 9.7.

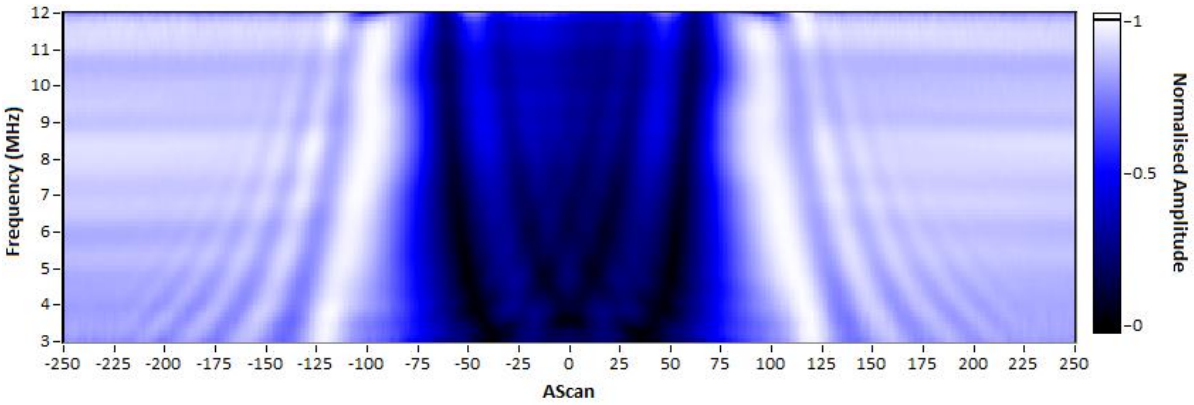

Figure 9.7: Normalised Spectrogram of the Roll Bite corresponding to Figure 9.6.

Figure 9.7 displays a distinctive 'curtain' pattern. It was hypothesised that this pattern is the result of the interference between the first reflection and reflections from the roll bite entry and exit, as described in §8.3.3. To ascertain if this pattern was consistent with the interference

pattern expected, the location of the interference maxima were calculated. This was based upon the relative time difference between the first and interfering reflections, if the interfering reflections were emanating from the roll bite entry and exit. These maxima are described by the following relationship, Equation 9.2.

$$b = a - \frac{v\sqrt{[(nc/2f) + d]^2 - d^2}}{60R_p} \qquad 9.2$$

Where b is the A-Scan number, a is the A-Scan number at the roll bite entry or exit relative to the roll bite centre, v the strip speed in m/min, R_p is the pulse repetition rate, d is the plug length, m is the interference mode, c is the speed of sound in the plug and f the frequency of the interference maxima. The values in Table 9.3, which are from the rolling case plotted in Figure 9.7, were entered into this equation to get the interference pattern in Figure 9.8.

Offset, a	-82 and 82
Strip Velocity, v	45 m/s
Mode, n	0 to 5
Rep. Rate, R	9 kHz
Plug Length, L	35 mm
Plug SoS, c	3247.72 m/s

Table 9.3: Interference Relationship Values.

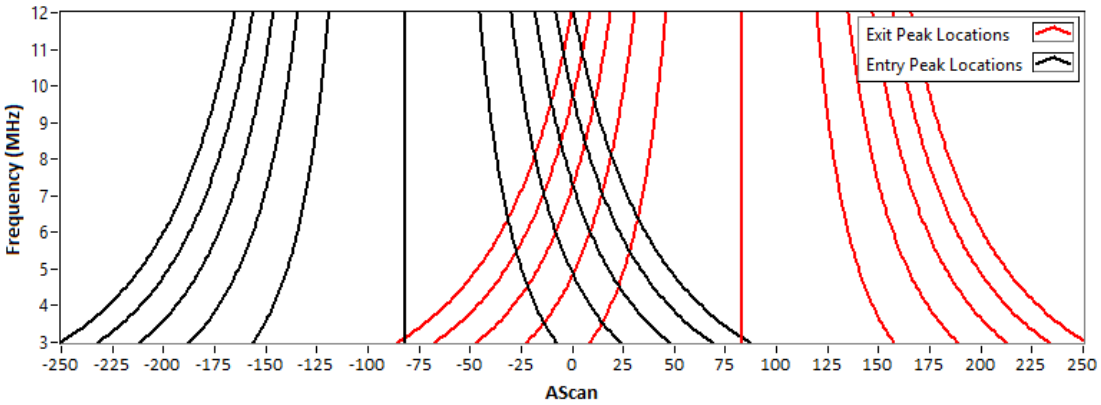

Figure 9.8: Interference Peaks from Equation 9.2 and values in Table 9.3.

A peak location algorithm was applied to Figure 9.7 to determine the location of the measured interference maxima. This data was then combined with Figure 9.8 to create Figure 9.9 which compares the theoretical and experimental values.

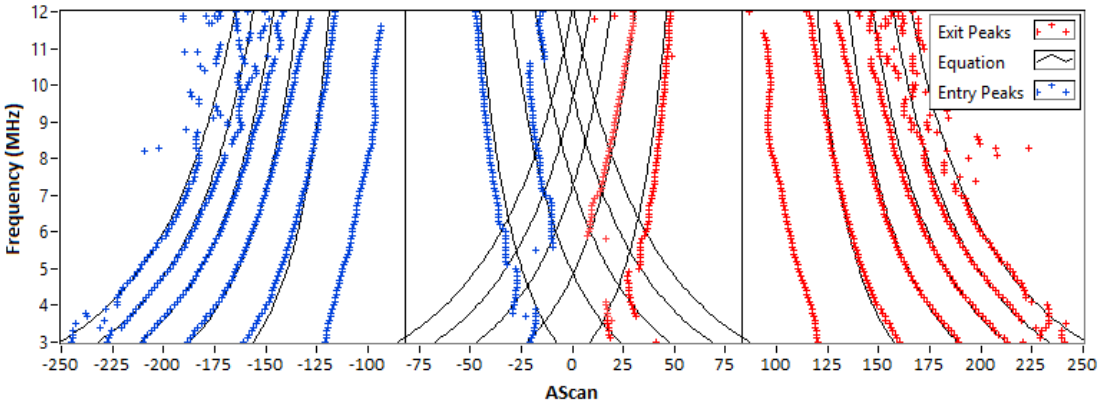

Figure 9.9: Comparison of Theoretical and Measured Interference Maxima Locations.

The results in Figure 9.9 show a strong correlation, clearly inferring that interference is occurring between the first reflection and reflections from the roll bite entry and exit. Unless accounted for such an interference will clearly affect the results of any amplitude measurements. To remove this effect firstly the A-Scans were cropped to leave only the first full cycle (1 wavelength at the pulse centre frequency) of the primary reflection. Next the difference in time of flight between the primary reflection and the interfering reflection was calculated for each A-Scan, using the method described in §8.3.3. A-Scans with a time separation between the two reflections of less than one cycle were assumed to contain interference and were discarded.

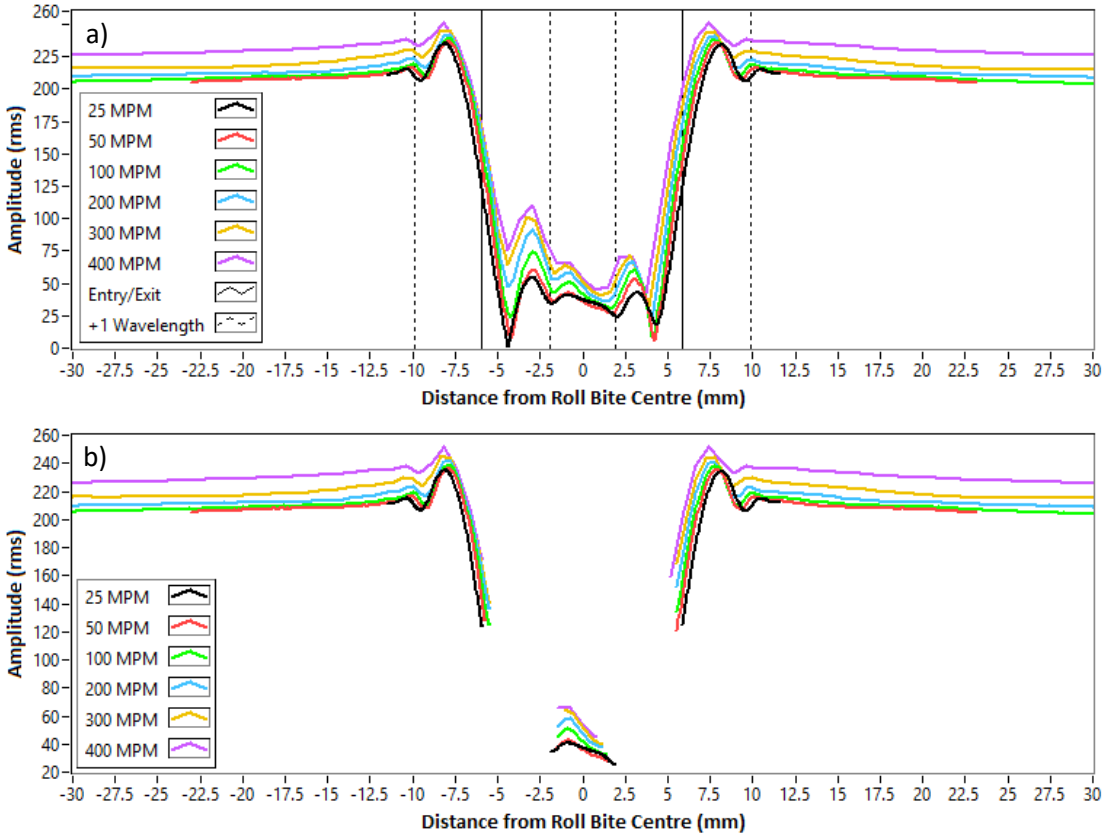

Figure 9.10: Amplitude across Roll Bite for different Rolling Speeds showing a) Entry, Exit and +1 Wavelength Points b) Interference Zone Removed.

A plot showing the amplitude with the roll bite entry and exit marked, along with the points at which the primary and interfering reflections are separated by one wavelength, is given in Figure 9.10a. The zones within 1 wavelength either side of the entry and exit show clear oscillations which result from the constructive then destructive interference that occurs as the time-separation increases between the two reflections. The same data with the interference zones removed is shown in Figure 9.10b.

This same approach has been adopted for all successive amplitude measurements in this chapter. It should be noted that in some test cases, especially where the rolling speed is high and roll bite contact length is small, the interference zones may overlap each other and there is no useable data in the roll bite.

9.4 Overall Interface Stiffness

The first stage in understanding the lubricant behaviour at the interface is to calculate the overall interface stiffness. This is extracted from the longitudinal amplitude, an example set of measurements across the roll bite for Test 6 at various speeds is given in Figure 9.11.

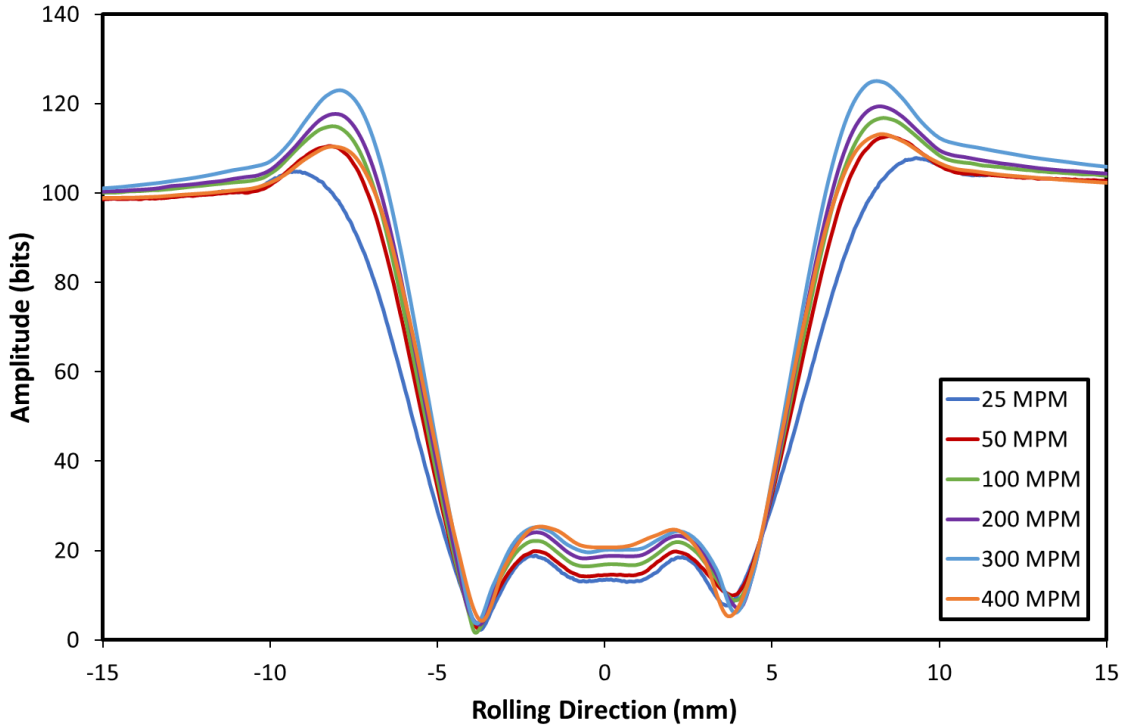

Figure 9.11: Longitudinal Amplitude across Roll Bite, Test 6.

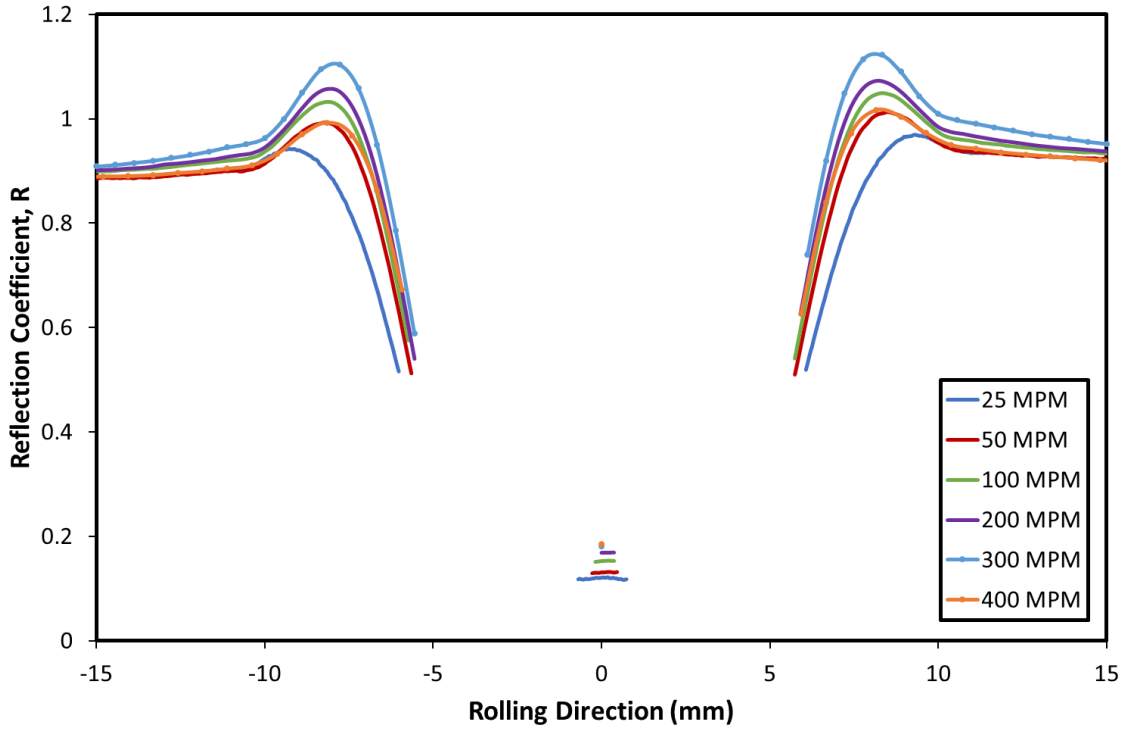

Figure 9.12: Cropped Longitudinal Reflection Coefficient across Roll Bite, Test 6.

The amplitude measurements were converted to reflection coefficient values by dividing through by a reference amplitude. This reference was taken when the observed interface was subject to air. The results where then cropped, as described in the previous section, to remove any interference effects. The resulting reflection coefficient values for the data in Figure 9.11 are shown in Figure 9.12. Using Equation 3.76 and a value for the longitudinal acoustic impedance of **46.703 MRayls**, the longitudinal stiffness was calculated. For the reflection coefficient data in Figure 9.12 the calculated stiffness's are given in Figure 9.13.

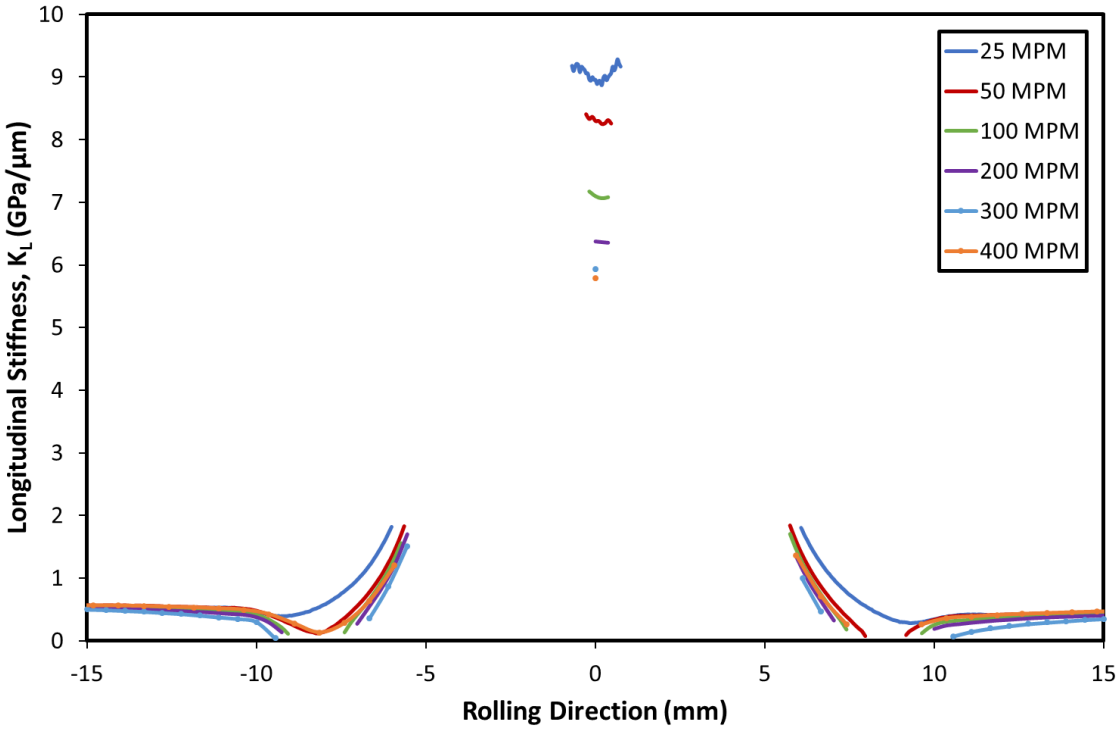

Figure 9.13: Cropped Longitudinal Stiffness across Roll Bite, Test 6.

The results show a clear decrease in interface stiffness with increasing rolling velocity. Due to the interference effects described earlier the usable data is limited to the centre of the roll bite and only single points have been recorded at higher rolling speeds.

The longitudinal stiffness was calculated for a number of different rolling cases. Figure 9.14 shows the resultant longitudinal stiffness at the centre of the roll bite for varying rolling speeds and elongations. For the thicker, rougher strip (Figure 9.14a) stiffness values in the range of 4 to 12 GPa/µm were reported. Tests 1 and 13 were performed with only recirculated lubricant, and these show a higher overall stiffness than the equivalent tests with directly applied lubricant, tests 6 and 11. This may in part be explained by more water being entrained in the roll bite. Water has a higher bulk modulus (2.19 GPa) than the rolling lubricant used (1.53 GPa). A liquid with a higher bulk modulus will give a greater stiffness for the same film thickness. The presence of water may disrupt the liquid layer formation and means the layer thickness is likely to be reduced, which will also contribute to a greater interface stiffness. These tests also show little change in the interface stiffness with rolling speed. The tests with directly applied lubricant on the other hand show a slight decrease in interface stiffness with higher rolling speeds. This may be explained by the formation of a thicker lubricant layer.

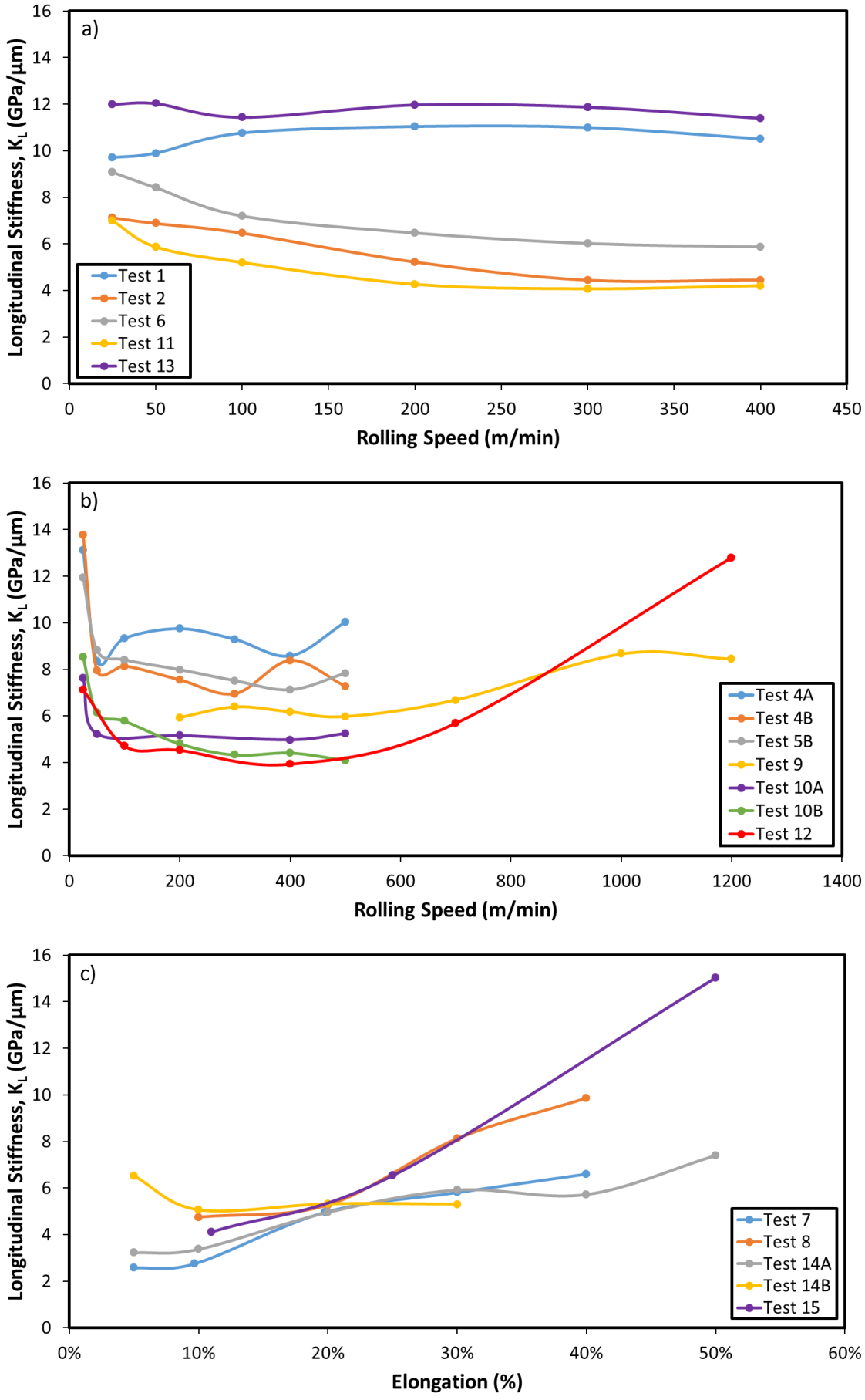

Figure 9.14: Longitudinal Stiffness at Roll Bite centre for Tests with a) 2.8mm Thick Strip and Varying Speeds b) 0.75mm Thick Strip and Varying Speeds c) Varying Elongation.

The interface stiffnesses for the thinner, smoother strip (Figure 9.14b) are of a similar magnitude to the thick strip. One key difference is that a significant drop in interface stiffness is observed between 25 and 50 m/min for all tests in which this data was recorded. This may be due to the formation of a thicker lubricant film as the speed increases. The stiffness of the interface increases at much higher rolling speeds, as seen in tests 9 and 12. This may be the result of the film thickness dropping as the interface is starved of lubricant. Figure 9.14c shows the effect of elongation. Broadly the results show an increase in the interface stiffness with increasing elongation. This is due to the rolling load going up, which results in the contact area going up and therefore the stiffness increasing.

9.5 Shear Interface Stiffness

The equivalent shear amplitude measurements for the cases shown in Figure 9.11 are given in Figure 9.15. The subsequent reflection coefficient values are shown in Figure 9.16. Unlike the longitudinal results the shear reflection coefficient is only a result of the solid stiffness from roll to strip contact, and should be unaffected by the lubricant.

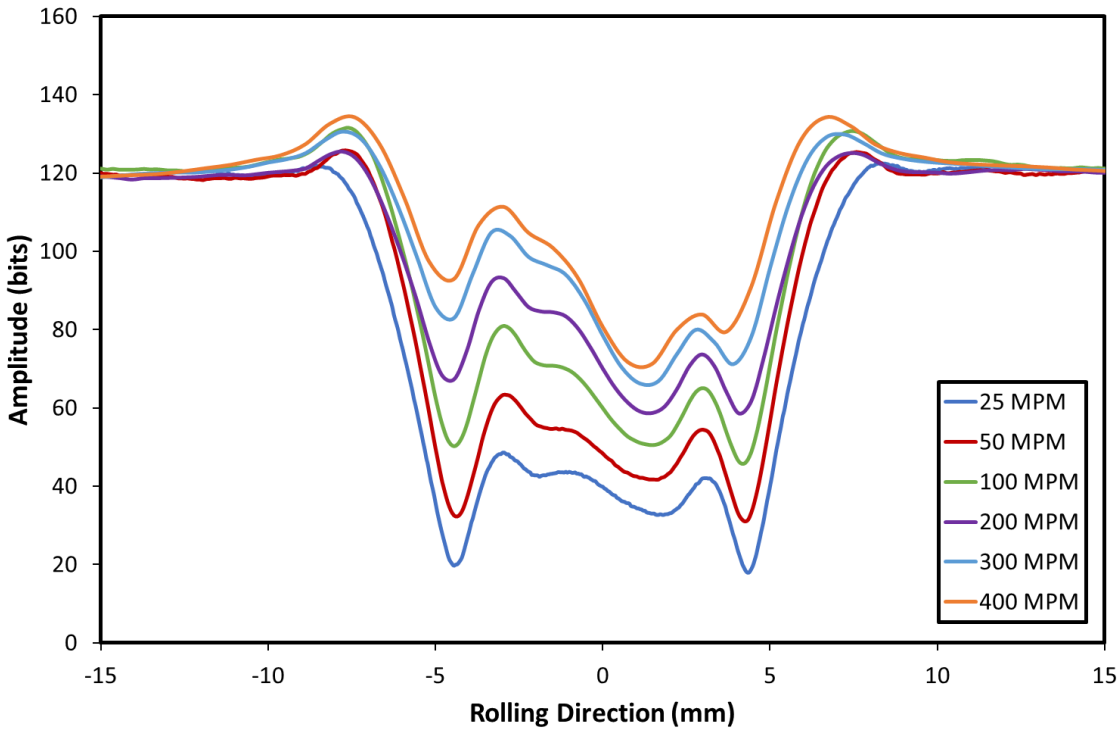

Figure 9.15: Shear Amplitude across Roll Bite, Test 6.

As with the longitudinal results, the data in Figure 9.16 has been cropped to remove any interference effects. This data was then converted to stiffness using Equation 3.76 and a value for the shear acoustic impedance of **25.313 MRayls**. The resulting stiffnesses are plotted Figure 9.17. The difference between each rolling case is much more marked than in the equivalent longitudinal measurements and the magnitude of the shear stiffness is several times smaller than the equivalent normal stiffness measured from the longitudinal data. There is a clear decrease in stiffness with increased rolling speed, implying reduced solid-solid contact. This is in agreement with the expectation of greater film thickness. There are more data points left across the roll bite after the data is cropped, this shows much more clearly the profile of stiffness across

the centre of the rollbite. The profiles show a consistent increase in stiffness across the roll bite in all the rolling cases plotted.

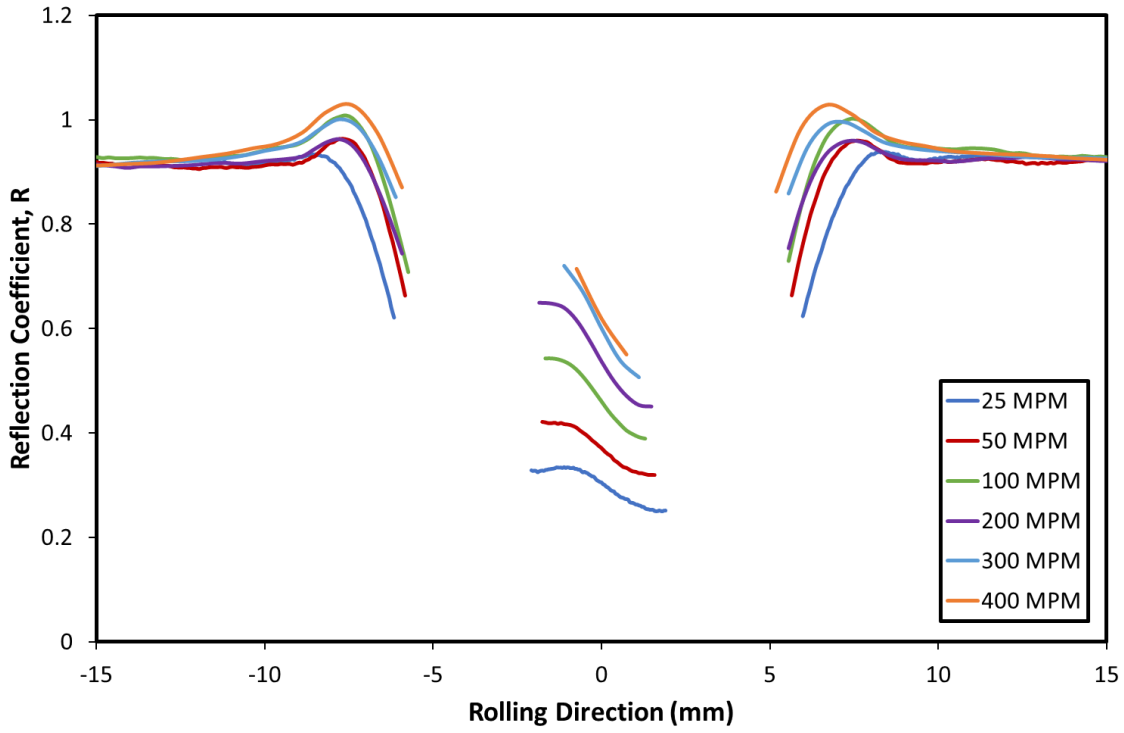

Figure 9.16: Cropped Shear Reflection Coefficient across Roll Bite, Test 6.

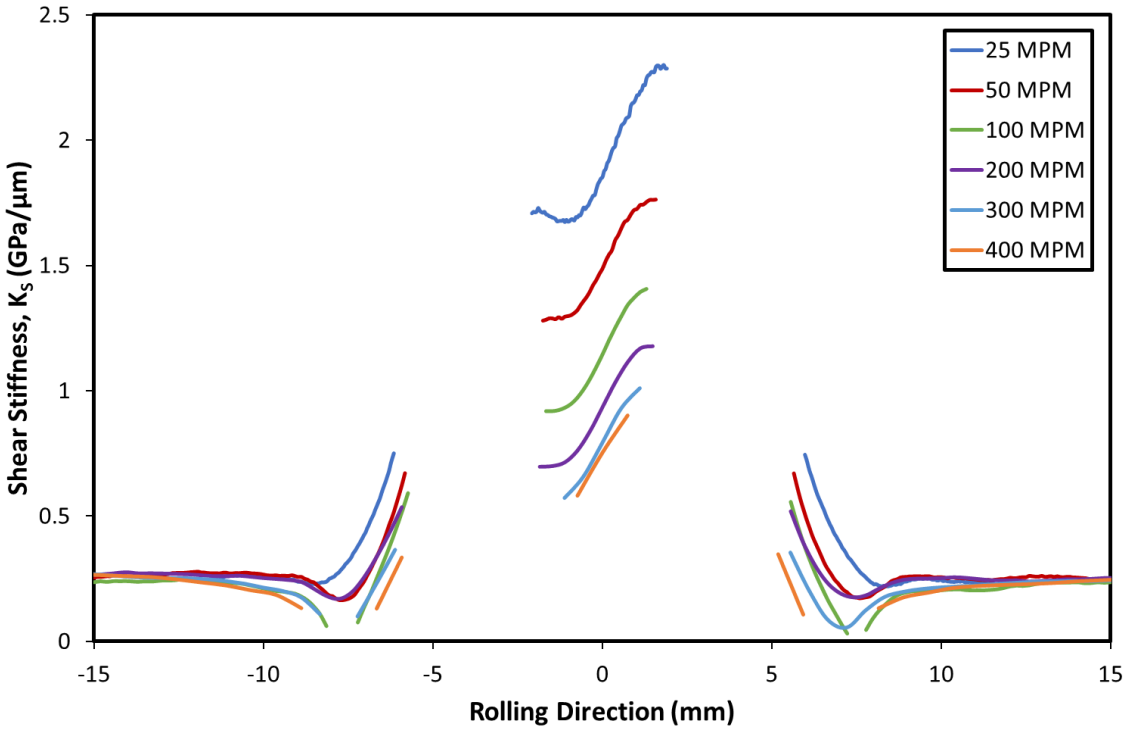

Figure 9.17: Cropped Shear Stiffness across Roll Bite, Test 6.

The stiffness at the centre of the roll bite has been extracted for the range of rolling conditions tested and are plotted in Figure 9.18. The tests for varying rolling speeds are shown in Figure 9.18a and Figure 9.18b, with the results for varying elongation in Figure 9.18c.

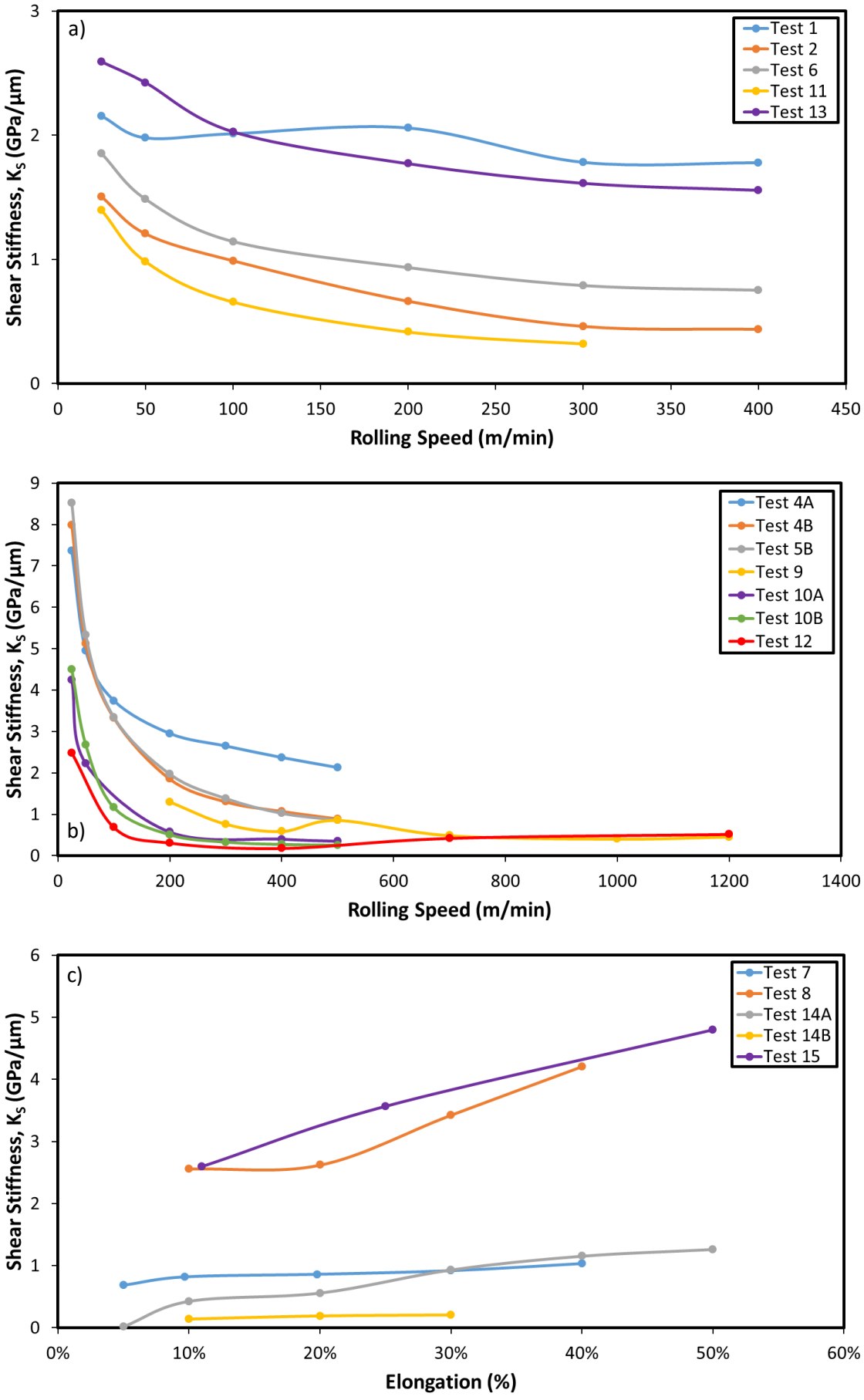

Figure 9.18: Shear Stiffness at Roll Bite centre for Tests with a) 2.8mm Thick Strip and Varying Speeds b) 0.75mm Thick Strip and Varying Speeds c) Varying Elongation.

For almost all cases the shear stiffness reduces with increased rolling speed. This corresponds to the reduced asperity contact expected with increased film thickness, and the change is most noticeable at slower speeds for the thinner, smoother strip. The only exceptions are tests 9 and 12 which included much higher rolling speeds and showed a slight increase in stiffness between 700 and 1200m/min. The results for the varying elongation show a general trend of an increasing stiffness with increasing elongation.

It is unsurprising to see a higher shear interface stiffness in Figure 9.18c for test cases 8 and 15. These represent tests with harder and smoother strip. What is perhaps surprising is that these differences are less manifested in the overall interface stiffness as measured by the longitudinal sensors and shown in Figure 9.14c, especially at lower speeds. As shown in § 3.5.3 the stiffness of the components of the interface are dependent upon their relative areas of contact. While the stiffness of the lubricant part of the interface will change linearly with a change in the real area of contact. The solid component however will increase exponentially with increasing real area of contact. The balance between the stiffness components from the solid and liquid parts of the interface perhaps explain the differences between the longitudinal and shear stiffnesses observed.

9.5.1 Interface Stiffness – Greenwood and Williamson

To check if the values for shear stiffness are reasonable, they are compared to values calculated using Greenwood and Williamson's (Greenwood & Williamson, 1966) simple asperity model (Equation 3.89). The pressure across the contact was assumed to be a simple elliptical distribution with maximum pressure at the centre of the roll bite. The normal load was recorded from the mill control system, these values are plotted in Figure 9.19. The maximum pressure was then calculated using Equation 2.18 from the load, strip width and the contact length measured ultrasonically (shown in Figure 8.31 and Figure 8.32). This value for maximum pressure was put into the simple asperity model. Where measured the combined roughness between the strip and roll, as stated in Table 9.2, was used. For test cases where the roughness had not been measured combined roughness values of **0.648µm** and **1.790µm** where used for the thin and thick strips respectively. Finally, to be able to compare the stiffness with the values obtained from the shear ultrasonic results it was necessary to convert from normal to shear stiffness. This was done using Equation 3.85 and a Poisson's ratio of **0.292**. This yielded the stiffness values shown in Figure 9.20.

The values shown in Figure 9.20 assume only solid-solid contact and do not account for the effect of lubricant in the interface. The difference this causes with the measured results is apparent in the tests with changing rolling speed. It is expected that thicker lubricant films will form as the rolling speed increases due to more lubricant being entrained within the roll bite. As the effect of the lubricant is not included in the asperity stiffness model, the change seen in the calculated stiffnesses at the different rolling speeds is much less than those seen in the measured data. There is also understandably no difference seen in the calculated results for different lubrication conditions between tests, unlike with the measured data.

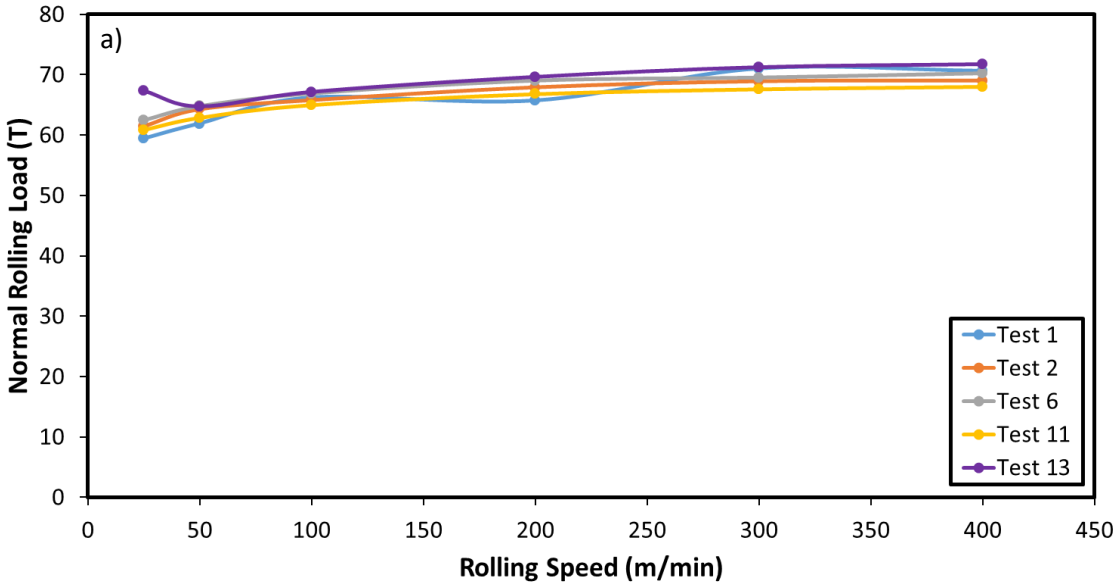

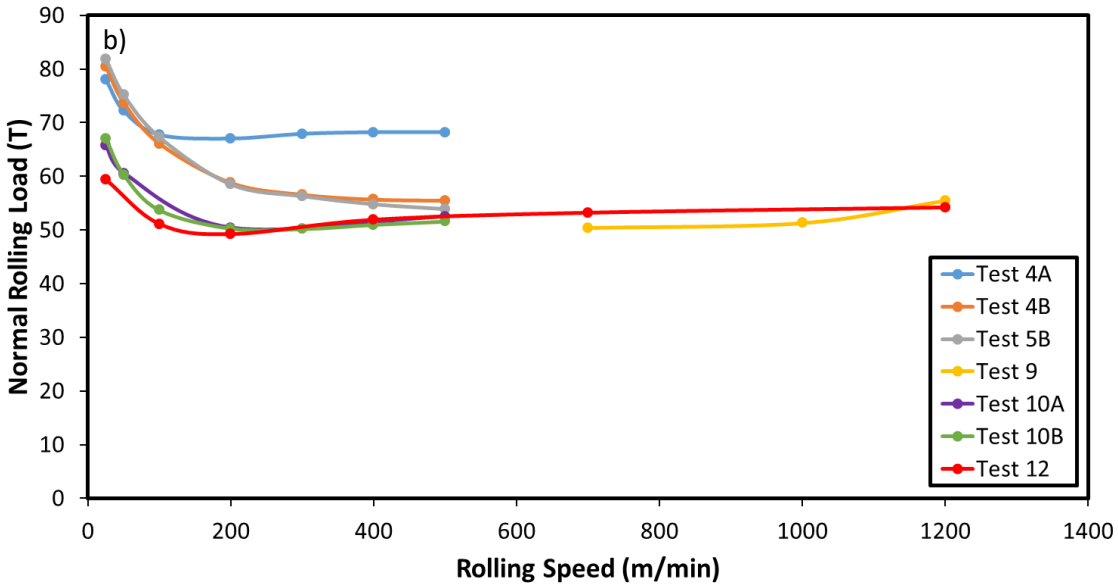

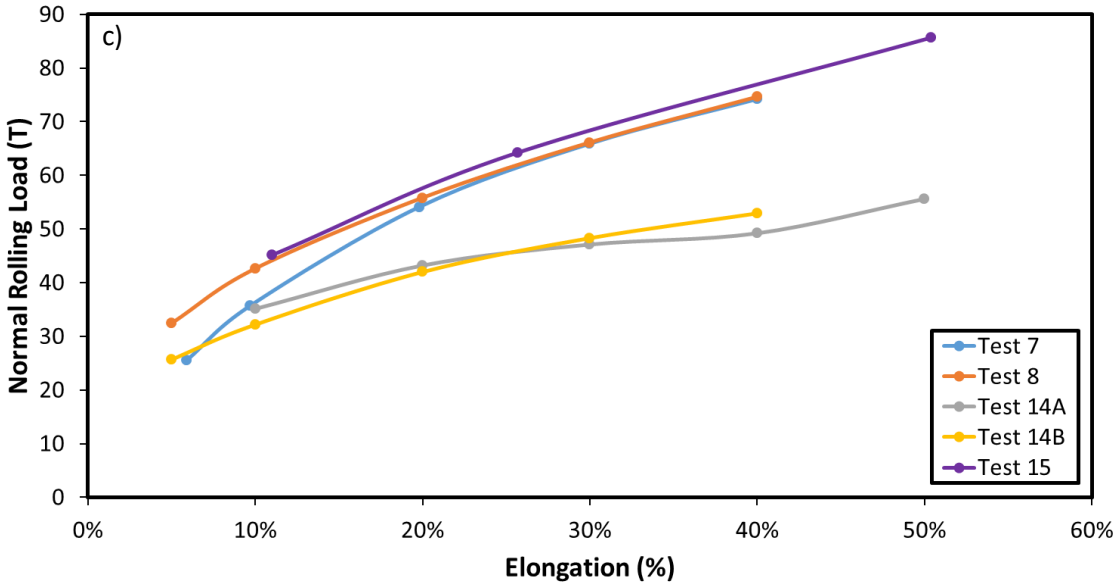

Figure 9.19: Normal Rolling Load for Tests with a) 2.8mm Thick Strip and Varying Speeds b) 0.75mm Thick Strip and Varying Speeds c) Varying Elongation.

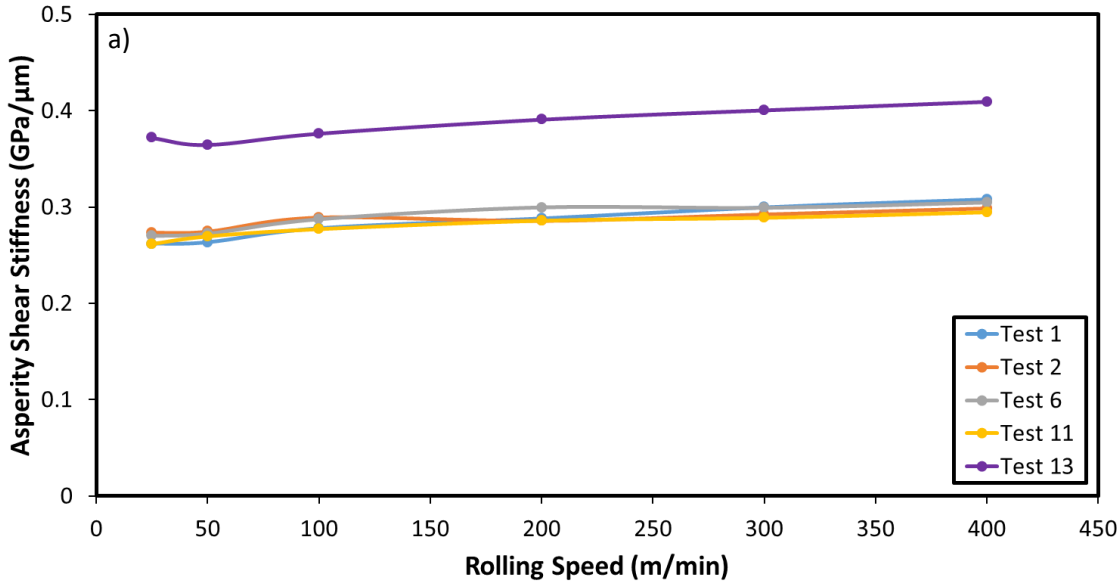

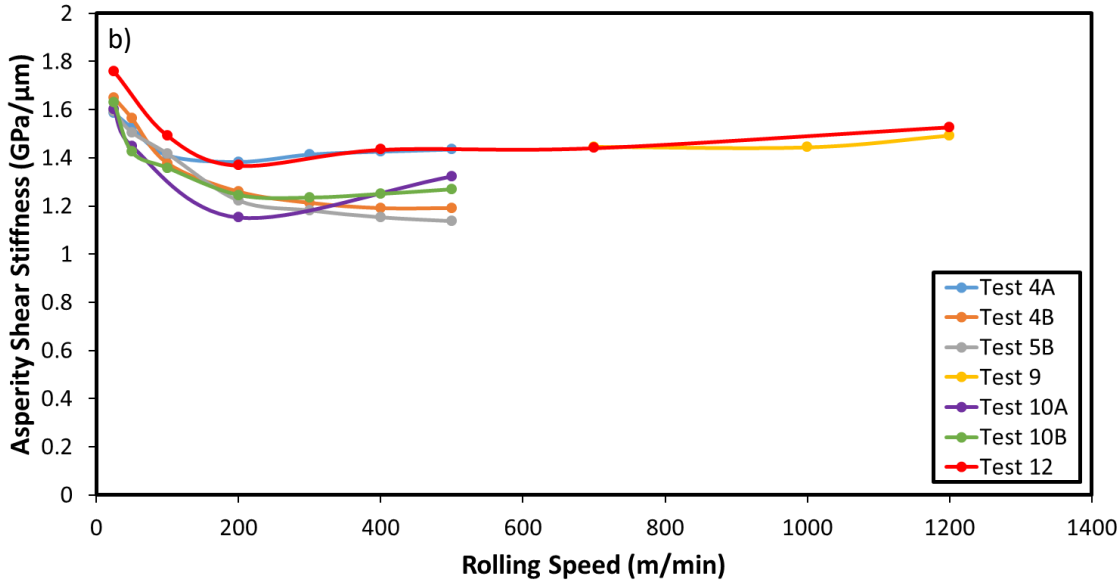

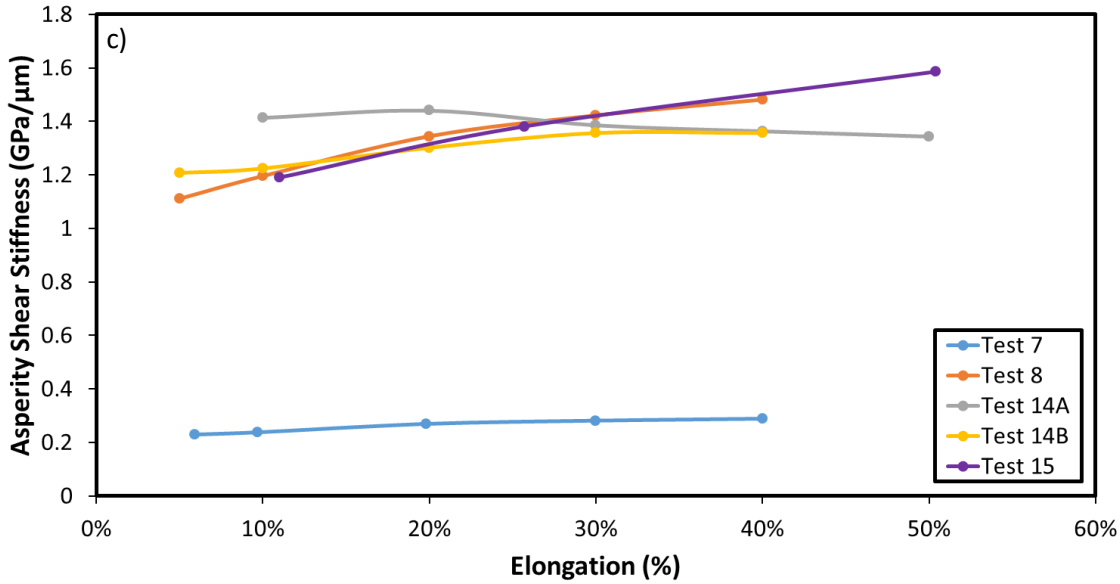

Figure 9.20: Stiffness calculated from Equation 3.85 for Tests with a) 2.8mm Thick Strip and Varying Speeds b) 0.75mm Thick Strip and Varying Speeds c) Varying Elongation.

The magnitudes of the results gained by calculation are of the same order as the experimental data. The values calculated for the rougher strip are consistently lower than those measured. The calculated values for the smoother strip under predict the stiffness at lower rolling speeds and over predict it at higher rolling speeds. The model results for the elongation data are a mixture with both higher and lower the values than those gained experimentally, but are broadly within the same range.

For the rougher strip the calculations show a slight increase in asperity shear stiffness with rolling speed, this differs from the experimental results which show a decrease. The greater surface roughness may result in more significant fluid film formation and therefore a greater influence on the stiffness of the lubricant. For the smoother strip the values for both measured and calculated stiffness both decrease at slower rolling speeds, however the effect seen in the calculated stiffnesses is much less marked. Both sets of results then show an increase in stiffness at higher rolling speeds, although the speed of this transition is lower in the calculated results. The results for increasing elongation, show agreement between modelled and measured stiffness, with both increasing for larger elongations.

9.6 Liquid Stiffness

The difference between the normal stiffness as calculated from the shear results, and the normal stiffness as measured by the longitudinal sensor was then taken to give the liquid stiffness, as shown in Equation 3.86. The liquid stiffness profile across the roll bite for the data shown in Figure 9.12 and Figure 9.17 is shown below in Figure 9.21.

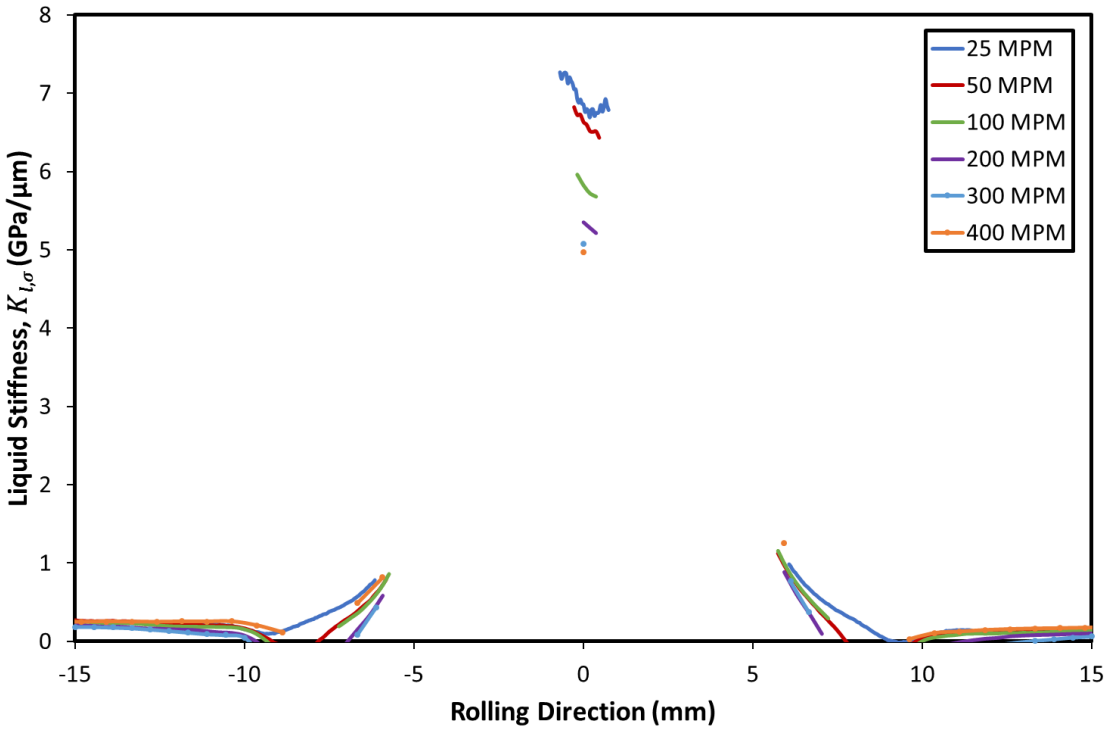

Figure 9.21: Liquid Stiffness across Roll Bite centre for Test 6.

Although more data is available across the roll bite for the shear stiffness, the limited longitudinal stiffness data in turn limits the amount of liquid stiffness data that can be calculated.

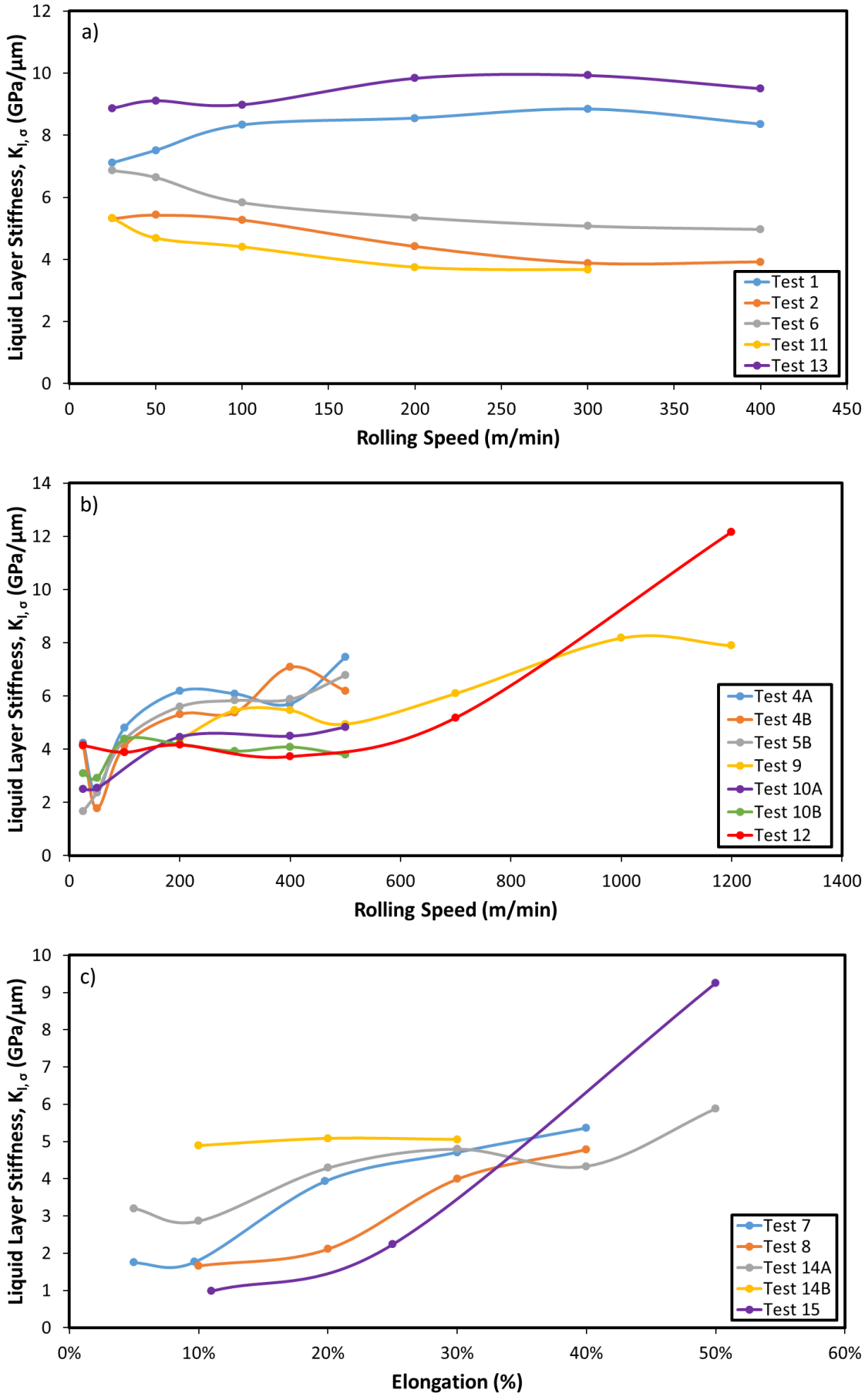

Figure 9.22: Liquid Stiffness at Roll Bite centre for Tests with a) 2.8mm Thick Strip and Varying Speeds b) 0.75mm Thick Strip and Varying Speeds c) Varying Elongation.

There is not enough data across the roll bite to give a clear indication of the profile across the roll bite. The data shows a clear decrease in liquid stiffness for increasing rolling speed.

As before the individual stiffness values at the centre of the roll bite for the range of rolling cases were extracted and are plotted in Figure 9.22. As was done previously these results have been split between tests with varying rolling speeds and those with varying strip elongations.

Tests 1 and 13 on thicker, rougher, strip with varying speed show a higher liquid stiffness which slightly increases with rolling speed up to 300m/min. Both Test 1 and 13 are only lubricated with a recirculated 2% emulsion. The other speed tests the thicker strip all have some form of directly applied lubricant and show decreasing liquid stiffness with rolling speed.

For the thinner, smoother, strip all tests show a drop in liquid layer stiffness from rolling speeds of 25 to 50m/min. The liquid layer stiffness then increases and levels out between 200 and 400m/min, before steadily again increasing above 400 m/min in most cases.

The tests for varying elongation show a trend of increasing liquid layer stiffness with increasing elongation in almost all cases.

9.7 Film Thickness

Having obtained a value for liquid layer stiffness, the liquid layer thickness can be calculated using the lubricant bulk modulus and the spring model (Equation 3.78). An example film thickness profile for the data in Figure 9.21 is shown below in Figure 9.23, which includes a close up view of the data around the centre of the roll bite. These values were calculated assuming a constant lubricant bulk modulus of **1.53 GPa** across the roll bite in all cases.

It has already been shown that the bulk modulus of the lubricant changes significantly with pressure and temperature. Assuming a simple elliptical pressure distribution the pressure at the centre of the roll bite could be calculated, as was done in §9.5.1. This pressure along with the input lubricant temperature as recorded from the mill lubrication system were used to estimate a value for the bulk modulus that was dependant on the specific rolling conditions. This assumed that the lubricant was entrapped in pockets between the interfacial surfaces and therefore was subject to the full rolling pressure. Any leakage of the lubricant will have allowed the pressure to reduce and thus invalidate this assumption.

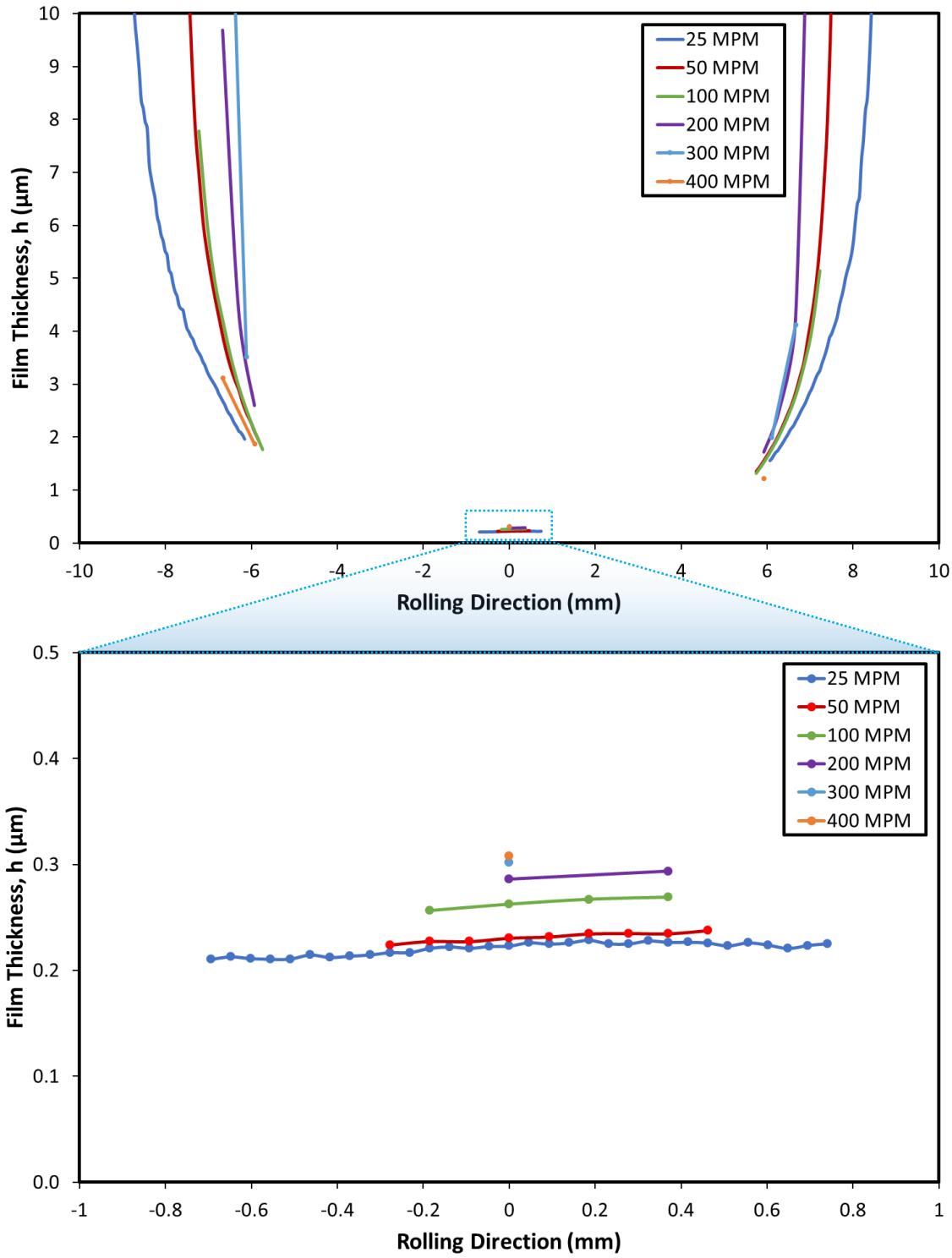

Figure 9.23: Lubricant Film Thickness Profile across Roll Bite for Test 6.

Figure 9.24 shows the film thickness values for a number of tests, before and after adjustment for the change in bulk modulus due to temperature and pressure. This adjustment results in larger values for film thickness due to the higher bulk modulus. However, although the magnitude of the film thickness has been scaled, the general trends for each case remain the same.

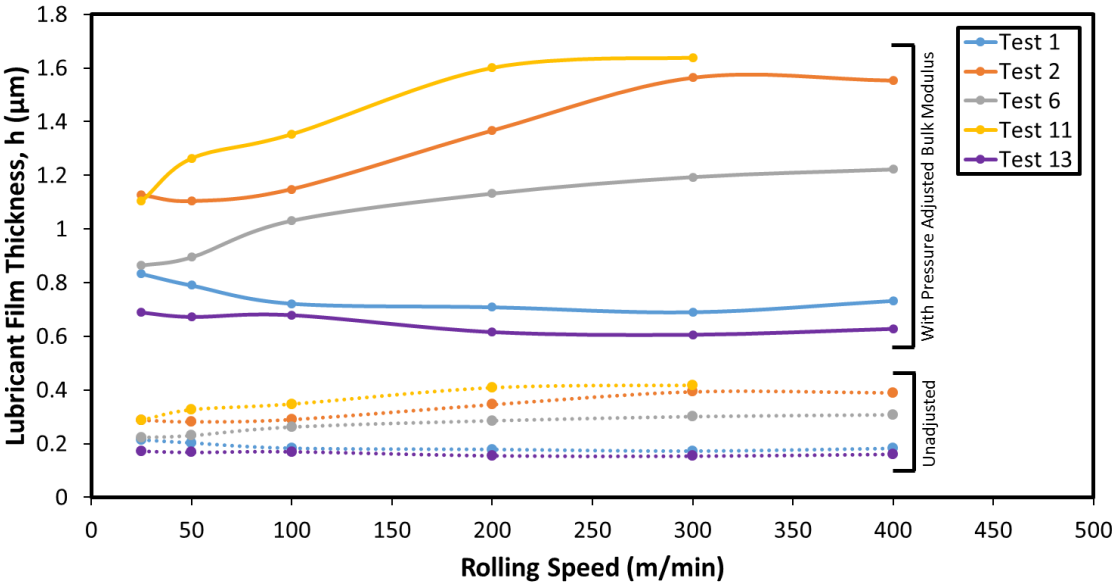

Figure 9.24: Liquid Film Thickness calculated at Roll Bite Centre using the Spring Model for Tests with 2.8mm Thick Strip, with and without the Lubricant Bulk Modulus adjusted for Pressure and Temperature.

The calculations were repeated for all test cases and the adjusted values for film thickness at the centre of the roll bite are shown in Figure 9.25. These are analysed in greater detail in later sections. In general terms the cases with thicker strip and only recirculated lubricant (Tests 1 and 13) show a thinner lubricant film which changes little with rolling speed. The other cases for the thicker strip have some form of directly applied lubricant and these show a slight increase in the lubricant film thickness with rolling speed. This implies that in these cases only the directly applied approach is effective in forming a stable fluid film, while the magnitude fluid film in the recirculated cases is solely down to the asperities resulting from surface roughness. For the thinner strip the lubricant film changes significantly between 25 and 50 m/min, but then remains stable up to 500 m/min. In the two test cases that go faster than 500 m/min (Test 9 and 12) a drop in lubricant film thickness is observed, this is consistent with contact starvation. All the tests of varying elongation show a decreasing film thickness with increasing elongation, as is expected due to increasing rolling load.

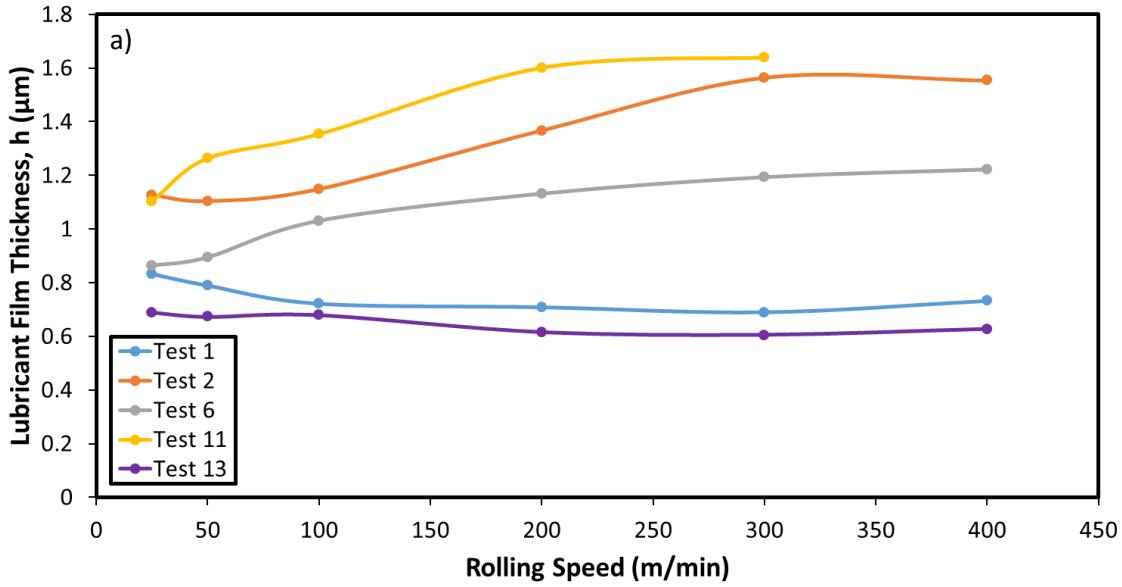

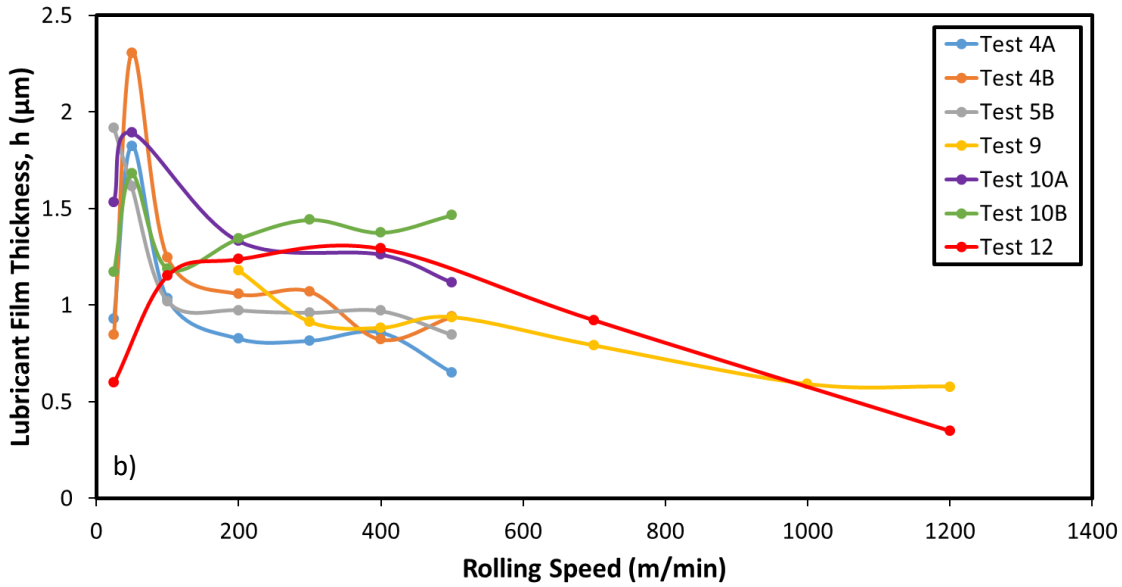

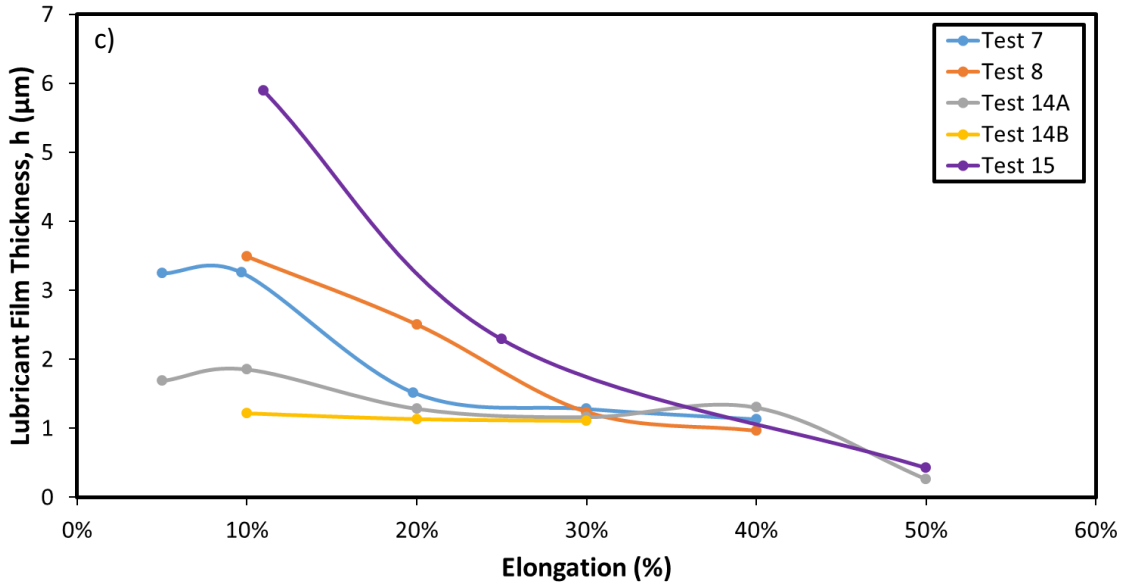

Figure 9.25: Liquid Film Thickness at Roll Bite centre for Tests with a) 2.8mm Thick Strip and Varying Speeds b) 0.75mm Thick Strip and Varying Speeds c) Varying Elongation.

9.7.1 Inlet Film Thickness

As there was no alternative measurement of the film thickness, to assess the validity of the thicknesses recorded ultrasonically they are compared to calculated thickness values. Estimating the thickness across the roll bite is complex, however the film thickness at the inlet to the roll bite can be determined by integrating Reynold's equation. Wilson and Walowit (Wilson & Walowit, An Isothermal Hydrodynamic Lubrication Theory for Hydrostatic Extrusion and Drawing Processes With Conical Dies, 1971) derived an expression for the inlet film thickness, h_s, which disregards the roughness of the roll and strip:

$$h_s = \frac{3\eta_0\alpha(v_{exit} + v_{roll})R'}{L\left(1 - \exp(-\alpha\sigma_y)\right)} \quad 9.3$$

Where η_0 is the viscosity of the lubricant at ambient pressure, v_{exit} is the strip exit velocity, v_{roll} is the roll surface velocity, *R'* is the deformed roll radius, *L* is the contact length, σ_y is the yield strength of the strip and α is the pressure-viscosity coefficient in the Barus equation (Equation 9.4) which links the variation of viscosity η with a change in pressure *p*.

$$\eta = \eta_0 \exp(\alpha p) \quad 9.4$$

The viscosity at ambient pressure and the pressure-viscosity coefficient (obtained from the data in §6.5) for the various rolling lubricants at 55°C are given in Table 9.4. Figure 9.26 shows the calculated inlet oil film thickness for Tests 2, 6, 11 and 13. In all cases the inlet film thickness is calculated as being less than the combined strip/roll roughness (1.790μm) this therefore predicts that the roll bite contact will be in boundary or mixed lubrication at the entry.

	Viscosity @ Ambient Pressure η_0 (mPa s)	Pressure-Viscosity Coefficient α (MPa^{-1})
Trenoil DA K-2	25.7	0.0144
Trenoil S 812 TCC	22.4	0.0139
Quakerol ARC-MK HV 2	68.4	0.0152
Gerolub 5525	20.2	0.0145

Table 9.4: η_0 and α values for each rolling lubricant at 55°C.

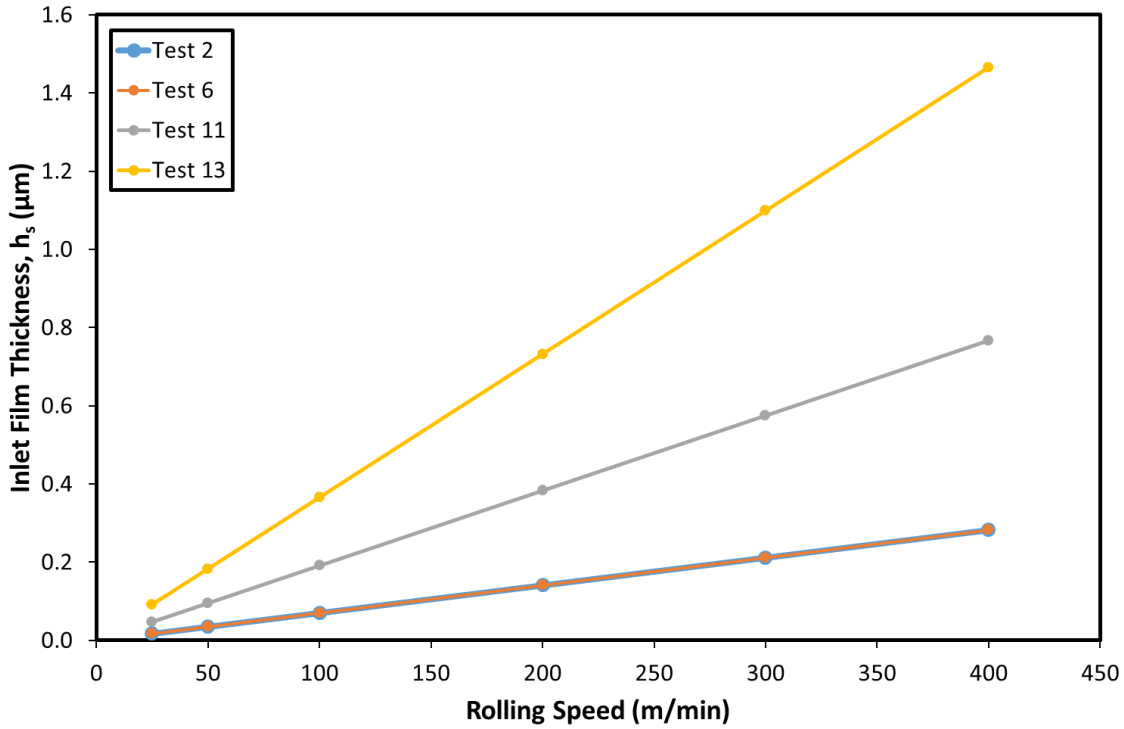

Figure 9.26: Inlet Film Thickness Calculated Equation 9.3 for Tests 2, 6, 11 and 13.

9.7.2 Effect of Lubricant Viscosity

The effect of lubricant viscosity can be studied by comparing test cases which are equivalent with the exception of the lubricant used. This was studied for directly applied lubricants by comparing 100% K2 @ 60°C (27 mPa.s) with 100% HV2 @ 60°C (70 mPa.s) in test 6 with 11. These tests had 2.8mm entry strip thickness and an elongation of 30%. Figure 9.27 shows the longitudinal and shear stiffnesses, while Figure 9.28 gives the calculated film thickness.

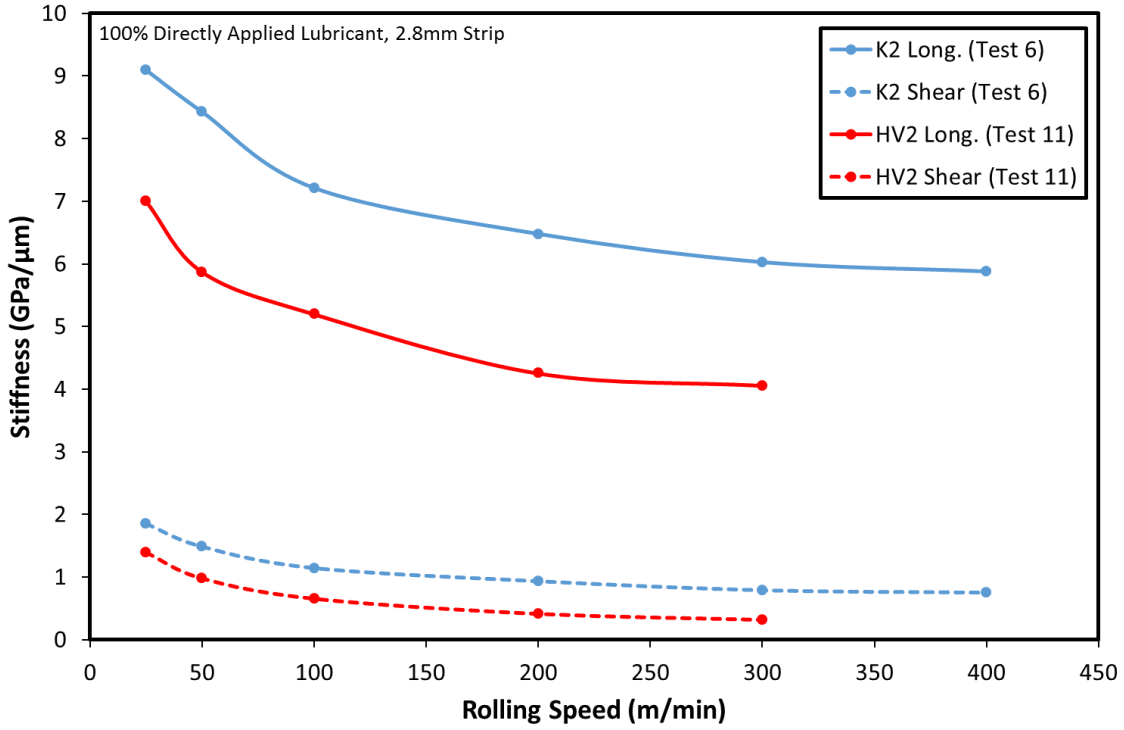

Figure 9.27: Longitudinal and Shear Stiffness for K2 and HV2 Lubricant Directly Applied.

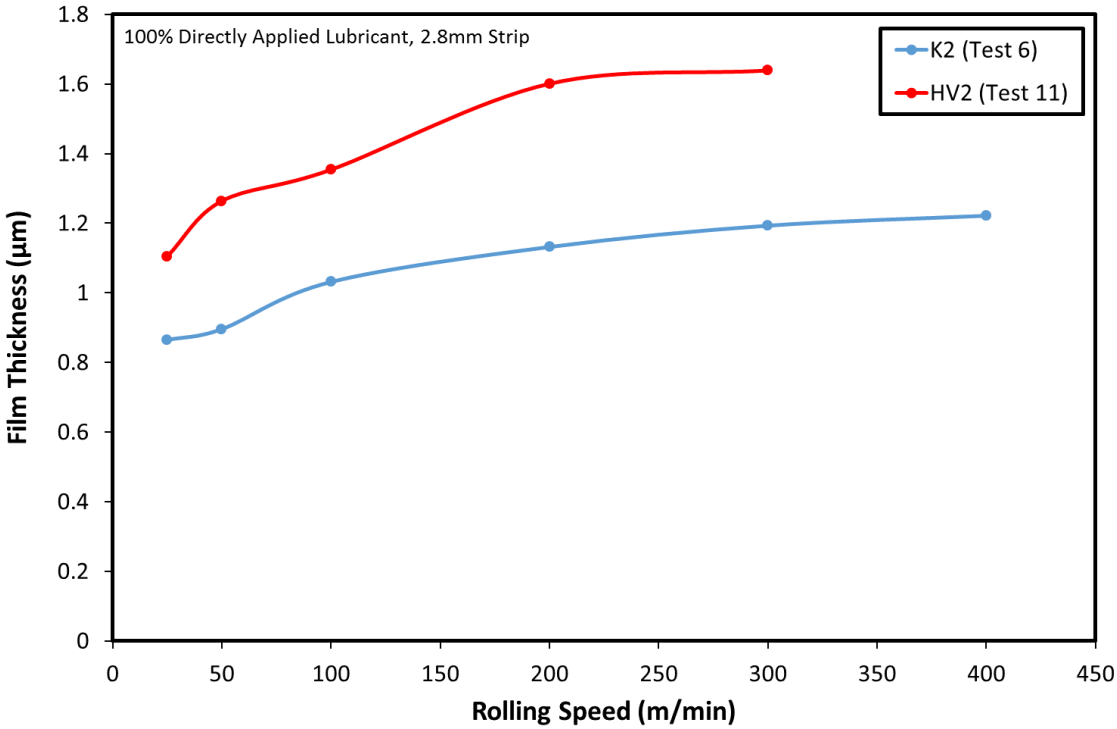

Figure 9.28: Film Thickness for K2 and HV2 Lubricant Directly Applied as calculated from the Longitudinal and Shear Stiffness's in Figure 9.27.

The test using the higher viscosity lubricant resulted in a comparatively less stiff and thicker films. Both tests show a marginal increase in film thickness with increased rolling speed. The shear stiffness in both cases is several multiples smaller than the equivalent longitudinal stiffness. Both shear and normal stiffness reduce consistently with increasing rolling speed. Next the effects of lubricant viscosity for recirculated application was studied by comparing 2% emulsions of K2 and HV2 in test 1 with 13.

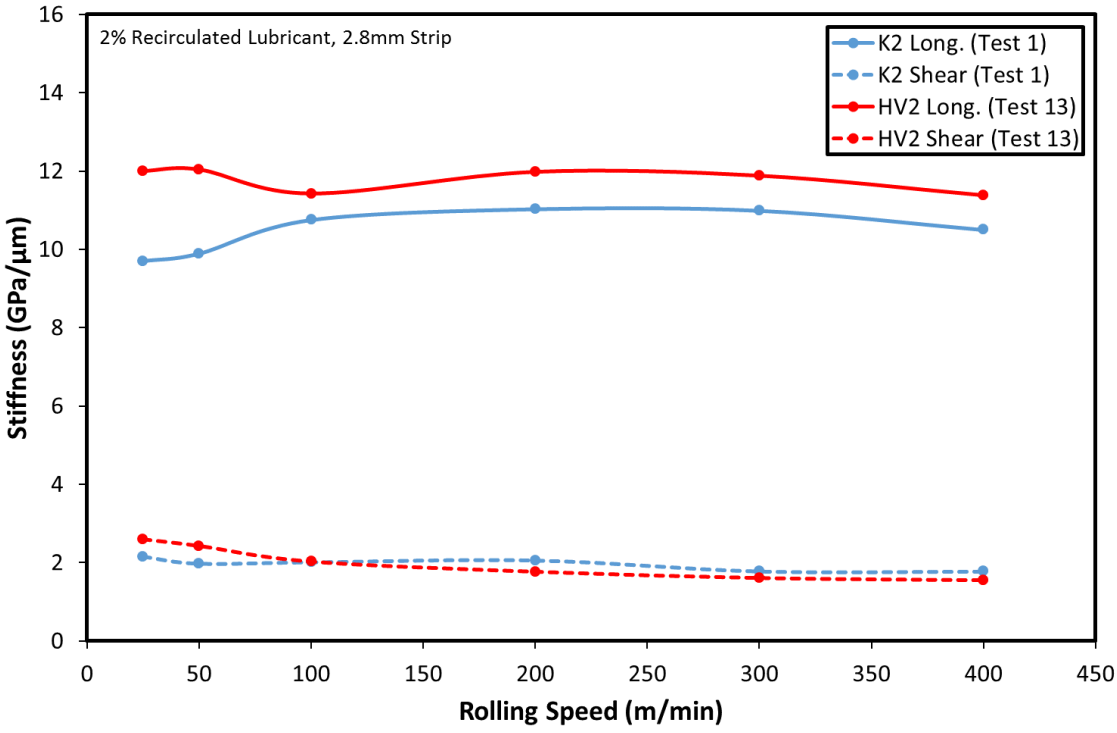

Figure 9.29: Longitudinal and Shear Stiffness for 2% K2 and HV2 Recirculated Emulsions.

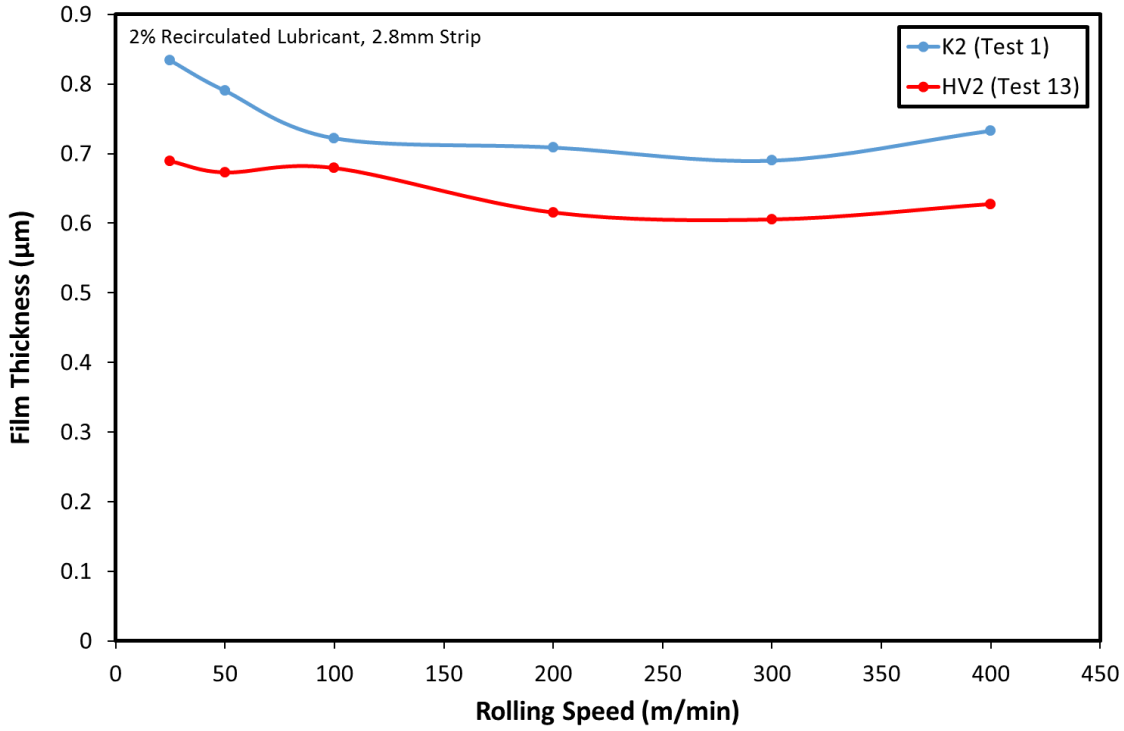

Figure 9.30: Film Thickness for 2% K2 and HV2 Recirculated Emulsions.

Again both tests had 2.8mm entry strip thickness and 30% elongation. Figure 9.29 gives the shear and longitudinal stiffnesses while Figure 9.30 gives the film thicknesses.

The stiffnesses recorded with recirculated lubricant are higher than those seen from directly applied lubricant. The shear stiffnesses in both cases are similar with the difference in the two test cases being seen in the longitudinal stiffness. The film thicknesses are smaller than those seen when using pure directly applied lubricant. In the cases tested the less viscous lubricant returns a larger film thickness measurement, although the difference between the two cases is much reduced in comparison to test cases 6 and 11. The change in film thickness with rolling speed is not as apparent as before.

If only viscosity is considered it would be expected that the more viscous lubricant would result in a thicker film, however the measurements show that this is not the case. It is possible that other factors are influencing the measurements taken, lubricant entrainment mechanisms into the roll bite are complex, especially where an emulsion is used and lubricant plate-out capacity may differ between the lubricants.

9.7.3 Effect of Strip Type and Roughness

The effect of different strip types was studied next by comparing 2.8mm thick DD14+Ti and 0.75mm thick ARCELOR06 strips with roughnesses stated in Table 9.1 and Table 9.2. The stiffnesses and film thickness for tests 5B with 6 are presented in Figure 9.31 and Figure 9.32 respectively. These both used 100% directly applied emulsions. Both tests had a 30% reduction.

The thinner strip shows higher stiffnesses, this is consistent with the smoother surface roughness. Again the shear stiffnesses in both cases show a consistent decrease with increased rolling speed. The measured film thicknesses are of the same order, with the thinner smoother strip having a slightly lower film thickness at higher rolling speeds.

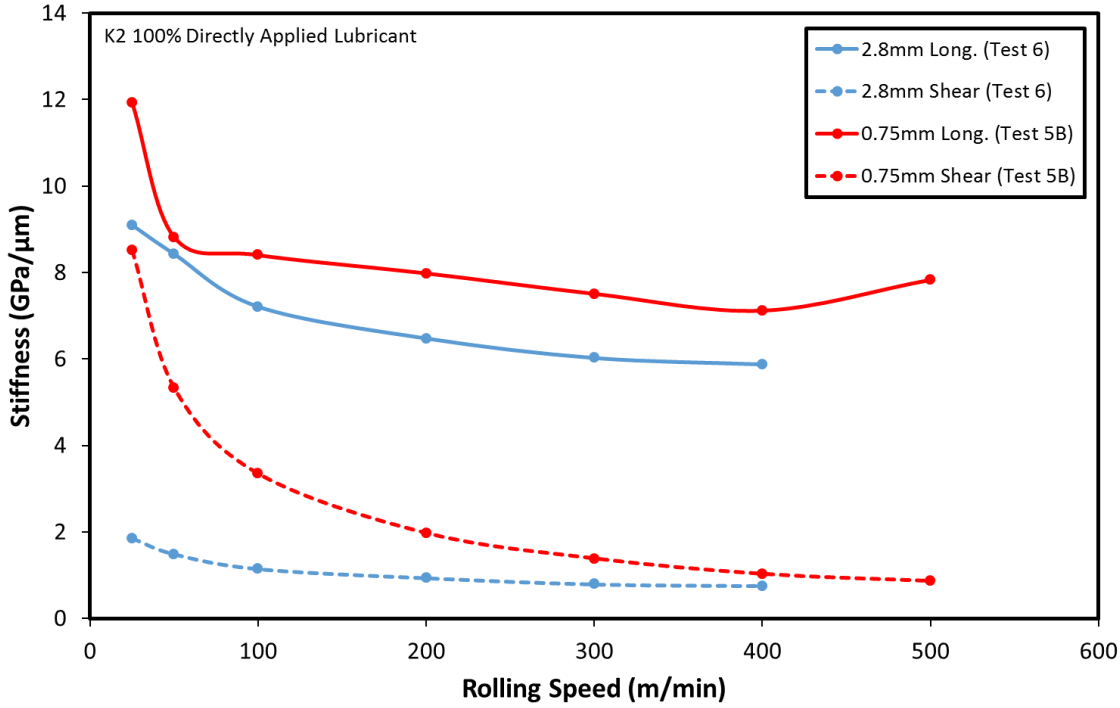

Figure 9.31: Longitudinal and Shear Stiffness for 2.8mm and 0.75mm Entry Strip Thickness.

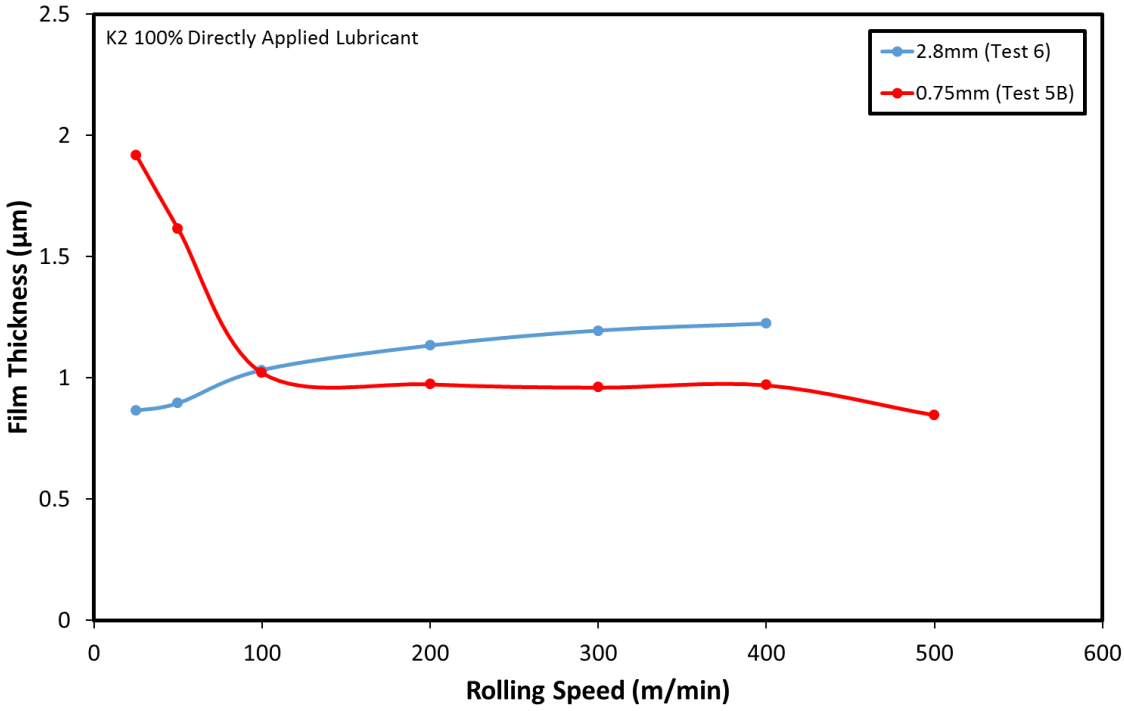

Figure 9.32: Film Thickness for 2.8mm and 0.75mm Entry Strip Thickness.

9.7.4 Effect of Lubricant Application Method

To compare the influence of the lubricant application configurations and emulsion percentages a mixture of setups were tested. This testing was done at speeds between 25 to 400 m/min for 100mm wide, 2.8mm thick strip and an elongation of 30%. Test 1, 2 and 6 are compared below, these used K2 lubricant applied as a recirculated 2% emulsion, as a recirculated 2% emulsion with a directly applied 20% emulsion and directly applied pure. The stiffnesses and film thicknesses are given in Figure 9.33 and Figure 9.34.

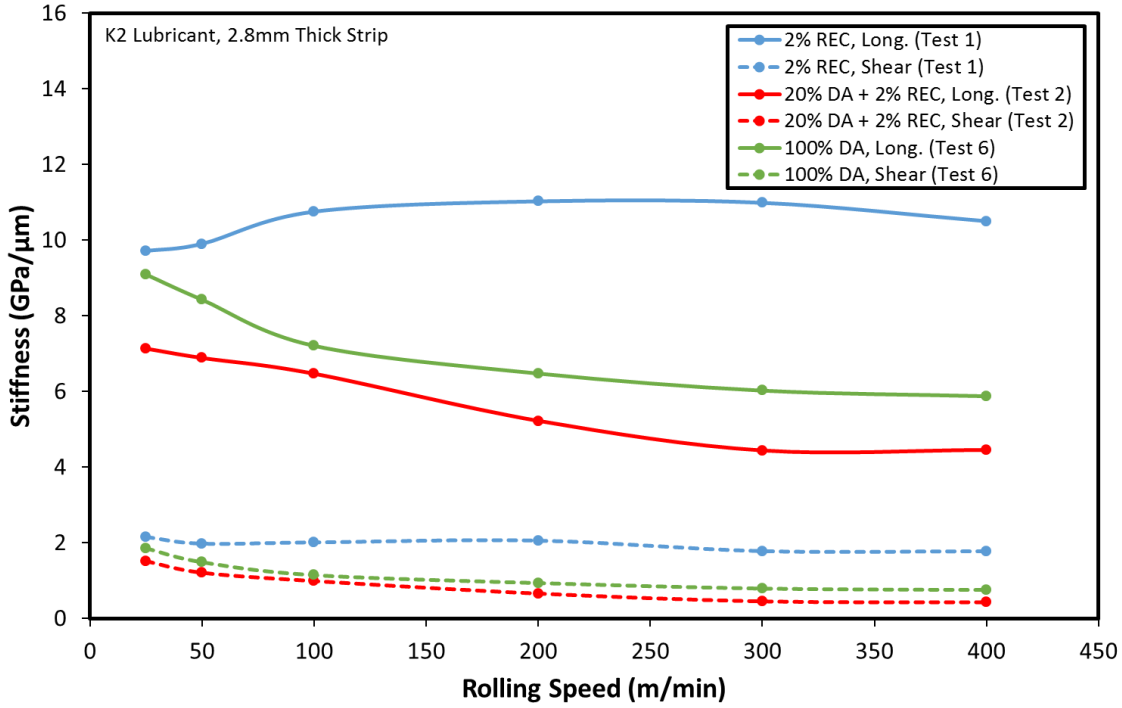

Figure 9.33: Longitudinal and Shear Stiffness for Various Lubricant Application Methods.

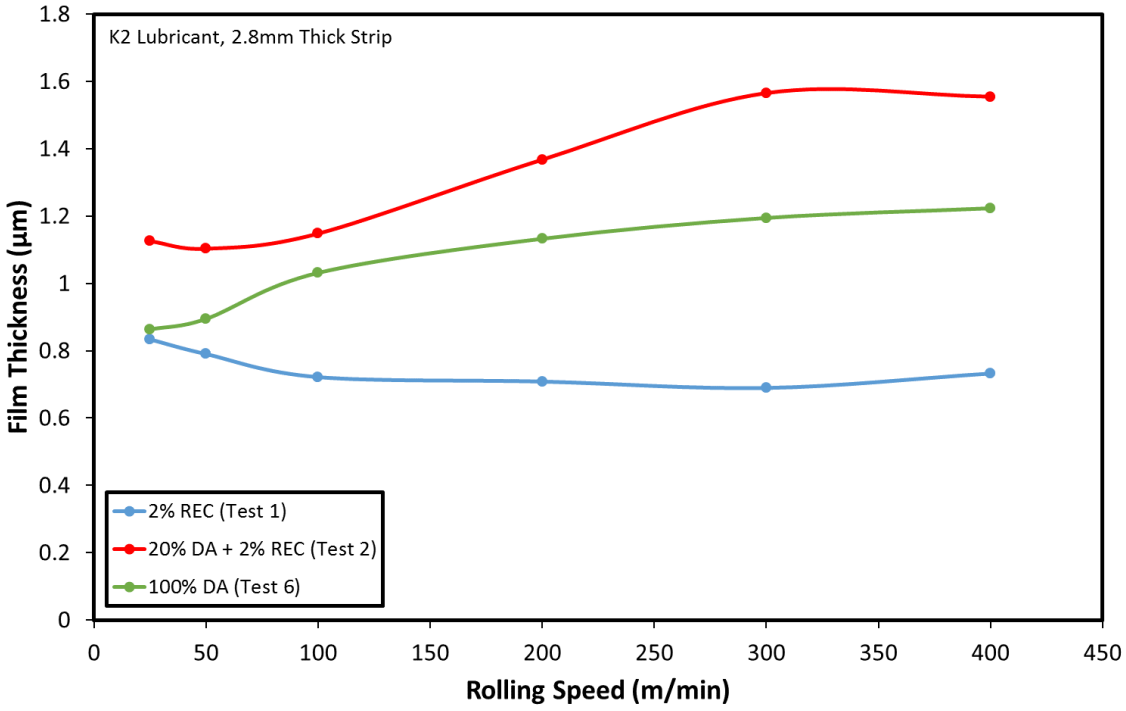

Figure 9.34: Film Thickness for Various Lubricant Application Methods.

The test cases which used directly applied lubricant (2 and 6) showed larger film thicknesses in comparison to the case where only recirculated lubricant was used. This is consistent with earlier results. Interestingly the thickest measured film thickness was recorded with a mixture of both directly applied and recirculated lubricants.

9.7.5 Effect of Temperature

The effect of lubricant temperature was studied by testing K2 lubricant, directly applied pure at both 40°C and 60°C. The temperature evolution of the lubricant through the roll bite was not measured explicitly, however indicative values for the simulated lubricant temperature and measured strip exit temperature are given in §11.3.6 (Table 11.9).

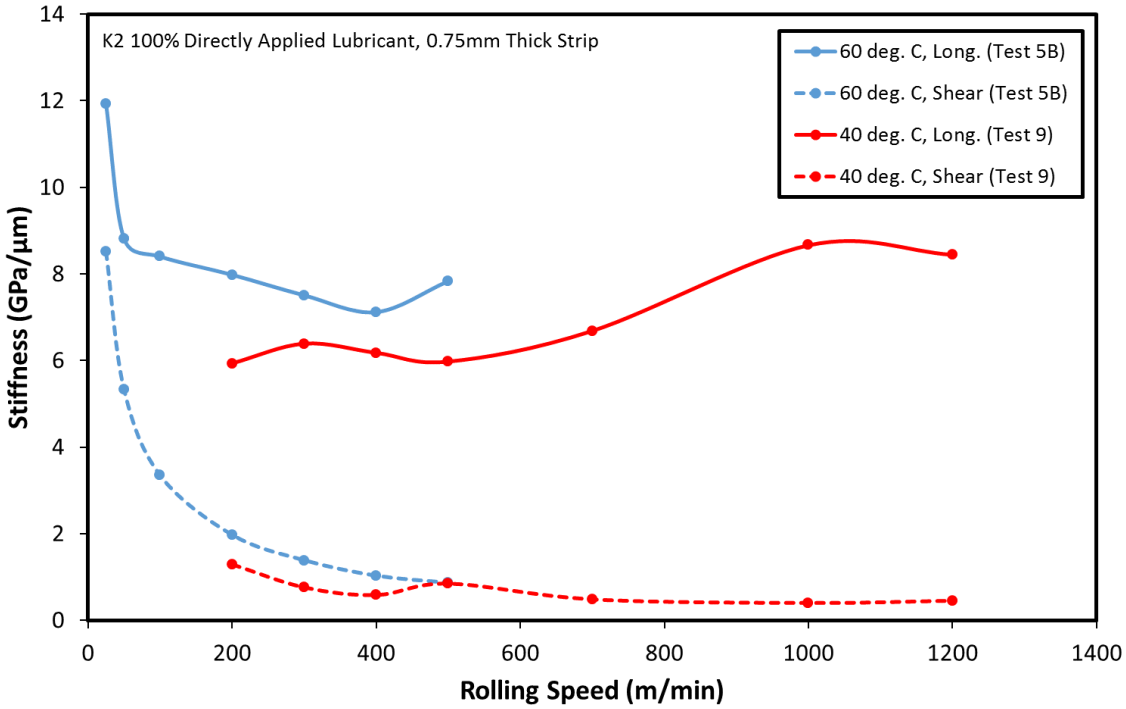

Figure 9.35: Longitudinal and Shear Stiffness for Lubricant Applied at 40°C and 60 °C.

This was completed in test 5B and 9 using 0.75mm entry strip thickness. The stiffnesses and film thicknesses are shown in Figure 9.35 and Figure 9.36.

Again the shear stiffness in both tests showed a consistent decrease with increased rolling speed. The longitudinal results are less consistent. The two tests were performed over a different speed range, only partly overlapping. The film thicknesses recorded show the two tests gave similar film thickness values for equivalent rolling speeds.

It was expected that the viscosity dependence of the lubricant would result in a thinner film for the hotter and therefore less viscous test conditions. However little difference is observed between the tests where lubricant is applied at 40°C and 60°C. It may be that the temperature of the roll or strip may dominate over the temperature of the applied lubricant, especially as the lubricant is applied a small distance from the roll bite. In addition, the film thickness values that are reported are for the centre of the roll bite and the heating within the roll bite may be of greater importance.

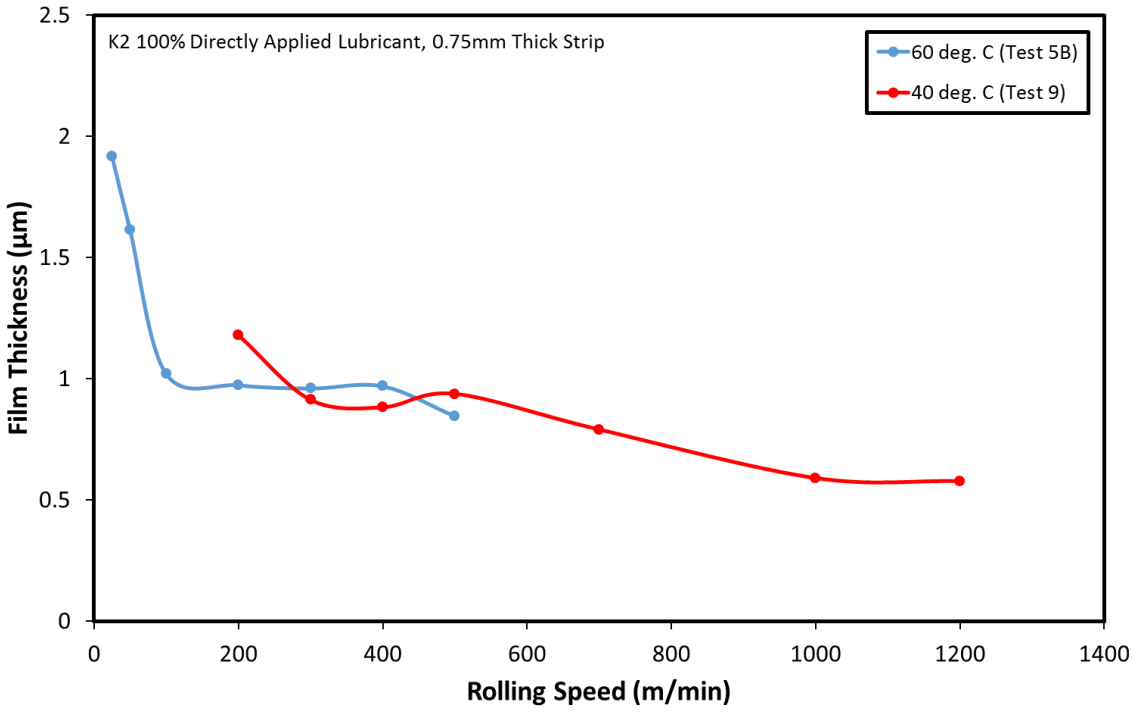

Figure 9.36: Film Thickness for Lubricant Directly Applied at 40°C and 60 °C.

9.8 Friction

The key parameter to be controlled by the mill lubrication system is the friction. In the tests completed no direct measurement for friction coefficient could be made, however it could be calculated by rearranging Equation 4.50, this yields

$$\mu = \frac{\theta^2}{4\left(\frac{\theta}{2} - \sqrt{\frac{S_f h_1}{R'}}\right)} \qquad 9.5$$

Where μ is the coefficient of friction, θ is the roll bite entry angle, S_f is the forward slip, h_1 is the strip exit thickness and *R'* is the deformed roll radius. Equation 2.8 was used to calculate the deformed roll radius and Equation 2.77 to calculate the roll bite entry angle. The forward slip was measured by the mill control system and the values obtained are given in Figure 9.37. The subsequently calculated friction coefficients are given in Figure 9.38.

The calculated friction coefficients all decrease with increasing rolling velocity, and with the exception of Test 7 remain reasonably constant with changing elongation. The drop in friction with increased rolling speed is expected as this indicates the formation of a thicker lubricant film.

It was noticed during data processing that there appears to be some correlation between the calculated friction and the measured shear stiffness. These values have been plotted in Figure 9.39 and Figure 9.40 for the thick (2.8mm) and thin (0.75mm) strips respectively. These plots show how the shear stiffness and friction coefficient vary approximately linearly for each test with varying rolling speed. Increased rolling speed results in lower friction and shear stiffness in all cases measured.

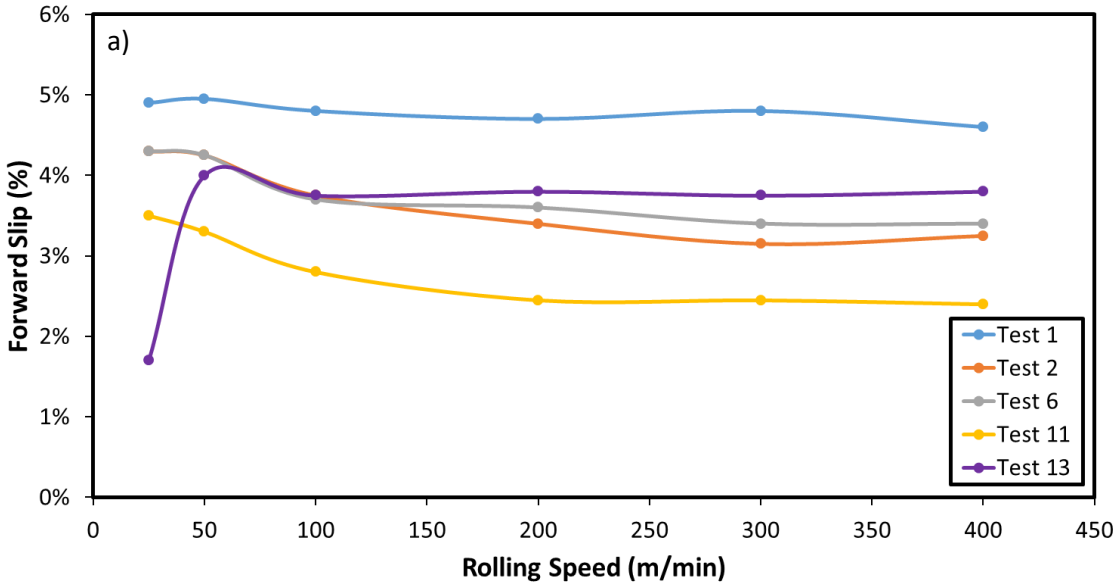

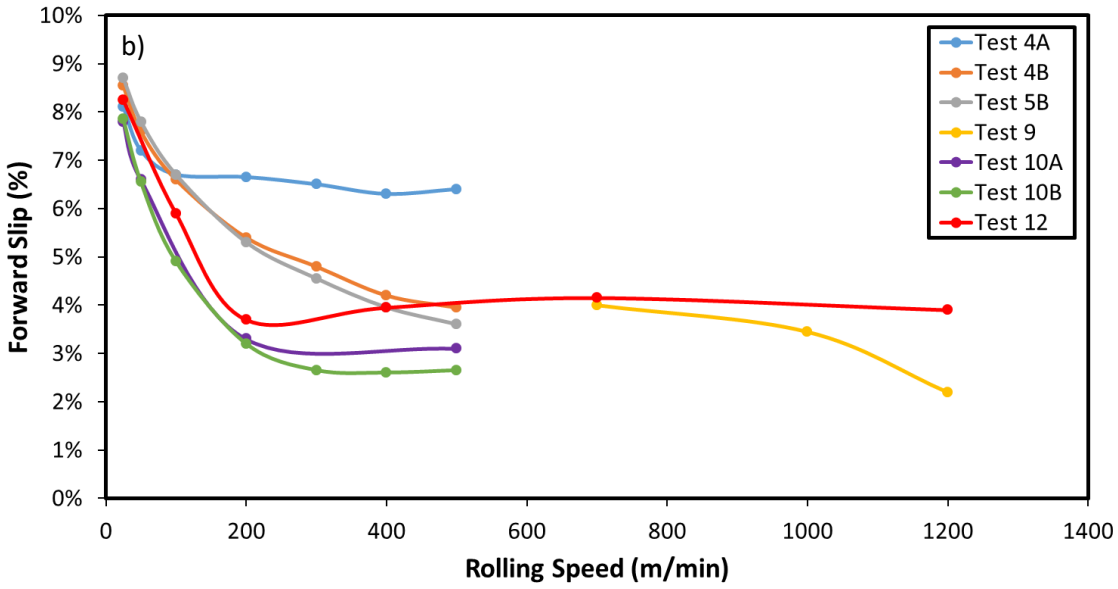

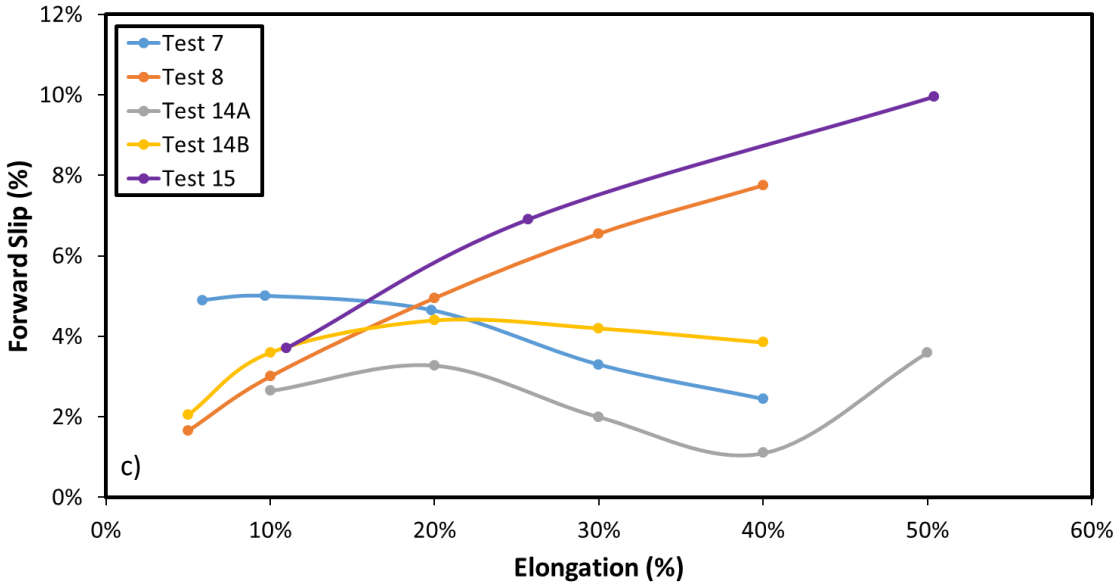

Figure 9.37: Forward Slip for Tests with a) 2.8mm Thick Strip and Varying Speeds b) 0.75mm Thick Strip and Varying Speeds c) Varying Elongation.

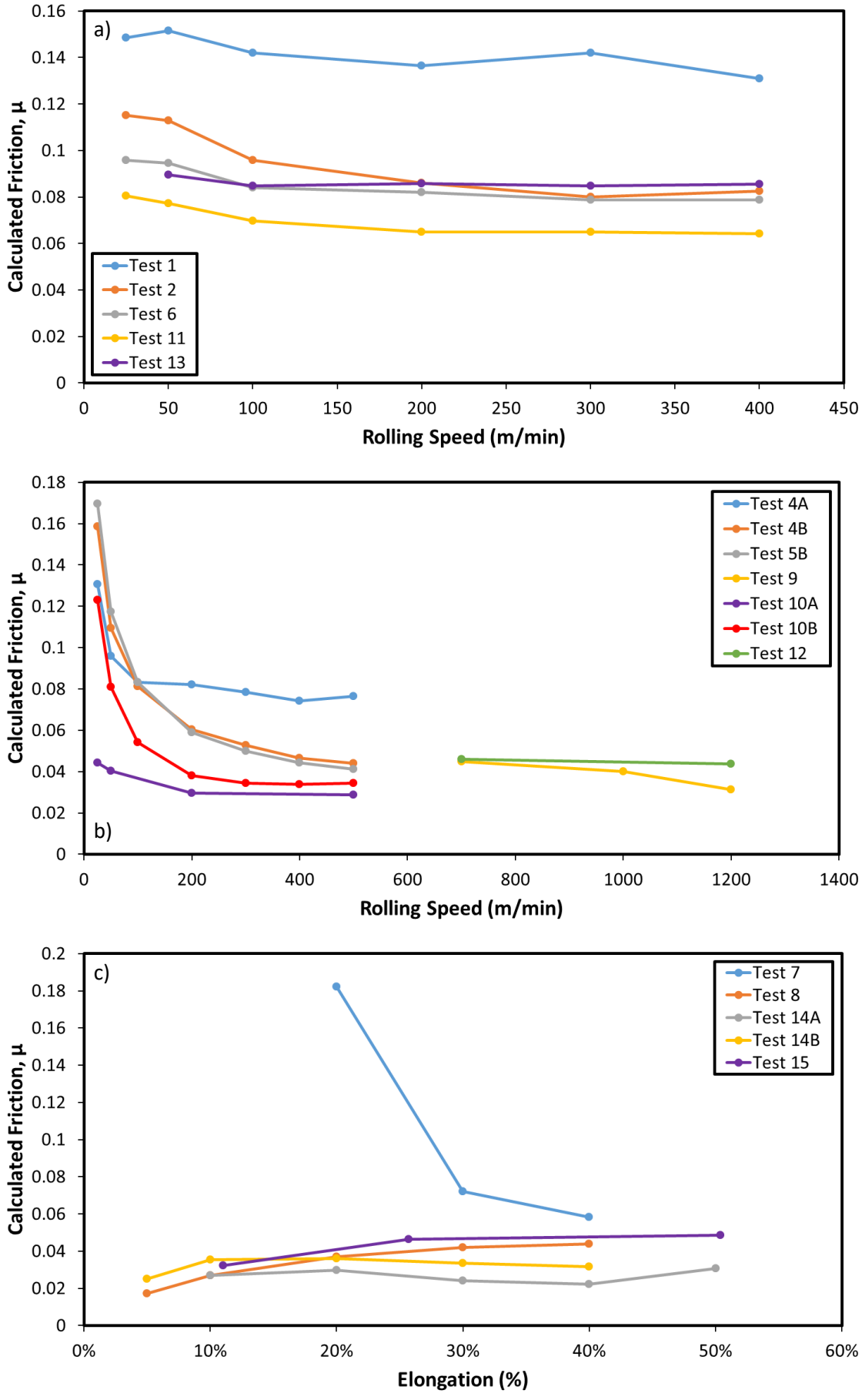

Figure 9.38: Friction Calculated from Equation 9.5 for Tests with a) 2.8mm Thick Strip and Varying Speeds b) 0.75mm Thick Strip and Varying Speeds c) Varying Elongation.

The reason for this apparent relationship is not explicit, however both friction and shear stiffness are dependent upon the real area of contact *A*. Therefore, if a reduction in one of these variables was seen due to a reduction in *A*, a similar drop in the other variable would be expected. This implies that an increase in rolling speed results in a reduced proportion of solid-solid contact.

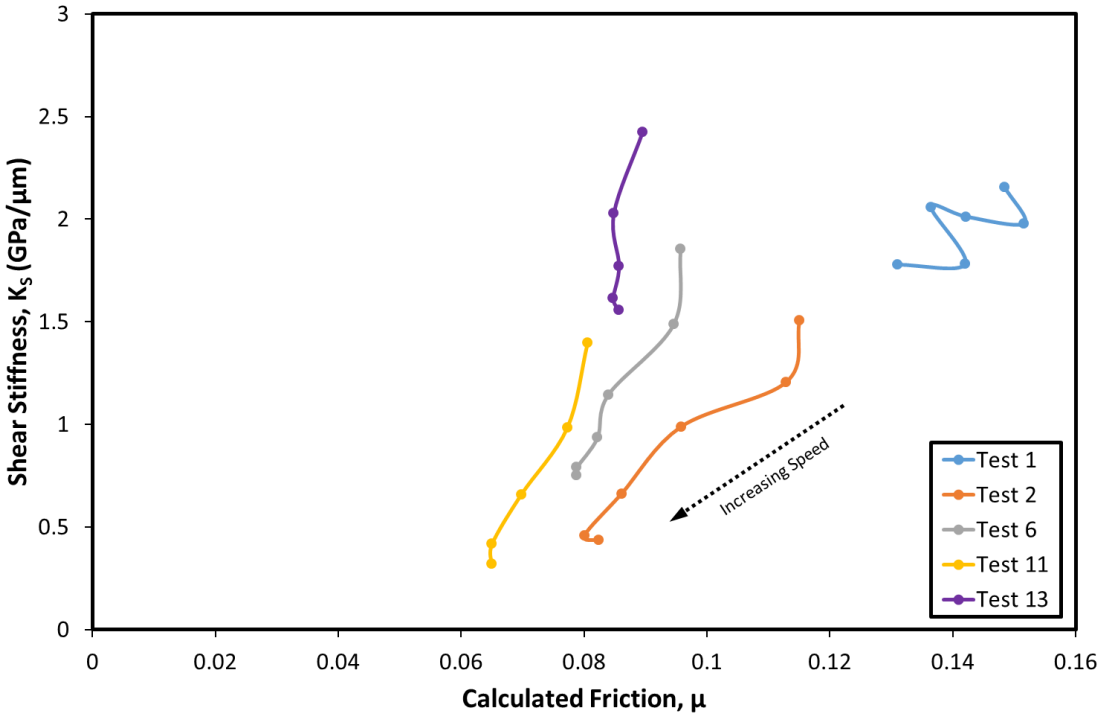

Figure 9.39: Shear Interface Stiffness for 2.8mm Thick Strip and Varying Speeds and Lubrication Conditions.

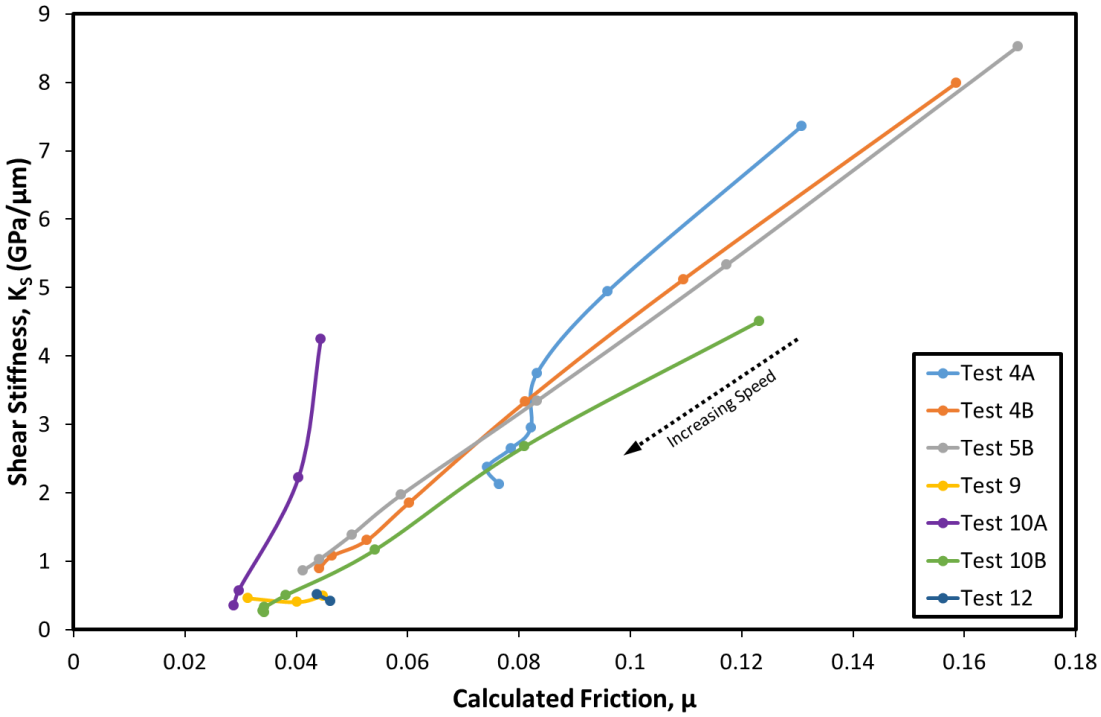

Figure 9.40: Shear Interface Stiffness for 0.75mm Thick Strip and Varying Speeds and Lubrication Conditions.

9.9 Conclusions

A range of rolling parameters and lubrication cases were successfully tested and the film thickness profile across the roll bite for these was measured ultrasonically. In general, the film thickness measurements taken gave values of a reasonable order of magnitude, and show a variation depending upon the rolling conditions.

Inlet film thickness calculations imply that the rolling conditions tested were all within mixed or boundary regimes, as expected. The roughness of the strip was therefore expected to effect the lubricant film thickness, and this was demonstrated in the ultrasonic results through a thicker lubricant film being measured for a rougher strip.

The lubricant film thickness at the centre of the roll bite showed a decrease with increased elongation. This was expected due to the higher rolling loads and increased strip surface. The layer thickness was seen to remain constant or slightly increase with increased rolling velocity for the thicker, rougher strip. The thinner smoother strip showed an increase in film thickness at the lowest speeds (25 m/min to 50 m/min), but then remained largely constant for speeds up to 500 m/min.

Some limitations to the measurement were encountered. The most evident were interference fringes experienced at the entry and exit of the roll bite. These rendered data in the vicinity of the contact edges unusable. However, data at the centre of the contact was still valid.

The pulse repetition rate was limited by the time-of-flight through the plug, this in turn restricted the resolution of data across the roll bite at higher rolling speeds. This could be resolved by shortening the ultrasonic path length.

It was necessary to adjust the value of the bulk modulus to account for pressure and temperature using a simulated pressure profile across the roll bite. This implies that the lubricant is trapped in the interface and experiences at least some proportion of the rolling pressure. A better understanding of the pressure at the interface is therefore required to yield accurate absolute values for film thickness.

A correlation between the calculated friction and the measured shear stiffness was observed although the reason for this is not entirely clear. Friction is a function of the contact area and interfacial shear stress. It may be that due to the nature of the interfacial asperity contact that the interface shear stiffness is related to the applied shear stress. If so this would explain why increased shear stress (and therefore increasing friction) in turn increases the shear stiffness of the interface. It may also be that the increase in speed results in greater lubricant film thickness. This reduces the proportion of solid-solid contact and therefore both the shear stiffness and friction.

10 Roll Stress and Deflection

The following chapter presents the results gained from measurements of the roll deflection and stress experienced during rolling. As with previous chapters the results presented were processed from data recorded on an Arcelor-Mittal semi-industrial pilot mill in Maizières-lès-Metz.

10.1 Test Conditions

A time domain response is required for the measurement of deflection and stress. This is the same response recorded for the film thickness measurements taken in Chapter 9. The same data was used and therefore the conditions shown in Table 9.1 were trialled. Although a range of lubricants were tested the relative effect of these on the stress experienced, comparative to the elongation, strip material and rolling speed was expected to be negligible. As before two different strip materials were rolled, DD14 and ARCELOR06, more details of which are given in §6.4.

To study the measurement of deflection and stress two test cases were selected. These were identical except in one case (Test 6) the rolling speed was varied, while in the other (Test 7) the strip elongation was changed. These two cases are studied in detail in this chapter.

In order to validate the results gained they are compared to the average radial stress profile as calculated from the model presented in §2.6. The following parameters were input into the model. The load was recorded from the mill control system, and the roll bite width measured ultrasonically.

Speed (m/min)	Rollbite Width (mm)	Load (Tonne)
25	13.385	62.5
50	13.756	64.8
100	13.464	66.9
200	13.319	69
300	13.437	69.5
400	13.322	70.2

Table 10.1: Test 6 Varying Speed Model Inputs.

Elongation (%)	Rollbite Width (mm)	Load (Tonne)
5	6.43	25.5
10	8.677	35.7
20	11.634	54.1
30	13.557	65.9
40	14.891	74.2

Table 10.2: Test 7 Varying Elongation Model Inputs.

10.2 Time of Flight Extraction

Both the roll deformation and stress were calculated from the Time-of-Flight (ToF) of an ultrasonic wave passing through the inspected material. This requires extremely accurate measurement of a pulse location in the time domain. Any pulse timing measurement must be unaffected by a change in pulse shape due to phase shifts introduced when the pulse reflects

from the contacting surface. To remove the effect of phase shift from the ToF measurement an approach that utilises the analytical envelope of the pulse was used. The envelope was calculated by combining the real and imaginary components of the wave in quadrature, the imaginary components being calculated using a Hilbert transform and hence the envelope is referred to in this work as the Hilbert envelope. A threshold, as calculated from a percentage of the maximum envelope value is set, and the point at which the envelope crosses this threshold was used to calculate the time of the pulse. The threshold was calculated as a percentage of the maximum as this removes the effect of any amplitude change in the reflected pulse. A low threshold value was chosen to ensure the threshold is crossed at a time close to the start of the pulse. Therefore, any interfering reflections occurring later in the time domain have a lesser effect.

This threshold approach means the exact start of the pulse is not calculated. Therefore, that absolute ToF of the pulse is not known, there will be some offset between this measurement and the absolute value. However, the measurements of interest in this chapter are only concerned with changes from the undeformed/unstressed state. As such only the relative change in ToF rather than the absolute value is required.

Due to data throughput limitations only a small time-domain window around the pulse of interest was recorded. This window had a fixed start and range. For some of the data recorded the start of the pulse shifted outside of this capture window. This was because the increasing speed of sound in the propagation material caused the pulse to occur earlier in the time domain, while the hardware record delay remained constant. An example pulse is shown in Figure 10.1. In this circumstance, the threshold point could not be captured accurately as it fell outside the captured window. To prevent this happening a larger tolerance could be set to increase the window width and reduce the likelihood of signal cropping. This would have the downside of increasing the amount of data acquired and therefore potentially reducing the maximum pulse repetition frequency, a particular issue when measuring high rolling speeds.

To prevent this from happening a larger threshold could be selected, this would shift the threshold later in the time domain. However, this causes inaccuracies on the data as described above. Therefore, an attempt to estimate and reconstruct this missing signal was made. Although this may introduce additional error in the measurement, as only a small amount of relevant data was lost (a few datapoints), it is expected that this error would not be significant. Three approaches were attempted.

The first approach was the simplest. A linear interpolation was used to extrapolate the Hilbert envelope past the start of the recorded data. This interpolation was based upon the gradient of the first two data points of the recorded data. This linear interpolation was used to construct a Hilbert envelope.

The second approach was based upon the assumption that the signal is expected to be zero before the pulse. Based upon this the existing data was prepended with zero-values. The Hilbert transform was then taken of this combined signal. The analytical signal was then calculated from this and processed as described above.

The final approach was the most complex. An FFT was calculated for the recorded part of the signal. This was then used to reconstruct the section of the ultrasonic response which had been

cropped. Once the A-Scan had been reconstructed a Hilbert transform was computed and the signal was processed as previous. The time domain data produced by the different approaches is shown in Figure 10.2, with the subsequent ToF calculated for 3% and 5% thresholds shown in Figure 10.3 and Figure 10.4 respectively.

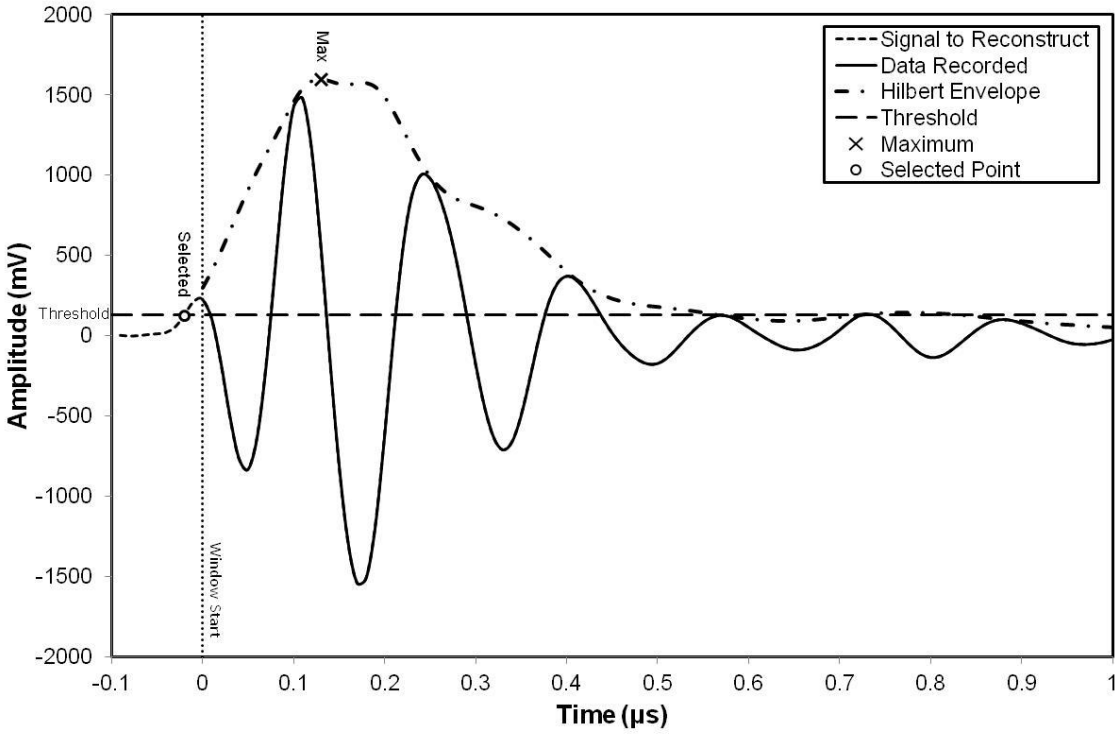

Figure 10.1: AScan showing Cropped Signal to Reconstruct.

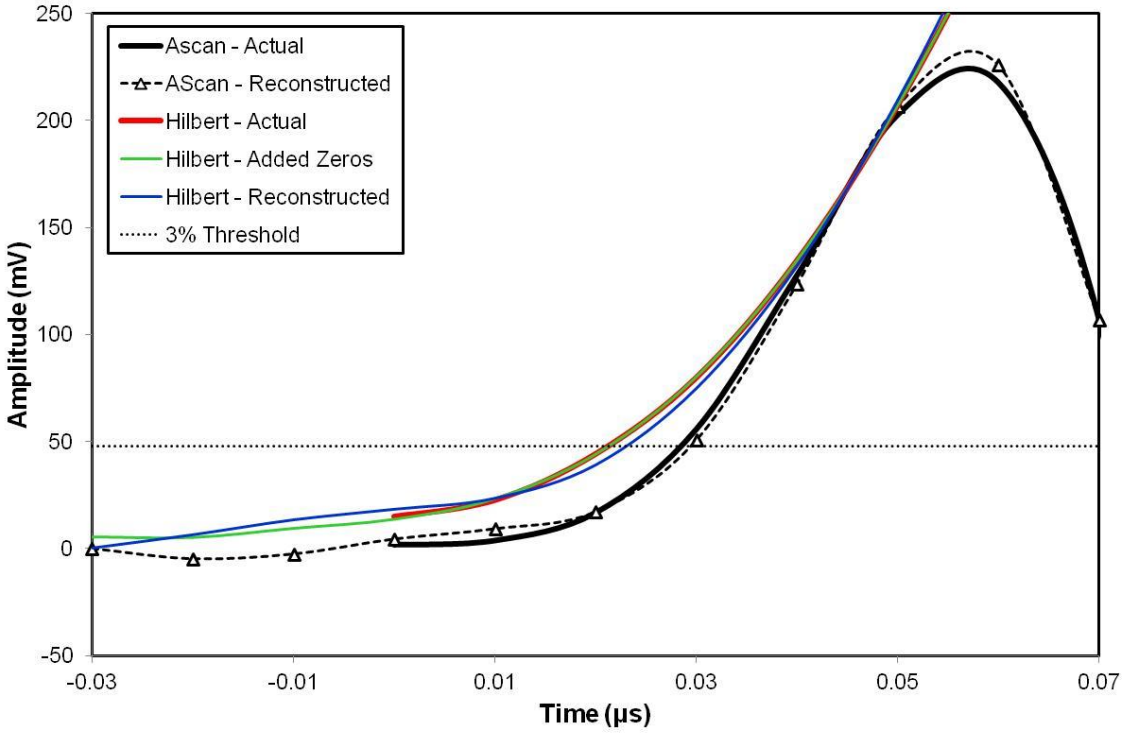

Figure 10.2: Various Techniques for Reconstructing Cropped Data.

All three techniques yielded similar values, especially for the 5% threshold. It was therefore decided to use a 5% threshold in all test cases, and the third A-Scan reconstruction technique in

the cases where data had been cropped from the A-Scan, as this offered the most robust approach.

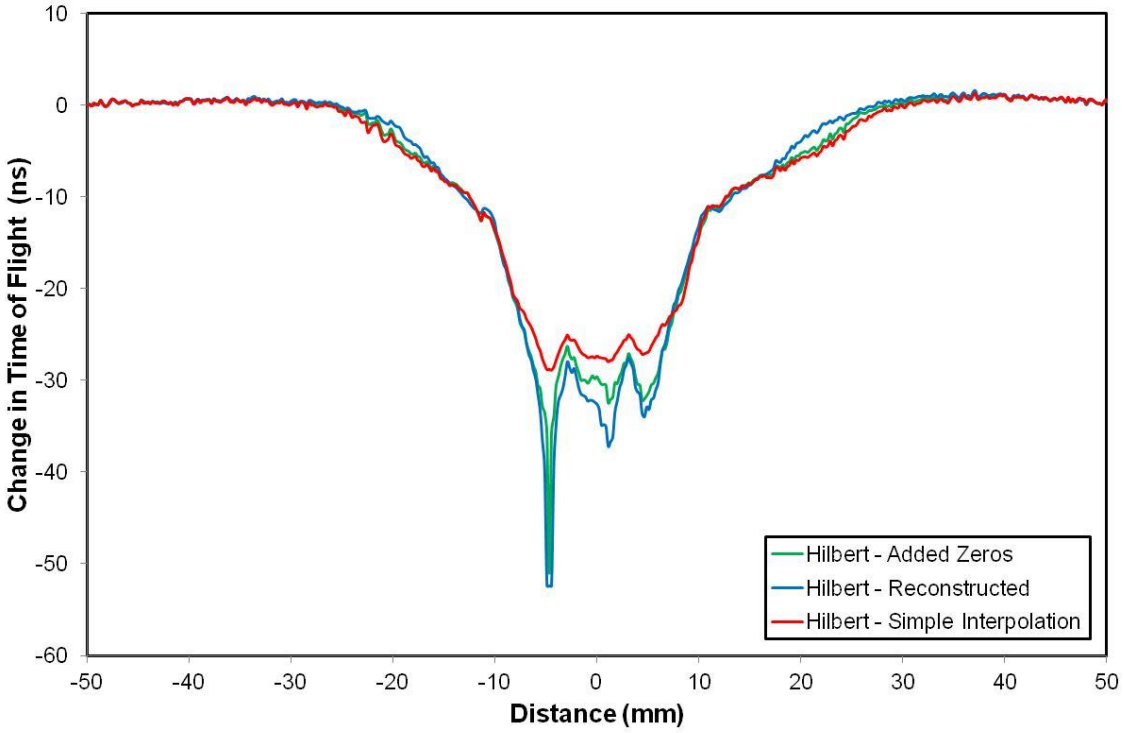

Figure 10.3: Various Techniques for Reconstructing Cropped Data, 3% Threshold.

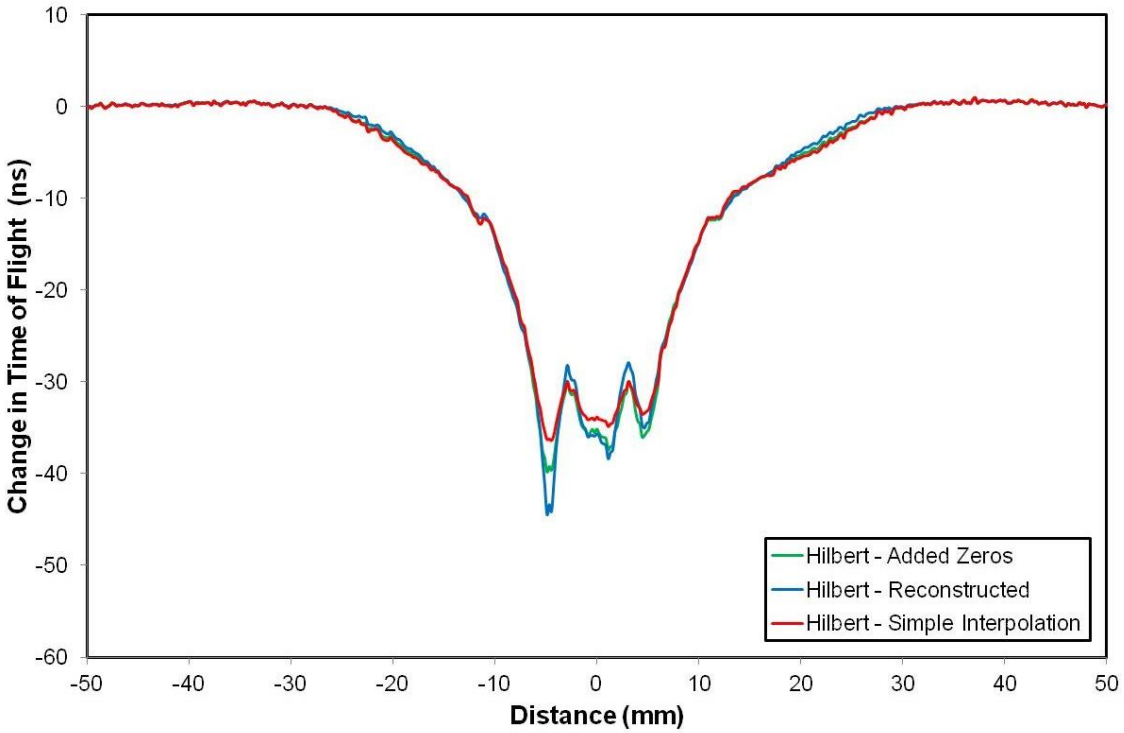

Figure 10.4: Various Techniques for Reconstructing Cropped Data, 5% Threshold.

In Figure 10.3 and Figure 10.4 sharp dips can be seen at the entrance and exit to the roll bite. In some cases a stress peak may occur at the first contact point, however in this case it is unclear if the peak occurs due to this or the entrance/exit interference as seen in the film thickness

measurements. As will be seen in the next section, data in these regions will be cropped out of the following analysis, however they may be worth future investigation.

10.3 Ultrasonic Data Capture and Processing

As in the previous chapter data was buffered at high speed and the individual time domain responses were separated in post processing. A set of example time domain responses and Hilbert envelopes from a shear sensor for a roll bite pass are given in Figure 10.5.

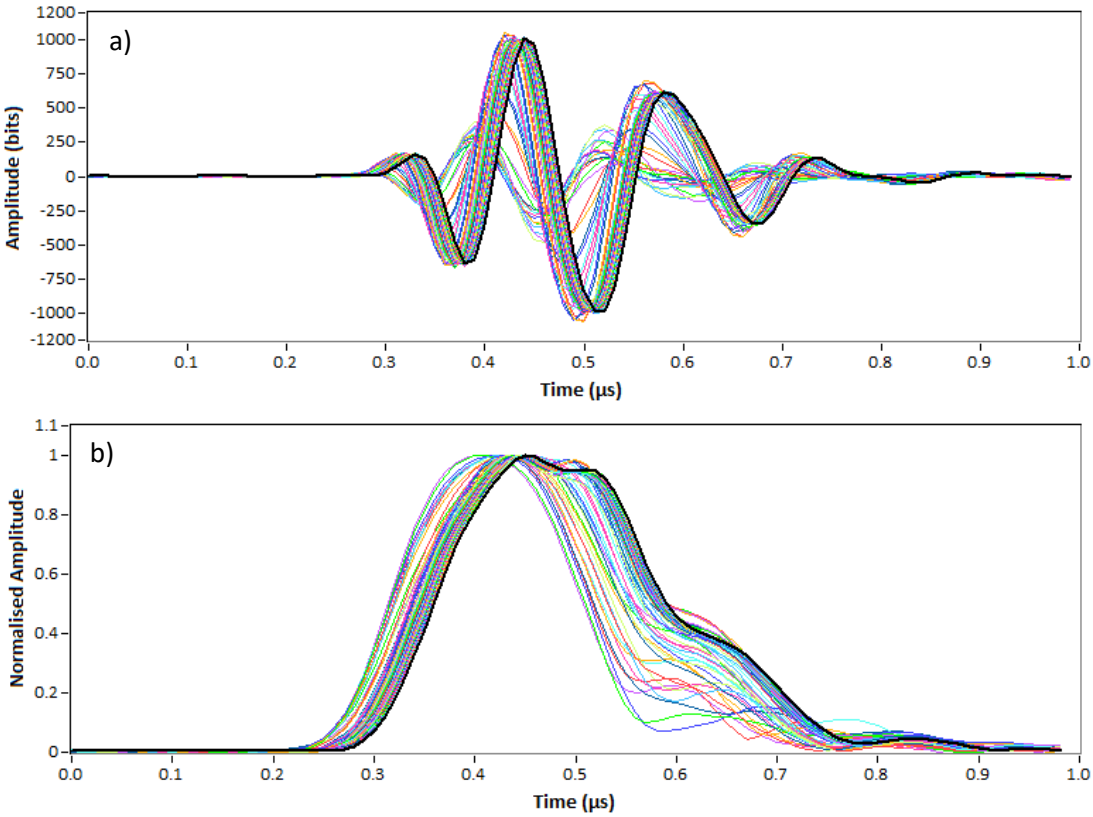

Figure 10.5: Ultrasonic Data showing a) Captured Pulse Time Domain Signals b) Hilbert (Analytical) Envelope.

These plots show a clear time shift in the leading edge of the pulse and envelope. This time shift was extracted using the threshold technique described above. The deformation and stress were then calculated using equations given in chapter 4. The parameters given in Table 10.3 were used in these calculations (combined from Table 7.3 and Table 8.5).

Undeformed Plug Length, d_0 (m)	0.035
Longitudinal SoS, c_L (m/s)	5992.11
Shear SoS, c_S (m/s)	3247.72
Density, ρ (kg/m^3)	7794.02
Poisson's Ratio, ν	0.292
Young's Modulus, E (GPa)	212.44
Shear Modulus, G (GPa)	82.21
Long. Acoustoelastic Constant, α_{xx}	-2.685
Shear Acoustoelastic Constant, α_{xy}	-1.757

Table 10.3: Parameters used to Calculate Deflection and Stress.

The time shift and associated surface deflection and stress from a set of example responses at a range of rolling speeds are shown in Figure 10.6. As with the previous chapter the results have

been cropped to remove areas of interference. Figure 10.6a shows the uncropped results, with a clear change in the time-of-flight observed. This change in ToF starts some way outside of the expected roll bite contact width of 13mm. The deformation is broadly symmetrical about the centre of the roll bite. Figure 10.6b shows the deflection calculated for the cropped results. These show a consistent deflection shape which slightly increases with rolling speed. The surface deflection appears to be of a reasonable magnitude. The associated radial stress is reported in Figure 10.6c. It should be noted that the stress values reported here represent an average radial stress along the ultrasonic path (plug length), and not the peak or surface stress. As the ToF change is the input to both the deflection and stress calculations it is noticeable that their form is the same.

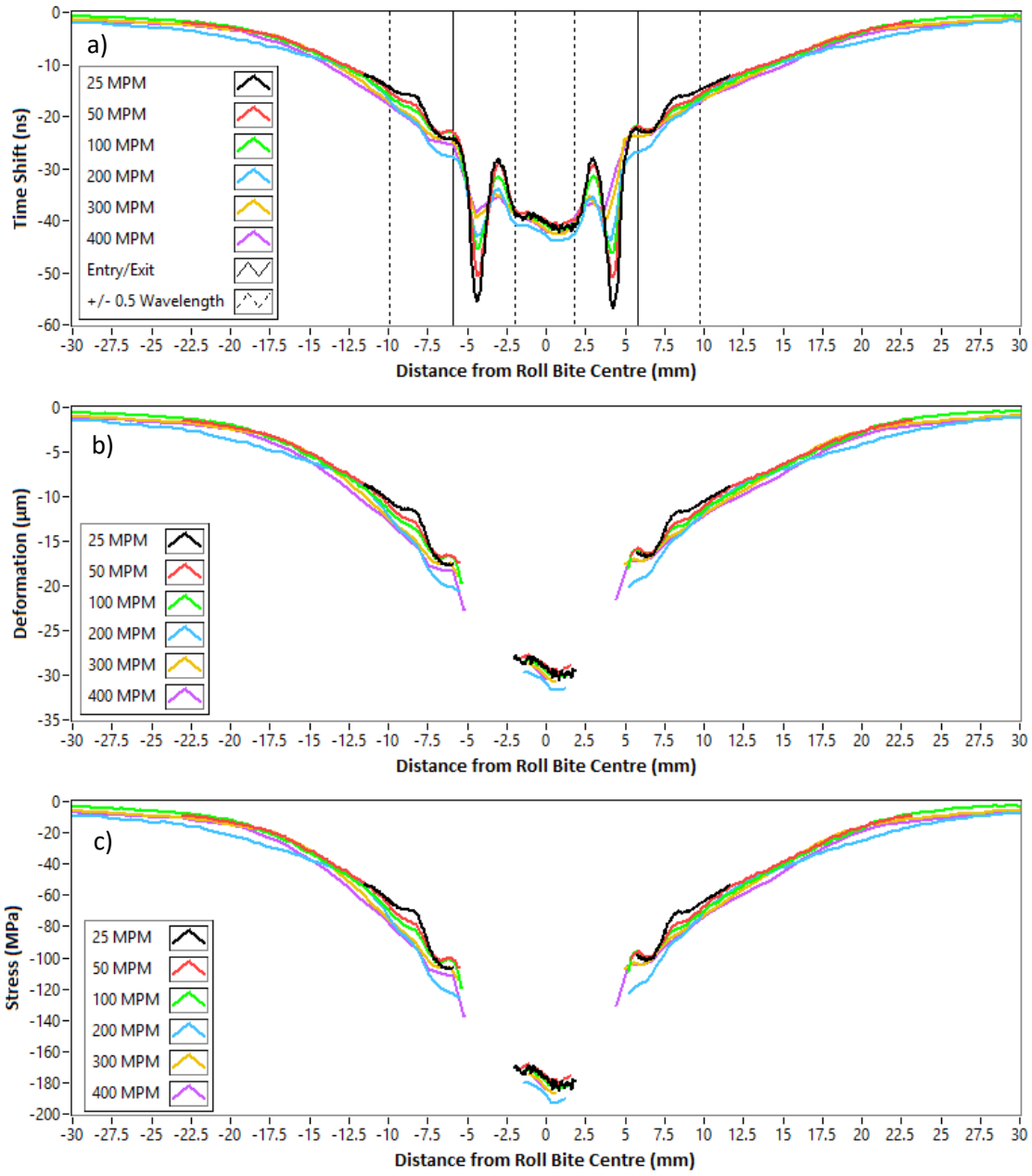

Figure 10.6: Example Profiles across Roll Bite a) Uncropped Time Shift b) Cropped Calculated Deformation c) Cropped Radial Stress.

The above indicates that it is possible to measure roll radial stress and deflection in the roll bite using ultrasound. To understand the effect that different rolling conditions have on the

deflection and stress two test cases have been studied in more detail below. Test 6 looks at the effect of varying rolling speed and Test 7 looks at the effect of varying strip elongation. Aside from the speed and elongation all other test parameters are kept the same between the tests.

10.4 Deflection and Stress with Rolling Speed

The following section uses data from Test 6. In this test a fixed 30% elongation was used with directly applied pure K2 oil at 60°C. The rolling speed was varied from 25 to 400 m/min.

10.4.1 Longitudinal Sensor Results

Firstly, the results obtained from the longitudinal sensor are studied. Figure 10.7 shows the unedited change in ToF of the first reflected pulse from the roll bite interface for several rolling speeds.

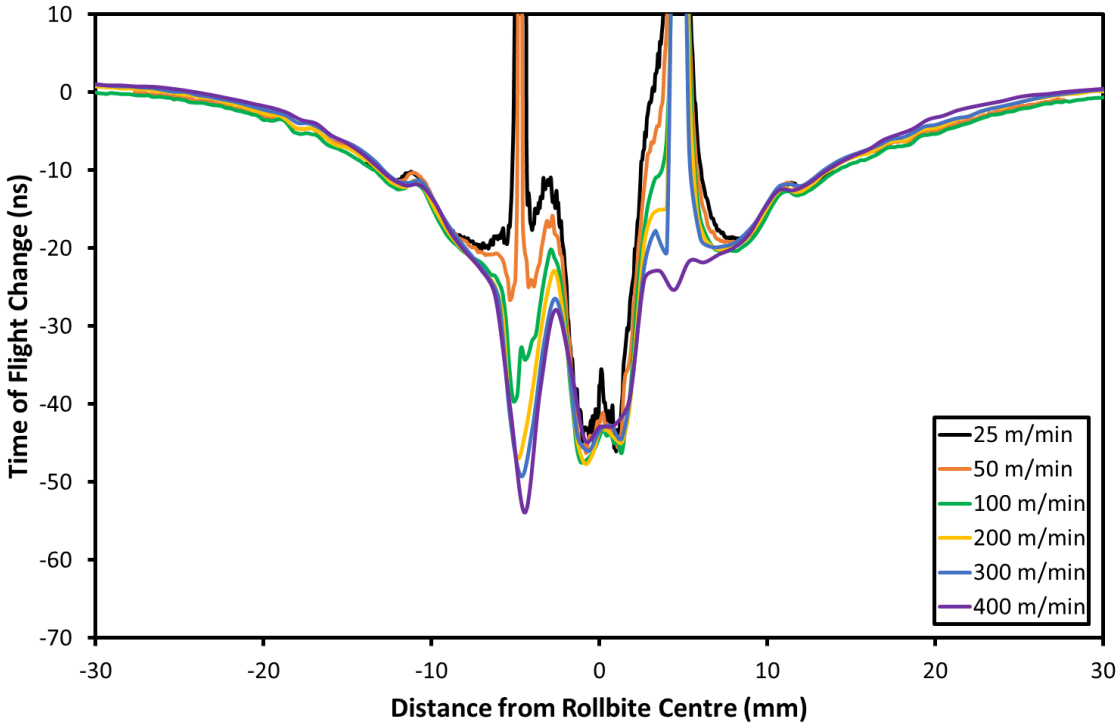

Figure 10.7: Change in Longitudinal Time of Flight across Roll Bite for Various Rolling Speeds.

A disrupted signal is seen at the roll bite entry and exit. These sections have been cropped as they were in chapter 9 to yield Figure 10.8. This figure shows a pattern in the ToF change which is consistent and of similar magnitude for all the rolling speeds tested. The change in ToF starts and ends approximately 30mm either side of the roll bite centre and reaches a maximum reduced ToF of around 45 ns at the roll bite centre.

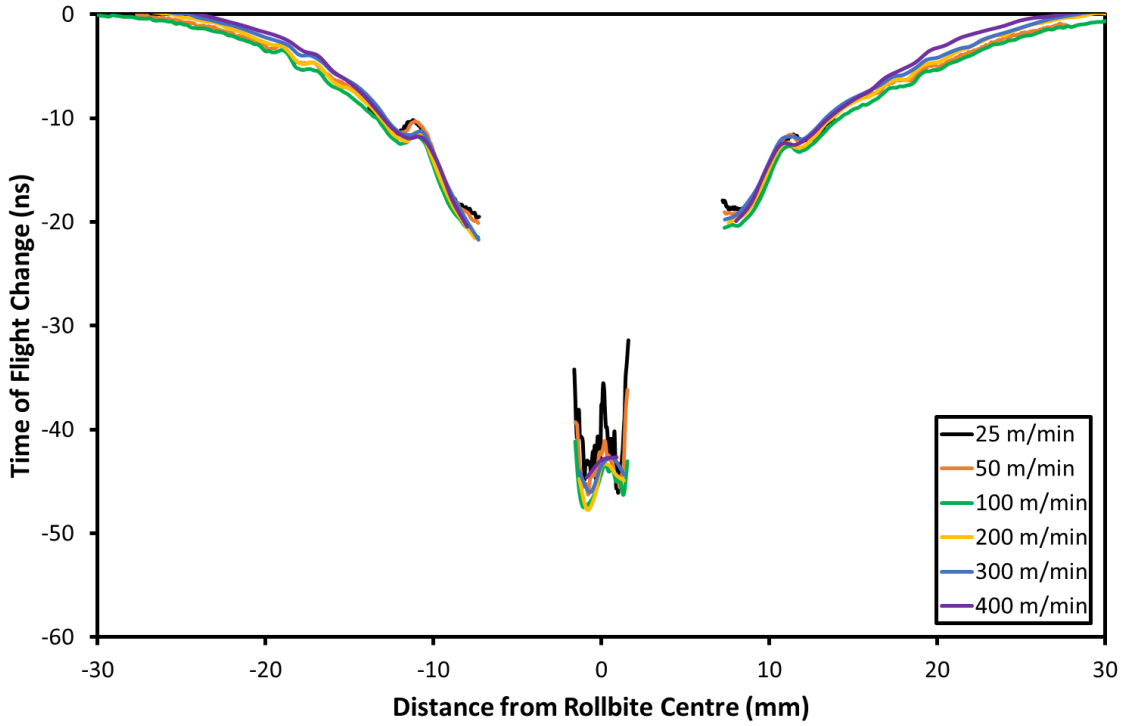

Figure 10.8: Change in Longitudinal Time of Flight across Roll Bite for Rolling Speeds Elongations, cropped to remove Interference Effects.

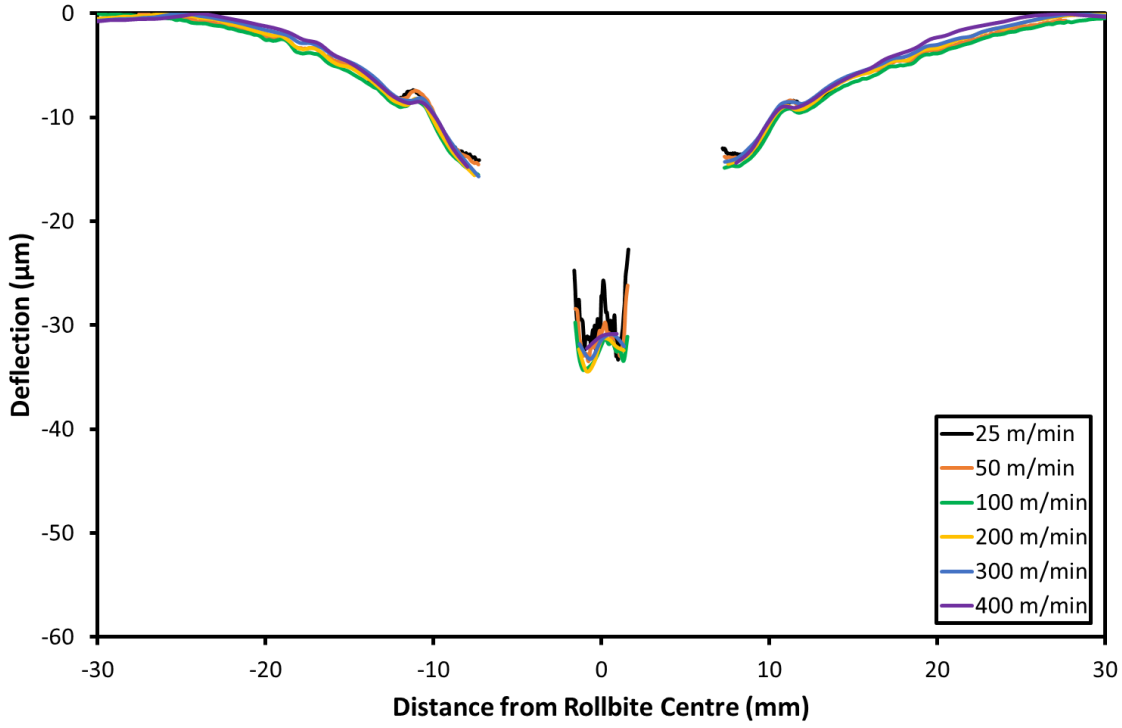

Figure 10.9: Deflection of Roll Surface measured using Longitudinal Sensor for various Rolling Speeds.

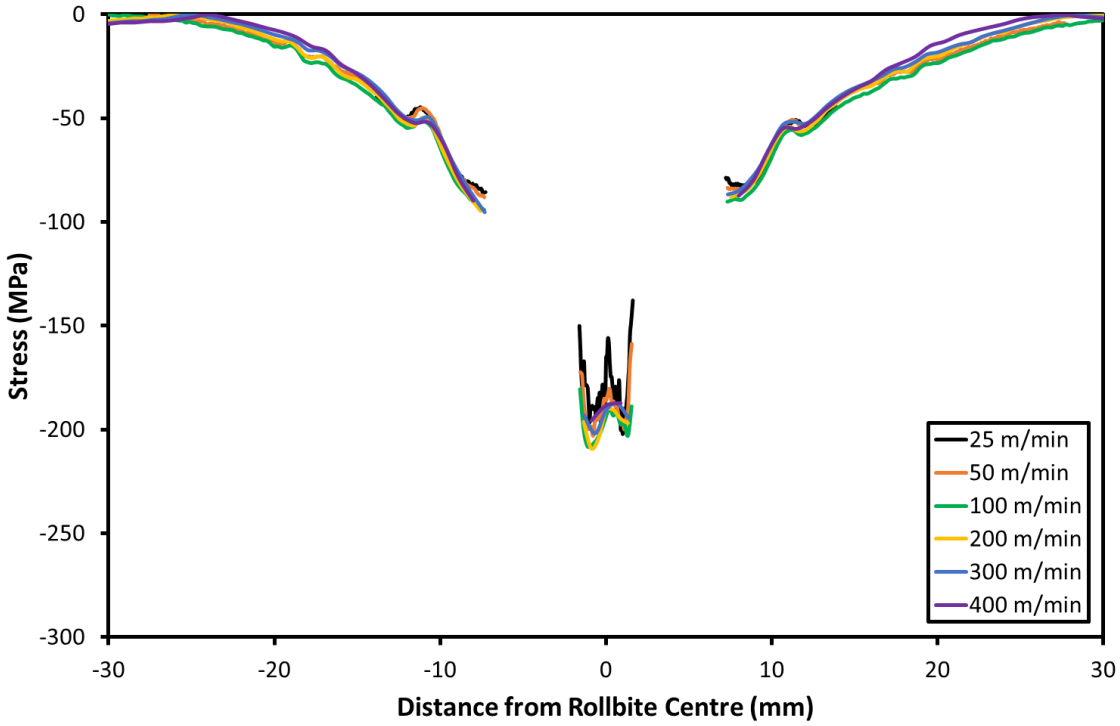

Figure 10.10: Average Radial Roll Stress from Longitudinal Sensor for various Rolling Speeds.

The surface deflection and radial stress calculated from this ToF are given in Figure 10.9 and Figure 10.10. The ToF, surface deflection and stress are all of the same form. All three show slight spikes at the edges and near the centre of the roll bite. The difference in the results between the different rolling speeds is minimal.

10.4.2 Shear Sensor Results

In addition to the longitudinal results data for the same tests was also recorded from a shear sensor. The change in the ToF recorded from this sensor are given in Figure 10.11.

As with the longitudinal results some interference is seen at the entry and exit of the roll bite. Again these results are cropped according to the method used in chapter 9. The cropping method is based upon the ultrasonic wavelength. The speed of sound of a shear wave is significantly smaller than a longitudinal wave and therefore the ultrasonic wavelength is also proportionally smaller. Because of this less of the shear signal is cropped in comparison to the longitudinal signal, as can be seen by comparing Figure 10.8 to the cropped shear sensor results in Figure 10.12.

By cropping less data, a better profile of the surface deflection and stress across the roll bite (as shown in Figure 10.13 and Figure 10.14) can be seen. The shear sensor results also appear to be more constant with no spikes at the roll bite entry, exit and centre as seen in the longitudinal results.

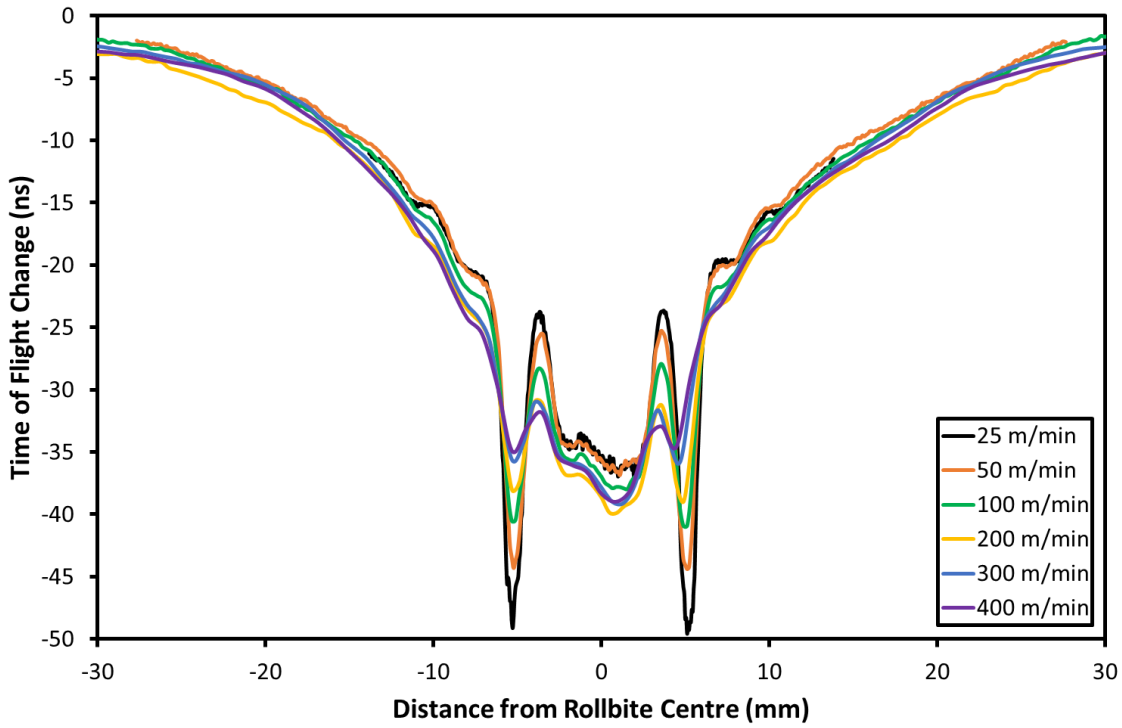

Figure 10.11: Change in Shear Wave Time of Flight across Roll Bite for various Rolling Speeds.

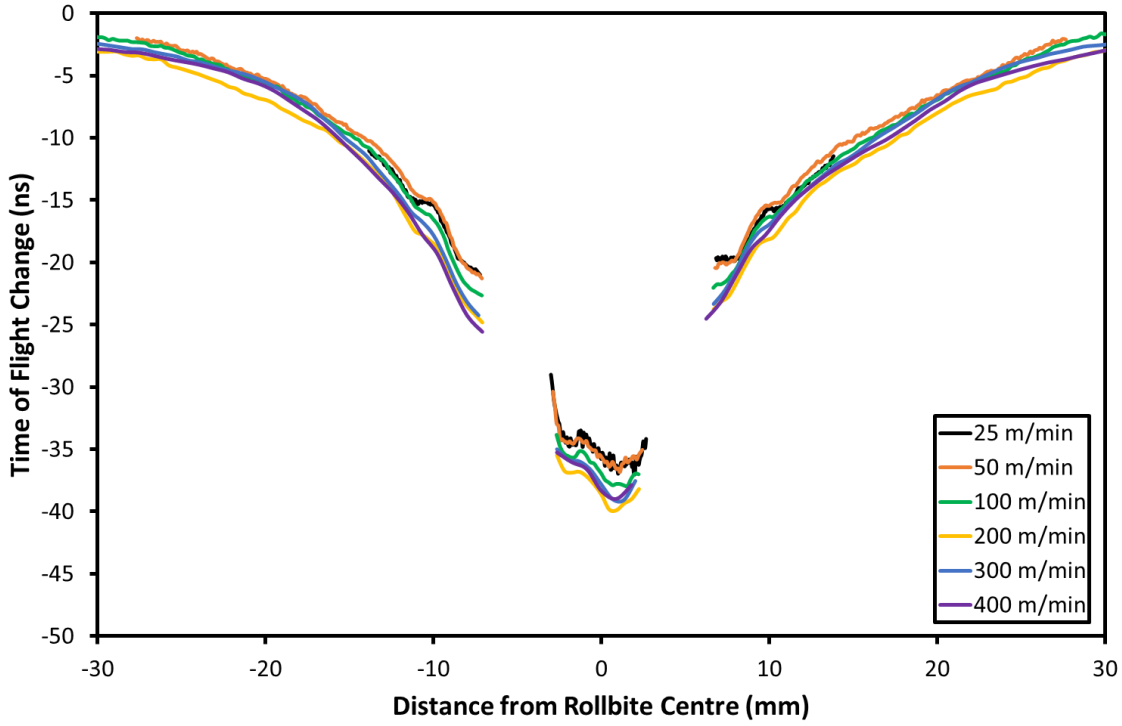

Figure 10.12: Change in Shear Wave Time of Flight across Roll Bite for various Rolling Speeds, cropped to remove Interference Effects.

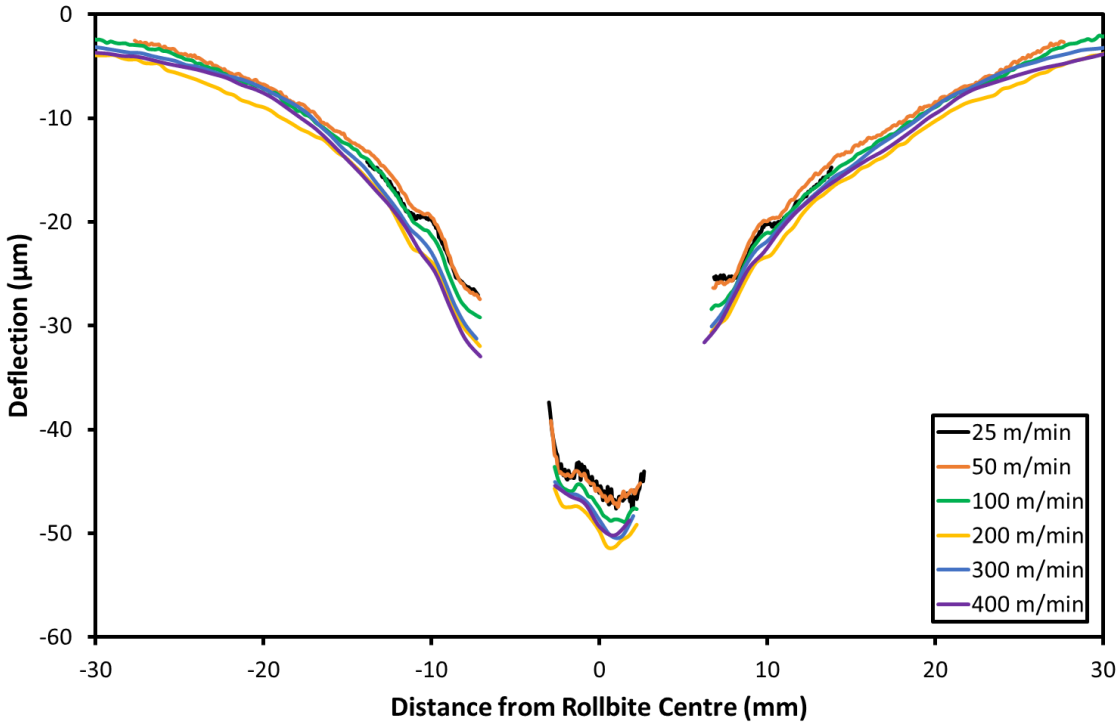

Figure 10.13: Deflection of Roll Surface measured using Shear Sensor for various Rolling Speeds.

As with the longitudinal results the shear wave results show a change in ToF occurring far outside of the expected roll bite contact. The results are similar for all rolling speeds tested. Across the roll bite the shear wave results, unlike the longitudinal results, seem to show a slight skew towards the roll bite exit. Both the deflection and stress reported increase slightly across the roll bite with higher values at the roll bite exit compared to the entrance. The maximum ToF change measured for the shear wave was smaller than for the equivalent longitudinal wave, however both the deflection and stress values are slightly higher, as can be seen by comparing Figure 10.10 and Figure 10.14.

There are several possible reasons for this. The measurements for radial stress from both sensor types assumes only simple normal compression of the roll, and ignores any tangential, axial or shear stresses. This is likely to result in some error as friction within the roll bite will result in traction forces at the interface and this will in turn have associated stresses. There may also be stresses induced due to roll bending. Finally, there may be an error in the acoustoelastic calibration performed, possibly resulting in an incorrect value for one or both of the acoustoelastic constants.

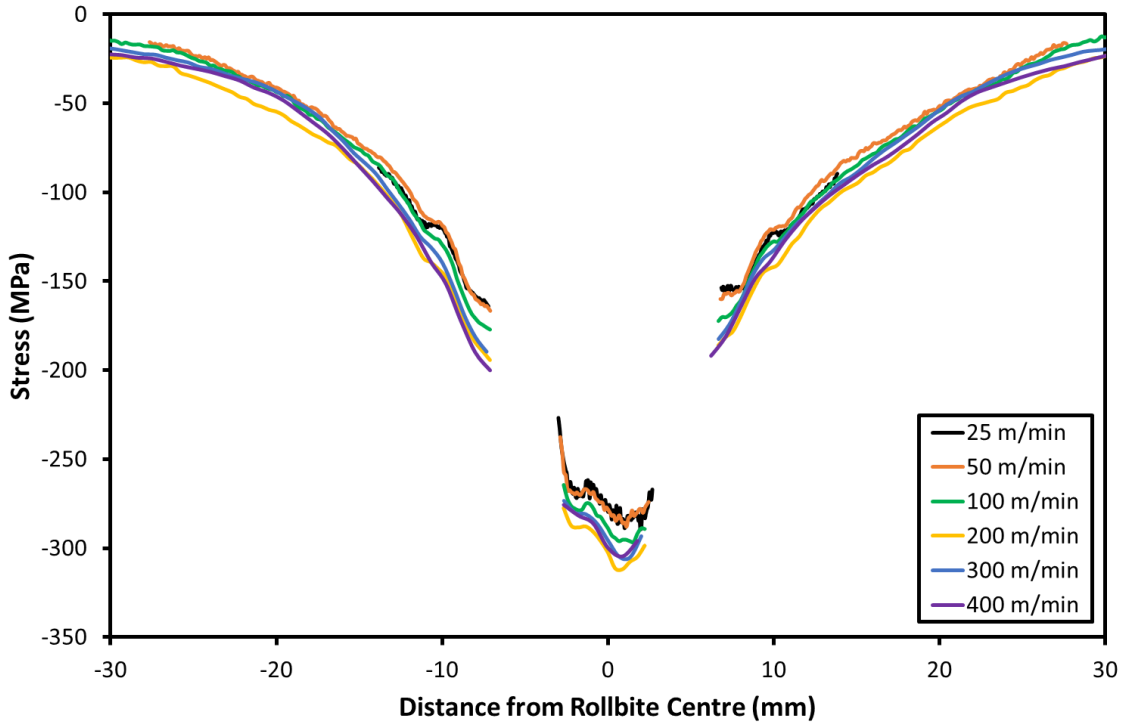

Figure 10.14: Average Radial Roll Stress measured using the Shear Sensor for various Rolling Speeds.

10.4.3 Model Results

With no independent measurement of surface deflection or stress having been recorded, in order to assess the validity of the results gained the rolling cases tested have been modelled using the stress model presented in §2.6 with parameters from Table 10.1. For the purposes of modelling it was assumed that the normal rolling force would dominate and that the frictional effects were negligible in comparison. Therefore, the friction coefficient was set to zero. The stress obtained from the longitudinal sensor and presented in Figure 10.10 have been overplotted with modelled results to give Figure 10.15.

There is a striking similarity in the shape of the stress curve between the cropped measured and modelled results. The modelled results do however appear to be offset from the measured results. The results could differ if there is an error in the acoustoelastic constant used. This would result in a scaling effect rather than a fixed offset. It also should not have any effect at zero-stress. Instead it is clear from the Figure that the results have a more consistent offset.

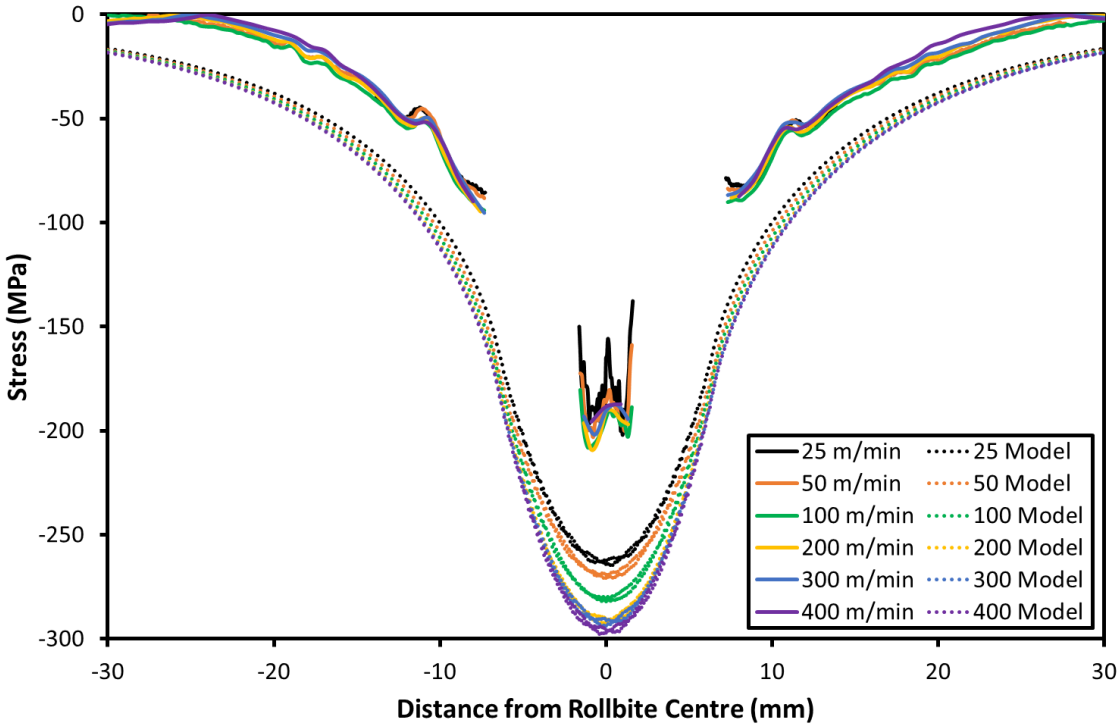

Figure 10.15: Radial Stress from Model and Longitudinal Sensor for various Rolling Speeds.

The stress is calculated from the change in ToF. This change is taken with respect to a "zero-value" of the time of flight. This zero-value is the ToF when the roll is not stressed, any error in this value will result in an offset in the measured stress, such as that observed. After the captured data was divided up by roll bite pass the zero ToF value was taken as the first sample recorded in each roll bite pass dataset. This was to ensure the zero value was taken outside of the roll bite. The value was retaken for each test to remove any effect on the ToF due to a change in plug temperature, this might occur throughout the test program due to heating from the rolling process or changes in temperature in the surrounding environment. If assumption that plug was under no stress when the zero value was taken was incorrect, then this would result in an offset such as that seen.

A possible reason for an incorrect zero value may be due to the plug used to fit the sensors to the roll. The plug on which the sensors were installed was 40mm diameter. From Figure 10.15 it can be seen that when over the centre of the roll bite a length larger than the plug diameter will be stressed, and therefore the entire plug surface will be undergoing some form of deflection. As the plug is only supported around it's circumference by friction from press fitting, it is possible that the plug will deform at a different rate to the surrounding roll material, and also at a different rate when compared to a complete roll which has not had a plug inserted. As the modelling assumes a complete roll this may result in some discrepancy. Also when the roll bite is not directly in contact with the plug, but is in contact with the surrounding roll material then the stress from the contact may not be transmitted to the plug. This will have been the arrangement when the ToF zero-values were recorded. If the plug was experiencing no stress at this point due to the material discontinuity, whereas a complete roll would be experiencing some stress, the zero-point would be assumed to be in an unstressed state when in fact it represents a stressed state in an actual roll. This would lead to an offset in the stress results reported in comparison to the modelled results.

To compare the form of the results a 28 MPa offset has been applied to the modelled results in order to better fit it to the experimental results. The resulting comparison is plotted in Figure 10.16. Although the shape of the results is similar, there is still a clear difference in the amplitudes not accounted for by offsetting the results.

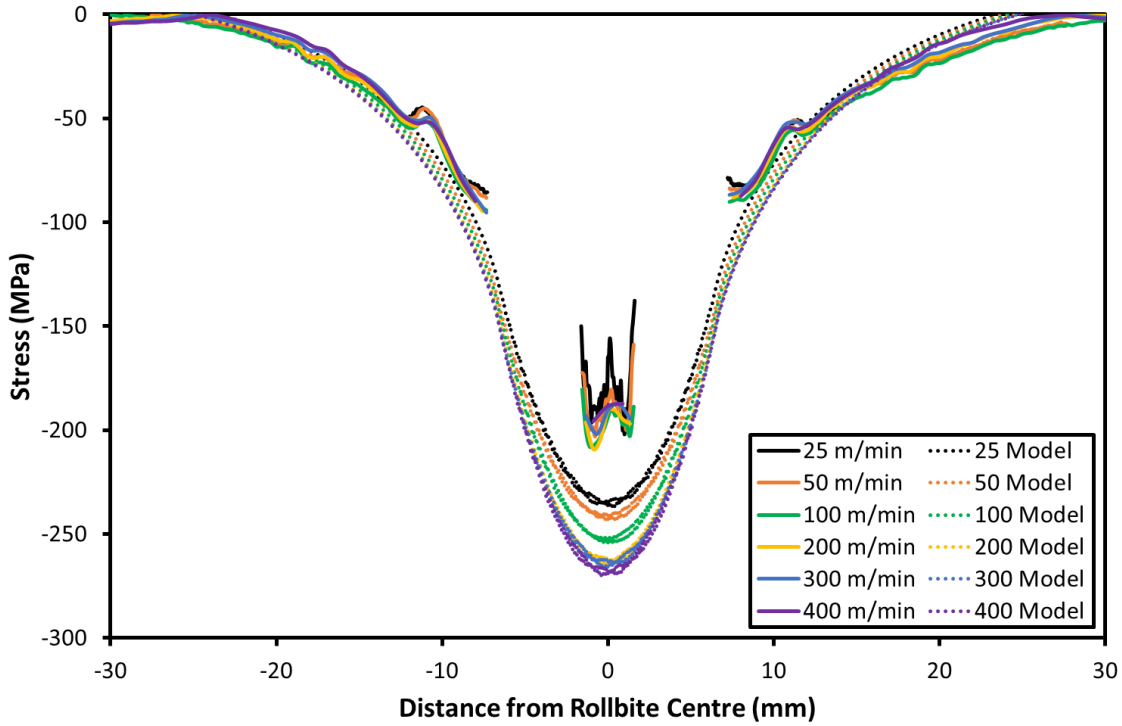

Figure 10.16: Radial Stress from Model and Longitudinal Sensor for various Rolling Speeds. A 28MPa offset has been applied to the modelled results.

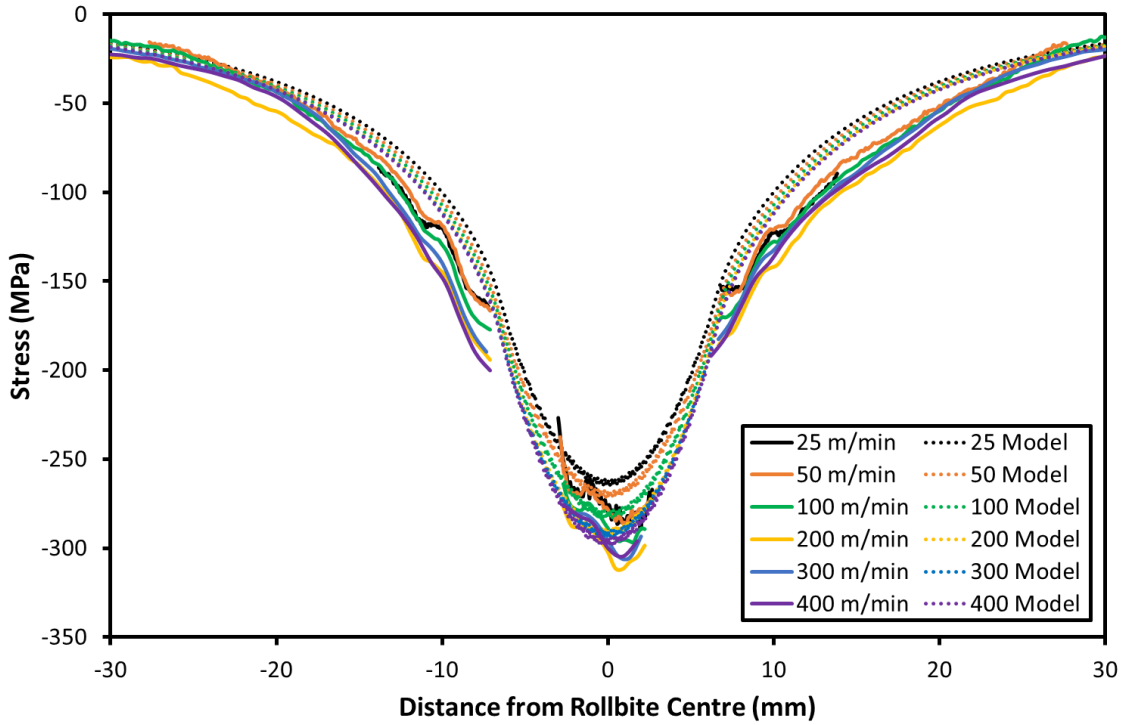

Figure 10.17: Radial Stress from Model and Shear Sensor for various Rolling Speeds.

The model results have also been overplotted on the shear results from Figure 10.14 in Figure 10.17. It should be noted that unlike the longitudinal results the stress model results plotted for the shear results have not been shifted.

Despite no offset being introduced, the shear results match very closely both in form and magnitude with the modelled results. The dips recorded from the measured results are slightly wider than the model. This is in part explained by the size of the sensing path, which will exaggerate the width of the measurement by the same width as the sensor.

The absence of an offset error is likely the result of less "zero-point" error. This may in part be due to lesser beam spread of the shear wave compared to the longitudinal wave, a result of the different transducer shape. A reduced beam spread would mean that the zero-value of the ToF could be taken closer to the roll bite without error.

10.4.4 Results Comparison

Although the model doesn't explicitly produce a value for surface deflection, a value was calculated using the stress-strain relationship for Young's modulus, as shown in Equation 10.1.

$$E = \frac{\sigma d_0}{\delta} \qquad 10.1$$

Where E is the Young's modulus, σ is the stress, d_0 is the undeformed plug length and δ is the deflection. This can simply be rearranged and the stress used to calculate the deflection. The deflection at the centre of the roll bite gained using this method on the modelled results, and measured using the longitudinal and shear sensors are plotted for comparison in Figure 10.18. The associated stress results are given in Figure 10.19.

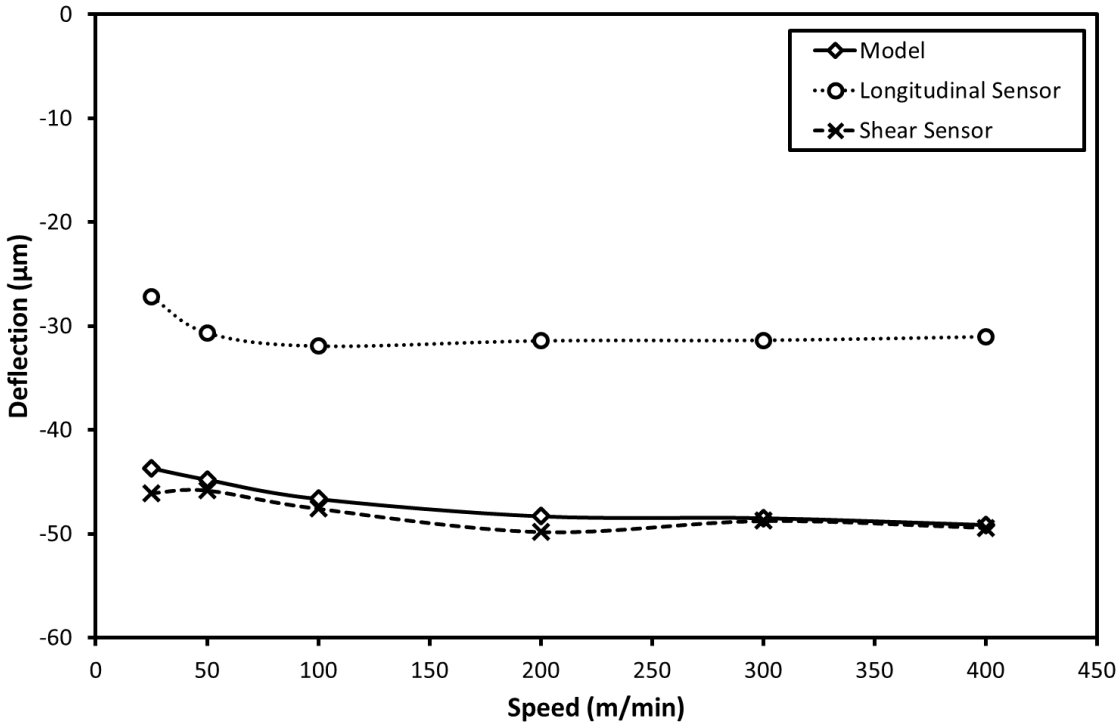

Figure 10.18: Longitudinal Sensor , Shear Sensor and Model Deflection at Centre of Roll Bite for various Rolling Speeds.

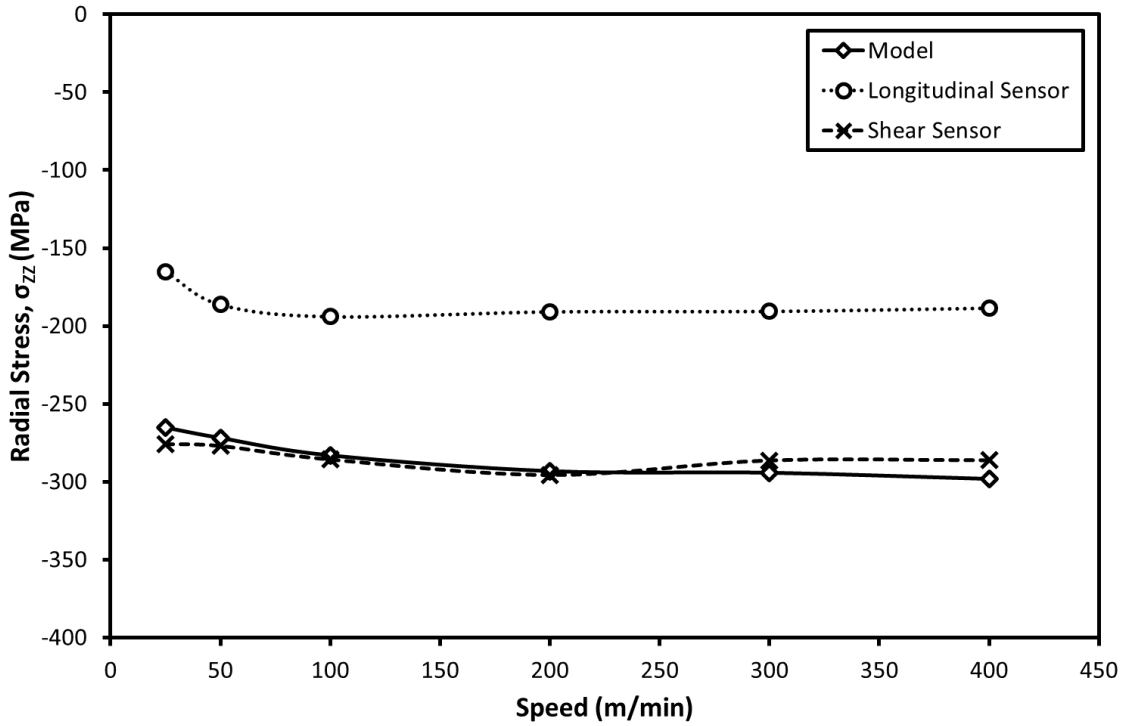

Figure 10.19: Radial Stress at Centre of Roll Bite for various Rolling Speeds calculated from the Longitudinal Sensor, Shear Sensor and Model.

These plots show a good agreement between the model and shear results for both deflection and stress. All results show little change in the deflection or stress across the range of rolling speeds tested. The longitudinal results show consistently less change than either the shear or modelled results. This is the case even if the offset applied above (28 MPa) was accounted for. The reason for the discrepancy between the longitudinal and shear results is not clear but may be due to a combination of the offset and an error in the acoustoelastic constant or other parameters used in the calculation of deflection and stress.

10.5 Deflection and Stress with Strip Elongation

To study the effect of strip elongation on roll surface deflection and stress the following section uses data from Test 7. In this test a fixed rolling speed of 100 m/min was used with directly applied pure K2 oil at 60^{o}C the same as in Test 6. The strip elongation was varied in steps from 5% to 40%

10.5.1 Longitudinal Sensor Results

The uncropped ToF change measured for a longitudinal wave across the range of strip elongations is given in Figure 10.20 with the cropped results shown in Figure 10.21. In the test cases with smaller elongations, and correspondingly small contact widths, cropping the results meant there were no values at the centre of the roll bite, as seen in Figure 10.21. Data at the centre of the roll bite is only available for elongations of 19.8%, 30% and 40%. Unlike with rolling speed, changing to the strip elongation results in a clear difference in the ToF with increased elongations showing increasing magnitudes of change. This is expected due to the increased rolling loads used, as shown in Table 10.2.

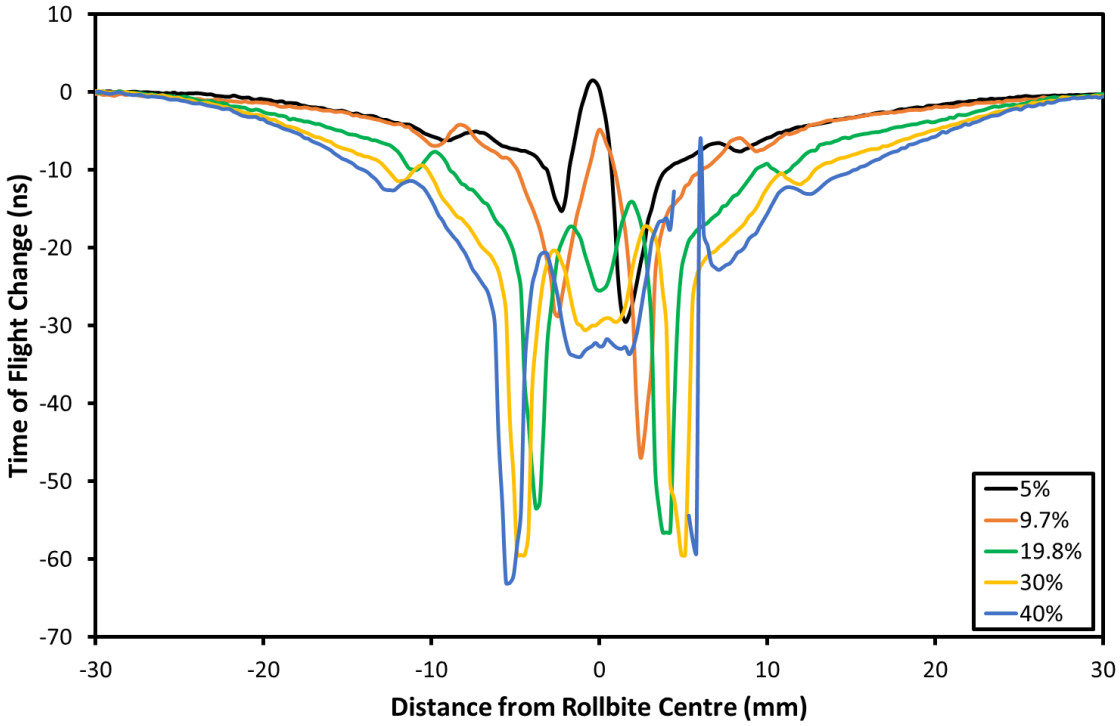

Figure 10.20: Change in Longitudinal Time of Flight across Roll Bite for various Strip Elongations.

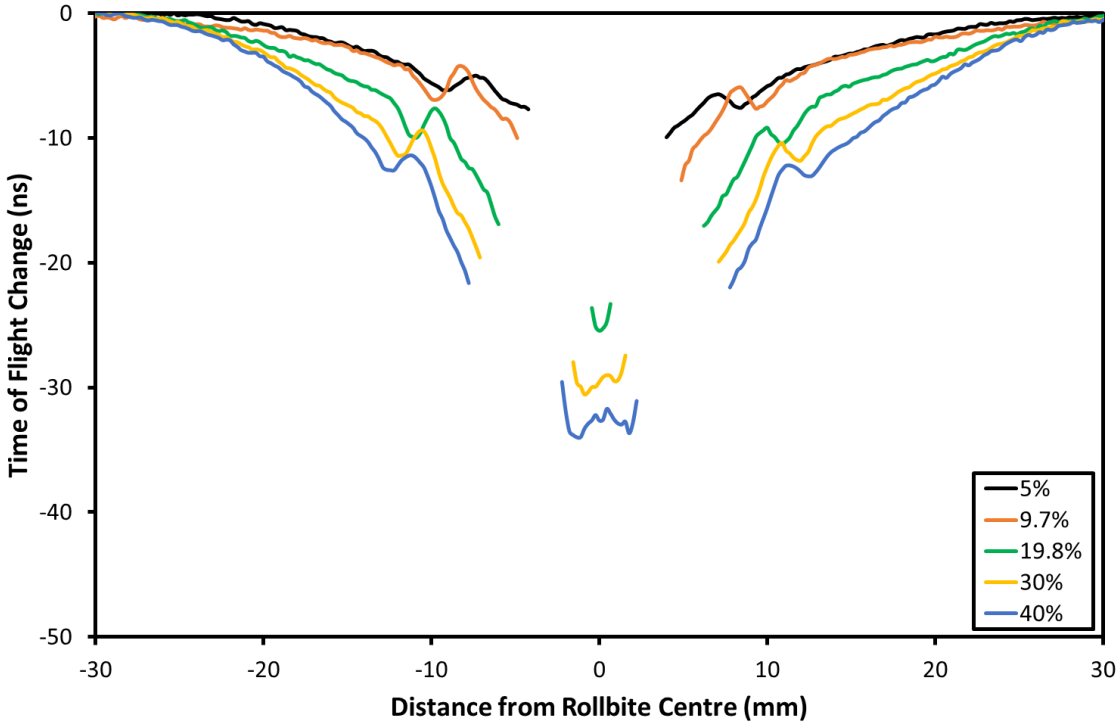

Figure 10.21: Change in Longitudinal Time of Flight across Roll Bite for various Strip Elongations, cropped to remove Interference Effects.

The surface deflection and roll stress calculated from the ToF are plotted in Figure 10.22 and Figure 10.23 respectively. The magnitude of the deflection for 30% strip elongation is similar to that seen in Test 6 for the same elongation and rolling speed (100 m/min). As before the stress plotted is an average over the path of the ultrasonic wave. Interestingly there does not appear to be a discontinuity in the stress between where the sensor plug is directly loaded (within ±20

mm of the roll bite centre) and where the plug is indirectly loaded via the surrounding material. This implies that the stress is being effectively transmitted across the roll-plug boundary with no slip.

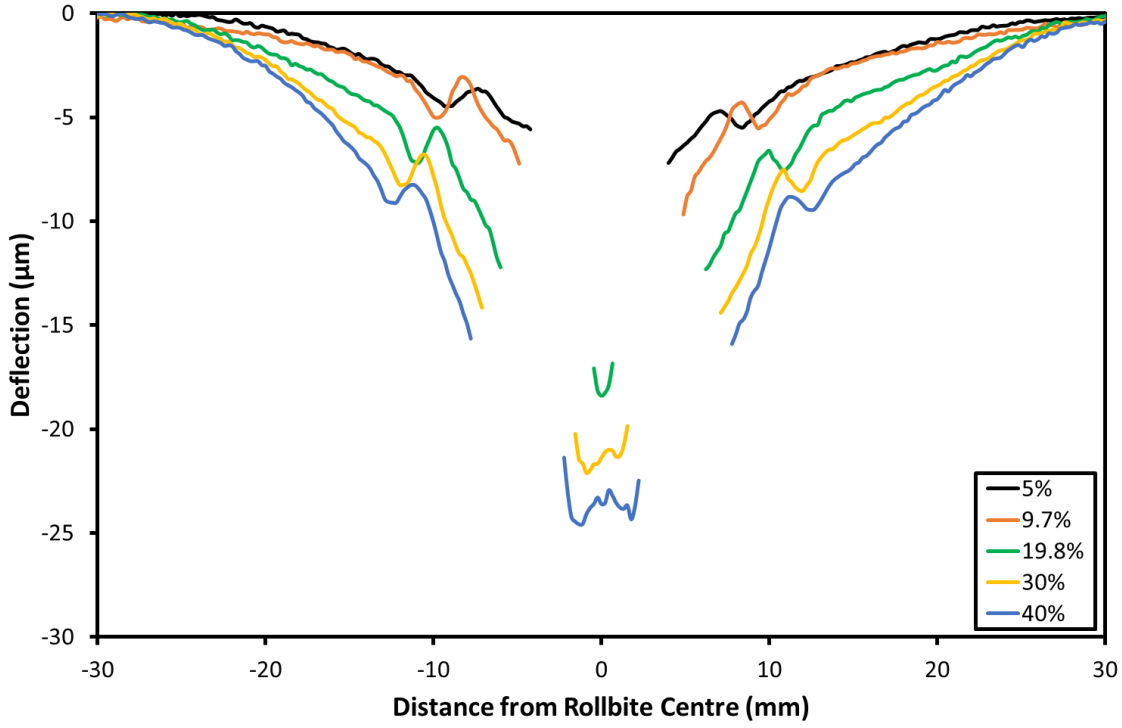

Figure 10.22: Deflection of Roll Surface measured using Longitudinal Sensor for various Strip Elongations.

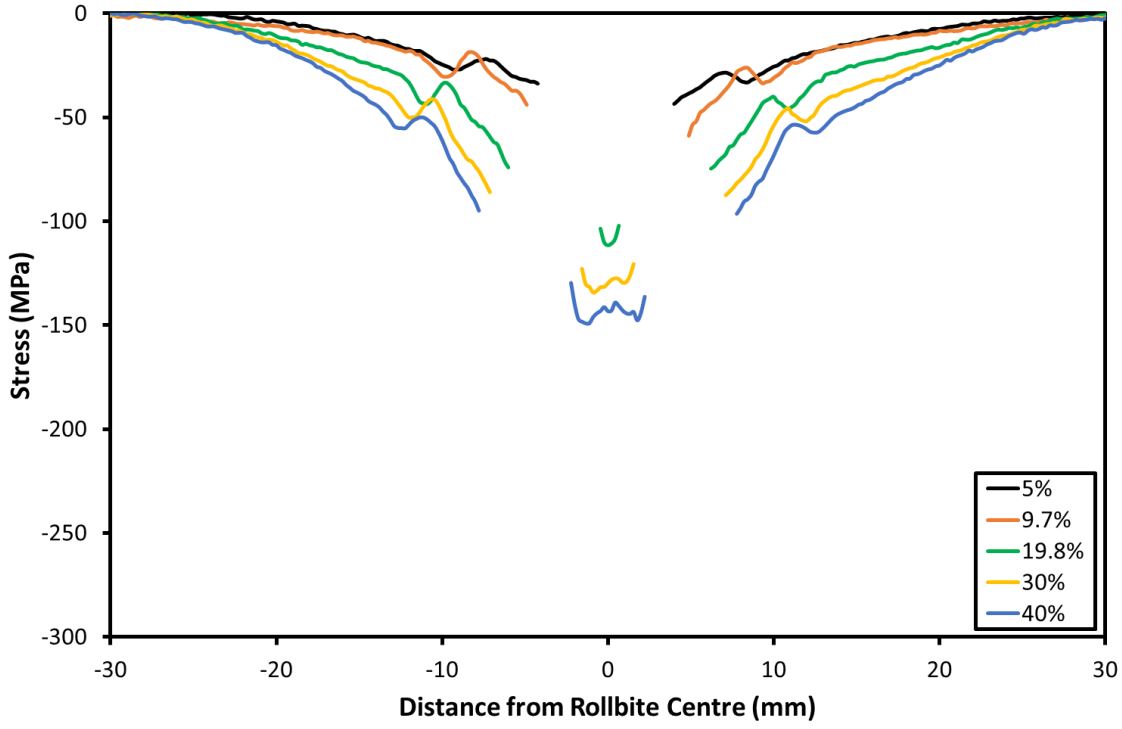

Figure 10.23: Average Radial Roll Stress measured using Longitudinal Sensor for various Strip Elongations.

10.5.2 Shear Sensor Results

The equivalent shear ToF results for the different strip elongations are given in their raw form in Figure 10.24 and cropped in Figure 10.25.

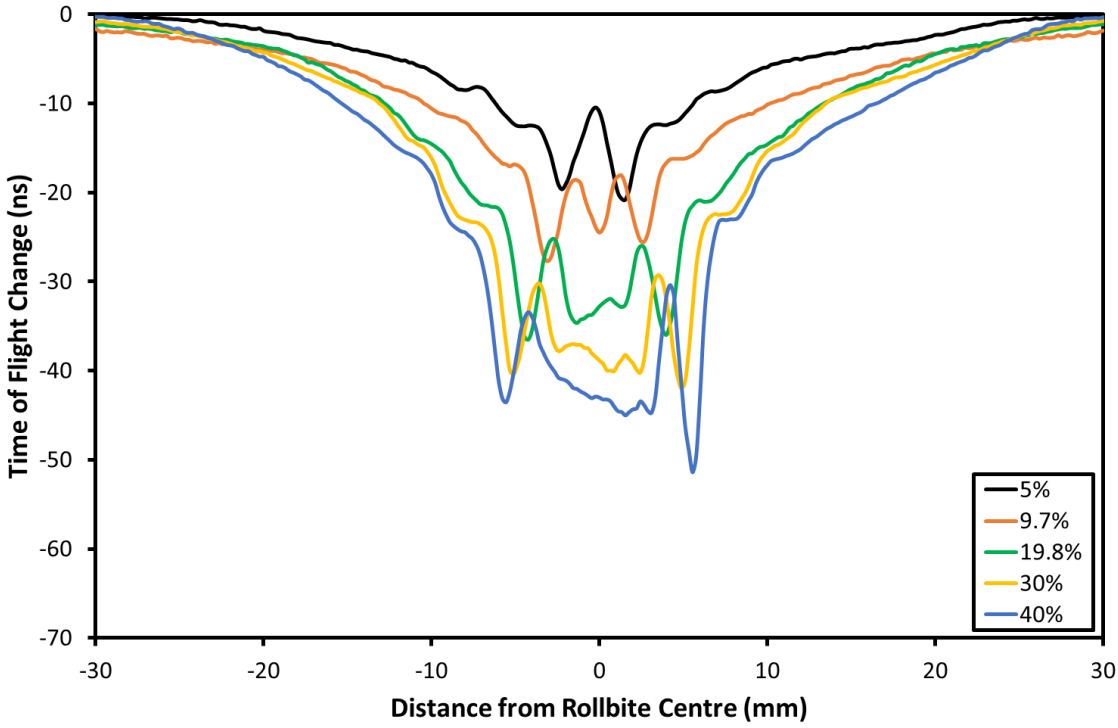

Figure 10.24: Change in Shear Time of Flight across Roll Bite for various Strip Elongations.

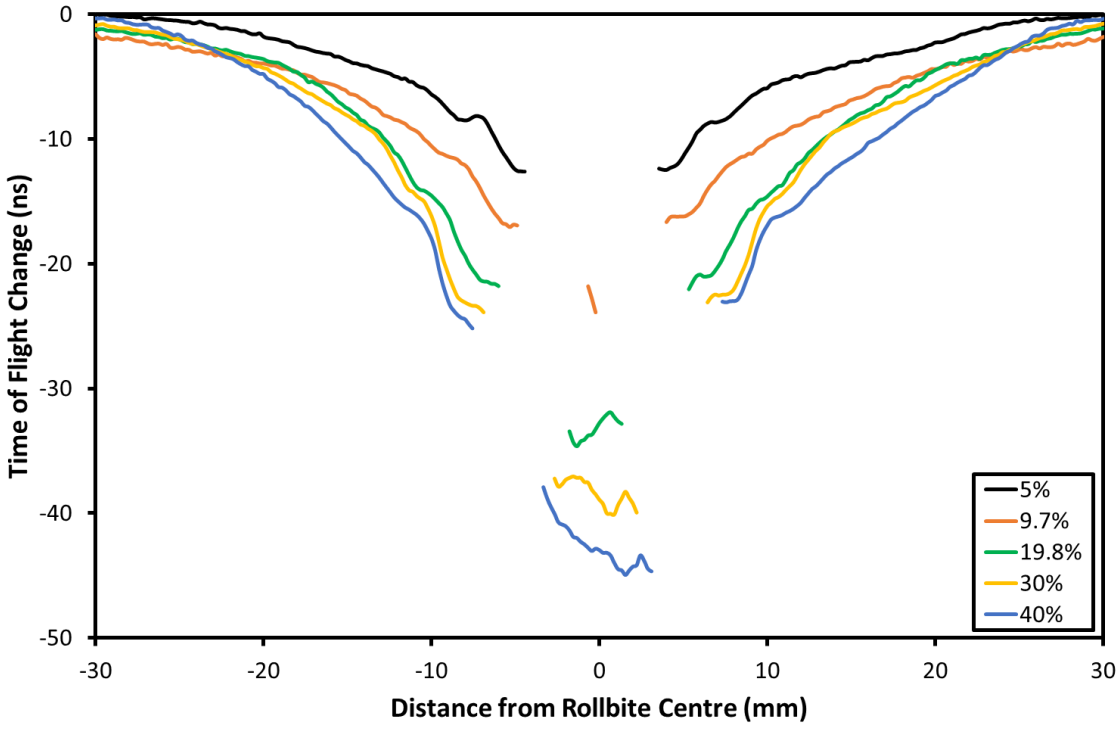

Figure 10.25: Change in Shear Time of Flight across Roll Bite for various Strip Elongations, cropped to remove Interference Effects.

Fewer data points are cropped from the shear results in comparison to the longitudinal results. This means that some data recorded from the centre of the roll bite for the 9.7% elongation case

is available in addition to the cases measured using the longitudinal sensor. The deflection and stress for this data are plotted in Figure 10.26 and Figure 10.27. These plots show a clear increase in the deflection and stress with increased strip elongation, as would be expected due to the increased rolling load. The shear wave measurements for both deflection and stress give much higher values than for the longitudinal waves.

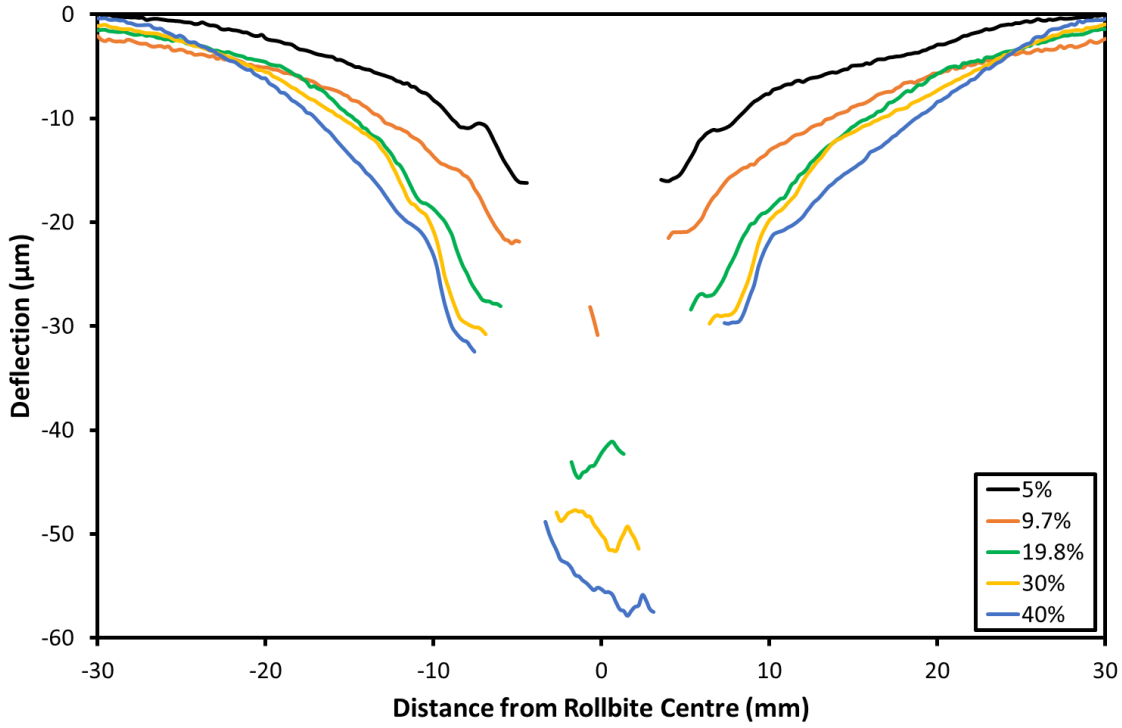

Figure 10.26: Deflection of Roll Surface measured using Shear Sensor for various Strip Elongations.

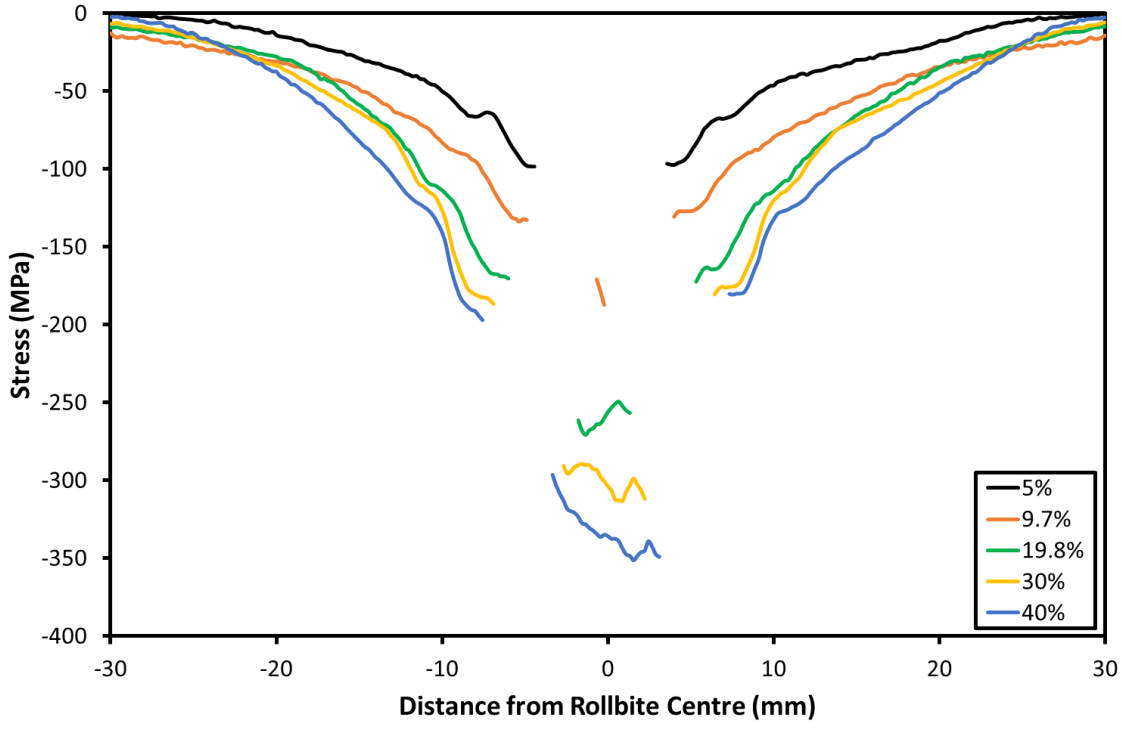

Figure 10.27: Average Radial Roll Stress measured using Shear Sensor for various Strip Elongations.

10.5.3 Model Results

As with the rolling speed tests, the results gained the rolling cases tested have been modelled using the stress model presented in §2.6 this time with parameters from Table 10.2. Again the friction coefficient was set to zero. The stresses obtained from the longitudinal and shear sensors have been overplotted with the respective modelled results and are given in Figure 10.28 and Figure 10.29.

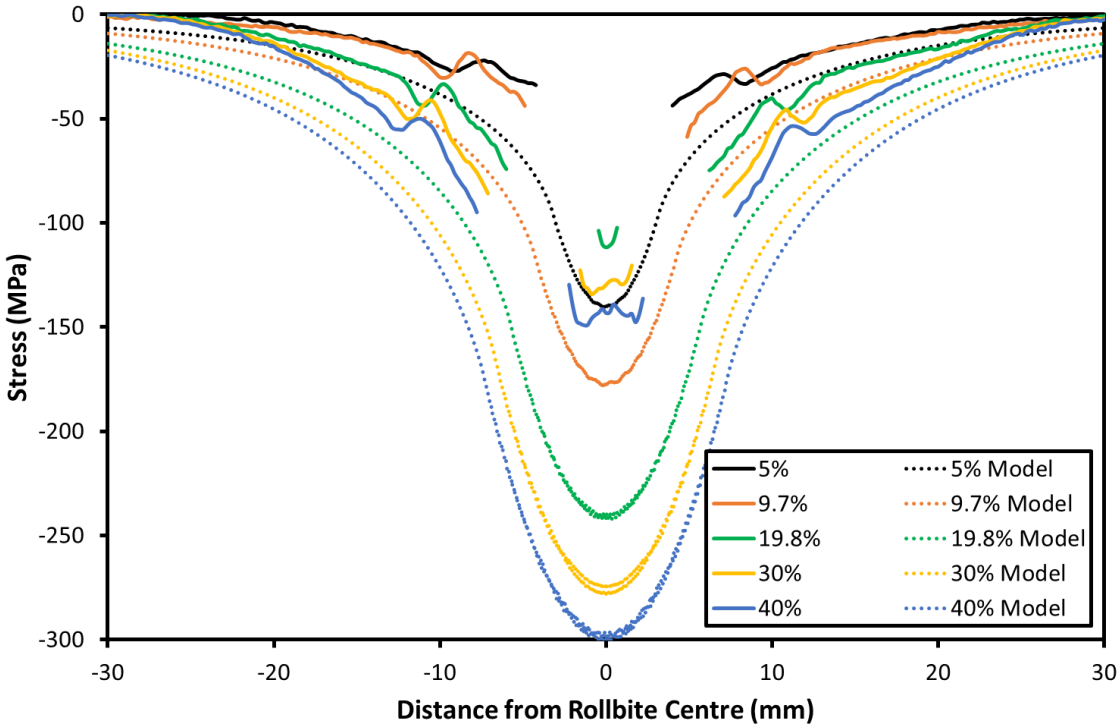

Figure 10.28: Model and Longitudinal Stress Profiles for various Strip Elongations.

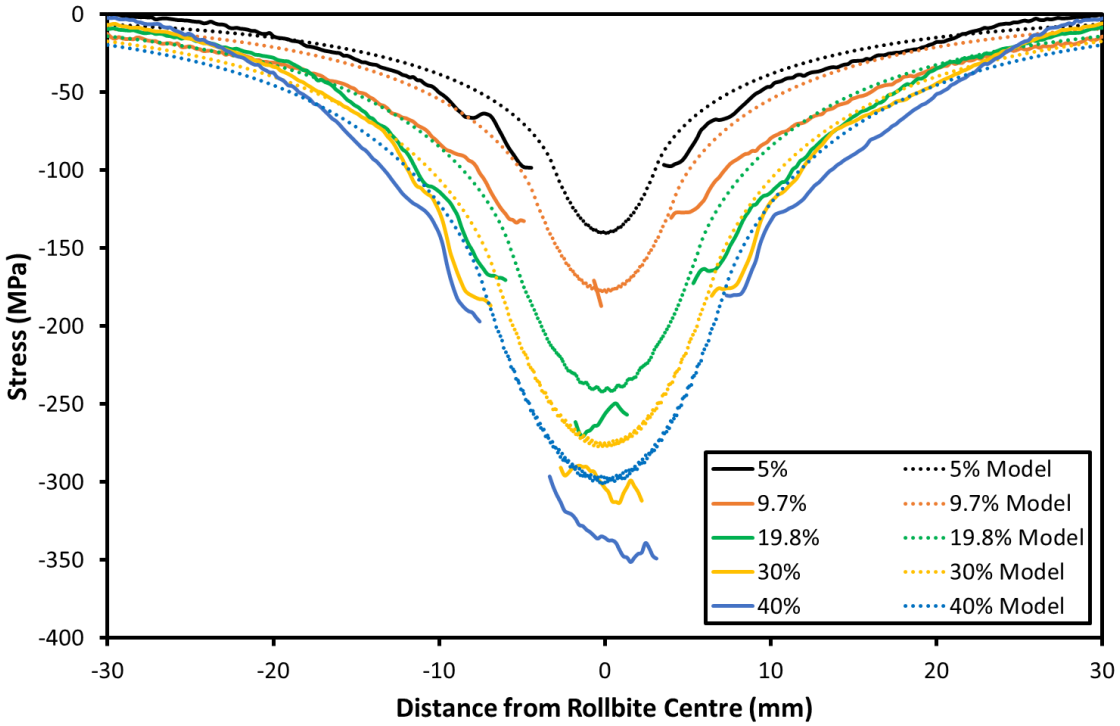

Figure 10.29: Model and Shear Stress Profiles for various Strip Elongations.

There is a similarity in the shape of the stress curves for each rolling case of both sensors. Again the magnitude of the experimental longitudinal results is less than the theoretical, while the shear results are of a similar scale. Both sets of data show that the stress curve maintains a consistent shape with increasing elongation with the only apparent difference being a scaling in the magnitude.

10.5.4 Results Comparison

In order to better compare the results obtained from the longitudinal and shear sensors, along with the output from the modelling, the values for deflection and stress at the centre of the roll bite for the various rolling cases have been extracted and are plotted in Figure 10.30 and Figure 10.31 respectively.

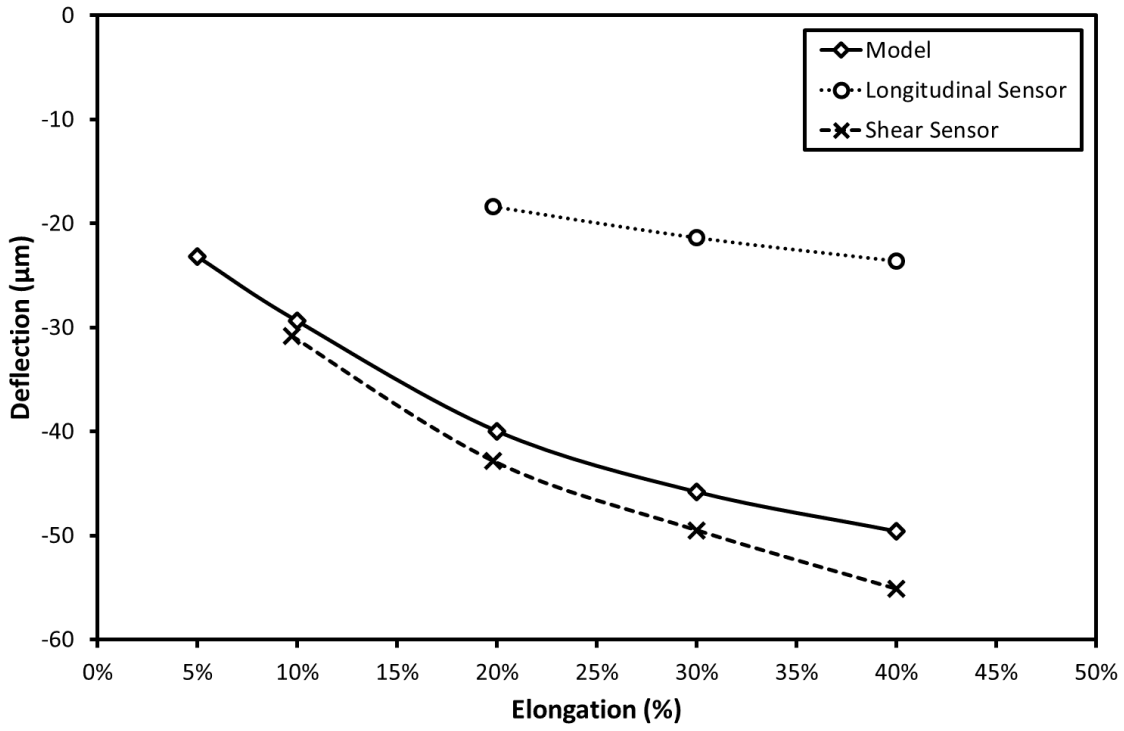

Figure 10.30: Longitudinal, Shear and Model Deflection at Centre of Roll Bite for various Strip Elongations.

These plots show the good agreement in the trend and magnitude between the shear and modelled results. Although less data is available for the longitudinal results, the data available shows a similar trend of increasing deflection and stress with increasing elongation albeit with some disagreement in the magnitude.

The relationship between deflection or stress and elongation is not linear for any of the approaches and a greater change is observed at smaller elongations in comparison to larger elongations. This is consistent with the relationship expected based upon a traditional contact mechanics modelling of a cylinder-on-cylinder, or cylinder-on-flat contact (the cylinder-on-flat contact being a special case of the cylinder-on-cylinder where the second cylinder is assumed to have an infinite radius).

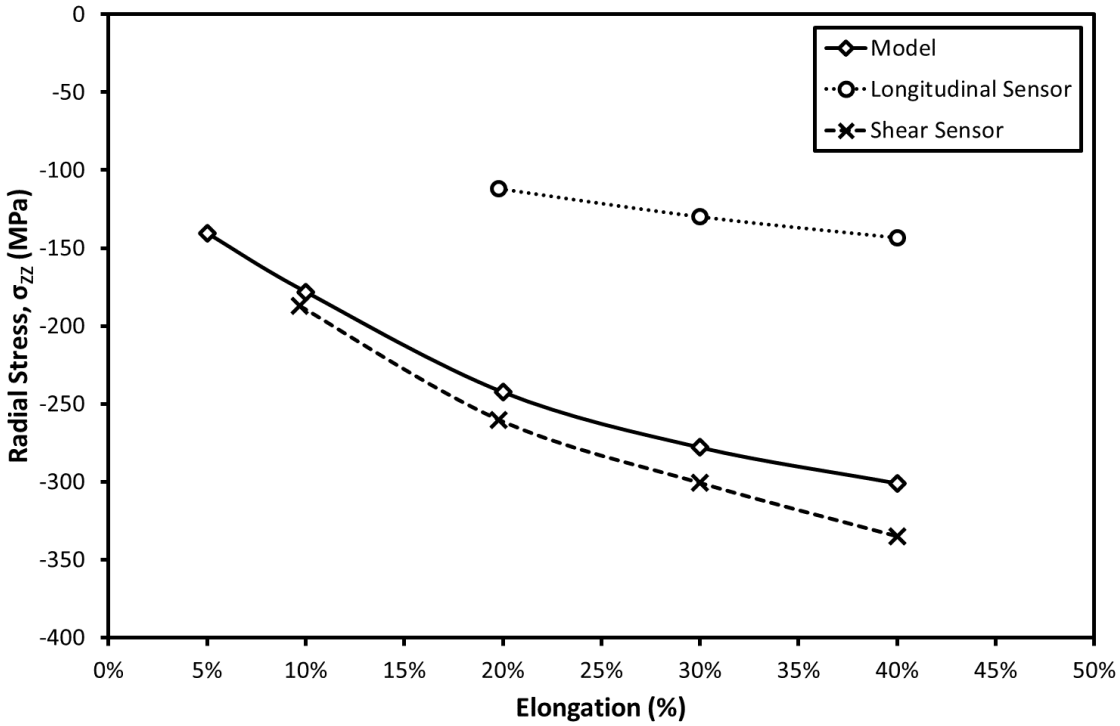

Figure 10.31: Longitudinal, Shear and Model Stress at Centre of Roll Bite for various Strip Elongations.

It is clear from Figure 10.30 that the deflection is not insignificant when considering the strip thickness (2.8 mm) and reduction. Assuming that the deflection is equal for the top and bottom work rolls then the total deflection will be double the value reported. The deflection compared to the draft is highest at lower elongations, with total deflection representing 21.6% of the draft for 10% elongation according to both the shear and modelled data, as shown in Figure 10.32.

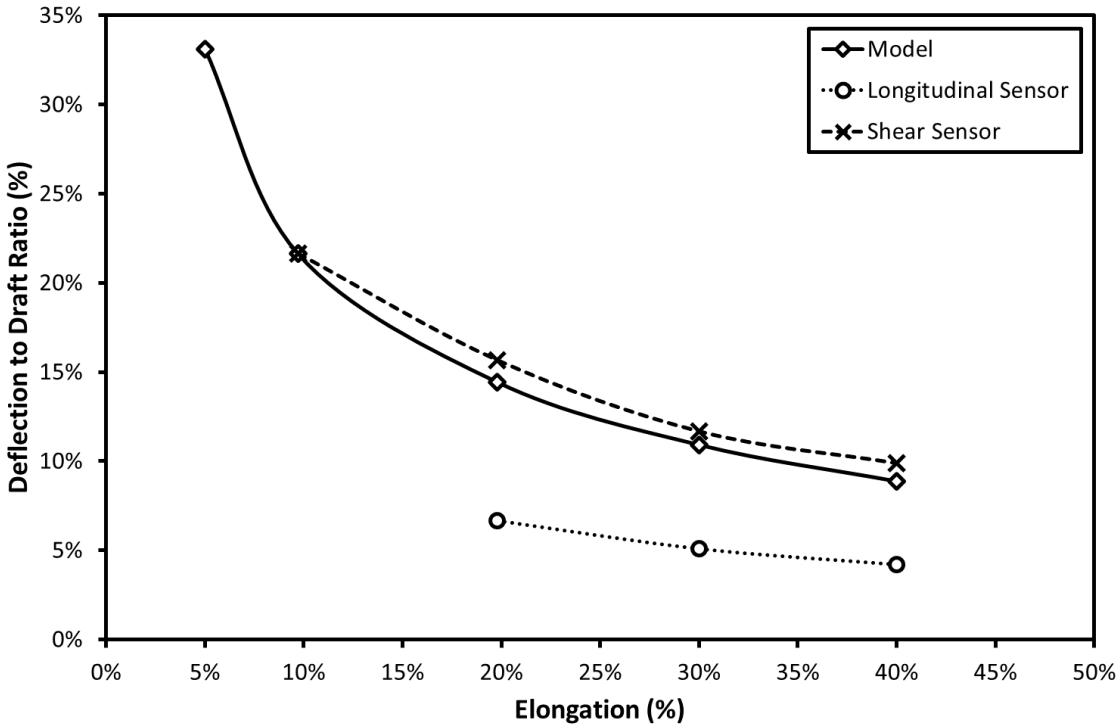

Figure 10.32: Ratio of Maximum Deflection of Rolls to Strip Draft for various Strip Elongations as calculated from Longitudinal Sensor, Shear Sensor and Model Data.

The size of the of deflection comparative to the draft is important as it represents a large potential source of error. The deflection stated here is at the centre of the roll bite. Due to the elastic recovery of the roll as it rotates away from the centre of the roll bite it does not necessarily translate directly into an error in the outgoing strip thickness. However, the centre of the roll bite is the region of plastic deformation, as shown in Figure 2.13. This could make accurately achieving the required rolled geometry difficult.

10.6 Comparison of Elongation and Rolling Speed

For the two test cases studied in detail above only the elongation and rolling speed were altered, all other test parameters were kept the same. By combining the results, it is possible to study the envelope over which these tests were taken and compare the tests where they overlap.

10.6.1 Model Results

Figure 10.33 and Figure 10.34 show the modelled deflection and stress from the centre of the roll bite for both Test 6 and 7. The data from Test 6 shows the increasing deflection and stress with rolling speed and Test 7 shows a clear increase with higher elongations. A test condition of particular interest is that at 30% elongation and 100 m/min as this point should be the same in both tests.

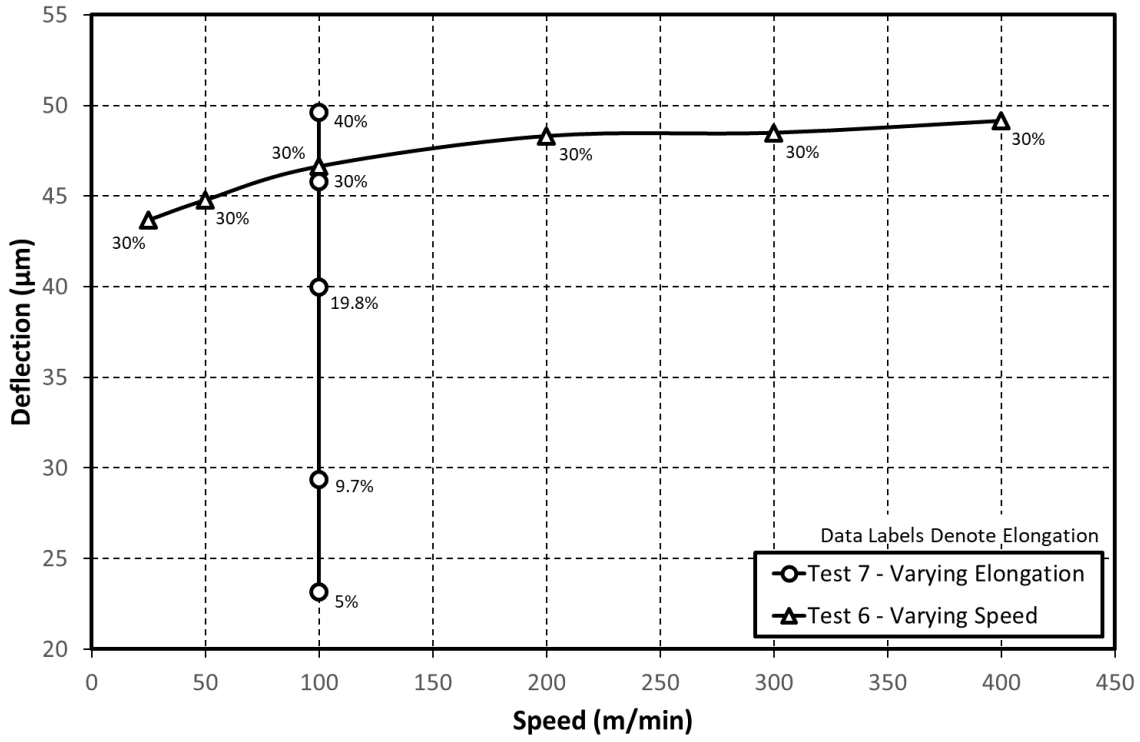

Figure 10.33: Deflection from Model for various Rolling Speeds and Strip Elongations.

These points show consistency with the result from Test 6 showing a marginally higher deflection and stress. This difference can be explained because the modelled results still rely upon a load set by and recorded from the mill control system, and contact width measurements taken ultrasonically. Both of these measurements will have an associated accuracy. It can be seen in Table 10.1 and Table 10.2 that the result from Test 7 had a slightly higher contact width and a slightly lower load. These differences are the cause of the differing outputs from the model for each test.

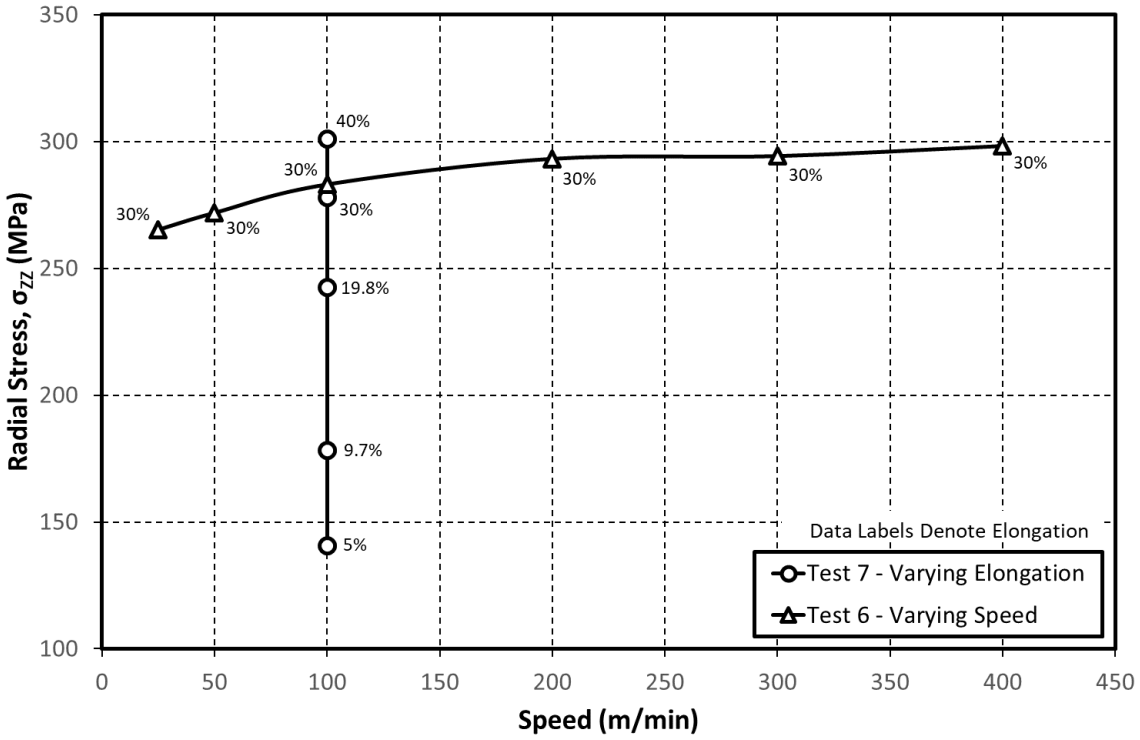

Figure 10.34: Stress from Model for various Rolling Speeds and Strip Elongations.

10.6.2 Longitudinal Sensor Results

The equivalent longitudinal results for Test 6 and Test 7 are given in Figure 10.35 and Figure 10.36. Unlike with the modelled data, these results do not compare, even for equivalent test conditions. The deflections and stresses reported in test 7 are significantly less than those in Test 6, for elongations both higher and lower than those recorded in Test 6.

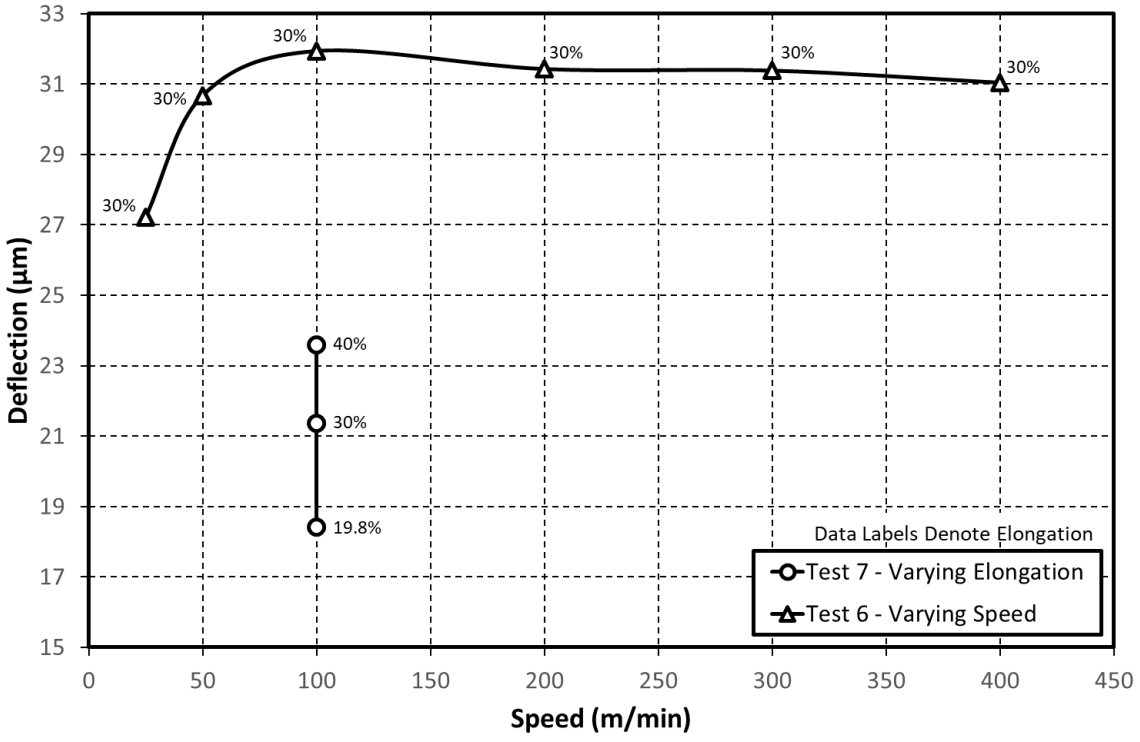

Figure 10.35: Deflection from Longitudinal Sensor for various Rolling Speeds and Strip Elongations.

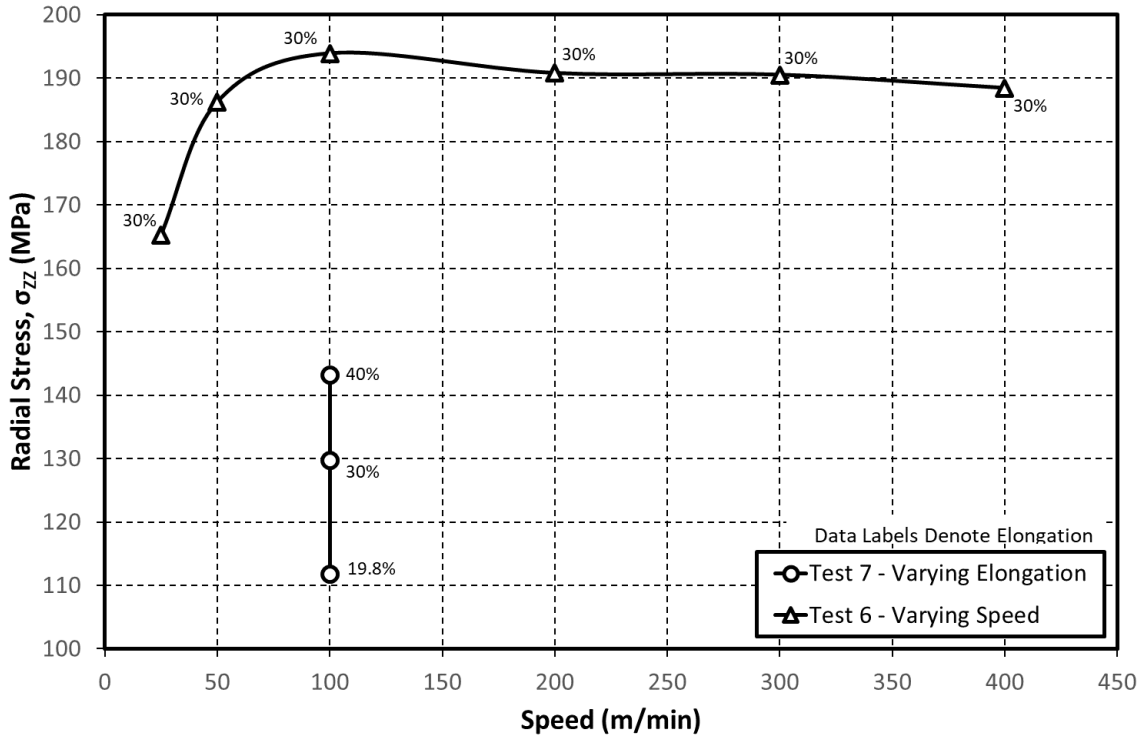

Figure 10.36: Stress from Longitudinal Sensor for various Rolling Speeds and Strip Elongations.

The disparity in the longitudinal sensor results between each test, combined with the difference when compared from the shear sensor and modelled results within each test, may imply that the longitudinal results are erroneous.

10.6.3 Shear Sensor Results

The deflection and radial stress results from the shear sensors are given in Figure 10.37 and Figure 10.38.

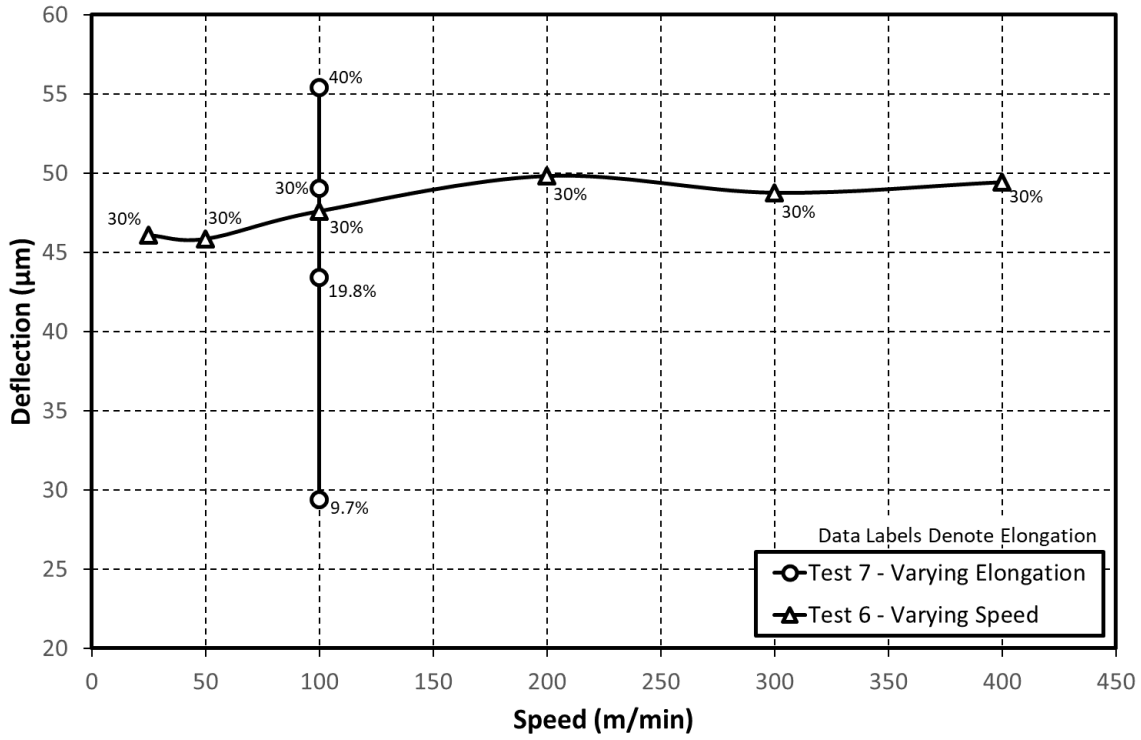

Figure 10.37: Deflection from Shear Sensor for various Rolling Speeds and Strip Elongations.

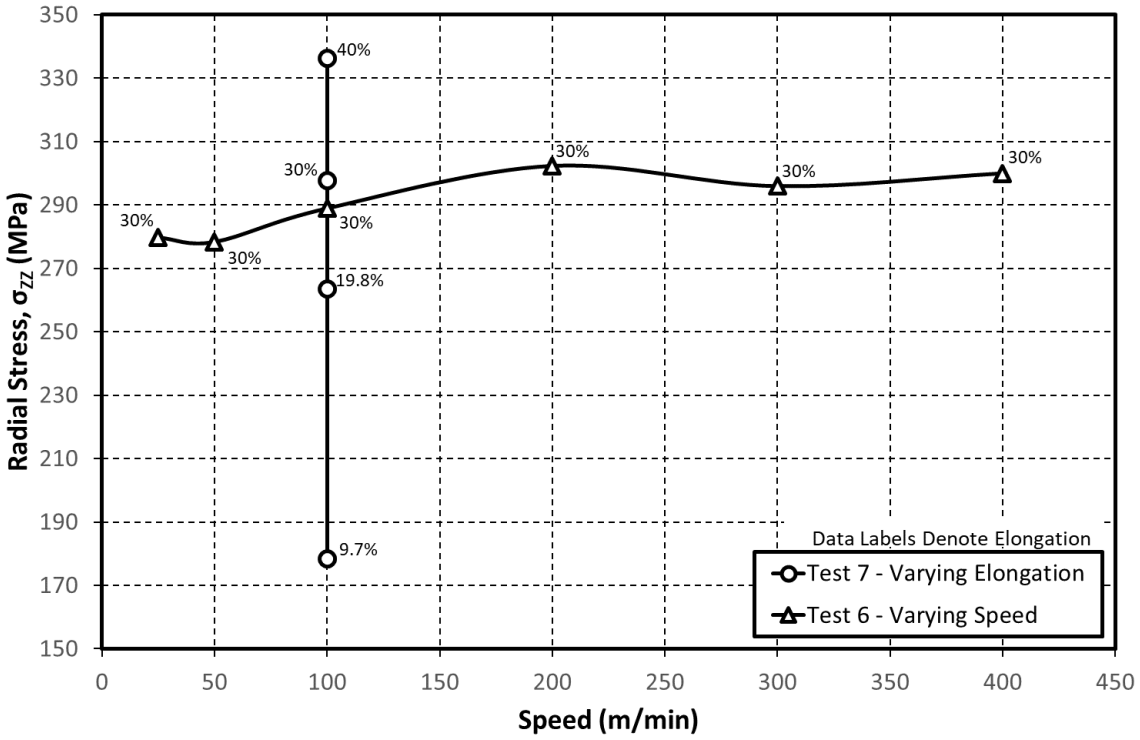

Figure 10.38: Radial Stress from Shear Sensor for various Rolling Speeds and Strip Elongations.

The data from the corresponding conditions (30% elongation, 100 m/min) for each test compare well, with Test 6 showing a slightly lower value for the deflection and stress in comparison to Test 7.

Test 6 shows a slight increase in the deflection and stress with rolling speed between 50 m/min and 200 m/min, however it is not as clear or consistent across the full range as with the modelled results. The change in deflection and stress due to elongation is shown clearly in Test 7.

10.7 Conclusions

In this chapter it has been shown that ultrasound can be used to measure both roll deflection and radial stress in-situ across the roll bite. While the deflection measured ultrasonically is the actual roll surface displacement, the radial stress measured represents the average radial stress over the ultrasonic path. Measurements have been processed and presented for a range of rolling speeds and strip elongations.

In order to calculate the deflection and stress it is first necessary to measure the Time-of-Flight (ToF) of an ultrasonic wave through the material. Several methods to extract the ToF of the returning pulse were assessed. The method chosen utilises a threshold of the analytic envelope.

Data was successfully recorded with both shear and longitudinal transducers. The stress and deflection were also modelled using the equations given in §2.6 along with the rolling load reported by the mill control system and the roll bite width measured ultrasonically. The shear sensor results show a good correlation with the modelled values while the longitudinal data showed similar trends but with changes of a much lower magnitude. The shear sensor results also showed good correlation for the same rolling parameters in different tests, while the

longitudinal results showed little consistency. It is therefore concluded that the longitudinal results are likely to be erroneous.

The measured deflection and stress profile reaches far outside of the roll bite contact. However, there is no apparent discontinuity in this measurement at the material interface between the sensor plug and supporting roll, implying this instrumentation technique is effectively supporting the rolling stress.

As with the film thickness measurements in the previous chapter some data is lost in interference regions at the entry and exit to the roll bite. The amount of data lost due to interference is reduced for the shear sensor results as the slower speed of sound of the shear wave allows for greater time separation between the primary reflection and subsequent interfering reflections. This means that data was recorded over a wider range of rolling conditions for the shear sensor than the longitudinal sensor.

An increase in both deflection and stress was observed with increasing strip elongation. A slight increase was also observed with increasing rolling speed; however, this was less marked across the range of speeds tested. The surface deflection is also shown to be significant compared to the draft and reduced strip thickness.

11 Numerical Modelling

In order to interpret the experimental results captured in the preceding chapters it is necessary to have an understanding of how the ultrasonic wave interacts with the system under measurement. While it is not possible to view the wave directly, it is possible to simulate the wave by computational modelling. Additionally, as there is no equivalent independent measurement of many of the variables measured during testing, this modelling can also help to validate the results. This chapter looks at a number of computer simulations which were run for these purposes.

11.1 Wave Propagation - PZFlex

In order to better understand the results gained ultrasonically it is important to understand the wave propagation within the roll. Some modelling was completed in §4.7 using custom written software to look into the effect of stress in the plug on the propagation of the ultrasonic wave. This modelling was simplified and used a ray tracing approach which accounted for the refraction of the wave due to stress induced change in speed of sound. This simulation did not account for any effects due to the geometry and internal reflections within the piezoceramic element, beam spread and the effect of plug contact with the strip.

11.1.1 Modelling Approach

To look into these effects in more detail a set of simulations were run using PZFlex, a finite element analysis package developed by Weidlinger Associates Inc. PZFlex is a time domain solver that specializes in large wave propagation problems (Abboud, et al., 1998). PZFlex uses an explicit method to model the wave propagation. This sets a time step to decouple the mesh nodes from each another. This approach is used as it is a more efficient way to model the ultrasonic pressure wave propagation than an implicit approach which models the effect of each node on every other node. PZFlex does also make use of the more computationally intense implicit approach to model piezoelectric materials. This is because the electrical wave propagation in a piezoelectric material is much faster than the mechanical ultrasonic wave and it travels effectively instantaneously between nodes (Reynolds, Krause, Carcione, Mould, & Vaughan, 2004). It was initially developed for medical ultrasound imaging devices but has now also been adopted for use in a wide range of engineering applications.

The simulation was run using the geometry shown in Figure 11.1. To understand the effect of the plug passing over the roll bite contact the mode was setup to allow three separate cases to be simulated. The first was the plug on its own, with nothing contacting the sensing surface. The second had a block in contact with the rolling surface covering half the roll bite contact width. The final case had an additional block covering the other half of the rolling face and effectively simulating strip being present across the entire contact width. The far side of the strip has been made an absorbing boundary such that nothing is reflected from it. The purpose of this is to ensure that only the influence of the upper interface between the roll and strip is observed. It was not possible to simulate the effects of stress in this model and so all cases presented here are unstressed and do not emulate roll or strip deformation. However, as the purpose of the model is to observe the wave propagation pattern, and the stress effects on this are expected to be slight, the model should approximate well.

The simulation was 2D and it should be noted that the model does not include any lubricant, and contact between the plug and blocks is assumed to be perfect. The sensor was modelled as a 1.4 mm x 0.2 mm piezoceramic (PZT5A), polarised as a longitudinal sensor and excited with a 7.5MHz pulse. The mesh size and computational time of the model are dependent upon the wavelength as defined by the frequency of the waves being simulated and the speed of sound. Higher frequencies require finer meshes and more processing time. For this reason, an excitation frequency at the lower end of the sensor bandwidth used during testing was selected to reduce the computational load while ensuring the results are still representative. The mesh was made such that there were 20 elements per wavelength for the slowest speed of sound, in this model the element size was 0.4mm. The modelling was completed before the actual plug material used had been selected. The plug and contacting blocks were modelled using a predefined material from the PZFlex library (iron) which had values for longitudinal and shear speed of sound of 5900 m/s and 3200 m/s respectively and a density of 7900 kg/m^3. These properties turned out to be close to the properties to the values measured for the actual materials.

Several outputs were recorded from the simulation. The shape of the wave propagation was captured by exporting 2D intensity plots of the pressure for each step as the model was run. The summation of the pressure at a cross sectional plane halfway down the plug, the location of which is shown in Figure 11.1, was also recorded. PZFlex is capable of modelling the electro-mechanical behaviour of materials, such as piezoceramics. It was also therefore possible to extract the voltage across the piezoceramic element; this is the equivalent of the measurement taken by the ultrasonic DAq in the real-world experiments.

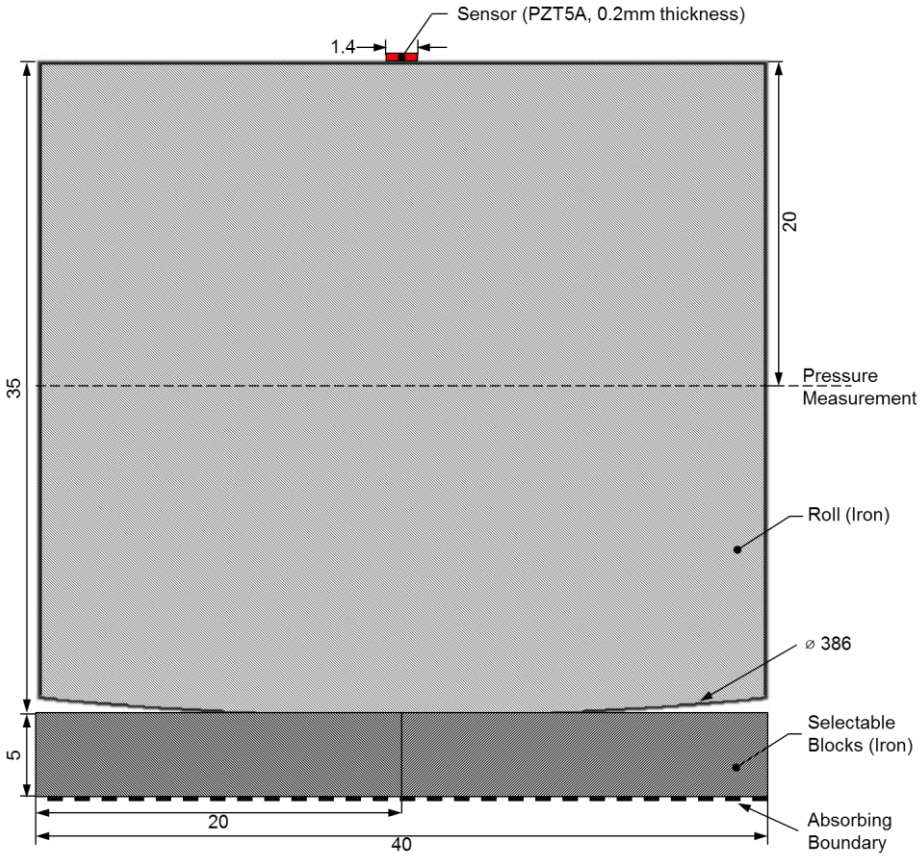

Figure 11.1: Wave Propagation Model.

A screenshot showing the model part way through execution for the case with no strip in contact is given in Figure 11.2. The 2D intensity plot of the wave-front can be seen on the left of the figure. The graph on the top right shows the pressure measured across the pressure measurement plane, in this image the graph shows all zero pressure as the wave has not yet reached the measurement plane. The graph on the bottom right shows the voltage across the piezoceramic element. This shows only the excitation pulse as no reflections have yet returned to the piezoceramic sensor.

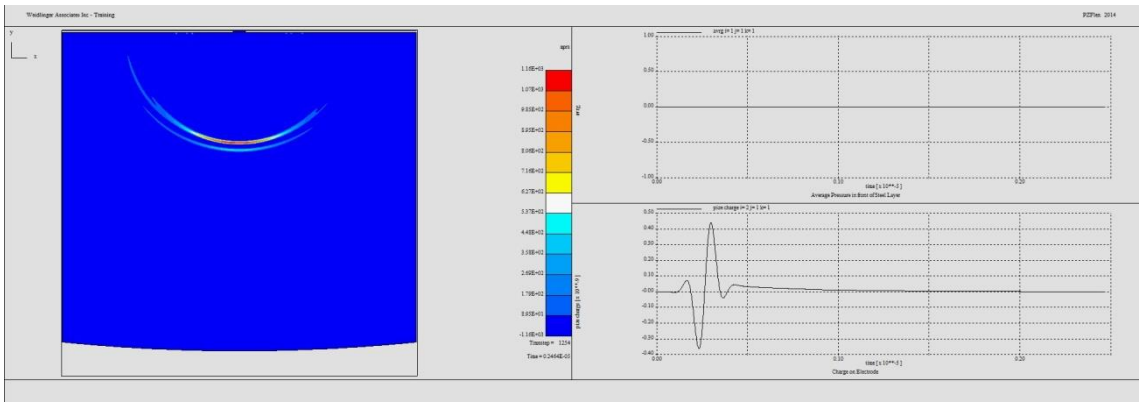

Figure 11.2: Model Running in PZFlex.

11.1.2 Ultrasonic Response

The time domain voltage response for no strip contact (air interface) from the simulation is compared to an equivalent experimental response in Figure 11.3. The measured response has been reduced by 66 dB to scale it to the simulated results. The test data was captured with a larger amplitude on purpose. This was to ensure the full range of the digitiser was utilised so that returned signal was captured with a good resolution. The larger amplitude was achieved by using a larger excitation pulse amplitude and amplification of the returned signal prior to digitiser.

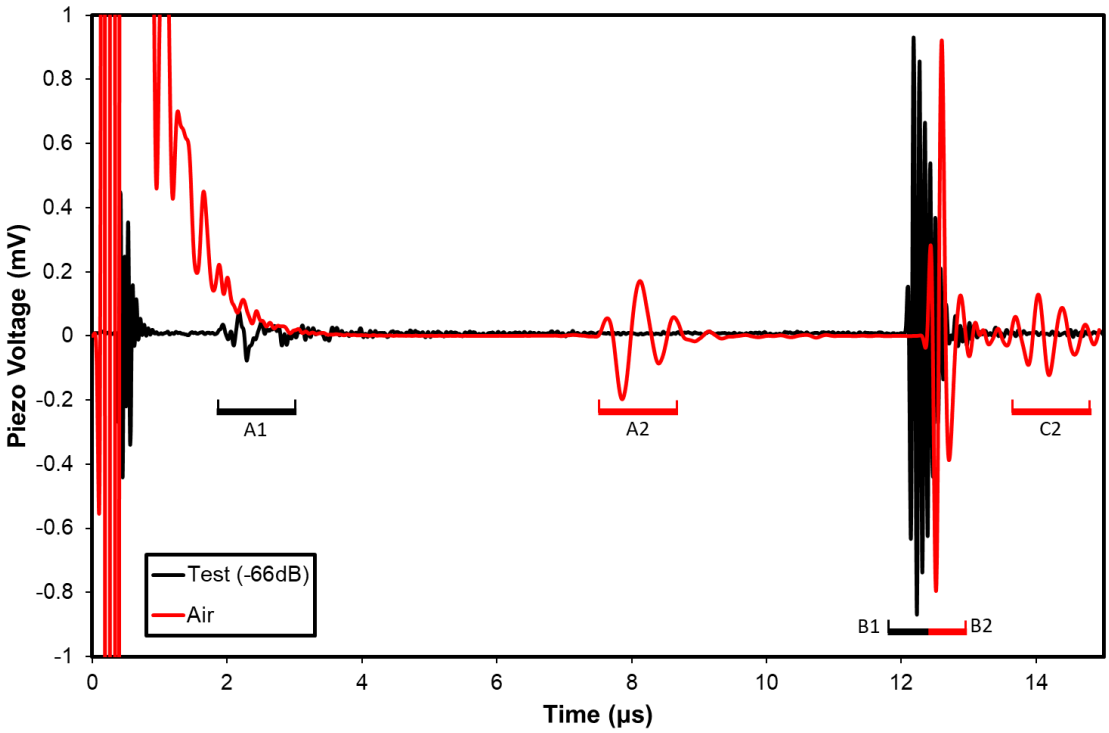

Figure 11.3: Simulated and Measured Time Domain Voltage Responses.

The two responses show some similarity. The main pulses (B1 and B2) are the reflections from the plug end surface. These are the pulses from which film thickness, stress and deflection measurements are taken. There is a small difference in the Time-of-Flight between these reflections. This is accounted for by the difference in the speed of sound used in the simulation compared to the actual value for the plug material. There will also be some error in the finite element time integration. The slight difference in the pulse frequencies caused by the different excitation pulses can be seen in the different wavelengths.

A number of additional pulses can be seen (A1, A2 and C2). It is possible that these are surface (Rayleigh) waves. The speed of a Rayleigh wave can be approximated from the shear wave velocity in a material using the relationship given in Equation 11.1 (Achenbach, 1984).

$$c_R = \frac{0.862 + 1.14\upsilon}{1 + \upsilon} c_S \qquad 11.1$$

Where c_R is the speed of the Rayleigh wave, υ is the Poisson's ratio and c_S is the shear wave speed. Taking the values for the plug material calculated in §8.2 (c_S is 3247.72 m/s and υ is 0.292) yields a Rayleigh wave speed of 3003.59 m/s. For a 20 mm surface (40mm path length) this translates to a Time-of-Flight for a returning wave of 13.32 µs. This matches well with reflection C2. The sensor arrangement in the actual testing differed slightly from that modelled. The sensors were inset into the plug, and the back face of the sensors damped with an epoxy backing. Also the shoulder of the plug was loaded against the supporting face within the roll. The backing epoxy and contact with the supporting face will have suppressed any surface waves on the back face of the plug, and for these reasons the surface wave seen in the simulations is not recorded in the experimental data.

The frequency spectra for each of reflections A2, B2 and C2 for the three simulated cases are given in Figure 11.4, Figure 11.5 and Figure 11.6.

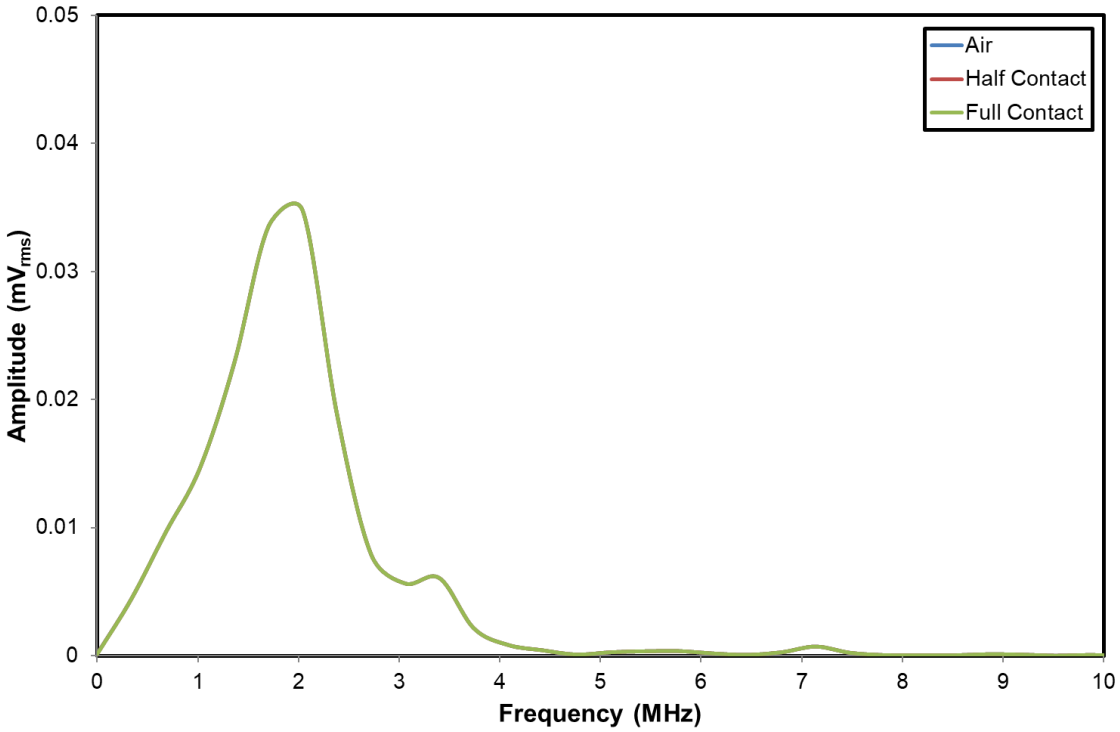

Figure 11.4: Frequency Spectra of reflection A2 from PZFlex model for three Simulated Cases. All three cases overlap perfectly.

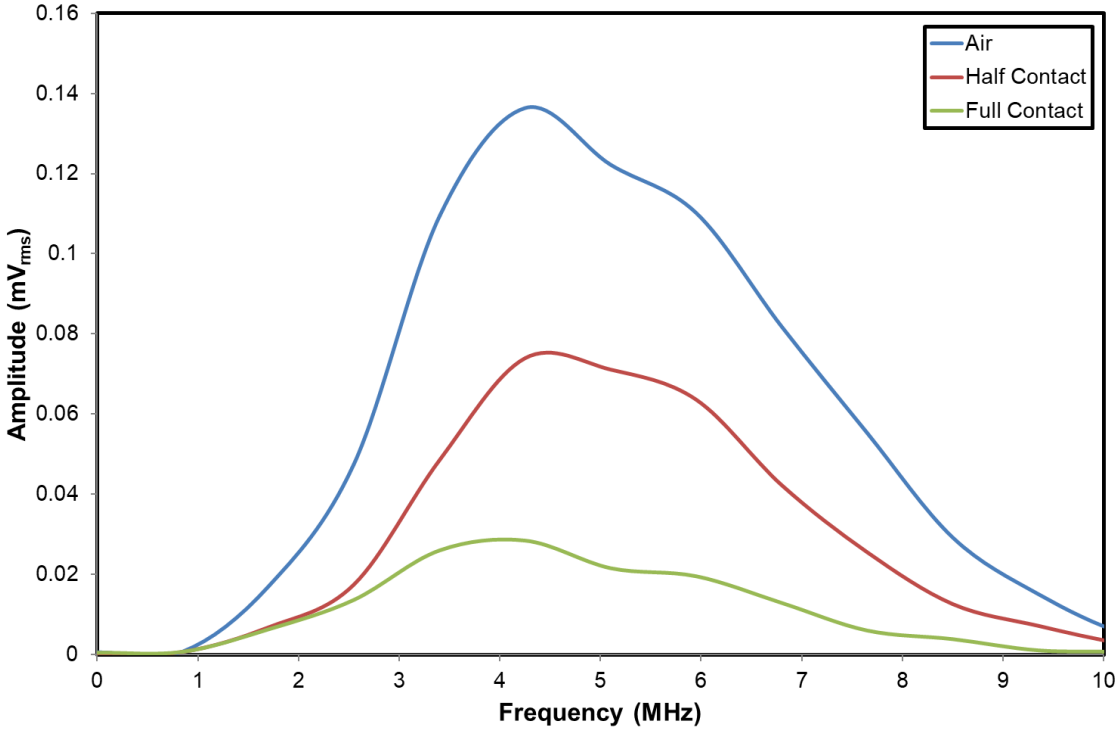

Figure 11.5: Frequency Spectra of reflection B2 from PZFlex model for three Simulated Cases.

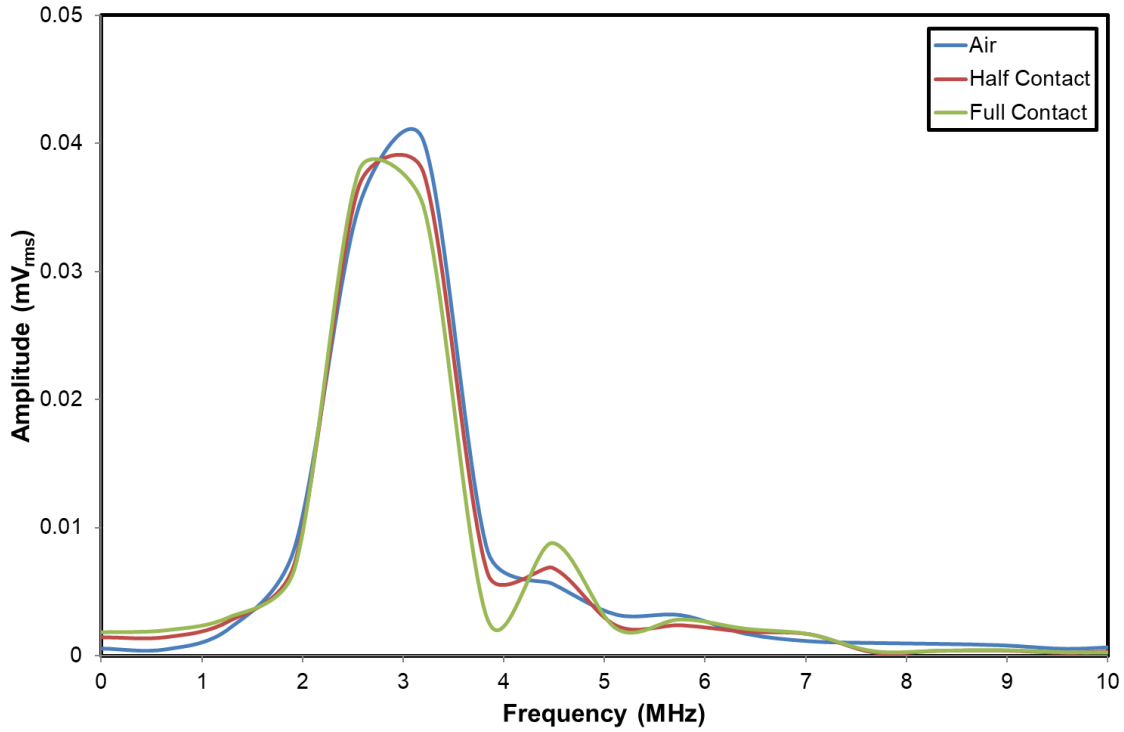

Figure 11.6: Frequency Spectra of reflection C2 from PZFlex model for three Simulated Cases.

The relatively little change between cases for reflections A2 and C2 imply that these do not originate from the far face of the plug (the upper face of the strip). Reflection B2 drops in amplitude as the contact size increases, implying that this reflection does emanate from the rolling face of the plug.

The time-domain voltage responses for the various interface contact cases are given in Figure 11.7. These clearly show that the only change occurs at reflection B2.

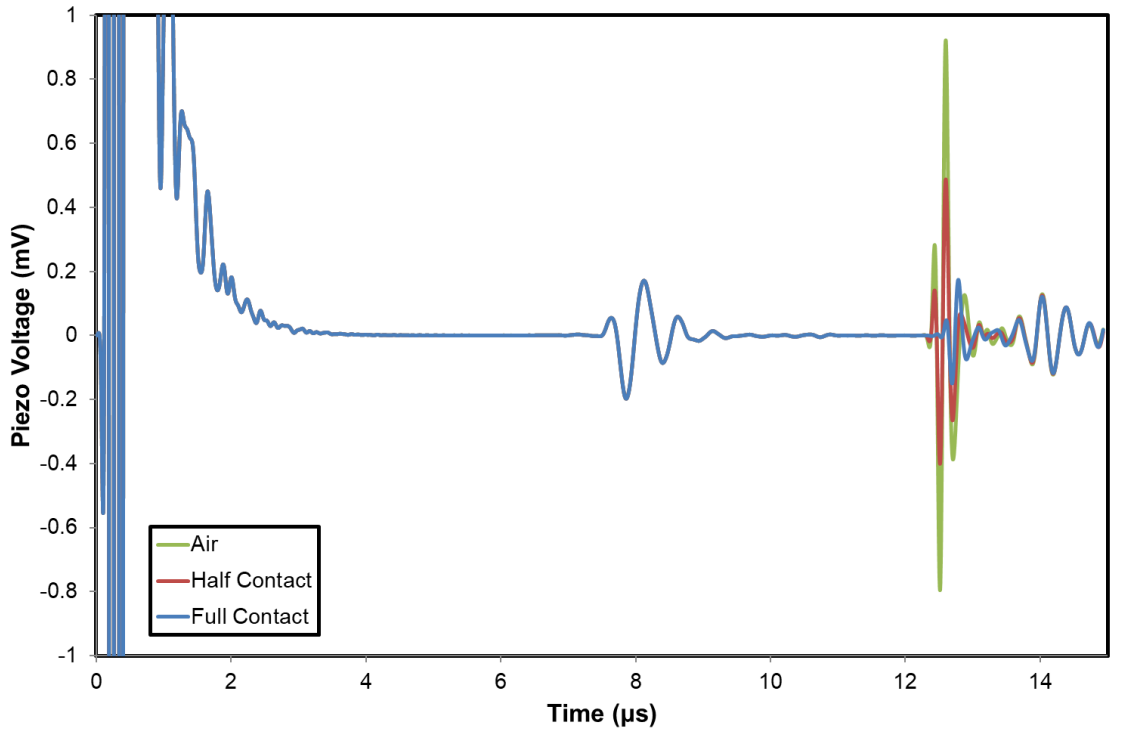

Figure 11.7: Voltage Response from PZFlex model for three Simulated Cases.

A closer view of this reflection for the 3 interface conditions is given in Figure 11.8.

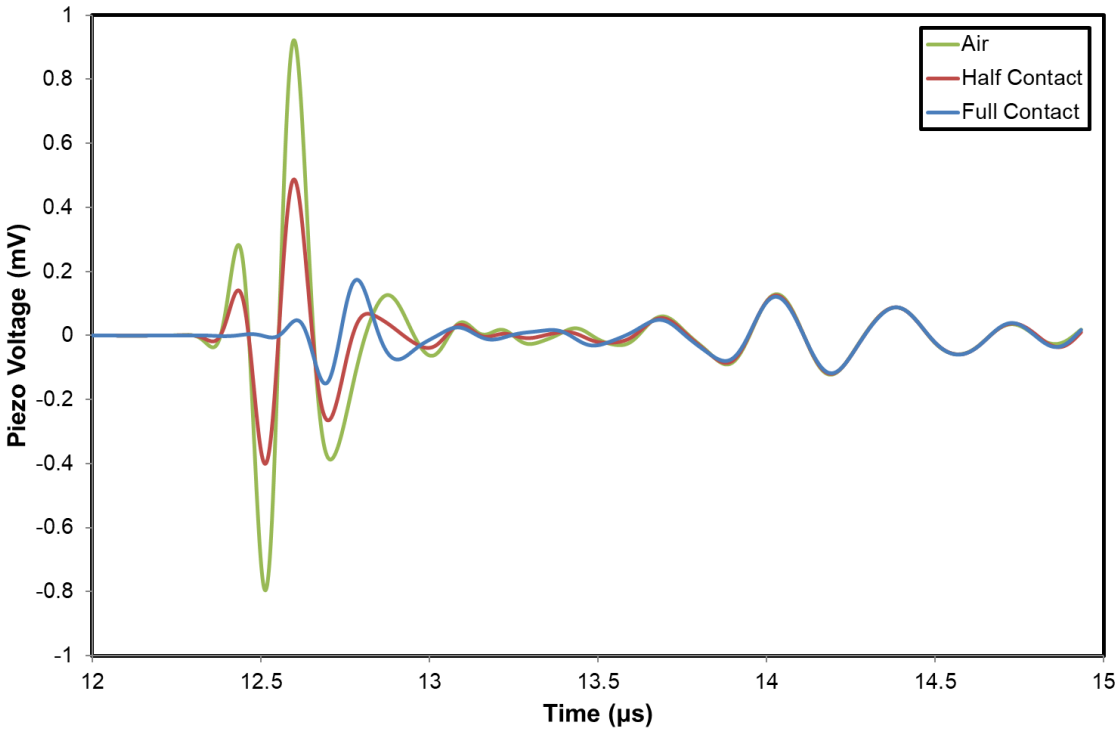

Figure 11.8: Voltage Response of First Reflections from PZFlex model for three Contact Cases.

The plot shows how the signal amplitude decreases as expected with greater contact at the interface, due to the higher proportion of the signal being transmitted into the contacting parts. Interestingly it also shows an apparent phase shift in the reflection only in the 'full contact' case.

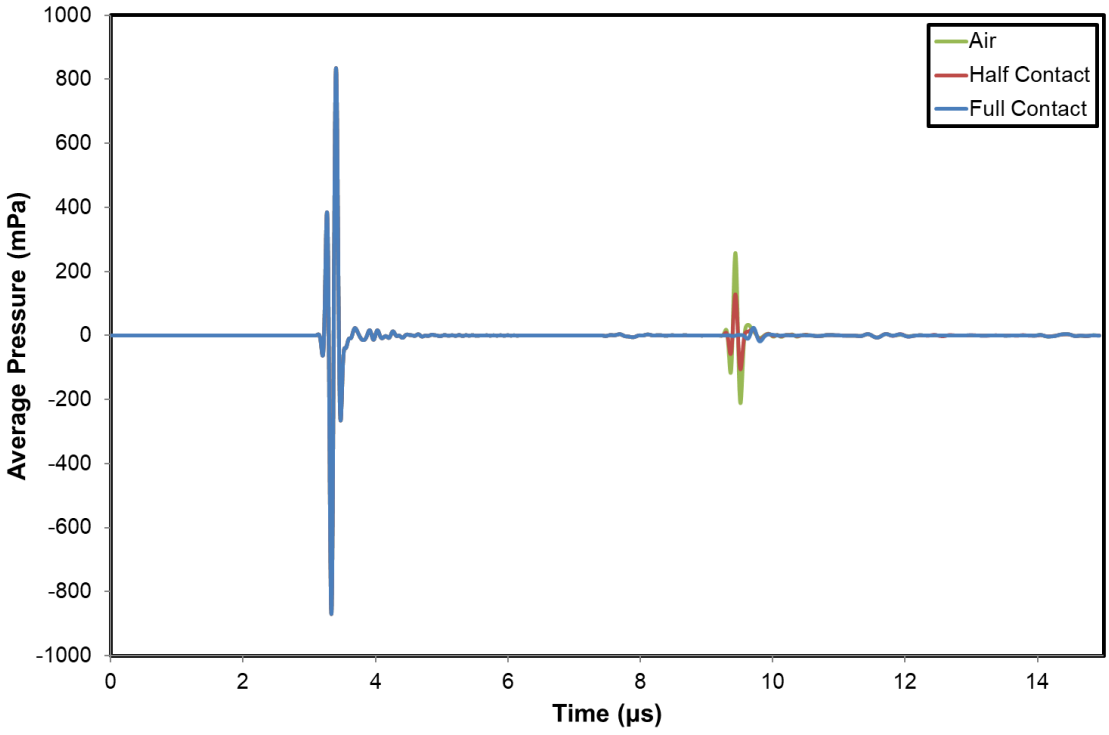

Figure 11.9: Mean Pressure from PZFlex model for three Simulated Cases.

Figure 11.7 and Figure 11.8 show the voltage responses recorded at the piezo, and these will therefore include any effects due to the response of the piezo, as well as surface waves. To help separate out the reflection just from the interface, the effect the mean pressure measured across the centre of the plug (location shown in Figure 11.1) for the three simulations is given in Figure 11.9. The first set of pulses in this figure are the incident wave, while the second set are the reflection from the interface. A zoomed view of the reflections is given in Figure 11.10.

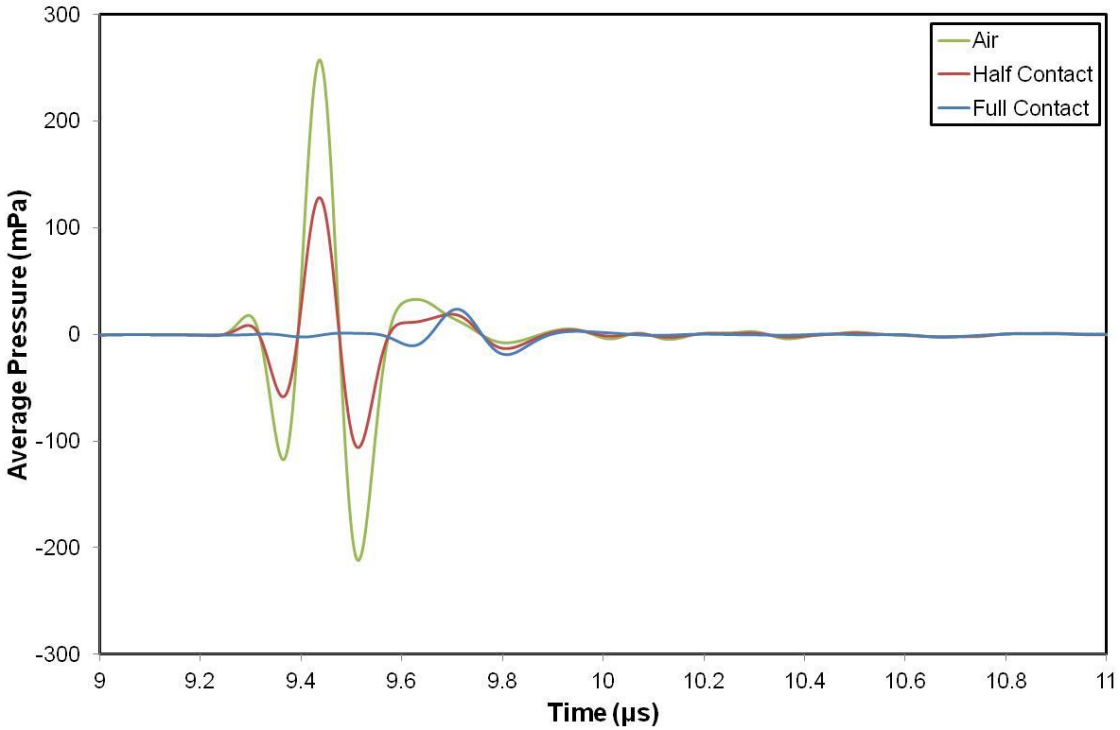

Figure 11.10: Mean Pressure of First Reflections from PZFlex model for three Simulated Cases.

Immediately it is clear that the pulses suspected to be from surface waves are no longer present. However the effect of the interface on the reflected waves is the same as observed in Figure 11.8, with a decrease in amplitude with increasing interface contact, and a phase shift seen in the 'full contact' case. The phase shift is even more pronounced for these measurements than the sensor voltage measurements. This may be because the pressure is being measured across the entire width of the plug and not just over the sensor area. As the wave travels it will spread, this will result in the parts of the ultrasonic beam taking an angled route across the plug, these will therefore have an increased ToF. This increase in ToF will explain the increased phase shift seen. The beam spread is of interest due to it's effect on the ultrasonics measurements taken, as described in previous chapters. For this reason it has been studied in greater detail in the following section.

11.1.3 Beam Spread

To be able to view the wave propagation pattern multiple 2D pressure intensity plots at 0.9 µs intervals were overlaid to show the progression of these wave-fronts. An example is shown in Figure 11.11.

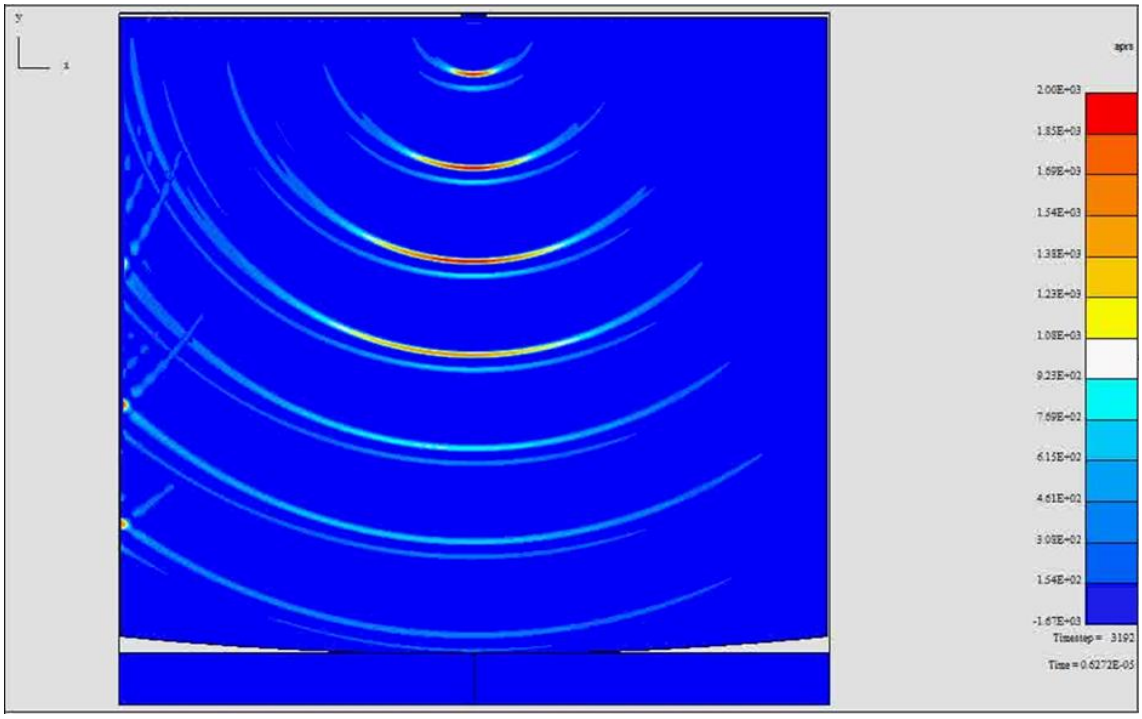

Figure 11.11: Multiple Pressure Intensity Plots overlaid at Intervals of 0.9µs. For clarity only the incident component has been plotted here, the reflected component has been neglected.

The plot only shows waves incident on the interface. These show a clear spherical wave pattern with some side wall reflections.

A threshold was applied to the pressure intensity plots in order to convert them to black and white images. This was done to highlight individual wave-fronts. The resultant images for each of the simulation cases are plotted in Figure 11.12. For clarity the plots for incident and reflected waves have been separated.

The plots in Figure 11.12 have been overlaid to yield Figure 11.13 which shows the reflected wave propagation for each contact case. The light grey wave fronts represent those from an entirely vacuum interface (no contact with the strip). This is the reference case where maximum energy is reflected. The full contact case is shown by the wave fronts given in red, this is where there is full contact with the strip and the maximum amount of energy is being absorbed. Between these extremes the proportion of the wave fronts emanating from the contact and non-contact zones is a function of how much of the interface is in contact with the strip.

The half contact case in Figure 11.13 has the strip across exactly half of the interface. As the sensor is half over the strip and half over the vacuum, it would intuitively be expected that half of the sensor receives a signal reflected from the vacuum, and half receives the response from the roll to strip interface. However, as can be seen by the green wave fronts, the beam spread results in the reflection from the vacuum reaching the whole sensor face. This is because the problem is not exactly symmetrical. Although the interface is exactly half cover, the sensor has a finite width which is not insignificant. The oblique components of the wave emanating from the sensor are the reason for the asymmetry of the returned pulses, as shown in the half-contact case. The effect of this on a measurement is to smooth the measurement across the entry and exit of the roll bite.

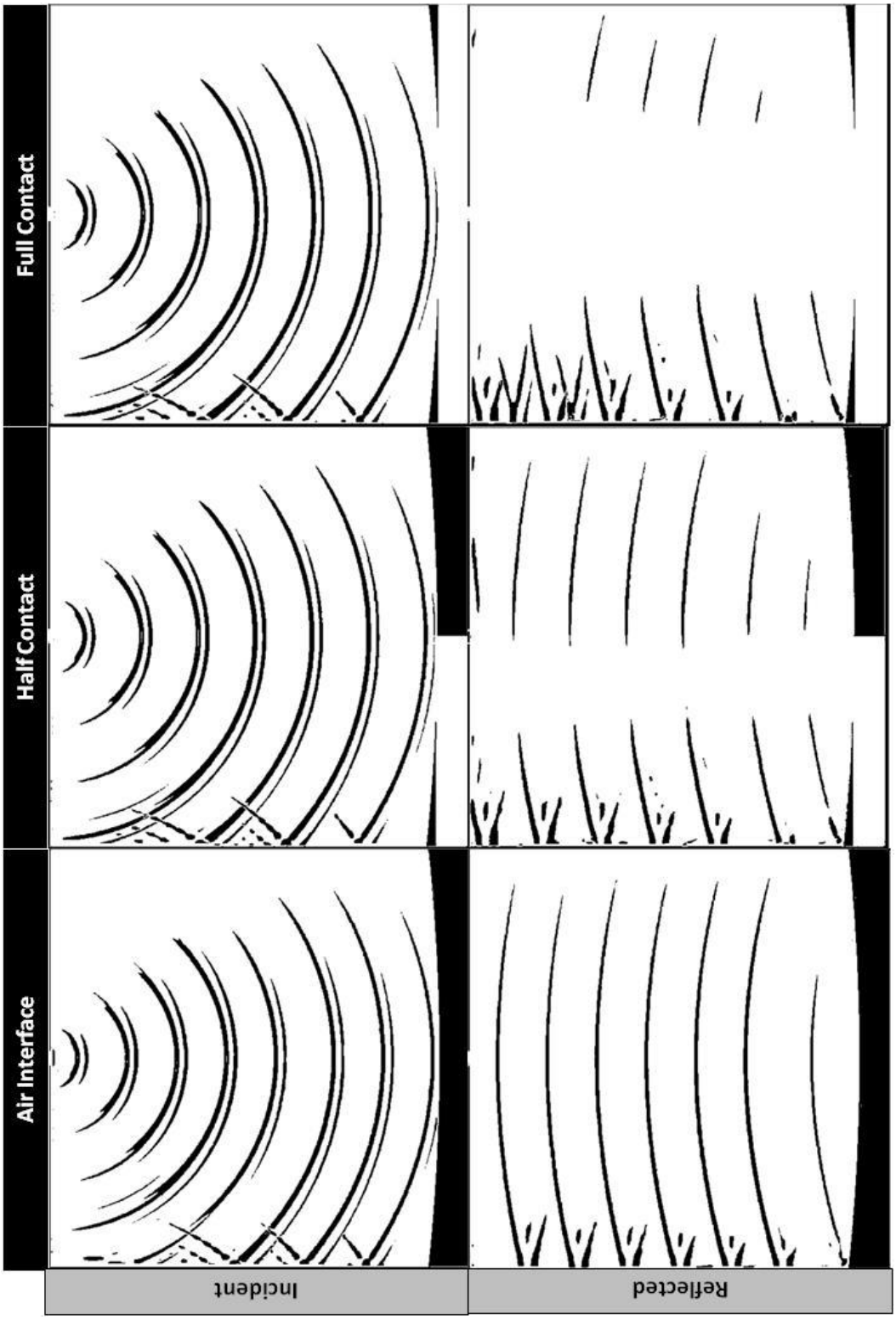

Figure 11.12: Incident and Reflected Wave Fronts overlaid at 0.9µs intervals.

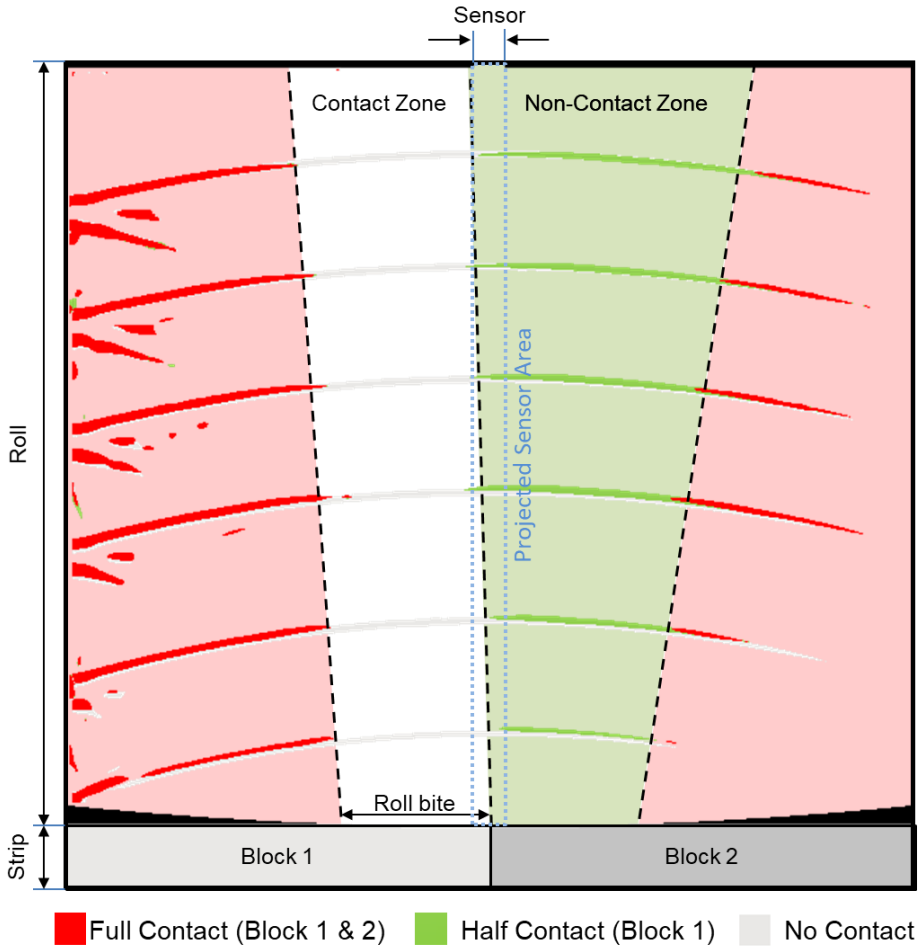

Figure 11.13: Reflected Wave Fronts for Full, Half and No Contact cases overlaid at 0.9µs intervals.

The purpose of the wave propagation modelling has not been to study the interface of interest explicitly, but rather understand how effects such as beam spread effect the measurement area, and if this causes any disruption to the expected measurement. The modelling has shown that the beam spread has a near spherical pattern. This combined with the width of the sensor means that the proportion of the wave received from the contact and non-contact parts of the interface is Non-symmetrical. Even in the half contact case it can be seen that the beam spread results in the reflection from the vacuum reaching the whole sensor face. The effect of this on a measurement will be to smooth the measurement across the entry and exit of the roll bite, and make the measurement of the contact appear larger.

11.2 Finite Element - Metafor

Two forms of rolling specific modelling were completed. The first set of modelling concentrated upon the stress conditions inside the roll itself. This was modelled using Metafor nonlinear finite element software. This models a cross section of a roll and strip during rolling. Metafor was developed by the Computational Mechanics laboratory of the Department of Aerospace and Mechanical Engineering at the University of Liège (Boman, Development of a Tridimensional Arbitrary Lagrangian Eulerian Formalism for Dynamic Implicit Problems. Application to Forming Processes. (in French), 2010) and the modelling in this section was completed in collaboration with Yves Carretta also of the University of Liège (Carretta Y. , et al., 2017).

11.2.1 Modelling Approach

Modelling was performed in three steps. Firstly the roll was moved down vertically into the strip. In the second step the rolling speed was increased from stationary to the specified rolling speed. The entry and exit tension was also increased from zero to the modelled tensions. In the final step the rolling velocity and strip tensions are kept constant and the simulation was stopped once twice the roll bite length had been rolled and steady state was reached. Modelling was completed using the example test conditions Table 11.1.

Coulomb friction is assumed in the modelling. In order to emulate the experimental results the friction coefficient was adjusted so that the rolling load and forward slip matched the experimental results. The parameters given in Table 11.2 were achieved.

Entry Strip Thickness, h_0	2.78 mm
Exit Strip Thickness, h_1	2.317 mm
Entry Tension, σ_1	39 MPa
Exit Tension, σ_2	117 MPa
Lubricant	4% Gerolub 5525
Strip Material	IF Steel
Roll Radius, R	193.325 mm
Rolling Velocity, V_R	100 m/min
Roll Roughness	0.54 µm
Entry Strip Roughness	1.015 µm
Strip Width, W	100 mm
Rolling Load, F	50.5 t
Forward Slip, S_f	5.5%

Table 11.1: Example Test conditions used in Metafor Modelling.

	Forward Slip, S_f (%)		Rolling Load, F (MN/m)	
Coulomb Friction	Experi.	Metafor	Experi.	Metafor
0.075	5.5	4.219	4.95	4.97

Table 11.2: Matched Test Conditions.

Two modelling approaches were used, Lagrangian and the Arbitrary Lagrangian Eulerian (ALE) method. The first is where the mesh is attached to the material being modelled. In the second the mesh can move arbitrarily to optimize the shapes of elements, while the nodes on the boundaries can move along the boundaries (with the material). The roll was meshed using the Lagrangian approach (Carretta Y. , et al., 2017). This is important as it means the material of the roll sticks to the mesh, which is necessary in order to keep track of the area covered by the ultrasonic sensors during rolling. It is then possible to export the change in plug length (the radial distance between the sensor position and the roll surface) for comparison with the experimental measurements.

The strip meshing used ALE for reasons explained by Boman and Ponthot (Boman & Ponthot, Finite Element Simulation of Lubricated Contact in Rolling using Arbitrary Lagrangian Eulerian Formulation, 2004).

Strip Modelling

For the purposes of modelling the strip is treated as IF Steel. The strip was meshed with 75 x 4 elements (Boman, Development of a Tridimensional Arbitrary Lagrangian Eulerian Formalism for Dynamic Implicit Problems. Application to Forming Processes. (in French), 2010) as shown in Figure 11.14.

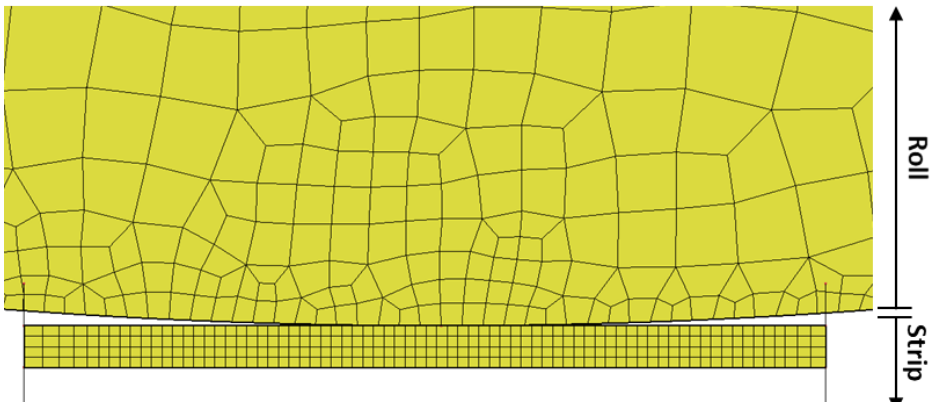

Figure 11.14: Strip Meshing.

Roll Modelling

A section of the roll directly above the strip was finely meshed, while the rest of the roll was more coarsely meshed. The centre of the roll has not been meshed as a rigid cylindrical axis one fifth of the roll radius has been used in order to impose the rotation of the roll by applying an appropriate displacement to this (Boman, Development of a Tridimensional Arbitrary Lagrangian Eulerian Formalism for Dynamic Implicit Problems. Application to Forming Processes. (in French), 2010). Figure 11.15 shows the mesh and stress field in the vertical Y-axis (σ_{YY}) for an example simulation once steady state had been reached. This was done to achieve the highest resolution of the stress around the contact zone while minimising the computational requirements of the model. The height of the finely meshed section was 61.69 mm, this is 1.5 times the distance between the sensor and the roll surface. The roll material was assumed to be elastic with a Young's modulus of 210 GPa.

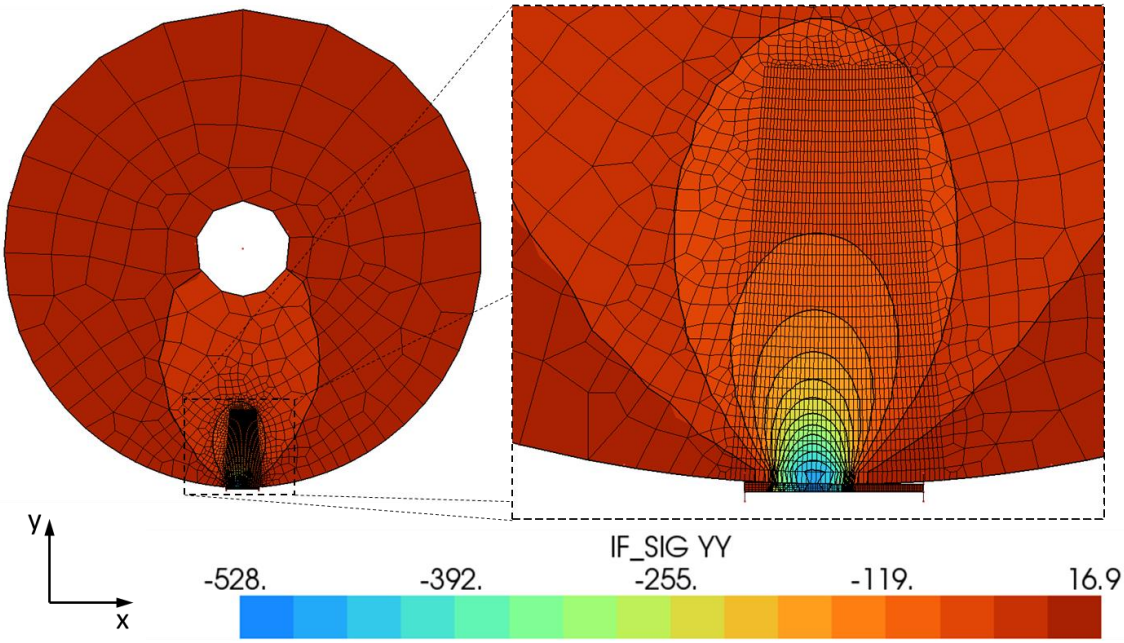

Figure 11.15: Roll Meshing showing σ_{YY} for an example simulation Wave Propagation Model.

11.2.2 Roll Deflection and Stress

The vertical, horizontal, shear and von Mises stresses where calculated, example profiles are shown in Figure 11.16. These show a strong similarity with the stress profiles calculated analytically and presented in §2.6.

The radial profile of the vertical stress (σ_{yy}) in the roll was extracted from the model. An example profile at the centre of the roll bite is given in Figure 11.17. This profile was taken at an x-axis position of -2.5638mm from the normal (vertical) line through the centre of the roll. In the main this profile is smooth and continuous as is predicted by standard contact mechanics. The only exception is the point on the rolling surface which shows a slight decrease in comparison to the next nearest data point. This could be explained due to the mesh sensitivity, most likely due to sub-optimal poor node position, or possibly inadequate mesh resolution at the interface.

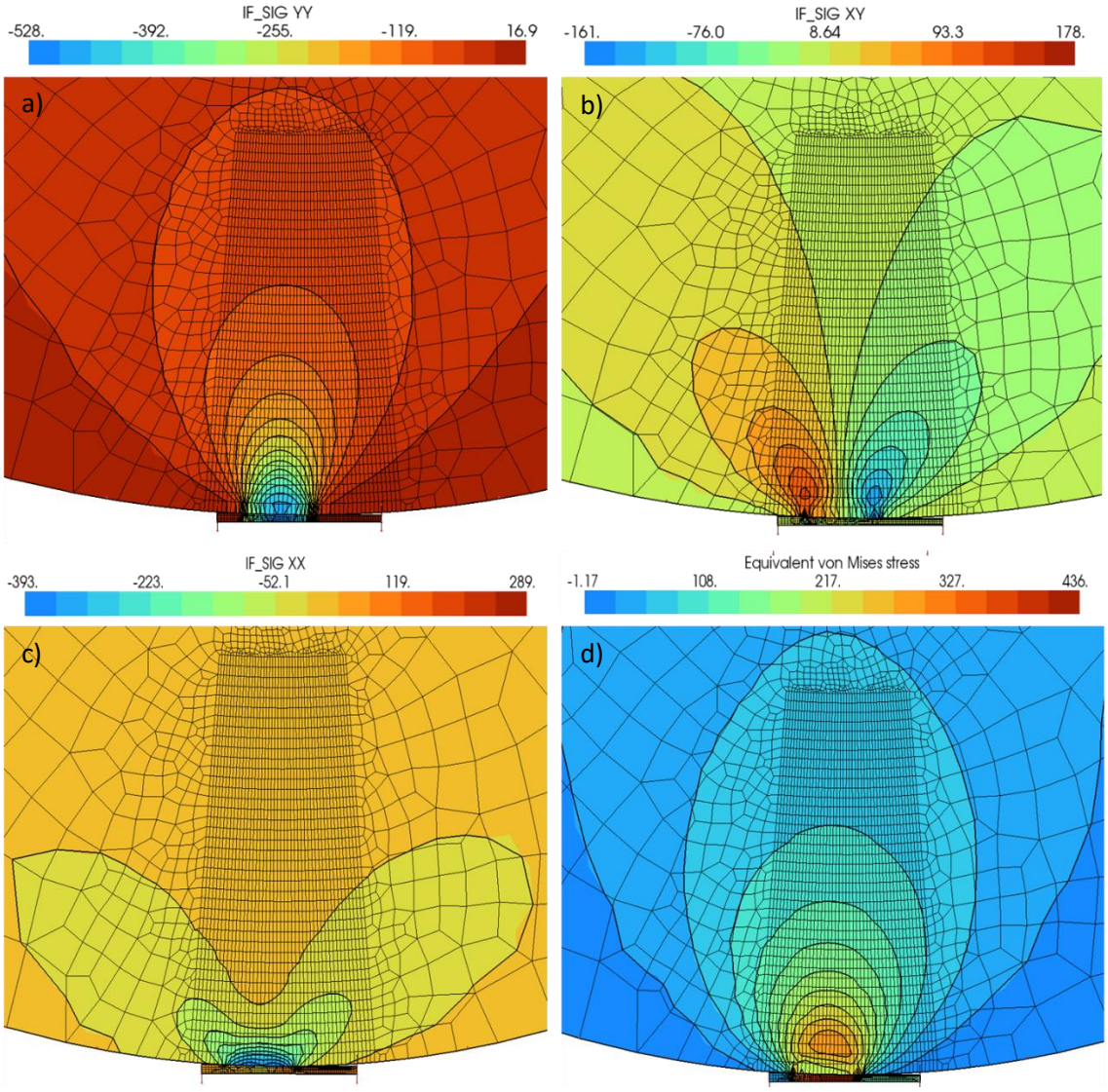

Figure 11.16: Modelled Stresses a) Vertical σ_{YY}, b) Shear τ_{XY}, c) Horizontal σ_{XX}, d) von Mises σ_V.

The stress measured ultrasonically is an average over the wave path. To get an equivalent result from the Metafor model the stress was averaged between the roll surface and the sensor position (40mm offset from the roll surface). It should be noted that this modelling was completed prior to finalisation of the plug dimensions used in testing, which actually had a length of 35mm at the point where the ultrasound travelled through. The stress was calculated

for the conditions in Test 7, with elongations from 10% to 40%. The outputs from the Metafor model for several elongations are plotted in Figure 11.18 against the analytical solutions given in §2.6. This plot shows that the stress calculated from both methods has a close similarity. The data for 10% elongation matches very well outside of the roll bite. The peak stress obtained from the finite element analysis within the roll bite is slightly lower than the analytical solution. The variation between the Metafor and analytical results are slightly higher for the cases with a larger elongation, but is less than 10% in all cases.

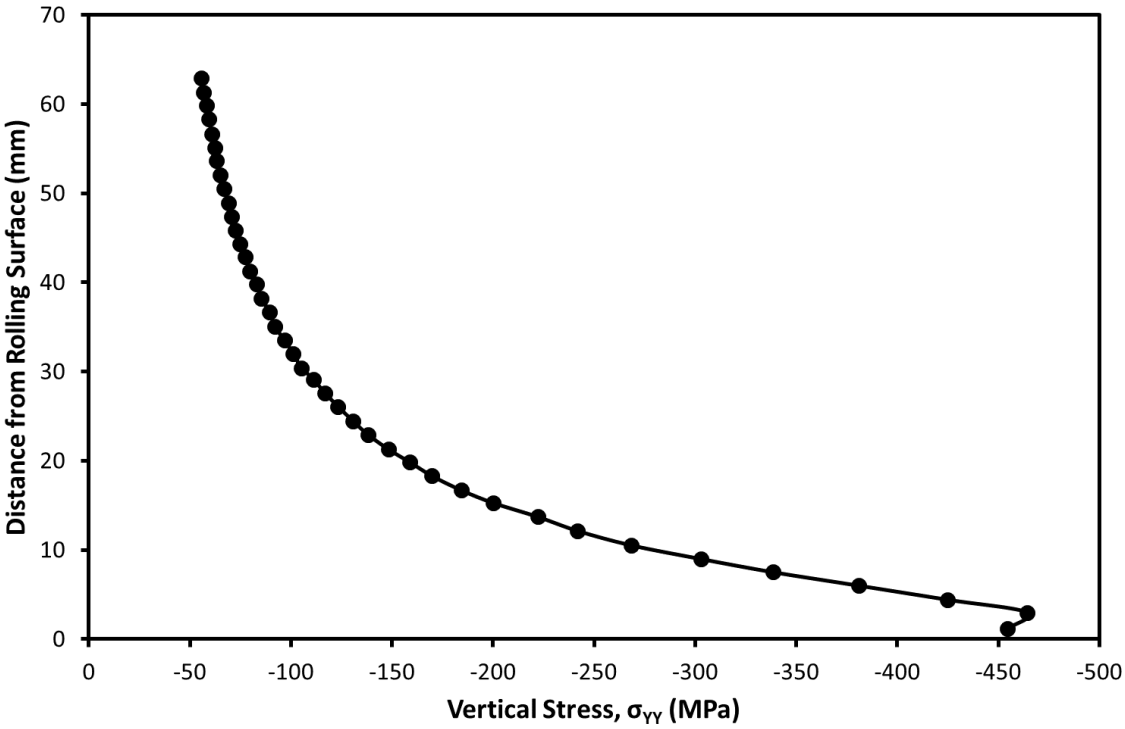

Figure 11.17: Example Radial Stress Profile in the Roll from the Metafor Model.

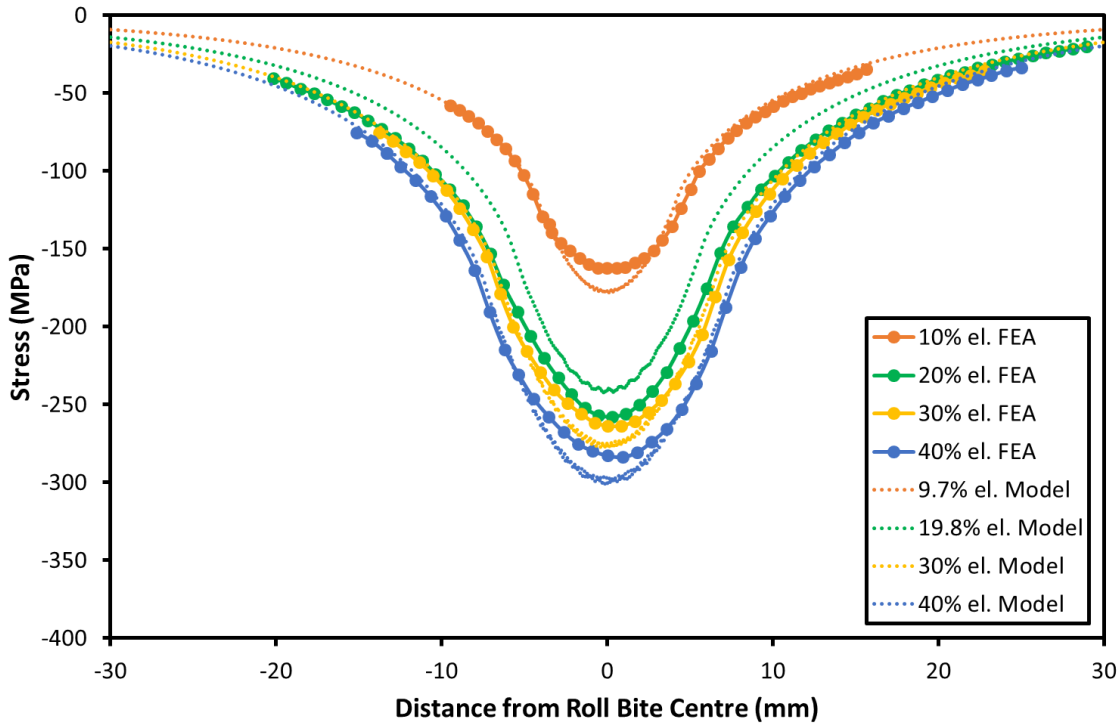

Figure 11.18: Roll Stress from Metafor FEA and Model.

The stress from the Metafor simulation is compared to the ultrasonic results in Figure 11.19, the ultrasonic results are for Test 7, details of which are given later in Table 11.10. The shape of the stress curves shows good similarity and similar magnitude at 10% and 20% elongation. They still show a similarity in shape at higher elongations, however the simulated results give a lower magnitude of the peak stress than those gained experimentally.

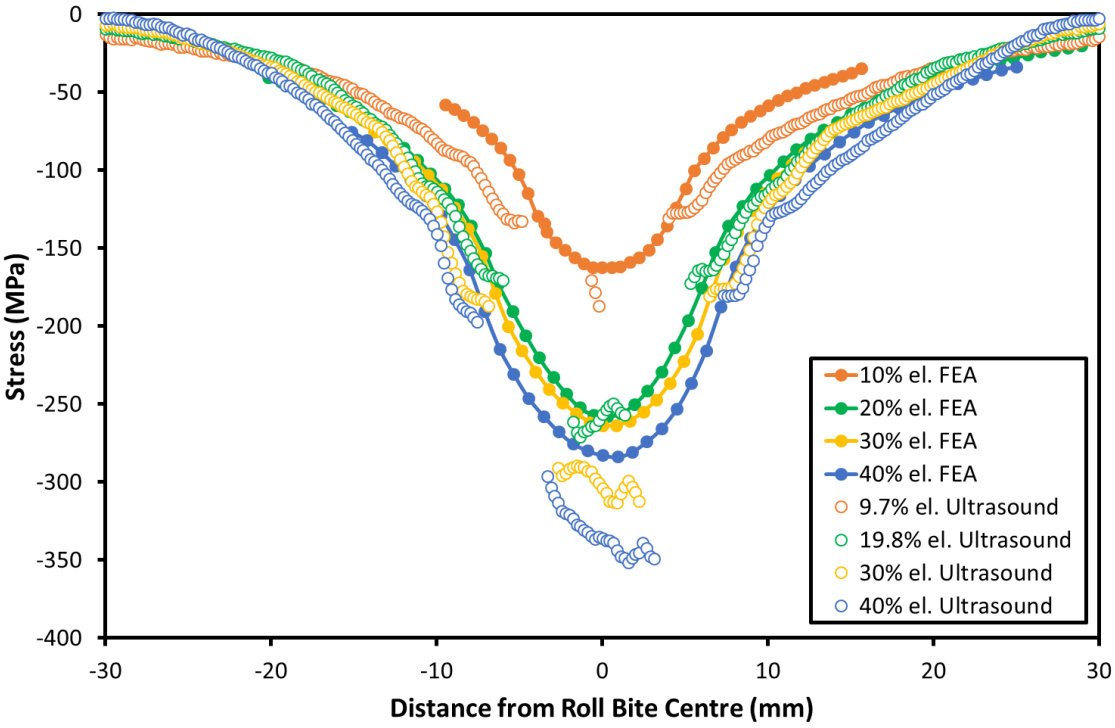

Figure 11.19: Roll Stress from Metafor FEA and Measured Ultrasonically.

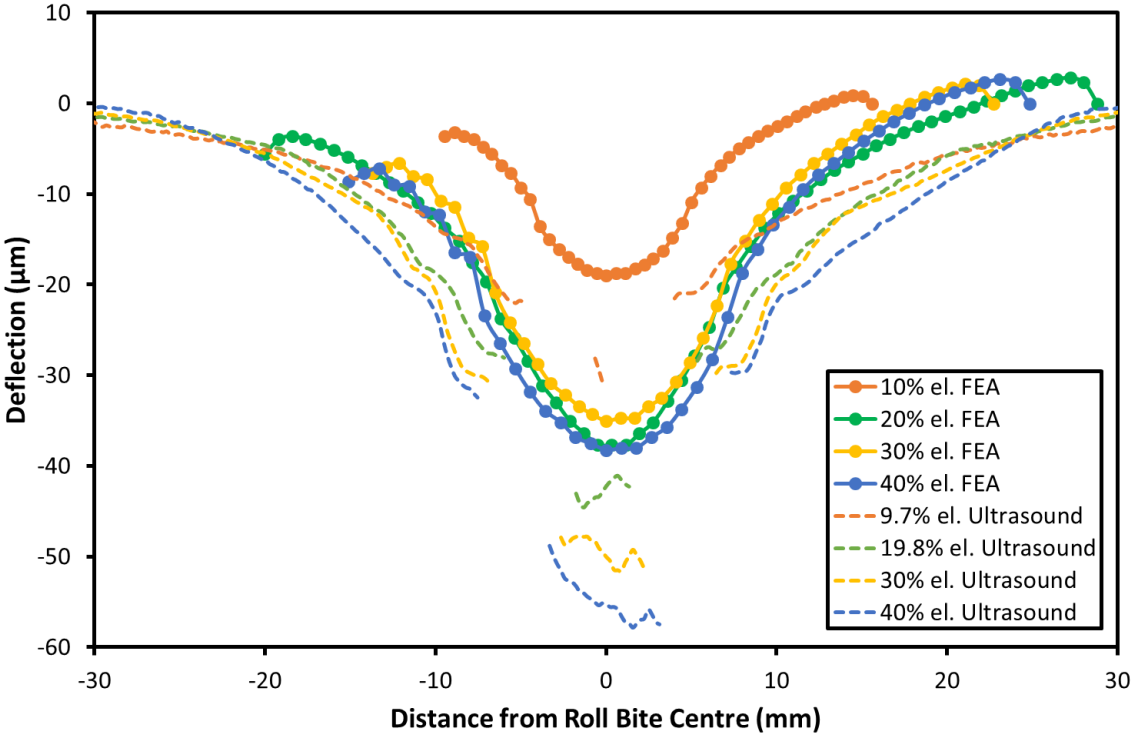

Figure 11.20: Roll Surface Deflection from Metafor FEA and Ultrasound.

In addition to the roll stress, Metafor was also capable of calculating the roll deformation. The calculated roll surface deflection is compared to the results obtained ultrasonically in Figure 11.20.

Again the shape of the deflection is similar for both the simulated and measured results. It should be noted that the ultrasonic results for deflection and stress were both calculated from the same Time-of-Flight measurement and so maintain the same order between test cases. There is a change in ranking between the modelled results for the deflection at 20% and 30% elongation, although the absolute difference in deflection values which results in this is very small. The could occur as the calculation of deflection and stress used separate methods (namely stress and node placement). These along with the discretisation of the mesh could explain the slight variation seen in the absolute results that are not similarly seen in the ultrasonic results. Both datasets show the same trends with larger elongations resulting in greater deflections as would be expected. Although they are of the same order of magnitude, the ultrasonic measurements consistently report a larger deflection than the equivalent simulated results. It is noticeable that there is less difference between the various simulated results for larger elongations, than there is between the equivalent ultrasonic measurements.

The similarities between the simulated and measured results indicate that the ultrasonic results have some validity both as a method for measuring surface deflection and internal roll stress. The differences in magnitude seen between the modelled and measured results could be the result of several different factors. Firstly, there are several sources of error in the ultrasonic measurements themselves. The ultrasonic method is indirect, requiring a conversion from speed of sound to stress. For this the acoustoelastic coefficient was obtained from testing, however for this testing only plain compression was applied. The effect of non-perpendicular and shear stresses was not accounted for. Although stresses non-parallel to the direction of ultrasonic propagation will have a lesser effect than those that are parallel, they will still have some additional influence on the ultrasonic ToF. As shown by Figure 11.16 horizontal and shear stresses are non-trivial. These unaccounted for stresses would cause the ultrasonic measurement to over-predict the magnitude of the deflection and stress measured, as is observed in the results obtained.

There are also a number of factors which will cause error in the modelling results. FEA is likely to have errors caused by the meshing approach and simplifying assumptions as described earlier. The parameters input into the finite element model were obtained from the mill control system which will have an associated error. The parameters input into the simulation were either nominal values, or values that were matched as closely as possible to those measured. For some of these parameters, for example slip and rolling force, perfect agreement could not be achieved as shown in Table 11.2. There will also be errors in the material properties used to emulate the strip and roll/plug for the simulation as literature values were used.

The FEA simulations assumed a sensor depth of 40mm from the rolling surface. The actual sensor depth during testing was slightly less than this for two reasons. For testing the sensors were inset into the plug by 5mm reducing the path length to 35mm. Upon installation the plug surface was ground to match the roll surface curvature, which will have further reduced the ultrasonic path length. The result of this is that the sensor was located closer to the high stress zone than calculated in the simulations, and therefore the average stress seen across the ultrasonic path would have been higher. Also the plug mounting method for the sensors will have influenced

the stress state in the plug as it meant there was no material supporting the plug directly behind the sensors. This was not accounted for in the modelling.

11.3 Strip Rolling Model – Metalub

A second set of rolling modelling was used to calculate the interfacial conditions in the roll bite contact, such as interface stiffness, lubricant film formation, lubricant pressure and contact length. An additional output from this modelling was the strip thickness evolution across the roll bite. This modelling was completed using Metalub software. Metalub is a 1D lubrication-coupled strip rolling model that simulates the interaction between strip and roll in the roll bite. As with Metafor this software, Metalub was developed at the *University of Liège* (Stephany, 2008) (Carretta, Boman, & Stephany, MetaLub - A Slab Method Software for the Numerical Simulation of Mixed Lubrication Regime in Cold Strip Rolling, 2011) and again the modelling presented in this section was performed in conjunction with Yves Carretta also of the *University of Liège* (Carretta Y. , et al., 2017) (Carretta Y. , 2015).

Previously the position along the roll bite has been stated relative to the roll bite centre, taken as the mid-point between the roll bite entry and exit. The coordinates in this section are based on those used by Metalub, which calculates the position along the roll bite relative to the point of minimum strip thickness.

11.3.1 Modelling Approach

Several types of numerical methods, ranging from 1D to 3D, are now available to model cold rolling depending on the process parameters and the required precision of the results. A review of rolling numerical models is presented by Montmitonnet (Montmitonnet, 2006). Metalub's 1D model was deemed acceptable in this circumstance as "a 1D model is perfect for a ratio between the length of the roll bite and the strip thickness higher than 3" (Montmitonnet, 2006).

The effect of the emulsion was not studied. Thermal transfer effects have also been neglected. Strip and roll roughness have been combined and applied only to the strip, the roll was smooth. This gives pure asperity flattening and no ploughing. The tangential stiffness of the roll was assumed to be infinite.

Where possible model inputs were chosen to match those recorded by the mill control system during testing. MetaLub outputs included profiles across the roll bite for strip thickness, local relative area of contact, local lubricant pressure and the local lubricant film thickness. These profiles were compared directly to the measurements taken ultrasonically.

Lubricant Modelling

The lubricant pressure is accounted for and determined using a form of Reynolds equation developed by Wilson and Marsault (Wilson & Marsault, Partial Hydrodynamic Lubrication With Large Fractional Contact Areas, 1998). In this equation two flow factors have been added to take into account the asperity presence on the fluid flow when a large relative contact area between asperities of the strip and the rolls occurs.

The piezo-viscosity dependence was modelled using an improved version (Bair, Mary, Bouscharain, & Vergne, 2013) of a modified William, Landl and Ferry (WLF) equation (Yasutomi, Bair, & Winer, 1984) as follows:

$$\log\left(\frac{\eta}{\eta_g}\right) = \frac{-C_1\left(T - T_g(p_l)\right)F(p_l)}{C_2 + \left(T - T_g(p_l)\right)F(p_l)} \quad 11.2a$$

$$T_g(p_l) = T_g(0) + A_1 \ln(1 + A_2 p_l) \quad 11.3b$$

$$F(p_l) = (1 + B_1 p_l)^{B_2} \quad 11.4c$$

This equation gives the lubricant viscosity η as a function of the lubricant pressure p_l and the temperature T. T_g is the glass transition temperature, η_g is the viscosity at the glass transition temperature and A_1, A_2, B_1, B_2, C_1 and C_2 are lubricant specific parameters that are identified experimentally. Parameters corresponding to the oils simulated are listed in Table 11.3 (Bouscharain & Vergne, Etude d'huiles de laminage sous hautes pressions, 2010).

	A_1 (°C)	A_2 (MPa^{-1})	B_1 (MPa^{-1})	B_2	C_1	C_2 (°C)	η_g (MPa.s)	$T_g(0)$ (°C)
Gerolub 5525	10.01	0.010010	0.26129	0.0128	16.00	24.26	1,000,000	-90.43
Trenoil K2	49.64	0.000365	0.00578	-0.565	16.11	26	1,000,000	-85.96
Quaker HV2	102.77	0.000226	0.00573	-0.547	15.95	26.98	1,000,000	-73.16

Table 11.3: Piezo-Viscosity Relationship Parameters obtained Experimentally for Pure Rolling Lubricants.

The rolling cases presented were assumed to be lubricated with pure oil and the temperature a constant 60°C across the roll-bite. Data from previous testing (§6.5) has shown how the bulk modulus of the lubricant will change with rolling pressure and temperature, this must therefore be accounted for in the measurement calculations. Because of this the lubricant pressure profile across the roll bite was added to the outputs of the modelling work.

Strip Modelling

MetaLub is based on the slab method (Bland & Ford, 1952) (Alexander, 1972) (Cosse & Economopoulos, 1968), which only takes into account the principal stresses in the strip, neglecting shear. The strip material was modelled using the hardening law given in Equation 11.5.

$$\sigma_{Yield}(\bar{\varepsilon}_{pl}) = (A + B\bar{\varepsilon}_{pl})(1 - Ce^{-D\bar{\varepsilon}_{pl}}) + E \quad 11.5$$

Where σ_{Yield} is the yield stress, $\bar{\varepsilon}_{pl}$ is equivalent plastic strain and A, B, C, D, E are material specific parameters. These parameters were obtained experimentally for the strip by fitting the results of a double punch test, giving the values listed in Table 11.4.

Strip Material	A	B	C	D	E
DD14+Ti	415 MPa	155 MPa	0.39	11.53	0
ARCELOR06	757	156	0	0	-100

Table 11.4: Hardening Law Parameters for Strip Materials.

Asperity Modelling

Asperity crushing is a critical phenomenon in the mixed lubrication regime as it controls the transfer of the work roll surface roughness to the strip. Several authors have proposed analytical crushing laws (Wilson & Sheu, Real Area of Contact and Boundary Friction in Metal Forming,

1988) (Sutcliffe, Surface Asperity Deformation in Metal Forming Processes, 1988). These relate the relative area of contact to the non-dimensional bulk strain rate and the non-dimensional effective hardness. Wilson and Sheu's (Wilson & Sheu, Real Area of Contact and Boundary Friction in Metal Forming, 1988) asperity crushing law was used In the simulations. Marsault (Marsault, 1998) proposed an asperity crushing model specifically related to strip rolling. This used a smooth rigid tool and a rough strip surface. The same assumption is used by MetaLub. The arithmetic roughness (R_a) was measured on the upper roll and on the strip before rolling. Measurements were very similar for all the test conditions discussed here. The asperity shape was assumed to be triangular and the quadratic roughness was inferred from arithmetic roughness using the following relationship:

$$R_q = \frac{2}{\sqrt{3}} R_a \qquad 11.6$$

The composite roughness of the strip and roll was calculated by adding the strip and roll roughness's in quadrature, as follows:

$$R_q = \sqrt{R_{q,strip}^2 + R_{q,roll}^2} \qquad 11.7$$

Where R_q is the composite roughness and $R_{q,strip}$, $R_{q,roll}$ are the quadratic roughness of the strip and rolls respectively. The half distance between asperities (*ll*) was computed assuming an asperity slope of 7°. The roughness and asperity details are summarised in Table 11.5.

$R_{a,roll}$ (µm)	$R_{q,roll}$ (µm)	$R_{a,strip}$ (µm)	$R_{q,strip}$ (µm)	R_q (µm)	Asperity Slope (°)	*ll* (µm)
0.616	0.77204	1.505	1.8862	2.0381	7	24.553

Table 11.5: Roughness and Asperity Parameters used for Simulation.

Friction Modelling

The mean shear stress (τ), defined locally at each point of the roll bite, is given by a sharing law which is an average of the solid-to-solid (τ_a) and the solid-to-fluid (τ_l) shear stresses weighted by the relative solid-to-solid (A) and solid-to-fluid contact areas ($1 - A$), as given by Equation 11.8.

$$\tau = A\,\tau_a + (1 - A)\tau_l \qquad 11.8$$

The solid-to-fluid shear stress is a function of the lubricant viscosity (η), the relative contact area A, the mean film thickness (h_l) and the sliding velocity between the rolls and the strip $(v_R - v_S)$ as given by Equation 11.9.

$$\tau_l = \eta \frac{(1 - A)(v_R - v_S)}{h_l} \qquad 11.9$$

The solid-to-solid friction stress is given by a Coulomb-limited-to-Tresca law as follows:

$$\tau_a = \min(\mu_C|\sigma_n|, \mu_T k) \qquad 11.10$$

Where σ_n and k are the normal stress and the yield shear stress respectively. This requires the definition of two coefficients μ_C and μ_T, which represent the Coulomb and Tresca coefficients respectively. The value of these depend on the strip and rolling conditions, as these parameters account for many complex mechanisms, they cannot be determined beforehand. To gain these values Coulomb's coefficient was iteratively adjusted in repeat simulations so that the rolling load and forward slip (defined as the difference between work roll and outlet strip velocities)

yielded the closest match between the simulated and measured results. It was not possible to achieve a perfect fit for both variables, and so a heuristic approach was adopted where each rolling case was matched by hand. A constant ratio between μ_T and μ_C of 2.6 was chosen ($\mu_T = 2.6\,\mu_C$). This friction sharing law and ratio were selected as they were deemed suitable in a previous study by Stephany (Stephany, 2008) which used the same software and similar rolling conditions to study numerical modelling of mixed lubrication contacts in cold rolling. The coefficients were kept constant along the roll bite. This iterative approach was the only practical way to obtain these parameters as they account for many complex mechanisms.

Work Roll Modelling

In the simulations conducted in this study, the deformation of the roll was computed using Jortner's formulation (Jortner, Osterle, & Zorowski, 1960). The rolls are modelled as tool steel with a Young's modulus of 210 GPa, Poisson's ratio of 0.3, radius of 192 mm and roughness parameters of R_a = 0.6 µm, Rsk = -0.3 and RPc = 100/mm. The roll radius differed slightly from that used in testing (193mm) as the modelling was performed prior to final definition of the test setup.

Thermal Effects

In these simulations the temperature was assumed to be constant throughout the roll bite. Lubricant temperature was set to 60°C, matching the sprayed lubricant temperature as measured by the mill lubrication system for the test cases simulated.

11.3.2 Strip Thickness

Firstly the strip thickness as calculated by Metalub is compared to the ultrasonic results. The test conditions simulated are those summarised in Table 8.10, the lubricant used was Gerolub 5525. The result of the slab method modelling along with the equivalent result obtained during testing are plotted in Figure 11.21.

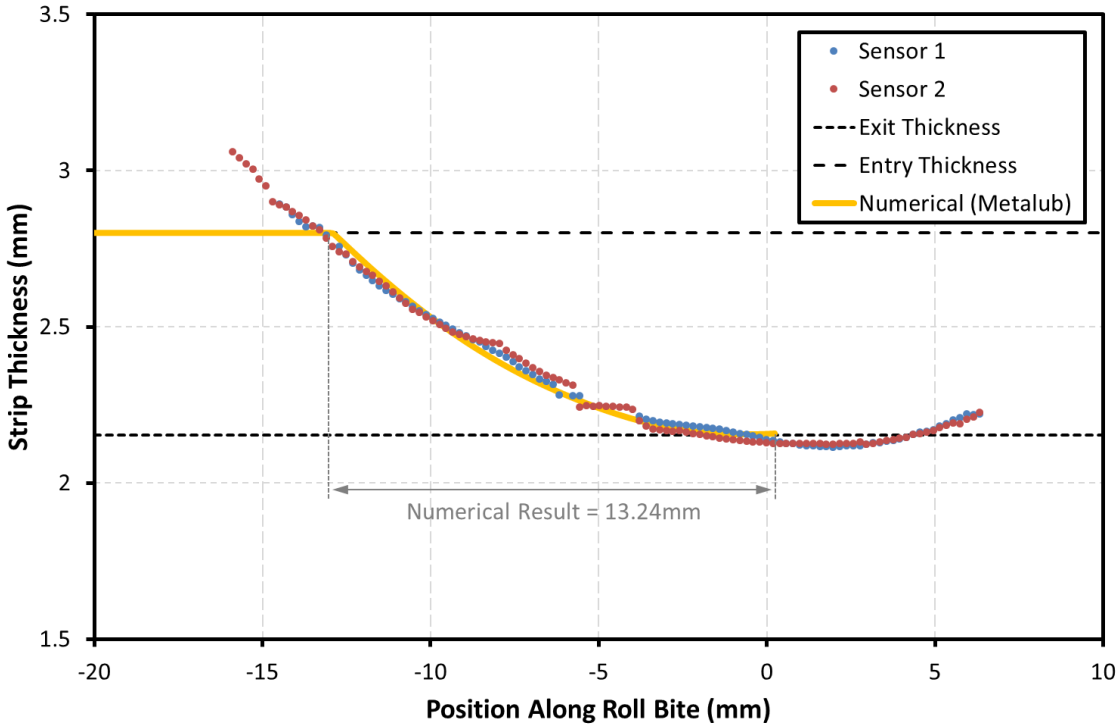

Figure 11.21: Strip Thickness Profiles from Metalub Simulation and Ultrasonically measured using two Shear Sensors.

In terms of strip thickness there is generally a good correlation between the modelled and experimental results. The experimental results appear to give a reading for strip thickness prior to the roll bite that is in excess of the entry strip thickness. The reason for this may be that the ultrasonic beam spreads as it propagates through a material, meaning the extremes of the beam will travel at an angle to the primary beam direction. This means that while the sensor position may appear to be outside of the roll bite, some of the signal at the extremes of the ultrasonic beam is returning from the roll bite. This signal will be travelling at an angle through the strip and so will have a longer path length than if it were travelling normally through the strip.

11.3.3 Roll Bite Length

Next the roll bite length computed with MetaLub was evaluated. For test the rolling configuration in the previous section the roll bite length is 13.24 mm, as shown in Figure 11.21. For this test case the ultrasonic method reported a length of 14.04 mm (see Figure 8.27). The difference between the two is 6%. Part of the reason for the difference may be the difficulty in accurately identifying the contact entry and exit points, particularly where the ultrasonic method reports strip thicknesses either side of the roll bite contact due to the beam spread.

To assess the roll bite width measurement in greater detail a number of test cases with varying strip elongations were simulated. The lubricant used was Gerolub 5525 and the test conditions are given in Table 11.7.

Strip Entry Thickness, h_0 (mm)	Elongation (%)	Entry Strip Tension, σ_1 (MPa)	Exit Strip Tension, σ_2 (MPa)	Rolling Velocity, V_R (m/min)	Rolling Load, F_y (N/mm)	Forward Slip, S_F (%)
2.8	10	38	119	97.5	3505	5.05
2.8	20	38	119	97.5	5300	4.65
2.8	30	38	119	97.5	6460	3.33
2.8	40	38	119	97.5	7267	2.47

Table 11.7: Test Conditions Simulation to assess Roll Bite length for different Strip Elongations.

The results from both the simulations and the ultrasonic testing are given in Figure 11.22. The experimental and numerical values correlate very well. Both datasets exhibit the same trends and have very similar magnitudes, the maximum relative difference is 3% which occurs for the strip elongation of 40%. This indicates that the ultrasonic method can be used to yield a reliable measurement of the contact width.

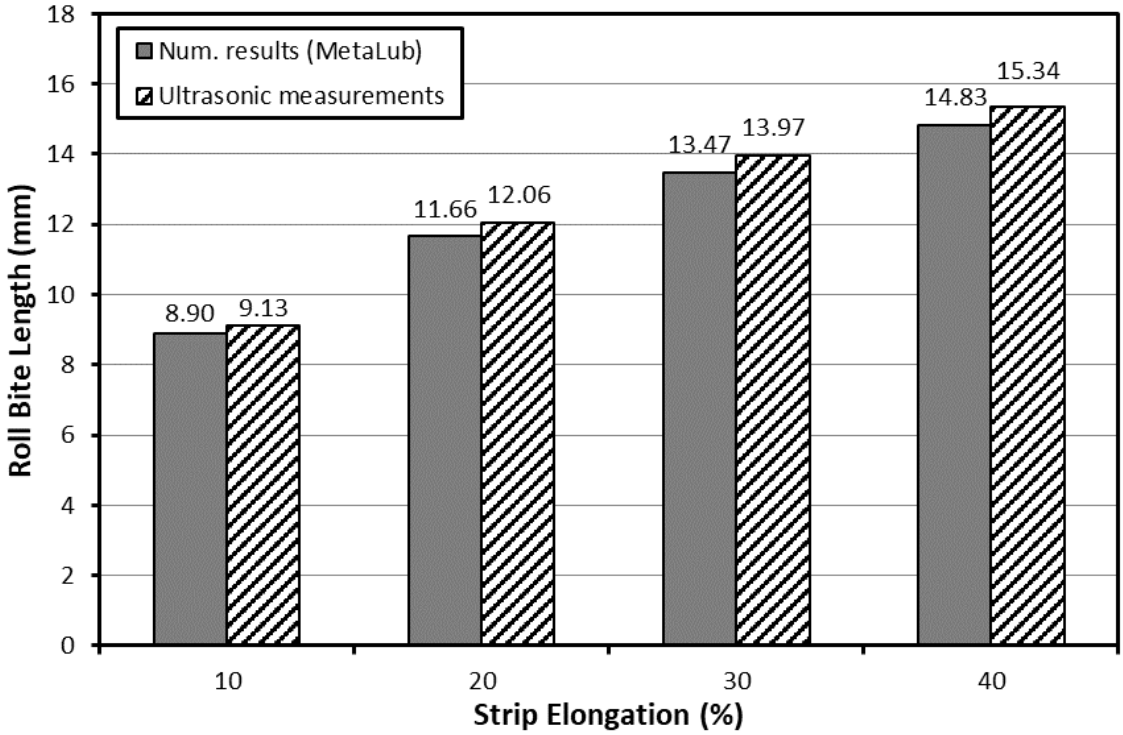

Figure 11.22: Roll bite length comparison: experimental measurements vs. numerical results.

11.3.4 Interface Pressure

The test parameters used for this modelling were a rolling velocity of 100 m/min with an elongation of 20% and lubricated with a 4% aqueous emulsion of Gerolub 5525. The simulation assumed pure oil and the contact was assumed to be fully lubricated (no starvation).

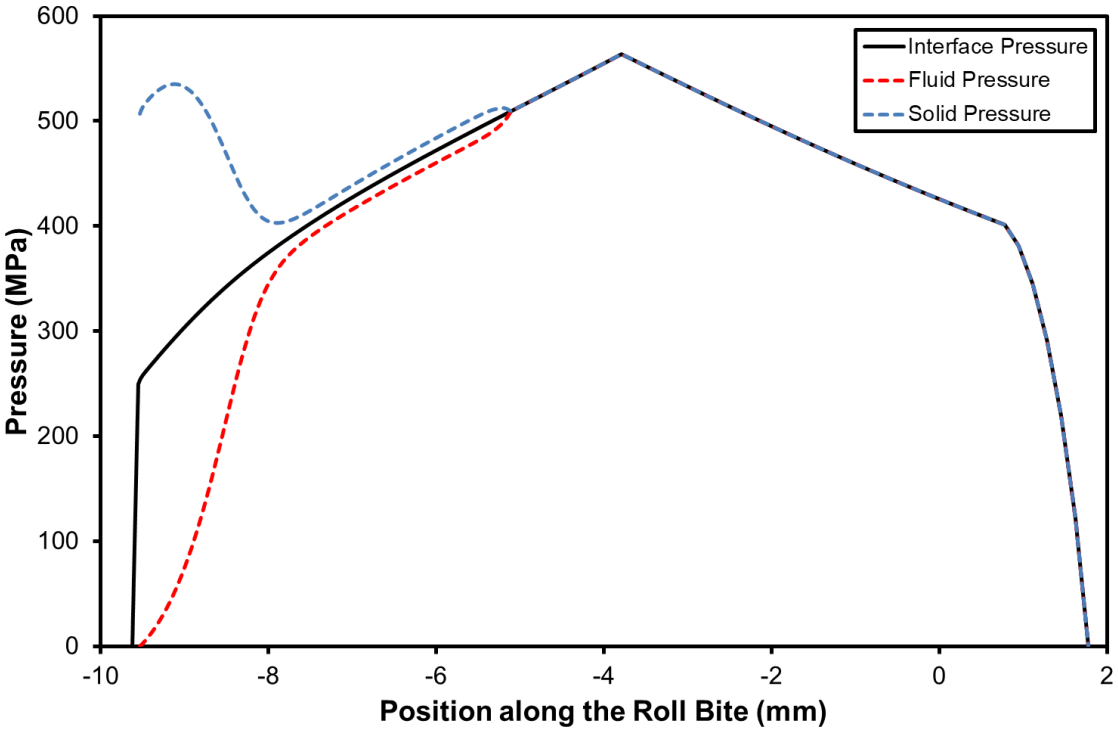

Figure 11.23: Interface Pressure Components across the Roll Bite from Metalub.

The pressure profile across the interface output from the Metalub model is given in Figure 11.23. This shows the pressure observed by both the fluid and solid components of the contact as well as the resultant interface pressure.

The fluid pressure can be used to calculate the fluid viscosity, the profile of which is given below in Figure 11.24.

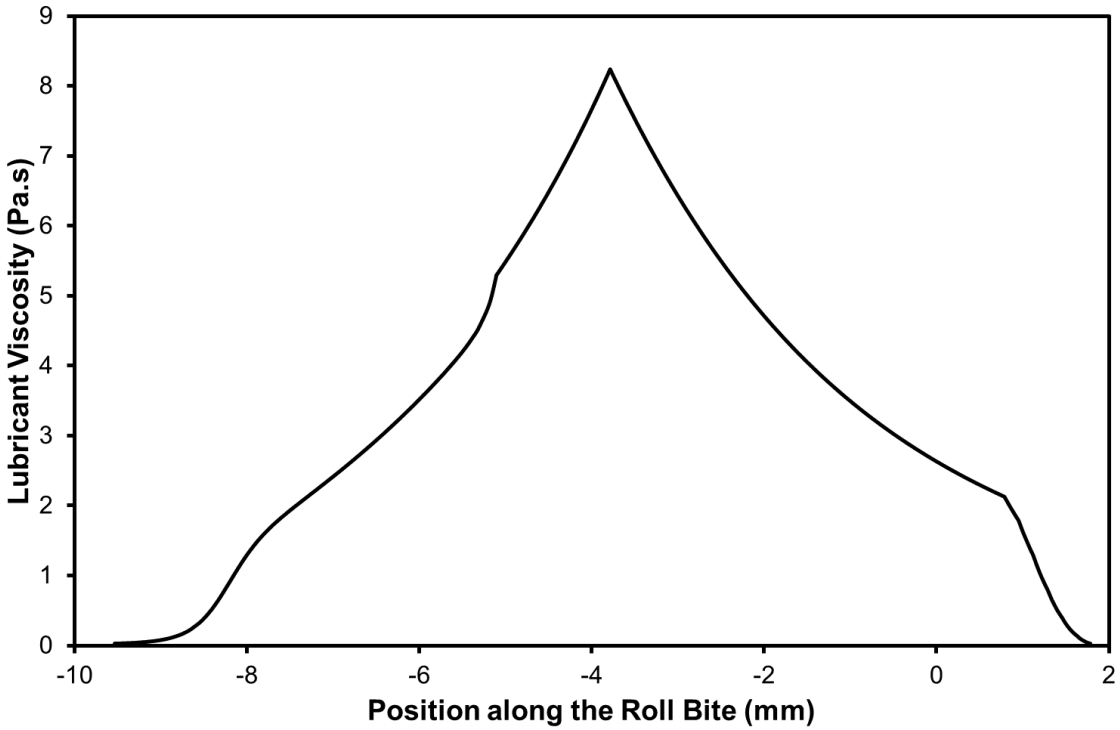

Figure 11.24: Lubricant Viscosity computed by Metalub.

It is also possible to account for the effect of pressure on the lubricant bulk modulus. The bulk modulus for Gerolub 5525 as a function of pressure for 55°C, the assumed lubricant temperature in this test, is given below (Equation 11.11) and shown in the Figure 11.25.

$$B(p_l) = -7.3 \times 10^{-6} {p_l}^2 + 0.012 p_l + 1.3 \qquad 11.11$$

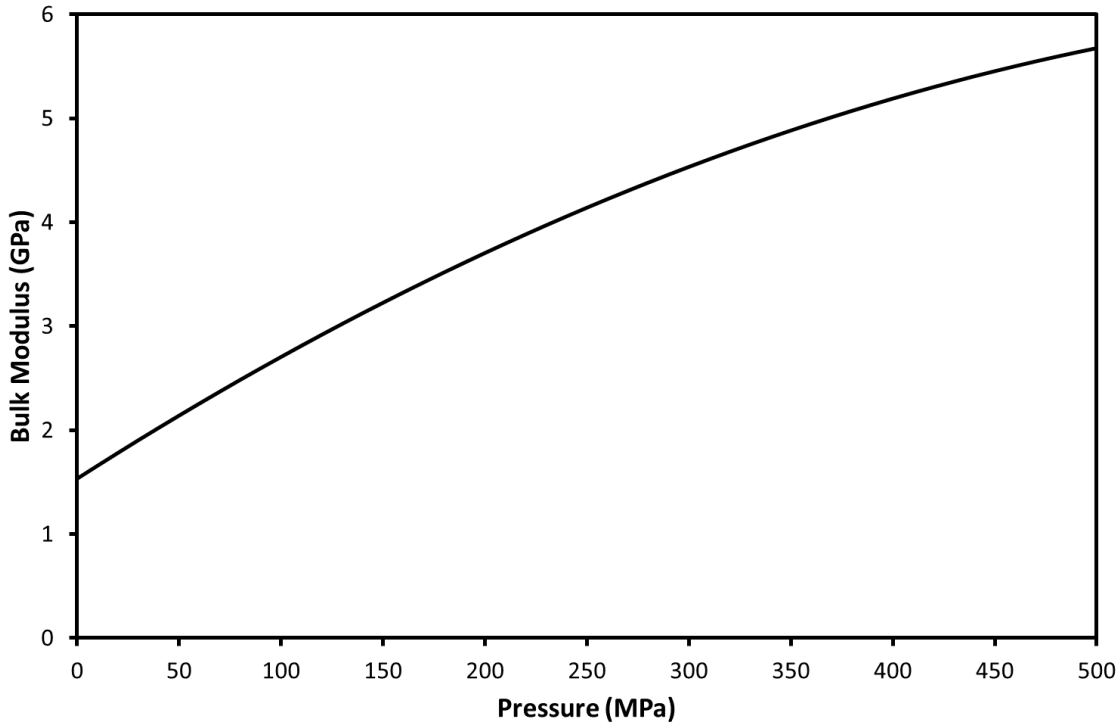

Figure 11.25: Bulk Modulus against Pressure for Gerolub 5525 at 55°C.

From the bulk modulus against pressure relationship and the lubricant pressure calculated by Metalub the bulk modulus was calculated across the roll-bite and is presented in Figure 11.26.

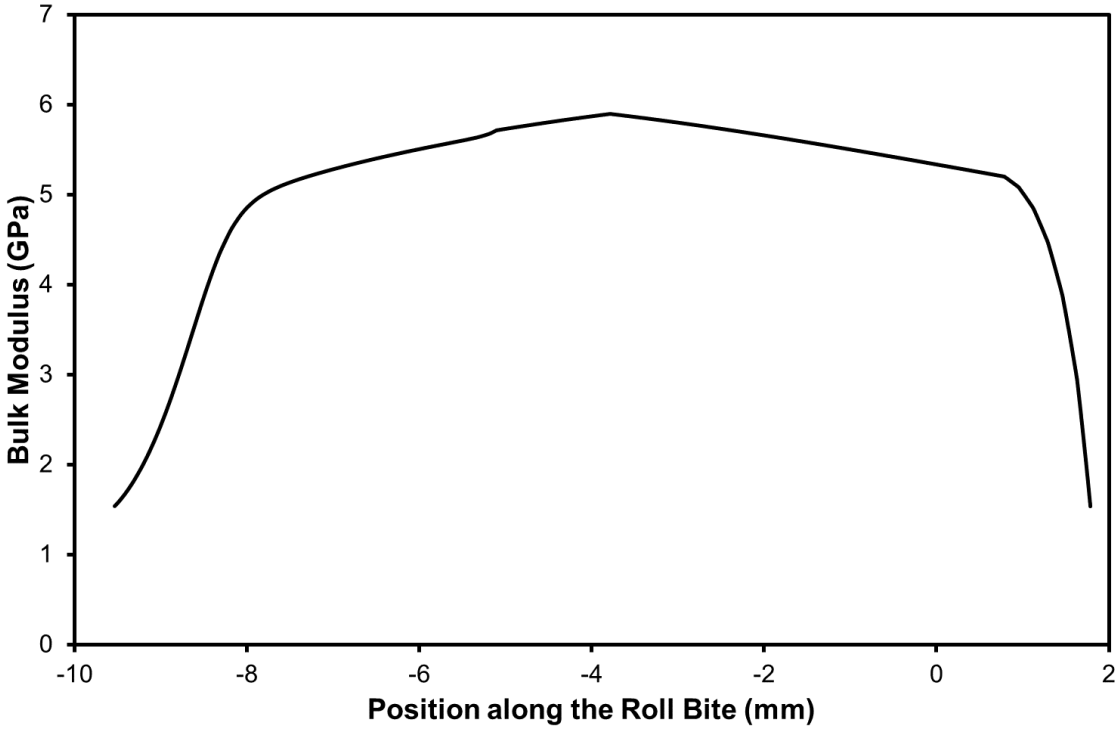

Figure 11.26: Bulk Modulus across the Roll Bite as calculated from Metalub Liquid Pressure.

11.3.5 Oil Film Thickness - Method

Once the bulk modulus profile across the roll bite had been calculated it was possible to determine a film thickness from the ultrasonic data using the spring model and the interface stiffness. The liquid stiffness $(K_l)_\sigma$, from both experimentation and computational modelling is given in Figure 11.27.

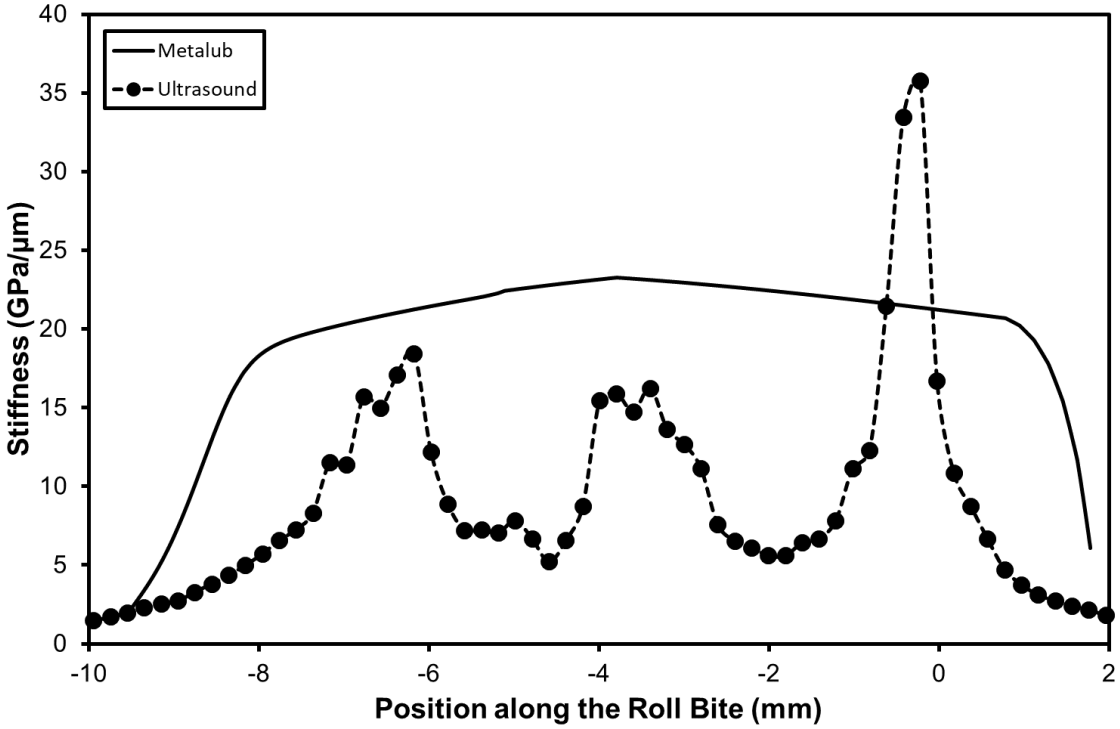

Figure 11.27: Liquid Stiffness $(K_l)_\sigma$ from Metalub and Ultrasonic Measurements.

Unlike in previous chapters no data has been cropped from the ultrasonic data in the regions where inference was encountered. Because of this the profile shows an unusual pattern, the cause of this is expected to be in part due to the interference, rather than an actual change in the fluid layer stiffness. The lubricant film thickness was computed from the stiffness and bulk modulus profiles are shown below, Figure 11.28.

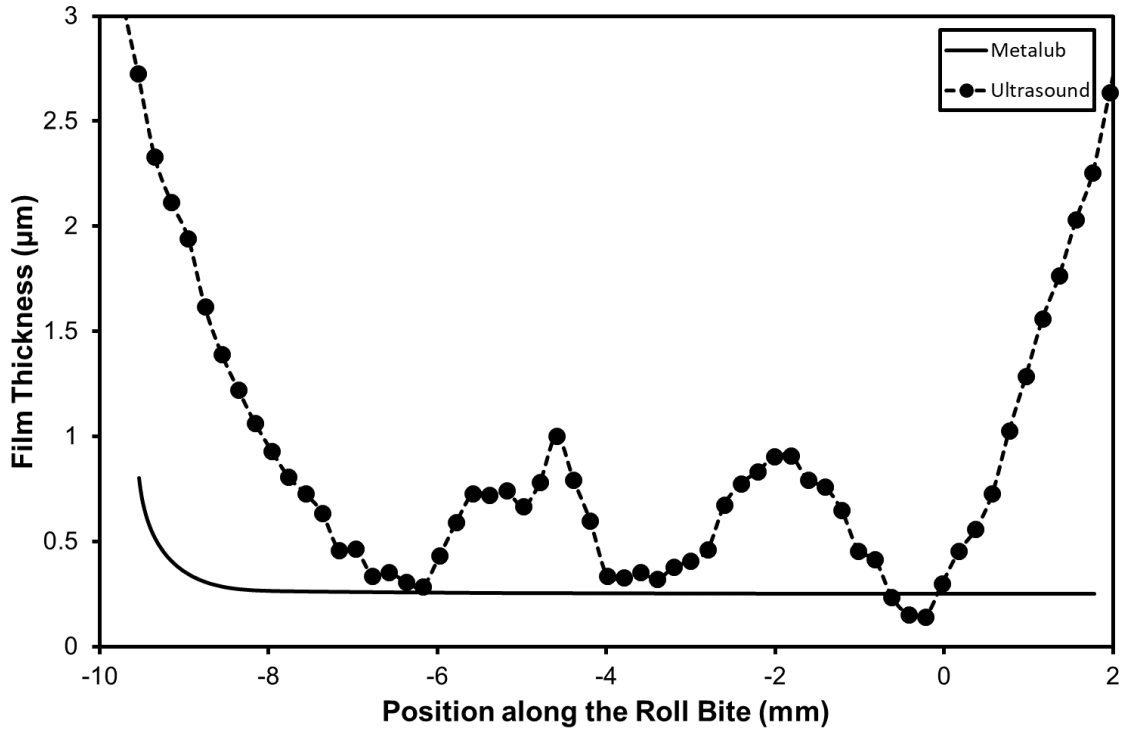

Figure 11.28: Lubricant Film Thickness from Metalub Modelling and Ultrasonic Measurements.

The Metalub results show how the lubricant film thickness drops across the roll bite not just due to the applied pressure. In fact, even when the lubricant pressure drops towards the exit of the roll bite, the lubricant film thickness still decreases. This is due to the elongation of the strip which results in a larger area for the lubricant to cover and therefore a thinner film for a given volume of lubricant.

The numerical and experimental results give stiffnesses and lubricant film thicknesses of the same order of magnitude. There is some inconsistency between the two datasets. Dips at -5mm and -2mm in the ultrasonic results for stiffness, and corresponding peaks in the film thickness, are not emulated in the simulated results. The reason for these is likely to be the aforementioned interference. In-between the film thickness peaks, at the geometrical centre of the roll bite, the simulation and test results have good agreement. For this reason only the results at the centre of the roll bite are considered in the following sections which compare the simulated and experimental results for a range of rolling speeds and strip elongations.

11.3.6 Oil Film Thickness – Rolling Velocity

The rolling conditions for a range of rolling speeds were simulated. These simulations emulated test case 12, the general conditions of which are given Table 11.8.

Test No.	Strip Thick. (mm)	Strip Material	Rolling Velocity, V_R (m/min)	Elong. (%)	Lubricant	Lubricant Temp. (°C)
12	0.75	ARCELOR06	25 to 1200	30%	HV2 100%	40

Table 11.8: Test Conditions for Test 12 varying Rolling Speed.

It was not possible to set all parameters directly in Metalub, some variables were calculated in the model based upon other input parameter values. Because of this it was not possible to exactly match these with the values recorded during actual testing, however the inputs were tuned to match as closely as practical. The values used for simulation and the equivalent experimental values are given in Table 11.9. The inlet and exit strip tensions used during the tests are respectively σ_1 = 114 MPa and σ_2 = 187 MPa.

Rolling Velocity, V_R (m/min)	Model Lubricant Temperature, T_{lub} (°C)	Experiment Exit Strip Temp., $T_{S,exit}$ (°C)	Rolling Load, F_{lam} (N/mm)		Forward Slip, S_F (%)	
			Model	Experiment	Model	Experiment
100	48	48.5	5004.2	5000	4.77	5.97
200	65	69	4912.8	4828	4.37	3.7
400	95	91.25	5154.5	5085	4.45	4
700	118	97	5138.8	5130	4.5	4.42
1200	155	106.5	5316	5317	4.7	4.06

Table 11.9: Experimental and Simulated Rolling Parameters for Varying Rolling Velocities.

As the velocity increases from 100m/min to 200 m/min, the rolling load and forward slip decreases. This is expected behaviour when lubricating with a pure oil. The higher the velocity, the more oil is dragged into the roll bite due to the hydrodynamic effect. Then, from 400m/min onwards the load increases which means there is an effect which counterbalances the impact of velocity.

It is likely this effect is due to the temperature. The strip temperature measured at the roll bite exit rises by 20°C from 200m/min to 400m/min. Then it keeps increasing to reach 106.5°C at a rolling speed of 1200m/min. The increase in temperature causes a decrease in oil viscosity. This reduces the effectiveness of the hydrodynamic effect at the roll bite entry. As less oil is entrained in the roll gap, the friction increases which results in the rise of the rolling load as seen from 200m/min to 1200m/min.

As described earlier it is necessary to iterate the model to ascertain a value for Coulomb's friction coefficient to match the rolling load and forward slip between the experimental and numerical results. The coefficient was adjusted to match the rolling load and forward slip at 100m/min and 400m/min with a constant lubricant temperature of 40°C and 65°C respectively. This led to a Coulomb friction coefficient of $\mu_C = 0.13$. Then using this value the lubricant temperature was adjusted for each velocity step in order to match the rolling load between experimental and numerical results. The resultant temperature level of the lubricant is of the same order of magnitude as the strip temperature measured at exit. The lubricant temperature values are larger than the measurements, this is realistic since the strip cools down slightly between the roll bite exit and the location where the strip measurement is achieved.

The consequence of matching the unkown numerical parameters with the experimental data is that the rolling load and forward slip are not predicted by the model. MetaLub can still give the lubricant film thickness profile in the roll bite for these the rolling load and forward slip values. The film thickness profiles output by Metalub for these test cases are shown in Figure 11.29. The actual rolling velocities achieved are stated, it should be noted that these vary marginally from the targeted values. These results confirm the expected trend drawn when observing the evolution of the experimental measurements with the temperature rise being sufficient to act against the velocity increase.

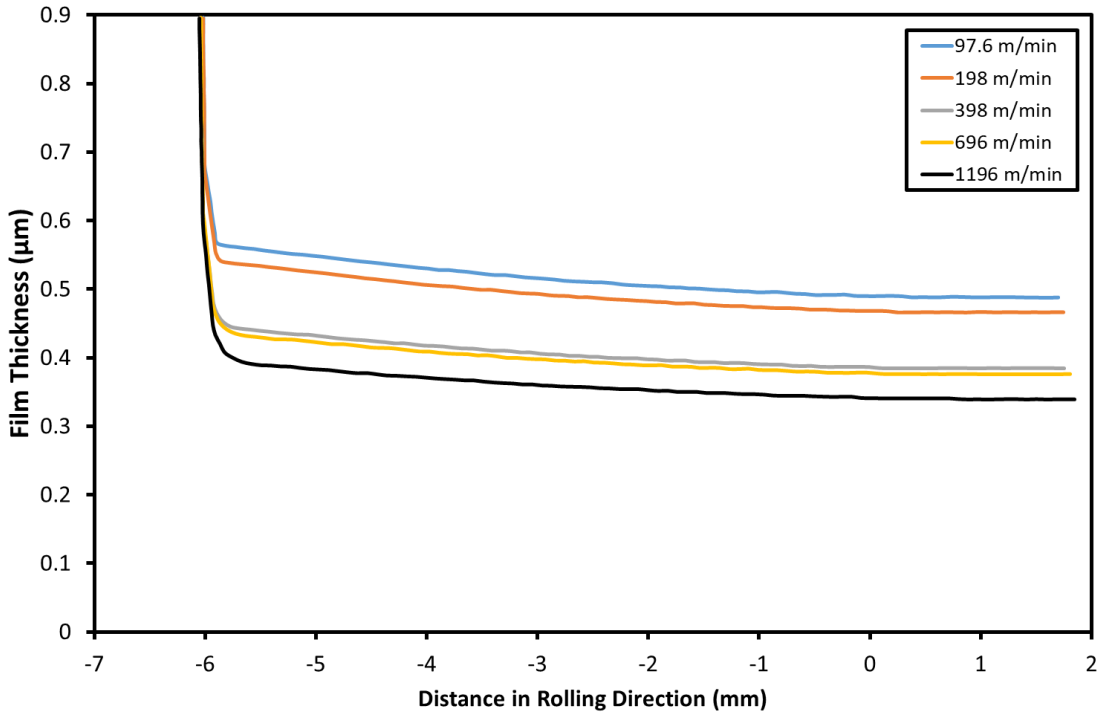

Figure 11.29: Lubricant Film Thickness Profiles from Modelling for a Range of Rolling Velocities.

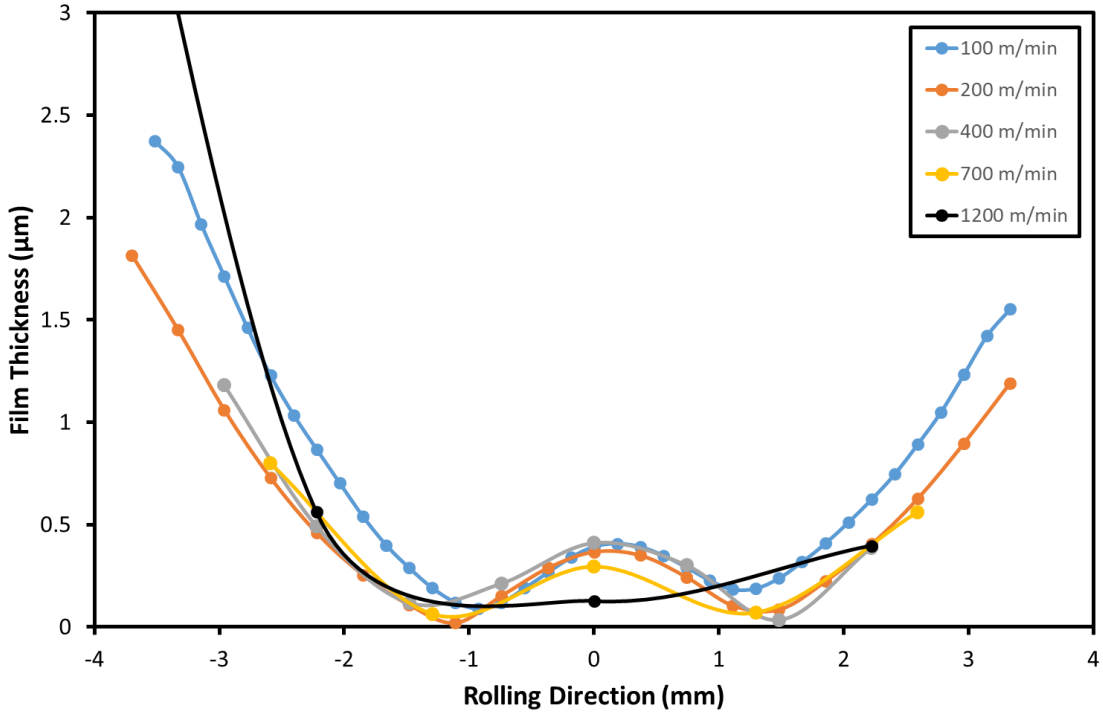

Figure 11.30: Ultrasonic Lubricant Film Thickness Profiles for a Range of Rolling Velocities.

The equivalent film thickness profiles measured ultrasonically are given in Figure 11.30. The values for film thickness at the centre of the roll bite for both the numerical and experimental results are presented in Figure 11.31.

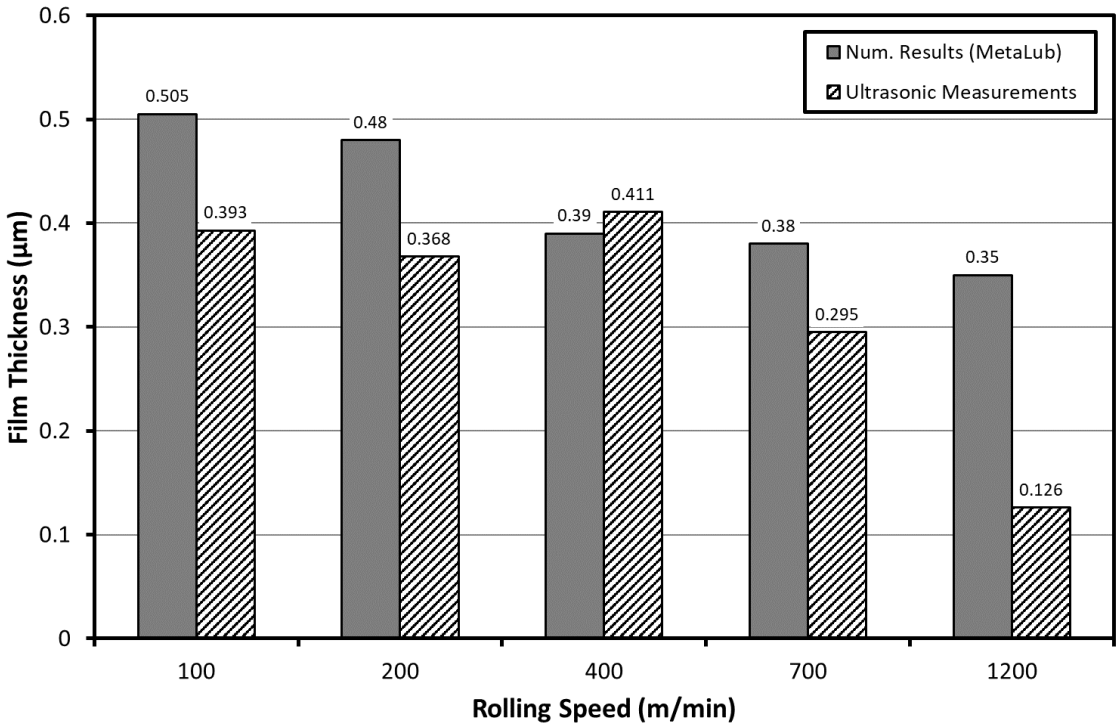

Figure 11.31: Lubricant Film Thickness at the Centre of the Roll Bite at Various Rolling Velocities for Numerical and Experimental Results.

The results show similar magnitudes, with the ultrasonic results giving generally slightly lower values. This may be due to the value of bulk modulus used, which will have been effected by the estimation of the lubricant pressure at the centre of the roll bite. Both sets of results show a downward trend in the lubricant film thickness with increased rolling velocity. At 1200m/min the drop off in the film thickness reported by the ultrasonic results is much greater than for the modelled results. There are a couple of possible explanations for this. The modelling results assume no starvation of the contact, and pure oil. These assumptions are less likely to hold true at higher rolling velocities. From the profile shown in Figure 11.30 it can be seen that very few points are recorded across the roll bite at 1200m/min, making inaccuracies likely.

11.3.7 Oil Film Thickness – Elongation

Finally the film thickness profiles for a range of strip elongations were modelled. These simulations emulated test case 7, the general conditions of which are given Table 11.10. The experimental rolling parameters for each case along with the exact Metalub simulation values are given in Table 11.11. Inlet and exit strip tensions are 38 and 119 MPa respectively.

As before Coulomb's friction coefficient was adjusted to match the rolling load and forward slip for each strip elongation level. The lubricant temperature used in the simulation was 60°C for stage 5% and 10% elongations, this was where the exit strip temperature was smaller than the applied oil temperature (60°C). For 20% elongation and above the lubricant temperature was set as the strip temperature measured at exit, to the nearest degree.

Test No.	Strip Thick. (mm)	Strip Material	Rolling Velocity, V_R (m/min)	Elong. (%)	Lubricant	Lubricant Temp. (°C)
7	2.8	DD14+Ti	100	5 to 40%	K2 100%	60

Table 11.10: Test Conditions for Test 7 varying Elongations.

Elong. (%)	Coulomb Friction Coeff., μ_c	Model Lubricant Temperature, T_{lub} (°C)	Experiment Exit Strip Temp., $T_{S,exit}$ (°C)	Rolling Load, F_{lam} (N/mm)		Forward Slip, S_F (%)	
				Model	Experiment	Model	Experiment
5	0.11	60	40	2527.9	2500	2.16	4.90
10	0.11	60	43.4	3396	3505	3.33	5.05
20	0.11	65	65.5	5300.3	5300	3.63	4.65
30	0.08	85	84.8	6446.2	6460	3.65	3.33
40	0.07	95	95.37	7316.2	7267	3.26	2.47

Table 11.11: Experimental and Simulated Rolling Parameters for Varying Elongations.

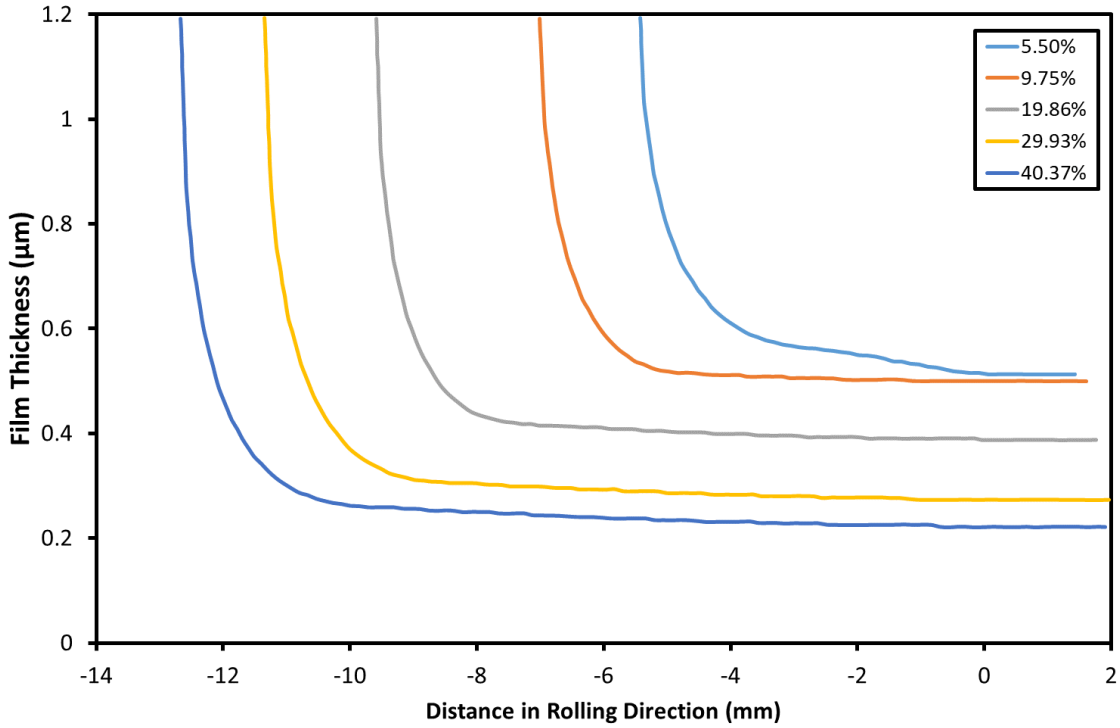

Figure 11.32: Lubricant Film Thickness Profiles from Modelling for a Range of Strip Elongations.

Using these parameters the lubricant film thickness profiles output by the model are plotted in Figure 11.32. A much greater difference in film thickness profile is observed due to elongation in comparison to the changes due to rolling velocity. The profiles also show the smaller contact lengths from smaller elongations. The equivalent ultrasonic profiles are shown in Figure 11.33.

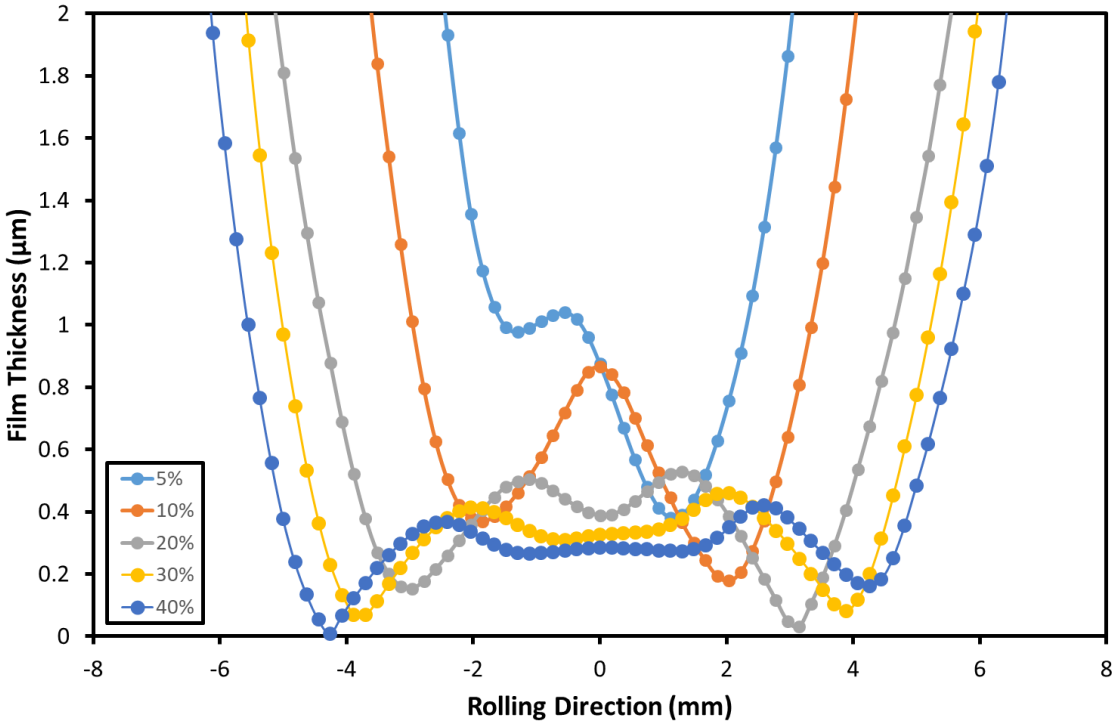

Figure 11.33: Ultrasonic Lubricant Film Thickness Profiles for a Range of Strip Elongations.

The values for film thickness at the centre of the roll bite for both the numerical and experimental results were extracted and are presented in Figure 11.34.

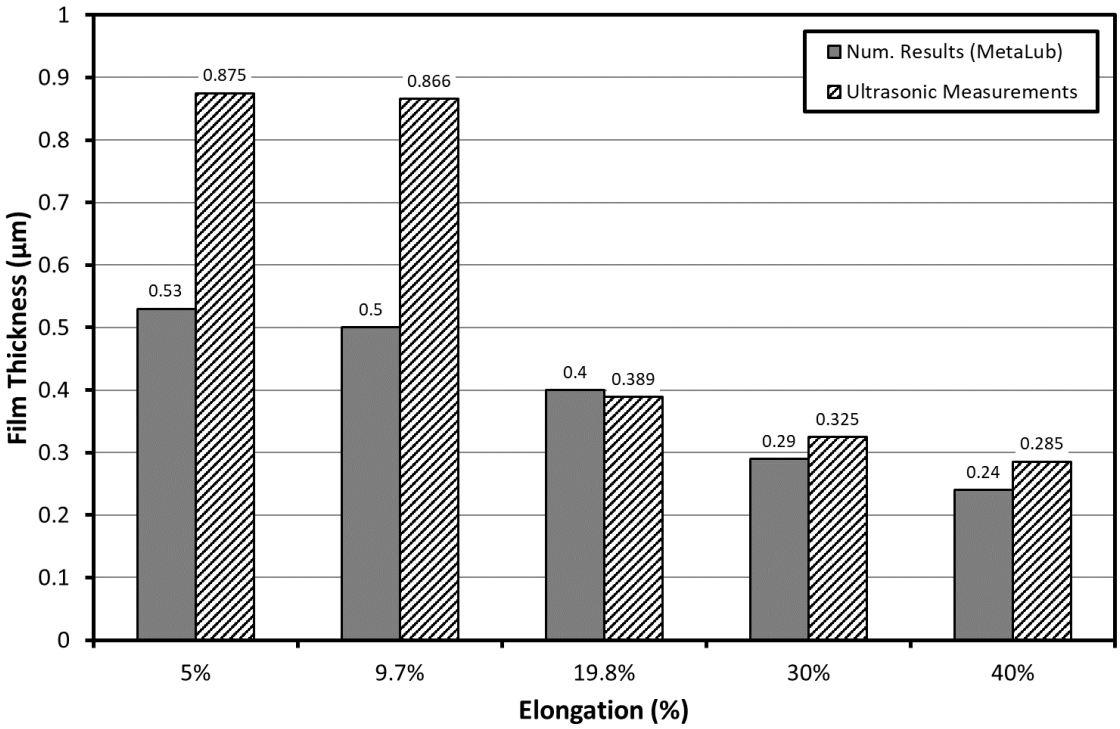

Figure 11.34: Lubricant Film Thickness at the Centre of the Roll Bite for Various Strip Elongations for Numerical and Experimental Results.

The agreement between the ultrasonic and numerical results for elongations ~20% and above is good. Both sets of data show a downward trend in the film thickness with increased elongation. However, it is clear from both the lubricant film thickness profiles, as well as the difference in

the central film thickness values from the simulated results, that the interference effecting the ultrasonic measurements prevents their use for smaller elongations.

11.4 Conclusions

In order to assess the validity of the ultrasonic methods presented in this thesis, it is important to compare their results with an independent measurement. However due to the harsh nature of cold rolling and the inaccessibility of the parts and interfaces of interest, there is no practical way of taking comparable measurements in-situ. Instead numerical models have been employed to simulate the conditions tested. The ultrasonic results have been compared to a number of different models dependent on the measurement being taken, which has yielded a number of useful insights.

Wave propagation modelling has shown the beam spread has a spherical pattern. Due to this the proportion of the wave reflecting from the contact and non-contact parts of the interface is not just a function of how much of the interface is in contact with the strip. Even in the half contact case it can be seen that the beam spread results in the reflection from the vacuum reaching the whole sensor face. The effect of this on a measurement is to smooth the measurement across the entry and exit of the roll bite.

Finite element modelling of the roll stress and deflection was completed using Metafor software. The resulting stress profiles show a strong similarity with the stress profiles calculated analytically. The average radial stress curves show good agreement in form and similar magnitudes at 10% and 20% elongations. At higher elongations the simulated results give a lower magnitude of the peak stress than those gained experimentally. Similarly, the deflection profile is similar for the simulated and measured results with both datasets showing larger elongations resulting in greater deflections. The similarity between the simulated and measured results indicate that the ultrasonic results have some validity both as a method for measuring surface deflection and internal roll stress.

Modelling of the roll strip interface was completed with Metalub software. There was strong correlation between the strip thickness results in both form and magnitude. The experimental results appear to give a reading for strip thickness before and after the roll bite that is in excess of the entry and exit strip thicknesses. It is proposed that the reason for this is the aforementioned beam spread. The ultrasonic method was also shown to yield a reliable measurement of the contact width, with a maximum relative difference between ultrasonic and numerical estimates of 3% occurring at the highest strip elongation (40%).

The pressure profile across the interface was calculated and split into its fluid and solid components. This fluid pressure was used to calculate the fluid viscosity and bulk modulus across the roll-bite.

There was some inconsistency between the numerical and experimental results for interface stiffness and lubricant film thickness. The results were of the same order of magnitude, however the ultrasonic results showed a variation, believed to be from interference discussed in previous chapters. In-between the areas of interference, at the geometrical centre of the roll bite, the simulation and test results gave good agreement. The central value was used for subsequent comparisons. Data was compared for various rolling speeds with the ultrasonic results giving generally slightly lower values than the simulated results. This may have been due to the value

of bulk modulus used, which was based upon a simplified estimation of the lubricant pressure at the centre of the roll bite. Both datasets showed a decrease in the lubricant film thickness with increased rolling velocity. This dropped off at the highest rolling velocity (1200m/min) with the change in the ultrasonic results more marked, possibly due to lubricant starvation of the contact.

The profiles for a range of strip elongations were also compared. The data showed a downward trend in the film thickness with increased elongation These compared well for larger elongations (≥20%). However, it was clear that the interference effecting the ultrasonic film thickness measurements prevents their use for smaller elongations.

12 Uncertainties, Conclusions and Future Work

This chapter starts by quantifying the uncertainties and measurement sensitivities relating to the work completed in this thesis. The purpose of this is to understand the accuracy of the measurements made so that their resolution and benefit can be assessed. This analysis does not just apply specifically to the measurements taken and reported in this work, but also aims to give a more general indication of the accuracies that could be expected if the measurements were more widely adopted. Following on from this, conclusions are drawn from the thesis as a whole and discussed. The chapter then concludes by recommending topics that would further research in this area.

The uncertainty analysis has been carried out using the methodology specified in "UKAS M3003:The Expression of Uncertainty and Confidence in Measurement" (UKAS) and the National Physical Laboratory's measurement good practice guide (Bell, 2001).

Firstly, it is worth noting that the terms *Error* and *Uncertainty* are commonly confused. Error is the difference between the measurement of a value, and the actual value. Uncertainty is the quantification of the doubt relating to a measurement (Bell, 2001). Any error whose value is not known is a source of uncertainty. Two numbers are needed in order to quantify an uncertainty. One is the width of the margin, or *interval*. The other is a *confidence level*. This states how sure it is that the 'true value' is within that margin.

In this analysis the contributions to uncertainty for each parameter are explored in turn and the resultant combined uncertainty for each parameter is presented. In order to appropriately compare uncertainties, it is important that they are expressed at the same confidence level. For this reason, uncertainties presented here are converted to a *Standard Uncertainty*, this is the uncertainty which covers one standard deviation, equivalent to a confidence interval of 68%.

To equate uncertainties from different sources sometimes it is necessary to apply an adjustment divisor. It is usual to assume that uncertainties taken from calibration certificates are normally distributed with a confidence interval of 95%. These must be divided by 2 to yield the uncertainty equivalent to one standard deviation. Similarly in order to gain the standard uncertainty for a rectangular or uniform distribution the half-width between the upper and lower limits is divided by √3 (Bell, 2001).

Expanded uncertainties at a confidence level of 99% are also given, this is calculated by multiplying the standard uncertainties by a coverage factor of 2.58 (the probability is assumed to have a normal distribution). Where uncertainties have been combined this has been done using summation in quadrature.

12.1 Time-of-Flight Uncertainty

In order to better understand the validity and significance of the measurements taken in the preceding chapters it is necessary to quantify the uncertainty of the results and methods used to yield them. For this purpose, it is useful to split the ultrasonic measurements in this thesis into two broad categories based upon their measurement technique. Measurements of material properties, roll stress, roll deflection and strip thickness utilise the ultrasonic Time-of-Flight (ToF) whereas contact width, interface stiffness and lubricant film thickness measurements are amplitude based.

ToF measurements have formed the basis of Non-Destructive Testing (NDT) thickness gauging and crack detection for many years. Because of this the uncertainty of ToF measurements have been widely studied elsewhere. Svilainis and Kitov offer an analysis looking into the effects on ToF estimation of digital signal processing (Svilainis & Kitov, Analysis of the Digital Signal Processing Influence on Time-of-Flight Estimation, 2010). Svilainis and Dumbrava also look into the influence of digitisation parameters (Svilainis & Dumbrava, The Time-of-Flight Estimation Accuracy versus Digitization Parameters, 2008) and interpolation techniques (Svilainis & Dumbrava, Analysis of the Interpolation Techniques for Time-of-Flight Estimation, 2008) including the zero-crossing method used in this thesis. For brevity their work has not been duplicated here. The methods used to capture the ToF are not particular to this work and therefore any errors in the ToF measurements are assumed to be of the same order as those seen in other applications.

12.2 Amplitude Uncertainty

Unlike with the ToF, the amplitude measurements taken are specific to this thesis, in particular the measurement of the lubricant film thickness. A more detailed analysis of these has therefore been completed.

12.2.1 Reflection Coefficient

The amplitude measurements rely on the reflection coefficient. The reflection coefficient measured during testing was calculated by comparing the live measurement to a reference value to give the proportion of returned signal. This is can be done in the time-domain by comparison of the peak-to-peak values of the reference and live signals. However for more robust results this testing adopts a method where the reference and live signals are first converted to the frequency domain. The amplitude at the reference peak frequency was then selected. By taking a reference any influence in terms of ultrasonic/electrical attenuation or conversion efficiencies are cancelled out. It in essence becomes a simple voltage measurement. The following are the key sources of error normally encountered with ultrasonic measurement systems.

Quantisation Error

Quantisation error is the result of the vertical resolution of the digitiser being used to capture the returned ultrasonic pulse. Digitiser resolution is commonly defined in bits. The *Least Significant Bit* (LSB) is the smallest interval that can be detected by the digitiser. A 12-bit digitizer, such as that used in the FMS100, has a LSB of 1/4096 = 2.4×10^{-4}. For a digitiser with a voltage range of +/-1 V this equates to 0.488 mV. This resolution is absolute and so will vary as a percentage of the digitised signal depending upon the signal amplitude. For low amplitude signals the percentage error is greater than higher amplitude. To reduce error due to quantisation the signal amplitude was matched though amplification to use as much of the digitiser range as possible.

ADC Internal Noise

The noise of an Analogue-to-Digital Convertor (ADC) is typically specified by the manufacturer of the chip, although different manufacturers state these errors in different ways, and have an incentive to overstate the accuracy of their devices by assuming idealised conditions not achievable in practical application. This makes accurate estimation of the actual ADC uncertainty difficult from the datasheet alone. It is assumed that the size of error due to the ADC internal noise will be negligible in comparison to the other sources of error when measuring the

reflection coefficient. The best approach to reduce the error from internal ADC noise is to ensure its temperature stability. Alternatively, a more precise digitiser can be used or the bandwidth can be reduced.

Time Skew

When signals from multiple sources are multiplexed rather than acquired simultaneously there is a time-skew error that occurs from switching between the channels. This is often called scan-clock or inter-channel skew. It is quoted as the aggregate speed for multiple channels. As the reflection coefficient is an amplitude not time based measurement it will be unaffected by this error.

Aliasing

Aliasing, also known as fold-over distortion, occurs when a frequency higher than the measurement bandwidth is present. This disrupts the results and can be seen as a fold-over in the frequency domain. To avoid this the signal is typically oversampled. Nyquist criterion theory dictates the lower bound for the sample rate for alias-free signal sampling. It is defined in terms of a function's bandwidth *B* and is stated as:

$$f_s = 2B \qquad 12.1$$

Where f_s is the constant sampling rate of the digitiser. This is based upon an infinite wave and so is not directly applicable to pulsed ultrasonics. Instead the number of oversamples used is selected heuristically and varies on application but the typical rule-of-thumb is 5 to 10 samples per period. The FMS100 has a 100 MHz digitiser and based upon this rule is suitable for frequencies up to 10 to 20 MHz without noticeable aliasing.

Radiated Noise (EMI)

Environmental noise from Electromagnetic (EM) sources can be induced in the conductors carrying the electrical signal. This is removed using the Faraday cage principle, electrically shielding cables and hardware. Co-axial cables were used for this purpose and the FMS100 was placed in a metal enclosure. The actual value of this will vary dependent upon the environment in which testing is completed as well as the cabling and hardware used. During slipring testing a signal to noise ratio (SNR) of 40:1 was measured.

Based upon the above errors an uncertainty analysis has been completed, as given in Table 12.1.

Source of Uncertainty	Value	Prob. Distribution	Divisor	Std. Uncertainty
Digitiser LSB ($2.4x10^{-4}$)	$1.2x10^{-4}$	Rectangular	√3	$6.928\ x10^{-5}$
Reference LSB ($2.4x10^{-4}$)	$1.2x10^{-4}$	Rectangular	√3	$6.928\ x10^{-5}$
Signal to Noise Ratio (40:1)	0.025	Normal	1	0.025
Combined Std. Uncertainty		Assumed Normal		0.025
Expanded Uncertainty (99%)		Assumed Normal		±0.065

Table 12.1: Reflection Coefficient Uncertainty Calculation.

The expanded reflection coefficient uncertainty of **±0.026**. This estimation assumes a simple peak-to-peak measurement. The uncertainty that occurs in converting the signal from the time to frequency domain has not been accounted for.

The above calculated only relies on a single measurement. In practice a minimum of 40 passes were averaged in each case. The reduction in signal uncertainty achieved through averaging is shown in Equation 12.2 (National Instuments, 2006).

$$\sigma_{SE} = \frac{\sigma}{\sqrt{N}} \qquad 12.2$$

Where σ_{SE} is the standard error, σ is the standard deviation and N is the number of averages. This yields the results given in Table 12.2.

Source of Uncertainty	Value	Prob. Distribution	Divisor	Std. Uncertainty
Digitiser LSB ($2.4x10^{-4}$)	$1.2x10^{-4}$	Rectangular	√3	$6.928\ x10^{-5}$
Reference LSB ($2.4x10^{-4}$)	$1.2x10^{-4}$	Rectangular	√3	$6.928\ x10^{-5}$
SNR (40:1) with 40 Averages	$3.953x10^{-3}$	Normal	1	$3.953x10^{-3}$
Combined Std. Uncertainty		Assumed Normal		$3.954x10^{-3}$
Expanded Uncertainty (99%)		Assumed Normal		±0.0102

Table 12.2: Reflection Coefficient Uncertainty Calculation assuming 40 Passes.

It can be seen that averaging has significantly reduced the expanded uncertainty of the reflection coefficient measurement to **±0.0102**.

From Table 12.2 it can still be seen that the SNR is still the primary source of uncertainty, being two orders of magnitude larger than the effect of the digitiser resolution in this case. Increasing the digitiser resolution is therefore unlikely to result in a noticeable improvement in the measurement of the reflection coefficient. Instead to yield better results attention should be paid to increasing the SNR. Dependent upon the source of the noise the simplest way to increase the SNR, is to simply increase the signal amplitude. The extent to which this can be done will be limited by the pulsing hardware capabilities, the digitiser range and the sensor characteristics. Alternatively, the noise the can reduced by careful system design and component selection, and through noise rejection techniques such as component shielding or signal filtering.

In addition to this it is shown that averaging is effective in reducing the measurement uncertainty. However practical implementation of large numbers of averages may be troublesome as it requires additional computational resources. It also assumes a time-invariant system and rolling is subject to many dynamic effects. Averaging can also result in a significant time-lag in the results, which can be problematic if the measurements are to be used in a feedback system.

12.2.2 Bulk Modulus

Bulk modulus is temperature and pressure dependent, and material specific. It must be evaluated for each material used in testing. A polynomial was fitted to the experimental data given in Figure 6.13 to give the relationship plotted in 6.15.

Errors will occur either due to poor measurement of this relationship, or due to poor estimation of temperature and/or pressure in the final application. It is assumed in this analysis that the uncertainties in profiling the fluid are negligible, as such only the uncertainties due to measurement of temperature and pressure are considered.

The temperature of the lubricant as it was applied during rolling was measured. Any heating effects due to rolling itself have been ignored. There was no instrumentation installed in the roll

for testing to take a direct measurement of the pressure in the rolling interface. Numerical values for pressure were used however without a direct measurement of pressure, it is not possible to evaluate the magnitude of the error due to this. Pressure measurement has been demonstrated in previous studies using a pin technique, first implemented by Siebel and Lueg (Siebel & Lueg, 1933). It has been assumed achievable uncertainties in the pressure measurements will be the same as those for typical commercial-off-the-shelf data acquisition hardware. Uncertainties based upon typical devices for pressure (±25 mbar) (Omega) and temperature (±0.75°C) (Pico Technology) measurement have been selected. Uncertainties resulting from these have been converted to their bulk modulus equivalents using the relationship in Equation 6.5 for nominal values of temperature and pressure of 50°C and 0 Pa. The uncertainty calculation is given in Table 12.3.

Source of Uncertainty	Value	Prob. Distribution	Divisor	Std. Uncertainty
Temperature (±0.75 ° C)	±5.498 MPa	Normal	2	2.746 MPa
Pressure (±2.5 kPa)	±31.37 kPa	Normal	2	15.69 kPa
Combined Std. Uncertainty		Assumed Normal		2.746 MPa
Expanded Uncertainty (99%)		Assumed Normal		±7.085 MPa

Table 12.3: Bulk Modulus Uncertainty Calculation.

The expanded uncertainty of the bulk modulus (±7.084 MPa) is very small compared to the nominal value. This is likely to be an optimistic estimate because the pressure reading is assumed to be very accurate, no uncertainty due to the liquid profiling has been accounted for and heating effects have been ignored. Also measurement of the lubricant temperature and pressure in situ is required to assess this uncertainty.

12.2.3 Acoustic Impedance

The acoustic impedance, *z*, of the roll and strip is measured from the speed of sound and density of a material using the following relationship:

$$z = \rho c \qquad 12.4$$

Where ρ and c are the density and acoustic velocity of the material respectively. As there is a different speed of sound for longitudinal and shear waves, there are also different acoustic impedances for each. Uncertainty of density measurements are typically around 0.2-0.5% (Ensminger & Bond, Ultrasonics: Fundamentals, Technologies, and Applications, 2011, p. 256). A value of ±0.25% has been used for the following calculations. Previous work has shown that an uncertainty in the speed of sound measurement of ±0.5 m/s is achievable. Based on the measurements in Table 8.5 steel with a nominal density of 7794 kg/m^3, and a longitudinal and shear speed of sound of 5992.11 m/s and 3247.72 m/s respectively has been used for the longitudinal and shear acoustic impedance calculations given in Table 12.4 and Table 12.5.

Source of Uncertainty	Value	Prob. Distribution	Divisor	Std. Uncertainty
Density (±0.25%)	±116.8 kRayl	Normal	2	58.38 kRayl
Speed of Sound (±0.5m/s)	±3.897 kRayl	Normal	2	1.949 kRayl
Combined Std. Uncertainty		Assumed Normal		58.41 kRayl
Expanded Uncertainty (99%)		Assumed Normal		±150.7 kRayl

Table 12.4: Longitudinal Acoustic Impedance Uncertainty Calculation.

Source of Uncertainty	Value	Prob. Distribution	Divisor	Std. Uncertainty
Density (±0.25%)	±63.28 kRayl	Normal	2	31.64 kRayl
Speed of Sound (±0.5m/s)	±3.897 kRayl	Normal	2	1.949 kRayl
Combined Std. Uncertainty		Assumed Normal		31.70 kRayl
Expanded Uncertainty (99%)		Assumed Normal		±81.79 kRayl

Table 12.5: Shear Acoustic Impedance Uncertainty Calculation.

The expanded uncertainty calculated is less than 0.33% of the nominal acoustic impedance in both cases. The variation in density and speed of sound between different materials, even different types of steel, means that for minimum error these values should be measured for each material used.

12.2.4 Frequency

The frequency used in the calculation comes from the point selected on the frequency spectrum used for the reflection coefficient measurement. The resolution of the FFT used to convert from time to frequency domain is defined by the number of points taken in the time domain and the time-step of the digitiser. This can be increased by recording a longer period of time, or increasing the digitizer resolution. Alternatively, the recorded signal can be padded with zero data, this has the effect of interpolating the frequency data. For the FMS100, which has a timestep of 10ns, 1000 datapoints either captured of padded, results in a frequency resolution of 100kHz. This has been used for the uncertainty analysis given in Table 12.6.

Source of Uncertainty	Value	Prob. Distribution	Divisor	Std. Uncertainty
FFT Resolution (100kHz)	50kHz	Rectangular	√3	28kHz
Combined Std. Uncertainty		Assumed Normal		28kHz
Expanded Uncertainty (99%)		Assumed Normal		±74 kHz

Table 12.6: Frequency Uncertainty Calculation.

12.2.5 Film Thickness Model

The uncertainties calculated for each of the model variables in the preceding analysis will now be combined to give an overall uncertainty for the model given in Equation 3.88. The conversion of each parameter uncertainty to equivalent film thickness uncertainty has been done using the nominal model values listed in Table 12.7.

Bulk Modulus, B	1.57 GPa
Frequency, f	10 MHz
Long. Acoustic Impedance, z_L	46.7 MRayls
Shear Acoustic Impedance, z_S	25.3 MRayls
Long. Reflection Coefficient, R_L	0.5
Shear Reflection Coefficient, R_S	0.5
Film Thickness, h	1.805 µm

Table 12.7: Nominal Model Values.

These uncertainties for a single measurement are combined in Table 12.8.

Source of Uncertainty	Value	Prob. Distribution	Divisor	Std. Uncertainty
B (±7.085 MPa)	±8.1 nm	Normal	1	±8.1 nm
R_L (±0.065)	±375.4 nm	Normal	1	±375.4 nm
R_S (±0.065)	±248.4 nm	Normal	1	±248.4 nm
z_L (±150.7 kRayl)	±17.0 nm	Normal	1	±17.0 nm
z_S (±81.79 kRayl)	±11.2 nm	Normal	1	±11.2 nm
Freq. (±74 kHz)	±13.4 nm	Normal	1	±13.4 nm
Expanded Uncertainty (99%)		**Assumed Normal**		**±450.9 nm**

Table 12.8: Model Uncertainty Calculation.

The uncertainties when averaging 40 passes, as was done during testing, are given in Table 12.9.

Source of Uncertainty	Value	Prob. Distribution	Divisor	Std. Uncertainty
B (±7.085 MPa)	±8.1 nm	Normal	1	±8.1 nm
R_L (±0.0102)	±144.0 nm	Normal	1	±144.0 nm
R_S (±0.0102)	±94.8 nm	Normal	1	±94.8 nm
z_L (±150.7 kRayl)	±17.0 nm	Normal	1	±17.0 nm
z_S (±81.79 kRayl)	±11.2 nm	Normal	1	±11.2 nm
Freq. (±74 kHz)	±13.4 nm	Normal	1	±13.4 nm
Expanded Uncertainty (99%)		**Assumed Normal**		**±174.3 nm**

Table 12.9: Model Uncertainty Calculation assuming 40 Passes.

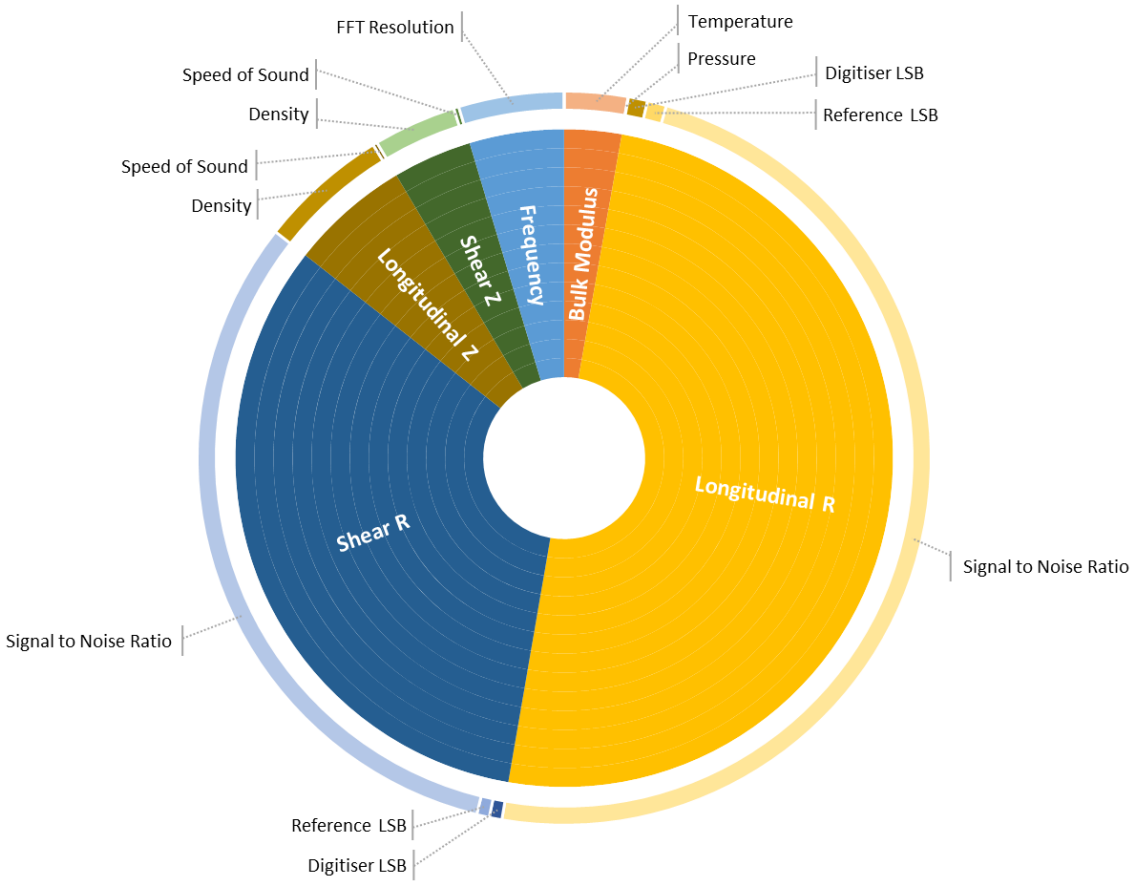

Figure 12.1: Contributions to Model Uncertainty.

The nominal values used therefore give a calculated film thickness of **1.805 µm ±0.451 µm** with a 99% certainty for a single reading. This is the equivalent of ±24.98% of the mean value. By

averaging 40 passes this is reduced to **1.805 μm ±0.174 μm** which is ±9.64% of the mean value with a 99% certainty. The breakdown of components that contribute to the uncertainty is shown in Figure 12.1. This clearly shows that the largest source of uncertainty is in the measurement of the reflection coefficient for both longitudinal and shear, and specifically the SNR. This therefore offers the largest area for improvement.

While it has been possible to quantify and account for a number of key sources of uncertainty, it is recognised that a number of assumptions have been made, the effects of which have not been enumerated. These include the effect of heating on the lubricant in the roll bite and the lack of in-situ pressure measurement. Additionally, the film thickness model itself relies on a number of simplifications including the modelling of the interface as a simple spring and the relationship used to convert between normal and shear stress.

12.3 Film Thickness Model Sensitivity

Model sensitivity analysis is primarily concerned with quantifying the robustness of a model to uncertainty. This is achieved by identifying the model inputs where uncertainty will cause a significant uncertainty in the model output. This helps to focus work on reducing uncertainty of the variables that will have the greatest effect on the final measurement.

A number of approaches are available to analyse the sensitivity of a model (Hamby, 1995), for this study a One-at-a-Time sensitivity analysis has been performed. Here nominal values are selected for each input, then one input at a time is varied. The effect on the model output, in this case the film thickness, is studied. This allows the effect of each variable to be presented independently. However, it cannot detect interactions between the model inputs. The nominal values used were those stated in Table 12.7. The only exception being that the longitudinal reflection coefficient was set to unity when the sensitivity of the shear acoustic impedance and reflection coefficient was calculated, and the same vice-versa with the shear reflection coefficient set to unity for the calculation of the longitudinal sensitivities. This was done as it was already known that for a given film thickness a relationship exists between the shear and longitudinal stiffness's. Setting the respective R values to unity removes their influence when calculating their counterpart values.

Equation 3.88 will be studied by this method. We can see from this Equation there are six inputs to the model, Layer Bulk Modulus, Wave Frequency, Longitudinal and Shear Acoustic Impedances and the Longitudinal and Shear Reflection Coefficients. To show the model sensitivity the relative change in the calculated film thickness for a relative change in each variable has been calculated. This has been done numerically with results plotted in Figure 12.2 to Figure 12.5. The results for the longitudinal and shear cases of both the acoustic impedance and reflection coefficient were the same, so only a single plot has been included for each of these.

The sensitivity of the input variables only needs to be considered across the range of values likely to be seen during testing. As material properties both the Bulk Modulus and Acoustic Impedance will remain fixed throughout a study. Only the sensitivity of values close to the nominal are of interest, this will show how the measurement error associated with these variables will affect the final result. The reflection coefficient will vary with film thickness and the frequency used

may vary based upon sensor characteristics and data processing selections. Therefore, these need to be considered across a much larger range.

The gradient of these plots tells us the factor by which a change in the input variable results in a change in the output variable. This is referred to as the model sensitivity factor. This value has been extracted using numerical differentiation. It is useful to define values for the sensitivity factor which are considered sensitive and insensitive. The selection of such values is subjective, however heuristically these are commonly selected as <5 for insensitivity and >10 for sensitivity. Values between these are considered neither sensitive or insensitive.

For the bulk modulus it is clear from that the gradient has a value of 1 for the values plotted in Figure 12.2. In fact, from a cursory inspection of Equation 3.88 it is clear that because it is in the numerator of the equation any relative change in *B* will always result in an equivalent relative change in the calculated film thickness. The model is therefore always insensitive to the Bulk Modulus. The sensitivity to the Acoustic Impedance does vary, however around the nominal value (±10%) again this approximates to a value of -1, meaning the model is also insensitive to the Acoustic Impedance.

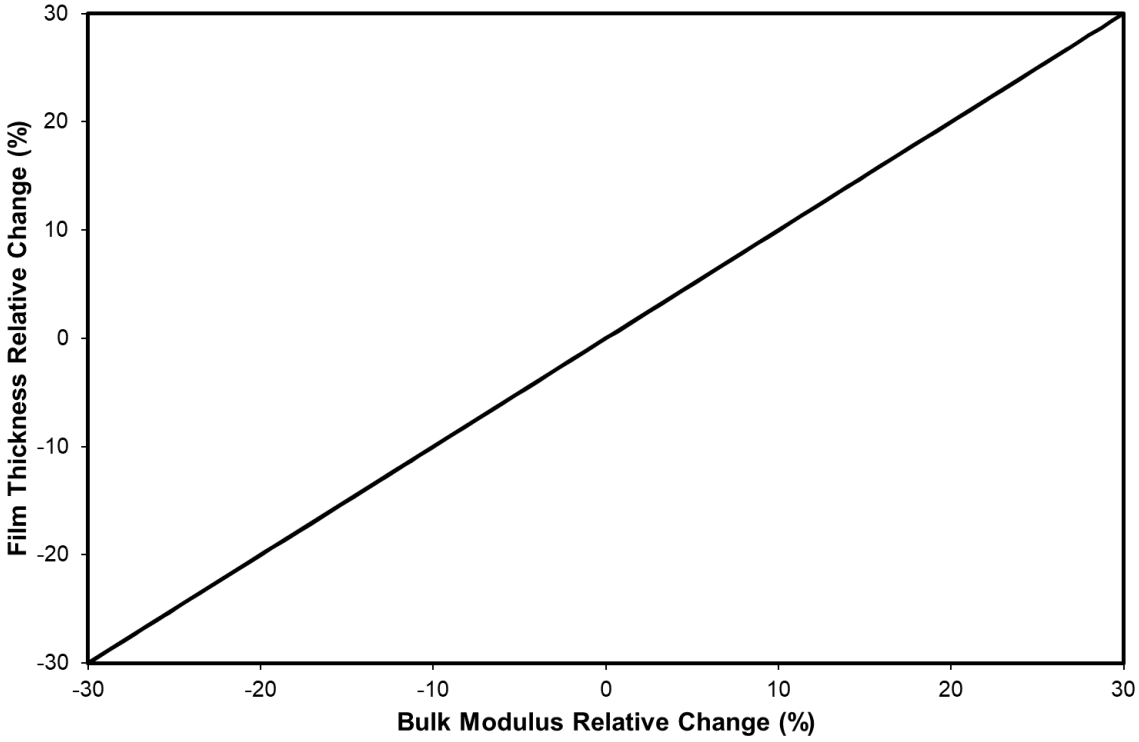

Figure 12.2: Film Thickness Model Sensitivity to Bulk Modulus.

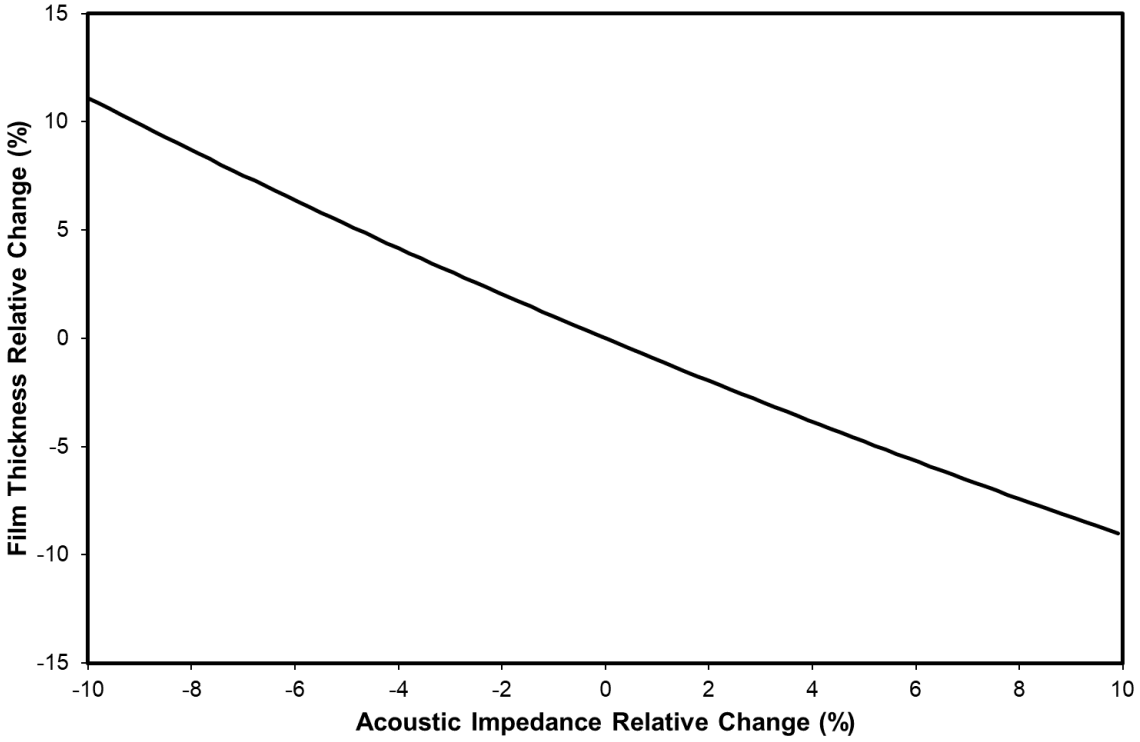

Figure 12.3: Film Thickness Model Sensitivity to Acoustic Impedance, applies to both Longitudinal and Shear.

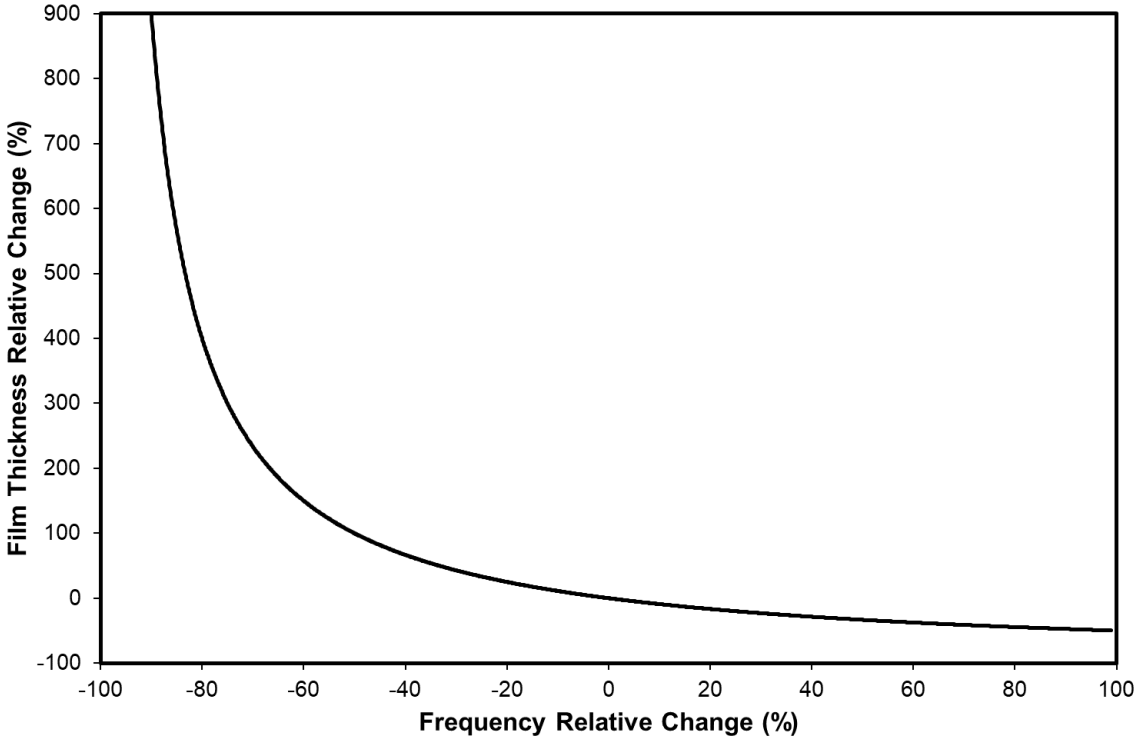

Figure 12.4: Film Thickness Model Sensitivity to Frequency.

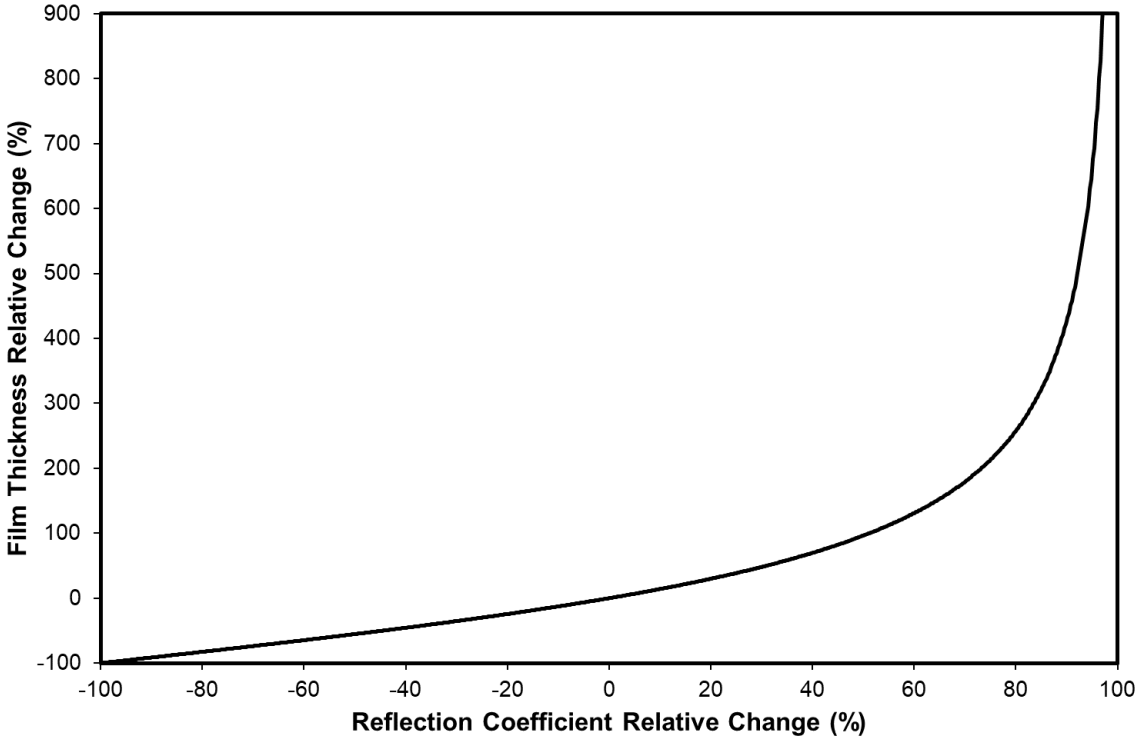

Figure 12.5: Film Thickness Model Sensitivity to Reflection Coefficient, applies to both Longitudinal and Shear.

As the Reflection Coefficient and Frequency show a changing sensitivity they have been studied in slightly greater detail. The sensitivity factor against the absolute value for each of these is shown in Figure 12.6 and Figure 12.7.

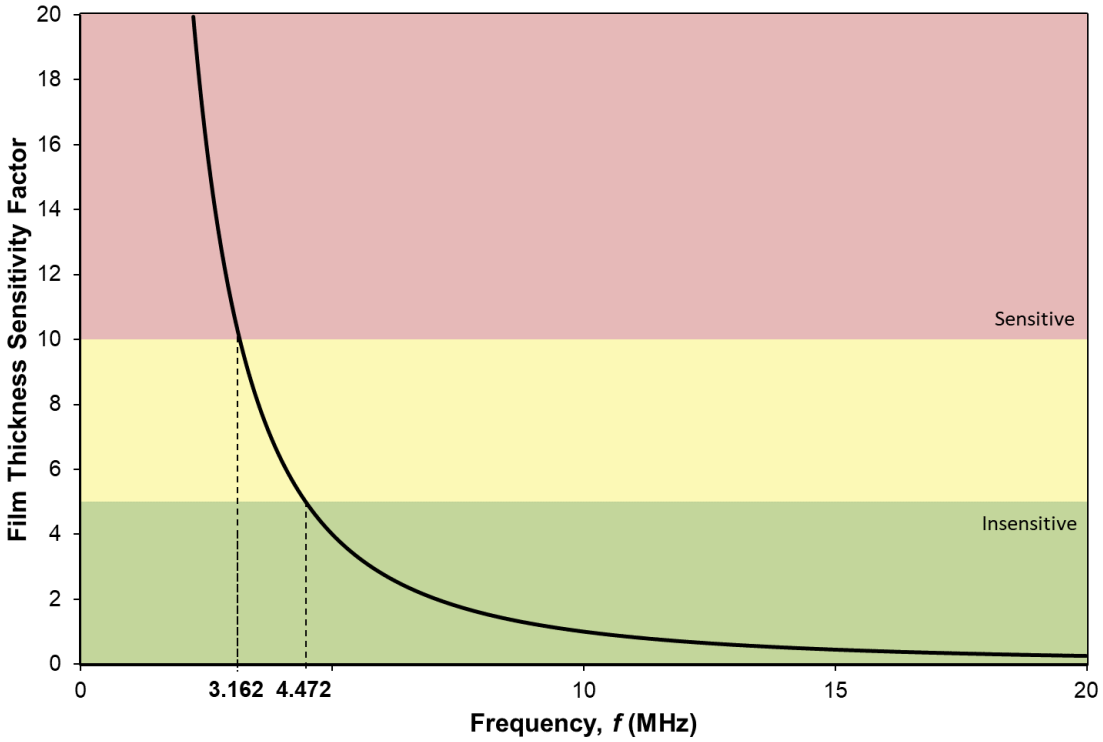

Figure 12.6: Model Sensitivity Factor against Frequency.

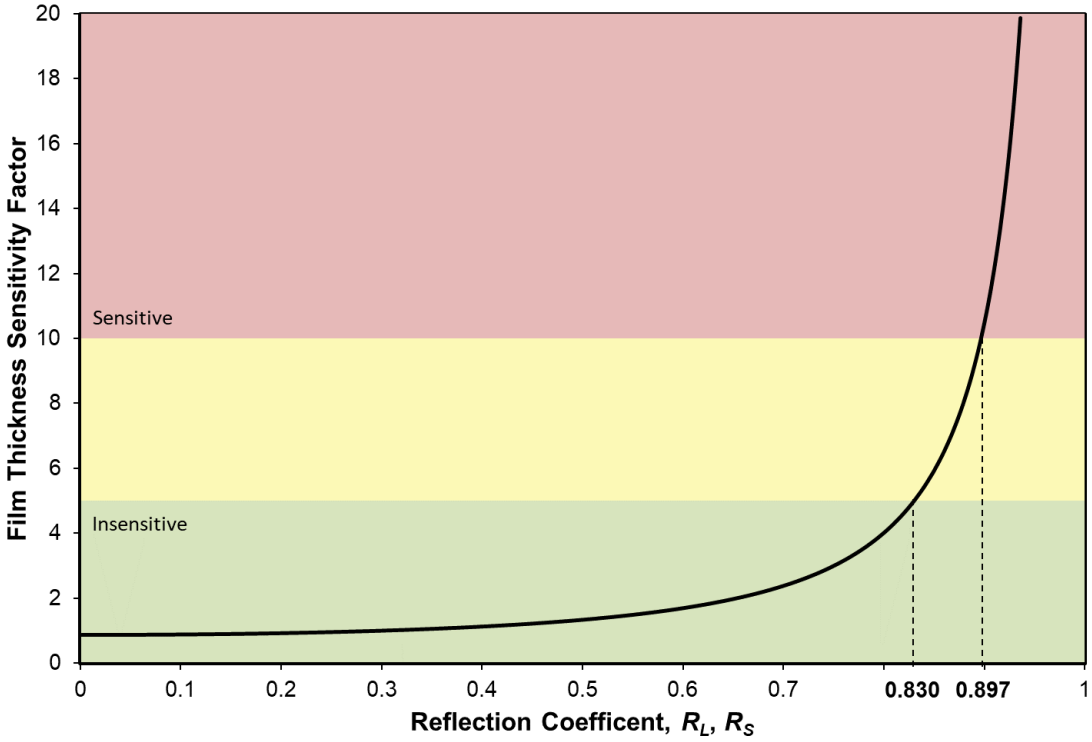

Figure 12.7: Model Sensitivity Factor against Reflection Coefficient, applies to both Longitudinal and Shear.

For frequency the plot shows the model becomes sensitive a values below **3.162 MHz** and is insensitive above **4.472 MHz**. It should be noted that the digitisation rate is fixed across the frequency range. Therefore, at lower frequencies the waveform is digitised in more detail due to the larger wavelength. This is likely to at least partially counteract the effect of the model sensitivity at lower frequencies. This highlights to need to select the transducer frequency based upon the expected range of film thicknesses being measured.

It is possible for the reflection coefficient to assume any value across the range depending upon the interface conditions being measured. Figure 12.7 shows that model becomes sensitive for values above **0.897**, which would be observed for thicker interfacial films, and insensitive below **0.830**. Careful consideration therefore needs to be given to reduce uncertainty in the reflection coefficient. Additionally, as reflection coefficient is frequency dependant, the sensor frequency should be selected based upon the expected film thickness to result in measurements of reflection coefficient below 0.897. Figure 12.8 shows the film thicknesses measurable by different frequency transducers, based upon an upper measurement limit of R = 0.897 and a lower limit of R = 0.1. This plot assumes a continuous fluid film, with no solid contact (R_S = 1).

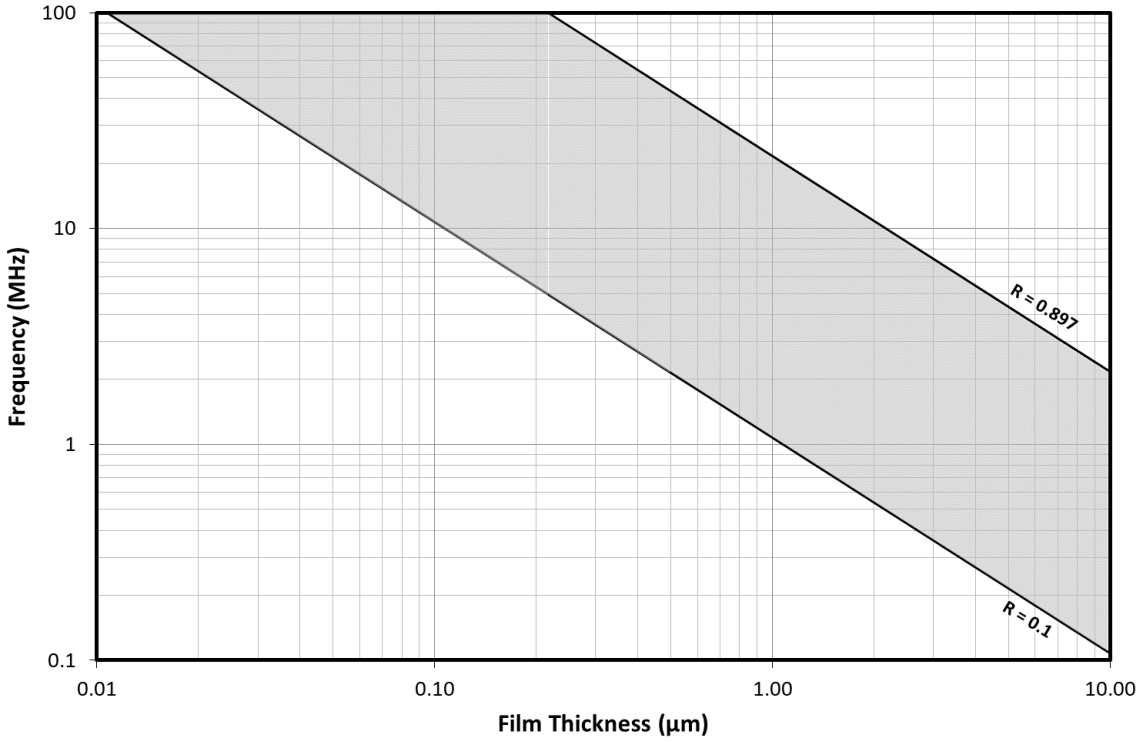

Figure 12.8: Sensor Frequencies against Film Thickness for R = 0.1 and 0.897. The shaded area indicates film thickness measureable with acceptable sensor sensitivity.

This above plot would require revision in the case of partial solid-solid contact. Although the sensitivity of the lubricant film component of the interface would remain unchanged, the presence of the solid component of the interface would alter the overall reflection coefficient for such an interface. This will be dependent on the material properties of the solid faces and the asperity shapes, which would influence the stiffness of the interface. This would need to be reconsidered for each new material and surface roughness profile.

The sensitivity analysis shows that the model is insensitive to errors in the material properties used. It is also insensitive to the frequency of ultrasound used, within the expected range of values. It is however sensitive to the reflection coefficient measured, particularly for higher values (>0.897).

Of all of the model inputs the uncertainty analysis showed that the largest uncertainty is in the value for the reflection coefficient. The combination of high uncertainty and sensitivity means that work should concentrate on reducing the errors in the reflection coefficient measurement.

Averaging is one approach that could be implemented dependent upon the application. Many errors can also be removed or reduced by way of calibration. Where possible a calibration of the method could be performed with an experimental setup as close to the final application as possible including identical materials, sensors, lubricants and processing techniques. This would yield the reflection coefficient against film thickness relationship and remove many of the sources of error.

12.4 Conclusions

Although detailed discussion of the findings reached in this thesis has been included in each chapter, a summary of the key results and conclusions is given below.

12.4.1 Theory

A number of contributions to the theory covering the measurement of cold rolling contacts using ultrasound have been made. A model for the ultrasonic response from a mixed mode interface has been developed. This model is a modified version of the spring model for thin embedded layers and separates the stiffness of the interface between the solid and liquid components. These stiffnesses are related to the longitudinal and shear reflection coefficients which can be measured using longitudinal and shear waves. The acoustic impedance of the materials either side of the interface, along with the bulk modulus of the interfacial film are required. This model also requires a conversion from the shear stiffness measured by the shear waves to normal stiffness. A commonly used model developed by Mindlin (Mindlin, 1949) was used, however this does represent a significant simplification compared to a real interface.

The theory behind the ultrasonic measurement of the acoustoelastic effect has been further developed. The effect on the change in time-of-flight of an ultrasonic pulse with applied pressure has been split into the contributions due to component deflection, elasticity change and density change. This density effect had not been considered in previous works. It was found that the proportion of each of these aspects remains the same for a given material, and is dependent on the particular material properties.

A numerical model of the effect of stress induced refraction was developed to aid the understanding of ultrasonic propagation in materials subjected to high pressure contacts, such as those seen in cold rolling. The stress field used in this model was calculated for a stick-slip contact. The results from this for conditions representative of cold rolling show a significant bending of the ultrasonic beam around the contact. In particular areas of high acoustic velocity gradient are seen at the entry and exit of the roll bite which result in significant deflection of the ultrasonic beam. The wave propagation modelling shows that the signals received by the sensor are subject to ultrasonic interference from the deflected beams in the entry and exit zones.

12.4.2 Implementation

A small hand fed pilot mill and a larger semi-industrial mill, both two-high (work rolls only), were successfully instrumented. The implementation of the proposed measurements onto these mills presented a number of technical challenges. Two similar approaches were trialled, one based upon inserting an instrumented plug into the roll and the other involved instrumenting a roll segment which was then attached to the roll. The plug approach was successfully used on both the pilot and semi-industrial pilot mills and attempted on an industrial mill roll. The roll segment approach was only attempted on the semi-industrial pilot mill. Both techniques were invasive, requiring modification of the roll and rolling surface. This makes these approaches difficult to retro fit, and as they both marked the strip they are unlikely to be unacceptable in an industrial setting.

Plugs of various sizes were used based upon the roll diameter, and they were variously secured using either a press fit, a transition fit and retaining compound, or an interference fit achieved by freeze shrinking with liquid nitrogen. The press and transition fit plugs were successful, demonstrating their viability for research applications. The sensors on the freeze-shrink plug survived the process, however the cabling failed on multiple occasions, further design work is therefore required before this approach could be adopted.

The roll segment approach involved removing a minor segment of the roll and replacing it with a similarly shaped instrumented component. This approach was a lower risk from an instrumentation perspective as, unlike with the plugs, the component could be removed and re-instrumented or replaced if required. It was also possible to place multiple sensors across the width of the roll bite. Unfortunately, the roll adapted for this approach demonstrated an imbalance which resulted in oscillations during rolling. These were especially problematic when rolling at higher speeds. The results obtained using this technique were therefore limited and superseded by data gained using the plug techniques.

Simple piezoceramic sensors, both longitudinal and shear polarised, were selected for testing. The method of instrumentation gave good sensor responses with reasonable bandwidth and pulse lengths. The bonding method was consistent with a good repeatability between similar sensors and robustness throughout the testing. During preliminary testing on the pilot mill the sensor aspect ratio was observed to be significant to the quality of the results obtained. Shear sensors with a low aspect ratio (1:1) demonstrated multimode resonance which made it difficult to determine measurements solely due to the rolling interface. Therefore, only sensors with a minimum aspect ratio of 10:1 were used.

The smallest sensors that respected the required aspect ratio were selected to reduce the measurement spot size. The beam intensity profile for the sensors was calculated and this showed that the measurement interface was outside of the sensor nearfield, but did show some beam spread. Wave propagation modelling was completed and showed significant beam spread with a near circular wave front due to the small transducer width. It was also demonstrated that this beam spread may confuse results when the ultrasonic beam is reflecting from a partially covered interface.

A data acquisition system was assembled and assessed for suitability. Ultrasonic pulsing hardware was selected to provide adequate pulse characteristics including pulse voltage, width and repetition rates as well as signal conditioning such as filtering and amplification. A high speed digitiser with 12-bit resolution was used. The ultrasonic signals gained showed a good amplitude and bandwidth. It was possible to capture a significant number of datapoints across the roll bite at lower rolling speeds, however the resolution dropped significantly for higher rolling speed, limited by the repetition rate of the ultrasonic hardware used and time-of-flight due to the plug length. The required cabling and slip ring where assessed for their effect on the ultrasonic signal. Cable attenuation and slip ring noise were quantified and found to be acceptable. Bespoke control software was written to control hardware and capture data.

12.4.3 Supporting and Preliminary Testing

The various measurement models proposed required information relating to the material properties of the rolling system. Testing was completed to evaluate these parameters.

Data for the lubricant speed of sound against temperature and pressure was used to estimate the bulk modulus. This value was used in the calculation of the lubricant film. This testing also included a crude estimate of lubricant solidification pressure. This was found to be within the upper range of rolling pressures expected during rolling and so may have had an influence on the results from testing.

The sensor responses against temperature were profiled. There was found to be some change in amplitude across the range of temperatures expected, however this was not expected to significantly affect the operation of the sensors. For testing a new reflection coefficient reference was taken for each test case when the roll was at temperature. This should have negated any change in the amplitude measurements taken.

Testing was completed to measure the longitudinal and shear acoustoelastic coefficients of the plug material. This testing also defined the ratio of the contributions from the density, deflection and elasticity effects. This compared well with values found in previous studies.

To validate the ultrasonic thin film measurement techniques described in this thesis an experiment was completed that aimed to validate the techniques against a calibrated laser interferometer and a capacitive displacement sensor. The testing was completed on a continuous fluid film with no asperity contact. The results from the film resonance method showed a very strong correlation to the calibrated devices. The accuracy appeared unaffected either by the liquid used or the surface finishes tested. This also shows robustness in the method. Only longitudinal sensors were used in this testing, so it was not possible to measure the mixed regime. It was therefore demonstrated that the minimum measureable film for the spring model was limited to the point of asperity contact between the opposing faces.

Pilot mill testing was completed with the aim of proving and de-risking the ultrasonic techniques prior to the more involved implementation required for the semi-industrial pilot. During these tests a clear difference in amplitude for the reflected longitudinal pulse was observed between the lubricated and unlubricated cases. No difference was observed between the equivalent shear cases. This implied that it was possible to detect the additional stiffness of the interface introduced by the presence of lubricant and thereby the lubricant film thickness. The calculated film thickness was comparable to the combined strip and roll roughnesses, although the bulk modulus used in this calculation was estimated.

For the pilot mill the contact size was comparable to, or smaller than, the ultrasonic spot size. This will have affected the accuracy of the results yielded. Additionally, the small reduction, large error in reduction setting, lack of strip tension and lack of force or speed measurement limited the range of rolling conditions that could be tested.

During this testing clear reflections were received from either side of the strip and the strip thickness was easily measured. A change in ToF across the instrumented plug, consistent with plug deformation was observed. This deformation also manifested as indentations in the strip. In addition to the plug deformation these indentations may also have been the result of the plug implementation. The relatively small amount of the plug supporting material may have been inadequate for the rolling load experienced, causing the plug to withdraw into the roll. This was important when considering the design of the plugs for the semi-industrial pilot testing.

Knowing the density and from the measurements of the longitudinal and shear speed of sound within the plug, it was possible to calculate a number of plug material properties. The Poisson's ratio, Young's modulus, shear modulus, bulk modulus, Lamé constant and both the longitudinal and shear acoustic impedances and attenuation coefficients where all measured and gave values that compared well with those found in literature for similar materials.

12.4.4 Rolling Mill Measurements

The results gained from the semi-industrial pilot mill testing were plotted as a set of B-Scans. Schematics were developed which show how these B-Scans should appear based upon the different expected geometries and acoustic velocities of the materials within the roll bite. It was clear from comparison between these and the measured responses that a clear reflection is seen from both sides of the strip. In addition to this a number of interfering waves were observed which met the roll surface reflection at the entry and exit to the roll bite. These were present in both the longitudinal and shear results.

The source of these interfering waves was not immediately apparent. Further analysis showed that their ToF was consistent with them having emanated from the region of the roll bite entry and exit. A potential explanation for the cause of these is ultrasonic beams deflected at the entry and exit of the roll bite due to stress, as observed in the acoustoelastic numerical model of the roll bite performed earlier.

The interference caused by these waves rendered the amplitude and ToF measurements around the roll bite entry and exit unusable. These sections of data were discarded from the analysis of roll stress and interface stiffness/film thickness. It may be possible in future work to minimise the effect of these interferences with a smaller sensor spot size, achieved through focusing.

Roll Bite Contact Length

The roll bite contact length was measured by taking a threshold of the signal amplitude across the roll bite. A reflection coefficient threshold of 0.5 yielded results consistent with simple geometry. Little change was observed between results for different speeds, but different roll bite widths were recorded for different elongations as would be expected. The result compared well with a numerical model of the roll bite length, with maximum relative difference of 3% between simulated and measured results. Dynamic measurements have also been demonstrated as the elongation was varied.

Strip Thickness

A range of strip thickness measurement methods have been assessed and a zero-crossing approach selected as the most suitable. The profile of the strip thickness across the roll bite was recorded. Comparison between this and the simulated strip thickness shown less than a 6% relative difference. The limit of the strip thickness measurement has been evaluated and has been demonstrated as a function of the ultrasonic pulse length.

Interface Stiffness

The ultrasonic signal amplitude was evaluated across the roll bite for multiple passes of each rolling case. This demonstrated the amount of variability present in the signal for steady-state conditions, which was deemed to be low. The proportion of the reflected signal for both the longitudinal and shear waves were converted to their respective stiffnesses.

The longitudinal results showed a small drop in overall interface stiffness with increased rolling speed for rougher strip up to 400 m/min. The same was seen for smoother strip up to 500 m/min, but an increase was then seen in the stiffness for rolling velocities above this. A

consistent increase in the interface stiffness was seen with higher elongations. This was expected due to the higher rolling load.

The change in shear stiffness, which was related to the solid asperity contact of the rolling interface, was much more apparent in all cases. The shear stiffness consistently dropped with increasing rolling velocities for all rolling conditions and for both rough and smooth strip. This demonstrated a reduction in the solid-solid contact, and it is hypothesised that this is the result of a thicker lubricant film. Conversely the shear stiffness grew with increasing elongation at a fixed rolling velocity.

The fluid stiffness was calculated from the shear and longitudinal stiffnesses. For the thinner, smoother, strip all tests show a drop in liquid layer stiffness from rolling speeds of 25 to 50m/min. The general trend was then for the liquid layer stiffness to increase with higher rolling velocities. The tests for varying elongation show a trend of increasing liquid layer thickness with increasing elongation in almost all cases.

Lubricant Film Thickness

The film thickness profile across the roll bite for the range of data that was usable was calculated. The amount of data available at higher rolling speeds was less due to the limitations of the pulse repetition rate. These results showed a consistent film thickness across the centre of the roll bite. If the ambient pressure and temperature value for the lubricant bulk modulus was used then the fluid layer thicknesses calculated were significantly below the magnitude of the surface roughnesses. If the bulk modulus was adjusted for pressure and temperature using a simulated pressure profile across the roll bite was used, the lubricant film thickness across the roll bite was found to be of the order of the combined surface roughness. This implies that the lubricant is trapped in the interface an experiences the full rolling pressure.

The lubricant film thickness at the centre of the roll bite showed a regular decrease with increased elongation. This was expected due to the higher rolling loads and increased strip surface area which results in the lubricant layer being spread more thinly.

The lubricant layer thickness was seen to remain constant or slightly increase with increased rolling velocity for the thicker, rougher strip. The thinner smoother strip showed an increase in film thickness at the lowest speeds (25 m/min to 50 m/min), but the thickness remained largely constant for speeds up to 500 m/min. Above this the calculated lubricant layer thickness dropped dramatically. This could be explained by starvation of the interface.

The results show similar magnitudes to numerical modelling across the range of rolling velocities tested, with the ultrasonic results giving generally slightly lower values. This may be due to the value of bulk modulus used, which will have been effected by the estimation of the lubricant pressure at the centre of the roll bite. The agreement between the ultrasonic and numerical results for elongations ~20% and above was good. It was clear from both the lubricant film thickness profiles, as well as the difference in the central film thickness values from the simulated results, that the interference effecting the ultrasonic measurements prevents their use for smaller elongations.

Different aspects of the lubrication conditions also yielded some interesting results. The testing using the higher viscosity lubricant resulted in a comparatively less stiff and thicker films. The

stiffnesses recorded with recirculated lubricant are higher than those seen from directly applied lubricant. The shear stiffnesses in both cases are similar with the difference in the two test cases being seen in the longitudinal stiffness. The film thicknesses are smaller than those seen when using pure directly applied lubricant.

The thinner strip tested showed higher stiffnesses, this is consistent with the smoother surface roughness. The measured film thicknesses were generally of the same order, the exception being that the thinner smoother strip had a slightly lower film thickness at higher rolling speeds.

The test cases which used directly applied lubricant showed larger film thicknesses in comparison to the case where only recirculated lubricant was used. Interestingly the thickest measured film thickness was recorded with a mixture of both directly applied and recirculated lubricants, the reason for this is unknown.

Friction

It was noticed during data processing that there appeared to be some correlation between the calculated friction and the measured shear stiffness. Plots show how the shear stiffness and friction coefficient vary approximately linearly for each test with varying rolling speed. Increased rolling speed results in lower friction and shear stiffness in all cases measured.

The reason for this apparent relationship is not entirely clear. Friction is a function of the contact area and interfacial shear stress. It may be that due to the nature of the interfacial asperity contact that the interface shear stiffness is related to the applied shear stress. If so this would explain why increased shear stress (and therefore increasing friction) in turn increases the shear stiffness of the interface. It may also be that the increase in speed results in greater lubricant film thickness. This reduces the proportion of solid-solid contact and therefore both the shear stiffness and friction.

Roll Deflection and Stress

Roll deflection was measured using both the longitudinal and shear waves. The usable data recorded showed profiles across the roll bite which matched the shape predicted through modelling. The magnitude of the deflection measured from the shear results corresponded very well with the modelled values. The longitudinal results showed the same trends but consistently returned values for deflection just over half those from the modelled or shear results. The same applied for both tests of varying speed and elongation.

The work in this thesis demonstrates that the large stresses seen in cold rolling mean that acoustoelasticity has a non-negligible effect. This was successfully used to measure the stress within the roll. The measurements taken were an average stress across the pulse path through the roll/plug.

The deflections and stresses recorded increased for increasing elongations and remained constant with rolling speed. Similar results between tests showed good similarity for the shear sensors, however an offset was observed in the longitudinal results between the same test conditions recorded as part of an elongation ramp and as part of a speed ramp. This implies there was some unexpected error in the longitudinal measurements.

The demonstrated that the shear wave ToF is a viable method for measuring in-situ roll stress and deflection.

12.5 Future Work

The results of the existing study could be improved and extended into a range of new areas. Some of the key topics are outlined below:

- Array of Sensors.

The results presented were taken from single pairs of sensors (one longitudinal and one shear) located centrally along the axis of the work roll barrel. This gave a sweep of the profile through the central plane of the roll bite. This could be extended by using an array of sensors mounted along the axis of the roll to give a 2D profile of the roll bite.

- Industrial Implementation.

The measurements taken have been demonstrated via laboratory experiments as well as on a small scale pilot mill and a semi-industrial pilot mill. Extending this work into an industrial setting is essential in progressing the measurements. Doing so would involve a significant amount of work to make the equipment and software both robust and rugged suitable for industrial conditions. Additionally, new methods for plug instrumentation need to be explored, as it is essential that the approach for instrumenting the roll does not result in damage to the end product (the strip), such as the indentations seen when using the plug technique.

- Non Invasive Sensors

It is clear throughout this study that the most challenging, costly and time consuming aspect has been the instrumentation of the work rolls. The techniques used also have questionable application in an industrial environment due to their effect on the strip being rolled. For these reasons it is suggested that an important next step is to investigate a non-invasive means of instrumenting the work roll. A few suggestions on how this might be achieved have been included below in Figure 12.9 along with advantages and disadvantages of each technique.

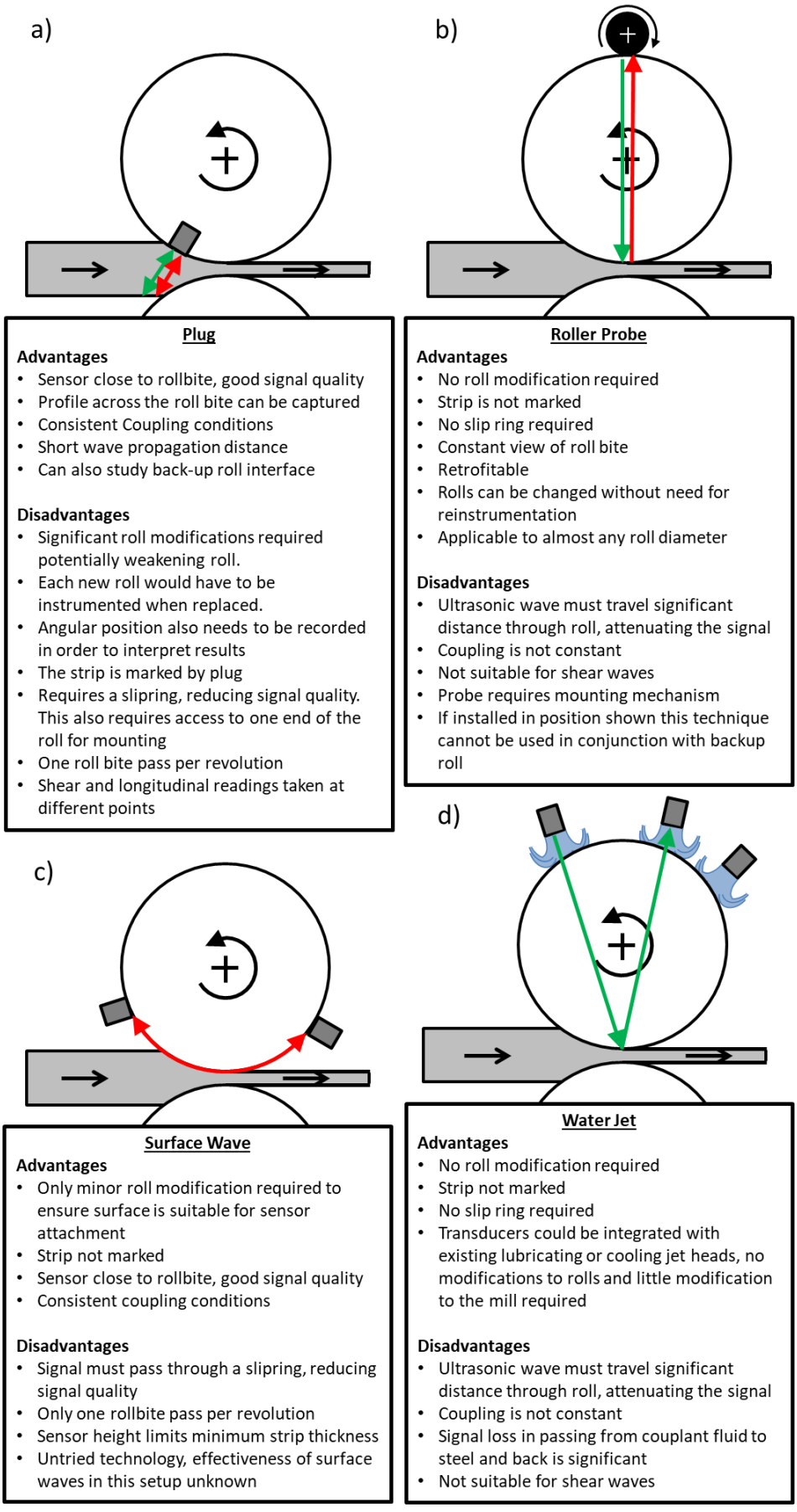

Figure 12.9: Sensor Mounting Arrangements a) Current Method b) Roller Probe c) Surface Waves d) Liquid Coupled Transducers.

The first proposed method is to couple to the outside of the work roll using a roller probe, this would be easily retrofitable. Alternatively, water jets (commonly known as bubbler probes) could be used. In both approaches the ultrasonic beam can be transmitted through the roll to the interface and the reflection picked up by a receiving transducer on the far side of the roll. As the ultrasonic beam reflects from the interface at an angle, both shear and longitudinal waves are produced simultaneously, as defined by Snell's law. This means both wave types can be measured at the same point. The coupling for both roller and water jet approaches does not allow for transmission of shear waves. Instead it would be necessary to only use longitudinal waves, or infer shear waves from mode-converted longitudinal waves at the roll surface.

The other suggested method would be to attach surface wave transducers to the surface of the roll, either side of the strip and transmit waves along the rolling surface in the direction of the roll axis, across the roll bite. No work has been done to understand the measurements possible with surface waves, and this approach would require research in this area.

- Digitise on the Roll.

The SNR could be increased by removing the need for a slip-ring. This would reduce parasitic noise and attenuation from the cabling. This could be achieved by mounting the digitising electronics directly onto the roll and then either storing the data locally for collected at a later time, or transmitting it wirelessly. This would remove the requirement to send sensitive and low amplitude signals through a slip ring. Small form factor and relatively low cost ultrasonic electronics are currently available in the market which may be suitable for this.

- Hot Rolling.

The concepts and measurements described in this thesis are not unique to cold rolling of steel, and could potentially be extended to include hot rolling. This will require further development of the sensors and cabling to accommodate the elevated temperatures. Temperature resistant piezo sensors and cabling already exist, but the suitability of these and a method for implementation them need to be explored.

- Lubricant Solidification.

A more detailed understanding of the lubricant bulk modulus is needed for reliable lubricant thickness calculations. This should include an understanding of how the lubricant pressure evolves across the roll bite, the effect that this has on the bulk modulus, if solidification of the lubricant is occurring and if so how this affects the measurements. It is expected that oil solidification would result in a significant change to the relationship between oil bulk modulus and pressure, a key material property used in the spring model method of determining oil film thickness. It may also be the case that oil solidification would allow the transit of shear waves across the oil component of the interface. This would invalidate a key assumption used in formulating the lubricant film thickness approach put forward in this thesis.

- In-Situ Lubricant Pressure and Temperature Measurement.

The lubricant bulk modulus, and therefore calculated film thickness, is dependent upon the lubricant pressure and temperature inside of the roll bite. No measurement of either of these values was taken inside of the roll bite. Other studies have demonstrated pressure and

temperature measurements in cold rolling. Combining a lubricant pressure and temperature measurement from the interface with simultaneous ultrasonic measurements would be extremely valuable in producing accurate measurements for the film thickness.

- Analytical Solution to Acoustoelastic Bending.

The effect of acoustoelastic bending was investigated in this thesis through numerical modelling. Given a known contact condition, and therefore stress field, it should be possible to derive analytical solutions to this problem. Similar equations, to help calculate the beam path and distance travelled, already exist for subsea sonar waves propagating through gradients of water with different densities. This is conceptually very similar to the acoustoelastic problem, and these equations could be adapted for this purpose.

- Interference Study and Sensor Focusing.

The cause of the interference fringes seen throughout this work, and methods for reducing/removing them need further investigation. This would allow reliable results to be taken across the whole length of the roll bite. One possible solution might be to focus the ultrasonic beam, reducing beam spread and measurement spot size.

- Inspection of the Top and Bottom Strip Interfaces.

During testing reflections were received from both the top and bottom faces of the strip. It should therefore be possible to inspect both interfaces simultaneously. An alternative approach would be to instrument both upper and lower work rolls. This would also allow through transmission to be used, where a signal is transmitted from the lower to upper roll.

- Shear Stiffness against Friction Relationship

The preliminary results presented indicate a possible correlation between the interface shear stiffness and the friction coefficient of the roll bite. The mechanism behind this, if there is such a mechanism, needs to be studied in more detail in order to understand if it exists and how it can be quantified.

13 References

A. Fouratier, F. Geißller, G. Endemann and B. Schmidt. (2002). *Lubrication during Cold-Rolling EUR 20092 EN.* Directorate-General for Research and Innovation, European Commission. doi:92-828-5191-5

Abboud, N., Wojcik, G. L., Vaughan, D. K., Mould, J., Powell, D. J., & Nikodym, L. (1998). Finite Element Modeling for Ultrasonic Transducers. *Medical Imaging*, 19-42.

Achenbach, J. D. (1984). *Wave Propagation in Elastic Solids.* North Holland.

Alexander, J. M. (1972). On the Theory of Rolling. *Proceedings of the Royal Society A, 326*, 535-563.

Allen, D. R., & Sayers, C. M. (1984, July). The Measurement of Residual Stress in Textured Steel using an Ultrasonic Velocity Combinations Technique. *Ultrasonics*, 179-188.

Anderson, W., Salant, R. F., & Jarzynski, J. (1999). Ultrasonic Detecction of Lubricating Film Collpase in Mechanical Seals. *Tribology Transactions, 4*, 801-806.

Annandale, C. (Ed.). (1894). *The Popular Encyclopedia* (Vol. VII). Blackie & Son.

(1987). *ANSI/IEEE 176-1987 - Standard on Piezoelectricity.* IEEE.

APC International Ltd. (2002). *Piezoelectric Ceramics: Principles and Applications.* APC International Ltd.

ArcelorMittal. (2010). *Data sheet: B3.1 - Cold Rolled Steel Sheet for Drawing and Forming.* ArcelorMittal South Africa Limited, Vanderbijlpark.

ArcelorMittal. (2016). *High Formability Steels for Drawing.* Retrieved from http://automotive.arcelormittal.com/saturnus/sheets/K_EN.pdf

Ashby, M. F., & Jones, D. R. (1996). *Engineering Materials 1.* Butterworth-Heinemann.

Atkins, A. G. (1974). Hydrodynamic Lubrication in Cold Rolling. *International Journal of Mechanical Sciences, 16*, 1-19.

Attenuation of Sound Waves. (n.d.). Retrieved 7 2015, 22, from NDT Resource Center: https://www.nde-ed.org/EducationResources/CommunityCollege/Ultrasonics/Physics/attenuation.htm

Bacon, D. R., & Jarvis, D. R. (n.d.). *Kaye & Laby: The Speed and Attenuation of Sound*. Retrieved June 27, 2015, from National Physical Laboratory: http://www.kayelaby.npl.co.uk/general_physics/2_4/2_4_1.html

Bair, S., Mary, C., Bouscharain, N., & Vergne, P. (2013). An Improved Yasutomi Correlation for Viscosity at High Pressure. *Proc. of IMechE Part J: Journal of Engineering Tribology, 227*, 1056-1060.

Banks, B., Oldfield, G. E., & Rawding, H. (1962). *Ultrasonic Flaw Dectection in Metals: Theory and Practice.* London: Iliffe Books Ltd.

Banks, B., Oldfield, G. E., & Rawding, H. (1962). *Ultrasonic Flaw Detection in Metals; Theory and Practice.* London: Iliffe Books.

Bauer, S., & Bauer, F. (2008). Piezoelectric Polymers and Their Applications. In W. Heywang, K. Lubitz, & W. Wersing, *Piezoelectricity* (Vol. 114, pp. 157-177). Springer.

Bell, S. (2001). *Measurement Good Practice Guide: A Beginner's Guide to Uncertainty of Measurement.* National Physical Laboratory, Centre for Basic, Thermal and Length Metrology.

Ben-Benjamin, J. S., & Cohen, L. (2015). Equations of Motion for Rays in a Snell's Law Medium. *Journal of the Acoustical Society of America, 137*(2), EL171-EL177.

Bergman, R. H., & Shahbender, R. A. (1958). Effect of Statically Applied Stresses on the Velocity of Propagation of Ultraasonic Waves. *Journal of Applied Physics, 29*.

Bernstein, R. A. (1961). Sound Waves in Deformed Perfectly Elastic Materials. *Journal of the Acoustical Society of America, 33*(2), 216-225.

Bland, D., & Ford, H. (1952). An Approximate Treatment of the Elastic Compression of the Strip in Cold Rolling. *Journal of the Iron and Steel Institute, 171*, 245-249.

Boman, R. (2010). *Development of a Tridimensional Arbitrary Lagrangian Eulerian Formalism for Dynamic Implicit Problems. Application to Forming Processes. (in French).* PhD Thesis, University of Liège.

Boman, R., & Ponthot, J.-P. (2004, Oct 1). Finite Element Simulation of Lubricated Contact in Rolling using Arbitrary Lagrangian Eulerian Formulation. *Computer Methods in Applied Mechanics and Engineering, 193*(39-41), 4323-4353.

Bouscharain, N., & Vergne, P. (2010). *Etude D'huiles de Laminage sous Hautes Pressions [Study of Rolling Oils under High Pressures].* Institut National des Sciences Appliquées de Lyon, Laboratoire de Mécanique des Contacts et des Structures.

Bouscharain, N., & Vergne, P. (2010). *Etude d'huiles de laminage sous hautes pressions.* INSA de Lyon, Laboratoire de Mécanique des Contact et des Structures.

Bouscharain, N., & Vergne, P. (2013). *Comportement Rhéologique D'huiles de Laminage sous Hautes Pressions [Rheological Behaviour of Rolling Oils under High Pressure].* Institut National des Sciences Appliquées de Lyon, Laboratoire de Mécanique des Contacts et des Structures.

Bray, D. E., & Stanley, R. K. (1996). *Nondestructive Evaluation: A Tool in Design, Manufacturing and Service* (1st ed.). CRC Press.

Bray, D. M. (1976). Measurement of Acoustoelastic and Third-Order Elastic Constants for Rail Steel. *Journal of the Acoustical Society of America, 60*, 741-744.

Brown, A. E. (n.d.). *Rationale and Summary of Methods for Determining Ultrasonic Properties of Materials at Lawrence Livermore National Laboratory.* Lawrence Livermore National Laboratory, Acoustic Properties of Materials Group.

BS EN 10111:2008 - Continuously Hot Rolled Low Carbon Steel Sheet and Strip for Cold Forming. Technical Delivery Conditions. (2008, May 30). BSI.

BS EN 10130:2006 - Cold Rolled Low Carbon Steel Flat Products for Cold Forming. Technical Delivery Conditions. (2006, December 29). *(0 580 49900 6)*. BSI.

C. Egenhofer, L. S. (17 December 2013). *The steel industry in the European Union: Composition and drivers of energy prices and costs.* CEPS Special Reports.

Calvert, J. R., & Farrar, R. A. (1999). *An Engineering Databook.* Basingstoke: Palgrave.

Cameron, A., & Gohar, R. (1963). Optical Measurement of Oil Film Thickness under Elasto-hydrodynamic Lubrication. *Nature, 200*, 458-59.

Cameron, A., & Gohar, R. (1963). Optical Measurement of Oil Film Thickness Under Elastohydrodynamic Lubrication. *Nature, 200*, 458-59.

Capital Market Days 2007. (2007). Retrieved November 25, 2012, from Andritz.com: http://atl.g.andritz.com/c/com2011/00/01/62/16211/1/1/0/683093797/gr-cmd-me-2007.pdf

Carretta, Y., Boman, R., & Stephany, A. (2011). MetaLub - A Slab Method Software for the Numerical Simulation of Mixed Lubrication Regime in Cold Strip Rolling. *Proc. IMechE Part J: Journal of Engineering Tribology, 225*, 894-904.

Carretta, Y., Hunter, A. K., Boman, R., Ponthot, J. -P., Legrand, N., Laugier, M., & Dwyer-Joyce, R. (2017). Ultrasonic roll bite measurements in cold rolling - Roll stress and deformation. *Journal of Materials Processing Tech., 249*, 1-13.

Carretta, Y., Hunter, A., Boman, R., Ponthot, J. -P., Legrand, N., Laugier, M., & Dwyer-Joyce, R. (2017). Ultrasonic roll bite measurements in cold rolling: Contact length and strip thickness. *Proc. IMechE Part J: J. Engineering Tribology*, 1-14.

Carter, F. W. (1926). On the Action of a Locomotive Driving Wheel. *Proceedings of the Royal Society of London. Series A, 112*(760), 151-157.

Cauchy, A.-L. (1829). Sur L'équilibre et le Mouvement Interieur des Corps Consideres comme des Masses Continues. *Exercices de Mathematiques, 4*, 293-319.

Challis, R. E., & Ivchenko, V. G. (2011, January 11). Sub-threshold sampling in a correlation-based ultrasonic spectrometer. *Measurement Science and Technology, 22*.

Chapter 4 - Capacitance per Unit Length. (n.d.). Retrieved 7 22, 2015, from Reference Designer: http://referencedesigner.com/books/si/capacitance-per-unit-len.php

Chapter 5 - Inductance. (n.d.). Retrieved 7 22, 2015, from Reference Designer: http://referencedesigner.com/books/si/inductance.php

(2010). *Characterization and verification of ultrasonic examination equipment - Probes.* BSI.

Cheeke, J. D. (2012). *Fundamentals and Applications of Ultrasonic Waves.* CRC Press.

Chen, C. T. (2001). *Digital Signal Processing.* New York: Oxford University Press.

Chen, W., Mills, R., & Dwyer-Joyce, R. S. (2015). *Direct Load Monitoring of Rolling Bearing Contacts using Ultrasonic Time of Flight.* University of Sheffield, Leonardo Centre for Tribology, Department of Mechanical Engineering.

Cobus, L. A., Ross, K. A., Scanlon, M. G., & Page, J. H. (2007). Comparison of Ultrasonic Velocities in Dispersive and Nondispersive Food Materials. *Journal of Adricultural and Food Chemistry, 55*, 8889-8895.

Cosse, P., & Economopoulos, M. (1968). Mathematical Study of Cold Rolling. *C.N.R.M., 17*, 15-32.

Crecraft, D. I. (1967, Jan). The Measurement of Applied and Residual Stresses in Metals using Ultrasonic Waves. *Journal of Sound and Vibration, 5*(1), 173-192.

Dargie, P. G., Harris, N. R., White, N. M., Atkinson, J. K., & Sion, R. P. (1998). An investigation of the effect of poling conditions on the characteristics of screen-printed piezoceramics. *Microelectronics International, 15*(2), 6-10.

Das Bakshi, S., Leiro, A., Prakash, B., & Bhadeshia, H. (2014, April 23). Dry Rolling/Sliding Wear of Nanostructured Bainite. *Wear, 316*, 70-78.

Davis, R. (1987). *John Wilkinson - Ironmaster Extraordinary.* The Dulston Press.

Dubey, S. P., Sharma, G. K., Shishodia, K. S., & Sekhon, G. S. (2005). A Study of Lubrication Mechanism of Oil-in-Water (O/W) Emulsions in Steel Cold Rolling. *Industrial Lubrication and Tribology, 57*(5), 208-212.

Duda, T. F. (2005). *Derivation of Ray Equations in Moving Media in Angle/Depth Form.* Woods Hole Oceanographic Institution, Applied Ocean Physics and Engineering Dept. Retrieved November 7th, 2015, from http://www.whoi.edu/science/AOPE/cofdl/tim/Ray_eqs.pdf

Dwyer-Joyce, R. S., Drinkwater, B. W., & Donohoe, C. J. (2003). The Measurement of Lubricant Film Thickness using Ultrasound. *Proc. R. Soc. Lond., 459*, 957-976.

Dwyer-Joyce, R. S., Drinkwater, B. W., & Donohoe, C. J. (2003). The Measurement of Lubricant Film Thickness using Ultrasound. *Proc. R. Soc. Lond. A, 459*, 957-76.

Dwyer-Joyce, R. S., Harper, P., & Drinkwater, B. W. (2004). A Method for the Measurement of Hydrodynamic Oil Films using Ultrasonic Reflection. *Tribology Letters, 17*(2), 337-348.

Dwyer-Joyce, R. S., Harper, P., Pritchard, J., & Drinkwater, B. W. (2006). Oil film Measurement in Polytetrafluoroethylene-Faced Thrust Pad Bearings for Hydrogenerator Applications. *Proc. IMechE Part A: Journal of Power and Energy, 220*, 619-628.

Dwyer-Joyce, R. S., Reddyhoff, T., & Zhu, J. (2011). Ultrasonic measurement for Film Thicknessand Solid Contact in Elastohydrodynamic Lubrication. *Journal of Tribology, 133*.

Einstein, A. (1906). Eine Neue Bestimmung der Molekul-Dimension [A New Determination of the Molecular Dimensions]. *Annalen der Physik, 19*(2), 289-306.

Electro Magnetic Acoustic Transducers. (n.d.). Retrieved August 14, 2016, from Sonatest: http://sonatest.com/products/range/transducers/emat/

Eley, P. (2012, May 23). *The Gosport Iron Foundry and Henry Cort*. Retrieved November 25, 2012, from Hampshire County Council: http://www3.hants.gov.uk/gdc/gosport-dc-local-studies/local-history-online/henry-cort

EMAT Technology. (n.d.). (Innerspec Technologies Inc.) Retrieved August 14, 2016, from Innerspec: http://innerspec.com/knowledge/emat-technology

Ensminger, D. (2008). *Ultrasonics: Data, Equations and Their Practical Uses.* CRC Press.

Ensminger, D., & Bond, L. J. (2011). *Ultrasonics: Fundamentals, Technologies, and Applications*. CRC Press.

EPA Office of Compliance. (1995). *Sector Notebook Project: Profile of the Iron and Steel Industry.* Washington D.C.

Eppelsheimer, D. (1938). The Development of Continuous Strip Mills. *Journal of the Iron and Steel Institute, II*, 185-303.

F. Feldmann, M. G. (2009). *Rolling Models: Adaptive Setup Models for Cold Rolling Mills.* ABB.

Fonseca, P., Santos, A. C., & Montenegro, E. C. (2007). A Very Simple Way to Measure Coaxial Cable Impedance. *The Brazilian Journal of Teaching Physics, 29*(3), 373-375.

Ford, H., Ellis, F., & Bland, D. R. (1951, May). Cold Rolling with Strip Tension, Part I - A New Approximate Method of Calculation and a Comparison with Other Methods. *Journal of the Iron and Steel Institue, 168*, 57-72.

Ford, R. A., & Foord, C. A. (1978). Laser-based fluorescence techniques for measuring thin liquid films. *Wear, 51*, 289-97.

Ford, R. A., & Foord, C. A. (1978). Laser-based Fluorescence Techniques for Measuring Thin Liquid Films. *Wear, 51*, 289-97.

Gamer, Y. P. (1985). Acoustoelastic Waves in Orthotropic Media. *Journal of the Acoustical Society of America, 77*(3).

Garcia-Rodriguez, M., Garcia-Alvarez, J., Yañez, Y., Garcia-Hernandez, M. J., Salazar, J., Turo, A., & Chavez, J. A. (2010). Low Cost Matching Network for Ultrasonic Transducers. *Physics Procedia, 3*, 1025 to 1031.

Graff, K. F. (1981). A History of Ultrasonics. In W. Mason, & R. N. Thurston, *Physical Acoustics Volume 15: Principles and Methods* (pp. 1-95). New York: Academic Press Inc.

Greenwood, J. A., & Williamson, J. B. (1966, December 6). Contact of Nominally Flat Surfaces. *Proc. R. Soc. Lond. A, 295*, 300-19.

Grice, N., Sherrington, I., Smith, E. H., O'Donnell, S. G., & Stringfellow, J. F. (1990). A capacitance based system for high resolution measurement of lubricant film thickness. *Proc. of Nordtrib '90 4th Nordic Symposium on Tribology, Lubrication, Friction and Wear*, 349-361.

Grice, N., Sherrington, N., Smith, E. H., O'Donnell, S. G., & Stringfellow, J. F. (1990). A Capacitance based System for High Resolution Measurement of Lubricant Film Thickness. *Proc. of Nordtrib '90 4th Nordic Symposium on Tribology, Lubrication, Friction and Wear*, 349-361.

H. Ford, F. E. (1951, May). Cold Rolling with Strip Tension, Part I - A New Approximate Method of Calculation and a Comparison with Other Methods. *Journal of the Iron and Steel Institue, 168*, 57-72.

Halmos, G. T. (Ed.). (2005). *Roll Forming Handbook, Manufacturing Engineering and Materials Processing Series.* CRC Press.

Hamby, D. M. (1995, Feb). A Comparison of Sensitivity Analysis Techniques. *Journal of Health Physics, 62*(2), 195-204.

Harper, P., Dwyer-Joyce, R. S., Sjödin, U., & Olofsson, U. (2004, September). Evaluation of an Ultrasonic Method for Measurement of Oil Film Thickness in a Hydraulic Motor Piston Ring. *Proceedings of the 31st Leeds-Lyon Symposium on Tribology*.

Henderson, T. (n.d.). *Sound Waves and Music - Lesson 2 - Sound Properties and Their Perception*. Retrieved 10 18, 2015, from The Physics Classroom: http://www.physicsclassroom.com/class/sound/Lesson-2/The-Speed-of-Sound

Henkel Limited. (29-11-2013). *BONDERITE L-RO 5525-2 known as Gerolub 5525-2.*

Henningsen, P., Arentoft, M., & Wanheim, T. (2006). Measurements of Normal and Frictional Forces in a Rolling Process. *Proc. IMechE Part B: J. Engineering Manufacture*.

Hertz, H. (1896). *Miscellaneous Papers.* London: Macmillan and Co Ltd.

Hitchcock, J. H. (1935). Elastic Deformation of Rolls Bearing During Cold Rolling. In *Roll Neck Bearings.* ASME Research Publication.

Hot Rolled Vs. Cold Rolled Steel. (n.d.). (Capital Steel & Wire Inc.) Retrieved June 25, 2014, from Capital Steel: http://www.capitalsteel.net/news/blog/hot-rolled-vs-cold-rolled-steel

How, C. (2015). Early Steps in Nail Industrialisation. In *Studies in Construction History: the proceedings of the Second Construction History Society Conference.*

Hubert, C., Dubois, A., Dubar, L., Laugier, M., Legrand, N., Boman, R., . . . Carretta, Y. (2015, July 15). Complementary Approaches for the Numerical Simulation of the Micro-Plasto-Hydrodynamic Lubrication Regime. *Key Engineering Materials, 651-653*, 492-497.

Jacobson, B. O. (1991). *Rheology and Elastohydrodynamic Lubrication.* ELSEVIER.

Jeswiet, J., Arentoft, M., & Henningsen, P. (2006). Methods and Devices Used to Measure Friction in Rolling. *Proc. IMechE Part B: Journal of Engineering Manufacture, 220*, 49-57.

Johnson, K. L. (1987). *Contact Mechanics.* Cambridge University Press.

Jortner, D., Osterle, J. F., & Zorowski, C. F. (1960). An Analysis of Cold Strip Rolling. *International Journal of Mechanical Sciences, 2*, 179-194.

Kalker, J. J. (1990). *Three-dimensional Elastic Bodies in Rolling contact.* Dordrecht: Kluwer Academic Publishers.

Kármán, T. v. (1925). Beitrag zur Theorie des Walzvorganges [Contribution to the theory of the rolling process]. *Zeitschrift für angewandte Mathematik und Mechanik, 5*(139).

Keith Wilson, D. (2003, February). The Sound-Speed Gradient and Refraction in the Near-Ground Atmosphere. *Journal of the Acoustical Society of America, 113*(2), 750-757. doi:10.1121/1.1532028

Kelly, D. S. (1953). Second-Order Elastic Deformation of Solids. *Physical Review, 92*(5), 1145-1149.

Kendall, K., & Tabor, D. (1971, June 22). An utrasonic study of the area of contact between stationary and sliding surfaces. *Proc. R. Soc. Lond. A, 323*, 321-340.

Kin, S., Lee, G. S., Shrout, T. R., & Venkataramani, S. (1991). Fabrication of Fine-Grain Piezoelectric Ceramic using Reactive Calcination. *Journal of Materials Science, 26*, 4411-4415.

KMM Metals. (n.d.). *KMM Metals*. Retrieved February 17, 2018, from Continuous casting description and history: http://www.kmmmetals.com/lat/kmm/nepartraukta_liesana2/

Kobasa, D., & Schultz, R. A. (1968). Experimental Determination of the Length of the Arc of Contact in Cold Rolling. *Iron and Steel Engineer Year Book*, 283-288.

Kosasih, P. B., & Tieu, A. K. (2007, May). Mixed film lubrication of strip rolling using O/W emulsions. *Tribology International, 40*(5), 709-716.

Krautkrämer, J., & Krautkrämer, H. (1977). *Ultrasonic Testing of Materials.* New York: Springer-Verlag.

Krautkrämer, J., & Krautkrämer, H. (1977). *Ultrasonic Testing of Materials.* New York: Springer-Verlag.

Krautkrämer, J., & Krautkrämer, H. (1977). Ultrasonic Testing of Materials. Springer-Verlag.

Krishnaswamy, S. (2003). Theory and Applications of Laser-Ultrasonic Techniques. In T. Kundu (Ed.), *Ultrasonic Nondestructive Evaluation: Engineering and Biological Material Characterization.* CRC Press.

Krsmanovic, D. (November 2009). *High Temperature Ultrasonic Gas Flow Sensor Based on Lead Free Piezoelectric Material.* PhD Thesis, University of Cambridge, Darwin College.

Laugier, M., Boman, R., Legrand, N., Ponthot, J. P., Tornicelli, M., Bech, J. I., & Carretta, Y. (2014, June). Micro-Plasto-Hydrodynamic Lubrication a Fundamental Mechanism in Cold Rolling. *Advanced Materials Research, 966-967*, pp. 228-241.

Lenard, J. G. (2013). *Primer on Flat Rolling.* Elsevier.

Leonardo da Vinci. (1488–1505). Paris Manuscript I, Folio 48v.

Liu, Y. J., Tieu, A. K., Wang, D. D., & Yuen, W. Y. (2001). Friction Measurement in Cold Rolling. *Journal of Materials Processing Technology, 111*, 142-145.

Liu, Y. J., Tieu, A. K., Wang, D. D., & Yuen, W. Y. (2001). Friction Measurement in Cold Rolling. *Journal of Materials Processing Technology, 111*, 142-145.

Lüthi, T. (1990, Decemeber). Determination of Biaxial and Triaxial Stress Distributions using Ultrasonics. *NDT International, 23*(6), 351-356.

M.-H. C. (1953). *Rolling Mills, Rolls, and Roll Making: A brief historical account of their development from the fifteenth century to the present day.* Pittsburgh, Pennsylvania.

Magnussen, F., Nordlund, E., Châtelet, S., & Sadarangani, C. (n.d.). *Measurements on Slip Ring Units for Characterization of Performance.* Royal Institute of Technology (KTH), Sweden.

Manufacturing Tutorial. (n.d.). Retrieved 12 13, 2015, from http://www.noliac.com/tutorials/manufacturing/

Marsault, N. (1998). *Modélisation du Régime de Lubrification Mixte en Laminage à Froid.* PhD Thesis, École Nationale Supérieure des Mines de Paris.

Matsuoka, Y., & Motomura, M. (1968). Variation of Coefficient of Friction Along the Arc of Contact, and the Length of the Arc [in Japanese]. *9*(86), 173.

Metals and Alloys - Bulk Modulus. (n.d.). Retrieved March 14, 2016, from The Engineering Toolbox: http://www.engineeringtoolbox.com/bulk-modulus-metals-d_1351.html

Metals and Alloys - Densities. (n.d.). Retrieved 7 21, 2015, from The Engineering Toolbox: http://www.engineeringtoolbox.com/metal-alloys-densities-d_50.html

Mindlin, R. D. (1949). Compliance of Elastic Bodies in Contact. *Journal of Applied Mechanics, 71*, pp. 259-268.

Modes of Sound Wave Propagation. (n.d.). Retrieved September 22, 2015, from NDT Resource Center: https://www.nde-ed.org/EducationResources/CommunityCollege/Ultrasonics/Physics/modepropagation.htm

Modulus of Rigidity of some Common Materials. (n.d.). Retrieved March 14, 2016, from The Engineering Toolbox: http://www.engineeringtoolbox.com/modulus-rigidity-d_946.html

Montmitonnet, P. (2006). Hot and Cold Strip Rolling Processes. *Computer Methods in Applied Mechanics and Engineering, 195*, 6604-6625.

Morgan Technical Ceramics Electroceramics. (n.d.). *Typical Values of Morgan Electro Ceramics Navy II Type Piezoelectric Ceramics.* Retrieved from www.morgantechnicalceramics.com

Morgan Technical Ceramics. (n.d.). *Piezoelectric Electrodes*. Retrieved from www.morganelectroceramics.com/products/piezoelectric/piezoelectric-electrodes/

Muir, D. D. (2009). *One-Sided Ultrasonic Determination of Third Order Elastic Constants using Angle-Beam Acoustoelasticity Measurements.* PhD Thesis, Georgia Institute of Technology, School of Electrical and Computer Engineering.

Mukdadi, O. (n.d.). *Biomedical Ultrasound.* MCEN4228 Lecture, University of Colorado Boulder. Retrieved September 22, 2015, from http://www.colorado.edu/MCEN/MCEN4228/index_files/biomedicalultrasound.pdf

Mukerjee, K. K. (1973). *A Critical Review of the Mechanics of Metal Rolling; It's application to the Design of Hot Strip Mills.* Masters Thesis, Sir George Williams University, Faculty of Engineering, Montreal.

Murnaghan, F. D. (1951). *Finite Deformation of an Elastic Solid.* New York: Wiley.

Nadai, A. (1939, June). The Forces Required for Rolling Steel Strip Under Tension. *Journal of Applied Mechanics*, A54-A62.

Nadai, A., & Wahl, A. M. (1931). *Plasticity: Mechanics of the Plastic State of Matter.* New York and London: McGraw-Hill.

National Instuments. (2006, Sept. 6). *Improving Accuracy through Averaging.* Retrieved Dec. 9, 2017, from National Instruments: http://www.ni.com/white-paper/3488/en/

NDT Resource Center. (n.d.). *Material Properties Tables*. Retrieved November 27, 2016, from NDT Resource Center: https://www.nde-ed.org/GeneralResources/MaterialProperties/UT/ut_matlprop_piezoelectrics.htm

Nikolić, B. D., Kegl, B., Marković, S. D., & Mitrović, M. S. (2012). Determining the Speed of Sound, Density, and Bulk Modulus of Rapeseed Oil, Biodiesel and Diesel Fuel. *Thermal Science, 16*(2), S505-S514.

Ocheltree, K. B., & Frizzell, L. A. (1989, March). Sound Field Calculation for Rectangular Sources. *IEEE Transactions on Ultrasonics, Ferroelectrics and Frequency Control, 36*(2), 242-248.

Olympus. (n.d.). *Contact Transducers*. (Olympus) Retrieved August 14, 2016, from Olympus NDT Instruments: http://www.olympus-ims.com/en/ultrasonic-transducers/contact-transducers/

Olympus. (n.d.). Manually Controlled Pulser-Recievers - 5072PR, 5073PR, 5077PR. Retrieved 02 21, 2016, from http://telab.vuse.vanderbilt.edu/docs/specs/Olympus-5072PR.pdf

Olympus NDT. (2006). *Ultrasonic Transducers Technical Notes.* Retrieved from http://www.olympus-ims.com/data/File/panametrics/UT-technotes.en.pdf

Omega. (n.d.). *PXM409 Pressure Transducer Datasheet.* Retrieved May 23, 2015, from Omega: http://www.omega.co.uk/Pressure/pdf/PXM409.pdf

Orowan, E. (1943). The Calculation of Roll Pressure in Hot and Cold Flat Rolling. *Proc. Institute of Mechanical Engineers, 150*(4), 140-167.

Palacio, M., & Bhushan, B. (2007). Surface potential and resistance measurements for detecting wear of chemically-bonded and unbounded molecularly-thick perfluoropolyether lubricant films using atomic force microscopy. *Journal of Colloid Interface Science, 315*, 261-69.

Palacio, M., & Bhushan, B. (2007). Surface potential and resistance measurements for detecting wear of chemically-bonded and unbounded molecularly-thick perfluoropolyether lubricant films using atomic force microscopy. *Journal of Colloid Interface Science, 315*, 261-69.

Pialucha, T., & Cawley, P. (1994). The detection of thin embedded layers using normal incident ultrasound. *Ultrasonics, 32*, 431-40.

Pico Technology. (n.d.). *USB TC-08 Manuals.* Retrieved May 23, 2015, from Pico Technology: https://www.picotech.com/download/datasheets/usb-tc08-3.pdf

Piezo. (2015, March 21). Retrieved from Merriam Webster Online Dictionary: http://www.merriam-webster.com/dictionary/piezo-

Piezo Elements Made by Pressing Technology. (n.d.). (PI) Retrieved 12 13, 2015, from PI Piezo Technology: http://www.piceramic.com/piezo-technology/manufacturing/pressing.html

Piezo Systems Inc. (2011). *Catalog #8 - Piezoceramic Application Data - Introduction to Piezoelectricity.* Retrieved from http://www.piezo.com/tech1terms.html

Piezo-ceramic Manufacturing Process - Proven Expertise in Piezo-ceramic Manufacturing. (n.d.). (CeramTec) Retrieved 12 13, 2015, from CeramTec: http://www.ceramtec.co.uk/ceramic-materials/piezo-ceramics/manufacturing-process/

POSCO. (n.d.). *Corporate Overview*. (POSCO) Retrieved June 25, 2014, from POSCO India: http://posco-india.com/website/company/corporate-overview.htm

Prandtl, L. (1923). Anwendungsbeispiele zu einem Henckyschen Satz über das Plastische Gleichgewicht [Application Examples for a Henckyschen Set on the Plastic Balance]. *Zeitschrift für Angewandte Mathematik und Mechanik [Journal of Applied Mathematics and Mechanics], 3*(6), 401-406.

R. G. Budynas, J. K. (2011). *Shigley's Mechanical Engineering Design.* New York: McGraw-Hill.

Rayleigh, L. (1912, February 28). On the Propagation of Waves through a Stratified Medium, with Special Reference to the Question of Reflection. *Proceedings of the Royal Society of London. Series A, Containing Papers of a Mathematical and Physical Character, 86*(586), 207-226.

Reddyhoff, T., Dwyer-Joyce, R. S., & Harper, P. (2006). A New Approach for the Measurement of Film Thickness in Liquid Face Seals. *Tribology Transactions, 51*(2), 140-149.

Reddyhoff, T., Kasolang, S., & Dwyer-Joyce, R. S. (2005). The Phase Shift of an Ultrasonic Pulse at an Oil Layer and Determination of Film Thickness. *Proceedings of the Institution of Mechanical Engineers Part J - Journal of Engineering Tribology, 219*, 387-400.

Reynolds, O. (1874). On the Refraction of Sound by the Atmosphere. *Proceedings of the Royal Society of London, 22*, 531-548.

Reynolds, P., Krause, R., Carcione, L., Mould, J., & Vaughan, D. (2004). Explicit Time Domain Modelling Techniques for Efficient Analysis of Piezoelectric Ultrasonic Transducers. *NIST-CTAP Workshop on Computational Tools for Mode.* Weidlinger Associates Inc.

Roberts, W. L. (1969). The Frictional Characteristics of Rolling Lubricants. (G. A. McGrann, D. W. Murphy, & F. E. Richardson, Eds.) *Proc. of the 11th Mechanical Working and Steel Processing Conference*, 299-314.

Roberts, W. L. (1978). *Cold Rolling of Steel.* New York: M. Dekker.

Rowe, G. W. (1977). *Principles of Industrial Metalworking Process.* London: Edward Arnold Publishers.

RP Acoustics. (n.d.). *PVDF Hydrophones*. Retrieved March 29, 2015, from RP Acoustics: http://www.rp-acoustics.de/english/PVDF_Hydrophone.htm

Schlengermann, U. (n.d.). *Forum: Near Zone Calculation.* Retrieved August 18, 2016, from NDT Net: http://www.ndt.net/forum/thread.php?msgID=204

Seibel, E. (1924). Berichte des Walzwerksausschusses [Reports of the Rolling Mill Committee]. *Verein deutscher Eisenhuttenleute, 37*.

Seibel, E., & Lueg, W. (1933). Untersuchungen über die Spannungsverteilung im Walzspalt [Investigations into the Distribution of Pressure at the Surface of the Material in Contact with the Rolls]. *Mitteilungen aus dem Kaiser-Wilhelm-Institut für Eisenforschung zu Düsseldorf, 15*(1).

Shull, P. J., & Tittmann, B. R. (2002). Ultrasound. In P. J. Shull (Ed.), *Nondestructive Evaluation: Theory, Techniques, and Applications* (pp. 143-44). CRC Press.

Si-Chaib, M. O., Menad, S., Djelouah, H., & Bocquet, M. (2001). An Ultrasound Method for the Acoustoelastic Evaluation of Simple Bending Stresses. *NDT&E International, 34*, 521-529.

Siebel, E., & Lueg, W. (1933). Untersuchungan über die Spannungsverteilung im Walzspalt. *Mitteilungen aus dem Kaiser-Wilhelm-Institut für Eisenforschung zu Düsseldorf, 15*(1).

Silk, M. G. (1984). Ultrasonic Transducers for Nondestructive Testing. CRC Press.

Sims, R. B. (1954, June). The Calculation of Roll Force and Torque in Hot Rolling Mills. *Proceedings of the Institution of Mechanical Engineers, 168*(1), 191-200.

SSAB Sheet Steel. (n.d.). (SSAB) Retrieved May 25, 2014, from SSAB: http://www.ssab.com/Products--Services/About-SSAB/Steel-making-process/Processing/Sheet-steel/

(2014). *Standard Guide for Evaluating Characteristics of Ultrasonic Search Units.* ASTM International. Retrieved from www.astm.org

(2013). *Standard Test Method for Measurement of Ultrasonic Attenuation Coefficients of Advanced Ceramics by Pulse-Echo Contact Technique.* ASTM International, West Conshohocken, PA. Retrieved from www.astm.org

Standards on Piezoelectric Crystals. (1949, December). *Proceeding of Institute of Radio Engineers, 37*(12), 1378-1395.

Steel Rolling & Drawing in the US: Market Research Report. (2012, August). Retrieved November 25, 2012, from Ibisworld.com: http://www.ibisworld.com/industry/default.aspx?indid=574

Steinhoff. (2008). *DHQ3 - Material Data Sheet.* Retrieved from http://www.steinhoff.eu/

Stephany, A. (2008). *Contribution à l'étude numérique de la lubrification en régime mixte en laminage à froid.* PhD Thesis, University of Liège, Laboratoire de Techniques aéronautiques et Spatiales.

Stobbe, D. M. (2005). *Acoustoelasticity in 7075-T651 Aluminum and Dependence of Third Order Elastic Constants on Fatigue Damage.* Georgia Institute of Technology, School of Mechanical Engineering.

Sutcliffe, M. P. (1988). Surface Asperity Deformation in Metal Forming Processes. *International Journal of Mechanical Sciences, 30*(11), 847-868.

Sutcliffe, M. P. (2002). Surface Finish and Friction in Cold Metal Rolling. In J. G. Lenard (Ed.), *Metal Forming Science and Practice.* Elsevier Science.

Svilainis, L., & Dumbrava, V. (2007). Evaluation of the ultrasonic transducer electrical matching performance. *Ultragarsas, 62*(4), 16 to 21.

Svilainis, L., & Dumbrava, V. (2008). Analysis of the Interpolation Techniques for Time-of-Flight Estimation. *Ultragarsas, 63*(4), 25-29.

Svilainis, L., & Dumbrava, V. (2008). The Time-of-Flight Estimation Accuracy versus Digitization Parameters. *Ultragarsas, 63*(1), 12-17.

Svilainis, L., & Kitov, S. (2010). Analysis of the Digital Signal Processing Influence on Time-of-Flight Estimation. *Ultragarsas, 65*(4), 22-27.

Technical Publication TP-238 Piezoelectricity. (n.d.). Retrieved from Morgan Electro Ceramics: www.morgan-electroceramics.com

The Speed of Sound in Other Materials. (n.d.). Retrieved 10 18, 2015, from NDT Resource Center: https://www.nde-ed.org/EducationResources/HighSchool/Sound/speedinmaterials.htm

Theobald, P. (n.d.). *Guide on Acoustic Emission Sensor Couplants*. Retrieved Feb 16, 2016, from National Physical Laboratory: http://www.npl.co.uk/acoustics/ultrasonics/research/guide-on-acoustic-emission-sensor-couplants

Toda, H. F. (1977). Preliminary Experiment on Acoustoelasticity for Stress Analysis. *Archives of Mechanics, 29*(5), 671-686.

Trinks, W. (1937). Pressures and Roll Flattening in Cold Rolling. *Blast Furance and Steel Plant, 25*, 617-619.

Tselikov, A. I. (1939). Effect of External Friction and Tension on the Pressure of the Metal on the Rolls in Rolling. *Metallurg*(6), 61-76.

Tyson, L. O. (1996). Sir Bevis Bulmer: An Elizabethan Adventurer. *British Mining*, 47-69.

UKAS. (n.d.). *The Expression of Uncertainty and Confidence in Measurement.*

Underwood, L. R. (1950). *The Rolling of Metals, Theory and Experiment* (Vol. 1). New York: John Wiley & Sons, Inc.

United States Steel Corporation, Association of Iron and Steel Engineers. (1985). Making, Shaping and Treating of Steel. In W. T. Lankford, *Making, Shaping and Treating of Steel.* United States Steel Corp; 10th Edn.

Van Rooyen, G. T., & Backofen, W. A. (1957). Friction in Cold Rolling. *J. Iron Sheet Inst., 186*, 235.

Wan, G. T., Kenny, P., & Spikes, H. A. (1984, December). Elastohydrodynamic Properties of Water-Based Fire-Resistant Hydraulic Fluids. *Tribology International, 17*(6), 309-315.

Wang, B., Takatsubo, J., Toyama, N., Akimune, Y., & Zhao, M. (2006). An Improved Ray Tracing Algorithm for Ultrasonic CT in Nondestructive Inspections. *ICSP2006 Proceedings*.

Wersing, W., & Lubitz, K. (n.d.). Electromechanical Frequency Filters. In W. Heywang, K. Lubitz, & W. Wersing (Eds.), *Piezoelectricity Evolution and Future of a Technology* (p. 198).

Whittingham, T., & Martin, K. (2010). Transducers and Beam-Forming. In P. R. Hoskins, K. Martin, & A. Thrush (Eds.), *Diagnostic Ultrasound: Physics and Equipment.* Cambridge University Press.

Wilson, W. R., & Chang, D.-F. (1996). Low Speed Mixed Lubrication of Bulk Metal Forming Processes. *Journal of Tribology, 118*, 83-89.

Wilson, W. R., & Marsault, N. (1998). Partial Hydrodynamic Lubrication With Large Fractional Contact Areas. *ASME Journal of Tribology, 120*(1), 16-20.

Wilson, W. R., & Sheu, S. (1988). Real Area of Contact and Boundary Friction in Metal Forming. *International Journal of Mechanical Sciencces, 30*(7), 475-489.

Wilson, W. R., & Sheu, S. (1988). Real Area of Contact and Boundary Friction in Metal Forming. *International Journal of Mechanical Sciences, 30*(7), 475-489.

Wilson, W. R., & Walowit, J. A. (1971, January). An Isothermal Hydrodynamic Lubrication Theory for Hydrostatic Extrusion and Drawing Processes With Conical Dies. *Journal of Lubrication Technology, 93*(1), 69-74.

Wilson, W. R., Sakaguchi, Y., & Schmid, S. R. (1993). A Dynamic Concentration Model for Lubrication with Oil-in-Water Emulsions. *Wear, 161*, 207-212.

Wood, R. W., & Loomis, A. L. (1927). The Physical and Biological Effects of High Frequency Sound Waves of Great Intensity. *Philosophical Magazine, 4*(22), 417-436.

Yasutomi, S., Bair, S., & Winer, W. O. (1984). An Application of a Free Volume Model to Lubricant Rheology I - Dependence of Viscosity on Temperature and Pressure. *ASME Journal of Tribology, 106*(2), 291-302.